

AEDC-TR-71-36

Copy 2

MAR 5 1971

APR 13 1971

JUN 25 1982

NOV 15 1984

MAR 23 1988

JAN 2 1990

**FREE TURBULENT MIXING: A CRITICAL
EVALUATION OF THEORY AND EXPERIMENT**



Philip Thomas Harsha

ARO, Inc.

February 1971

**TECHNICAL REPORTS
FILE COPY**

This document has been approved for public release and
sale; its distribution is unlimited.

**ENGINE TEST FACILITY
ARNOLD ENGINEERING DEVELOPMENT CENTER
AIR FORCE SYSTEMS COMMAND
ARNOLD AIR FORCE STATION, TENNESSEE**

PROPERTY OF U S AIR FORCE
AEDC LIBRARY
F40600-71-C-0002

NOTICES

When U. S. Government drawings specifications, or other data are used for any purpose other than a definitely related Government procurement operation, the Government thereby incurs no responsibility nor any obligation whatsoever, and the fact that the Government may have formulated, furnished, or in any way supplied the said drawings, specifications, or other data, is not to be regarded by implication or otherwise, or in any manner licensing the holder or any other person or corporation, or conveying any rights or permission to manufacture, use, or sell any patented invention that may in any way be related thereto.

Qualified users may obtain copies of this report from the Defense Documentation Center.

References to named commercial products in this report are not to be considered in any sense as an endorsement of the product by the United States Air Force or the Government.

FREE TURBULENT MIXING: A CRITICAL
EVALUATION OF THEORY AND EXPERIMENT

Philip Thomas Harsha
ARO, Inc.

This document has been approved for public release and
sale; its distribution is unlimited.

FOREWORD

The work reported herein was sponsored by the Air Force Office of Scientific Research under Program Element 61102F, Project 9711.

The results of the research presented were obtained by ARO, Inc. (a subsidiary of Sverdrup & Parcel and Associates, Inc.), contract operator of the Arnold Engineering Development Center (AEDC), Air Force Systems Command (AFSC), Arnold Air Force Station, Tennessee, under Contract F40600-71-C-0002. The investigation was conducted under ARO Project No. RW5008 from June 1969 to June 1970, and the manuscript was submitted for publication on September 9, 1970.

The author wishes to acknowledge the assistance of Dr. W. T. Snyder of the University of Tennessee; Dr. C. E. Peters, ARO, Inc.; and Dr. S. C. Lee of the University of Missouri. The material reported herein was submitted to the University of Tennessee as partial fulfillment of the requirements of the degree of Doctor of Philosophy.

This technical report has been reviewed and is approved.

Marion L. Laster
Research and Development
Division
Directorate of Technology

Harry L. Maynard
Colonel, USAF
Director of Technology

ABSTRACT

The problem of the analysis of free turbulent mixing is complex, and some empiricism is always necessary to obtain a solution. This has led to a proliferation of experiments and of semi-empirical models for the turbulent shear stress. All of these models will correlate experimental data well in some region of a particular flow, but not in others. None has been tested over as broad a range as is possible. The ultimate goal of this study is to confront each important model for the turbulent shear stress with as broad a range of experimental data as possible. From this confrontation come two sets of conclusions--one detailing those models presently suitable for engineering use, and the second establishing the models which show promise of becoming more generally applicable with further development.

TABLE OF CONTENTS

CHAPTER	PAGE
INTRODUCTION	1
1. METHODS OF ANALYSIS OF THE EXPERIMENTAL DATA. . .	7
General Criteria.	7
Methods of Presentation	12
2. CONSTANT-DENSITY SINGLE STREAM FLOWS:	
EXPERIMENTAL DATA	16
The Two-Dimensional Jet	16
The Two-Dimensional Mixing Layer.	39
The Circular Jet.	60
Summary	93
3. CONSTANT-DENSITY TWO-STREAM FLOWS:	
EXPERIMENTAL DATA	102
Two-Dimensional Jet with Nonzero Secondary. . .	103
Axisymmetric Jets with Nonzero Secondary:	
Coaxial Jets.	119
Two-Dimensional Wakes	150
Axisymmetric Wakes.	161
Two-Stream, Two-Dimensional Mixing Layers . . .	176
Summary	182
4. VARIABLE-DENSITY SINGLE-STREAM FLOWS:	
EXPERIMENTAL DATA	195
The Compressible Circular Jet	196

CHAPTER	PAGE
Circular Jets with Density Difference Caused by Temperature and Composition Differences. .	212
Other Flows	236
Summary	245
5. VARIABLE DENSITY TWO-STREAM FLOWS:	
EXPERIMENTAL DATA	253
Coaxial Jets.	254
Axisymmetric Wakes.	301
Summary	310
6. LOCALLY-DEPENDENT THEORETICAL MODELS IN CONSTANT DENSITY FLOW.	318
Introduction.	318
Mixing Length Theory.	320
Vorticity Transport Theory.	323
The Inductive Hypothesis.	325
Constant Exchange Coefficient Models.	327
Summary	329
7. LOCALLY-DEPENDENT THEORETICAL MODELS IN VARIABLE DENSITY FLOW	332
Introduction.	332
Ferri Eddy Viscosity Model.	334
Alpinieri Eddy Viscosity Model.	334
Zakkay Eddy Viscosity Model	335
Schetz Displacement Thickness Model	336
Compressibility Corrections	340

CHAPTER	PAGE
Compressibility Transforms.	341
Summary	343
8. HISTORY-DEPENDENT THEORETICAL APPROACHES.	346
Introduction.	346
Eddy Viscosity Rate Equation.	347
The Turbulent Kinetic Energy Approach	351
Summary	363
9. CONFRONTATION OF THE THEORETICAL MODELS WITH	
EXPERIMENTAL DATA	367
Resume of the Selected Experiments.	367
Resume of the Selected Theoretical Models	375
Confrontation I: The Mixing Length Theory.	386
Confrontation II: Prandtl Eddy Viscosity	
Model	388
Confrontation III: Schetz "Unified Theory"	401
Confrontation IV: Ferri Model.	423
Confrontation V: Zakkay Model.	438
Confrontation VI: Alpinieri Model.	447
Confrontation VII: Turbulent Kinetic Energy.	460
Confrontation VIII: Compressibility	
Correction.	474
Confrontation IX: Compressibility Transforms	481
Summary	488
Prandtl mixing length	491
Prandtl eddy viscosity.	491

CHAPTER	PAGE
Schetz "unified theory"	493
Ferri eddy viscosity model.	494
Zakkay eddy viscosity model	495
Alpinieri eddy viscosity model.	496
Kinetic energy theory	496
Donaldson and Gray correction	497
Libby transform	498
10. RESULTS AND RECOMMENDATIONS	499
Selection of Theoretical Models	500
Additional Results for Coaxial Hydrogen-Air	
Mixing.	514
Recommendations for Future Experimental Work. .	523
Recommendations for Turbulent Shear Stress	
Models--Present Use	526
Recommendations for Turbulent Shear Stress	
Models--Further Development	528
BIBLIOGRAPHY	532
APPENDICES	547
A. EVALUATION OF THE MOMENTUM INTEGRAL	548
B. EVALUATION OF AXIAL DECAY OF CENTERLINE	
VELOCITY FOR INCOMPRESSIBLE FLOW.	557
C. CONDITIONS FOR SELF-PRESERVATION.	563
D. DETAILS OF THE TING-LIBBY TRANSFORMATION IN	
TWO-DIMENSIONAL AND AXISYMMETRIC FLOW	577
E. THE NUMERICAL SOLUTION TECHNIQUE.	583
F. INITIAL CONDITIONS FOR THE CALCULATIONS	602

LIST OF TABLES

TABLE	PAGE
2.1. The Two-Dimensional Jet-into-Still-Air.	24
2.2. Tests for which Velocity Profile are Given;	
A. J. Chapman [16].	48
2.3. The Constant-Density Circular Jet-into-Still-	
Air	65
2.4. Velocity Decay data from Reference [27]	72
2.5. Comparison of Core Length Predictions	75
2.6. Momentum Integral Results for Data of	
Corrsin	80
2.7. Correlation between Low-Frequency Limit and	
Error in Measurement of Turbulent Shear	
Stress.	87
3.1. The Two-Dimensional Constant-Density Jet with	
Nonzero Secondary	109
3.2. Coaxial Constant-Density Jets	126
3.3. Two-Dimensional Wakes	151
3.4. Axisymmetric Wakes.	165
4.1. Compressible Jet into Quiescent Air	200
4.2. Circular Jets into Quiescent Air with	
Temperature or Concentration Differences.	214
4.3. Other Variable-Density Flows with Zero	
Secondary Velocity.	240

TABLE	PAGE
5.1. Variable-Density Coaxial Mixing	255
5.2. Comparison of Measured Concentration Potential Core Length with those Predicted by Equation (5.2)	298
5.3. Axisymmetric Compressible Wakes	302
9.1. Characteristics of the Selected Experiments . .	368
9.2. Theoretical Models for the Turbulent Shear Stress.	376
10.1. Recommendations for the Use of Locally- Dependent Turbulent Shear Stress Models . . .	527
E.1. Source Terms in the Transformed Equations . . .	590

LIST OF FIGURES

FIGURE	PAGE
1. 1. Control Volume for Free Mixing	8
2. 1. 2D Jet with Zero External Velocity- Definition Sketch.	17
2. 2. Axial Decay of Centerline Velocity Ratio, Two-Dimensional Jet-into-Still-Air	21
2. 3. Comparison of Axial Decay Data of Heskestad [7] with that of Albertson, et al., [8].	23
2. 4. Comparison of Centerline Decays, 2D Jet.	27
2. 5. Velocity Profiles from Reference [8]	29
2. 6. Centerline Velocity Decay.	32
2. 7. Axial Turbulent Intensity Variation, 2D Jet- into-Still-Air	33
2. 8. Lateral Turbulent Intensity Variation, 2D Jet-into-Still-Air.	34
2. 9. Turbulent Shear Stress Variation, 2D Jet- into-Still-Air	35
2.10. Ratio of Turbulent Shear Stress to Turbulent Kinetic Energy, 2D Jet-into-Still-Air.	38
2.11. Types of Two-Dimensional Mixing Layers	40
2.12. Ratio of Turbulent Shear Stress to Turbulent Kinetic Energy, 2D Mixing Layer Data of Mueller [14] and Haugen and Dhanak [15].	45

FIGURE	PAGE
2.13. Mean Velocity Profiles, 2D Mixing Layer, Chapman, Test 5.	50
2.14. Mean Velocity Profiles, 2D Mixing Layer, Chapman, Test 15	52
2.15. Mean Velocity Profiles, 2D Half Jet.	55
2.16. Relation between Turbulent Shear Stress and Turbulent Kinetic Energy, 2D Mixing Layer. .	56
2.17. Lateral Profile of a_1 , 2D Mixing Layer. . . .	58
2.18. Comparison of Experimentally Measured Shear Stress with Shear Stress Calculated from Assumed Velocity Profile, 2D Mixing Layer. .	59
2.19. Circular Jet-into-Still-Air.	61
2.20. Axial Velocity Decay, Circular Jet, Zero Secondary: Data from Baines [21].	63
2.21. Axial Decay of Centerline Velocity Ratio, Circular Jet-into-Still-Air.	67
2.22. Axial Decay of Centerline Velocity Ratio, Data of Albertson, Dai, Jensen, and Rouse [8].	71
2.23. Effect of Jet Reynolds Number on Axial Decay of Centerline Velocity, Data from Reference [27]	73
2.24. Comparison of Empirical Relation with Axial Velocity Decay Data of Alexander, et al., [27]	76

FIGURE	PAGE
2.25. Velocity Profiles in the Fully-Developed Region, from Wygnanski and Fiedler [20]: Circular Jet, Zero Secondary	78
2.26. Decay of Axial Mean Velocity, Circular Jet- into-Still-Air	79
2.27. Comparison of Measurements of Axial Turbulent Intensity, Data of Corrsin [23] and of Corrsin and Uberoi [25]	82
2.28. Axial Component of Turbulent Intensity, Circular Jet-into-Still-Air.	89
2.29. Lateral Component of Turbulent Intensity, Circular Jet-into-Still-Air.	90
2.30. Distribution of Turbulent Shear Stress, Circular Jet-into-Still-Air.	91
2.31. Relation between Turbulent Shear Stress and Turbulent Kinetic Energy, Circular Jet- into-Still-Air	92
2.32. Distribution of the Ratio of Turbulent Shear Stress to the Turbulent Kinetic Energy, Circular Jet-into-Still-Air.	94
3. 1. Geometry of the Two-Dimensional Jet, Nonzero Secondary.	104
3. 2. Velocity Profiles, 2D Jet, Nonzero Secondary: Weinstein, Osterle, and Forstall [37], Series I, $U_o/U_j = 0.5$, Near Field.	107

FIGURE	PAGE
3. 3. Velocity Profiles, 2D Jet, Nonzero Secondary: Weinstein, Osterle, and Forstall [37], Series I, $U_o/U_j = 0.5$, Far Field	108
3. 4. Axial Decay of Centerline Velocity Ratio, Two-Dimensional Jet, Nonzero Secondary . . .	110
3. 5. Axial Decay of Centerline Velocity Ratio, Two-Dimensional Jet, Nonzero Secondary. Data of Bradbury and Riley [38].	111
3. 6. Comparison of Data from Weinstein, Osterle, and Forstall [37] with Data from Bradbury [39] for the Small-Perturbation (Self- Preserving) 2D Jet	113
3. 7. Comparison of Centerline Velocity Decay Predicted by Empirical Correlation of Bradbury [39] with Measured Data	115
3. 8. Relation between Turbulent Shear Stress and Turbulent Kinetic Energy, 2D Two-Stream Jets. Data from Bradbury [34]	117
3. 9. Lateral Variation of the Parameter a_1 in the Self-Preserving Region of a Two-Dimensional Two-Stream Jet; Data from Bradbury [34]. . .	118
3.10. Idealized Coaxial Mixing	120
3.11. Experimental Approximations to True Coaxial Free Mixing.	121

FIGURE	PAGE
3.12. Test for Local Similarity: Paulk [42], $U_o/U_j = 0.125$, $\rho_j/\rho_o = 0.93$	124
3.13. Test for Self-Preservation: Paulk [42], $U_o/U_j = 0.125$, $\rho_j/\rho_o = 0.93$	125
3.14. Comparison of Centerline Velocity Decays; Coaxial Axisymmetric Jets.	129
3.15. Comparison of Axial Decays Measured by Paulk (Unducted) with Those Measured in Various Ducted Experiments	130
3.16. Evidence for Data Shift with Reynolds Number, Forstall Data [40]	132
3.17. Calculated Centerline Velocity Decay as a Function of Assumed Initial Boundary Layer Thicknesses, Prandtl Eddy Viscosity Model, $\epsilon = kb U_{\max} - U_{\min} $, $k_I = 0.007$, $k_{II} = 0.011$.	134
3.18. Variation in Axial Decay Rate with Initial Velocity for Coaxial Jets with Unity Velocity Ratio. Data from Fejer, et al., [45]	136
3.19. Centerline Velocity Decay, Coaxial Axisymmetric Jets.	139
3.20. Comparison of Centerline Velocity Decay Data of Fejer, et al., [45] with Other Investigators.	140

FIGURE	PAGE
3.21. Axial Decay of Centerline Velocity, Data of Curtet and Ricou [44].	143
3.22. Axial Decay of Centerline Velocity, Data of Zawacki and Weinstein [35]	145
3.23. Relation between Turbulent Shear Stress and Turbulent Kinetic Energy, Coaxial Jets . . .	147
3.24. Radial Variation of Ratio of Turbulent Shear Stress to Turbulent Kinetic Energy, from Curtet and Ricou [44].	148
3.25. Radial Variation of a_1 (= Ratio of Turbulent Shear Stress to Turbulent Kinetic Energy), Zawacki and Weinstein Data [35], $U_o/U_j = 3.4$	149
3.26. Increase of Centerline Velocity, 2D Wake . . .	153
3.27. Relation between Turbulent Shear Stress and Turbulent Kinetic Energy in the Initial Region of a 2D Wake.	155
3.28. Relation between Turbulent Shear Stress and Turbulent Kinetic Energy in the Self- Preserving Region of a 2D Wake	156
3.29. Self-Preservation of Turbulent Kinetic Energy, Townsend [50].	158
3.30. Ratio of Turbulent Shear Stress to Turbulent Kinetic Energy, Two-Dimensional Wake, Data of Townsend [5] and [50]	159

FIGURE	PAGE
3.31. Test for Self-Preservation of Turbulent Intensity, Chevray and Kovasznay [52], 2D Wake.	160
3.32. Test for Self-Preservation: Turbulent Shear Stress Profiles. Chevray and Kovasznay [52], 2D Wake.	162
3.33. Evolution of the Ratio of the Turbulent Shear Stress to the Turbulent Kinetic Energy in a Two-Dimensional Wake. Data of Chevray and Kovasznay [52]	163
3.34. Test for Self-Preservation, Axisymmetric Wake of a Square Plate 0.2 in. on a Side (b = 0.2 in.), Data of Cooper and Lutzky [56].	167
3.35. Comparison of Centerline Velocity Decays, Axisymmetric Wake.	168
3.36. Relation between Turbulent Shear Stress and Turbulent Kinetic Energy, Axisymmetric Wakes.	171
3.37. Evolution of the Parameter a_1 in the Middle Region of the Axisymmetric Wake of a Disk. Data from Carmody [57]	172
3.38. Evolution of the Parameter a_1 in the Early Region of the Axisymmetric Wake of an Aerodynamic Body, Data from Chevray [58]	173

FIGURE	PAGE
3.39. Evolution of the Parameter a_1 in the Middle Region of the Axisymmetric Wake of an Aero- dynamic Body. Data from Chevray [58]. . . .	174
3.40. Velocity Profiles in Initial Region of Mixing between Two Different Velocity Streams with Initial Boundary Layers. Data from Lee [51]	177
3.41. Test for Similarity, Two-Stream Mixing, Lee Data, Reference [51]	179
3.42. Similarity Plot of Kinetic Energy Measure- ments from Watt [62]	180
3.43. Similarity Plot of Shear Stress Measurements from Watt [62]	181
3.44. Relation between Turbulent Shear Stress and Turbulent Kinetic Energy for Two- Dimensional Two-Stream Mixing Layers	183
3.45. Comparison of Data--Single-Stream and Two- Stream Mixing Layers	184
3.46. Development of the Lateral Variation of the Parameter a_1 in the Initial Region of a Two-Dimensional Two-Stream Mixing Layer. . .	185
4. 1. Supersonic Jet into Quiescent Surroundings . .	198
4. 2. Comparison of Compressible Free Jet Data with Effectively Incompressible Data; Decay of Centerline Velocity.	207

FIGURE	PAGE
4. 3. Variation of Core Length with Mach Number, Compressible Jet-into-Still-Air.	208
4. 4. Axial Decay of Centerline Velocity; Compressible Jet-into-Still-Air.	209
4. 5. Similarity Plot, Jet-into-Still-Air ($T_{O_j}/T_a = 1.0$) and Comparison with Commonly Used Profiles	213
4. 6. Comparison of Axial Component of Turbulent Velocity, Hot and Cold Jets. Data from Corrsin and Uberoi [25].	219
4. 7. Relation between Turbulent Shear Stress and Turbulent Kinetic Energy, Hot Jet.	221
4. 8. Comparison of Ratio of Turbulent Shear Stress to Turbulent Kinetic Energy, Hot and Cold Jets	222
4. 9. Comparison of Axial Decay of Centerline Velocity, Isothermal and Nonisothermal Jets	223
4.10. Axial Decay of Centerline Temperature Ratio. .	225
4.11. Radial Temperature Distribution ($T-T_O$)/(T_C-T_O) versus $r/r_{1/2}$, where $r_{1/2} = r$ for $U/U_C = 0.5$	226
4.12. Radial Temperature Distribution ($T-T_O$)/(T_C-T_O) versus $r/r_{1/2T}$, where $r_{1/2T} = r$ for ($T-T_O$)/(T_C-T_O)	227

FIGURE	PAGE
4.13. Effect of Nonunity Temperature Ratio on Velocity Profile, Compressible Jet-into- Still-Air.	229
4.14. Test for Geometric Similarity--High Enthalpy N ₂ Jet-into-Still-Air--Reference [77]. . . .	230
4.15. Centerline Decay of Velocity, Stagnation Enthalpy, and Concentration, High Temperature Jet-into-Still-Air	231
4.16. Effect of Initial Temperature Ratio on Centerline Velocity Decay.	233
4.17. Effect of Initial Temperature Ratio on Centerline Decay of Total Enthalpy	234
4.18. Axial Decay of Centerline Velocity, Circular Jets of Various Gases into Air, Keagy and Weller [76].	235
4.19. Axial Decay of Centerline Composition, Circular Jets of Various Gases into Air, Keagy and Weller [76].	237
4.20. Effect of Initial Molecular Weight Ratio on Centerline Decay of Axial Velocity	238
4.21. Comparison of Determinations of Variation of σ with Mach Number	243
5. 1. Axial Decay of Centerline Velocity, Compressible Coaxial (Air-Air) Jets.	261

FIGURE	PAGE
5. 2. Similarity Plot for Velocity Ratio, Compressible Coaxial Jets.	263
5. 3. Axial Decay of Centerline Velocity and Temperature Ratio, Subsonic/Subsonic Coaxial Jets. Data from Landis and Shapiro [43]	265
5. 4. Axial Decay of Centerline Velocity, Temperature and Composition, Coaxial Subsonic/Subsonic Mixing	266
5. 5. Axial Decay of Centerline Velocity, Freon-Air Mixing, Reference [35]. $\rho_o U_o / \rho_j U_j > 1.0, U_o / U_j > 1.0$	269
5. 6. Axial Decay of Centerline Velocity Ratio, Air-Air and Freon-Air Coaxial Mixing. Data from Reference [92].	270
5. 7. Axial Decay of Centerline Concentration, Air-Air and Freon-Air Coaxial Mixing. Data from Fejer, et al., [92]	273
5. 8. Axial Decay of Centerline Velocity Ratio, H_2 -Air Mixing. $\rho_o U_o / \rho_j U_j > 1.0, U_o / U_j < 1.0$. Data from Chriss [90].	274
5. 9. Axial Decay of Centerline Composition, Coaxial Hydrogen-Air Mixing. Data of Chriss [90].	276

FIGURE	PAGE
5.10. Radial Velocity Profile. Data of Chriss [90].	277
5.11. First Regime Radial Velocity Profile. Data of Chriss [90]	278
5.12. Radial Composition Profile. Data of Chriss [90]	279
5.13. Velocity-Enthalpy Relationship for Hydrogen- Air Tests. Data of Chriss [90].	281
5.14. Axial Decay of Centerline Velocity Ratio, Coaxial Mixing of CO ₂ and Air. Data from Alpinieri [84]	282
5.15. Centerline Concentration Decay, Coaxial Subsonic/Subsonic Mixing. Data from Alpinieri [84]	283
5.16. Initial Profiles of Concentration and Velocity at X/D = 2.5. Hydrogen-Air Mixing. Reproduced from Reference [84]. . .	285
5.17. Centerline Composition Decay, Coaxial Bromine-Air Mixing [89].	287
5.18. Axial Decay of Centerline Composition, Subsonic/Supersonic Coaxial Mixing. Data of Zakkay and Krause [85].	288
5.19. Axial Decay of Centerline Composition, Subsonic/Supersonic and Supersonic/ Supersonic Jets. Data from Zakkay, et al., [93]	290

FIGURE	PAGE
5.20. Axial Decay of Centerline Composition, Subsonic/Supersonic Coaxial Jets. Mass Flow Ratio $\rho_o U_o / \rho_j U_j > 1.0$	292
5.21. Axial Decay of Centerline Composition. Subsonic/Subsonic Coaxial Jets, Mass-Flow Ratio > 1.0	293
5.22. Axial Decay of Centerline Composition (or Temperature Ratio), Subsonic/Subsonic Coaxial Jets, Mass-Flow Ratio < 1.0	294
5.23. Core-Length Correlation, Variable-Density Coaxial Mixing	297
5.24. Comparison of Experimental Data with Empirical Prediction	299
5.25. Axial Increase of Centerline Mach Number, Axisymmetric Supersonic Wakes.	303
5.26. Comparison of Centerline Velocity Decay Rates, Axisymmetric Wakes.	304
5.27. Axial Decay Curves in Self-Preserving Coordinates Data of Demetriades [99]	306
5.28. Normalized Axial Velocity and Temperature Profiles. $M_o = 3$. Axisymmetric Wake Data from Reference [97], $X/D = 17.00$ to 68.28	308
5.29. Axial Increase of Centerline Mach Number, Axisymmetric Supersonic Wakes.	309

FIGURE	PAGE
5.30. Comparison of Initial Decay Curves with x^{-2} Decay, Axisymmetric Compressible Wakes.	311
9. 1. Comparison of Predicted Axial Decay of Centerline Velocity using Prandtl Mixing Length: Integral Analysis and Finite- Difference Analysis.	377
9. 2. Comparison of Calculated Velocity Decay using Schetz Theory: Schetz Calculation [121] and Present Study.	380
9. 3. Comparison of Fully-Normalized Profiles Predicted by Various Models with Coaxial Air-Air Mixing Data. Data from Forstall [40], $U_o/U_j = 0.2$, $x/D = 24$	383
9. 4. Comparison of Semi-Normalized Velocity Profiles Predicted by Various Methods with Coaxial Air-Air Mixing Data of Forstall [40]: $U_o/U_j = 0.2$, $x/D = 24$	385
9. 5. Comparison of Predictions of Mixing Length Theory with Jet-into-Still-Air Data.	387
9. 6. Comparison of Predictions of Mixing Length Theory with Coaxial Air-Air Data of Paulk [42]	389

FIGURE	PAGE
9. 7. Comparison of Predictions of Mixing Length Theory with Coaxial Air-Air Mixing Data. Data of Forstall [40].	390
9. 8. Comparison of Predictions of Mixing Length Theory with Coaxial H ₂ -Air Mixing Data of Chriss [90].	391
9. 9. Comparison of Prediction of Mixing Length Theory with Data for the Initial Region of an Axisymmetric Wake. Data of Chevray [58]	395
9.10. Comparison of Prediction of Mixing Length Theory with Data for the Initial Region of a Two-Dimensional Wake. Data of Chevray and Kovasznay [52]	396
9.11. Comparison of Predictions of Prandtl Eddy Viscosity Theory with Jet-into-Still-Air Data	398
9.12. Comparison of Predictions of Prandtl Eddy Viscosity Theory with Coaxial Air-Air Data of Paulk [42].	399
9.13. Comparison of Predictions of Prandtl Eddy Viscosity Theory with Coaxial Air-Air Mixing Data. Data of Forstall [40].	400

FIGURE	PAGE
9.14. Comparison of Prandtl Eddy Viscosity Theory with Coaxial H ₂ -Air Mixing Data of Chriss [90].	402
9.15. Comparison of Prediction of Prandtl Eddy Viscosity Theory with Data for the Initial Region of an Axisymmetric Wake. Data of Chevray [58]	406
9.16. Comparison of Prediction of Prandtl Eddy Viscosity Theory with Data for the Initial Region of a Two-Dimensional Wake. Data of Chevray and Kovasznay [52]	407
9.17. Comparison of Predictions of Schetz "Unified Theory" with Jet-into-Still-Air Data	409
9.18. Comparison of Semi-Normalized Velocity Profiles Predicted by Various Theoretical Models for the Jet-into-Still-Air at x/D = 20	410
9.19. Comparison of Predictions of Schetz "Unified Theory" with Coaxial Air-Air Data of Paulk [42]	412
9.20. Comparison of Predictions of Schetz "Unified Theory" with Coaxial Air-Air Mixing Data. Data of Forstall [40].	413

FIGURE	PAGE
9.21. Comparison of Schetz "Unified Theory" with Coaxial H ₂ -Air Mixing Data of Chriss [90].	415
9.22. Comparison of Calculated Velocity and Shear Stress Profiles at Two Axial Stations: Coaxial H ₂ -Air Mixing, Schetz Model.	420
9.23. Comparison of Prediction of Schetz "Unified Theory" with Data for the Initial Region of an Axisymmetric Wake. Data of Chevray [58]	421
9.24. Comparison of Prediction of Schetz "Unified Theory" with Data for the Initial Region of a Two-Dimensional Wake. Data of Chevray and Kovasznay [52]	422
9.25. Comparison of Predictions of Three Models for the Two-Dimensional Wake Data of Chevray and Kovasznay [52]	424
9.26. Comparison of Predictions of Ferri Model with Jet-into-Still-Air Data.	426
9.27. Effect of Change of Constant in the Prandtl Eddy Viscosity Model	428
9.28. Comparison of Predictions of Ferri Model with Coaxial Air-Air Data of Paulk [42].	429

FIGURE	PAGE
9.29. Comparison of Predictions of Ferri Model with Coaxial Air-Air Mixing Data. Data from : Forstall [40].	430
9.30. Comparison of Predictions of Ferri Model with Coaxial H ₂ -Air Mixing Data of Chriss [90]. .	432
9.31. Comparison of Prediction of Ferri Model with Experimental Data for the Initial Region of an Axisymmetric Wake. Data of Chevray [58]	436
9.32. Comparison of Prediction of Ferri Model with Data for the Initial Region of a Two- Dimensional Wake. Data of Chevray and Kovaszny [52]	437
9.33. Comparison of Predictions of Zakkay Model with Jet-into-Still-Air Data	439
9.34. Comparison of Predictions of Zakkay Model with Coaxial Air-Air Mixing Data of Paulk [42]	441
9.35. Comparison of Predictions of Zakkay Model with Coaxial Air-Air Mixing Data. Data from Forstall [40]	442
9.36. Comparison of Predictions of Zakkay Model with Coaxial Hydrogen-Air Mixing Data of Chriss [90].	443

FIGURE	PAGE
9.37. Comparison of Prediction of Zakkay Model with Experimental Data for the Initial Region of an Axisymmetric Wake. Data of Chevray [58]	448
9.38. Comparison of Prediction of Zakkay Model with Data for the Initial Region of a Two- Dimensional Wake. Data of Chevray and Kovasznay [58]	449
9.39. Comparison of Predictions of Alpinieri Model with Jet-into-Still-Air Data	452
9.40. Comparison of Predictions of Alpinieri Model with Coaxial Air-Air Data of Paulk [42]. . .	454
9.41. Comparison of Predictions of Alpinieri Model with Coaxial Air-Air Mixing Data. Data from Forstall [40]	455
9.42. Comparison of Predictions of Alpinieri Model with Coaxial H ₂ -Air Mixing Data of Chriss [90]	456
9.43. Comparison of Predictions of Kinetic Energy Theory with Jet-into-Still-Air Data.	463
9.44. Comparison of Predictions of Kinetic Energy Theory with Coaxial Air-Air Mixing Data of Paulk [42]	465

FIGURE	PAGE
9.45. Comparison of Predictions of Kinetic Energy Theory with Coaxial Air-Air Mixing Data. Data of Forstall [40].	466
9.46. Comparison of Predictions of Kinetic Energy Theory with Coaxial H ₂ -Air Mixing Data of Chriss [90].	468
9.47. Comparison of Prediction of Kinetic Energy Theory with Experimental Data for the Initial Region of an Axisymmetric Wake. Data of Chevray [58]	473
9.48. Comparison of Prediction of Kinetic Energy Theory with Data for the Initial Region of a Two-Dimensional Wake. Data from Chevray and Kovasznay [52]	475
9.49. Comparison of Calculations of Centerline Velocity Decay for Incompressible Coaxial Mixing	477
9.50. Comparison of Predictions of Prandtl Eddy Viscosity Model for Coaxial Hydrogen-Air Mixing with and without Donaldson and Gray Correction	478
9.51. Comparison of Prediction of Prandtl Eddy Viscosity Model with and without Donaldson and Gray Correction, for Supersonic Jet-into- Still-Air, Data from Eggers [72]	480

FIGURE	PAGE
9.52. Comparison of Predictions of the Libby Transform with Coaxial Hydrogen-Air Mixing Data. Data of Chriss [90]	484
9.53. Comparison of Predictions of Centerline Velocity Decay by Libby Transform and by Donaldson and Gray Correction for Coaxial Hydrogen-Air Mixing. Experimental Data from Chriss [90]	486
9.54. Comparison of Predictions of Centerline Composition Decay by Libby Transform and by Donaldson and Gray Correction, for Coaxial Hydrogen-Air Mixing. Experimental Data from Chriss [90]	487
9.55. Comparison of Centerline Decay Predictions Normalized with Respect to Computed Velocity Potential Core Length; Libby Transform and Donaldson and Gray Correction.	489
10. 1. Comparison of Best Predictions with Composite Data for Incompressible Jet-into-Still-Air.	501
10. 2. Comparison of Best Predictions with Data for the Compressible Jet-into-Still-Air. Data from Eggers [72], $M_j = 2.22$	503
10. 3. Comparison of Best Predictions with Coaxial Air-Air Mixing Data of Paulk [42].	504

FIGURE	PAGE
10. 4. Comparison of Best Predictions with Coaxial Air-Air Mixing Data of Forstall [40]	505
10. 5. Comparison of Best Predictions with Coaxial Hydrogen-Air Mixing Data of Chriss [90]. . .	509
10. 6. Comparison of Best Predictions with Axisymmetric Wake Data of Chevray [58] . . .	512
10. 7. Comparison of Best Predictions with Two- Dimensional Wake Data of Chevray and Kovaszny [52]	513
10. 8. Comparison of Velocity Profile Predictions of the Various Models with Representative Hydrogen-Air Data.	515
10. 9. Velocity Decay Predictions for Coaxial Hydrogen-Air Mixing using Schetz Model and Kinetic Energy Theory. Data from Chriss [90].	516
10.10. Comparison of Centerline Composition Decay and Half-Radius Growth Predictions of Schetz Model and Kinetic Energy Theory with Hydrogen-Air Data. Data from Chriss [90]. .	517
10.11. Comparison of Predicted Centerline Velocity Decay According to Schetz Model and Kinetic Energy Theory with Hydrogen-Air Mixing Data. Data from Chriss [90].	520

FIGURE	PAGE
10.12. Comparison of Centerline Decay and Half-Radius Growth Predictions of Schetz Model and Kinetic Energy Theory with Hydrogen-Air Data. Data from Chriss [90], $U_o/U_j = 0.416$	521
A. 1. General Axisymmetric Flow.	549
A. 2. Non-Symmetric Two-Dimensional Flow	554
B. 1. Nomenclature	558
C. 1. Symmetrical Jet with Arbitrary Secondary-Stream Velocity.	564
E. 1. Finite-Difference Grid	597

NOMENCLATURE

a	Parameter in generalized parabolic equation (E.13)
A	Universal constant in Nee and Kovasznay equation (8.7)
a_1	Ratio of turbulent shear stress to turbulent kinetic energy
a_2	Dissipation constant in turbulent kinetic energy equation
b	{ Cavity width, Chapter 2
	{ Characteristic dimension, axisymmetric wake, Chapter 3
	{ Mixing layer width, Chapter 6
	{ Parameter in generalized parabolic equation (E.13)
B	Constant in Nee and Kovasznay equation (8.7)
$b_{1/2}$	{ Half-velocity width, Chapter 3
	{ Half-width ($= 2r_{1/2}$), Chapter 7
c	{ Constant in mixing length equation, Chapter 6
	{ Parameter in generalized parabolic equation (E.13)
C_c	Centerline composition
C_j	Jet gas composition (normally = 1)
d	{ Characteristic diameter of wake producing body, Chapter 3
	{ Parameter in generalized parabolic equation (E.13)
D	{ Nozzle diameter
	{ Decay term for Nee and Kovasznay equation (8.7)

F	General scalar quantity, Chapter 8
g	Gravitational constant
g ₁₁	<div style="display: inline-block; vertical-align: middle; font-size: 3em; line-height: 1;">}</div> Functions in self-preservation analysis, Appendix C
g ₂₂	
g ₁₂	
G	Production term for Nee and Kovaszny equation (8.7)
h	Slot height, two-dimensional jet
H	<div style="display: inline-block; vertical-align: middle; font-size: 3em; line-height: 1;">{</div> Total enthalpy Non-dimensional shape parameter = $(\delta^*/\theta)^{r+1}$, Appendix C
H _c	Total enthalpy on centerline
H _j	Total enthalpy of jet
H _o	Total enthalpy of surrounding stream
J	Jacobian of coordinate transformation, Appendix D
k	<div style="display: inline-block; vertical-align: middle; font-size: 3em; line-height: 1;">{</div> Constant, Chapters 1 and 6 Turbulent kinetic energy/unit mass
K _A	Coefficient in Alpinieri eddy viscosity formulation
K _F	Coefficient in Ferri eddy viscosity formulation
K _P	Coefficient in Prandtl eddy viscosity formulation
K _{PO}	Coefficient in Prandtl eddy viscosity model, incompressible flow
K _S	Coefficient in Schetz eddy viscosity model
K _Z	Coefficient in Zakkay eddy viscosity model
K ₂	Constant in velocity ratio expression (1.3)

ℓ	{	Distance to reattachment, Chapter 2
		Prandtl mixing length, Chapter 6
ℓ_k		Length scale for turbulent energy dissipation
ℓ_T		Mixing length for vorticity theory, Chapter 6
L	{	Slot length, two-dimensional jet
		Length scale in Nee and Kovasznay equation (8.7)
L_O		General width scale, Appendix C
M	{	Momentum integral parameter, Chapter 2
		Mach number
M_C		Centerline Mach number
M_j		Jet Mach number
M_m		Mach number at half-velocity point
\dot{m}_G		Mass flow rate at boundary G per unit area
n	{	Exponent for axial decay curve, Chapter 1
		Total turbulent viscosity, Chapter 8
P		Static pressure
P_a		Ambient pressure
P_e		Nozzle exit pressure
P_o		Total pressure
Pr		Prandtl number
Pr_k		Prandtl number for turbulent kinetic energy
q		Excess flow rate
r		Radial coordinate
r_B		Width scale for first regime (Figure 5.11)
r_I		First regime inner radius
r_j		Jet radius

r_m	Radius at which $\partial u / \partial r$ is a maximum
r_o	Radius at which $U = U_o$; jet radius, Chapter 2
$r_{1/2}$	Radius at which $U = U_o + 1/2 (U_c - U_o)$
$r_{1/2C}$	Radius at which $C/C_j = 1/2$
$r_{1/2T}$	Radius at which $T = T_o + 1/2 (T_c - T_o)$
R	{ Gas constant Outer integration limit, Appendix A
Re_D	
Re_x	Reynolds number based on length
T	Total temperature
T_a	Ambient temperature
T_o	Total temperature
T_{oj}	Jet total temperature
u	Axial component of turbulent fluctuations
u'	Axial component of turbulent fluctuation (rms)
U	Axial component of mean velocity
U_c	Centerline velocity
U_D	Velocity difference $U_c - U_o$
U_j	Jet velocity
U_o	Outer stream velocity
v	Lateral component of turbulent fluctuation
v'	Lateral component of turbulent fluctuation (rms)
V	Lateral component of mean velocity
$\bar{u}v$	Turbulent shear stress
w	Z-component of turbulent fluctuation
x	Axial coordinate

x_c	Potential core length
x_o	Virtual origin distance
x_v	
x	
y	Lateral coordinate
Y	Outer integration limit, 2D flow, Appendix A Howarth coordinate, Chapter 7 Transformed coordinate, Appendix D
Y	
Y	
α	Coefficient, = 0 for plane flow, = 1 for axisymmetric
γ	Ratio of specific heats
δ_o	Initial boundary layer thickness
δ^*	Displacement thickness
δ_r^*	Axisymmetric displacement thickness
ϵ	Eddy viscosity
ϵ_o	Constant in Pai eddy viscosity formulation
η	Nondimensional coordinate, defined as used
θ	Momentum thickness Temperature fluctuation, Chapter 4
θ	
μ	Thermal conductivity
λ	Constant, Chapter 2 U_j/U_o , Chapter 3 U_o/U_j , Appendix B
λ	
λ	
Λ	Coefficient in Reichardt hypothesis
μ_T	Turbulent dynamic viscosity
ν	Kinematic viscosity

ξ	Transformed X-coordinate
ρ	Density
σ	<div> <div>{</div> <div>Mixing layer width parameter, Appendix B</div> <div>General transport coefficient, Appendix E</div> </div>
σ_o	Mixing layer width at $x = x_c$, Appendix B
τ	Turbulent shear stress
τ_L	Laminar shear stress
ϕ	<div> <div>{</div> <div>Any profile quantity</div> <div>General dependent variable</div> </div>
ϕ_H	$(H - H_o)/(H_c - H_o)$
ϕ_u	$(U - U_o)/(U_c - U_o)$
ψ	Stream function
ψ_I	Stream function at inner boundary
ψ_E	Stream function at outer boundary
ψ_j	$r_j(\rho_j U_j / \rho_o U_o)^{1/2}$
ω	Nondimensional stream function
Ω	Diffusion velocity for turbulent kinetic energy
∇	Gradient operator

Subscripts

B	General boundary
D	Downstream station
DD	Interpolated point, downstream station
G	General boundary
U	Upstream station
UU	Interpolated point, upstream station

INTRODUCTION

Free turbulent mixing may be defined as that class of turbulent flows in which there is no direct effect of solid boundaries on the flow. There may be an indirect effect; the free mixing process may have been generated by the action of a solid boundary, as for example, in the wake. Although turbulent flows contained within ducts are included in this study, the turbulent flow cannot impinge on a wall. The class of flows considered in this study is further restricted to coflowing streams, with zero axial pressure gradient. Thus the ducted flows covered must be contained within ducts sufficiently large for the pressure gradient to be negligible.

The understanding of the process of free turbulent mixing is of fundamental importance to the description of the phenomena that occur in many devices of practical engineering interest. Such phenomena include the fuel-oxidizer mixing processes in propulsive devices such as the scramjet and air-augmented rocket, in the combustion systems of turbojet engines, and the turbulent mixing processes in jet pumps and in wakes. In another field, the study of the acoustic properties of jets itself involves the understanding of their turbulent structure. In all of these flows, the fundamental problem remains the same: although the appropriate equations of motion can be

formulated, they cannot be solved in closed form; indeed, the mathematical statement always contains more unknowns than equations, and thus empirical information must always be included before the solution to the problem may be sought.

Considerable experimental work has been done in recent years on various free turbulent mixing flows, both in the investigation of their mean flow field and, through the development of vastly improved hot wire anemometer equipment, in the investigation of their fine scale turbulent structure. The rapid development of computer technology in recent years has made feasible theoretical approaches to the problem which are capable of treating the problem of turbulent mixing in much more detail than has heretofore been possible. But at the same time the recent appearance of these advances has pointed up the lack of any reliable guide to the available experimental results and theoretical models in the field.

The earliest theoretical models of turbulent flow sought to reduce the mathematical formulation of the problem to one similar to a laminar flow, since techniques were then known for the analytical treatment of laminar flow problems. The result of these attempts was the modelling of a turbulent flow as analogous to a laminar flow with the laminar viscosity, a function only of the fluid, replaced by an "eddy viscosity" which is a function only of the flow process. As information concerning the

unsteady structure of turbulent flows became available, it became increasingly apparent that turbulent flows behaved physically quite differently from laminar flows. Thus the analytical and experimental work proceeded in two separate directions--on the one hand theoretical treatments using eddy viscosity models and experiments in which the gross mean flow characteristics were measured for flows of practical interest, and on the other hand statistical theoretical treatments, which often were bereft of engineering usefulness, and experiments in which the turbulent fluctuations were measured in flows of purely academic interest. Further, theoretical treatments often tended towards the development of a model to fit one experiment without regard to its general implications and experiments often were made solely to test a specific model.

After four decades of this sort of development, the field of free turbulent mixing presents a rather formidable maze of often conflicting models combined with many experimental investigations of different facets of the overall problem. The practicing engineer, faced with this chaotic situation, can only investigate a small fraction of the available literature, and often does not have time to evaluate and compare the results he obtains with other results in the field. In this study such an analysis and comparison of all of the major experimental work which has been done in the field of free turbulent mixing is

performed. From the results of this evaluation a group of reliable experiments covering the broadest possible range of turbulent free mixing flows is selected. The second phase of this study then involves the selection of the most commonly used analytical models for the free turbulent eddy viscosity, as well as models which, while not commonly used as yet, appear to show some interesting aspects, and models in which the eddy viscosity is replaced by more direct relationships for the turbulent shear stress.

All of the models selected, ranging from the classical mixing-length concept of Prandtl through the relatively recent displacement thickness eddy viscosity model and the kinetic energy theory, in which the turbulent shear stress is related directly to the turbulent kinetic energy, are then used to compute analytically the selected flow fields. These computations are made using a recently developed finite-difference computational technique which has been modified and developed to allow calculations to be made of free mixing flows with arbitrary eddy viscosity models; or with the use of the turbulent kinetic energy equation to evaluate the turbulent shear stress. The results of these calculations are used to evaluate the performance of the various predictive models against a large cross-section of experimental information. Because the same computational technique is used in all calculations,

the differences that remain between predictions must be caused by the eddy viscosity model chosen.

The overriding consideration in the evaluation of these theoretical models is how well a given model stands up to the challenge of comparison of its predictions with experiments throughout the entire range of free turbulent flows. Those models for eddy viscosity or turbulent shear that best meet this challenge are those which have the widest range of applicability and thus the greatest engineering usefulness. In this study, specific recommendations are presented concerning those models which appear to be most useful and reliable for engineering calculations of free turbulent mixing.

The work described in this study can be divided into two main parts. In the first part the review and evaluation of the experimental data are described. Because it is imperative for the confrontation of theory and experiment that follows in the second part that each experiment be closely examined, this first part is necessarily lengthy. However, in each Chapter the most important conclusions of the evaluation have been assembled in a summary section, which can be read independently, with each Chapter then serving to contain the supporting material for the conclusions stated in its summary. If only the summaries are used, the reader will gain a reasonably quick overview of the experimental data on free turbulent mixing.

In the second part, experiments selected from those described in the first part are used to confront the predictions of various models. Once again, for a quick review of the various models to be considered, the summaries of the appropriate Chapters will suffice, but here it is recommended that both the discussion of results in Chapter 9 and the conclusions and recommendations in Chapter 10 be read in detail. Finally, liberal use of appendices is made in order to facilitate a detailed investigation of various facets of this study that do not conveniently fit into any particular Chapter.

The material covered in this study involves work reported up to March, 1970. Because of this obviously arbitrary cutoff date, some interesting recent work has had to be neglected. The reader will also note that there is little reference to the extensive Russian literature on the subject of free turbulent mixing. This is primarily caused by the demands of this study for extensive and detailed reporting of both experiments and theoretical treatments. The Russian literature, at least as it is available in this country, is in general not reported in sufficient detail to be used here.

CHAPTER 1

METHODS OF ANALYSIS OF THE EXPERIMENTAL DATA

General Criteria

The first question in the evaluation of a given set of experimental data must obviously be "what experimental results are presented?" There can be a great variety of answers for any given flow. Most commonly in free mixing flow experiments the velocity profiles at several axial stations are presented, along with axial distributions of the centerline velocity. If the flow involves temperature or composition differences between two streams or between a single stream and its surroundings, lateral profiles and axial distributions of the centerline value of the temperature or composition are commonly presented.

To define the minimum necessary amount of data for the purposes of this study, it is necessary to discuss the basic check which will be made on a given piece of data. The primary check, applicable to all free mixing flows, involves the momentum flow rate through any arbitrary control volume enclosing the flow. Figure 1.1 depicts such a control volume schematically; it is taken as extending far enough into the external flow so that the axial velocity equals the constant external velocity.

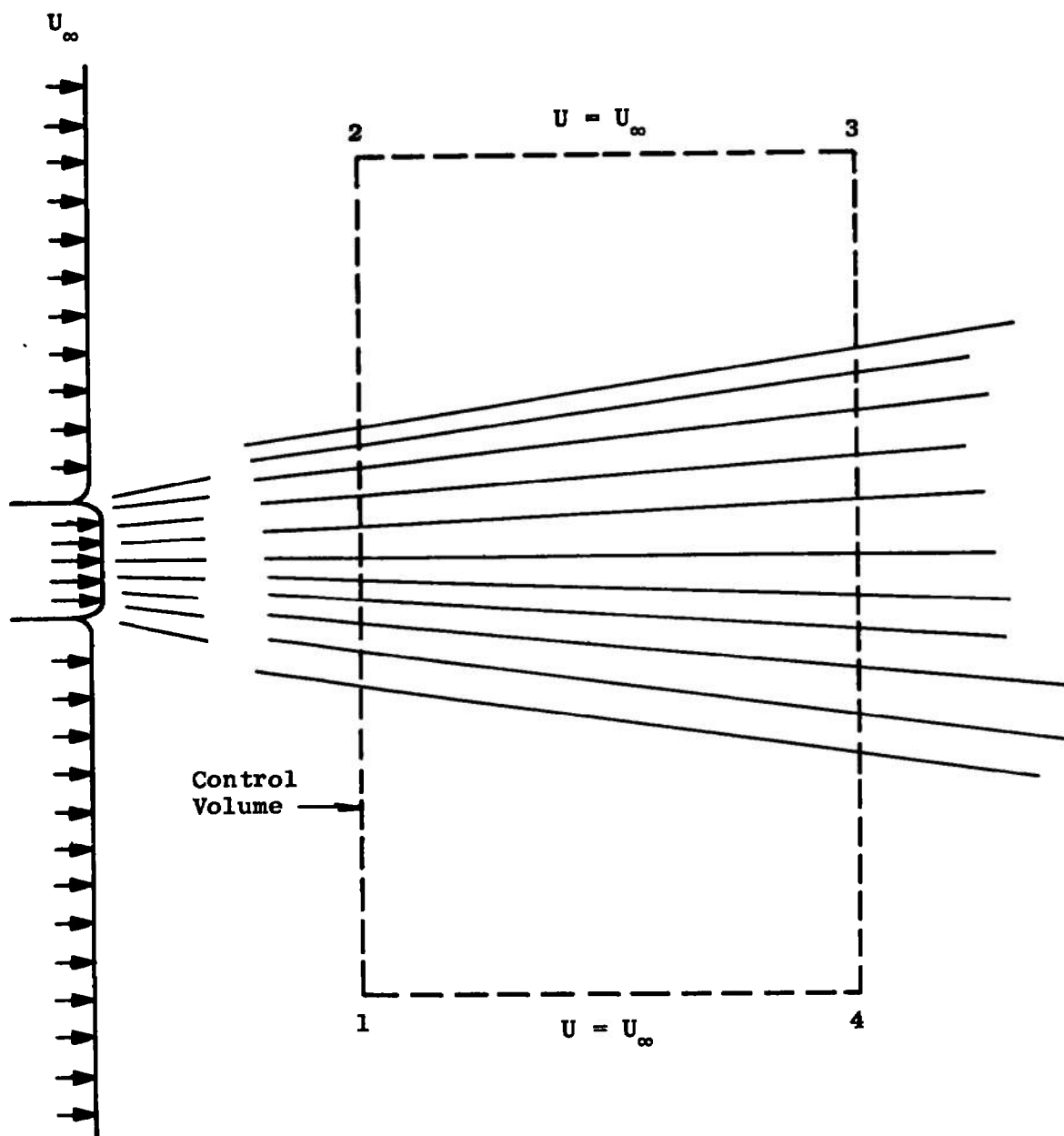


Figure 1.1. Control volume for free mixing.

Newton's second law for any control volume states that the net force acting on the surfaces of the control volume is equal to the change in momentum flow rate through the control volume. But none of the surfaces of this control volume (1-2-3-4 on Figure 1.1) are physical walls or boundaries of the flow; therefore, in the absence of a pressure gradient there can be no net force exerted on them. The change in momentum flow rate in a free mixing flow must then be zero, so that at any lateral plane in the flow, such as 1-2, the momentum flow rate must equal that across any other section, i.e., 4-3 on Figure 1.1. If an axial pressure gradient exists in the flow then there must be a change in the momentum flow rate through the control volume of exactly sufficient magnitude to balance the pressure forces acting on the control volume; further, the external velocity U_{∞} will no longer be constant.

The primary test for a given set of zero axial pressure gradient free mixing data is then that it exhibit a constant value of momentum flow rate from one axial station to the next. In this study, the excess momentum flow rate is used instead of the total momentum flow rate. This parameter represents the increase in momentum flow rate of a particular flow over the momentum flow rate represented by the constant background velocity, and is a considerably more sensitive parameter than the total

momentum flow rate. For a wake, in which velocities are lower than the background velocity, this parameter of course becomes a momentum deficit.

To unequivocally evaluate the excess momentum flow rate, it is necessary to know lateral profiles of the velocity and density at several axial stations, as is shown in Appendix A, assuming constant static pressure. This requirement may be eased slightly in an incompressible flow that exhibits geometric similarity, which is defined below. The evaluation of the excess momentum flow rate in this case is also described in Appendix A. But in general, in order to judge the accuracy of a given experiment, the fundamental requirement is that it contain sufficient data to evaluate the excess momentum flow at several lateral cross sections. (Because this quantity is evaluated by integrating the local excess momentum flow rate per unit area over the area represented by a lateral end of the control volume, with its edges taken to $\pm \infty$, it is referred to in the following text as the excess momentum flux integral or simply momentum integral.)

A second test of a given experiment is of course how well it compares with other similar experiments. This is essentially a subjective test, but it is unlikely that two experiments with similar configurations will both satisfy the momentum integral criterion and yet show widely different behavior. If something of this order occurs, it

may indicate that one of the two flows is not really the same flow configuration as the other. An example of this situation might be two coaxial free mixing experiments, one of which shows a markedly greater initial rate of decay of centerline composition than the other. If the different flows have markedly different jet-to-external-stream velocity ratios, such that the ratio in the case which shows a greater centerline decay is very much less than unity, then it may be that the much-less-than-unity case is exhibiting a somewhat wake-like behavior in the early part of the mixing region, while the other flow behaves more like an ordinary coaxial-jet free mixing process. The wake-like behavior referred to may perhaps be manifested in strong pressure gradients and the existence of regions of local recirculation.

In recent years a new approach to the theory of free turbulence has been developed which involves using the turbulent kinetic energy equation to evaluate the turbulent shear stress. Such a method of course depends on the existence of a fairly general relationship between the turbulent shear stress, τ , and the turbulent kinetic energy per unit mass, k . Because of its importance in the kinetic energy theory, the existence of a relationship between τ and k is evaluated in this study for all experiments which include sufficient data, and it is found that a linear relationship

$$\tau = a_1 \rho k \quad (1.1)$$

where a_1 may be a function of the lateral coordinate is quite general. Further it is found that the shape of the lateral variation of a_1 is reasonably consistent from experiment to experiment in a given flow configuration. Thus Equation (1.1) and the consistent lateral behavior of a_1 provide additional criteria for judging those experiments for which sufficient data are available.

Summarizing, the primary criteria are that the experimental results be complete enough for an unequivocal evaluation of the excess momentum flux integral, and that the value of this integral be nearly constant. To further define the phrase "nearly constant," it has been observed in the course of this study that acceptable experiments generally show deviations from a constant value of the excess momentum integral of ten percent or less. A secondary criterion is that the results be consistent with other results for similar configurations. Further, the relationship between turbulent shear stress and turbulent kinetic energy can be used to provide additional evidence in those flows for which data is available.

Methods of Presentation

It has been commonly observed that if U_c represents the centerline velocity, U_o the free stream velocity, and $r_{1/2}$ the lateral position at which $U - U_o = 1/2(U_c - U_o)$,

then for all axial stations greater than a certain axial station (which varies with the type of flow), one can collapse the measured velocity profile data to a single function

$$\frac{U - U_o}{U_c - U_o} = f\left(\frac{r}{r_{1/2}}\right) \quad (1.2)$$

This is true for two-dimensional and axisymmetric jets with still surroundings ($U_o = 0$), wakes, and for two-stream jets. With some modification an expression similar to Equation (1.2) can be written for two-dimensional mixing layers. Indeed, the function itself is grossly the same for all free mixing flows. In cases in which temperature and concentration differences appear between streams in a flow, it is observed that the total enthalpy and concentration ratios also exhibit geometric similarity.

Because of this observation of geometric similarity, the axial decay curves, i.e., the curves of $U_c - U_o/U_j - U_o$ versus x/D , where U_j is the nozzle exit velocity and D the nozzle diameter (or width) become important parameters in comparing experiments with each other and in comparing the results of calculations with experiment. There are a number of ways in which axial decay curves may be presented. As will be discussed below, all free-mixing jet flows can be divided into two mixing regimes, the first of which is called the potential core.

It is empirically observed that downstream of the end of this potential core the decay curves for a given configuration tend to all have the same behavior, which may be described by a function of the form

$$\frac{U_c - U_o}{U_j - U_o} = k \left(\frac{x}{D}\right)^{-n} \quad (1.3)$$

where k is a constant for any given flow. Therefore, if $\log (U_c - U_o / U_j - U_o)$ is plotted versus $\log (x/D)$, a family of straight lines of slope $(-n)$ results. This fact makes it particularly easy to compare various results with one another, and to determine for a theoretical analysis both its level of agreement with the data and the trend this agreement shows with increasing x ; i.e., whether the agreement can be expected to improve or become worse with increasing axial distance. Because of these advantages, logarithmic plots of axial velocity-, temperature-, and composition-ratio decay will be used as the primary medium for comparison of results.

Since it is observed that all of the axial decay curves for a given configuration have about the same slope downstream of the end of the potential core, but that the potential core length x_c varies from experiment to experiment, it is natural to investigate how the potential core

effect may be removed from the results. Because of the logarithmic nature described above, this may best be done by plotting

$$\frac{U_c - U_o}{U_j - U_o} = k_2 \left(\frac{x}{x_c}\right)^{-n} \quad (1.4)$$

where k_2 is another constant. Indeed, it is shown in Appendix B that for certain simple flows, if geometric similarity is assumed, the integral momentum flux is constant, and the local width scale $r_{1/2}$ is assumed to vary proportionally to x^n , then the determining parameter for the flow is x_c/D . However, even in the simplest flows no universal way is known to evaluate x_c/D . Thus Equation (1.4) does not provide any information of practical interest.

CHAPTER 2

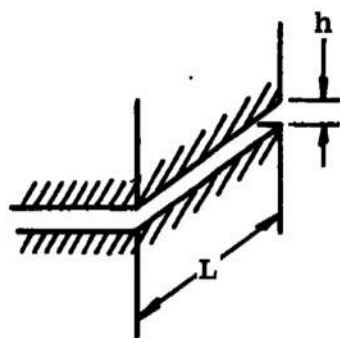
CONSTANT-DENSITY SINGLE-STREAM FLOWS:

EXPERIMENTAL DATA

Conceptually, the constant-density single-stream flow (sometimes referred to as the submerged jet) is, with the possible exception of the incompressible wake, the simplest class of free mixing flows. Thus it is no surprise that this class of flows is the most thoroughly investigated in the field of free turbulent mixing. Because there are no density gradients, and the flow velocities are low, the application of hot-wire equipment to the investigation of the turbulent structure in such flows is straightforward. Most of the available information on turbulent structure is concerned with such constant-density single-stream flows as will be described in this Chapter. The individual flows to be investigated include the two-dimensional and circular jet, and the two-dimensional mixing layer.

The Two-Dimensional Jet

The flow field produced by a two-dimensional jet exhausting into still surroundings can, in general, be broken into two regimes. Where the jet exits from the nozzle, as shown schematically in Figure 2.1, regions of turbulent mixing are formed at either edge of the slot.



$$U_{\infty} = 0$$

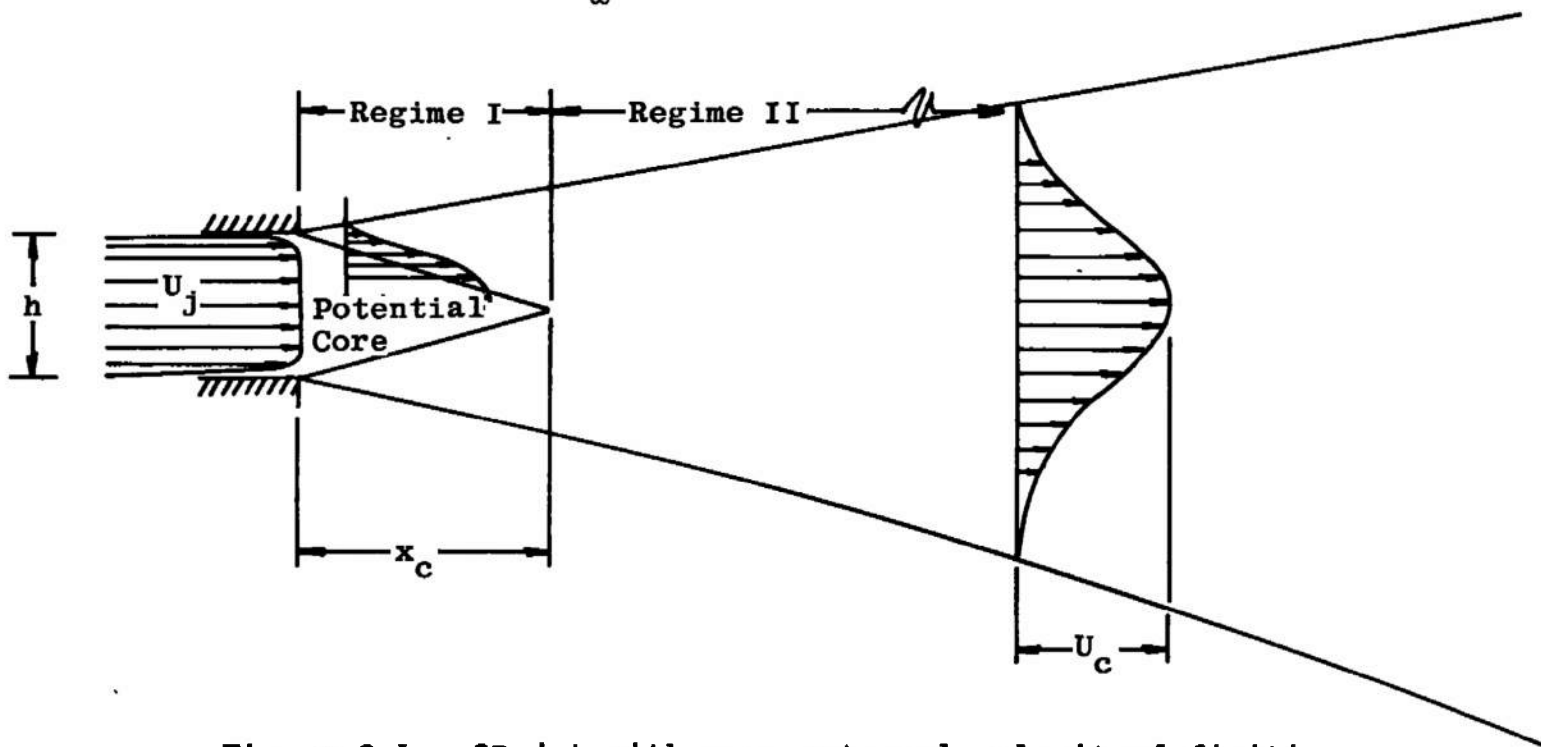


Figure 2.1. 2D jet with zero external velocity-definition sketch.

The width of the turbulent mixing region expands in the downstream direction, so that it encroaches both on the external still fluid and on the non-turbulent potential core region between the two mixing layers. At the point where the two mixing layers meet, the potential core disappears, and the potential core region, or first regime of mixing, undergoes a transition to the second regime in which turbulent flow is encountered all the way across the jet.

The mixing model just described is idealized. In reality, there is ordinarily some low level of turbulence existing in the potential core, and the lines of demarcation between the turbulent mixing region and non-turbulent fluid are not distinct. If a fast response probe is held close to the edge of a turbulent jet, it will sense alternate periods in which both turbulent and non-turbulent patches of fluid are swept by. This phenomenon, called intermittency, has been observed in all free turbulent flows (in the two-dimensional jet by Hannum and Griffith [1]).¹ The presence of intermittency means that the boundary between the turbulent mixing region and non-turbulent fluid is random; it "blurs" the lines of demarcation. Further, the change from regime I to regime II is not abrupt, as idealized in Figure 2.1; rather there

¹Numbers in brackets refer to similarly numbered references in the bibliography.

is a transition regime where the behavior of the flow gradually changes from the characteristic behavior of the first regime to that of the second. Nevertheless, the idealized picture of Figure 2.1 is important in two respects: as an aid to the understanding of the characteristics of the two-dimensional jet flow and as a model for the mathematical simulation of the flow.

A truly two-dimensional flow is difficult to realize experimentally, as the physical necessity of limiting the length of the slot (L on Figure 2.1) unavoidably introduces three-dimensional end effects into the flow. A true two-dimensional flow can only be approximated, and this only through the use of a suitably high aspect ratio, L/h on Figure 2.1. The maintenance of two-dimensionality also limits the downstream distance over which the jet may be measured. Van der Hegge Zijnen [2] states that the slot jet will approximate the true two-dimensional case in the plane of symmetry perpendicular to the slot provided that the downstream distance is not farther than $2L$. Newman [3] regards the end effects as distorting some experimental results by causing the rate of growth of the mixing layer to be too slow, presumably through the action of end vortices which induce spanwise flows and thus thin the mixing layer. An additional problem arises when the slot jet has to be for practical reasons enclosed in a duct. Care must be taken that the

duct be sufficiently large compared to the slot. Foss and Jones [4] report that the structure of a rectangular jet enclosed in a duct can be significantly different from that of a free jet.

The ideal two-dimensional jet has no characteristic length (Townsend [5], page 173), which means not only that the fluid viscosity and jet velocity completely specify the whole flow, but also that a characteristic Reynolds number for the whole flow cannot be defined. This in turn implies that all two-dimensional jets are dynamically similar. Under this condition it can be shown from the equations of motion (see for example, Newman [3], also Appendix C) that in the self-preserving region, in which the profiles of velocity and shear stress exhibit similarity, the centerline velocity ratio U_c/U_j varies as $(x/h)^{-1/2}$ and the jet width is proportional to $(x/h)^{1/2}$. All of the two-dimensional jet experiments reported in this Chapter exhibit over some region an " $x^{-1/2}$ " decay of centerline velocity, as is indicated by Figure 2.2. The region beyond which similarity prevails is reported as $x/h > 20$ by Miller and Comings [6] but Heskestad [7] reports similarity occurring only for $x/h > 65$. In this connection, however, the definition of "similarity" is important as the velocity profile is observed to take on a similar profile shape (i.e., one in which the velocity profile, plotted as U/U_c versus y/x , does not vary with x)

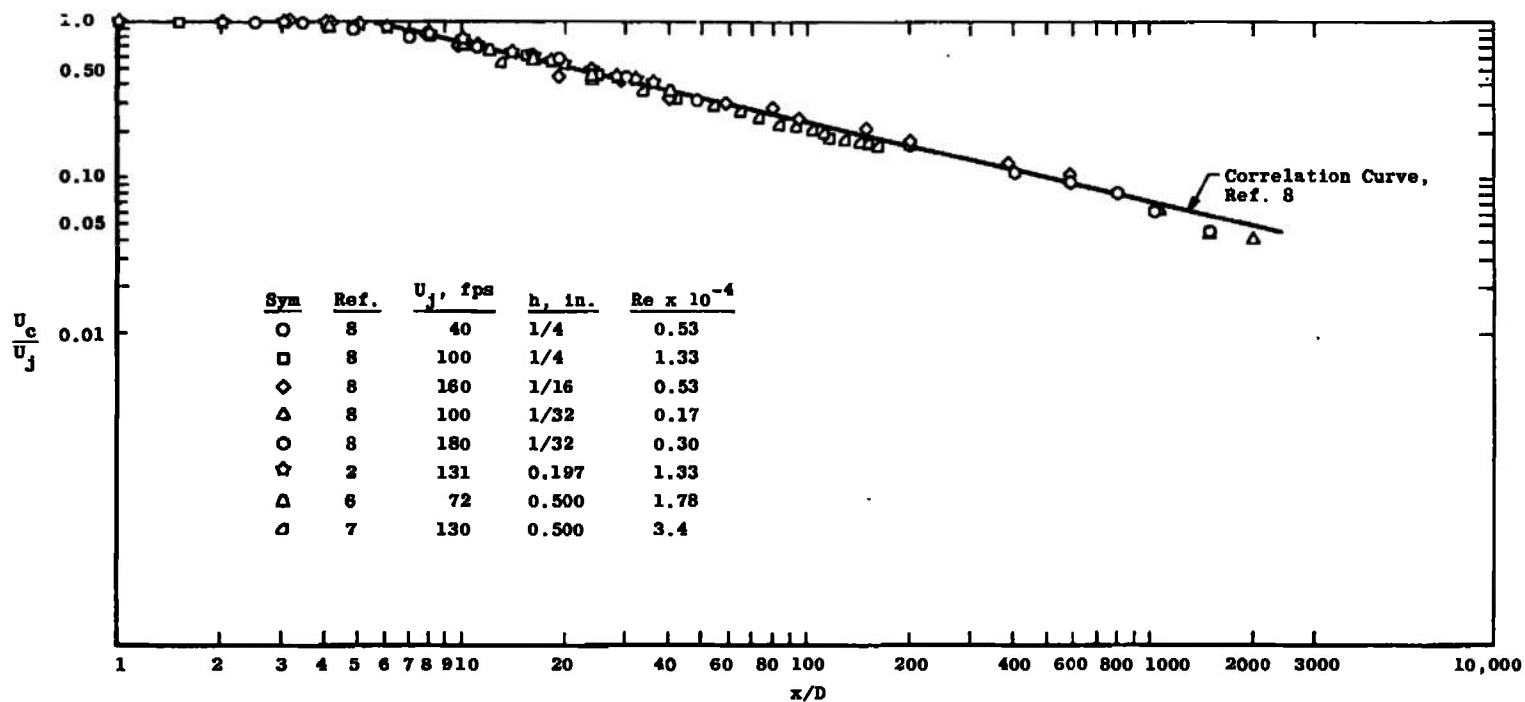


Figure 2.2. Axial decay of centerline velocity ratio, two-dimensional jet-into-still-air.

earlier than the turbulent shear stress profile. In addition, Heskestad reported that a "subrange" existed in his jet in the region $10 \leq x/h \leq 30$ in which the centerline velocity decay approximated a self-preserving form, although a different form than that exhibited further downstream.

Although there can be no Reynolds number defined for the whole flow in an ideal flow, a Reynolds number for the actual jet can be defined at the jet exit, and in the early part of the flow some variation of centerline velocity decay behavior with this Reynolds number is observed. From an examination of experimental data, Newman [3] concludes that there are no important variations due to changes in slot conditions beyond a few tens of slot heights downstream. However, as Figure 2.3 shows, there is an apparently persistent data shift present between Heskestad's [7] data and that reported by Albertson, Dai, Jensen, and Rouse [8]. As is shown in Table 2.1, the Reynolds number (based on the slot height) for the latter data ranged from 0.17×10^4 to 1.1×10^4 , while Heskestad's measurements were made at a Reynolds number of 3.4×10^4 . There is thus a Reynolds number change of a factor of between 3 and 20 between the two experiments. Some recent work, by Flora and Goldschmidt [9] indicates that this type of shift may be not so much because of Reynolds number differences, but rather because of differences in initial

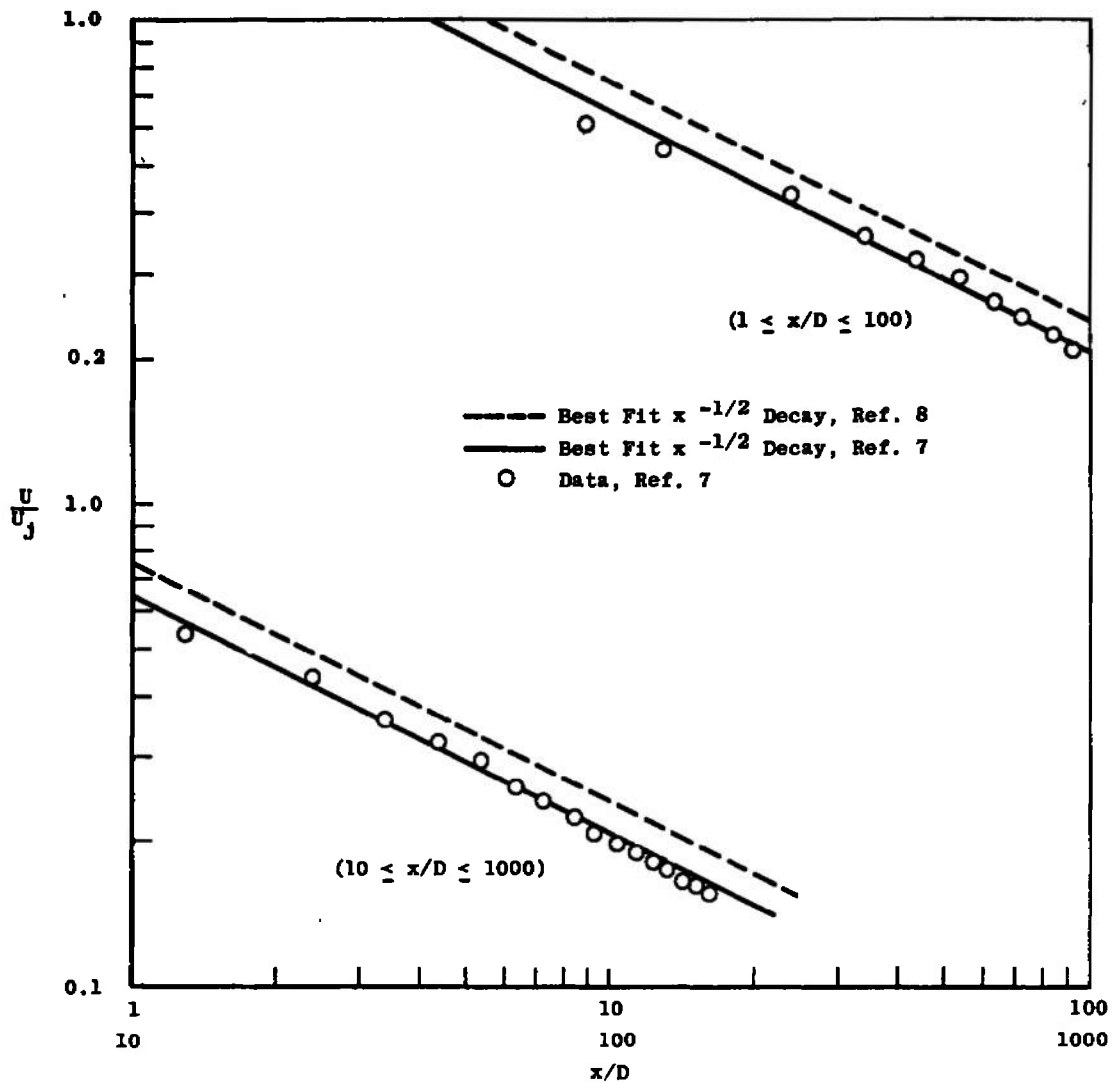


Figure 2.3. Comparison of axial decay data of Heskestad [7] with that of Albertson, et al., [8].

TABLE 2.1
THE TWO-DIMENSIONAL JET-INTO-STILL-AIR

Experimenter	Ref.	Year	$Re^a \times 10^{-4}$	Slot Aspect Ratio	Maximum x/h	x_{max}/L	Momentum Check, ^b Percent
Forthmann ^c	3	1934	7.1	20	25	1.25	-
van der Hegge Zijnen	2	1949	1.33	20	40	2.0	4
Albertson, Dai, Jensen, and Rouse	8	1950	0.17-1.33	288-2300	2000	0.87	10
Reichardt ^c	3	1951	2.4	21	100	4.77	-
Miller and Comings	6	1958	1.78	40	40	1.0	4.25
Nakaguchi ^c	3	1961	0.9-1.6	133	100	0.75	-
Olson ^c	3	1962	0.9	12	16	1.33	-
Knystautas ^c	3	1964	0.7-1.3	98-195	350	3.57-1.79	-
Gartshore ^c	3	1965	1.7	167	200	1.20	-
Heskestad	7	1966	3.4	120	162	1.35	6
Prosser and Fisher	10	1966	-	-	16	-	-

^aBased on slot height, h .

^bMaximum deviation, percent of average.

^cSummarized in Newman [3].

turbulent intensity. Presumably this would also explain why there is less difference between the $Re = 0.17 \times 10^4$ and the $Re = 1.1 \times 10^4$ measurements of Albertson, Dai, Jensen, and Rouse [8] than between their $Re = 1.1 \times 10^4$ results and Heskestad's $Re = 3.4 \times 10^4$ results.

An interesting point raised by Figure 2.3 involves the fact that the curves shown will collapse together if plotted versus x/x_c rather than x/d , providing that x_c , the potential core length, is obtained by extrapolating the line $U_c/U_j \propto (x/d)^{-1/2}$ to the line $U_c/U_j = 1.0$. This implies that the effect of the conditions at the origin of mixing is felt at least as far downstream as 100 slot heights.

The important parameters of the available two-dimensional jet-into-still-air experiments are given in Table 2.1. Some of these experiments have not been included in the discussion which follows; the data are from Newman [3] and are included here for completeness. One item from this table worthy of note is that although the decay measurements of Albertson, Dai, Jensen, and Rouse [8] are carried down to $x/h = 2000$, the slit width used is so small that x_{max}/L remains less than 1. Most of the measurements can be seen to fall within the two-dimensionality requirement described by van der Hegge Zijnen [2] with the exception of those of Reichardt and of Knystautas, both reported by Newman [3]. It can also be seen from Table 2.1

that the Reynolds number range of the measurements is quite small, with only the measurements of Forthmann, reported by Newman [3] and Heskestad [7] being at a substantially different Reynolds number than the others.

Two of the experiments to be considered in this section are primarily concerned with mean flow measurements (as opposed to measurements of the turbulent fluctuations); these are the experiments of van der Hegge Zijnen [2] and Albertson, Dai, Jensen, and Rouse [8]. Both of these experiments involved substantially the same Reynolds number range, and as would be expected, the axial decay of center-line velocity data from these two experiments agree quite well. This is shown in Figure 2.4, in which the axial range plotted is limited to $1 < x/h < 100$. There is some deviation between the results at $Re_h = 1.33 \times 10^4$ and $Re_h = 0.53 \times 10^4$, but it is not sufficiently greater than the experimental scatter to be significant. The solid curve indicates the $x^{-1/2}$ decay predicted by similarity considerations.

Both van der Hegge Zijnen [2] and Albertson, Dai, Jensen, and Rouse [8] indicate that the velocity profiles obtained became approximately similar for $x/h > 20$, the approximation becoming better further downstream. Individual profiles are not available from Reference [2] because of the small size of the figures in that reference.

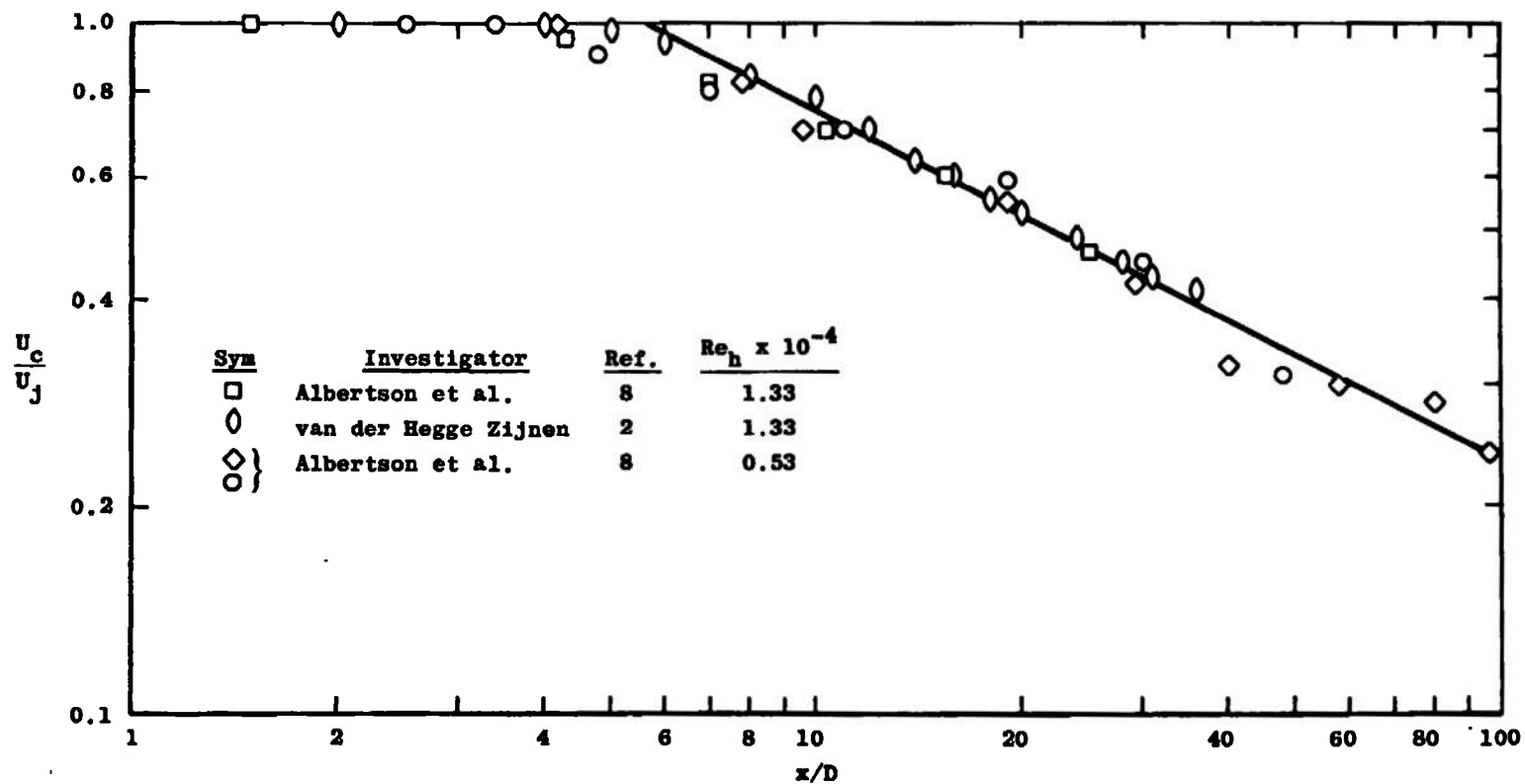


Figure 2.4. Comparison of centerline decays, 2D jet.

It is possible to obtain similar data from Reference [8]. Representative profiles obtained from Reference [8] are presented in Figure 2.5.

Measurements of turbulence intensities are presented in three of the papers considered. Experiments in which the turbulent intensity components u' and v' and the turbulent shear correlation \overline{uv} were measured in a two-dimensional jet are presented by van der Hegge Zijnen [2]. These measurements were made in a jet from a 1.0×25 cm (0.394×9.84 inch) slot at $U_j = 2000$ cm/sec (65.6 ft/sec). Miller and Comings [6] made measurements of the turbulent velocity fluctuation v' , the mean velocity U and the average static pressure \bar{p} in a 72 ft/sec jet from a 0.5×20 inch slot. From these measurements, v' , V , and the turbulent shear stress τ were deduced using the integral forms of the continuity, x-momentum, and y-momentum equations. Both van der Hegge Zijnen and Miller and Comings carried out lateral profile measurements at several downstream locations; the former at $x/h = 17.5, 20, 22.5, 30, \text{ and } 35$, and the latter at $x/h = 10, 20, 30, \text{ and } 40$. On the other hand, Heskestad [7] measured the components of the turbulent kinetic energy equation (except for the pressure-velocity correlation) as well as u' , v' , w' , and \overline{uv} , providing more detail, but at only one station in the flow, $x/h = 101$.

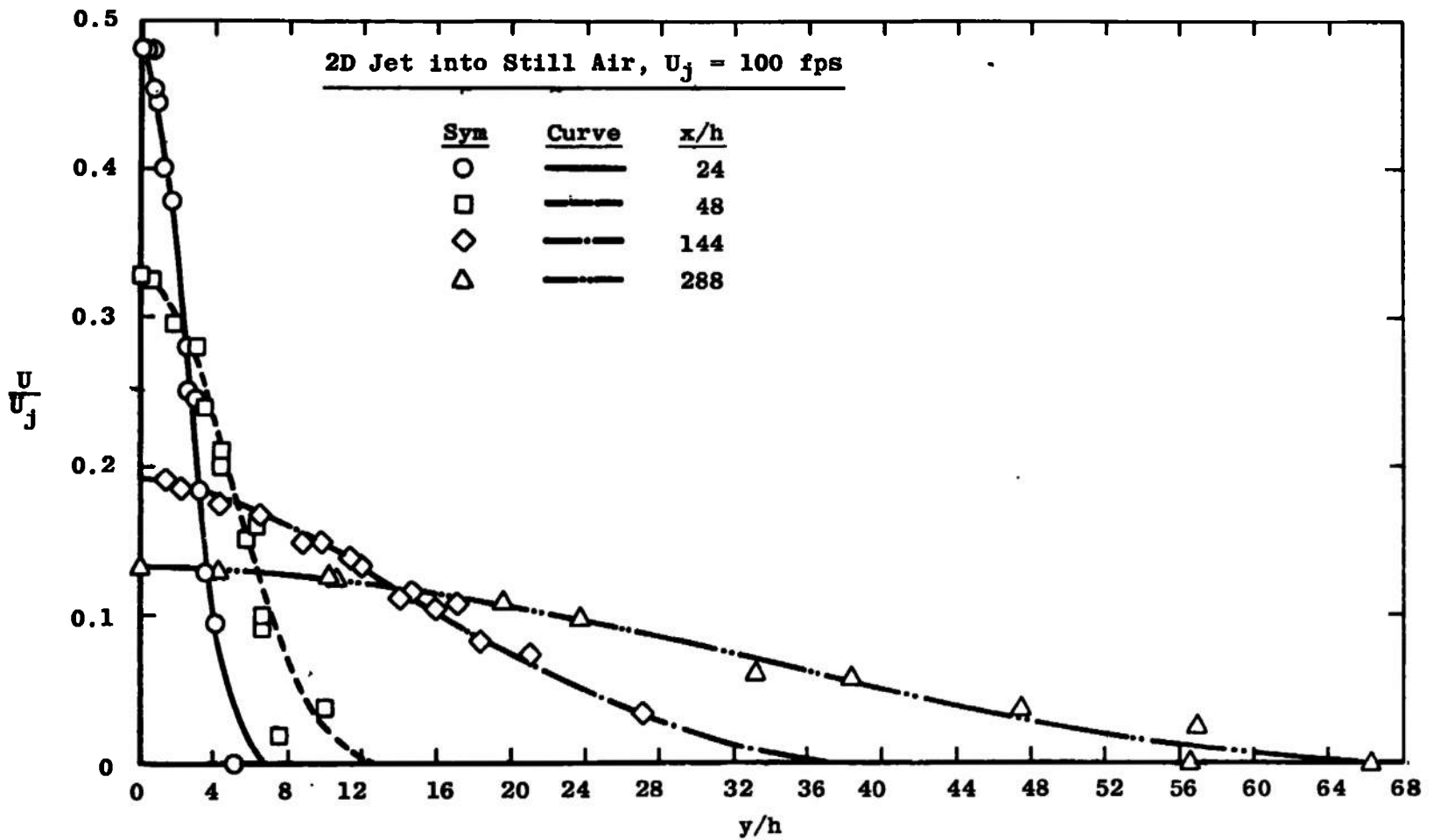


Figure 2.5. Velocity profiles from Reference [8].

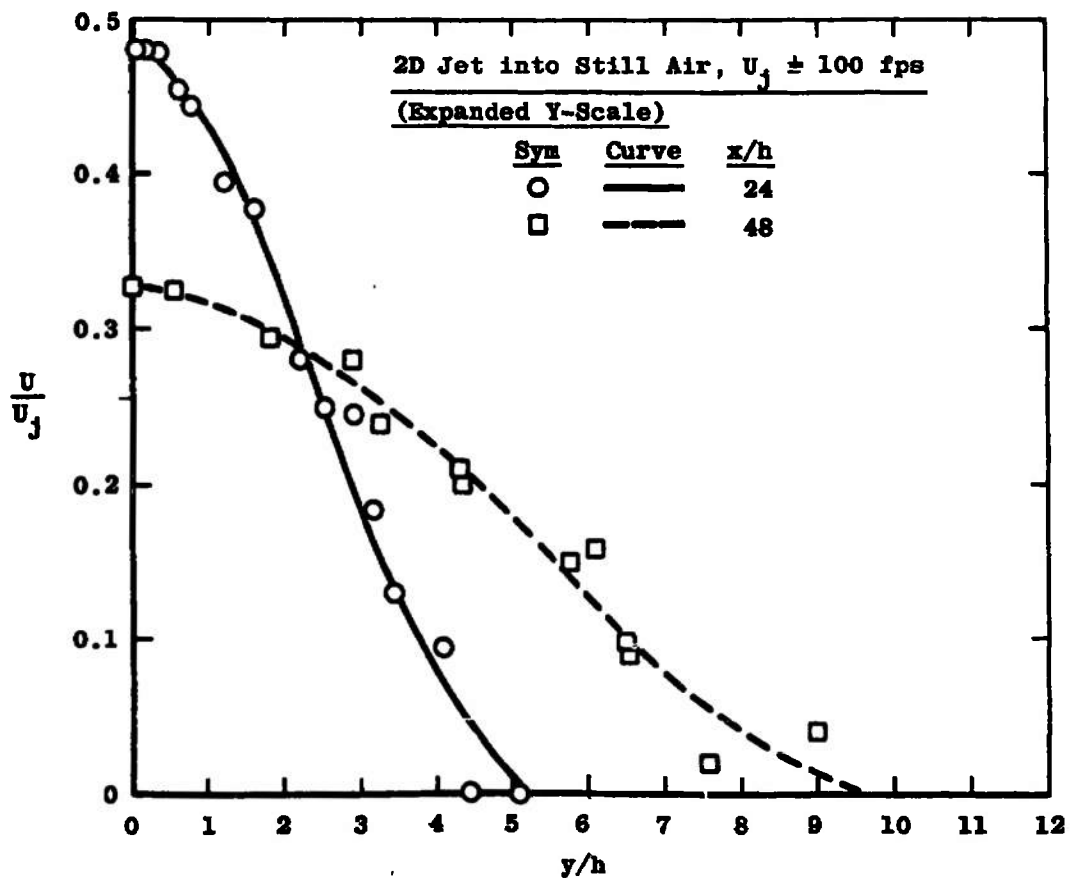


Figure 2.5. (continued)

Centerline velocity decay data are shown for these three experiments in Figure 2.6. As can be seen from Table 2.1, page 24, the Heskestad data are at a jet exit Reynolds number of 3.4×10^4 , which is about twice the Reynolds number for the other two cases. As would be expected from the previous discussion of the persistence of the effect of the initial conditions, lines of $U_c/U_j \propto x^{-1/2}$ passed through the data exhibit a quite obvious shift with jet exit Reynolds number. The $x^{-1/2}$ proportionality is that demanded by conservation of momentum under the assumptions of similar velocity profiles and linear spread rate; both of these assumptions are borne out by the experimental data under consideration.

Figures 2.7, 2.8, and 2.9 compare, respectively, profiles of u'/U_c , v'/U_c , and $\tau/\rho U_c^2 (= |\overline{uv}|/U_c^2)$ versus the nondimensional lateral coordinate η ,

$$\eta = y/(x-x_v) \quad (2.1)$$

where x_v is the virtual origin length. This quantity arises from the classical model of a jet flow, in which the flow is characterized as emerging from a point source. To relate a real flow to this classical model, it is necessary to define a point, usually upstream of the actual physical origin of the jet (although it can also be downstream) from which an equivalent point source jet would have issued. This is usually accomplished by extrapolating the observed

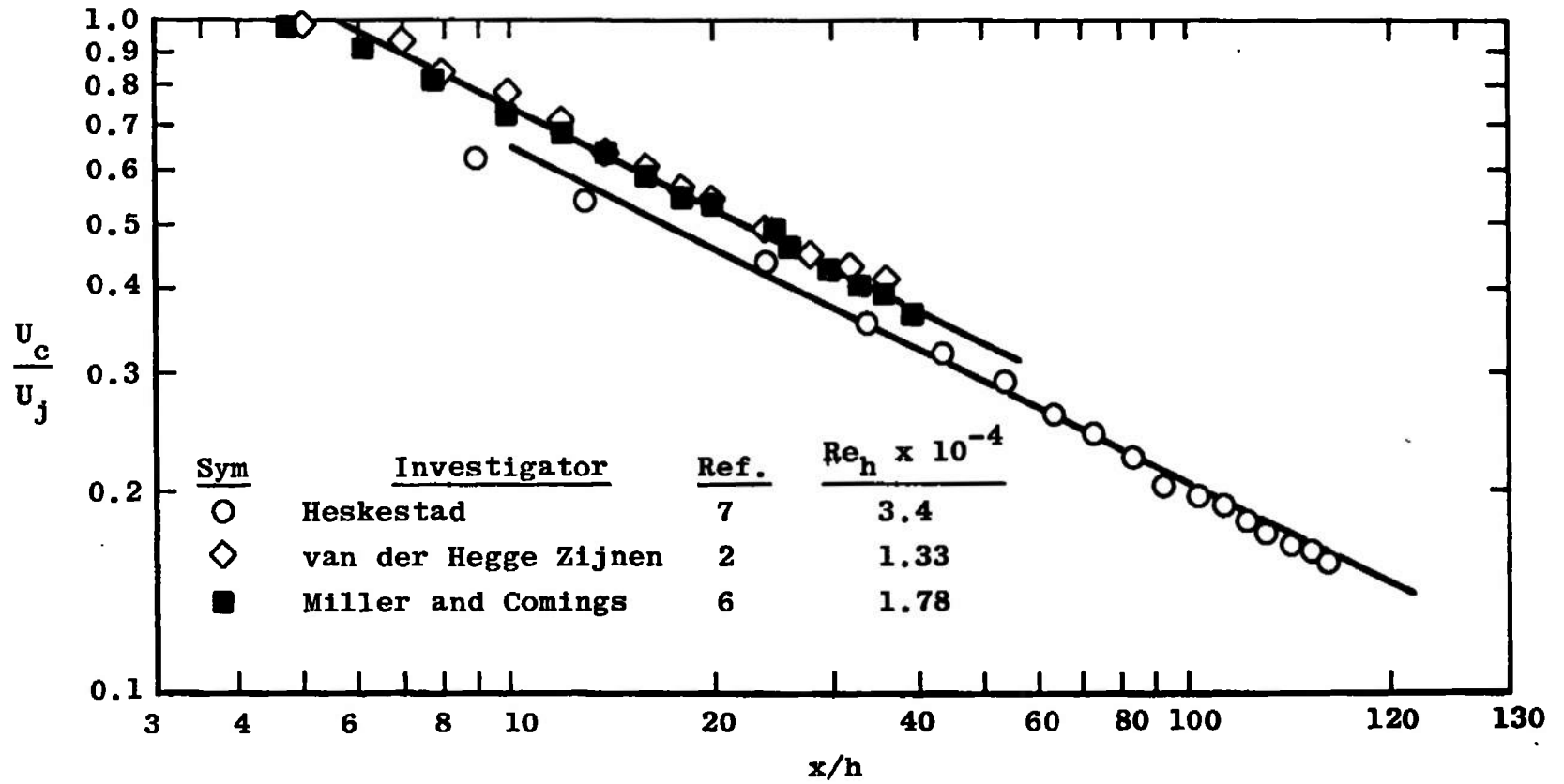


Figure 2.6. Centerline velocity decay.

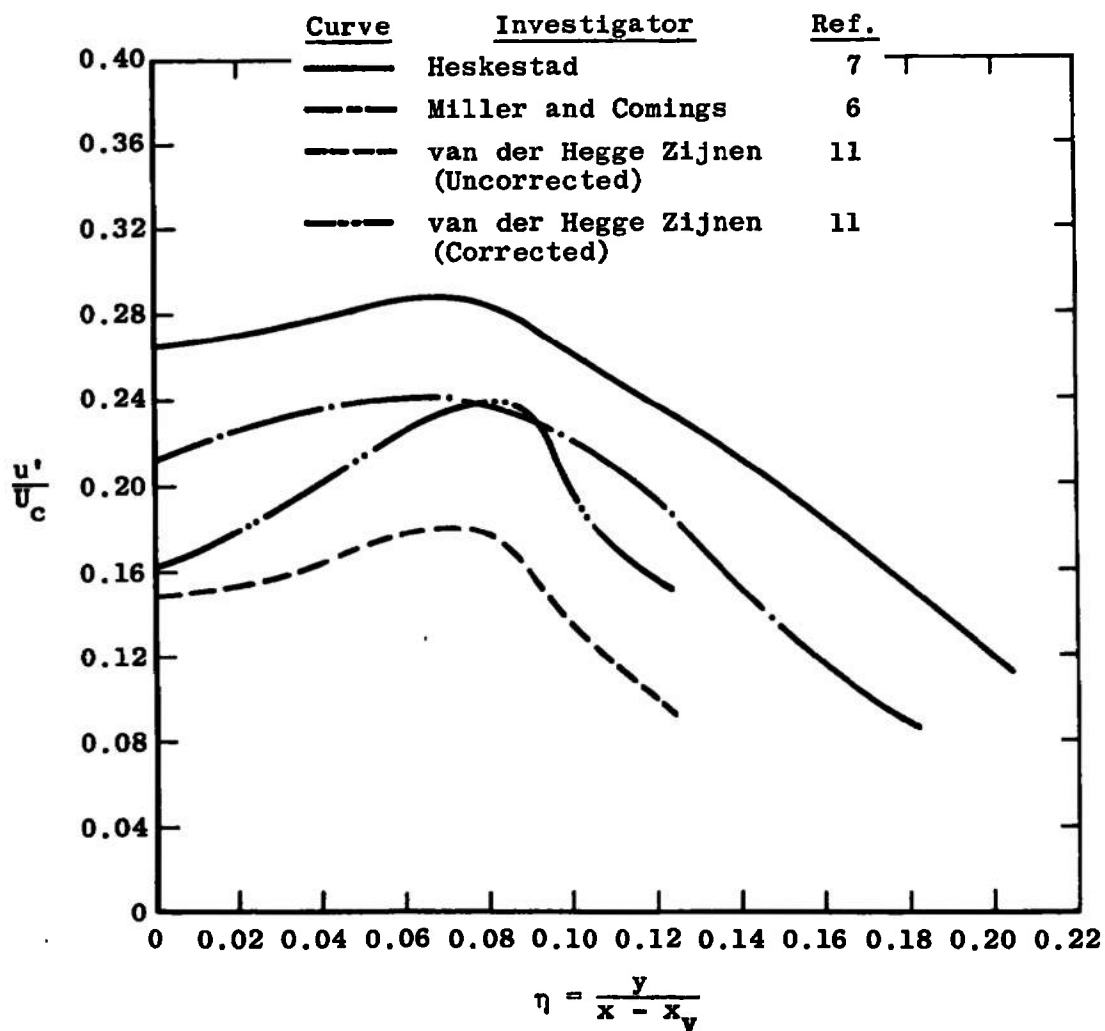


Figure 2.7. Axial turbulent intensity variation, 2D jet-into-still-air.

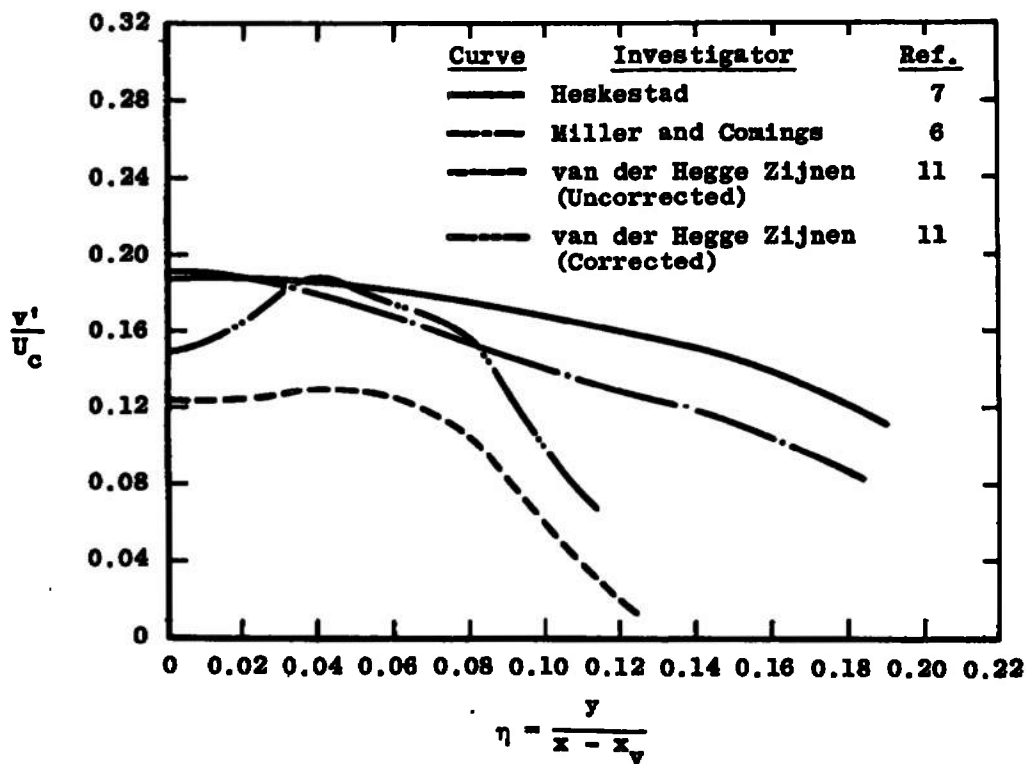


Figure 2.8. Lateral turbulent intensity variation, 2D jet-into-still-air.

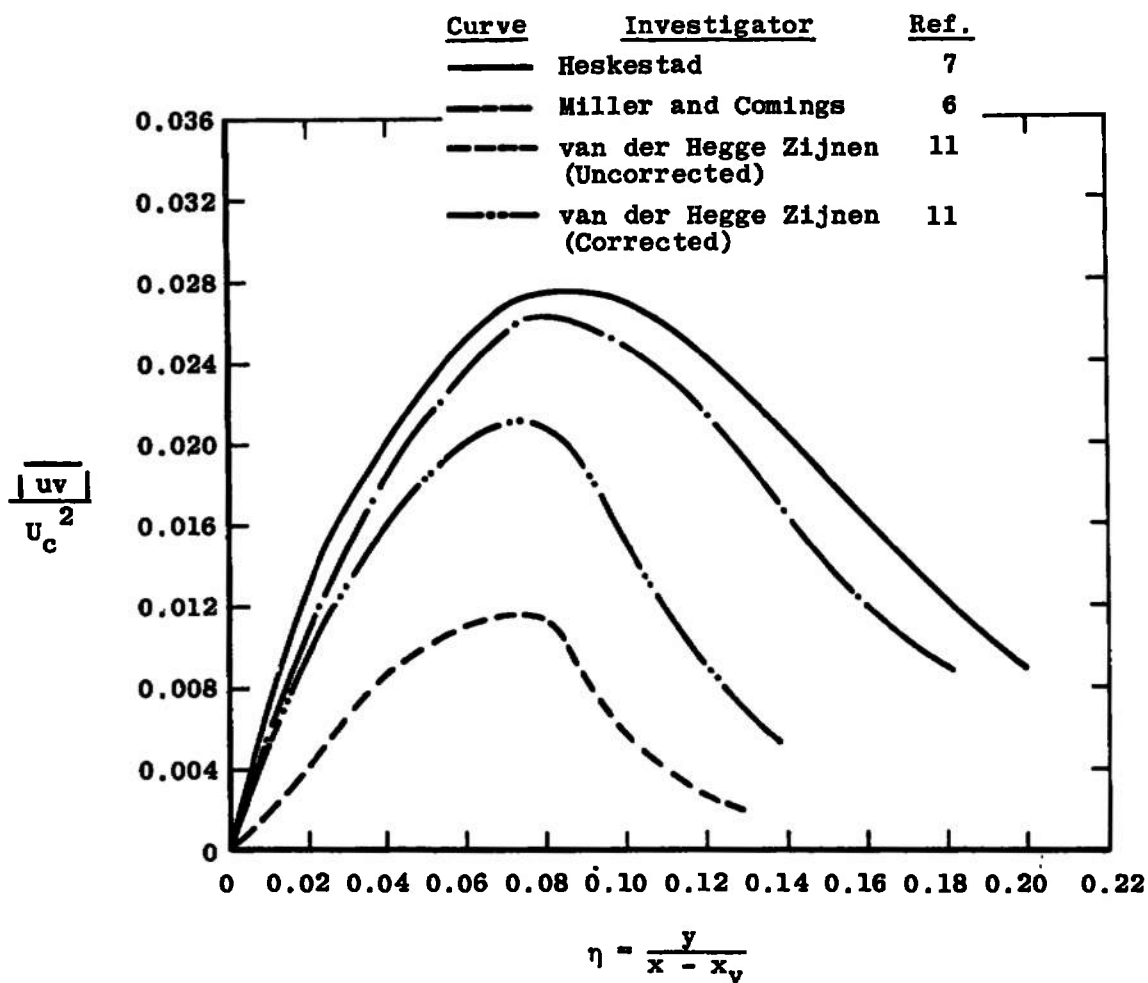


Figure 2.9. Turbulent shear stress variation, 2D jet-into-still-air.

downstream rate of spread back to the point of zero thickness. There are two profiles in each case for the van der Hegge Zijnen [11] measurements, one representing his "corrected" data and the other his "uncorrected" data. His correction brings the measured turbulent shear stress level up to that obtained by integration of the mean flow velocity profiles. Both the van der Hegge Zijnen measurements and those of Miller and Comings [6] were made at $x/h = 20$; Heskestad's measurements were at $x/h = 101$. If similarity exists for the turbulent intensity and shear profiles by $x/h = 20$, all of the curves (excepting possibly the van der Hegge Zijnen "uncorrected" case) should coincide. Looking at the u'/U_c , v'/U_c , and $|\overline{uv}|/U_c^2$ plots (Figures 2.7 through 2.9), it seems that complete similarity does not exist by $x/h = 20$. This of course agrees with Heskestad's conclusion. It must be noted in considering these figures that the only one of the three quantities depicted that was actually measured by Miller and Comings was u'/U_c , and that the data of van der Hegge Zijnen can be obtained from the curves of Reference [11] only with great difficulty (and probably great error), because of the small size of the figures presented.

From Figures 2.7 through 2.9, it appears that the data of Miller and Comings [6], obtained with a minimum of measurements, agree fairly well with that of Heskestad. There is, however, an alternate way of comparing these

experiments. It has been shown in Reference [12] that an approximate linear relationship exists between the turbulent shear stress, $\tau = \rho \overline{uv}$, and the turbulent kinetic energy per unit mass $k = 1/2[u'^2 + v'^2 + w'^2]$ over a wide range of experimental conditions. This relationship can be expressed as

$$\tau = a_1 \rho k \quad (2.2)$$

where a_1 is approximately constant over a portion of the flow field, but approaches zero on the centerline and at the outer edge. If the data shown in Figures 2.7 through 2.9 are used to obtain

$$a_1 = \frac{\tau / \rho U_c^2}{k / U_c^2} \quad (2.3)$$

as a function of η , Figure 2.10 results. From Figure 2.10, it can be seen that both the uncorrected and the corrected van der Hegge Zijnen data agree well with the Heskestad data (the corrected better than the uncorrected), while the data of Miller and Comings deviate strongly, particularly for the large η . Because both van der Hegge Zijnen and Heskestad made independent measurements of both turbulent intensities and the turbulent shear stress, while Miller and Comings did not, the deviation shown in Figure 2.10 indicates that the latter data should be treated with some suspicion.

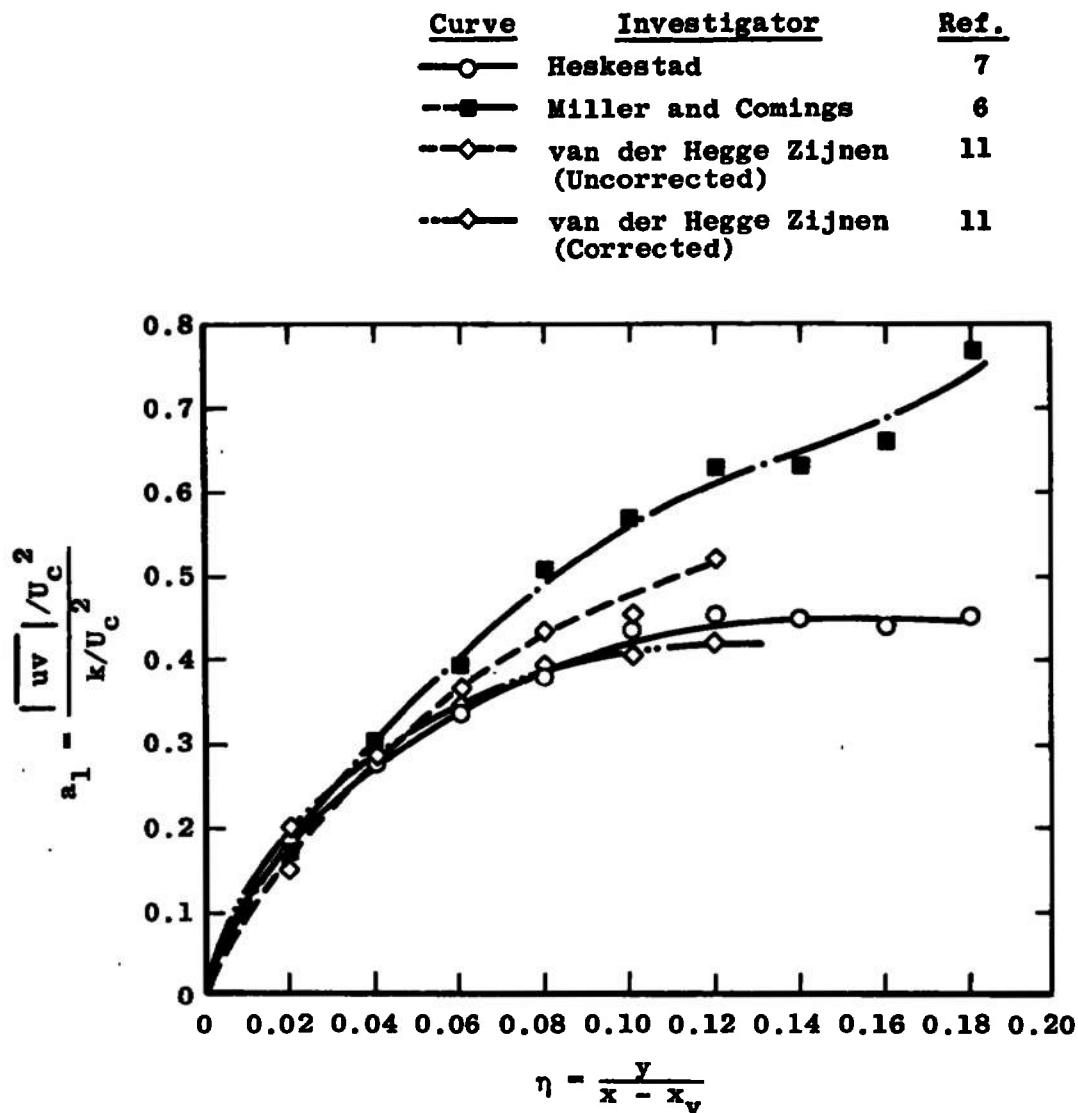


Figure 2.10. Ratio of turbulent shear stress to turbulent kinetic energy, 2D jet-into-still-air.

Before leaving the subject of the two-dimensional jet into still air, one further experiment should be mentioned, although it does not add anything further insofar as experimental information is concerned. This is the investigation into the structure of a two-dimensional jet carried out by Csanady [13]. Primarily aimed at the problem of jet noise suppression, it is one of a number of analyses which look for relationships between the sound produced by a jet and the turbulent intensity in the jet. Of greatest interest to the present report is Csanady's conclusion, based on his own experiment and others', that the production, diffusion, and dissipation of turbulent energy may be expressed in terms of an eddy viscosity, eddy diffusivity of turbulent energy, and a turbulence microscale, respectively, all being constant for a given cross-section. This conclusion is of some importance to the application of the turbulent kinetic energy method to free turbulent mixing.

The Two-Dimensional Mixing Layer

The ideal two-dimensional mixing layer is a hypothetical flow which can be visualized as occurring when a uniform semi-infinite stream, initially separated from a region at rest by an infinitesimal divider, mixes with a stagnant region. Then at $x = 0$, Figure 2.11 (a), a mixing region develops and propagates into both the stream at rest and the moving stream. Since boundary layer development on the dividing plate is unavoidable, the ideal two-dimensional

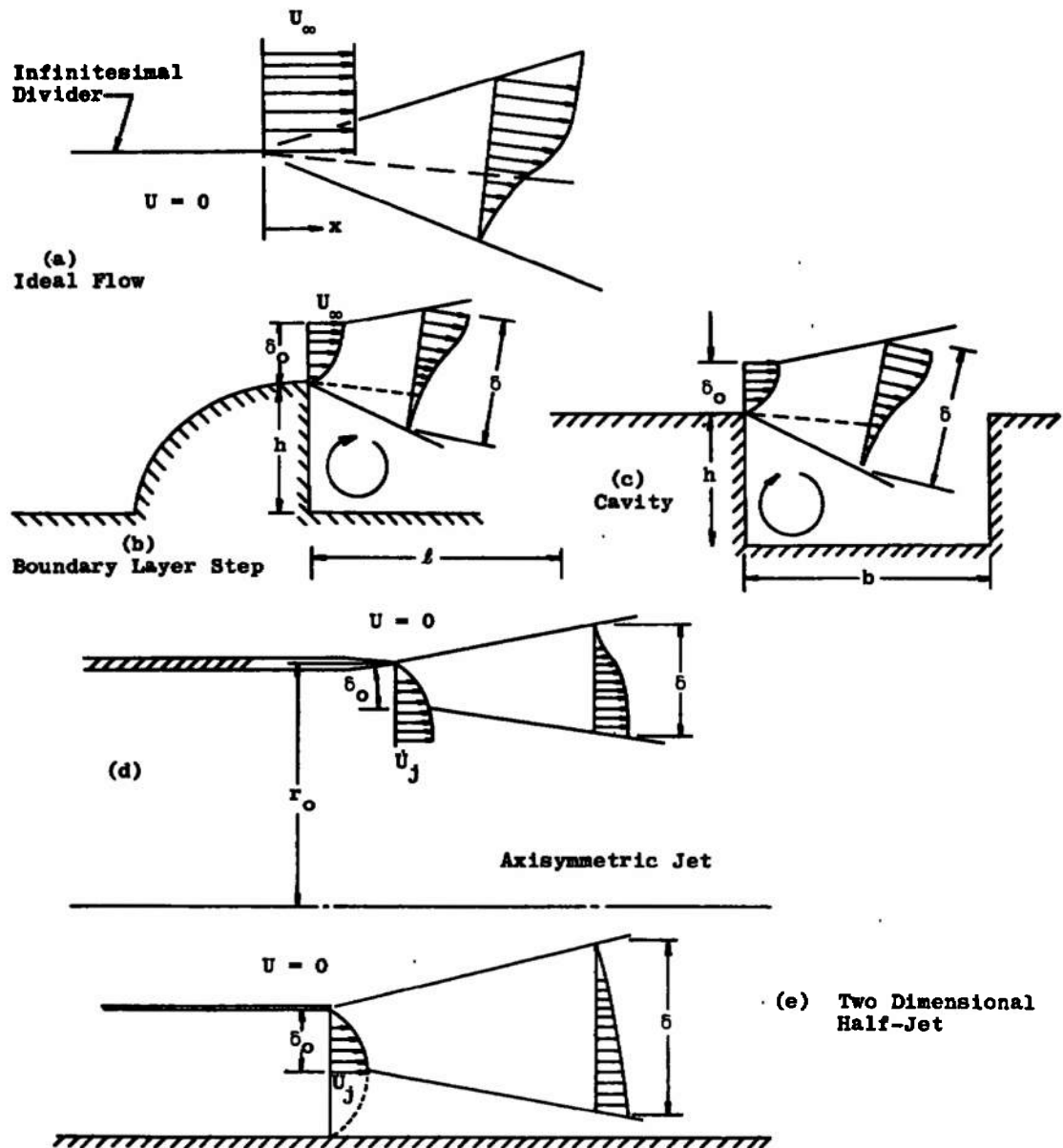


Figure 2.11. Types of two-dimensional mixing layers.

mixing layer can in practice only be approximated. There are a number of different ways in which the approximation can be done. Four different approaches to it are described in this section.

The flow from the edge of a boundary layer bump, as shown schematically in Figure 2.11 (b), will approximate a two-dimensional mixing layer for a part of the distance down to where the separated boundary layer reattaches to the plate. Such a flow has been experimentally investigated by Mueller [14]. Another approximation with some of the characteristics of the configuration of Mueller is the flow of a boundary layer into a cavity, as shown schematically in Figure 2.11 (c). In both of these flows there is a characteristic ratio, step height/distance to reattachment (h/l) in Figure 2.11 (b) and cavity height/cavity width (h/b) in Figure 2.11 (c), which determines to some extent the behavior of the flow; in both cases there also exist vortices (one or more) in the flow below the mixing region. Because of the existence of these vortices the mixing layer is not actually interacting with a stagnant flow. Haugen and Dhanak [15] have investigated the free mixing portion of a cavity flow in some detail.

Somewhat better approximations to the ideal two-dimensional mixing layer are provided by the next two flows to be considered. The mixing layer at the edge of an axisymmetric jet flowing into still air will approximate a

two-dimensional mixing layer as long as the jet radius r_0 , is sufficiently greater than the mixing layer thickness, δ , as shown in Figure 2.11 (d). Such a configuration was investigated by A. J. Chapman [16]. Finally, the closest approximation to the ideal mixing layer flow is achieved in the first regime of a two-dimensional jet. By dividing the jet with a splitter plate and investigating one side of the first regime, the "half jet" flow, investigated by Liepmann and Laufer [17] is formed. Such a flow is shown schematically in Figure 2.11 (e).

In the ideal flow there can be no characteristic Reynolds number, as there is no characteristic dimension of the flow. On the other hand, in the real flows a characteristic dimension might be taken to be the boundary layer thickness at the start of the free mixing process, δ_0 , and a characteristic Reynolds number defined. It is observed for the two-dimensional mixing layers formed in the first regime of both two-dimensional [17] and axisymmetric [18] jet that by an x-Reynolds number ($U_j x/\nu$) of 3.5×10^5 the velocity profiles have become fully developed; that is that the measurements collapse together when U/U_j is plotted as a function of $\eta = y/x$. Based on the assumption of similar velocity profiles, it is shown in Reference [17] that the spreading rate of the two-dimensional mixing layer is linear with distance.

The separated boundary layer flow of Mueller [14] and the cavity flow of Haugen and Dhanak [15] have certain superficial similarities, as described above, and thus they will be discussed together. Mueller measured the turbulent fluctuations u' and v' and the shear stress correlation \overline{uv} in a flow configuration such as that sketched in Figure 2.11 (b), page 40. For a step height of 0.75 inch corresponding to a Reynolds number $Re_h = 3.6 \times 10^4$, he was able to achieve fully developed turbulent mixing in the free mixing layer.² Mueller also experimented with step heights of 0.5 and 0.25 inch. Presumably these did not produce free mixing layers long enough for fully developed mixing to occur. The boundary layer thickness at the point of departure from the edge of the step was of the order of 0.75 inch, so that the Reynolds number based on initial boundary thickness was also 3.6×10^4 . The length ℓ to reattachment was 5.15 inches.

Haugen and Dhanak [15] investigated the flow into a cavity, such as sketched schematically in Figure 2.11 (c). Their apparatus enabled them to adjust both the cavity width b and the initial boundary layer thickness δ_0 . Measurements were made of the fluctuating velocity component in the

²However, even at the point of reattachment, $x/h = 6.8$, the x -Reynolds number is 2.48×10^5 , somewhat lower than the Reynolds number required for a fully developed profile as described by Liepmann and Laufer [17] and Bradshaw, et al., [18].

x-direction, u' , and the turbulent shear stress \overline{uv} . These measurements were made at $x/b = 0.50$, so that with a cavity width b of 2.50 inches, $Re'_x = 6.63 \times 10^4$, which is far below the apparent requirement for a fully developed profile.

The turbulence intensity measurements made by Mueller [14] indicate that in this configuration $v'/U \approx 2 u'/U$. It is unlikely that the unmeasured fluctuation component w'/U would also be twice u'/U , so that for these data the following assumption has been made: For Mueller's data

$$\begin{aligned} \frac{k}{U^2} &= \frac{1}{2} \left[\left(\frac{u'}{U} \right)^2 + \left(\frac{v'}{U} \right)^2 + \left(\frac{w'}{U} \right)^2 \right] \\ &\approx \frac{1}{2} \left[\left(\frac{w'}{U} \right)^2 + \left(\frac{v'}{U} \right)^2 + \left(\frac{u'}{U} \right)^2 \right] \\ &\approx \frac{1}{2} \left(\frac{v'}{U} \right)^2 + \left(\frac{u'}{U} \right)^2 \end{aligned} \quad (2.4)$$

Because Haugen and Dhanak [15] use somewhat the same configuration, but measure only u'/U , the following assumption is made:

$$\frac{k}{U^2} \approx \frac{1}{2} \left[\left(\frac{u'}{U} \right)^2 + \left(\frac{2u'}{U} \right)^2 + \left(\frac{u'}{U} \right)^2 \right] = 3 \left(\frac{u'}{U} \right)^2 \quad (2.5)$$

Under these assumptions, calculations of k/U^2 and $\overline{uv}/U^2 = -\tau/\rho U^2$ result in Figure 2.12, which indicates that the

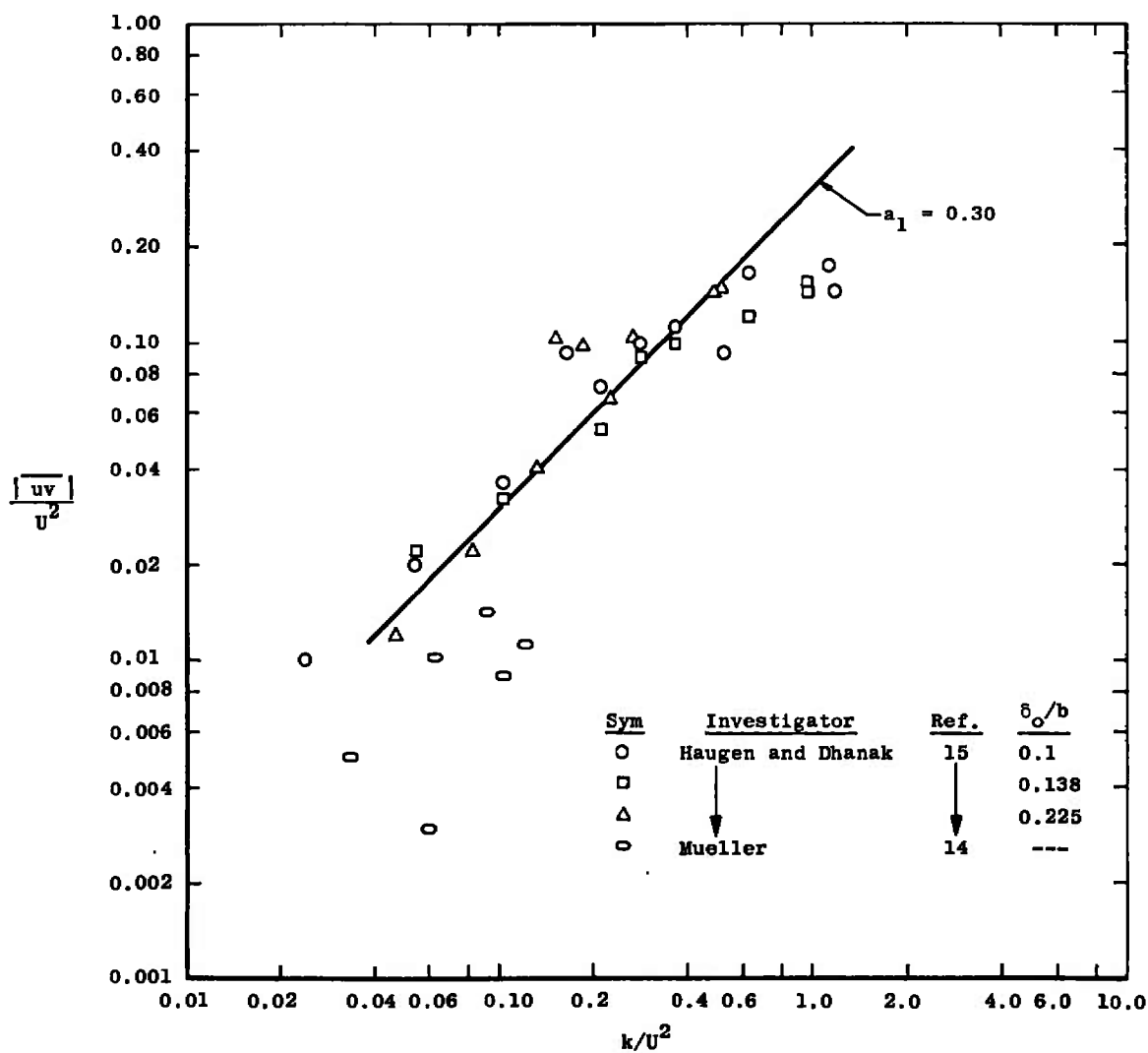


Figure 2.12. Ratio of turbulent shear stress to turbulent kinetic energy, 2D mixing layer data of Mueller [14] and Haugen and Dhanak [15].

average value of $a_1 = \tau/\rho k$ may be somewhat less here than it is for other configurations, such as the two-dimensional jet into still air, and as will be seen, axisymmetric jets and wakes. However, the experimental scatter and the assumptions necessary to obtain Figure 2.12 preclude reaching any detailed conclusion from these data. Further, the extremely large values of k/U^2 measured by Haugen and Dhanak, which arise from values of u'/U of 0.6 or more, cast serious doubts on the accuracy of these measurements.

Chapman [16] experimentally investigated the approximately two-dimensional mixing layer, unbounded on both sides, found in the first regime of a circular free jet. This configuration is similar to Figure 2.11 (d), page 40. The jet diameter for most of his tests was 2.50 inches (63.5 mm). Various lengths of nozzle section, ranging from 9 to 65 mm were used to generate different initial boundary layer thicknesses and different exponents for the assumed power-law variation of velocity profile. Of the sixteen different experiments, with different initial thicknesses δ_0 and exponents m ,³ nozzle exit boundary layer data are given for three and velocity ratio plots at several downstream locations for five. Only two of the initial boundary layer plots are for tests for which the downstream data are given. Tests for which velocity profile data are

³ m is defined by the equation $U/U_0 = (y/\delta_0)^{1/m}$.

available are summarized in Table 2.2. All profiles are presented by Chapman in transformed coordinates, U/U_0 versus $\eta = \lambda y/x$ where λ is a constant, x is a coordinate measured along the free streamline, and y is a coordinate normal to x . Sufficient information to convert to physical coordinates is given only for the $m = 4.0$ and $m = 7.0$ cases. Chapman encountered difficulty in converting the other cases, with large discrepancies appearing between the theoretically predicted conversion factor and the one necessary for good agreement with experimental data. One possible explanation for some of these discrepancies is apparent in Table 2.2. If one very crudely relates the two-dimensionality of the flow to the error resulting from assuming that the flow area per unit length (circumference) is simply δ , the mixing layer thickness, it is quickly shown that the fractional error involved is of the order of δ/D , where D is the jet diameter. From Table 2.2 it can be clearly seen that this ratio is substantial, for all but the $m = 7.0$ case, even at the initial station, indicating that the assumption of two-dimensionality for this flow is not particularly good. Interestingly enough, momentum checks (made without assuming two-dimensional flow) for the two cases which can be converted to physical variables indicate that the more nearly two-dimensional flow measurements are also quite accurate.

TABLE 2.2

TESTS FOR WHICH VELOCITY PROFILE DATA ARE GIVEN; A. J. CHAPMAN [16]

Jet Velocity U_o (cm/sec)	δ_o (mm)	δ_o/D_j	m	Axial Stations for Velocity Profile Data, x/δ_o	Initial Boundary Layer Profile?	Momentum Check Percent of Average
4520	7.4	0.116	2.3	0.95, 2.7, 4.7, 7.4	yes	-
4700	7.4	0.116	3.0	3.0, 7.0, 13.8	no	-
4650	9.5	0.150	4.0	1.6, 3.2, 6.4, 10.75	yes	4.77
4370	10.0	0.158	5.0	2.0, 4.0, 6.0, 8.0	no	-
6550 ^a	3.0	0.068	7.0	2.0, 3.3, 4.7, 9.7	no	0.37

^aUsed 0.875 inch (22.2 mm) nozzle exit.

Velocity profiles for the $m = 7$ case and the $m = 4$ case, converted to physical variables, are presented in Figures 2.13 and 2.14, respectively.

The two-dimensional half jet experiment of Liepmann and Laufer [17] was a configuration such as that sketched in Figure 2.11 (e), page 40. Such a configuration is, with the closely similar first regime of a two-dimensional jet (the half-jet being as the name implies half of the two-dimensional jet), the closest approximation to the ideal two-dimensional mixing layer attainable. The reason for the dividing plate which reduced the configuration to a half-jet is, according to Liepmann and Laufer, to reduce the influence of any draft in the room on the half jet and improve its two-dimensional character. Csanady [13], however, cautions that it is conceivable that the presence of the divider could introduce a somewhat different large-eddy pattern to the flow than might be the case without it; however, Csanady's analysis indicates that even if so this would not introduce a significant influence.

In Liepmann and Laufer's apparatus the jet emerged from a 7.5-inch by 60-inch slot, for an 8:1 aspect ratio, at 59 feet per second. The boundary layer at the end of the slot was laminar, 0.1 cm thick; the mixing layer underwent a transition to turbulent flow at $x \approx 6$ cm and became fully-developed (based on velocity profile similarity) for $x \approx 30$ cm, or at a length Reynolds number of 3.7×10^5 . The

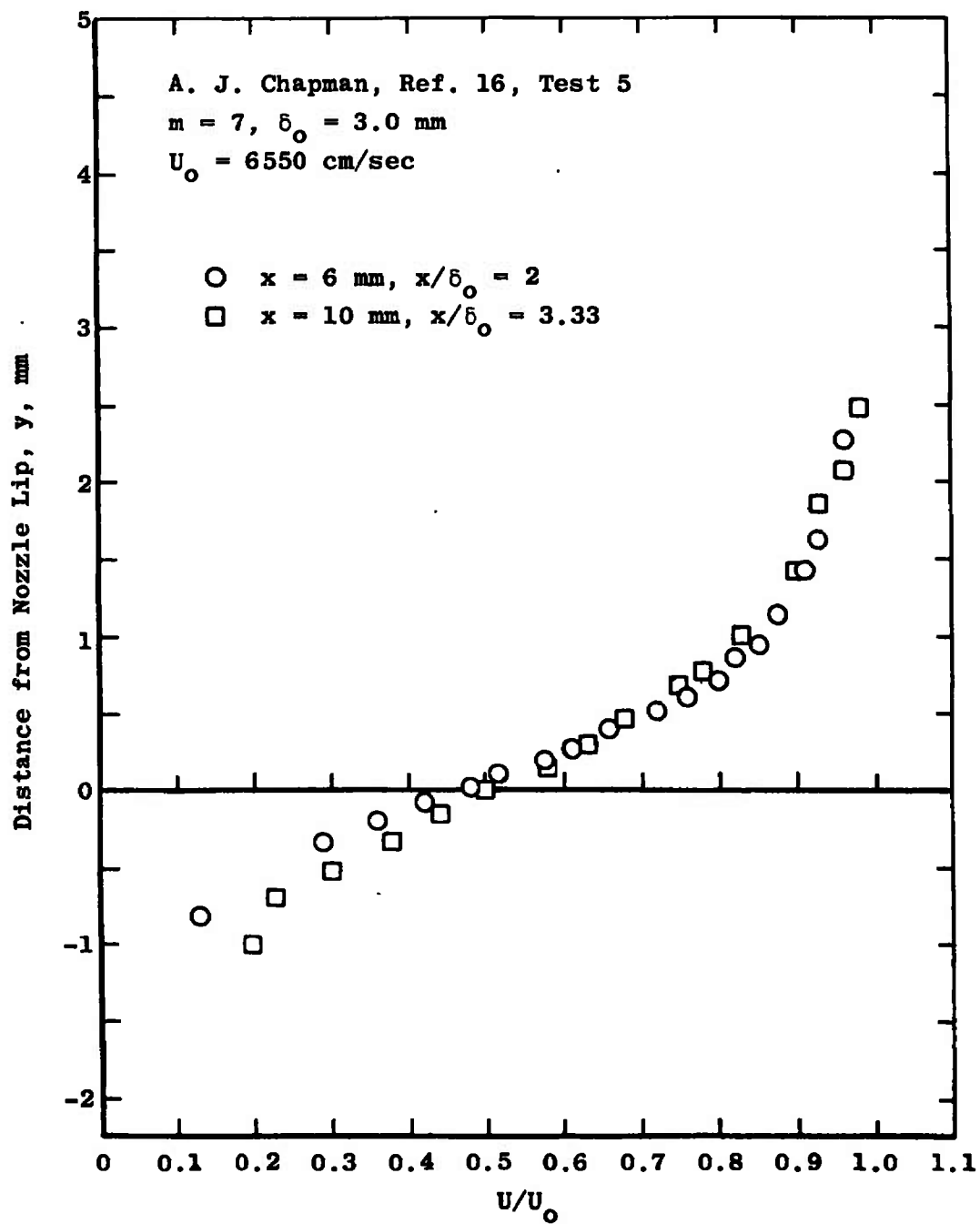


Figure 2.13. Mean velocity profiles, 2D mixing layer, Chapman, test 5.

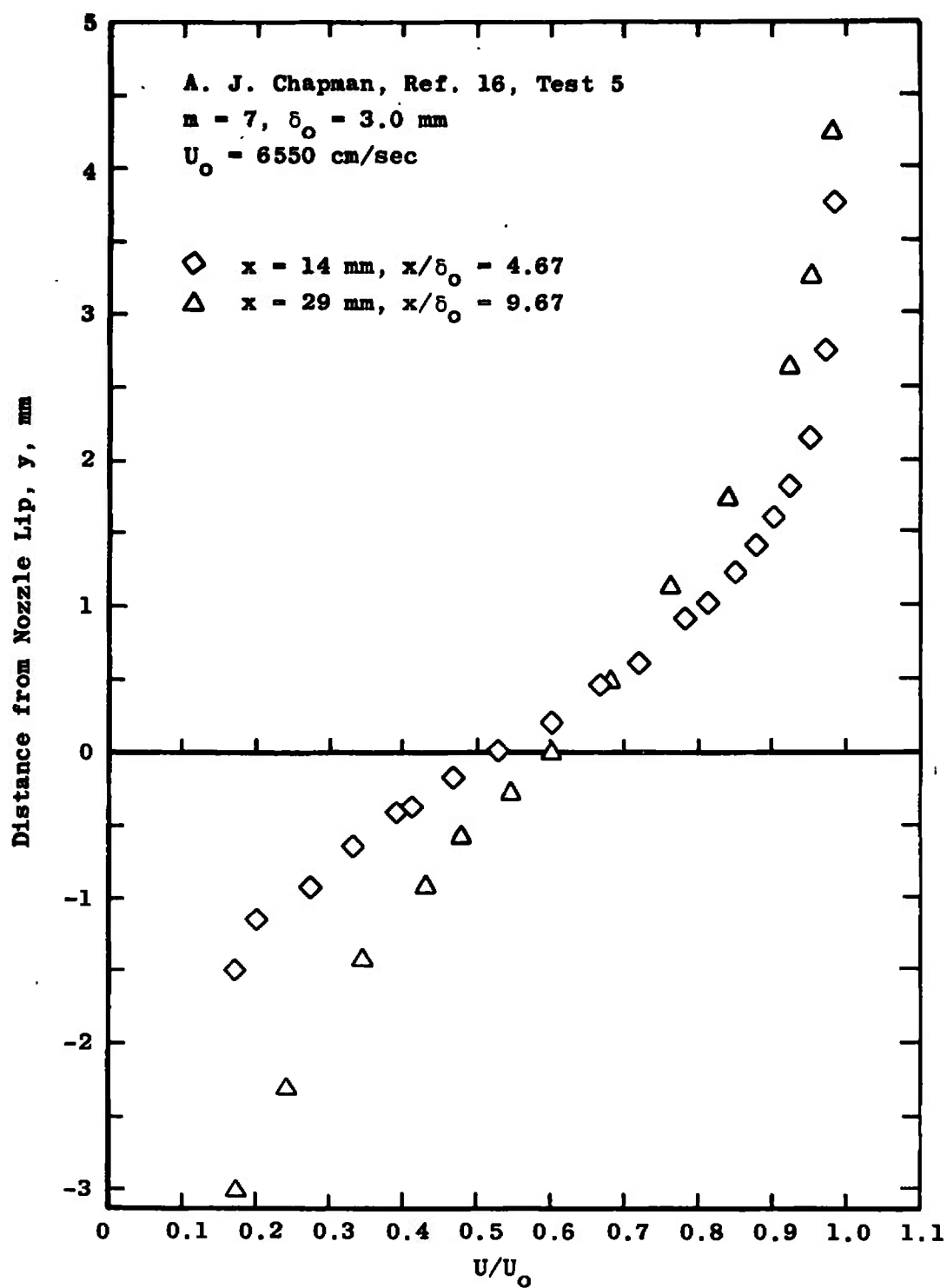


Figure 2.13. (continued)

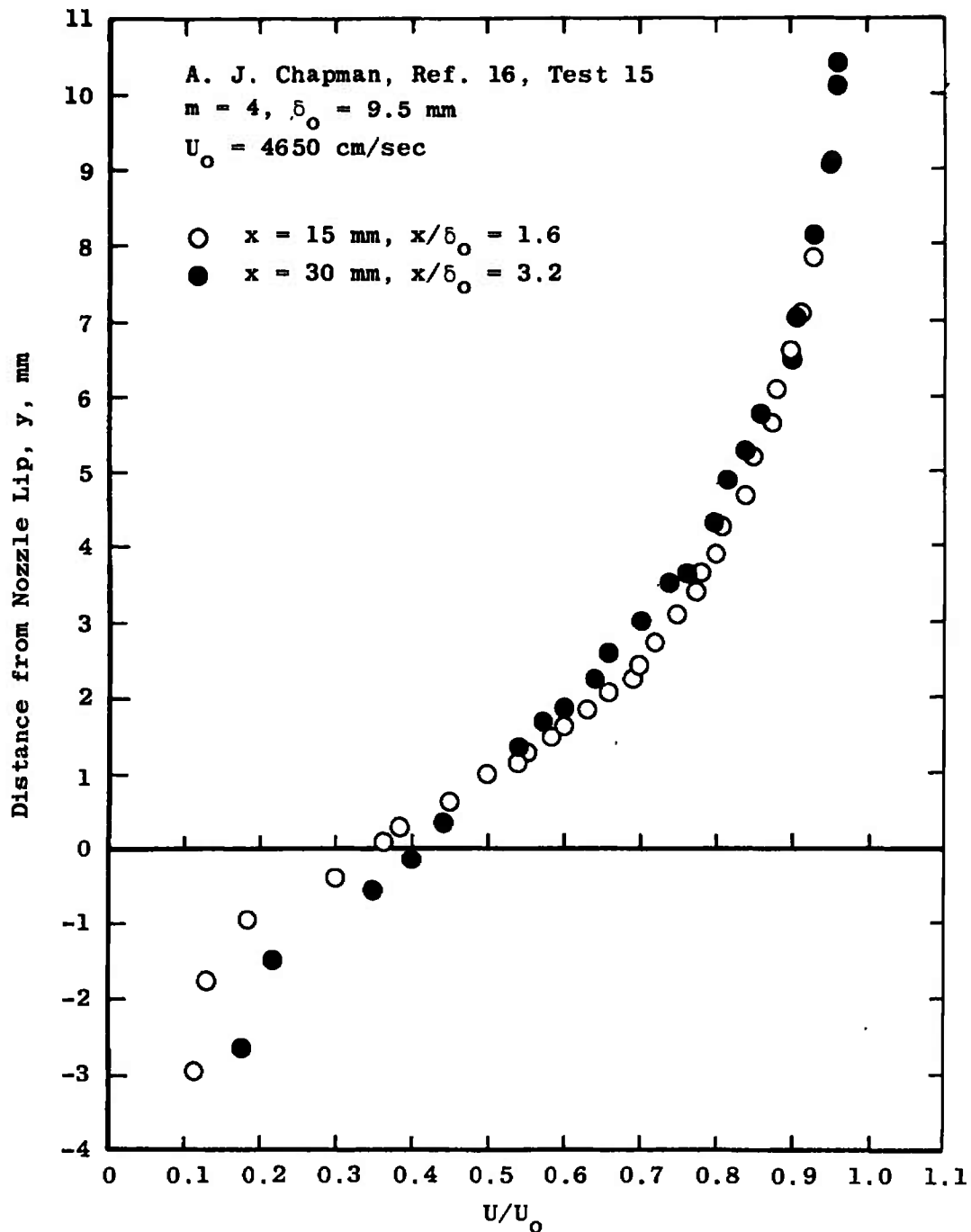


Figure 2.14. Mean velocity profiles, 2D mixing layer, Chapman, test 15.

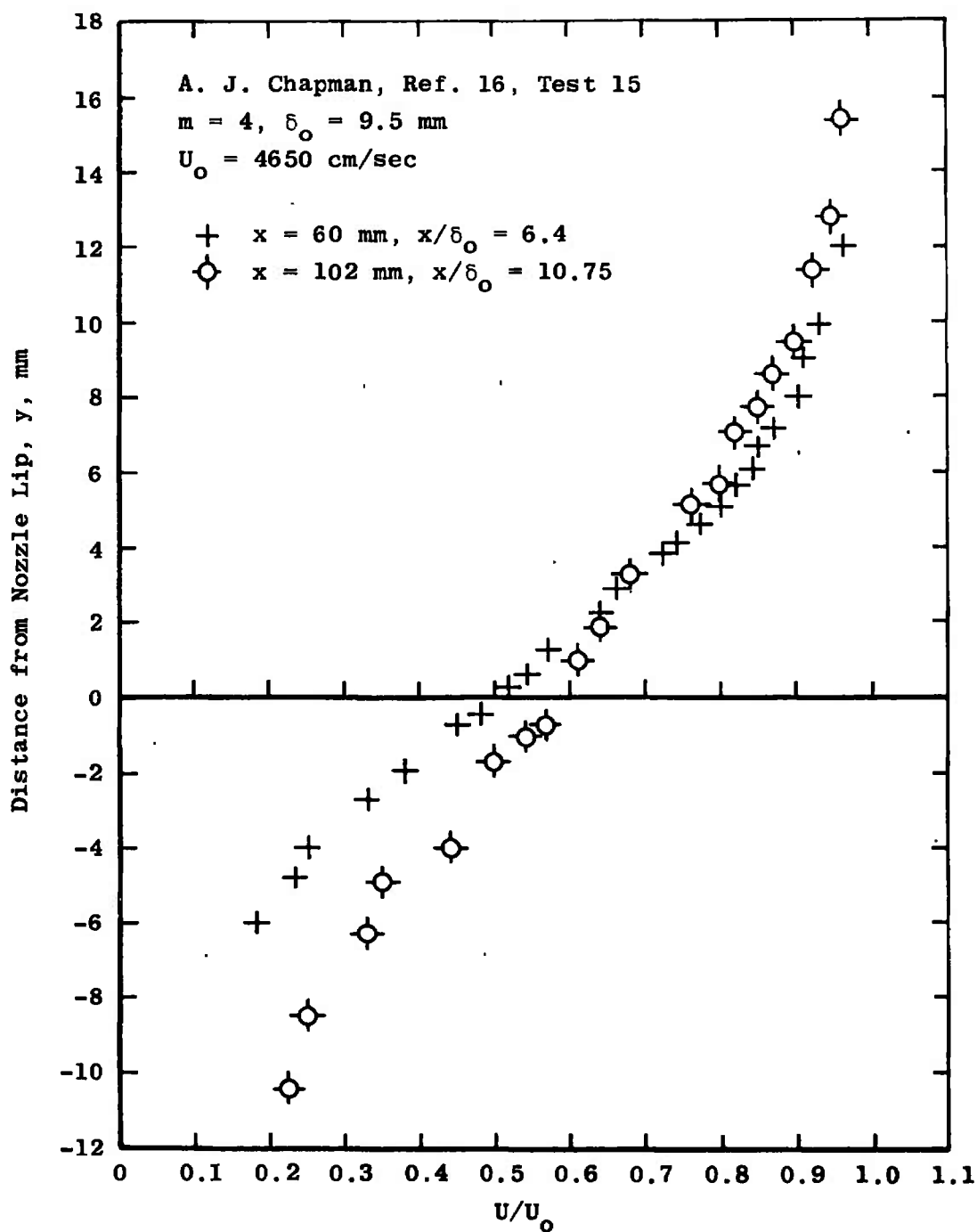


Figure 2.14. (continued)

result that the flow was fully-developed at $Re_x = 3.7 \times 10^5$ was confirmed by Bradshaw, et al., [18] in the first regime of a circular jet.

Liepmann and Laufer presented mean velocity profiles, distributions of the longitudinal and lateral components of the fluctuating turbulent velocity, and of the turbulent shear, and distributions of correlation coefficients and terms of interest in the kinetic energy equation, at three axial stations: $x = 30, 54.3, \text{ and } 75 \text{ cm}$. All distributions were presented with the lateral coordinate y nondimensionalized by θ , where

$$\theta = \int_{-\infty}^{\infty} \frac{U}{U_0} \left(1 - \frac{U}{U_0}\right) dy \quad (2.6)$$

is the momentum defect thickness at the axial station. The exception was the mean velocity, which was presented both as a function of y/θ and of y . During the course of the present investigation, θ was evaluated and the values obtained are given in Figure 2.15 along with a comparison of the velocity profiles obtained from the nondimensional profiles and the profiles given as a function of the physical variable y by Liepmann and Laufer.

The linear relationship between turbulent shear and turbulent kinetic energy demonstrated in Reference [12] is well supported by this data, as shown in Figure 2.16, while a profile of the parameter a_1 versus the lateral

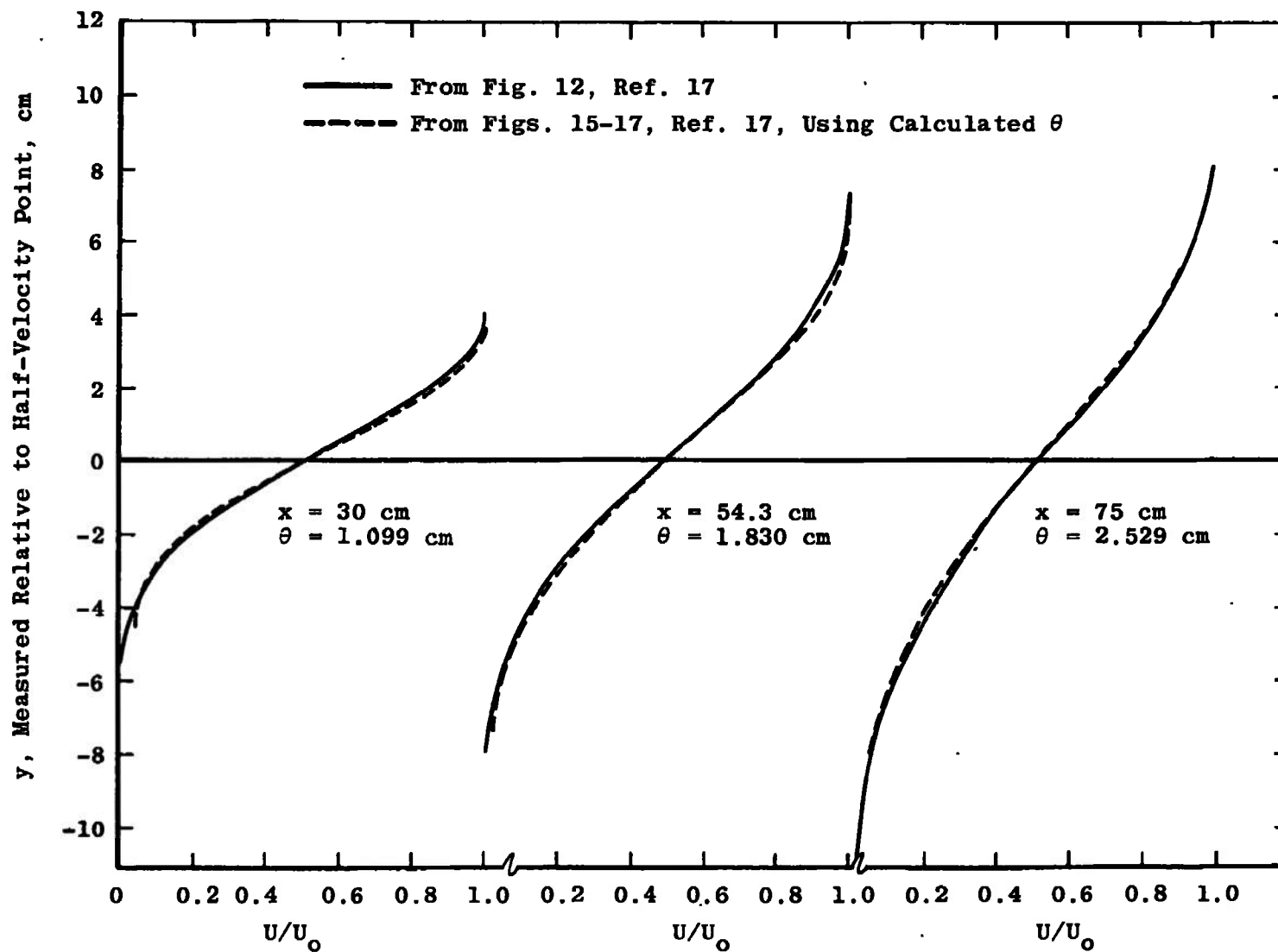


Figure 2.15. Mean velocity profiles, 2D half jet.

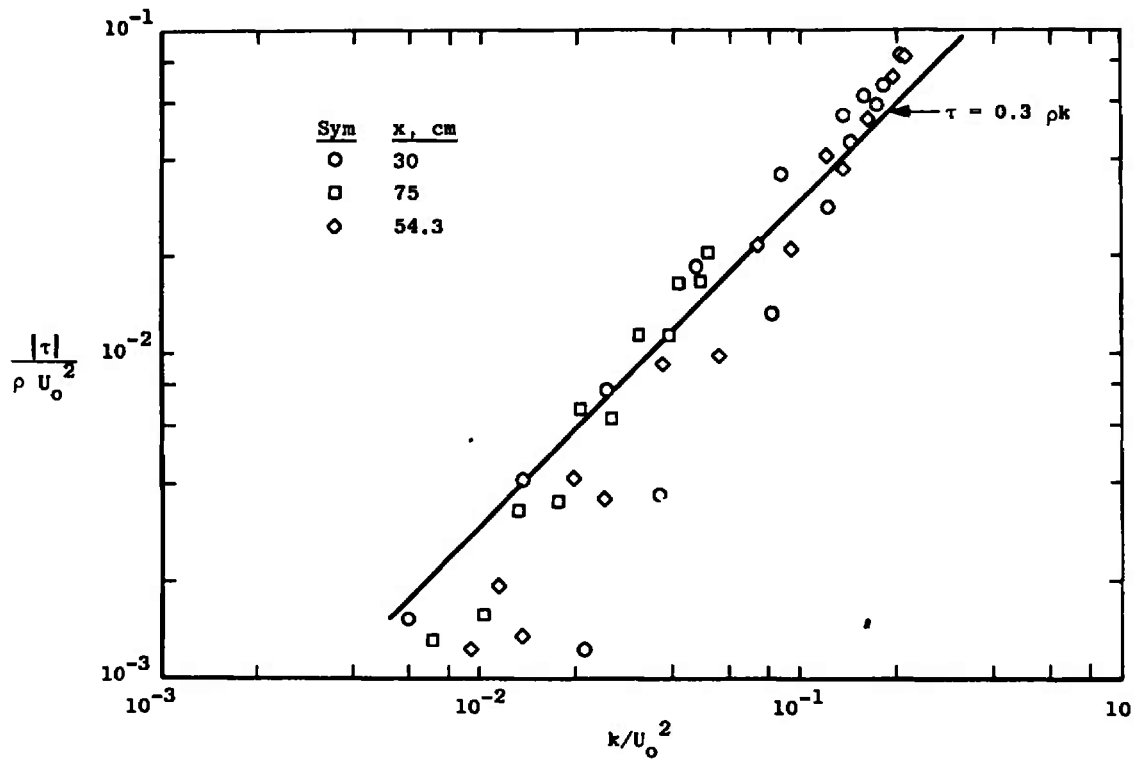


Figure 2.16. Relation between turbulent shear stress and turbulent kinetic energy, 2D mixing layer.

coordinate qualitatively similar to those already seen for the two-dimensional jet is also obtained. This is shown in Figure 2.17. Results of the evaluation of the momentum deficit integral for this experiment indicate that these measurements achieved a good level of accuracy; the maximum deviation in the integral momentum deficit is 2.4 percent of its average value.

Liepmann and Laufer compared the hot-wire shear stress profiles they measured with shear stresses calculated using an integral technique and assuming an error-function velocity profile, which is in good agreement with their experimental results. W. L. Chow [19] repeated these calculations, using the same form for the velocity profile and the same method for evaluation of the constants involved as Liepmann and Laufer used, and found that the latter work was in error. Furthermore, Chow stated that the value of the constant of integration chosen by Liepmann and Laufer was based on incorrect physics; the turbulent shear stress does not have its maximum at the inflection point of the profile for an error function profile. Figure 2.18 illustrates the results obtained by Liepmann and Laufer and by Chow, in comparison with the experimental data. It should be noted that discrepancies between the measured turbulent shear stress and that obtained from the mean flow profile are encountered in nearly every turbulent flow experiment.

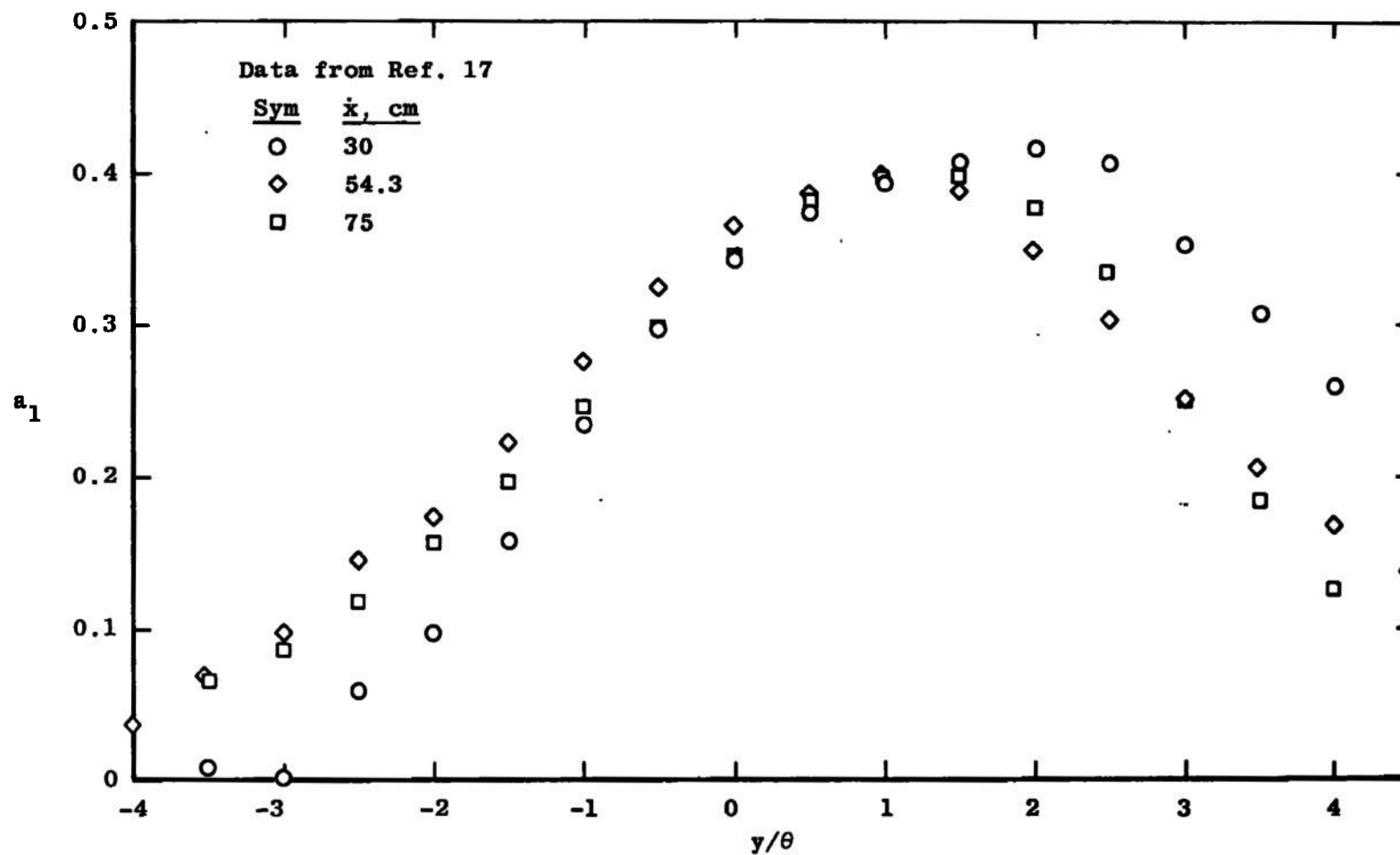


Figure 2.17. Lateral profile of a_1 , 2D mixing layer.

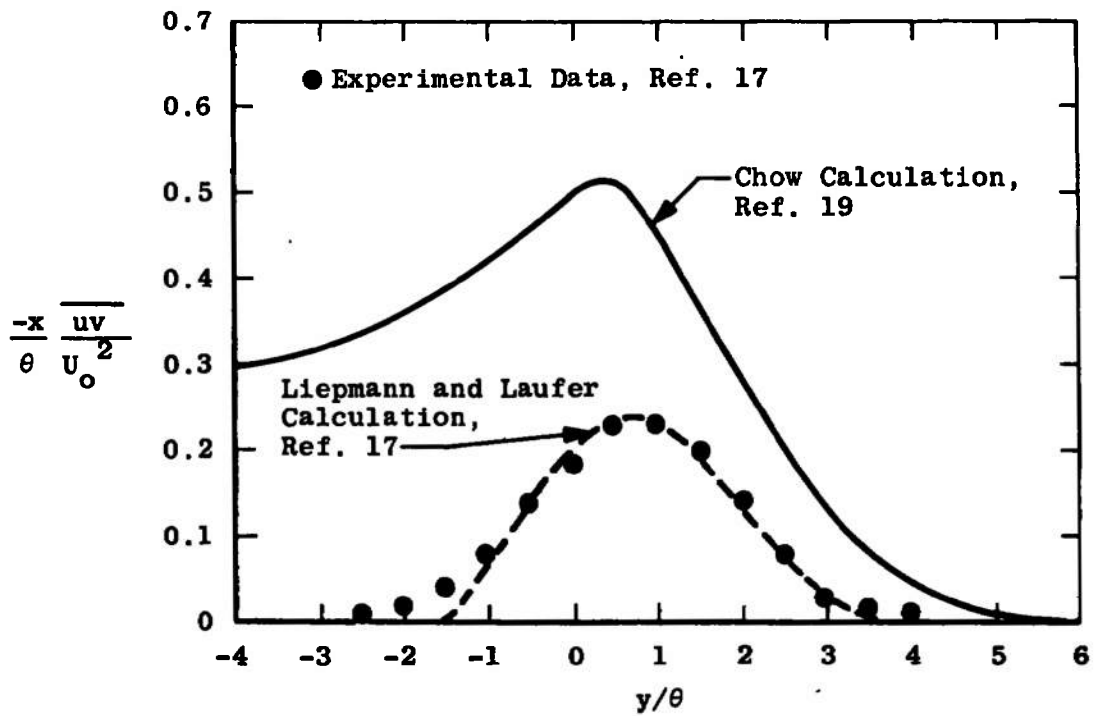
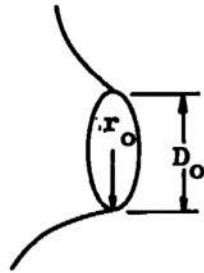


Figure 2.18. Comparison of experimentally measured shear stress with shear stress calculated from assumed velocity profile, 2D mixing layer.

The Circular Jet

The largest single group of experiments in free turbulent mixing is that concerned with the circular jet into still air, as this configuration is probably the easiest to realize experimentally. In general, the flow resembles the two-dimensional jet into still air already described. As shown in Figure 2.19, the flow can be divided into two major regimes, coupled together by one transition regime and separated from the nozzle by another transition regime. This first transition regime, in which the turbulent structure changes from a boundary-layer character to that of a free mixing layer, is usually small compared with the nozzle dimensions, probably comparable in length to the thickness of the boundary layer at the exit of the nozzle. It is followed by a quasi-plane mixing layer in which the flow is self-preserving, and velocity and intensity profiles are geometrically similar when plotted against $(\eta = y - r_0)/x$ [18]. This regime is called "Regime I" on Figure 2.19. Departures from similarity begin as the thickness of the mixing layer becomes an appreciable fraction of the nozzle radius, and the flow enters a second transition region. Some distance downstream a second self-preserving state is reached. The distance from the nozzle exit to this region (Regime II in Figure 2.19) is given variously as 10 diameters [8] to 20 diameters [18]; Wygnanski and Fiedler [20], on the other hand, state that



$$U = 0$$

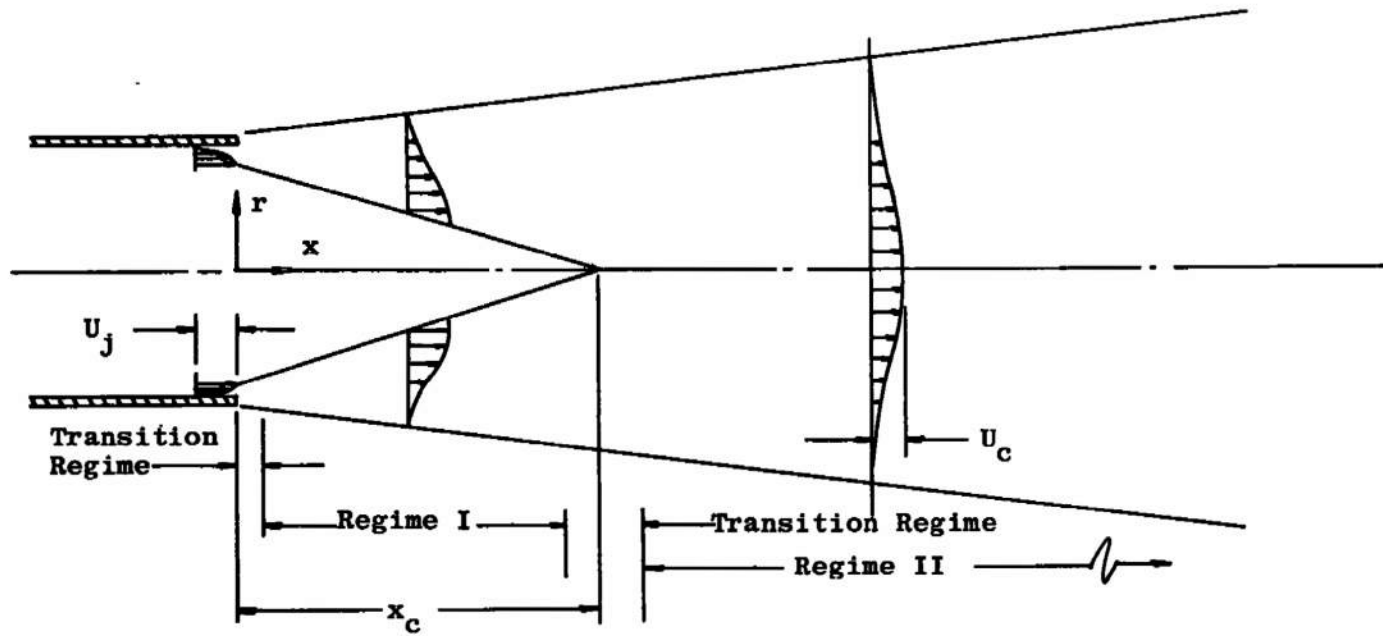


Figure 2.19. Circular jet-into-still-air.

"true" self preservation--i.e., geometrically similar profiles of not only the mean flow quantities but also the turbulence intensities and the turbulent shear stress, as well as $U_c/U_j \propto x^{-1}$ and lateral width scale proportional to x --is not reached until more than 70 diameters downstream. For the purpose of discussion, the beginning of the second regime will be taken to be at the point where the mean velocity profiles become geometrically similar, i.e., by $x/D = 20$.

As for the two-dimensional jet, there is a scale effect of the jet Reynolds number which seems to persist quite far downstream, as shown in Figure 2.20 taken from Baines [21]. Newman [3] (see Appendix C), shows that for the circular jet in still surroundings under the assumption of similar velocity profiles in the variable

$$\eta = r/b$$

where b is the local width, $U_c/U_j \propto (x/D)^{-1}$ and $b \propto x$ for self-preservation. It can be seen from Figure 2.20 that the data of Baines remain shifted as long as these relations hold. Indeed it can be shown (Appendix B) that under the assumption of similar profiles the equations for the decay of mean flow quantities can be written for the circular jet, as for the two-dimensional jet, in terms of one parameter, the nondimensionalized core length, x_c/D . It can also be shown (as in Appendix B) that for incompressible coaxial

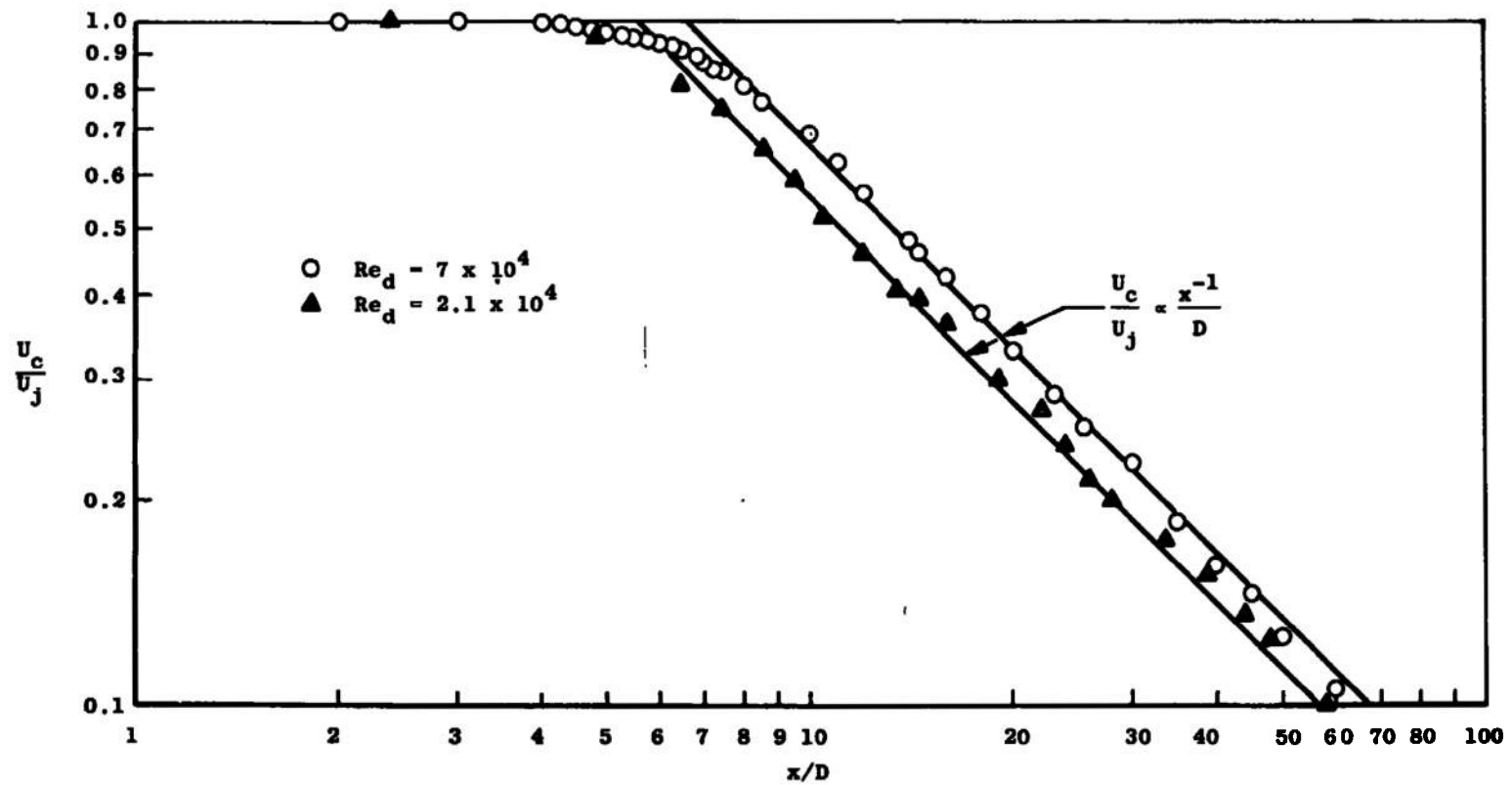


Figure 2.20. Axial velocity decay, circular jet, zero secondary: data from Baines [21].

jets, similar profiles and the equation of conservation of momentum lead to expressions for the velocity decay containing only the potential core length and the stream velocity ratio.

This dependence of the downstream decay rates on the potential core length makes the flow visualization experiment performed by Binnie [22] of some interest. By using a jet of a mixture of a solution of iodine in potassium iodide with a solution of starch, a deep blue color is obtained. The jet drops through a short airspace into a tank, filled with a solution of sodium thiosulfate ("hypo"), which instantly removes the color. By this means the potential core region is selectively visualized. Although the experiment is flawed by the density discontinuity that the jet undergoes in passing from air to liquid, not to mention the free-surface effects, the observation that the core ends in a "wagging tail" is of interest. This may indicate the presence of alternating vortices at the end of the core. It may also be, as far as free mixing is concerned, an entirely spurious effect of the peculiar geometry used; however, the technique appears to be worth adapting to a true free mixing flow.

Table 2.3 gives the important parameters for the circular jet experiments included in this section. All of the regimes of interest have been investigated, with the exception of the first transition regime. Diameter Reynolds

TABLE 2.3
THE CONSTANT-DENSITY CIRCULAR JET INTO STILL AIR

Investigator	Ref.	Year	U_j ft/sec	D_j in.	Re $\times 10^{-4}$ ^a	Maximum x/D	Momentum Check, ^b Percent
Corrsin	23	1943	32.7	1.0	1.75	40	35 at $x/D=40$
Hinze and van der Hegge Zijnen	24	1949	131.0	1.0	6.7	40	-
Baines	21	1950	-	-	2.1	58	-
			-	-	7.1	60	-
Albertson, et al.	8	1950	102.5	1.0	5.45	65	<10 at $x/D=60$
			165.0	0.5	4.38	120	(author's
			170.0	0.25	2.26	250	measurement)
Corrsin and Uberoi	25	1950	65-115	1.0	3.4-6.1	25	<10 ^c
Taylor, et al.	26	1951	390.0	0.9	18.6	31.5	< 4
Alexander, et al.	27	1953	49.0	0.898	2.33	30	-
			57.0		2.71	30	-
			92.0		4.38	30	-
			104.0		4.95	30	-
			177.0		8.43	30	-
			363.0		17.25	30	<4 at $x/D=10$ ^d
			403.0		19.18	30	-
			803.0		38.22	30	-
Davies, et al.	28	1963	($M=0.2$)	1.0	-	10	-
Bradshaw, et al.	18	1964	($M=0.3$)	2.0	35.0	7.5	<1 at $x/D=7.5$
Sami	29	1966	35.0	12.0	22.0	10	5 at $x/D=10$
Wyganski and Fiedler	20	1969	236.0	1.04	13.0	97.5	7 at $x/D=45$ ^e
			167.0		9.24	97.5	8 at $x/D=97.5$ ^e

^aReynolds number based on jet diameter, D_j .

^bMomentum check in maximum percent deviation from average.

^cCalculated using similarity expressions and measured width.

^dAuthor's measurement.

^eTwo sets of curves, one $30 \leq x/D \leq 50$, second $60 \leq x/D \leq 97.5$.

numbers range from 2.3×10^4 to 3.8×10^5 , with measurements being carried to 250 diameters downstream. Axial and radial distributions of the mean flow velocity have been obtained by a number of investigators, as summarized in Table 2.3. Centerline velocity ratio decay data taken from these experiments are summarized in Figure 2.21, from which it can be seen that all of the experiments adhere fairly closely to the family of curves $U_c/U_j \propto (x/D)^{-1}$ as demanded by conservation of momentum under the assumption of self-preservation of velocity profiles. The two lines drawn indicate the limits of nozzle exit Reynolds number encountered in these tests. It can be seen that the length of the velocity potential core increases with increasing Reynolds number. This curve does not, however, take into account the effects of turbulent intensity level at the nozzle exit, as these data are not generally reported. Changes in the level of turbulent intensity at the jet exit may also have an influence on the length of the potential core, as described by Flora and Goldschmidt [9].

The experiments of Taylor, Grimmer, and Comings [26] are reported in terms of the ratio of the square root of the momentum flux density to the density $\sqrt{\rho U^2/\rho}$, rather than the normally reported velocity. This is due to questions that arise when a total head tube is used in a turbulent flow concerning the effect of instantaneous turbulent velocity fluctuations on the pressure reading. In an

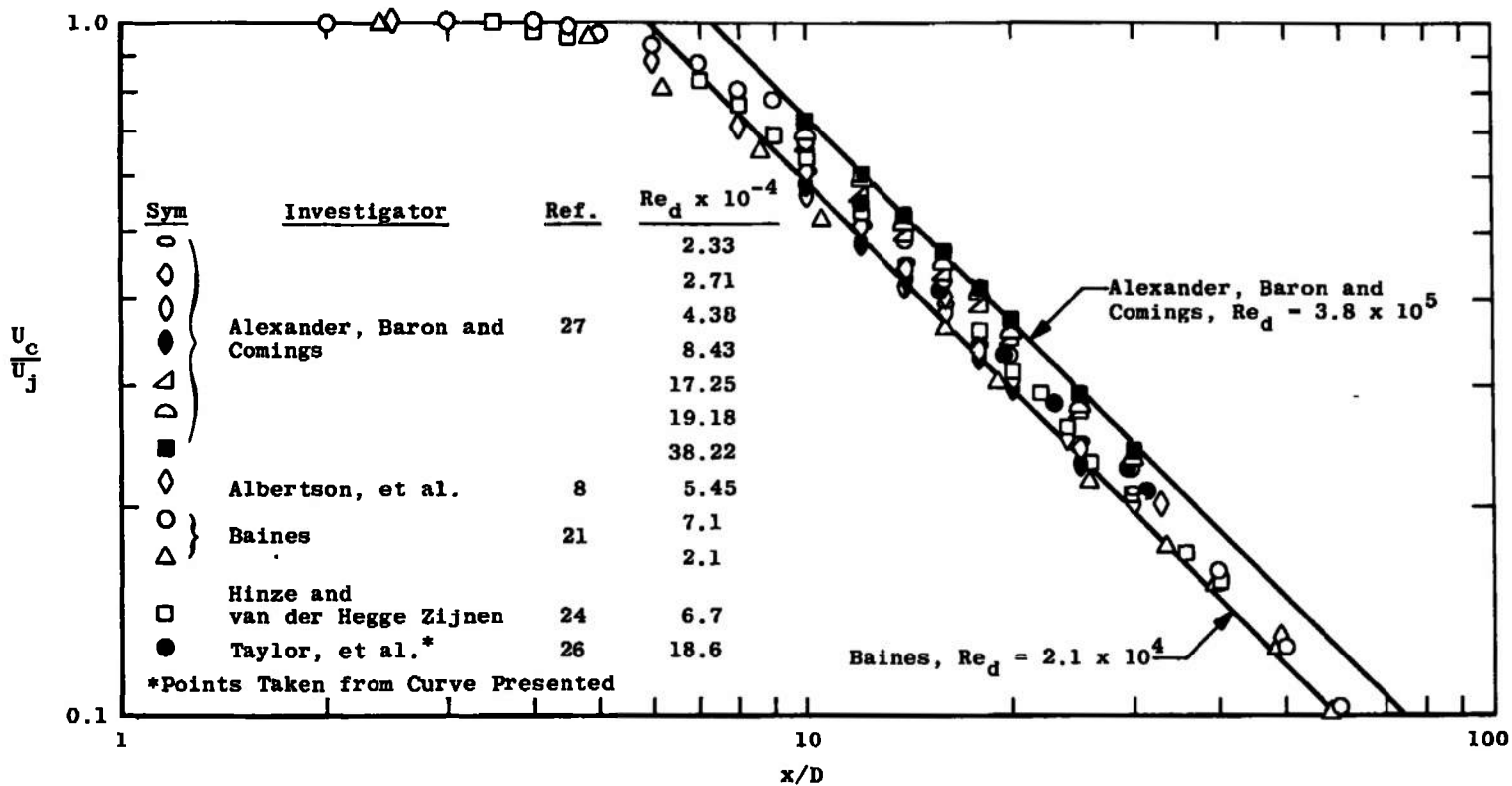


Figure 2.21. Axial decay of centerline velocity ratio, circular jet-into-still-air.

incompressible flow if the instantaneous velocity is written as the sum of an average velocity \bar{U} and a fluctuating velocity u (whose time-average is zero), one has

$$U = \bar{U} + u$$

so

$$U^2 = \bar{U}^2 + 2\bar{U}u + u^2$$

Taking the time average

$$\overline{U^2} = \overline{\bar{U}^2} + \overline{2\bar{U}u} + \overline{u^2} = \bar{U}^2 + \overline{u^2} \text{ as } \bar{u} \equiv 0$$

Thus, in incompressible flow, $\bar{\rho} = \rho$ and

$$\overline{\rho U^2} = \bar{\rho} \bar{U}^2 + \bar{\rho} \overline{u^2} \tag{2.7}$$

so that

$$\overline{\rho U^2} = \bar{\rho} \bar{U}^2$$

Equation (2.7) implies that the reading of a total head tube will increase with increasing turbulent intensity. However, as reported by Hinze [30, page 135], when this effect was investigated by Alexander, Baron and Comings [27], they found that the total head tube reading decreased markedly with increasing relative turbulent intensity. Because of observations such as this, and the fact that from Equation (2.7)

$$\overline{\rho U^2} = \bar{\rho} \bar{U}^2 [1 + (\overline{u^2}/\bar{U}^2)] \quad (2.8)$$

so that for

$$u'/U = \sqrt{\overline{u^2}}/U = 0.2$$

$$\overline{\rho U^2} = 1.04 \bar{\rho} \bar{U}^2$$

the deviation of the total head tube reading caused by changes in turbulent intensities are commonly ignored.

Hinze and van der Hegge Zijnen [24] present their data both in uncorrected form and using a correction similar to Equation (2.8) with intensity data taken from Corrsin [23]. There is no significant difference between the results, particularly at the scale represented by the figures in Reference [24]. In addition to measuring the momentum flux in the jet, they also made measurements of temperature distribution in a jet heated to approximately 30°C above the surroundings, and mass transfer measurements in a jet seeded with town gas at an initial concentration of one percent by volume. These measurements indicate that heat and mass mix appreciably faster than momentum, and that the rates of spread of temperature and concentration are equal. They find that the temperature spreading rate is slower than that reported by Corrsin [23]; however, the accuracy of the experiments of Reference [23] must be seriously questioned, as will be discussed below.

Albertson, Dai, Jensen, and Rouse [8] measured the axial decay of centerline velocity in a circular jet down to 250 diameters from the jet exit. Data taken from their work are shown in Figure 2.22, from which it can be seen that these data follow the " x^{-1} " decay characteristic of flows with similar profiles quite well.

Alexander, Baron, and Comings [27] measured centerline velocity ratio decays for a 0.898 inch diameter jet over the Reynolds number (based on jet diameter) range from 2.3×10^4 to 3.8×10^5 . In their experiments their pitot pressure measurements were assumed to represent the quantity $\overline{\rho U^2}$; in the following discussion, the assumption $U = \sqrt{\overline{\rho U^2} / \rho}$ has been made, which from the work of Hinze and van der Hegge Zijnen [24] introduces very little error, especially on the centerline. Table 2.4 lists the centerline velocity ratios measured by Alexander, Baron, and Comings for seven tests in the Reynolds number range listed above. These data are plotted in Figure 2.23, in which straight lines representing the relation $U/U_c \propto (x/D)^{-1}$ have been drawn through the data. The intersections of these lines with the line $U_c/U_j = 1$ defines the length of the potential core. These data have been used in this study to obtain an empirical relation for the core length as a function of jet Reynolds number, which is given by

$$\frac{x_c}{D} = 2.13 (Re_d)^{0.097} \quad (2.9)$$

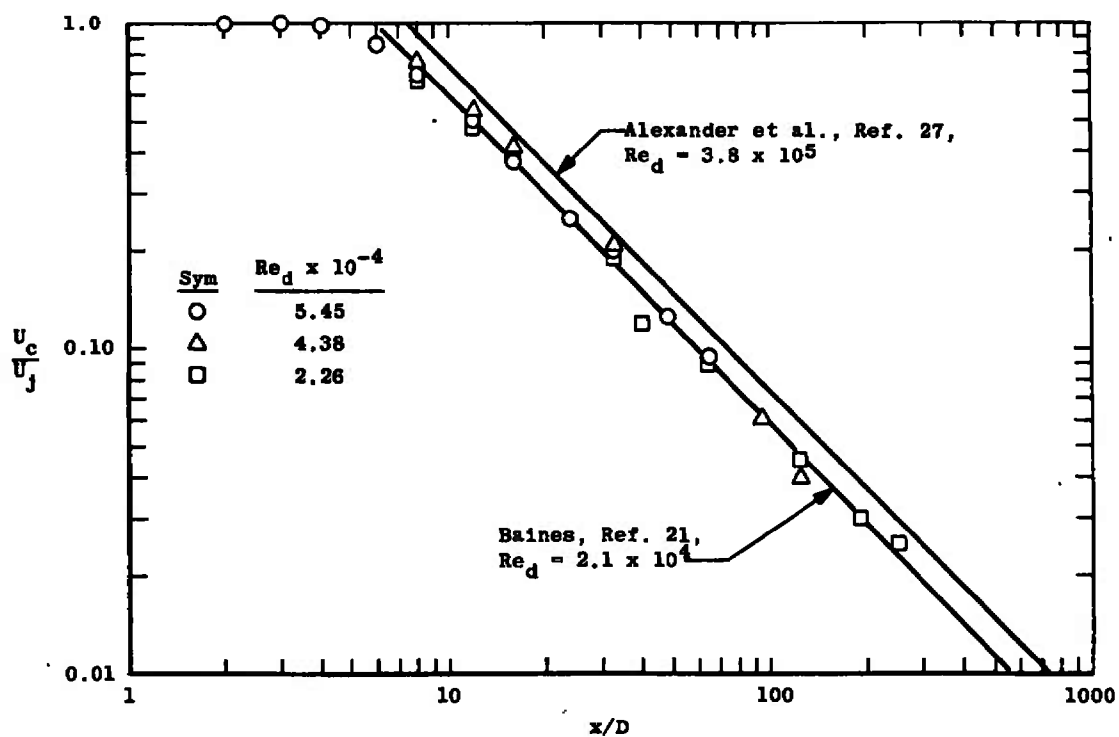


Figure 2.22. Axial decay of centerline velocity ratio, data of Albertson, Dai, Jensen, and Rouse [8].

TABLE 2.4
VELOCITY DECAY DATA FROM REFERENCE [27]

U_o (ft/sec)	49	57	92	104	177	403	803
$Re_D (x10^{-4})$	2.33	2.71	4.38	4.95	8.42	19.18	38.22
U/U_o x/D							
10	0.620	0.608	0.556	0.567	0.664	0.683	0.716
12	0.521	0.510	0.477	0.484	0.559	0.585	0.604
14	0.449	0.440	0.422	0.424	0.484	0.509	0.527
16	0.392	0.383	0.374	0.379	0.431	0.445	0.465
18	0.346	0.338	0.331	0.334	0.389	0.396	0.414
20	0.315	0.307	0.298	0.302	0.346	0.352	0.370
25	0.249	0.243	0.231	0.237	0.272	0.274	0.288
30	0.210	0.202	0.202	0.200	0.226	0.232	0.237

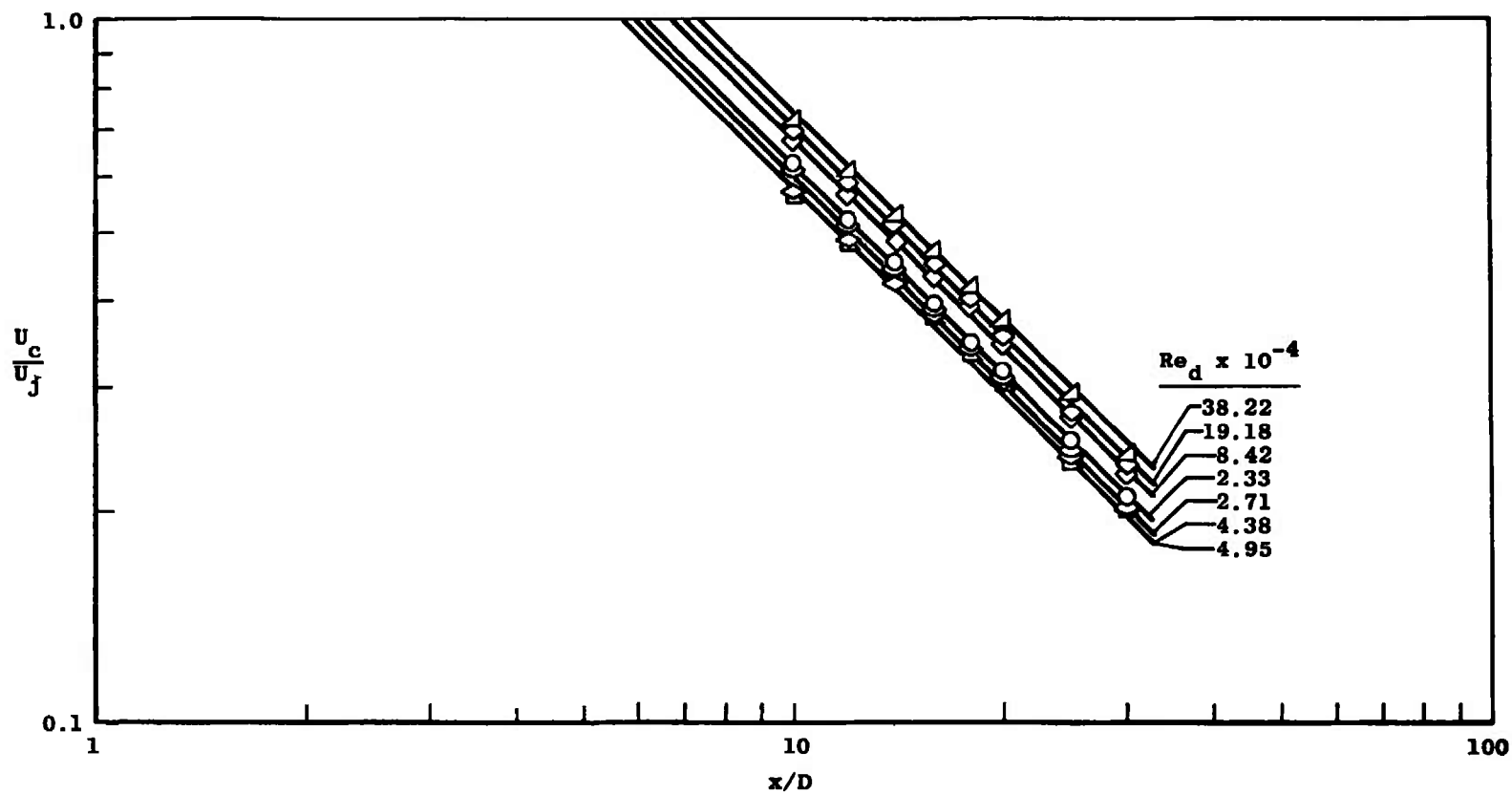


Figure 2.23. Effect of jet Reynolds number on axial decay of centerline velocity, data from Reference [27].

A comparison of the core lengths predicted by Equation (2.9) with those obtained from the experimental data in the same manner is presented in Table 2.5; in all but one case the empirical relation comes within 10 percent of the actual core length and it is generally considerably better.

This empirical correlation can be carried one step further. Baines [21] and Albertson, et. al., [8] show that under the assumption of similar velocity profiles and linear spreading rate, conservation of momentum leads to the result

$$\left. \begin{aligned} \frac{U_c}{U_j} &= 1 \text{ for } x \leq x_c \\ \frac{U_c}{U_j} &= \frac{x_c}{x} \text{ for } x > x_c \end{aligned} \right\} \quad (2.10)$$

Combining (2.9) and (2.10),

$$\left. \begin{aligned} \frac{U_c}{U_j} &= 1 \text{ for } \frac{x}{D} \leq 2.13 (Re_d)^{0.097} \\ \frac{U_c}{U_j} &= 2.13 (Re_d)^{0.097} \left(\frac{x}{D}\right)^{-1} \end{aligned} \right\} \quad (2.11)$$

These relations are also derived in Appendix B. Figure 2.24 shows a comparison of these relations with one set of the experimental data of Reference [27]. It should be noted that

TABLE 2.5
COMPARISON OF CORE LENGTH PREDICTIONS

Investigator	Ref.	Turbulence Intensity, Percent	$Re_D \times 10^{-4}$	x_c/D Predicted	x_c/D Measured	Error Percent ^a
Baines	21	0.008	7.0	6.35	7.0	10.0
		0.004	7.0	6.35	6.05	5.0
		0.008	3.0	5.85	6.05	3.33
		0.004	3.0	5.85	5.60	4.46
Corrsin	23	0.005	1.75	5.4	5.6	3.56
Hinze and van der Hegge Zijnen	24	n.a. ^b	6.7	6.25	6.5	3.85
Taylor, et al.	26	n.a. ^b	1.86	5.45	6.5	15.8
Albertson, et al.	8	n.a. ^b	5.45	6.2	6.2	0
Corrsin and Uberoi	25	n.a. ^b	3.55-6.1	5.9-6.3	6.5	3.1-9.25
Wyganski and Fiedler	20	n.a. ^b	9.24	6.6	6.4	3.2

^aPercent of measured value.

^b"n.a." indicates data not reported.

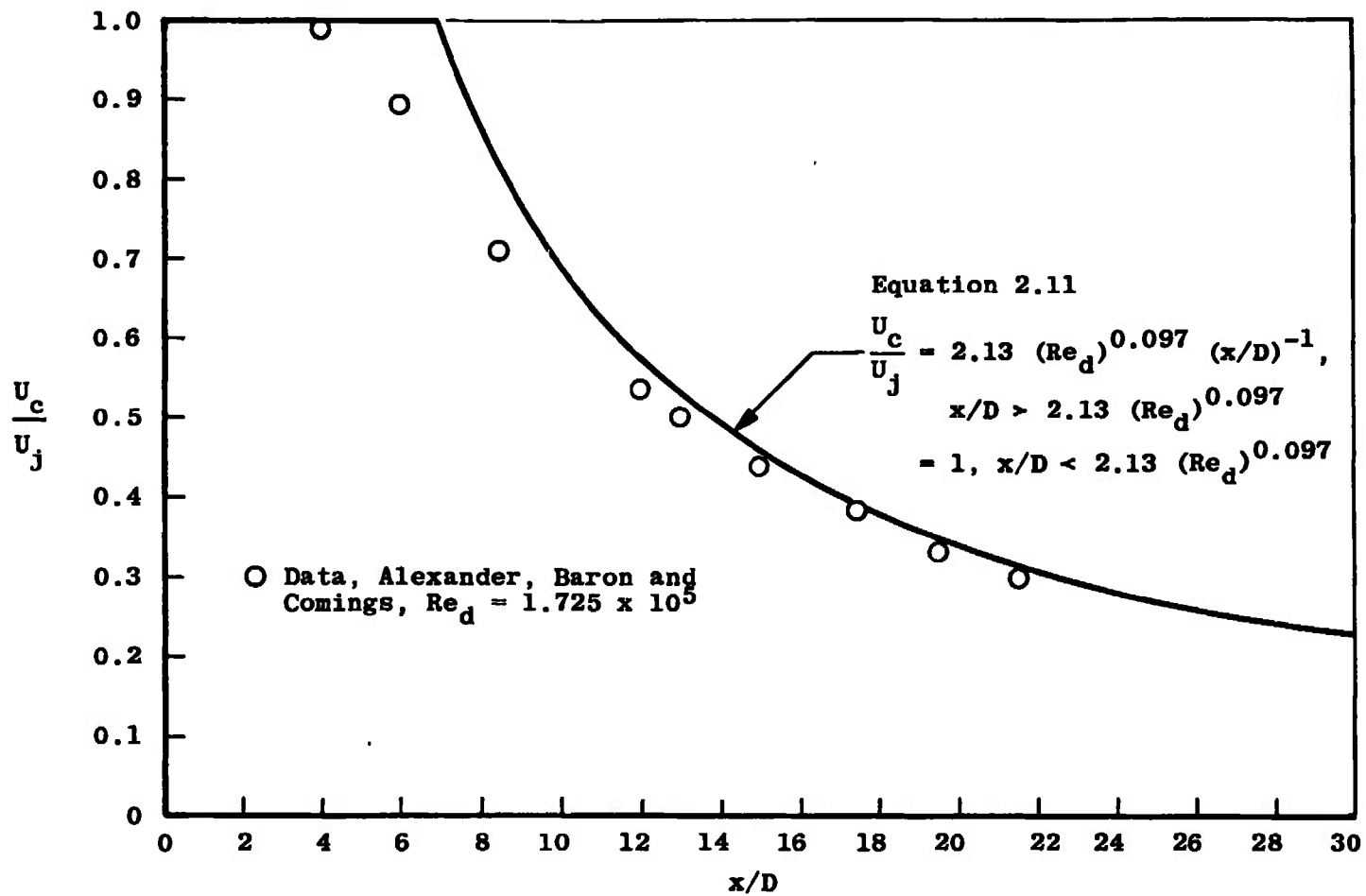


Figure 2.24. Comparison of empirical relation with axial velocity decay data of Alexander, et al., [27].

equations such as (2.11) are unable to represent the actual centerline decay behavior in the transition region from $x/D = 2$ to about $x/D = 10$.

Similarity of mean velocity profiles is always observed in the circular jet into still air. For large x/D , these profiles take on a self-preserving shape becoming a function only of the self-preserving coordinate r/x . Figure 2.25 provides an example of the shape of the velocity profile encountered.

Axial mean velocity decay data from three experiments concerned with measurements of the turbulence structure are shown in Figure 2.26. The axial decay curve for the data of Baines [21] is also shown. The convergence of the data of Wagnanski and Fiedler [20] and that of Baines [21], despite the wide variation in jet exit Reynolds number, is not easily explained. The turbulence intensities (u'/U) at the jet exit were reported by Wagnanski and Fiedler to be 0.001 and by Baines to be 0.004. If, as reported by Flora and Goldschmidt [9], the effect of increasing turbulence intensity is to enhance the mixing, decreasing the length of the potential core, while by Equation (2.9) the effect of increasing jet exit Reynolds number is to increase the length of the potential core, one would expect the data of Wagnanski and Fiedler to be considerably shifted relative to that of Baines. It must be noted that the effect of either the jet exit Reynolds number

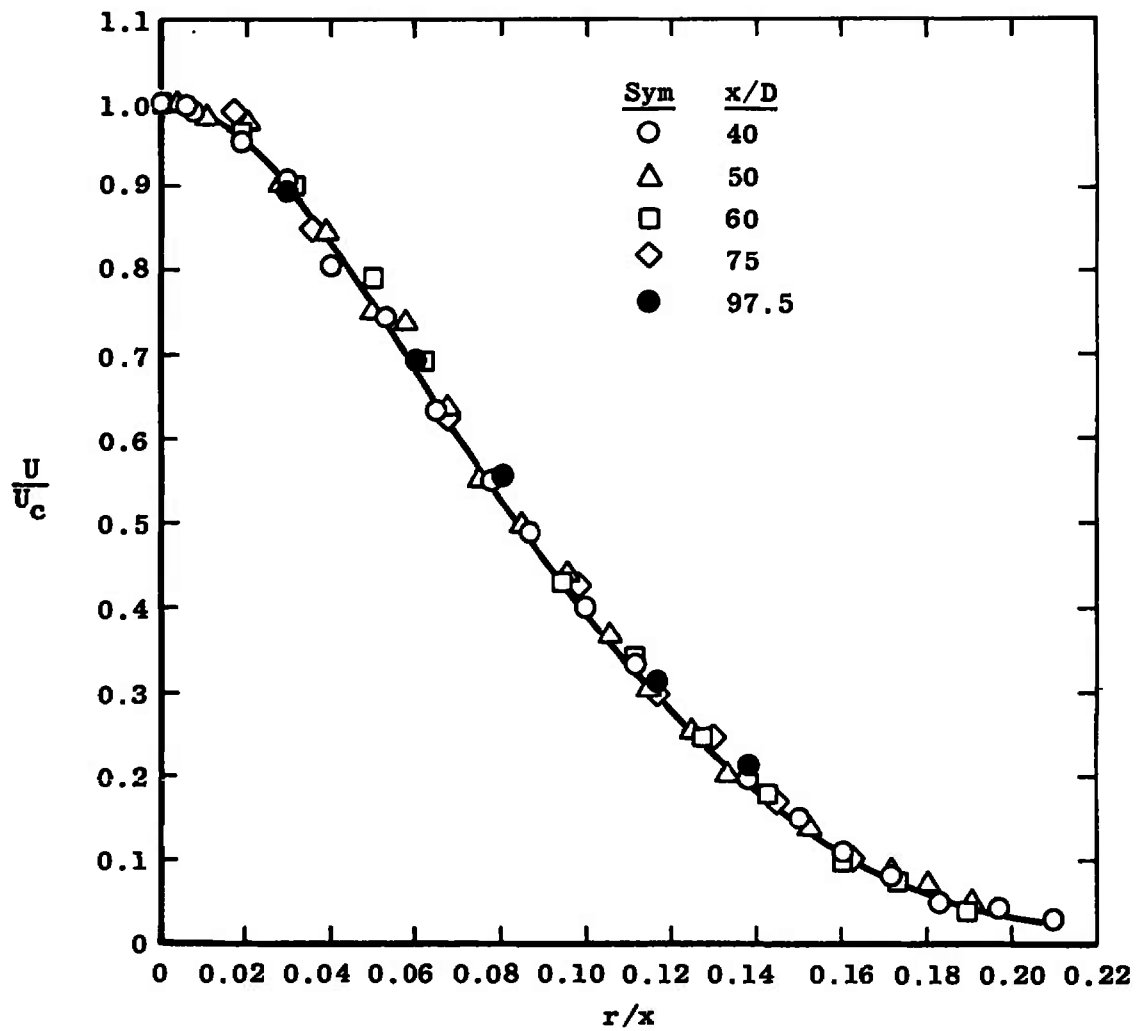


Figure 2.25. Velocity profiles in the fully-developed region, from Wagnanski and Fiedler [20]: circular jet, zero secondary.

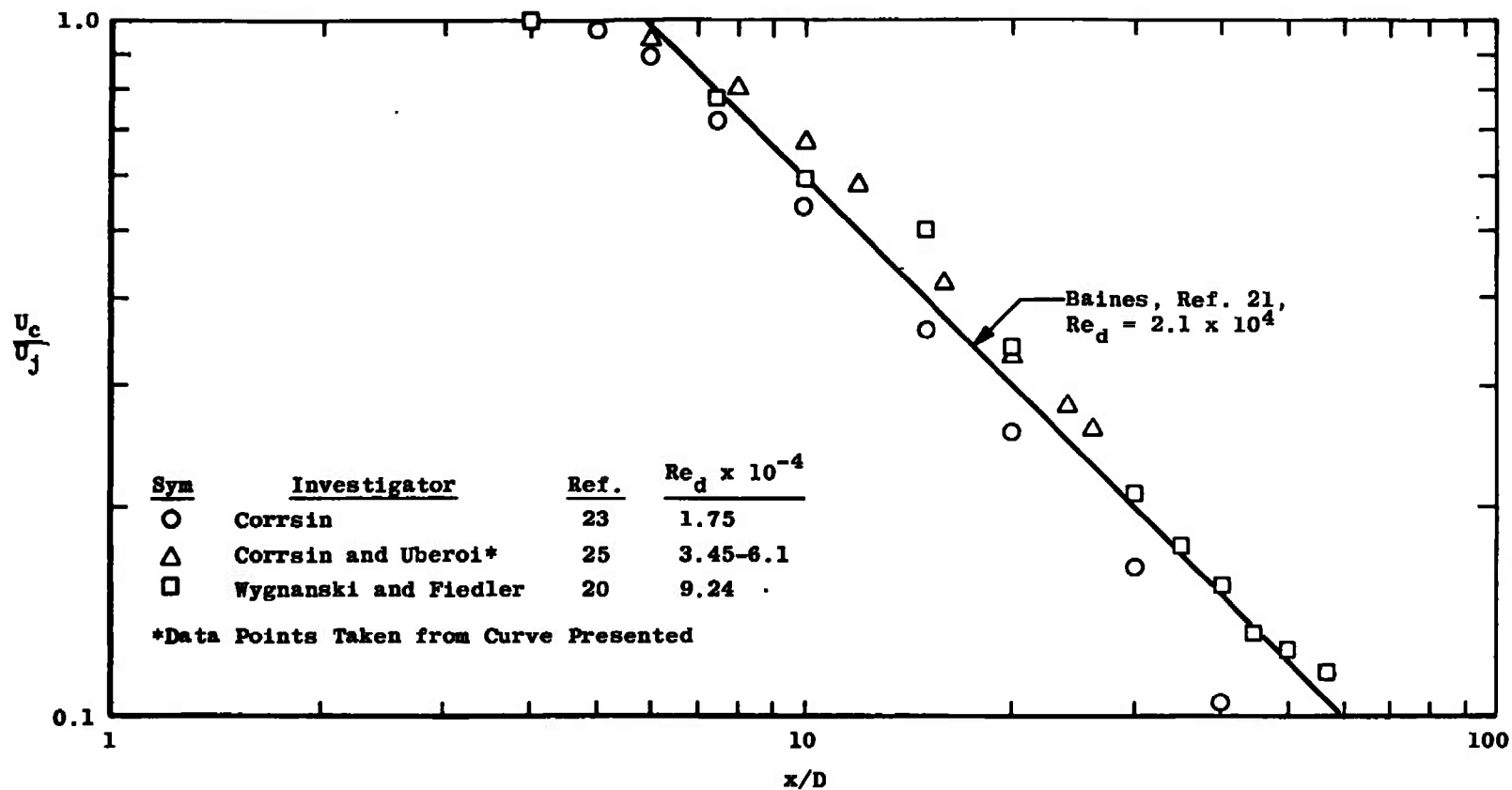


Figure 2.26. Decay of axial mean velocity, circular jet-into-still-air.

or the initial level of turbulence intensity on the length of the potential core is very incompletely understood.

It can clearly be seen from Figure 2.26 that the axial decay data of Corrsin deviate markedly from the trend established by all of the other data for this configuration. This deviation is consistent with the fact that the momentum integral is not satisfied for this flow. Table 2.6 below lists in detail the results of the calculation of the parameter M, where

$$M = \int_0^{\infty} \left(\frac{U}{U_j} \right)^2 r dr \quad (2.12)$$

TABLE 2.6
MOMENTUM INTEGRAL RESULTS FOR
DATA OF CORRSIN

x/D	M
5	0.5304
10	0.7223
20	0.4118
30	0.3652
40	0.2995

The values of M shown in Table 2.6 were calculated using the measured velocity profiles of Reference [23]; the continual

decrease in the value (which to satisfy the criterion of conservation of momentum should be constant) agrees with the data of Figure 2.26 which show a continual decrease in the value of U/U_j on the centerline for the Corrsin data compared to other available data for this flow.

Further evidence of the existence of this discrepancy is shown in Figure 2.27 which compares with the axial turbulent intensities measured by Corrsin [23] with those measured by Corrsin and Uberoi [25] in a similar apparatus. The investigation of Corrsin and Uberoi was primarily concerned with the flow of a highly-heated jet into still surroundings; however, some check data were taken in a one inch jet with only a small temperature difference (15°C). These latter data were used in constructing Figure 2.27. Comparison of the original Corrsin data with that of Corrsin and Uberoi shows that there is substantial disagreement, despite the similarity of conditions and axial position. If, however, the value of the centerline velocity ratio is adjusted from the value of 0.255 measured at $x/D = 20$ by Corrsin, to the value of 0.33 measured at $x/D = 20$ by Corrsin and Uberoi (whose data satisfy the criterion of the constancy of the momentum integral to within ten percent--Table 2.3, page 65), the curve labeled "corrected U_c " on Figure 2.27 is obtained. This curve is seen to provide much better agreement with the data of Corrsin and Uberoi.

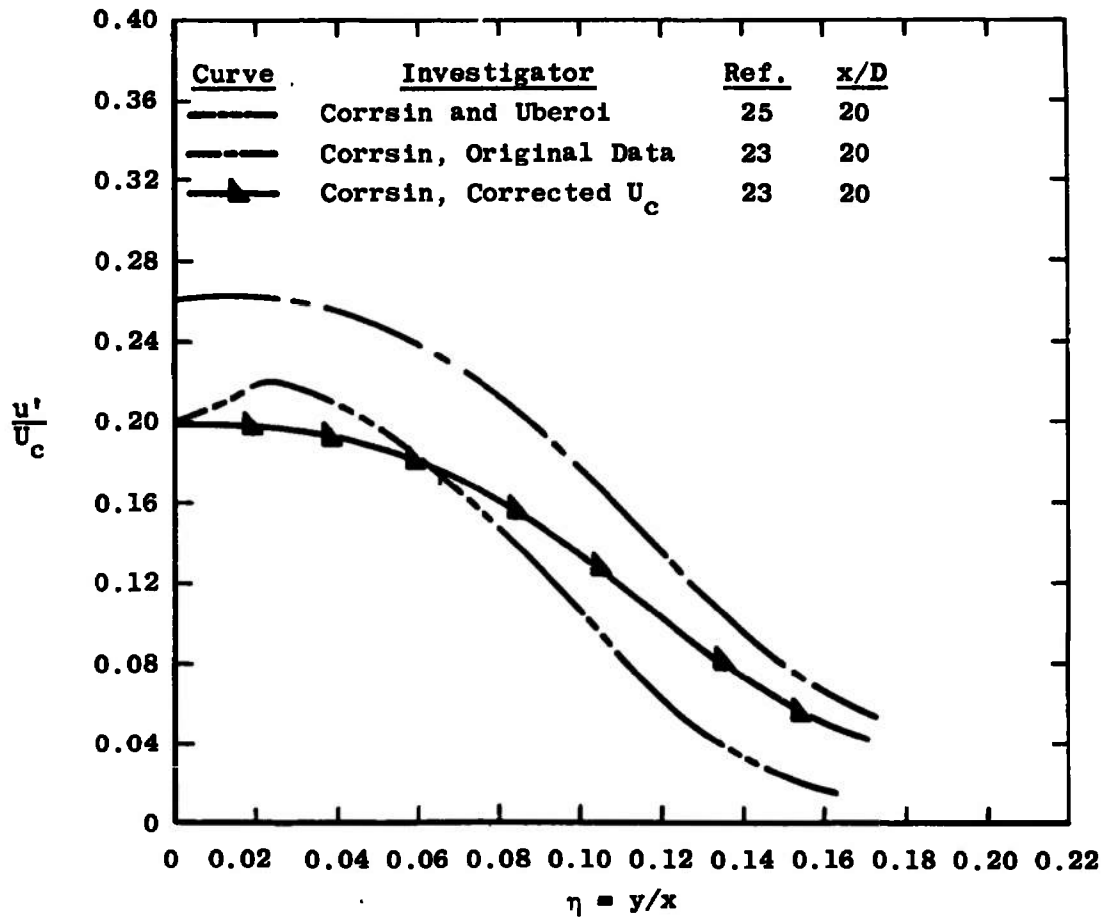


Figure 2:27. Comparison of measurements of axial turbulent intensity, data of Corrsin [23] and of Corrsin and Uberoi [25].

Two of the turbulence structure experiments were concerned primarily with the first regime of mixing--those of Davies, et al., [28] (also Davies [31]) and Bradshaw et al., [18]. The first of these is primarily an investigation of the noise production of a turbulent jet and hence provides little experimental information of interest in this study. The description provided by Davies, et al., [28] of the flow in the first regime is however of some interest:

. . . there is an initial zone in which the turbulence intensity grows rapidly. The extent of this is only a few inches and depends on the dimensions of the boundary layer flow at the jet orifice. Beyond this is a region extending well past the end of the potential core in which the intensity is constant and the flow is in equilibrium. . . . The present results indicate that a . . . self-preserving region extends from eight or so diameters to close to the jet orifice. . . .

Two points are of interest in this description. One is that a self-preserving region exists well past the end of the first regime (the length of the potential core in this experiment was 4.5 diameters) through the transition region and into the second regime. The other is the description of an "initial zone in which the turbulent intensity grows rapidly." This phenomenon will be encountered again in the study of the developing wake flow behind a flat plate.

An investigation of the same flow region, from $x/D = 0$ to $x/D = 7.5$ was performed by Bradshaw, et al., [18]. In this case profiles of the three components of the turbulent intensity and the turbulent shear stress were measured at three stations: $x/D = 2$, 4, and 7.5. Sami [29]

performed a detailed study of this region, measuring at axial locations $x/D = 1, 3, 6$, and 10 , all three intensity components, the turbulent shear stress, and all of the terms encountered in the turbulent kinetic energy equation except the pressure-velocity correlation. A not completely successful attempt was made to measure this quantity also. Sami's work thus complements that of Bradshaw, et al., [18] and extends it somewhat farther into the second regime. Results of these two experiments will be seen to agree quite well.

The detailed experiments of Wygnanski and Fiedler [20] may well be the most significant of this section. In these experiments a linearized constant-temperature hot-wire anemometer was used to probe the flow in the "truly self-preserving" region of a jet into still air. The "truly self-preserving" region is that in which not only the mean velocity profiles but also the turbulent intensity profiles exhibit self-preservation. In addition to measuring profiles of the turbulent intensities and shear stress, as well as the spectral quantities and distributions of the terms of the turbulent kinetic energy equation, Wygnanski and Fiedler critically examined the assumptions underlying the use of hot-wire anemometry. This examination may have solved one of the most vexing problems in the use of hot-wire anemometry, which is the apparent inability of the hot-wire anemometer to accurately measure the level of the

turbulent shear stress as compared to values of the turbulent shear stress obtained from the mean-flow velocity and density profiles.

The apparent inability of the hot-wire anemometer to measure accurately the turbulent shear stress level has been mentioned before and will be encountered in later discussions. Most commonly this discrepancy arises when the measured turbulent shear stresses are compared with those calculated by integration of the mean flow velocity profile (see for example, Reference [24]), but it has also appeared in the comparison of measurements made by two or more methods. Thus Jezdinsky [32] in comparing the results obtained from hot-wire probes and pressure probes of a novel design in the same flow, finds that the hot-wire measurement of the turbulent intensity is lower than the pressure-probe measurement by 10 percent and the discrepancy in shear stress is 13 percent in the same direction. Wygnanski and Fiedler [20] attribute this type of error to low-frequency response errors in the hot-wire equipment previously used. Their results indicate that if the hot-wire signal is clipped at 2 Hz, an error of 27 percent will result in the measurement of $\overline{u^2}$ with corresponding errors in the other quantities. It should be noted here that the turbulent shear stress profiles are measured using a x-wire array, which is also used to obtain the intensity profiles, by appropriate manipulation of the hot-wire output signal.

Thus, if as Wagnanski and Fiedler indicate, errors are encountered due to electronic clipping of the signal, it would be expected that these errors would be found in all components of the turbulence measured. The error in the shear stress measurement would be the most obvious, as this quantity, unlike the turbulent intensities, can also be obtained from mean-flow measurements. The fact that, given the Wagnanski and Fiedler hypothesis, similar errors would be made in all turbulence components as well as in the turbulent shear stress measurement is of obvious importance in the interpretation of the calculation of the parameter a_1 . Wagnanski and Fiedler [20] quote a comparison between their measurements of $\overline{u^2}$ at $x/D = 20$ (using a correlator of their own design tested for linearity to 0.05 Hz) and those of Corrsin and Uberoi [25] at the same point (using equipment whose frequency response was not tested below 7 Hz); the measured values of Corrsin and Uberoi are 25 percent lower than those of Wagnanski and Fiedler. Further results obtained by Wagnanski and Fiedler using "standard" equipment--linear response to 5 Hz--showed $\overline{u^2}$ profiles "significantly lower" than those measured with the equipment linear to 0.05 Hz and thus in better agreement with the Corrsin-Uberoi data.

In an attempt to investigate this result further, Table 2.7 was constructed from the available data for a number of configurations. While the evidence is not

TABLE 2.7

CORRELATION BETWEEN LOW-FREQUENCY LIMIT AND ERROR IN
MEASUREMENT OF TURBULENT SHEAR STRESS

Investigator	Year	Ref.	Flow Configuration	Estimated Error in Shear Measurement ^a	Low Frequency Limit, Hz
Corrsin and Uberoi	1950	25	Axisymmetric Jet	12%, low	7
Sami	1966	29	Axisymmetric Jet	15%, low	n.a. ^b
van der Hegge Zijnen	1958	12	Plane Jet	20%, low	n.a. ^b
Carmody	1964	33	Wake	30%, low	n.a. ^b
Bradbury	1965	34	Plane Jet ^c	0%, slightly low	0 ^d
Zawacki and Weinstein	1968	35	Coaxial Jets	20%, low	n.a. ^b
Wynanski and Fiedler	1970	36	Mixing Layer	0%, slightly low	0.05

^aIn percent of mean flow shear.^bIndicates data unavailable.^cNonzero secondary.^dQuoted as "d.c."

overwhelming, due to a common lack of information about the low-frequency limit of the equipment used, there is nothing in Table 2.7 to contradict the conclusion of Wygnanski and Fiedler. Clearly hot-wire experiments in which care is taken to provide linear frequency response to the lowest limit possible would be of interest in a variety of configurations.

Figures 2.28 through 2.30 compare the measurements of u'/U_c , v'/U_c , and \overline{uv}/U_c^2 made by Corrsin [23], Corrsin and Uberoi [25] (u'/U_c only), Sami [29], Bradshaw, et al., [18], and Wygnanski and Fiedler [20] for the circular jet into still air. Except in Figure 2.28, Corrsin's data are shown both in "corrected U_c " and "uncorrected U_c " forms. Possible corrections to account for low-frequency errors as described above have not been made; they would not change the general conclusions. From these figures it is clear that there is a steady increase in the values of all of these quantities (over most of the profile) with x/D . Since if similarity existed for the turbulent components the curves would collapse together, the conclusions of Reference [20] regarding "true self-preservation" seem substantiated. There is, however, a general similarity of profile shape in the "grossly self-preserving" part of the second regime, for $x/D \geq 20$.

Figure 2.31 shows that the linear relationship between turbulent shear stress and turbulent kinetic energy

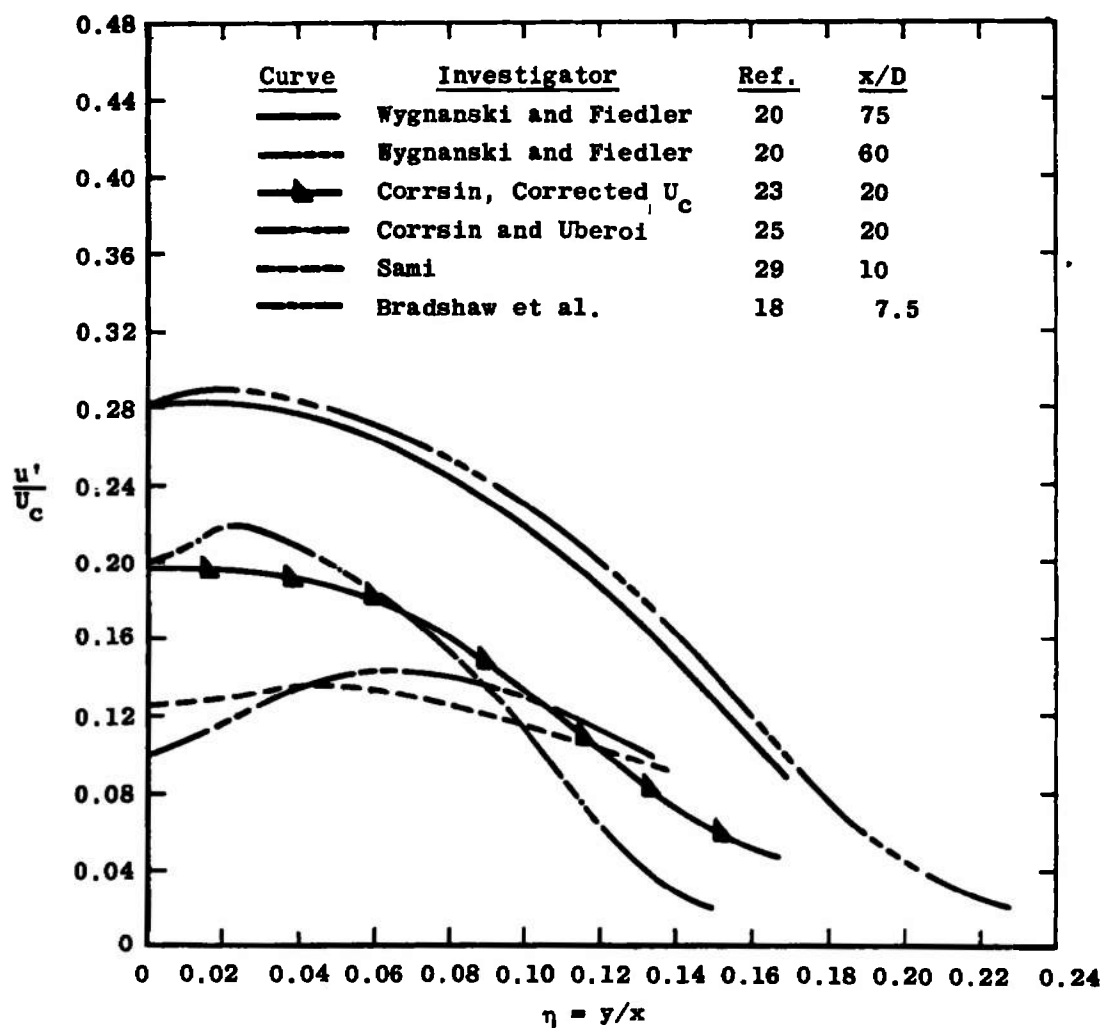


Figure 2.28. Axial component of turbulent intensity, circular jet-into-still-air.

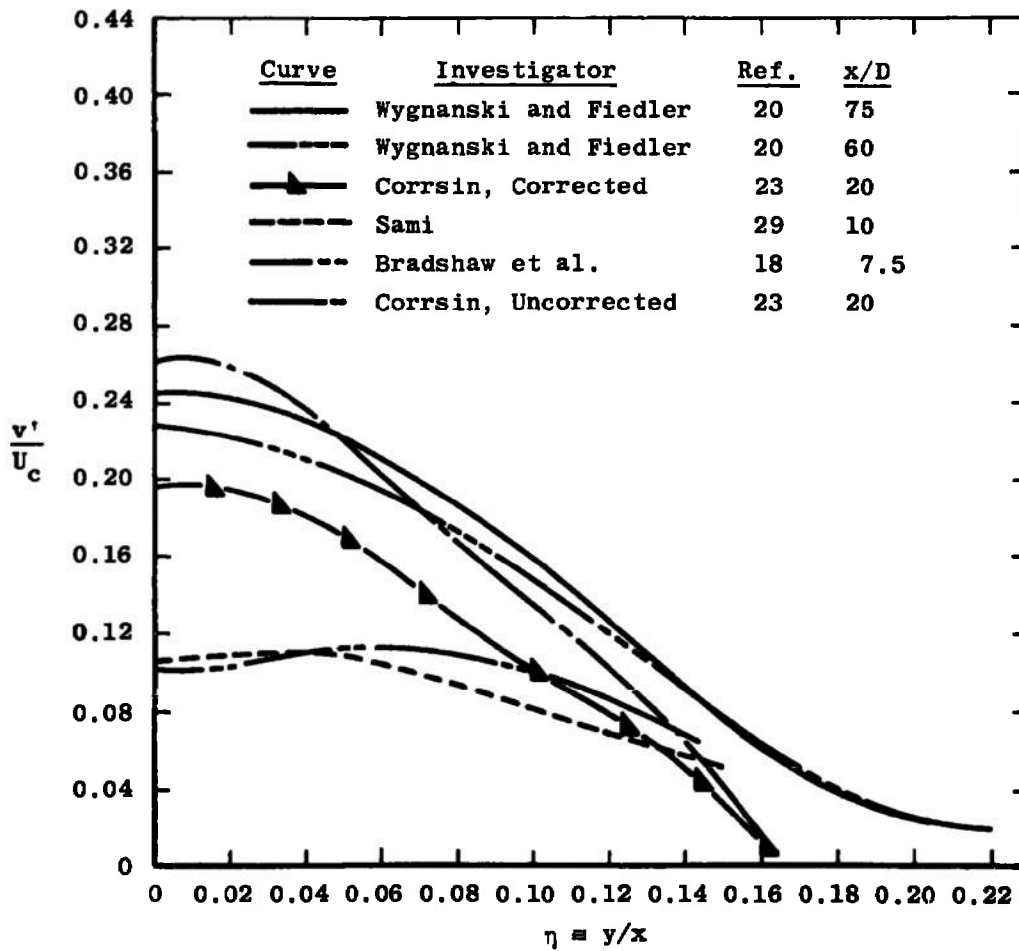


Figure 2.29. Lateral component of turbulent intensity, circular jet-into-still-air.

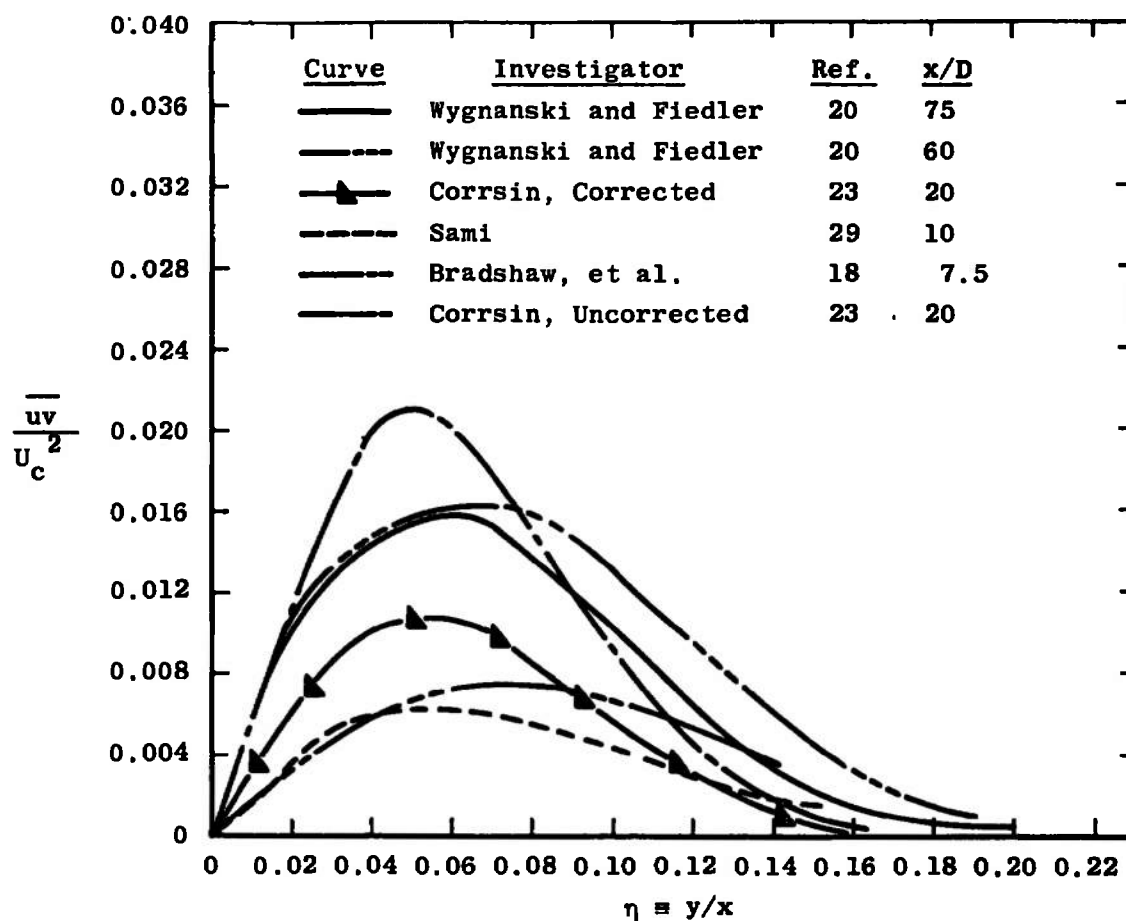


Figure 2.30. Distribution of turbulent shear stress, circular jet-into-still-air.

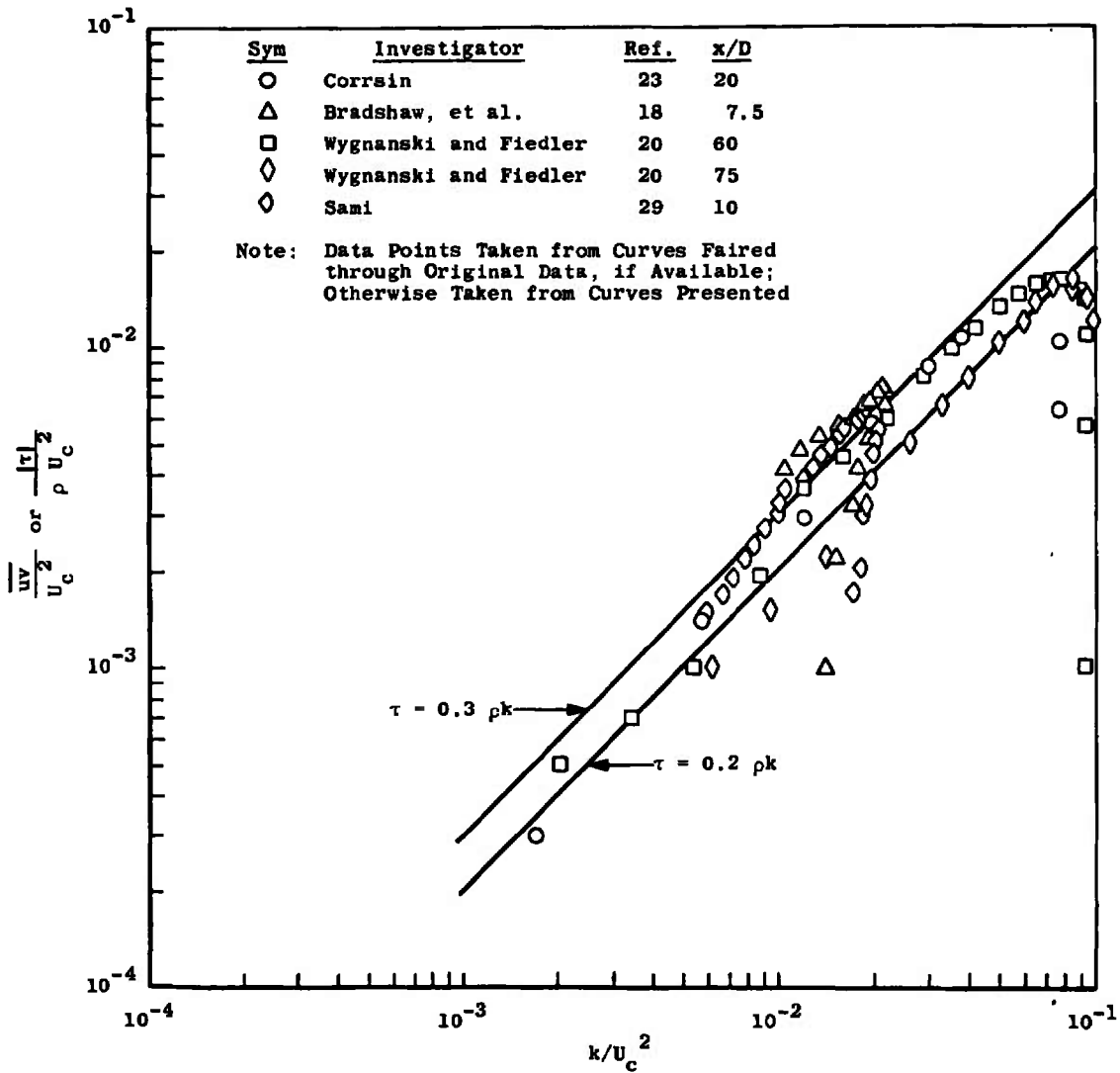


Figure 2.31. Relation between turbulent shear stress and turbulent kinetic energy, circular jet-into-still-air.

already described, Equation (2.2), is well substantiated by these data, although there appears to be a drift of the average value of the parameter a_1 from a value of 0.3 in the early part of the second regime to 0.2 in the later part. Figure 2.32 illustrates that, allowing for some scatter in these measurements, the parameter a_1 keeps qualitatively the same sort of profile throughout the second regime, rising from zero at the centerline to its peak value around $\eta = 0.10$ and then decreasing slowly. The same behavior is observed in the two-dimensional jet. The measurements of Bradshaw, et al., [18], at $x/D = 7.5$, may well be in the transition region between the first and second regimes; this may explain the shape discrepancy that these data show.

Summary

The velocity decay predicted by self preservation considerations for the two-dimensional jet, $U_c/U_j \propto (x/D)^{-1/2}$ is closely followed in the second regime of mixing by all of the two-dimensional jet results investigated. Comparison of the centerline velocity decay curves over a range of Reynolds numbers (evaluated at the nozzle exit) indicates that a definite shift in the curves of U_c/U_j versus x/D occurs, with the higher Reynolds number results exhibiting an earlier drop from a unity value of U_c/U_j . This indicates

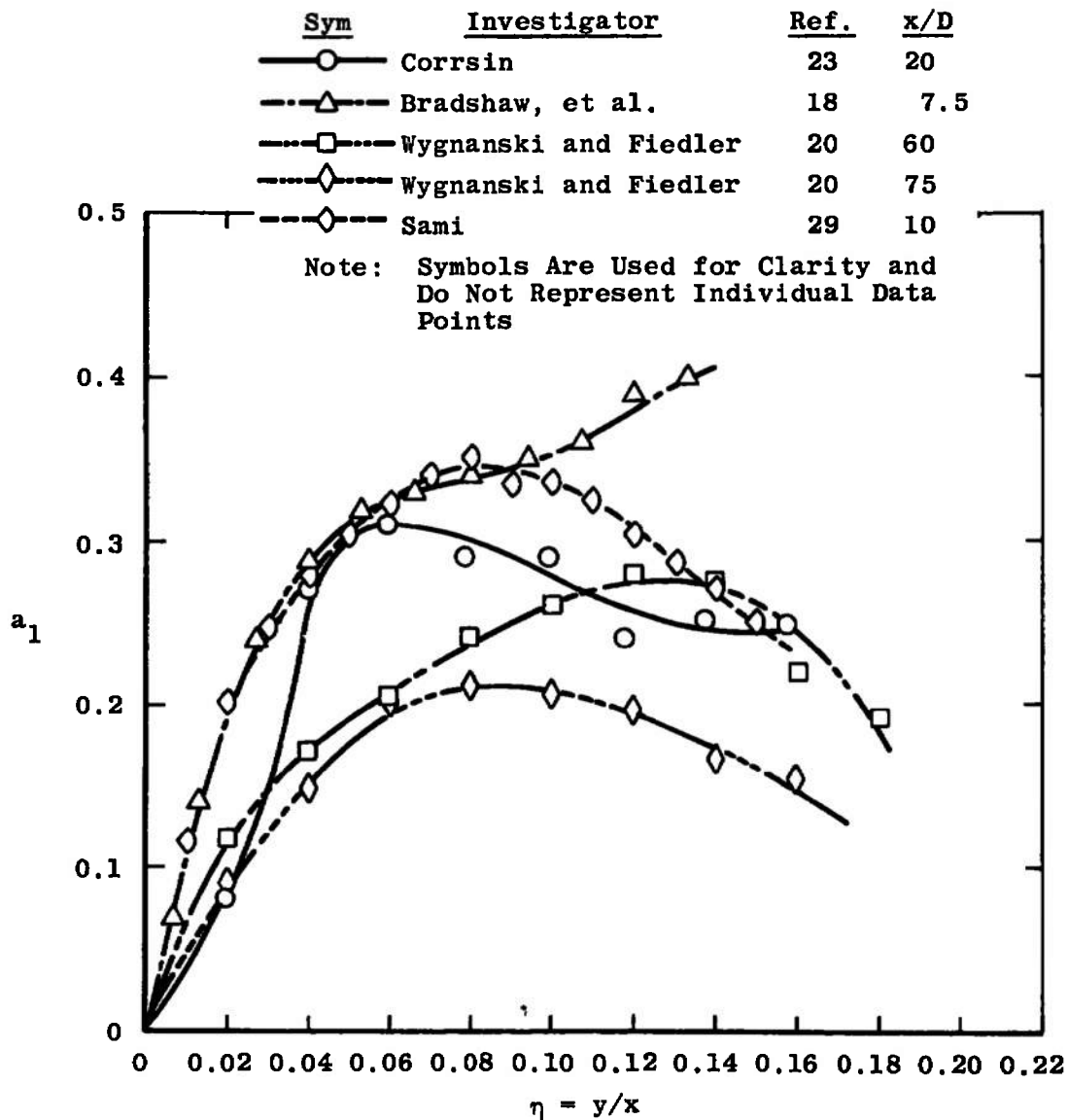


Figure 2.32. Distribution of the ratio of turbulent shear stress to the turbulent kinetic energy, circular jet-into-still-air.

that the potential core (or first regime) length decreases with increasing Re_h . Flora and Goldschmidt [9] give evidence that the potential core length is a function of the turbulence intensity at the jet exit, and that this parameter may indeed be more important than the jet exit Reynolds number in some circumstances. For the circular jet, for which considerably more data is available, the data show an increasing potential core length with increasing Reynolds number. Thus the variation observed for the two-dimensional jet may be entirely a result of the turbulent intensity.

Geometric similarity for the mean-flow velocity profiles in the two-dimensional jet is achieved by $x/h = 20$ [6, 8] but complete self-preservation, involving the profiles of u' and \overline{uv} as well as the mean velocity U does not appear to be achieved before $x/h = 65$ [7]. Turbulence data are obtained in both the similarity region [12] and the self-preserving region [7]. These data exhibit comparable behavior of the parameter a_1 , which is the ratio of the turbulent shear stress to the turbulent kinetic energy, with an average value of about 0.3 being appropriate.

Only a limited amount of data is available for the two-dimensional turbulent mixing layer. Two of the available experiments concern free mixing layers developed from boundary layers [14, 15] and are relatively limited both in number of measurements and spatial extent of these measurements. The third is the classic two-dimensional half jet

experiment of Liepmann and Laufer [17]. The half jet measurements are carried into the region of fully-developed flow, which occurs by a length Reynolds number Re_x of 3.7×10^5 .

In contrast to the situation for the two-dimensional mixing layer, a great deal of experimental information is available for the circular jet into still air. These data all support the centerline velocity expression $U_c/U_j \propto (x/D)^{-1}$ quite well in the second regime of mixing. Geometric similarity of velocity profiles is achieved between ten [8] and twenty [18] diameters, but full self-preserving behavior (of turbulent components as well as mean flow quantities) is not achieved until some seventy diameters [20]. Unlike the two-dimensional jet, the length of the potential core increases for increasing jet Reynolds number [27]. There is sufficient data available in the case of the circular jet into still air to determine an empirical correlation for the core length as a function of jet Reynolds number Re_d ; the result is

$$\frac{x_c}{D} = 2.13 (Re_d)^{0.097}$$

It is also possible, given geometric similarity and assuming a self-preserving form for the axial variation of the local length scale, to show that the axial decay of centerline velocity depends only on the length of the potential core.

This is demonstrated in Appendix B, following References [8] and [21]. The results are

$$\frac{U_c}{U_j} = 1 \text{ for } \frac{x}{D} \leq \frac{x_c}{D}$$

$$\frac{U_c}{U_j} = 2.13 (Re_d)^{0.097} \left(\frac{x}{D}\right)^{-1} \text{ for } \frac{x}{D} > \frac{x_c}{D}$$

which gives fairly good results for this simple configuration.

The first regime of the constant-density jet-into-still-air has been extensively investigated [18, 28, 29, 31]. These investigations have produced a relatively detailed description of the initial development of a free turbulent mixing layer, which is probably valid for other configurations as well. There is seen to be an initial region, of the order of a few thicknesses of the initial nozzle wall boundary layer, in which the turbulent intensity (and turbulent shear stress) increases rapidly. Beyond this a region in which the turbulent intensity is constant exists, and extends "well past the end of the potential core" [28]. A transition follows to a situation in which turbulent mixing occurs from the centerline to the edge of the jet.

All of the experiments on two-dimensional jets into still surroundings that were evaluated showed good agreement with the criterion that the momentum integral be

constant, as well as showing satisfactory two-dimensionality. The results of Albertson, et al., [8] are noteworthy in that the measurement of profiles and axial decays was carried out to $x/h = 2000$. Turbulence structure investigations were carried out by both van der Hegge Zijnen [11] and Heskestad [7]; however, the former results are spoiled somewhat by the extremely small plots presented in Reference [11], while the latter measurements were performed at only one axial station. Heskestad's results are, however, quite detailed, including an analysis of the terms of the turbulent kinetic energy equation. Miller and Comings [6] present relatively few measurements for comparison with other results--their emphasis was primarily on the pressure field in the two-dimensional jet--and their use of the conservation equations to obtain unmeasured quantities complicates analysis of their data.

As mentioned above, experimental information on the two-dimensional mixing layer is relatively limited. Both Mueller [14] and Haugen and Dhanak [15] investigated mixing layers formed by boundary layers; Mueller studying the free mixing layer formed from the boundary layer over an obstruction on a plate and Haugen and Dhanak studying a cavity-flow free mixing layer. Their data are relatively limited and exhibit considerable scatter. The two-dimensional mixing layer measured by Chapman [16] is such only in an approximate sense, as it is formed on the edge of

a circular jet. However, at least part of Chapman's results exhibit two-dimensional behavior reasonably well. Chapman's work is also noteworthy because of the documentation of the initial boundary layers at the nozzle lip. The half-jet of Liepmann and Laufer [17] while subject to some criticism regarding the applicability of the results to a full two-dimensional jet flow [13], is both accurate and detailed. Chow [19] has shown that their calculation of turbulent shear stress results for comparison with their experimental results is incorrect. The actual measurements of turbulent shear stress are themselves accurate within the usual limitations of hot-wire shear stress measurements of that time.

The circular jet into still surroundings is probably the single most extensively studied free mixing flow, as the eleven experiments listed in Table 2.3, page 65, indicate. With one exception, all of the experiments for which the momentum integral can be calculated provide satisfactory agreement with the momentum integral criterion. This exception is the early (1943) data of Corrsin [23] which fails to hold a constant value of the momentum integral by some 35 percent.

As in the case of the two-dimensional jet into still surroundings, the data of Albertson, et al., [8] are again noteworthy for the extreme axial distance to which measurements of profiles and axial decays are carried--in

this case 250 diameters. Alexander, et al., [27] and Baines [21] both demonstrate variations in the length of the potential core with the jet Reynolds number, the former investigating this effect over a Reynolds number range of 2.33×10^4 to 3.82×10^5 . Corrsin [23], Hinze and van der Hegge Zijnen [24], Corrsin and Uberoi [25], Bradshaw, et al., [18], Sami [29], and Wygnanski and Fiedler [20] all present measurements of the turbulence structure; Bradshaw, et al., and Sami in the first and transition regimes, Hinze and van der Hegge Zijnen in the second regime, and Wygnanski and Fiedler in the second regime past the onset of self-preservation. The work of Hinze and van der Hegge Zijnen again suffers from the very small plots presented in Reference [24].

Perhaps more important than their detailed structural measurements is the possible solution that Wygnanski and Fiedler [20] give to the vexing problem of turbulent shear stress measurement. Their conclusion that the reason that hot-wire turbulent shear stress measurements commonly are some twenty percent lower than the shear stresses obtained by other means is that a large portion of the turbulent shear stress is at the very low frequency end of the spectrum (and therefore involved with the very largest eddies) clearly should be further investigated.

The greatest need in the investigation of the mixing of a circular jet with still surroundings is of an

experiment in which detailed profiles in the first regime of mixing are followed by careful axial decay measurements in the second regime. This problem is lessened somewhat by the relatively narrow band in which most axial decay of center-line velocity curves fit (Figure 2.21, page 67), and by the typical $(x/D)^{-1}$ decay behavior of all of the curves represented. Using these observations, the experiment selected from the circular-jet-in-still-surroundings to be used in confrontation with theory to follow is then made up from the initial conditions measured by Bradshaw, et al., (at $x/D = 1$) [18] followed by an essentially arbitrary $(x/D)^{-1}$ decay curve. Sami's [29] profiles at $x/D = 1$ could also be used.

CHAPTER 3

CONSTANT-DENSITY TWO-STREAM FLOWS:

EXPERIMENTAL DATA

While the jet into still air is the simplest conceivable free mixing jet flow, embedding the jet in a moving secondary stream has distinct advantages. The primary advantage of this technique is that it simplifies measuring the very small mean velocities that exist near the edges of a jet-into-still-air. In particular, measurement of the turbulent fluctuations, which is extremely difficult when the fluctuating velocities approach the order of magnitude of the mean velocity, is considerably simplified. This is because the assumptions made in relating the heat-transfer-rate fluctuations of the hot-wire to the velocity fluctuations break down when the fluctuations are of the same order of magnitude as the mean velocity, rendering the interpretation of the measurements difficult if not impossible. Embedding the jet in a moving stream reduces the importance of the problem, as there is always a significant "background" velocity level. Much the same advantages are apparent in the measurement of pitot pressure in a two-stream flow.

The price paid for easing the measurement problem is the introduction of an additional parameter into the experiment, which is the velocity ratio between the two

streams. In addition, because of the finite size and capacity of laboratory equipment, it is often necessary to enclose the outer stream in a duct. This in turn means that great care must be taken to minimize the effect of the axial pressure gradient if the results are to be meaningful as an approximation to free mixing.

In addition to free mixing between a two-dimensional stream and a moving secondary and an axisymmetric stream and a moving secondary, wakes, which can be considered as two-stream mixing with zero primary velocity, will also be covered in this section. In the case of wakes, there is of course no velocity ratio parameter encountered, but there are differences in wake development depending on the shape and type of body that produces the wake.

Two-Dimensional Jet with Nonzero Secondary

A schematic representation of a two-dimensional jet embedded in a moving secondary is shown in Figure 3.1. As for the zero-secondary case, the jet emerges from a rectangular nozzle of length L and width h . Also as for the zero-secondary case, the aspect ratio of the nozzle, L/h , must be large to insure two-dimensionality. Above and below the center or primary jet a secondary stream emerges. The length of the secondary-stream nozzle is ordinarily the same as the primary nozzle; the width is ordinarily considerably greater. In the true free mixing case two mixing processes occur simultaneously as the jets leave the nozzle, one

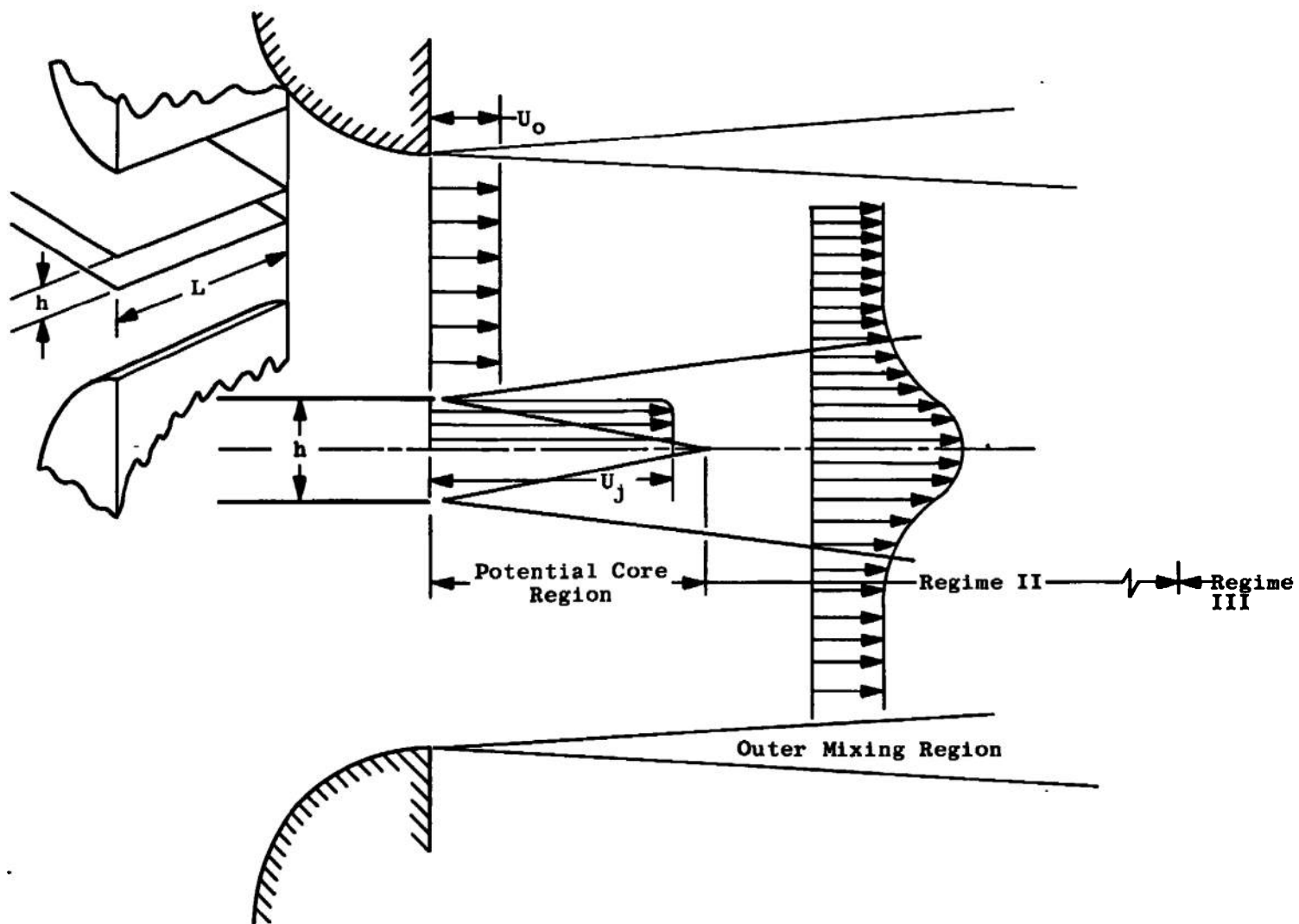


Figure 3.1. Geometry of the two-dimensional jet, nonzero secondary.

between the primary and secondary streams and the other between the secondary stream and the surroundings. The process of greatest interest is the mixing between the primary and secondary streams. Like the two-dimensional jet-into-still-surroundings this mixing process can be divided into two regions. In the first regime, or potential core, the region of turbulent mixing expands both inward and outward, until the inward expansion reaches the centerline. At this point the second regime begins. In the true free-mixing case, the outer stream also mixes on its outer edge with the quiescent surroundings. This mixing region also expands downstream, until some distance downstream the outer edge of the mixing region between primary and secondary streams intersects with the mixing region between the outer stream and the quiescent surroundings. At this point the third regime begins and the character of the flow changes, becoming gradually more like the mixing of a jet-into-still-surroundings. Generally, only the first and second regimes are of interest.

The length of the second regime can be increased by increasing the width of the secondary stream, at the cost of increased mass flow requirements, or it can be increased by enclosing the outer stream in a duct. In the latter case the second regime length is increased as the boundary layer that forms on the duct wall increases in width much more slowly than would a free-mixing region. However, the

ducting of the flow induces an axial pressure gradient which, if of sufficient magnitude, can distort the flow from its free-mixing (and zero pressure gradient) form.

Figures 3.2 and 3.3, taken from the data of Weinstein, Osterle, and Forstall [37] illustrates the evolution of the velocity profile in a two-dimensional two-stream mixing flow.

Table 3.1 lists the important parameters of the two-stream two-dimensional flows considered. The Weinstein, Osterle, and Forstall data represent a series of mean flow measurements for several secondary-stream-to-primary-stream velocity ratios ranging from 0.33 to 0.67. Both Bradbury [34] and Bradbury and Riley [38] present turbulent structure measurements in relatively low velocity ratio flows, where the introduction of a non-zero secondary stream velocity is aimed at improving the accuracy of hot-wire measurements. It should be noted that the data appearing in Bradbury and Riley [38] are presented in nondimensional form without sufficient information to convert to the parameters used here. However, the same data (presumably) are presented in Bradbury [39] in a somewhat more suitable form; the data from the latter paper have been used in the present work.

Axial decay curves for the centerline velocity ratio for a number of the tests considered here are plotted in Figures 3.4 and 3.5. The data of van der Hegge Zijnen [2] for a two-dimensional jet with zero secondary velocity

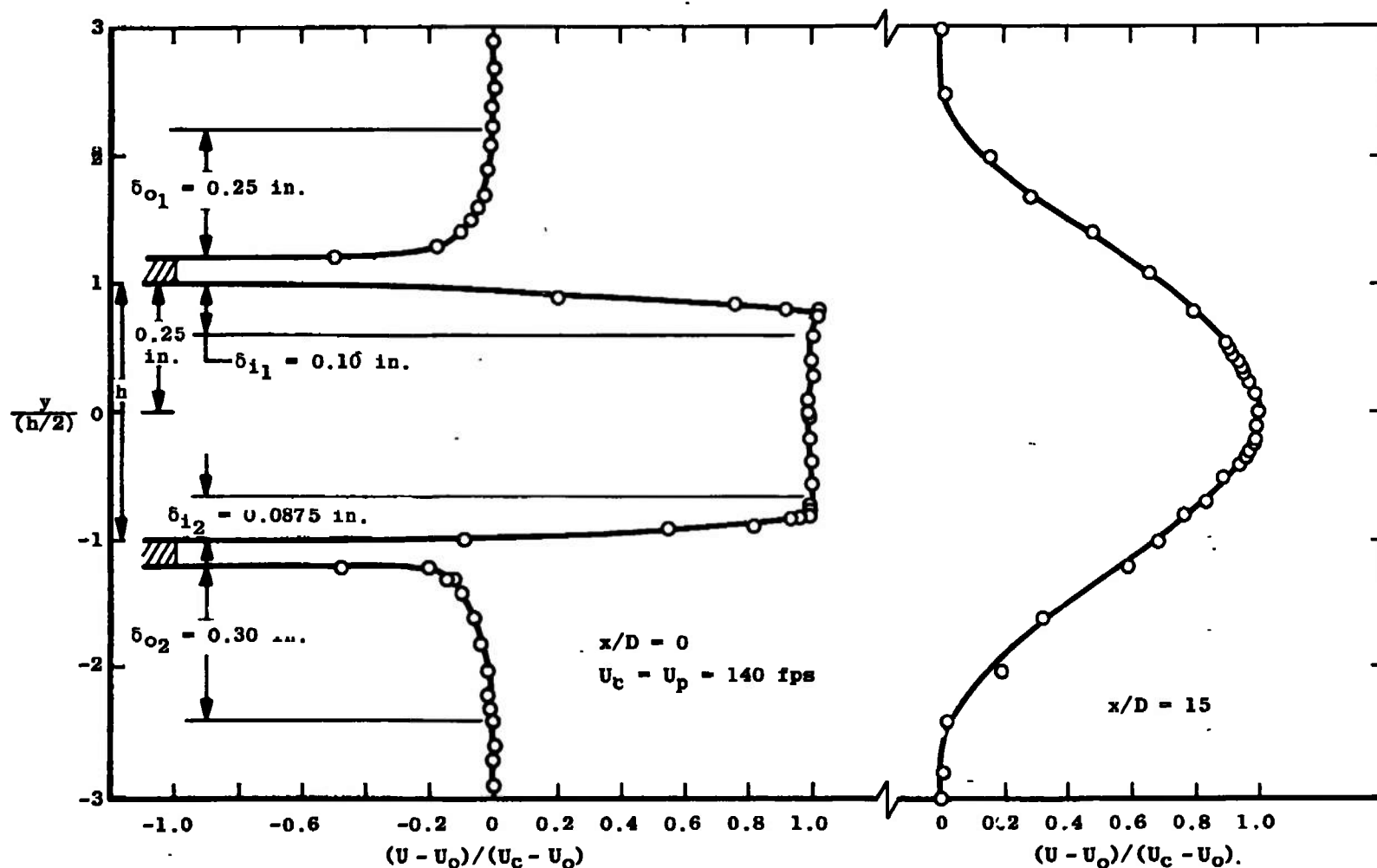


Figure 3.2. Velocity profiles, 2D jet, nonzero secondary:
 Weinstein, Osterle and Forstall [37], series I,
 $U_c/U_j = 0.5$, near field.

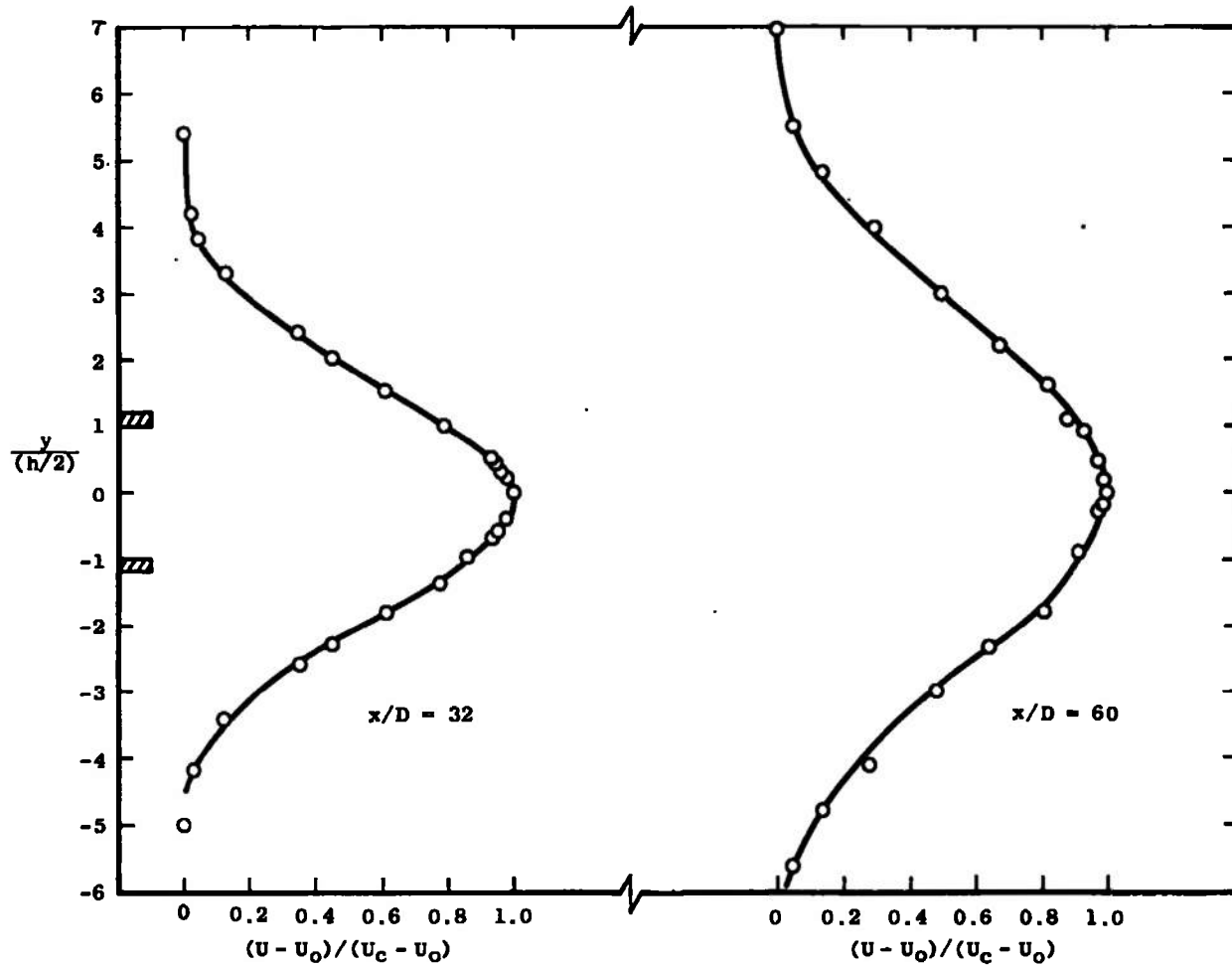


Figure 3.3. Velocity profiles, 2D jet, nonzero secondary:
Weinstein, Osterle, and Forstall [37], series I,
 $U_0/U_j = 0.5$, far field.

TABLE 3.1

THE TWO-DIMENSIONAL CONSTANT-DENSITY JET WITH NONZERO SECONDARY

Investigator	Year	Ref.	Slot Width (in.)	Aspect Ratio	U_j ft/sec	U_o/U_j	$Re \times 10^{-4}$ ^a	Maximum x/L	Momentum Check, Percent ^b
Weinstein, et al.	1956	37	0.5	24	120	0.33	3.2	2.5	6.5
			0.5	24	140	0.50	3.7	2.5	
			0.5	24	100	0.50	2.6	2.5	
			0.5	24	120	0.67	3.2	2.5	
Bradbury	1965	34	0.375	48	155	0.16	3.0	1.425	4
Bradbury and Riley	1967	38	0.375	48	155 ^c	0.07	3.0 ^c	-	5 ^d
			0.125	144		0.16			
			0.125	144		0.31			

^aReynolds number based on slot height h .

^bMaximum deviation from average.

^cPresumed for the aspect ratio 48 case to be equal to Bradbury (1965).

^dAuthor's measurement.

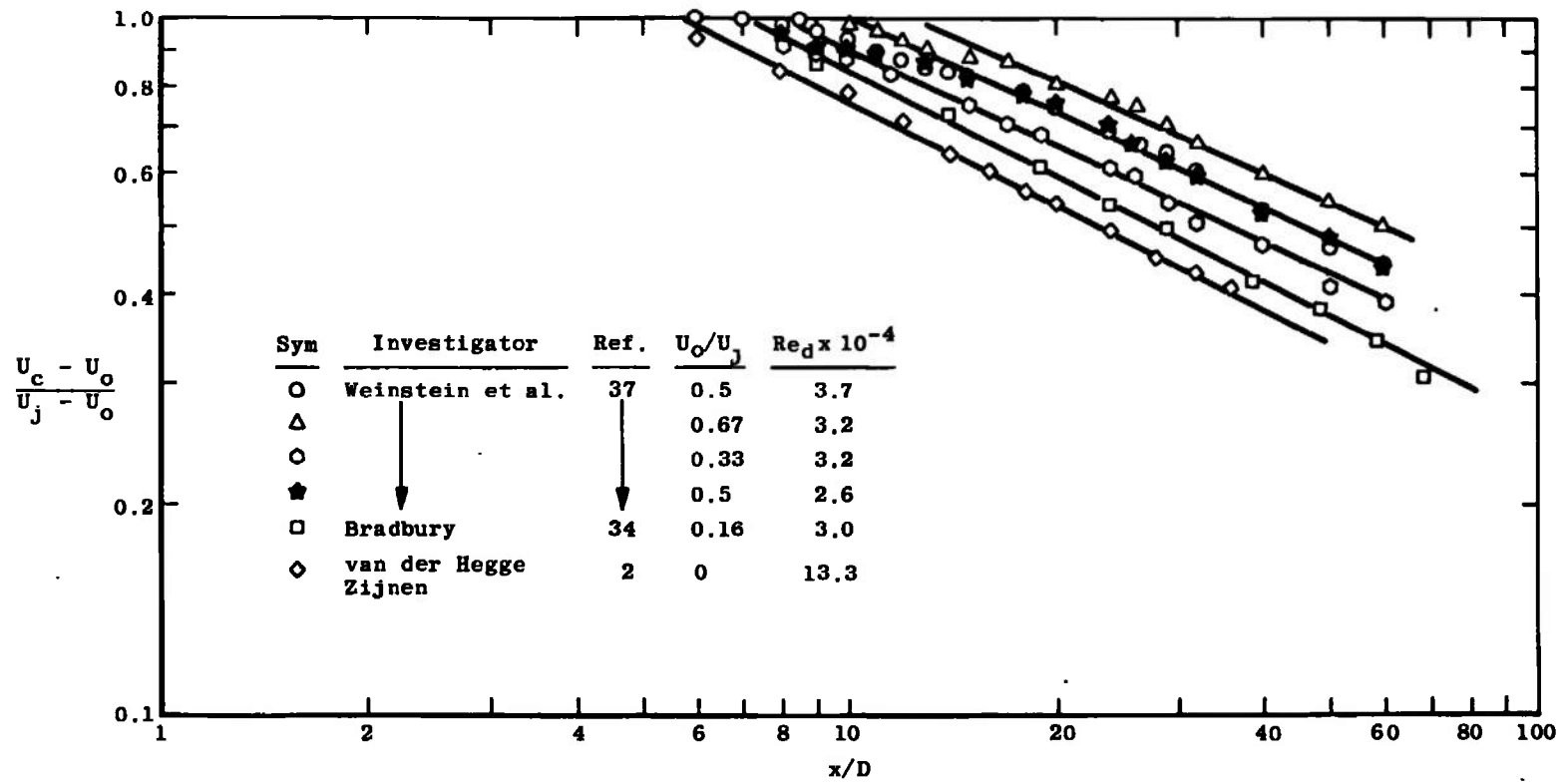


Figure 3.4. Axial decay of centerline velocity ratio, two-dimensional jet, nonzero secondary.

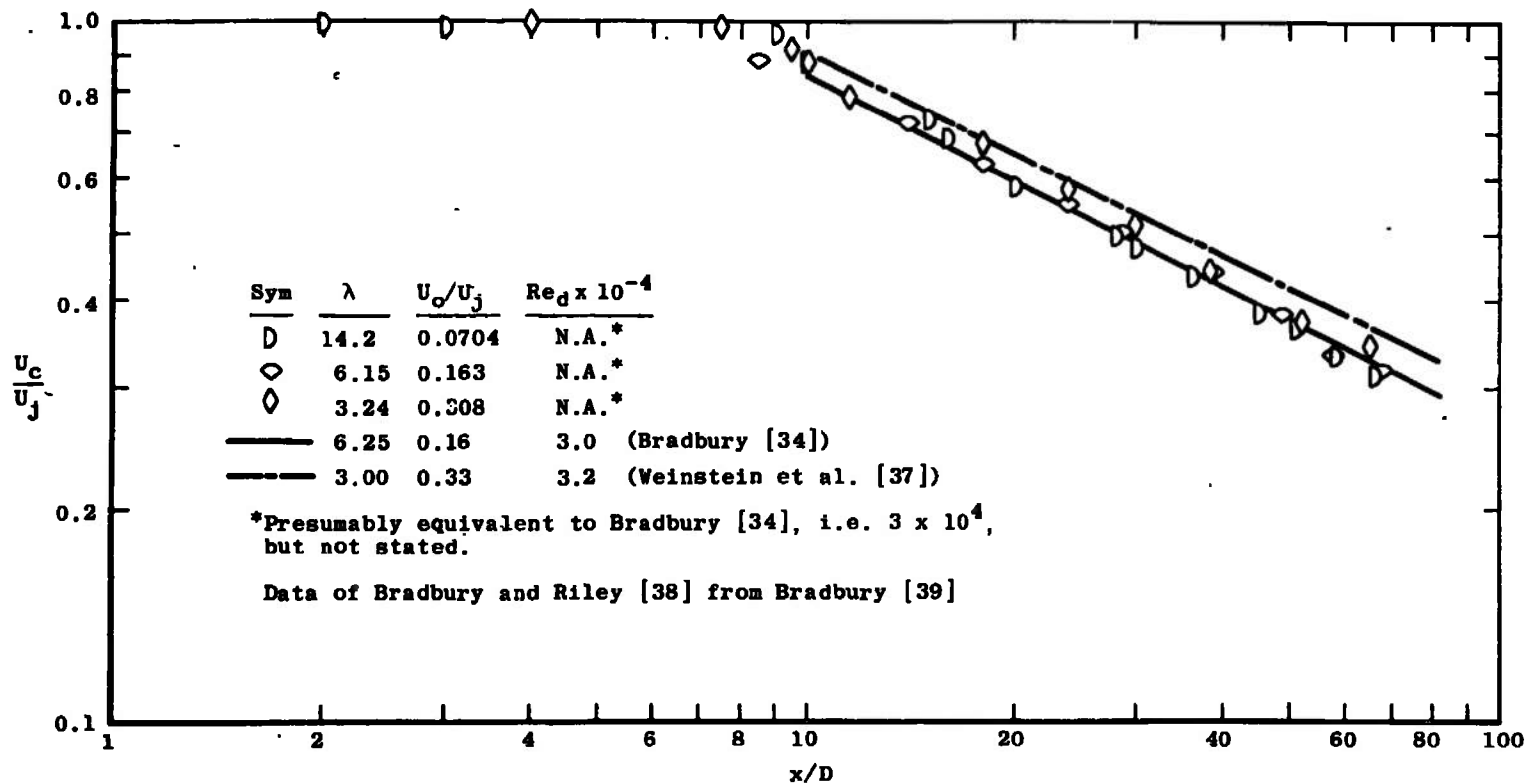


Figure 3.5. Axial decay of centerline velocity ratio, two-dimensional jet, nonzero secondary. Data of Bradbury and Riley [38].

is included for comparison. From these figures the quite definite influence of the jet velocity ratio is clearly apparent. No Reynolds number effect such as was found for the jet in still surroundings is observed. However, any shift with primary jet Reynolds number would be masked by the velocity ratio effect in these experiments.

As is demonstrated by Figure 3.6, downstream of the potential core region the mean velocity profiles for the two-stream two-dimensional jet can be fit quite well with a function of the similarity variable $\eta = y/b_{1/2}$. The parameter $b_{1/2}$ is the ordinate at which the mean velocity $U = U_o + (U_c - U_o)/2$. Newman ([3], see Appendix C) shows that true self-preservation--in which the whole flow scales with two parameters, a width scale and a velocity scale--only exists in an approximate sense for the two-dimensional two-stream jet, when the velocity increment $U_c - U_o$ is large compared to U_o , or in the opposite case, when $U_c - U_o$ is small compared to U_o . For the two-dimensional jet, self-preservation in the large velocity increment case requires that the velocity ratio $(U_c - U_o)/(U_j - U_o)$ be proportional to $x^{-1/2}$. Assuming that $(U_c - U_o)/(U_j - U_o) \propto x^{-1/2}$, as required for self-preservation, and that $(U - U_o)/(U_c - U_o) = f(\eta)$, as experimentally observed, Bradbury [39] shows that, with the additional assumption that the flow in the downstream region is dependent only on the overall excess momentum flux in the jet, equations can be written for the

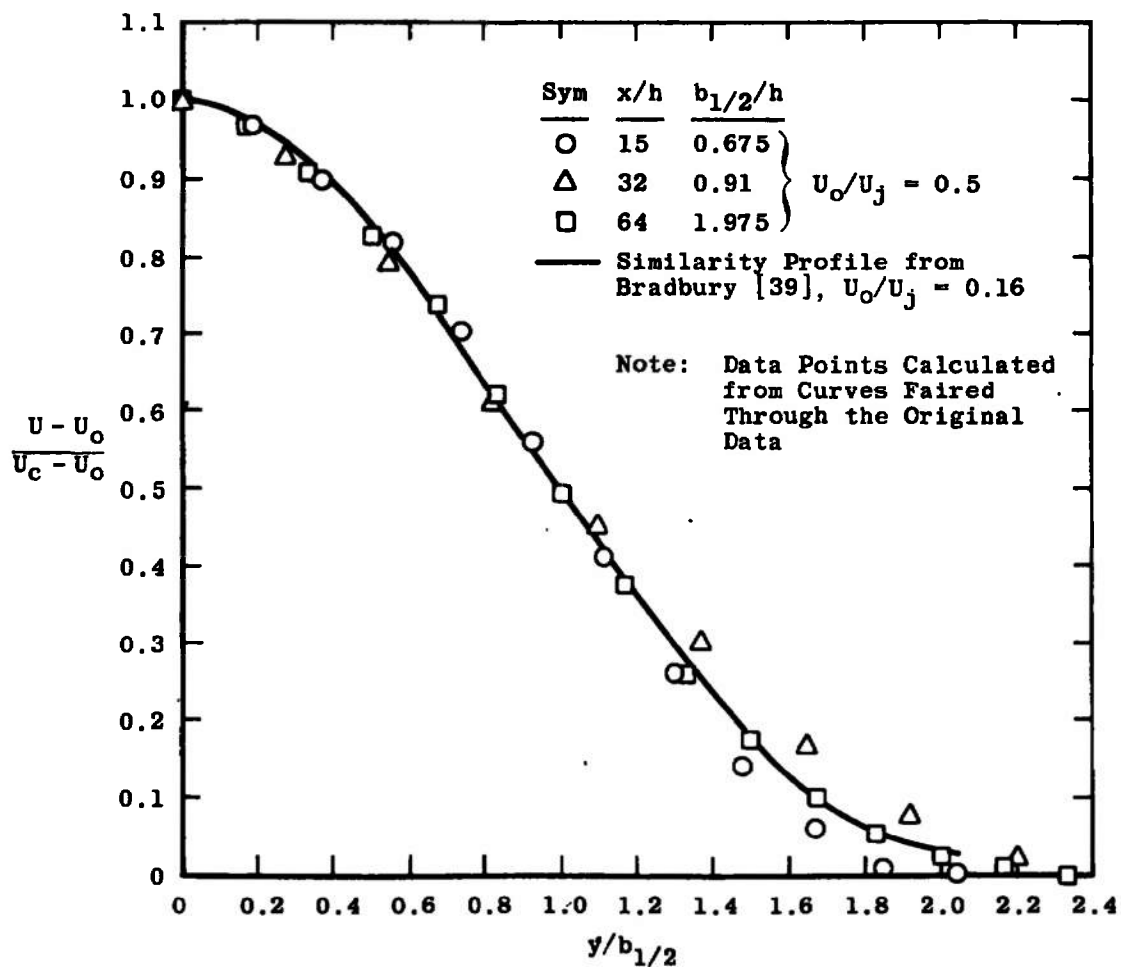


Figure 3.6. Comparison of data from Weinstein, Osterle, and Forstall [37] with data from Bradbury [39] for the small-perturbation (self-preserving) 2D jet.

axial decay of centerline velocity ratio and the increase of width of the jet, in terms of the virtual origin x_v and the ratio of velocities $\lambda = U_j/U_o$. Axial decay equations can be written in the same manner for the circular jet with nonzero secondary. Further, Bradbury [39] recommends taking $x_v = 0$, which results in equations which are functions only of the parameter λ . Thus:

$$\frac{U_c - U_o}{U_j - U_o} = 2.5 \sqrt{\frac{\lambda}{\lambda-1}} \left(\frac{x}{h}\right)^{-1/2} \quad (3.1)$$

and

$$\frac{b_{1/2}}{h} = 0.109 \frac{x}{h} \frac{1}{1 + \frac{0.55}{\sqrt{\lambda(\lambda-1)}} \sqrt{\frac{x}{h}}} \quad (3.2)$$

Figure 3.7 shows a comparison between the velocity decays predicted by Equation (3.1) with experimentally measured decays. For $x/h > 10$, Equation (3.1) provides a reasonably good prediction of the centerline velocity decay for $\lambda = U_j/U_o > 2.0$. The prediction improves as U_j/U_o increases, as would be expected as the criteria for approximate self-preservation is that $U_c - U_o/U_o \rightarrow \infty$.

The measurements of turbulent intensities and turbulent shear stress carried out by Bradbury [37] were made in the self-preserving region of the jet. In Bradbury's usage, the condition for self-preservation is

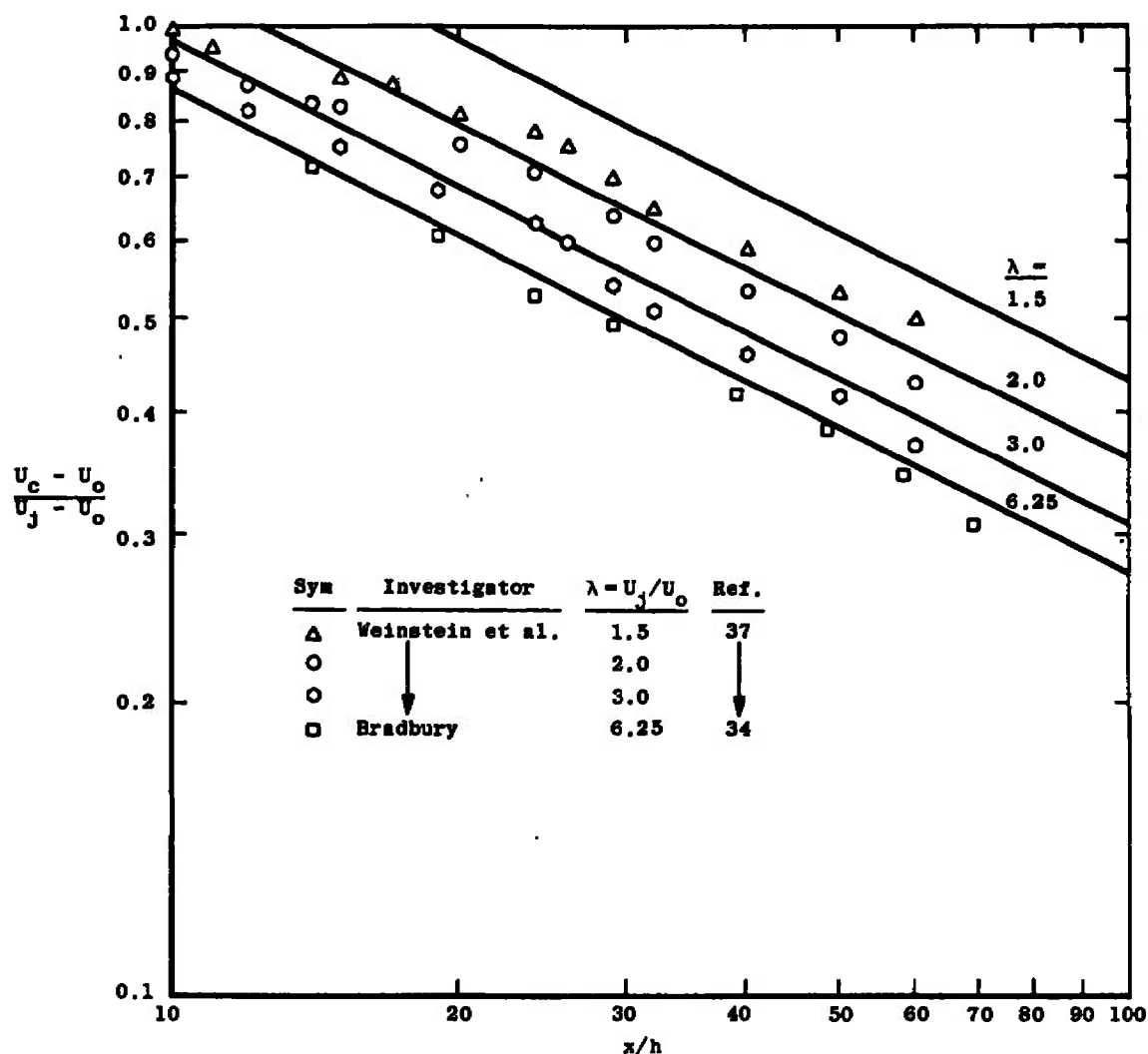


Figure 3.7. Comparison of centerline velocity decay predicted by empirical correlation of Bradbury [39] with measured data.

taken to be that $(U_c - U_o) \propto x^{-1/2}$; this is observed to occur for $x/h > 30$. Bradbury notes that the empirical expression which fits his velocity decay curve implies, given conservation of momentum, that the width is not exactly proportional to x , as self-preservation would require. However, the departure from self-preservation is small.

Calculations of the turbulent shear stress and turbulent kinetic energy were made from the data presented in Reference [34], in the self-preserving region. Figure 3.8 shows that the ratio of turbulent shear stress to turbulent kinetic energy follows the linear relationship encountered earlier quite well. The lateral variation of the parameter a_1 as shown in Figure 3.9 is also at least qualitatively in agreement with measurements made in other flows.

Bradbury also presents measurements of turbulence structure in the self-preserving region. His measurements show that a significant amount of the turbulent shear stress is tied up in the large eddies. This conclusion is contrary to Townsend's [5] large eddy hypothesis (which in part predicts that the majority of the turbulent shear stress is tied up in the smaller eddies of the flow); however, it does agree with some of the measurements of Wygnanski and Fiedler [20] in the axisymmetric jet into still surroundings. In this latter work, as discussed in Chapter 2, it was found

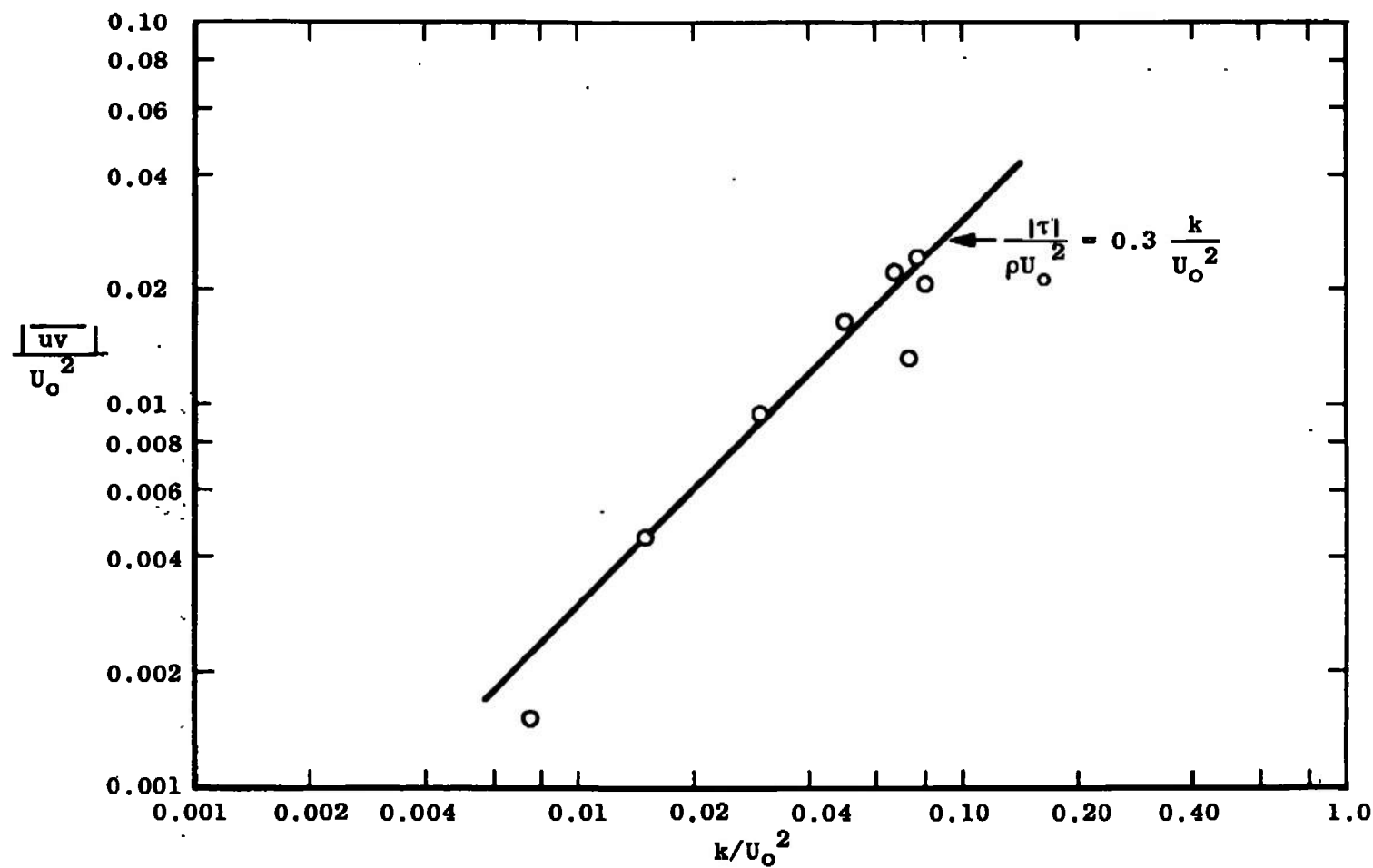


Figure 3.8. Relation between turbulent shear stress and turbulent kinetic energy, 2D two-stream jets. Data from Bradbury [34].

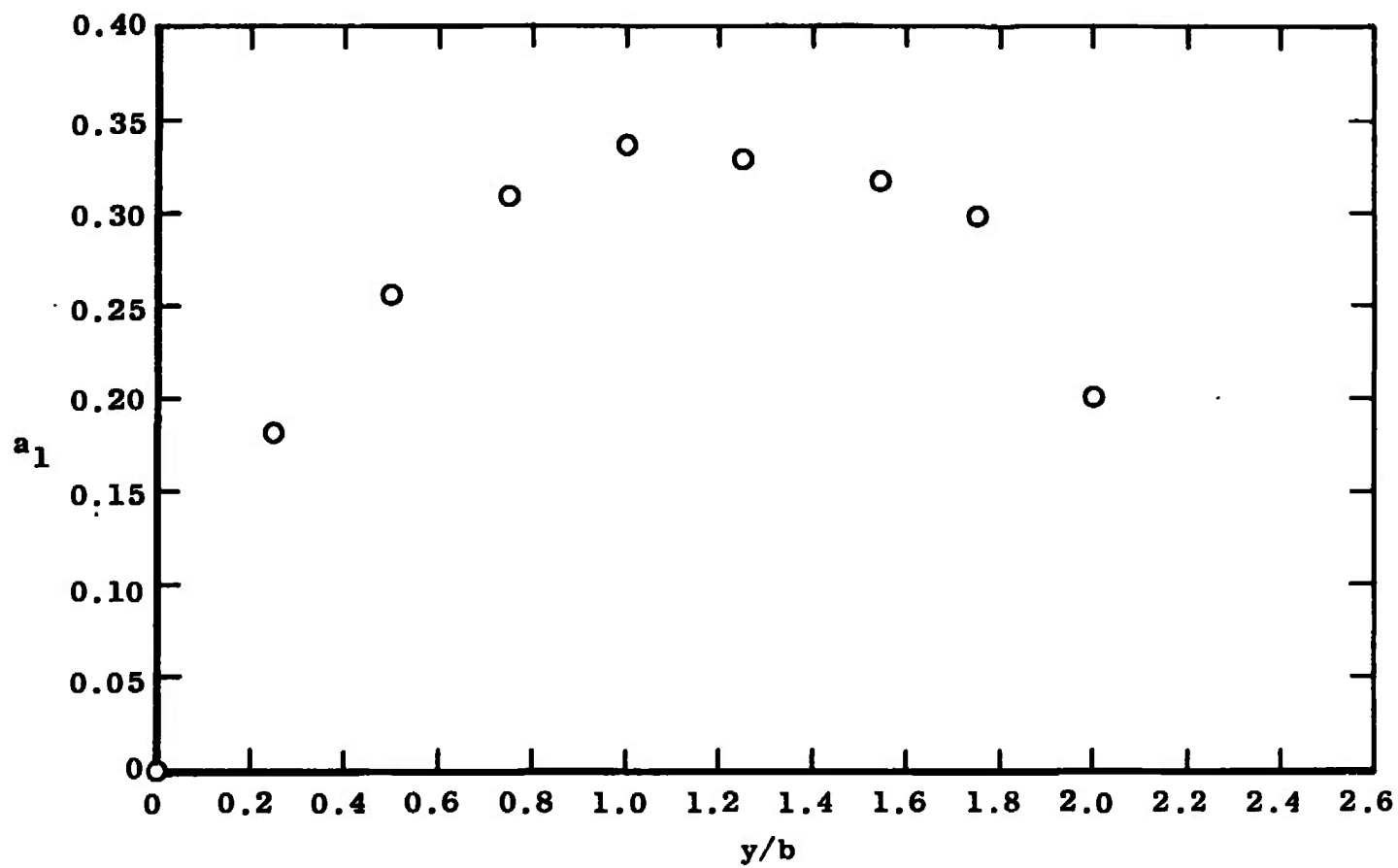


Figure 3.9. Lateral variation of the parameter a_1 in the self-preserving region of a two-dimensional two-stream jet; data from Bradbury [34].

that a significant portion of the shear stress occurs in the lowest frequency part of the turbulence spectrum, which implies the largest eddies. In this connection it is noteworthy, in light of the discussion of the measurement of turbulent shear stress in Chapter 2, that Bradbury's measurements of turbulent shear stress agree quite well ([34], Figure 13) with the turbulent shear stress calculated by integration of the mean velocity profiles.

Axisymmetric Jets with Nonzero Secondary: Coaxial Jets

As can be seen from the flow schematic of Figure 3.10, the idealized coaxial mixing flow is quite similar to the idealized two-dimensional two-stream mixing flow, and the same description applies. Thus there are three flow regimes: the potential core, the region of complete mixing of the primary and secondary streams, and the region of complete mixing of both streams and the surrounding quiescent fluid. As for the two-dimensional case, in the idealized flow the surrounding stream extends to $\pm \infty$, and the surrounding stream velocity U_0 remains constant for all x . This ideal is of course not realizable in practice; two representative actual approaches are shown in Figure 3.11.

Figure 3.11 (a) represents a common experimental approach to coaxial free mixing, exemplified by the apparatus used by Forstall [40, 41]. In this apparatus the secondary air stream is drawn through a duct surrounding the

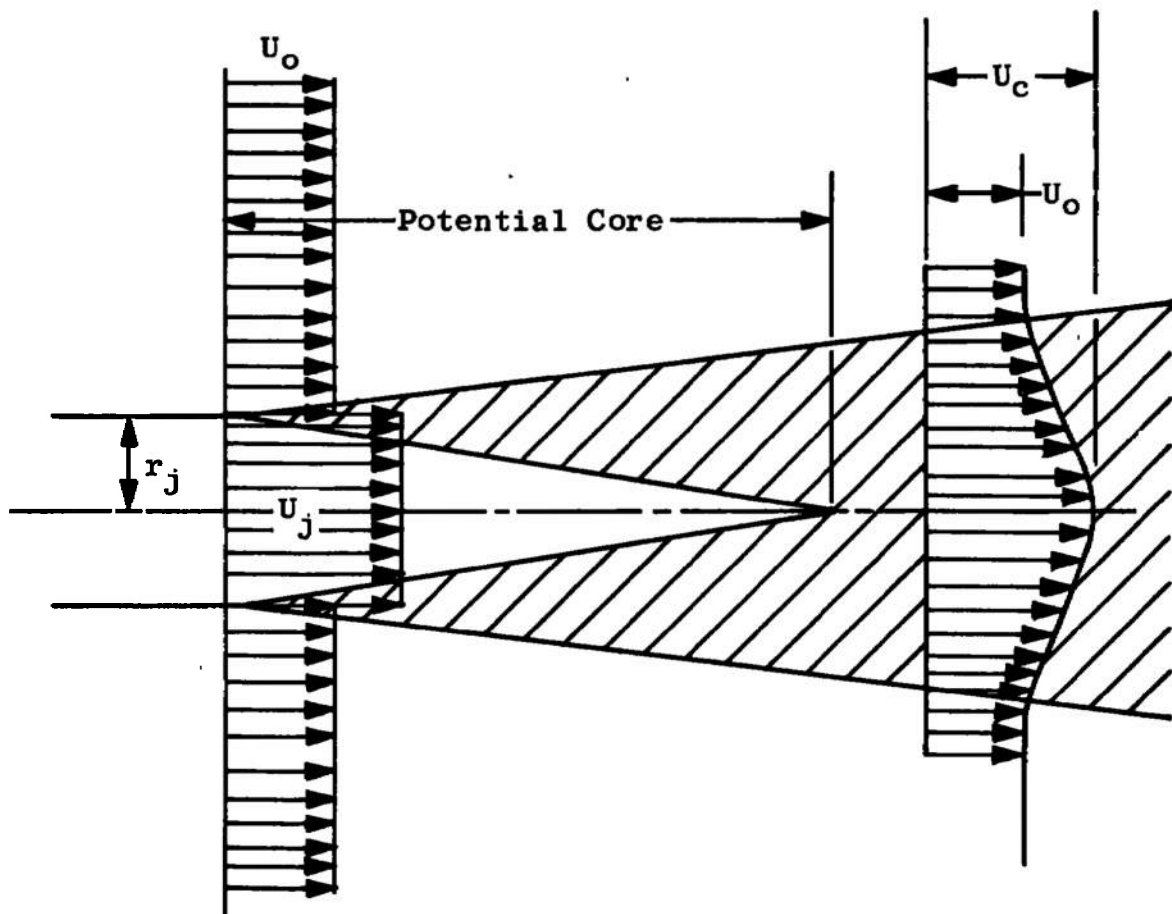
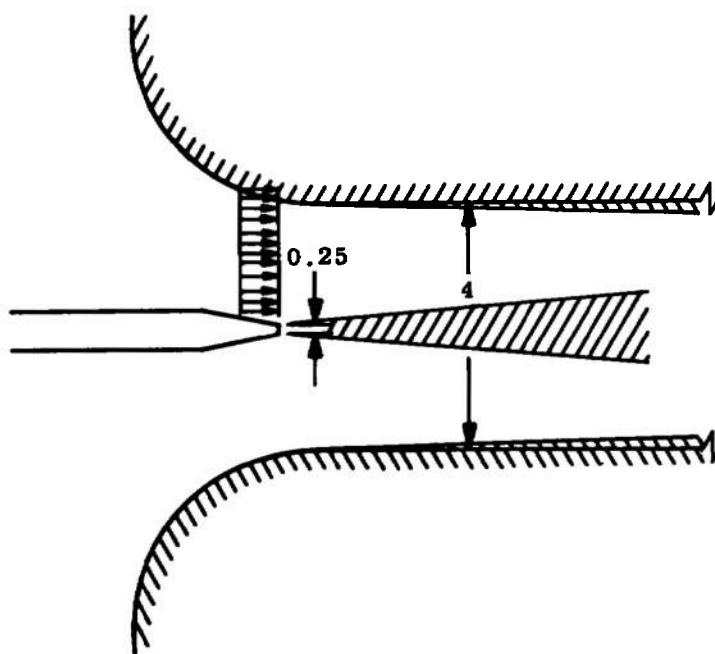
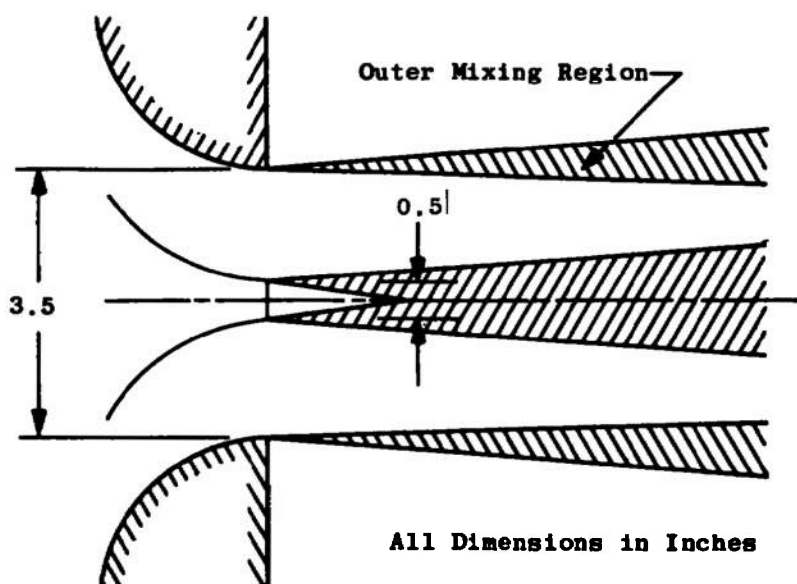


Figure 3.10. Idealized coaxial mixing.



a. Apparatus of Forstall (Schematic)



b. Apparatus of Paulk (Schematic)

Figure 3.11. Experimental approximations to true coaxial free mixing.

primary jet. While ensuring a relatively long second regime and providing an experimental setup requiring only a modest flow capacity, this type of apparatus has the disadvantage of involving nonzero pressure gradient effects, which can distort the flow from a true free mixing flow. Figure 3.11 (b) represents a configuration in which the zero pressure gradient criterion can be closely approached. The particular apparatus sketched is that used by Paulk [42]. The advantage of a nearly constant-pressure flow is obtained in this apparatus at the cost of a drastically reduced second regime. This is caused by the fact that the outer stream, mixing with quiescent air, mixes faster than the inner stream, mixing with a moving stream. Thus, for realistic outer jet sizes the second regime of mixing is abbreviated.

The concepts of local similarity of mean flow profiles and of self-preservation of the coaxial jet flow are both useful in the analysis of coaxial free mixing. Of the two, the former is far more widely applicable. To test for local similarity the question asked is whether the mean flow velocity profile (or profile of some other quantity) is reducible to a function of the lateral coordinate divided by some suitable local reference length. The local reference length is commonly taken to be the half radius of the particular profile: for the velocity profile $r_{1/2}$ is the ordinate at which $U = U_o + (U_c - U_o)/2$. Paulk's data for a

velocity ratio $U_o/U_j = 0.125$ [42] is reducible in this form as Figure 3.12 shows.

Self-preservation of the flow is shown by Newman ([3], see Appendix C) to exist for a coaxial free mixing flow only in an approximate sense, when $(U_c - U_o)/U_o \gg 1$ or $(U_c - U_o)/U_o \ll 1$. The first case represents a high ratio of primary to secondary velocity, and the second a jet with primary velocity very much less than the secondary. The criteria for self-preservation in the first case are that the centerline velocity difference $U_c - U_o$ be proportional to $1/x$ while at the same time the width scale is proportional to x . Thus self-preservation for coaxial jets requires that the velocity profiles be reducible as a function of $\eta = r/x$. Figure 3.13 shows that the same data shown to exhibit local similarity in Figure 3.12 does not exhibit self-preservation. The conclusion is clearly that local similarity may be exhibited where self-preservation is not.

Table 3.2 lists the important parameters for the coaxial free mixing tests to be considered in this section. Of these tests, those of Paulk [42] are the only ones in which the outer stream was not ducted. In four of these experiments the density ratio was not unity. Forstall [40], Fejer, et al., [45], and Paulk [42] used a trace gas, using helium, argon, and hydrogen, respectively, in order to investigate the transfer of mass, while both Landis and

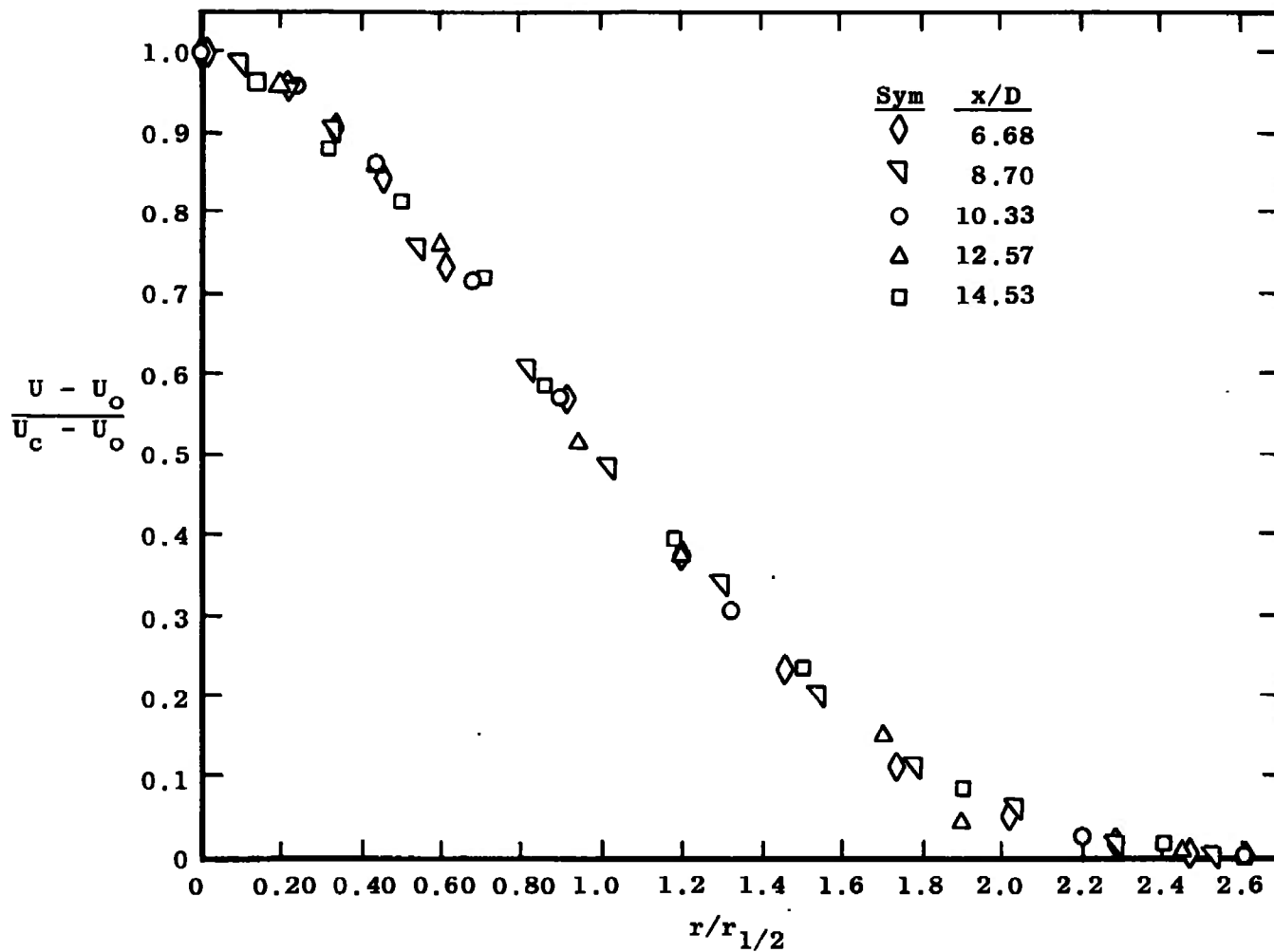


Figure 3.12. Test for local similarity: Paulk [42],
 $U_o/U_j = 0.125$, $\rho_j/\rho_o = 0.93$.

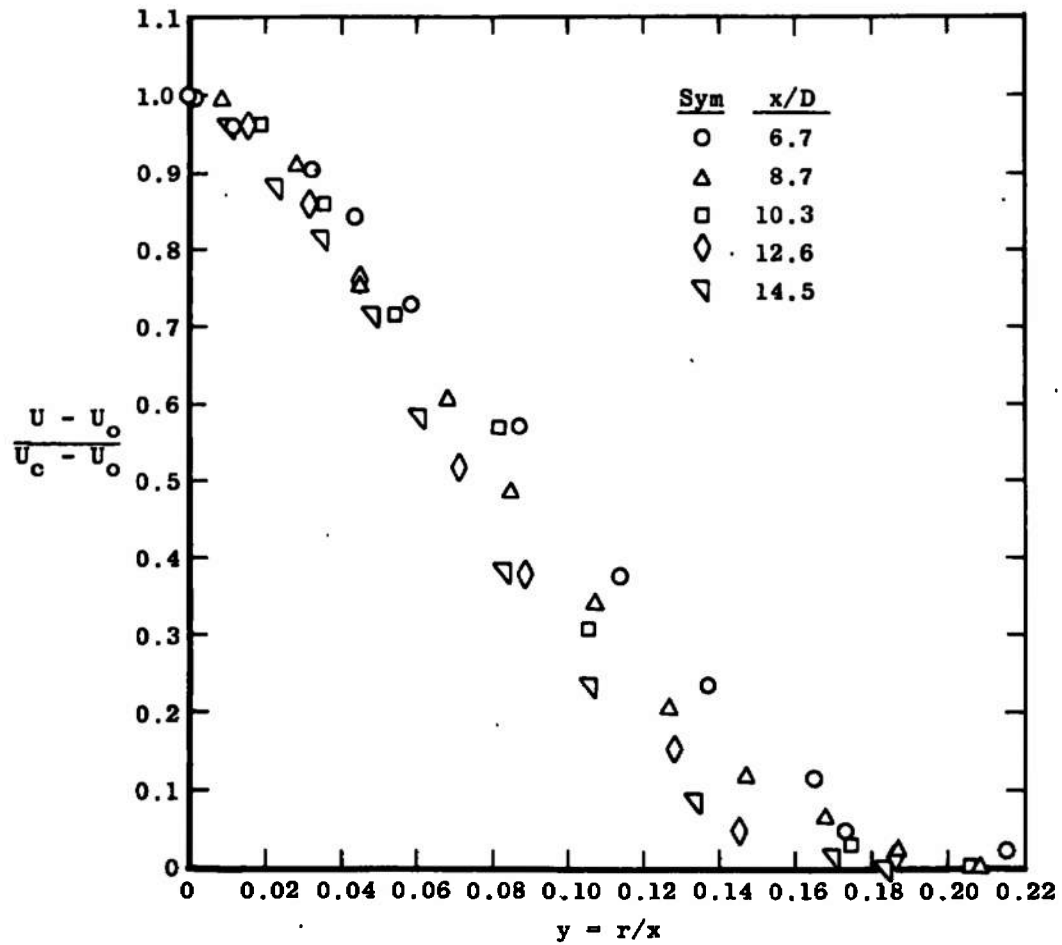


Figure 3.13. Test for self-preservation: Paulk [42],
 $U_o/U_j = 0.125$, $\rho_j/\rho_o = 0.93$.

TABLE 3.2
COAXIAL CONSTANT-DENSITY JETS

Investigator	Year	Ref.	D_j (in.)	Duct Dia. (in.)	U_j (ft/sec)	U_o/U_j	Re $\times 10^{-4}$ ^a	ρ_j/ρ_o	Last x/D	Momentum Check, ^b Percent
Forstall (Forstall and Shapiro)	1950	40 (41)	0.25	4.0	180	0.5	2.38	0.92	120	-
			0.25	4.0	225	0.2	2.98	0.92	80	10
			0.25	4.0	120	0.25	1.59	0.92	80	8
			0.25	4.0	90	0.5	1.19	0.92	135	23
			0.25	4.0	120	0.75	1.59	0.92	130 ^c	-
Landis and Shapiro	1951	43	0.5	4.0	200	0.25	5.3	0.92	32	10 ^d
			0.5	4.0	220	0.46	5.84	0.92	32	-
			0.5	4.0	180	0.75	4.77	0.92	32	-
Curtet and Ricou	1964	44	0.48	3.22	125	0.49	3.2	1.0	50	1 ^e
			0.48	3.22	226	0.27	5.8	1.0	-	-
Fejer, et al.	1967	45	1.0	6.0	50-400	1.0	2.7-21	1.0	48 ^c	-
			1.0	6.0	200	0.5	10.6	1.0	36	-
			1.0	6.0	300	0.33	15.9	1.0	36	-
			1.0	6.0	300	0.67	15.9	1.0	36	-
			1.0	6.0	400	0.25	21.2	1.0	36	-
Zawacki and Weinstein	1968	35	0.356	8x8 ^f	14.1	3.4	0.8	1.0	21.0	5 ^g
			0.356	8x8 ^f	6.0	8.0	0.34	1.0	14.1	5.5
			0.356	8x8 ^f	3.0	16.0	0.17	1.0	14.1	6.5
			0.356	8x8 ^f	1.69	28.5	0.095	1.0	11.2	17.0
			0.356	8x8 ^f	1.21	39.5	0.069	1.0	11.2	5.5
Paulk	1969	42	0.50	none	401.0	0.477	10.65	0.89	18	2.0
					405.0	0.125	10.75	0.93	14.5	5.0

^aBased on jet diameter D_j and velocity U_j .

^bMaximum deviation from average.

^cCenterline concentration measurements only.

^dAssumes similarity of velocity profiles.

^eIncludes axial pressure gradient term; author's measurement.

^fSquare duct.

^gMomentum check calculation begins at first "jet-flow" station.

Shapiro [43] and Paulk [42] used a heated central stream to investigate the transfer of heat. In all cases the small deviations from unity density ratio do not seem to influence the results.

The effects of ducting of the outer stream can be seen in the momentum check for Forstall's data. Forstall's data are carried to much larger x/D than the other experiments, and as was pointed out by Maczynski [46] the data for large x are apparently influenced by the presence of the walls. It would be expected that the influence of the presence of the walls (and the pressure gradients thereby generated) would be greater for the more nearly equal velocity ratio cases, for in these tests the level of turbulent shear stress is lower than in cases in which there is a large velocity difference between the streams. Such an effect shows up in the momentum check. Thus the $U_o/U_j = 0.5$ case, which is the highest velocity ratio case for which sufficient data are provided by Forstall [40] to perform a momentum analysis, is much further out of momentum balance than the $U_o/U_j = 0.2$ and 0.25 cases. It is also notable that in the experiments of Landis and Shapiro [43] which used substantially the same type of apparatus as was used by Forstall, measurements were not reported beyond $x/D = 32$. In all of these calculations the axial pressure gradient was assumed zero; no pressure measurements were presented by Forstall or by Landis and Shapiro. The apparent lack of a

wall effect in the Curtet and Ricou [44] momentum balance is explained by their measurement of the axial pressure gradient and inclusion of the appropriate term in the momentum balance.

The data of Zawacki and Weinstein is interesting because of the very high velocity ratios U_o/U_j measured; however, the behavior of these flows involves large regions of recirculating flow, as has been described by Rozenman [47].

Of the experiments listed in Table 3.2, only those of Forstall [40] (and not Reference [41]) and Zawacki and Weinstein [35] include measurements of profiles at $x = 0$, and as will be discussed below, both of these experiments are in certain ways beset by problems.

Figure 3.14 presents measured axial decay of centerline velocity curves selected from the experiments considered in this section in which the outer stream was enclosed in a duct. As for the two-dimensional case, a strong dependence on the velocity ratio parameter can be seen; the decay beginning progressively later as the velocity ratio increases. Forstall's data exhibits a somewhat anomalous behavior which will be gone into in more detail below.

Certain of the ducted mixing experiments are compared in Figure 3.15 with the zero pressure gradient Paulk [42] data. No strong conclusions can be reached

Sym	U_o/U_j	U_j , ft/sec	D_j , in.	Re_{D_j} $\times 10^{-4}$	Investigator	Ref.
○	0.2	225	0.25	2.98	Forstall	40
△	0.25	120	0.25	1.59	Forstall	40
●	0.27	226	0.476	3.2	Curtet and Ricou	44
◆	0.46	220	0.50	5.84	Landis and Shapiro	43
◻	0.49	228	0.476	5.77	Curtet and Ricou	44
◇	0.50	180	0.25	2.38	Forstall	40
□	0.50	90	0.25	1.19	Forstall	40
◊	0.67	300	1.0	16.0	Fejer et al..	45

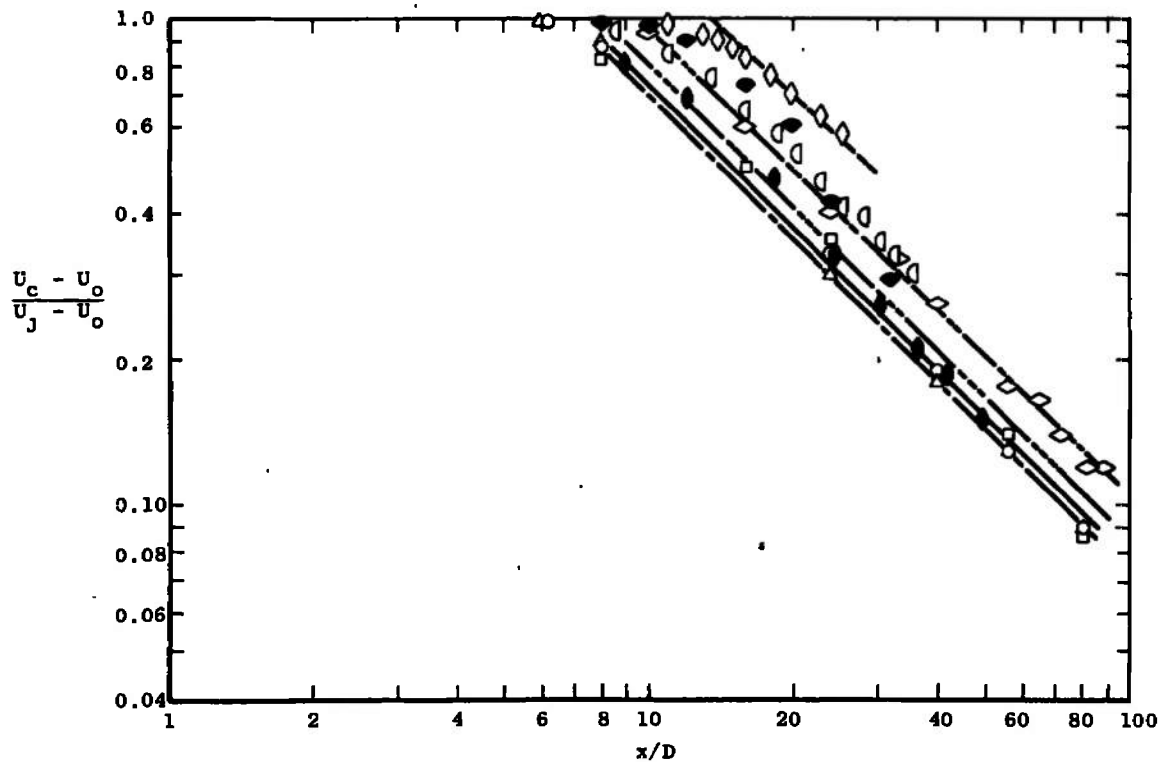


Figure 3.14. Comparison of centerline velocity decays; coaxial axisymmetric jets.

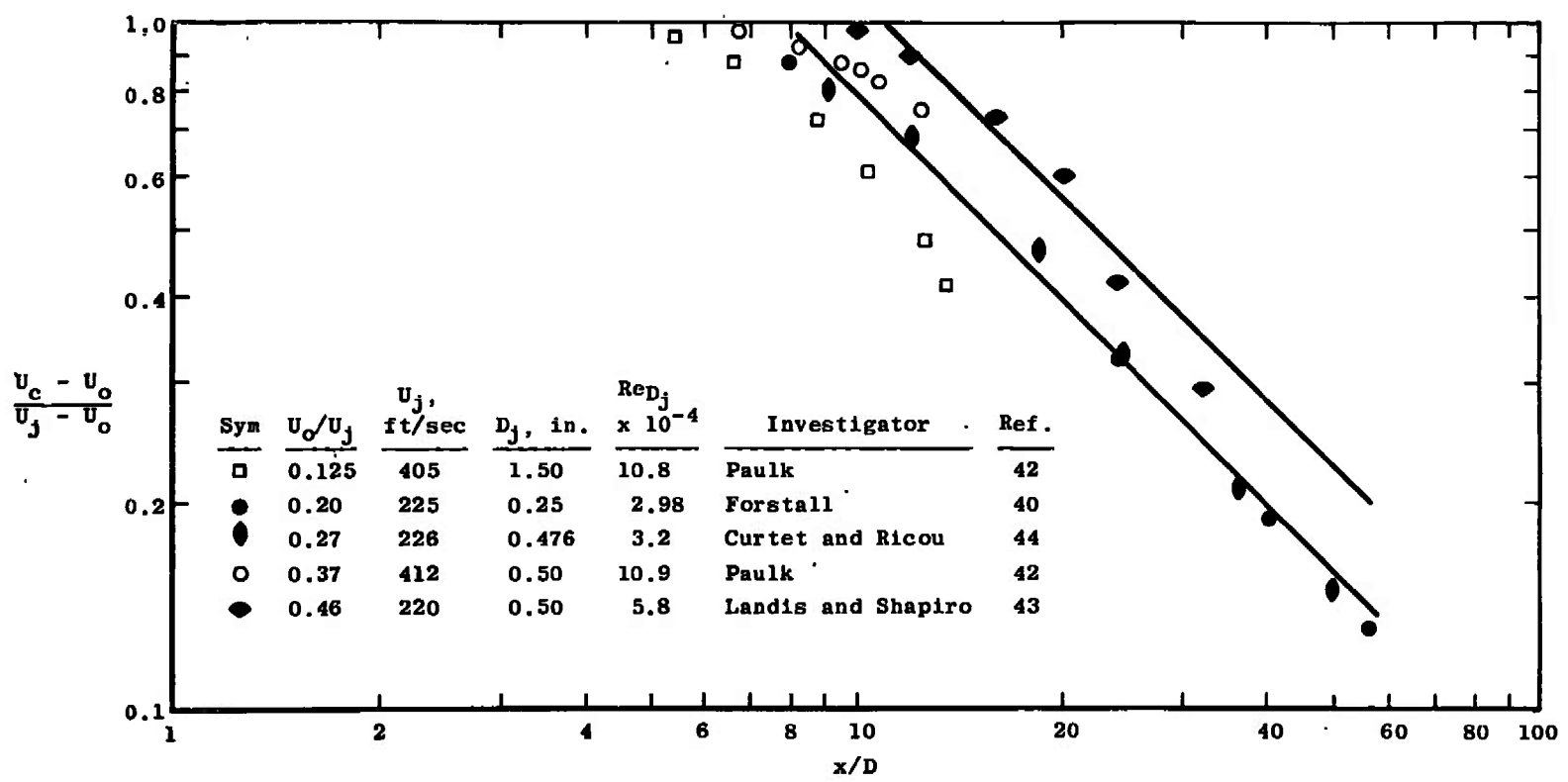


Figure 3.15. Comparison of axial decays measured by Paulk. (unducted) with those measured in various ducted experiments.

because of the extremely short second regime investigated by Paulk; however, the data fall in the appropriate region compared to the ducted data, exhibiting a lengthening potential core as the velocity ratio approaches unity.

Forstall's experiments [40, 41] involved the mixing of two coaxial streams of air at low velocities, with the center jet incorporating about ten percent by volume helium as a tracer. As shown in Table 3.2, page 126, both Forstall's $U_o/U_j = 0.2$ and $U_o/U_j = 0.25$ cases show only moderate deviation from momentum balance. His $U_o/U_j = 0.5$ case deviates substantially, while for the $U_o/U_j = 0.75$ case there is not sufficient information available to perform a momentum check. Closer inspection of Forstall's $U_o/U_j = 0.5$ case shows several features that are unfortunately not at all uncommon and which deserve further discussion.

As Figure 3.16 shows, there are at least two different axial decay curves presented in Reference [40] for the $U_o/U_j = 0.5$ case. Two of these represent different nozzle (and secondary stream) velocities, and thus different primary jet Reynolds numbers. Figure 3.16 can thus be taken as evidence for the same sort of shift of the decay curve with primary jet Reynolds number as is seen in the circular jet-into-still-surroundings. In addition, Forstall performed measurements with two different nozzles, one 1/4 inch diameter and the other 1 inch diameter, with the larger nozzle being used for the near field investigation.

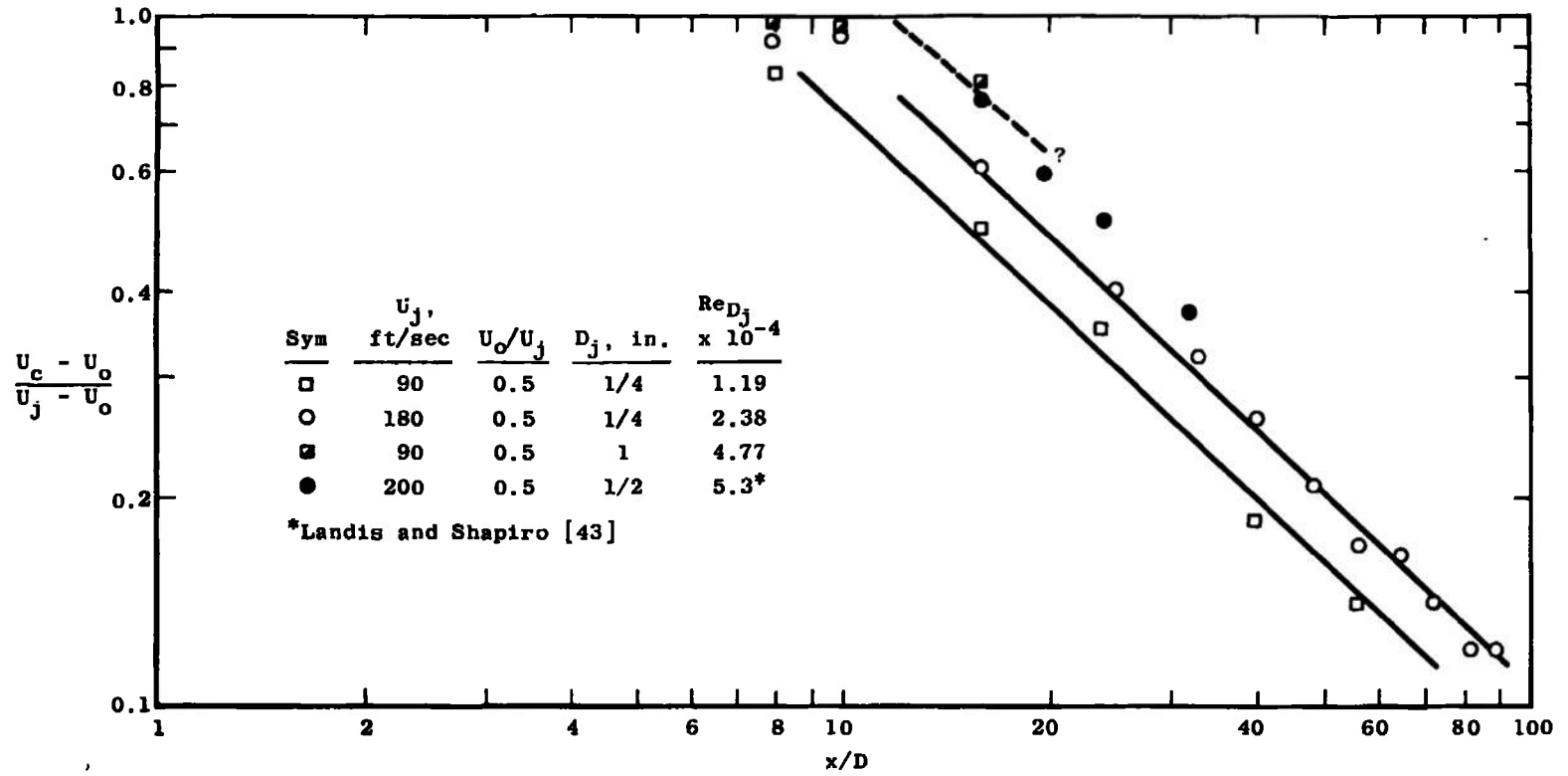


Figure 3.16. Evidence for data shift with Reynolds number,
Forstall data [40].

Forstall's $U_o/U_j = 0.5$ decay data also show, besides the two distinct curves already mentioned, what appears to be the beginning of a third decay curve, marked "?" on Figure 3.16. Since these data only extend to $x/D = 16$, presumably they represent data from the one inch diameter nozzle, and thus data at a nozzle Reynolds number $Re_d = 47,700$. This conjecture is strengthened by comparison with the data of Landis and Shapiro [43] at $Re_d = 53,000$.

As was mentioned above, Forstall in Reference [40] presents initial velocity profiles at the jet exit, $x/D = 0$. These profiles are not presented in Forstall and Shapiro, Reference [41]. If finite-difference techniques are to be used for comparison with the downstream decay rates, these profiles (and measured boundary layer thicknesses) are important, particularly so as the stream velocity ratio approaches unity. (This is because as the stream velocity ratio approaches unity the free mixing turbulent shear stress level decreases and the details of the initial conditions of the flow become more important.) Unfortunately, the initial profile data presented by Forstall [40] show a marked asymmetry; further, for the $U_o/U_j = 0.5$ case, initial profiles are presented only for the 0.25 inch nozzle. The effect of the resulting uncertainty in the initial boundary layer thickness is shown in Figure 3.17, in which the results of a finite difference calculation of Forstall's $U_o/U_j = 0.5$ case are presented as a function of the initial

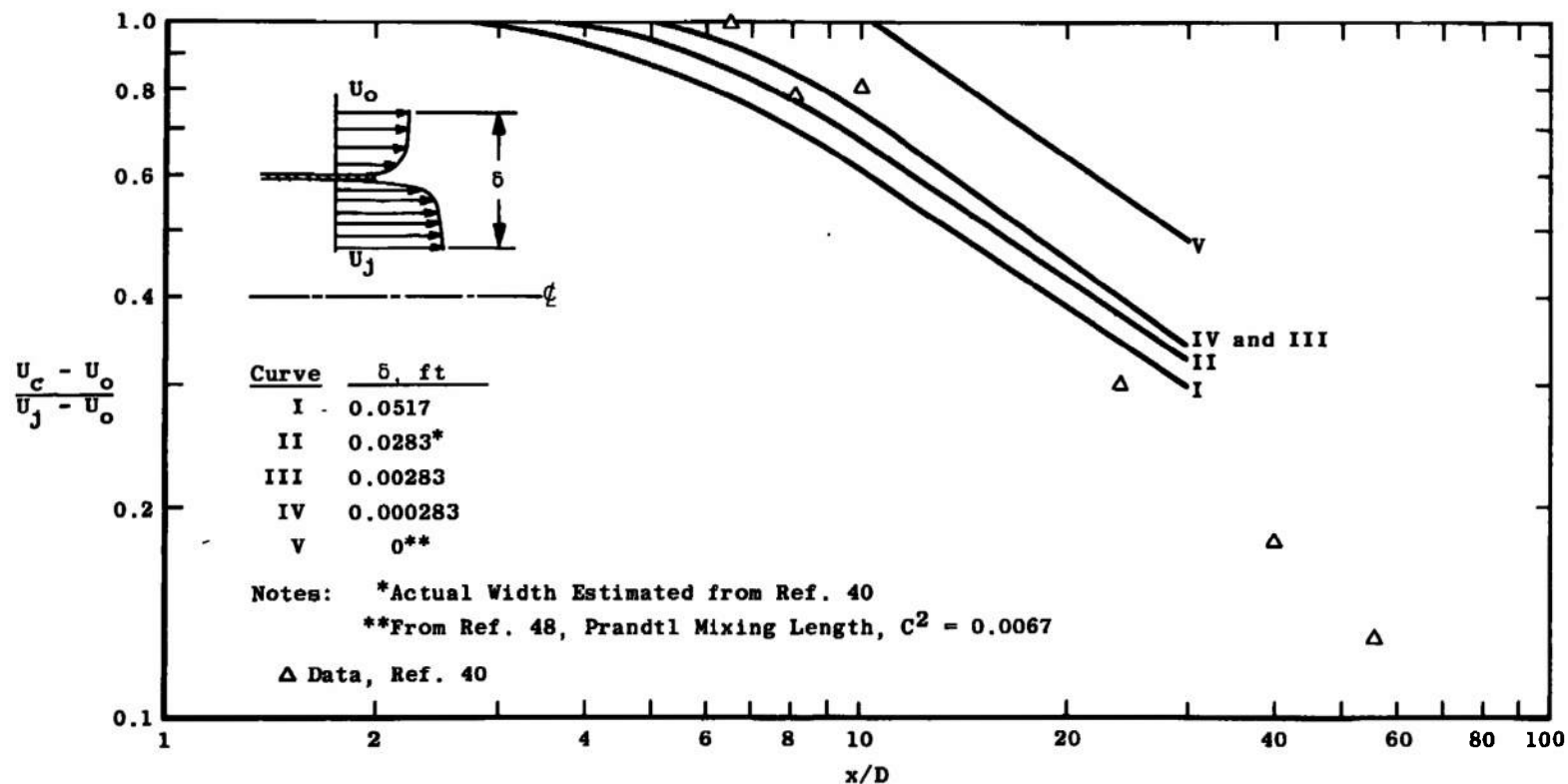


Figure 3.17. Calculated centerline velocity decay as a function of assumed initial boundary layer thicknesses, Prandtl eddy viscosity model, $\epsilon = kb|U_{\max} - U_{\min}|$; $k_I = 0.007$, $k_{II} = 0.011$.

boundary layer thickness. The calculations for this example used the Prandtl eddy viscosity model--although the particular eddy viscosity model used is unimportant--and used the numerical technique described in Appendix E. The influence of the choice of initial boundary layer thickness is apparent. Further, it can be seen that beyond a certain value of the initial thickness, the results are unchanged, as would be expected. The "negligible thickness" curves also show essentially the same slope as predicted by the Squire and Trouncer [48] integral (and hence zero initial boundary layer thickness) calculation at this velocity ratio. The difference in potential core lengths is due to a different choice of shear stress model--Squire and Trouncer use Prandtl's mixing length to evaluate the shear stress at the half-velocity radius. In the second regime both the Prandtl eddy viscosity model and the Prandtl mixing length, with the constants used here, give substantially the same value for the shear stress at the half-velocity radius.

Experimental evidence for the importance of initial conditions as the velocity ratio approaches unity is strikingly illustrated by Figure 3.18. This figure shows centerline composition (of argon tracer) decay profiles from the data of Fejer, et al., [45] for a velocity ratio U_o/U_j of 1.0. The different curves are a result of changes in the center jet velocity U_j (and obviously of concomitant changes in the external velocity U_o) from 50 ft/sec

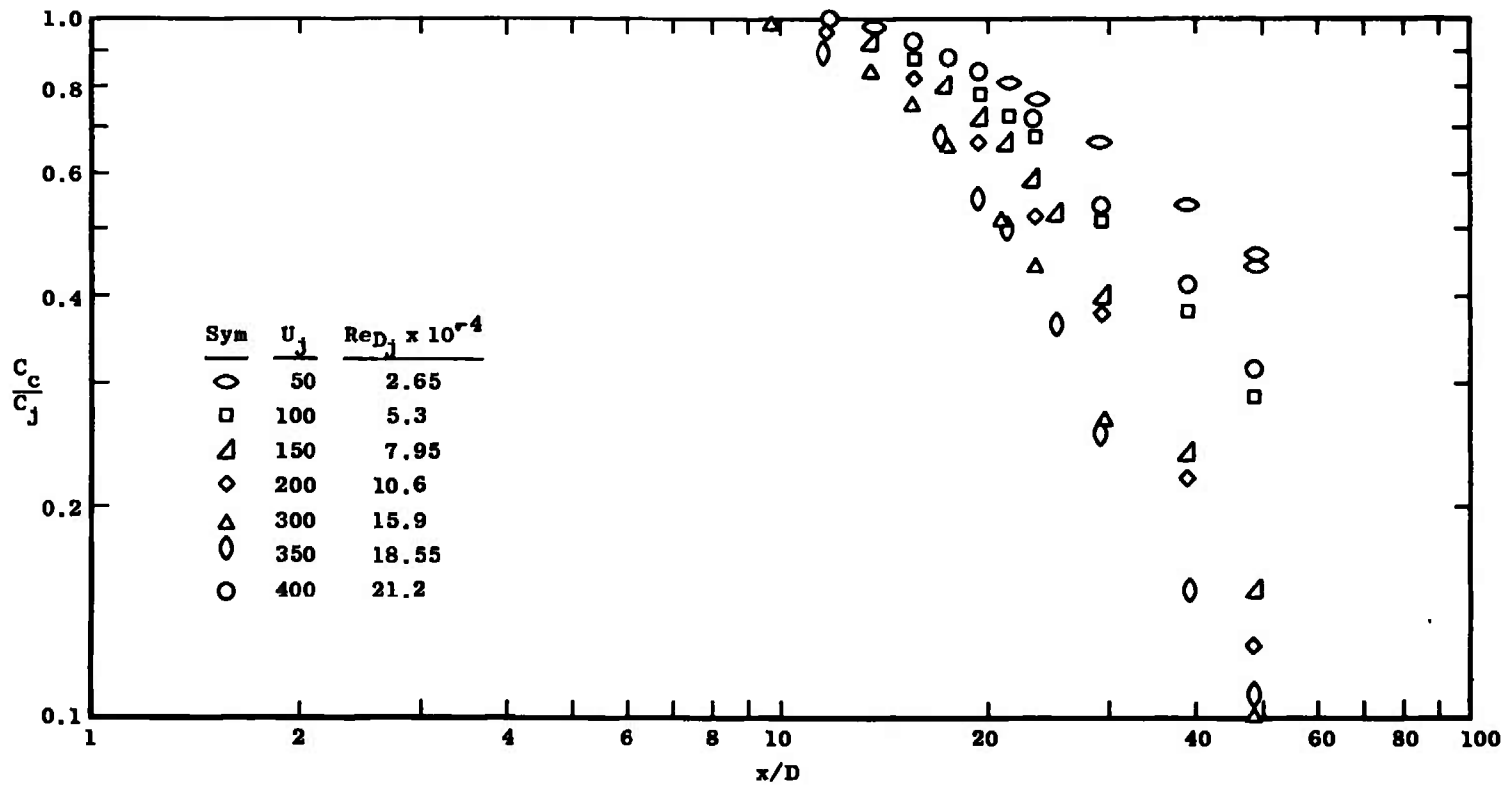


Figure 3.18. Variation in axial decay rate with initial velocity for coaxial jets with unity velocity ratio. Data from Fejer, et al., [45].

($Re_D = 2.65 \times 10^4$) to 400 ft/sec ($Re_D = 21.2 \times 10^4$). Apart from the anomalous behavior of the 400 ft/sec case--which it is argued in Reference [45] is caused by boundary layer transition effects increasing the mixing rate for all other cases--there is a steady progression toward increased mixing rates at increased velocities. This progression is surprisingly counter to the trend observed in both the jet into still air and the $U_o/U_j = 0.5$ data of Forstall [40], Figure 3.14, page 129, for which an increase in core length and decrease in extent of mixing (at a given axial station) with increase in velocity is shown. Fejer, et al., [45] report no correlation between turbulent intensity level in the jet and the rate of mixing. Further, the effect of the ducting of the outer jet on the mixing rate at this velocity ratio is unknown, so that the cause of the variation both in core length and in mixing rate (as evidenced by the increasing slope of the decay curves with increasing velocity) must remain mysterious. It may be that effects of a laminar-turbulent transition are included in the observed behavior. Figure 3.18 does, however, illustrate the need for an adequate understanding of the initial region in flows which, because of their near-unity velocity ratio, are dominated by their initial conditions.

Landis and Shapiro [43] extended the work of Forstall [40, 41] to the case in which the central stream temperature is heated above the outer stream temperature,

thus complementing the mass transfer measurements of Forstall with measurements of the diffusion of heat. Most of the data of Reference [43] was taken at temperature ratios large enough to influence the mixing process; however, as listed in Table 3.2, page 126, some of the data are at temperature (and thus density) ratios not much different from unity. Figure 3.19 shows a comparison of the data of Landis and Shapiro with that of Forstall. As might be expected from the discussion above, the Landis and Shapiro $U_o/U_j = 0.75$ case shows a strong deviation from a linear decay curve. However, considering only the early region of the curve, it is evident that a strong shift with velocity ratio exists, as has already been pointed out. Figure 3.19 also shows further evidence of a shift in the data with the primary-jet Reynolds number in the comparison of Landis and Shapiro $U_o/U_j = 0.25$ data (at $Re_D = 5.3 \times 10^4$) with Forstall's $U_o/U_j = 0.25$ data, taken at $Re_D = 1.6 \times 10^4$.

In addition to the velocity ratio 1.0 case, Fejer, et al., [45] measured centerline velocity decay data for several other velocity ratios, ranging from 0.25 to 0.67. Figure 3.20 shows a comparison between their centerline decay data and those measured by other investigators at different primary-jet Reynolds numbers. In this case, the data of Fejer, et al., which in each case is at a larger primary-jet Reynolds number than the data with which it is

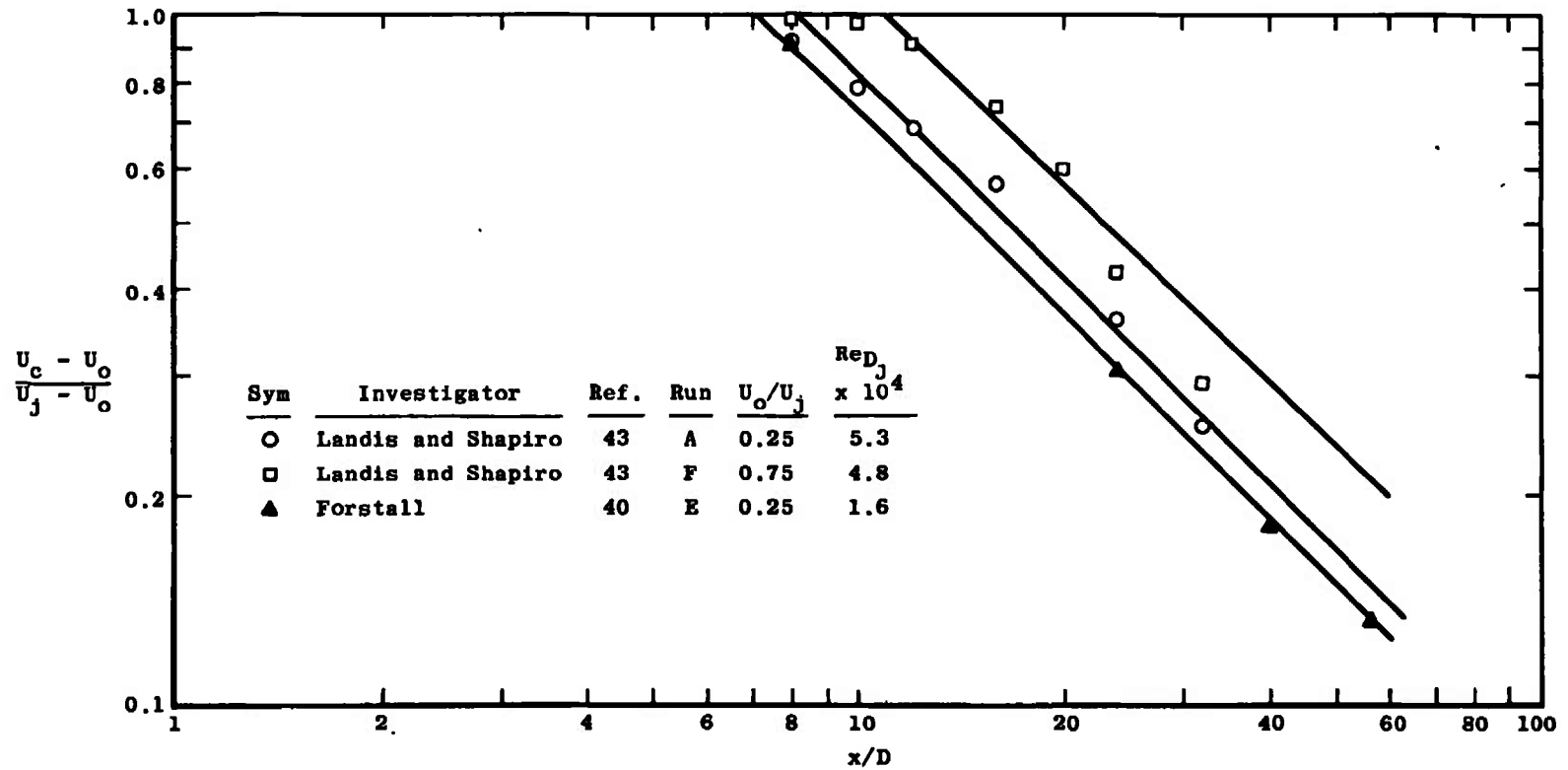


Figure 3.19. Centerline velocity decay, coaxial axisymmetric jets.

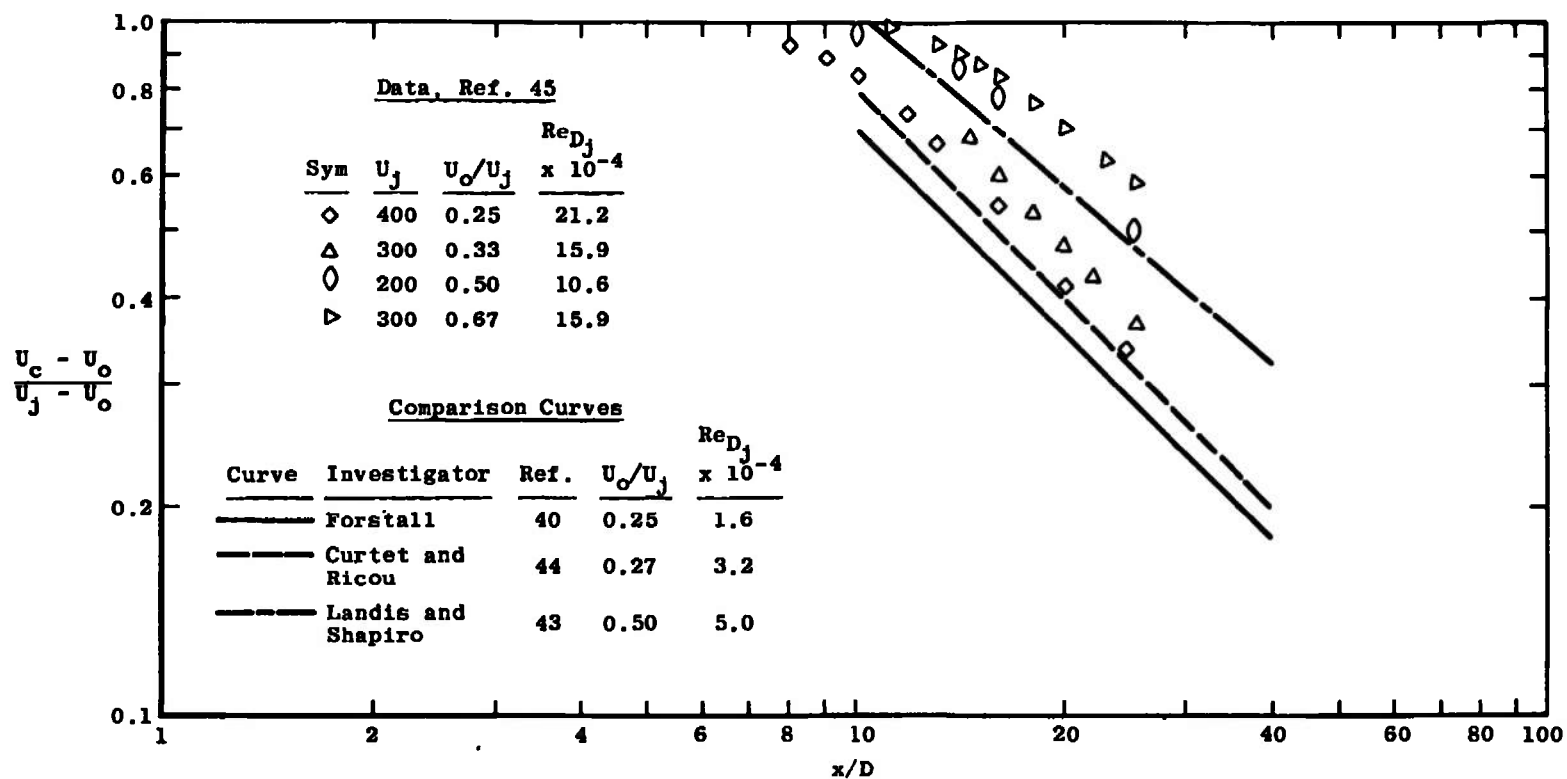


Figure 3.20. Comparison of centerline velocity decay data of Fejer, et al., [45] with other investigators.

compared, can be seen to indicate a decrease in the amount of mixing at a given axial station with increase in primary jet Reynolds number.

It should be noted that for $U_o/U_j = 0.2, 0.25,$ and 0.33 , Fejer, et al., [45] present the radial variation of the eddy viscosity, ϵ , defined by

$$\epsilon = \frac{\tau/\rho}{\frac{\partial u}{\partial r}}$$

These values are obtained in a manner similar to that used by Paulk; i.e., through integration of the measured profiles to various stations, to evaluate the shear stress from the integral momentum equation. The value of shear stress at a given radial location is then divided by the value of $\partial u/\partial r$ obtained using a finite-order polynomial fit to the radial velocity profile. Surprisingly, however, Fejer, et al., [45] do not report velocity profiles corresponding to the eddy viscosity profiles they report.

Paulk's measurements [42] have already been described briefly. His apparatus consisted of a central jet of air with a hydrogen tracer surrounded by a coaxial jet of air. The outer flow was not ducted, which resulted in an extremely short second regime. In addition to profiles of mean flow velocity and concentration, Paulk obtained the turbulent shear stress through use of the integral mean flow

momentum equation and the measured mean flow velocity, concentration, and enthalpy profiles.

All of the data considered to this point indicate that the mean velocity decays approximately as x^{-1} , as is required by self-preservation considerations. The velocity profiles are locally similar, and can be fit by error function or cosine profiles, although with some inaccuracy [41, 42, 43]. The experiments run with trace gases or temperature traces indicate that both mass and heat diffuse more rapidly than momentum and that the turbulent Prandtl and Schmidt numbers are both approximately equal to 0.70.

Curtet and Ricou [44] and Zawacki and Weinstein [35] both investigated the turbulence structure in coaxial free jets. An additional study was made by Kobashi [49]; however, in this case mean velocity profiles are given for one jet, turbulent fluctuation profiles for a second, and turbulent shear stress profiles for still a third. Thus, this experiment can add little to the former two.

The axial decay of centerline velocity for two of the cases investigated by Curtet and Ricou [44] is presented in Figure 3.21. Measurements of two other velocity ratios were made by Curtet and Ricou, but in these cases the effect of the pressure gradient due to ducting of the jet was substantial. Of the two cases presented here, the

$U_o/U_j = 0.267$ case is nearly constant-pressure, and the

$U_o/U_j = 0.494$ flow is in a slightly favorable pressure

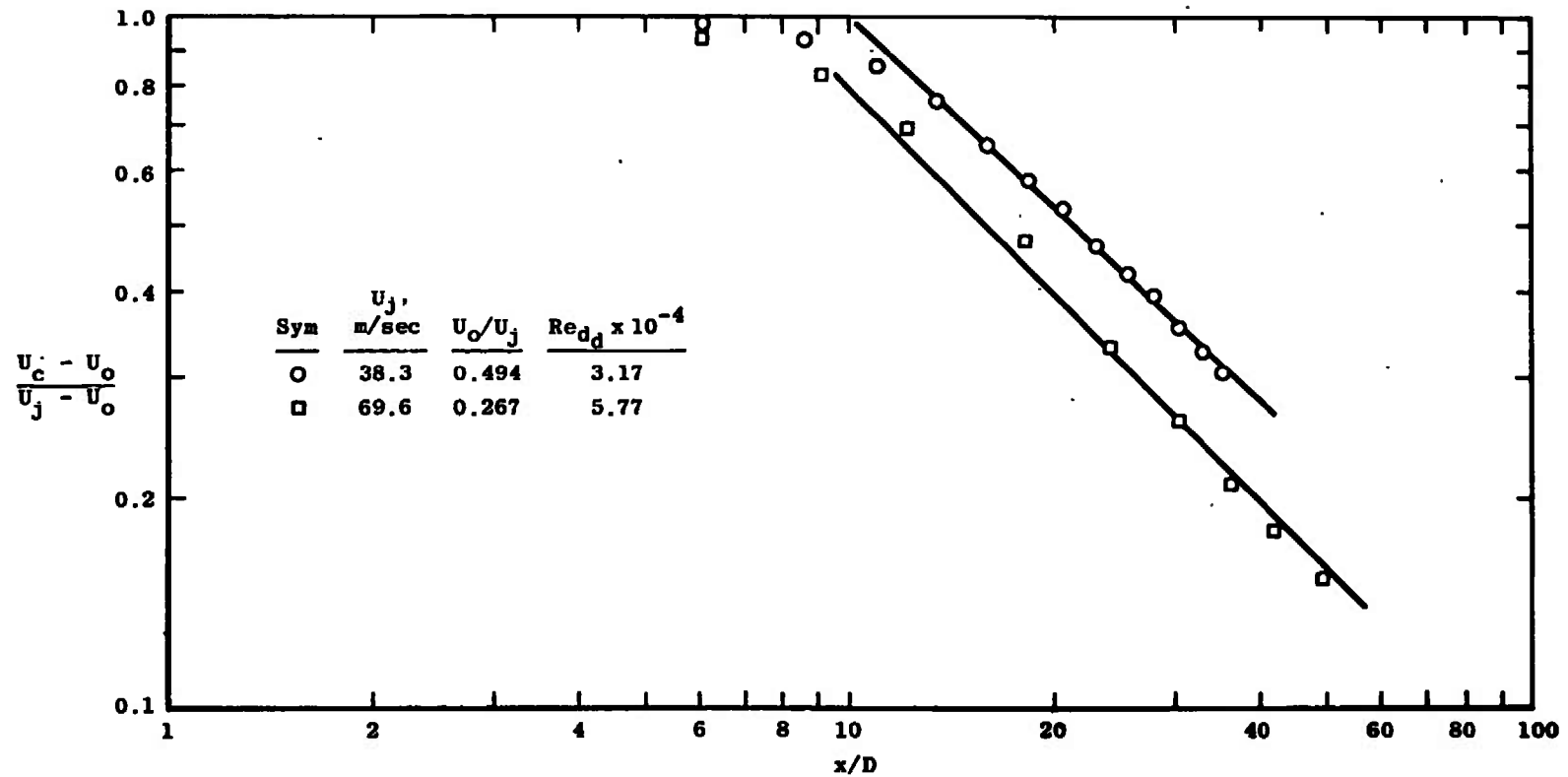


Figure 3.21. Axial decay of centerline velocity, data of Curtet and Ricou [44].

gradient. This difference in pressure gradient is probably the explanation for the apparent slight difference in slope of the decay curve for the two runs. Measurements of turbulent intensities and turbulent shear stress were made by Curtet and Ricou for the $U_o/U_j = 0.267$ case; as for other hot-wire measurements discussed, the turbulent shear stress measured is some 20 percent lower than predicted by integration of the mean flow profiles.

Axial decays for the data of Zawacki and Weinstein [35] are presented in Figure 3.22. Rozenmann [47] has investigated the flow in the initial region of this configuration in detail, and he states that for a velocity ratio U_o/U_j greater than 13 a recirculation region forms in the primary jet. Thus, it might be expected that for velocity ratios greater than 13 the axial decay data of Zawacki and Weinstein [35] will not look like other coaxial free jet decay data, and from Figure 3.22 this can be seen to be the case. Zawacki and Weinstein measured the three components of the turbulent intensity fluctuation and the turbulent shear stress, using a hot film probe, for all of the velocity ratios listed in Figure 3.22 (and Table 3.2, page 126). Like Curtet and Ricou [44] their measured shear stress profiles disagree with those obtained through integration of the mean flow momentum equation, being some 20 percent low.

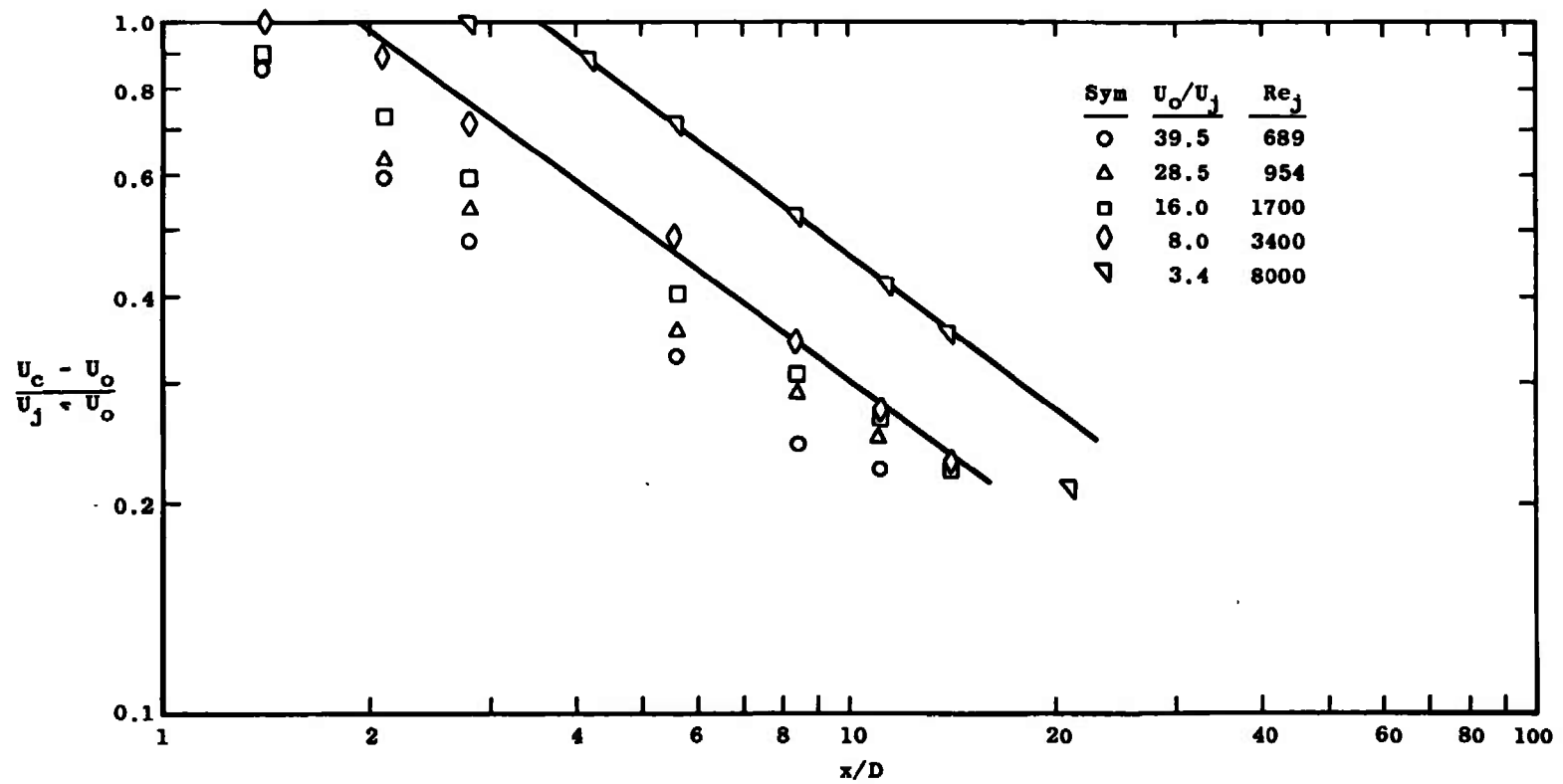


Figure 3.22. Axial decay of centerline velocity, data of Zawacki and Weinstein [35].

Figure 3.23 shows that the linear relation between the turbulent shear stress and the turbulent kinetic energy holds for both the data of Curtet and Ricou and that of Zawacki and Weinstein. Figures 3.24 and 3.25 show that the details of the lateral variation of the ratio of turbulent shear stress to turbulent kinetic energy are qualitatively similar, but also show some interesting differences. In Figure 3.24, the parameter a_1 is plotted versus the non-dimensional radius--the physical radius divided by an "effective radius," defined in Reference [44] as the radius of a cylinder with a volume equal to the excess flow rate

$$q = 2\pi \int_0^{r_o} (U - U_o) y dy$$

where r_o is the radius at which $U = U_o$, and a height equal to $U_c - U_o$. This definition of "effective radius" precludes direct comparison of the radial variation obtained by Curtet and Ricou [44] and Zawacki and Weinstein [35]. Figure 3.24 shows that the lateral profiles of a_1 are quite similar in shape at various downstream stations, as is also the case, although not nearly so strikingly, for the data of Zawacki and Weinstein [35], Figure 3.25. However, in the coaxial jet of Curtet and Ricou, at $U_o/U_j = 0.267$, the peak value of a_1 increases from $x/D = 5$ to 15, and then decreases from $x/D = 15$ to 20, while the peak for the Zawacki and Weinstein data occurs at $x/D = 3.4$ and then continually decreases. The

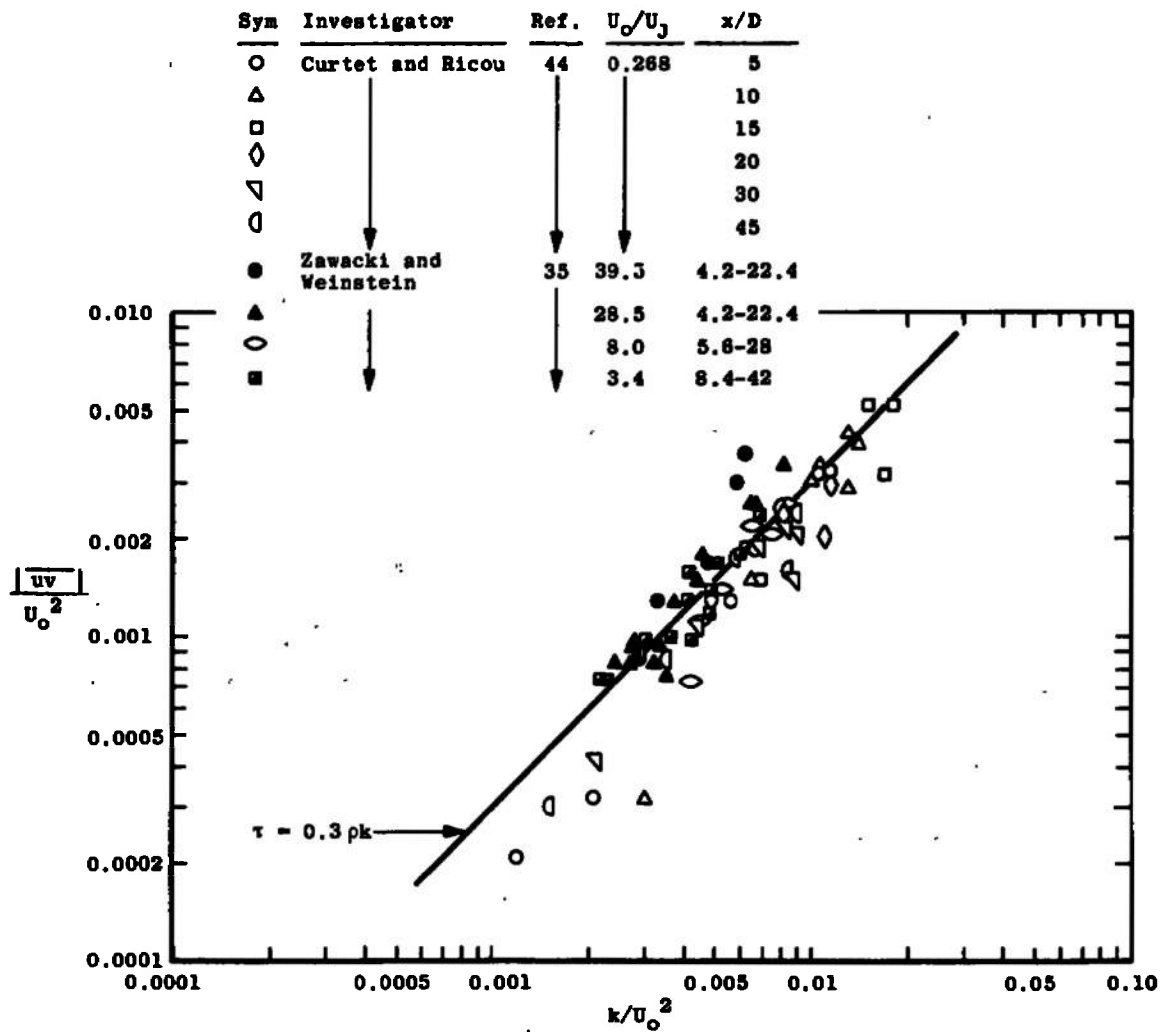


Figure 3.23. Relation between turbulent shear stress and turbulent kinetic energy, coaxial jets.

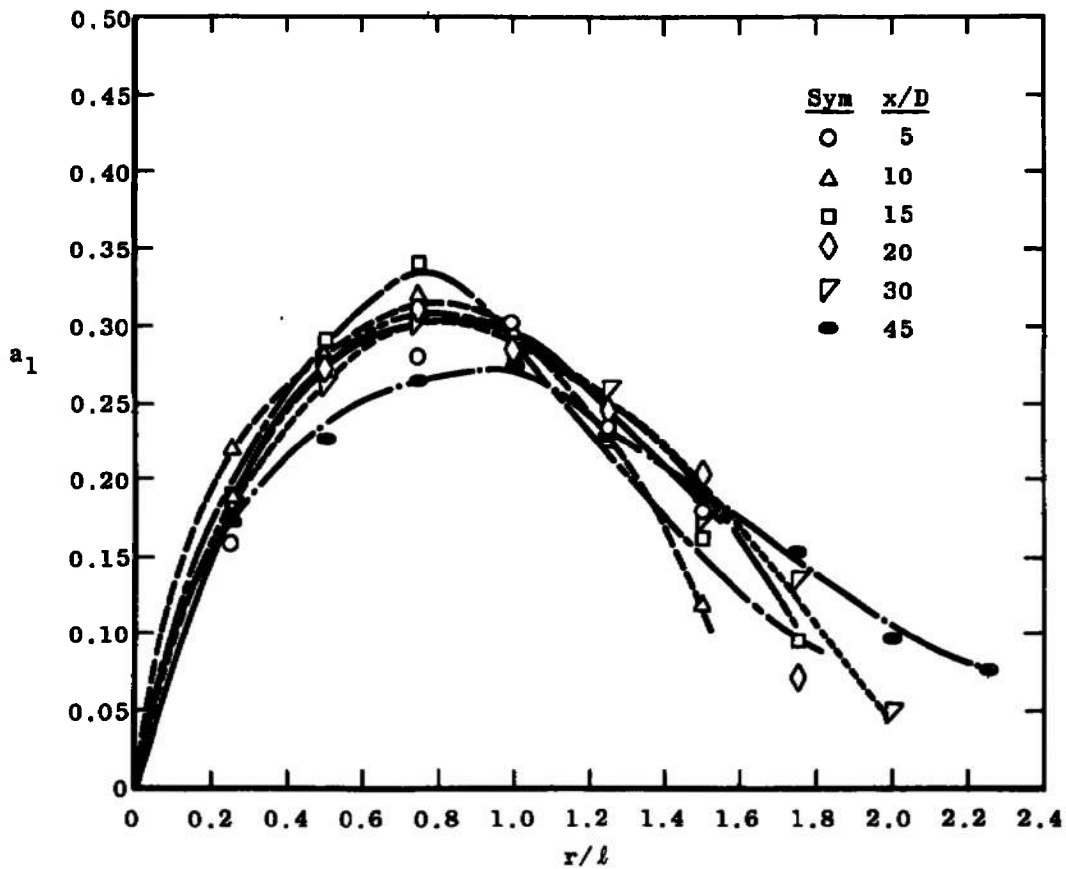


Figure 3.24. Radial variation of ratio of turbulent shear stress to turbulent kinetic energy, from Curtet and Ricou [44].

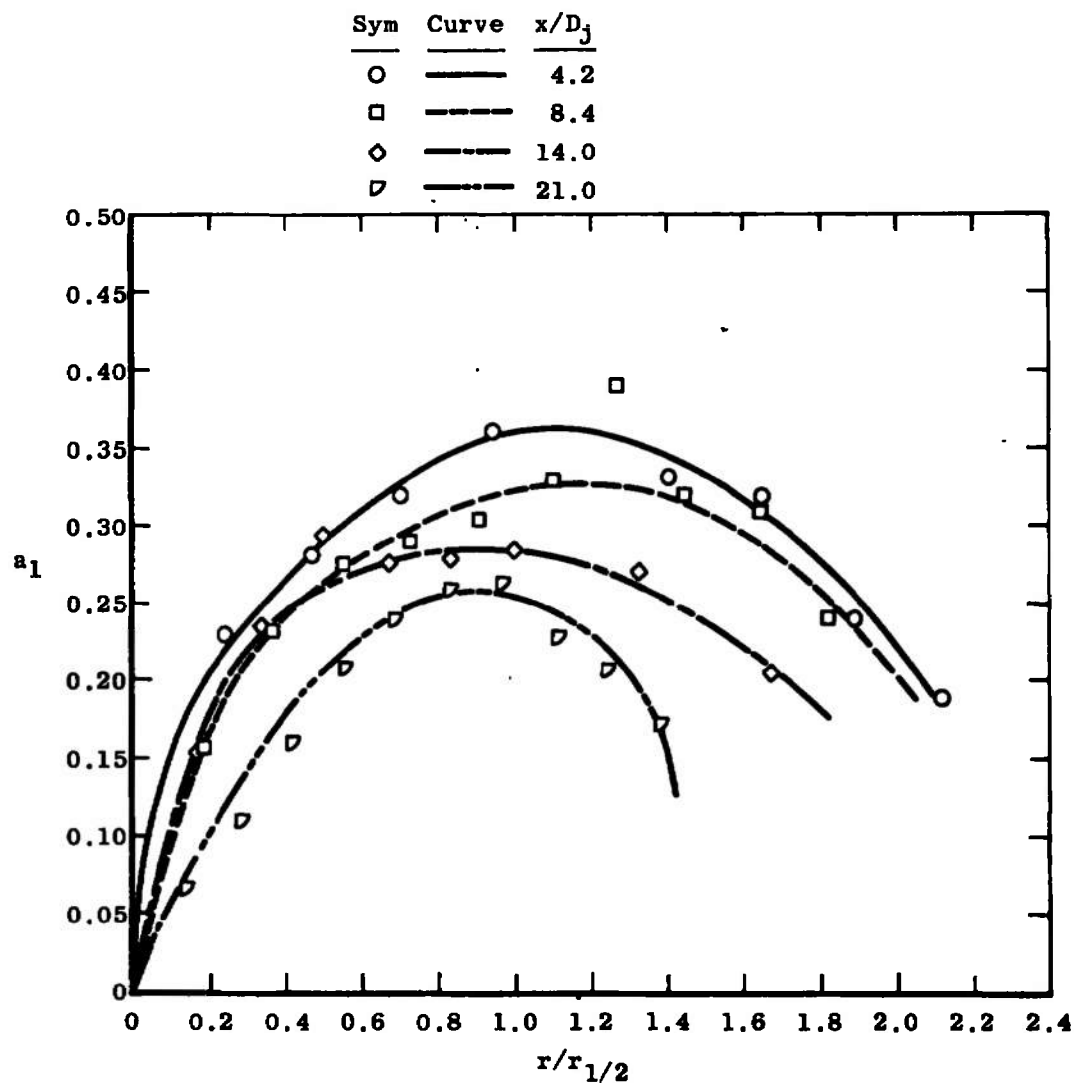


Figure 3.25. Radial variation of a_1 (= ratio of turbulent shear stress to turbulent kinetic energy), Zawacki and Weinstein data [35], $U_o/U_j = 3.4$.

difference between the flows is quite probably due to the strong changes in behavior of the flow as U_o/U_j becomes greater than unity, while the behavior of the data of Reference [44] may reflect a change from the first regime of mixing to the second.

Two-Dimensional Wakes

When a uniform flow passes over a two-dimensional body, that is, one which is essentially infinite in one direction, the action of viscosity in the fluid layers closest to the body causes those layers to slow. Thus, the flow leaving the body is no longer uniform but has a velocity gradient. If the characteristic Reynolds number $U_o d/\nu$, where d is some characteristic dimension of the body, is high enough, the flow leaving the body will be turbulent and the velocity deficit caused by the retarding action of the body will become smoothed out due to the action of turbulent mixing.

The three flows listed in Table 3.3 all represent two-dimensional wakes; they differ in the shape of the body used to create the wake. In the classic experiment of Townsend [5, 50] the two-dimensional wake is created by a 0.0625 inch diameter circular cylinder spanning a 15 x 15 inch wind tunnel through which flows a 42 ft/sec stream. Lee [51] generates an effectively two-dimensional wake by passing a nominally 100 ft/sec stream over an aerodynamic

TABLE 3.3
TWO-DIMENSIONAL WAKES

Investigator	Ref.	Year	Type	Character- istic Re x 10 ⁻³	Basis	Measure- ment Range ^a	Momentum Check
Townsend	50	1949	Circular Cylinder	1.36 4.0 ^b	Cylinder Diameter	500-950 1120-2280 ^b	- -
Lee	51	1966	Aerodynamic Body	24.0	Momentum Thickness ^c	0-120	4%
Chevray and Kovaszny	52	1969	Flat Plate	1.6	Momentum Thickness ^c	0-414	1.6% at x/θ ₀ = 86

^aBasis same as Re.

^bFrom Newman [3].

^cDefined as $\theta = \int_0^{\infty} \frac{U}{U_1} (1 - \frac{U}{U_1}) dy$.

body. The two-dimensional wake investigated by Chevray and Kovasznay [52] is formed by passing a 13 ft/sec stream over a flat plate.

Newman ([3], see Appendix C) shows that the small increment wake, i.e., the wake for which $U_c - U_o \ll U_o$, is approximately self-preserving, and that for a two-dimensional self-preserving wake the velocity deficit $U_c - U_o \propto x^{-1/2}$ and the width scale $b \propto x^{1/2}$. Townsend [50, 5] finds that self-preservation in the two-dimensional wake is only achieved for $x/d > 500$, where d is the cylinder diameter, and his measurements are carried out downstream of this point.

On the other hand, both Lee [51] and Chevray and Kovasznay [52] made detailed investigations of the initial region of a two-dimensional wake. Both investigators found that there is an extremely rapid increase in velocity on the wake centerline starting immediately at the trailing edge of the body. This increase is so rapid that both Lee [51] and Chevray and Kovasznay [52] found a finite velocity on the wake centerline as near as they were able to get to the trailing edge, as shown in Figure 3.26.

Because of its simplicity, and the fact that there is a finite background velocity on which the turbulent motion is superimposed, the two-dimensional wake has been extensively used for studies of the structure of turbulent flow [5, 53, 54]. All of the experiments considered here

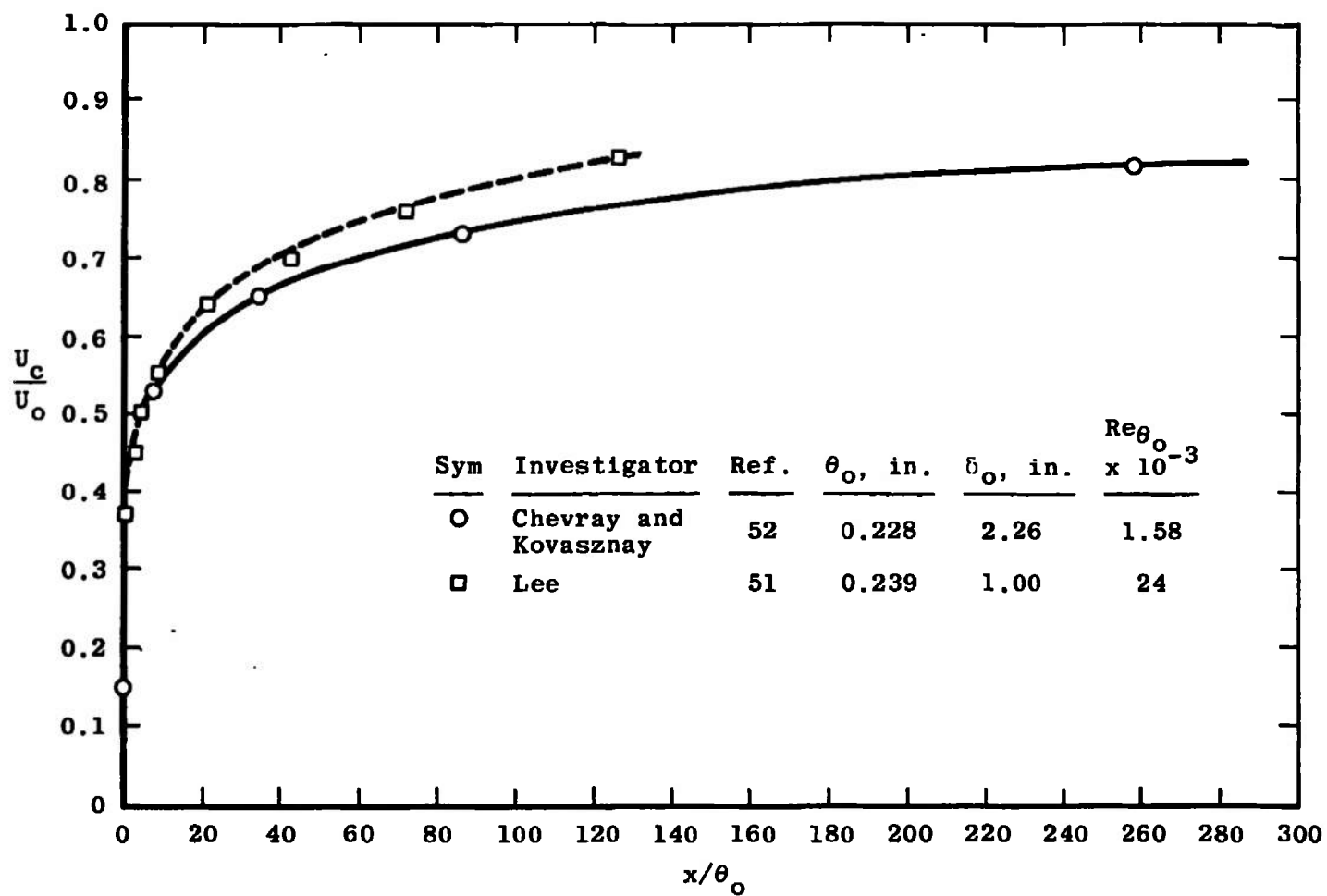


Figure 3.26. Increase of centerline velocity, 2D wake.

involved measurements of the turbulent intensities and turbulent shear stress; Townsend also measured the terms of the turbulent kinetic energy equation in the self-preserving region. Figures 3.27 and 3.28 show that the linear relationship between turbulent shear stress and turbulent kinetic energy observed in all other flows considered to this point holds also for the two-dimensional wake. However, Figure 3.28 shows that in the self-preserving region the average value is considerably different than in the initial region. It might be noted that the behavior exhibited in these two figures is somewhat anomalous; one would expect a decrease in turbulent shear stress downstream in the wake as the flow approaches isotropic conditions without perhaps an equivalent decrease in turbulent kinetic energy, and thus a decrease in the value of a_1 rather than the observed increase.

As described before, self-preservation requires that $U_c - U_o \propto x^{-1/2}$ and $b \propto x^{1/2}$. Thus to test for self-preservation the lateral variable should be $(y/d)/\sqrt{(x - x_v)/d}$ or $y/\sqrt{(x - x_v)d}$ where x_v is the virtual origin of the flow. If similarity is assumed, then

$$(u')^2 = (U_c - U_o)^2 g(\eta) ; \eta = y/b$$

from Newman ([3], Appendix C), and

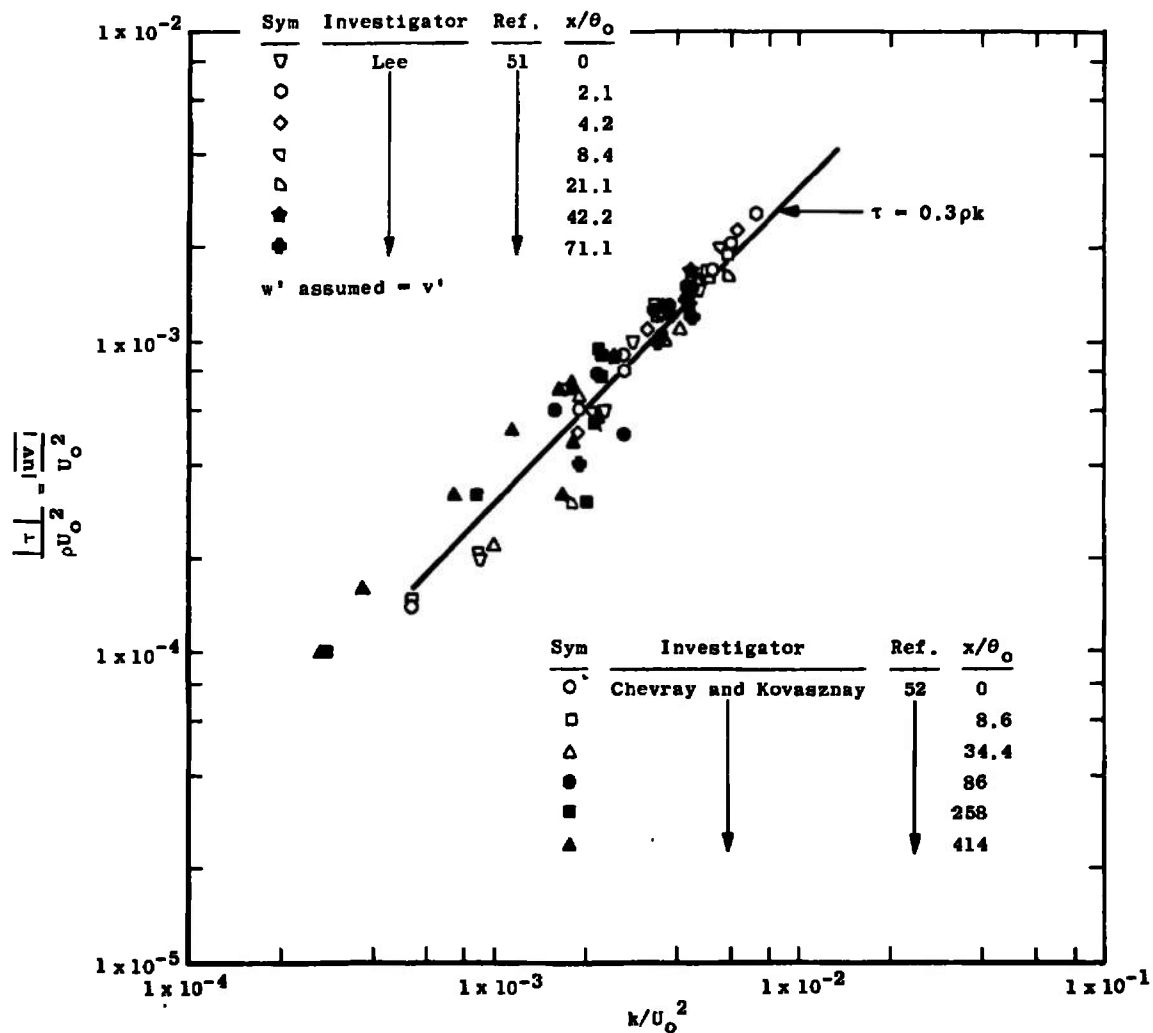


Figure 3.27. Relation between turbulent shear stress and turbulent kinetic energy in the initial region of a 2D wake.

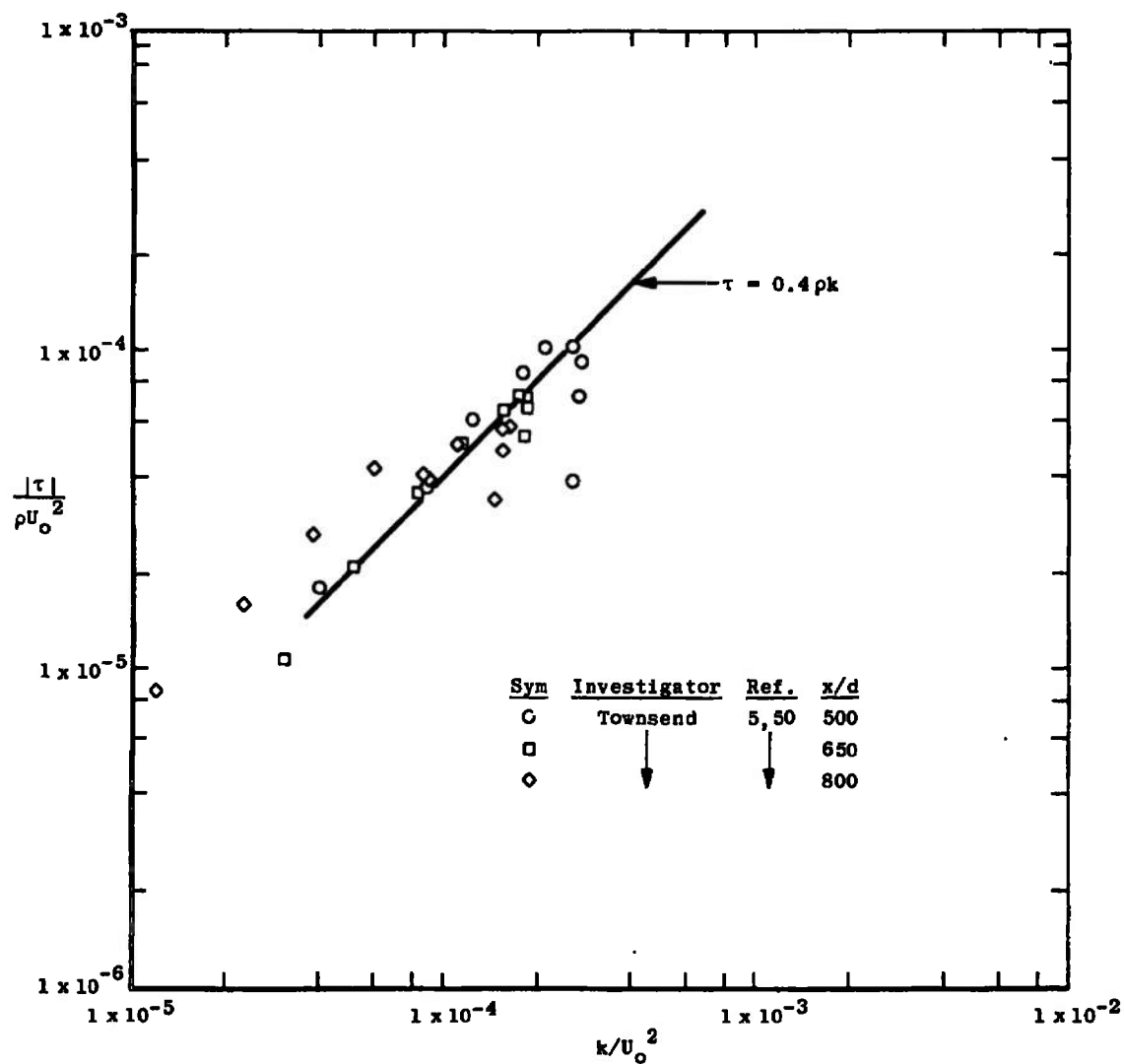


Figure 3.28. Relation between turbulent shear stress and turbulent kinetic energy in the self-preserving region of a 2D wake.

$$\frac{(u')^2}{U_o^2} = \left(\frac{U_c - U_o}{U_o} \right)^2 g(\eta)$$

but

$$U_c - U_o \propto (x - x_v)^{-1/2}$$

so

$$\frac{U_c - U_o}{U_o} = C \sqrt{\frac{x - x_v}{d}}$$

and thus

$$\left(\frac{u'}{U_o} \right)^2 \frac{x - x_v}{d} = \frac{1}{C} g(\eta)$$

The same development can be used for any other component of the turbulence structure. Thus, if the flow is self-preserving, it should be possible to plot any mean flow or structure quantity ϕ on a single curve of

$$\phi\left(\frac{x - x_v}{d}\right) \text{ versus } \frac{y}{\sqrt{(x - x_v)d}}$$

Figures 3.29 and 3.30 show that this is indeed the case for both the turbulent kinetic energy k and the parameter a_1 for Townsend's data.

That the initial region of a two-dimensional wake is not self-preserving is clearly shown by Figure 3.31 and

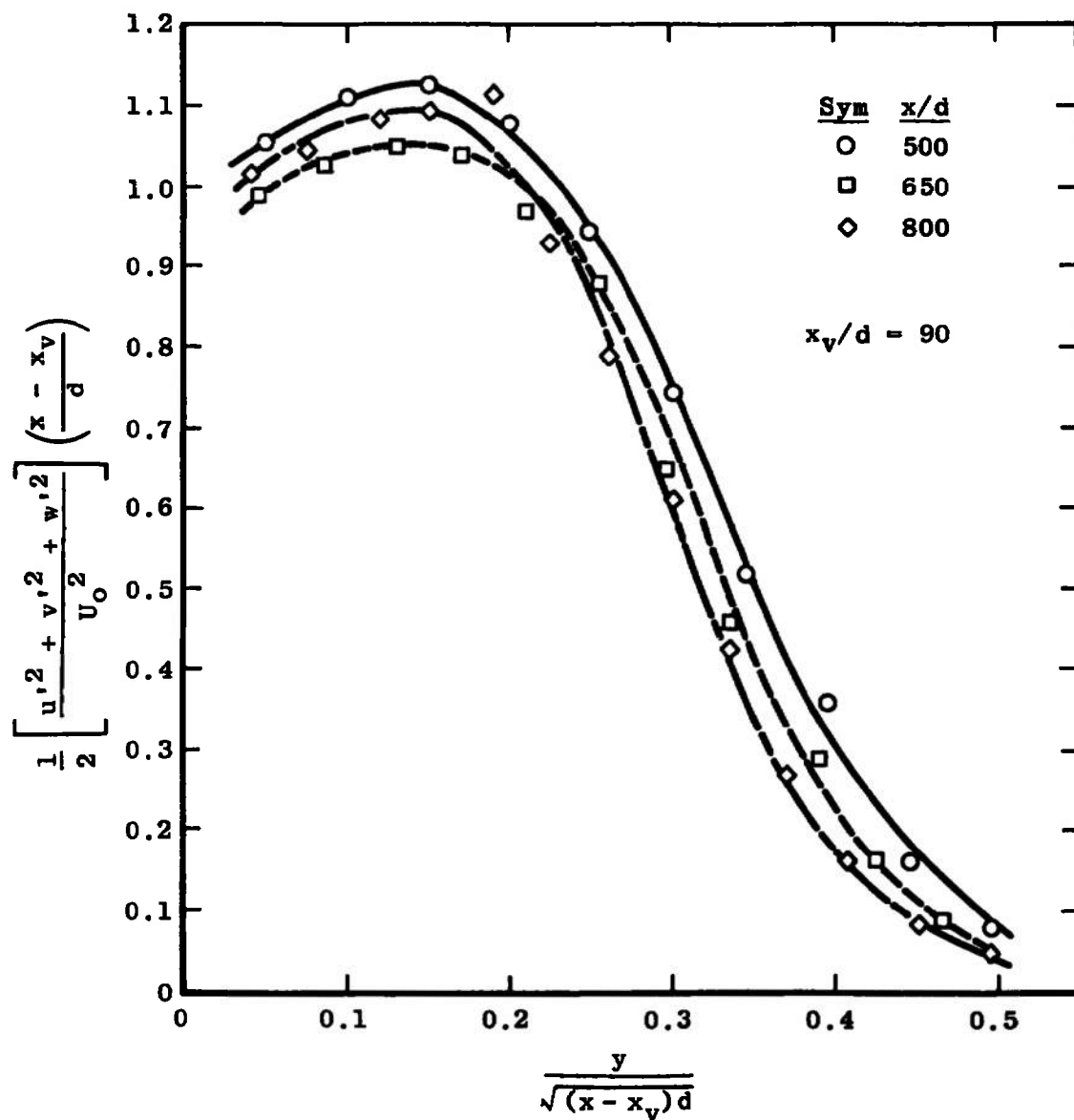


Figure 3.29. Self-preservation of turbulent kinetic energy, Townsend [50].

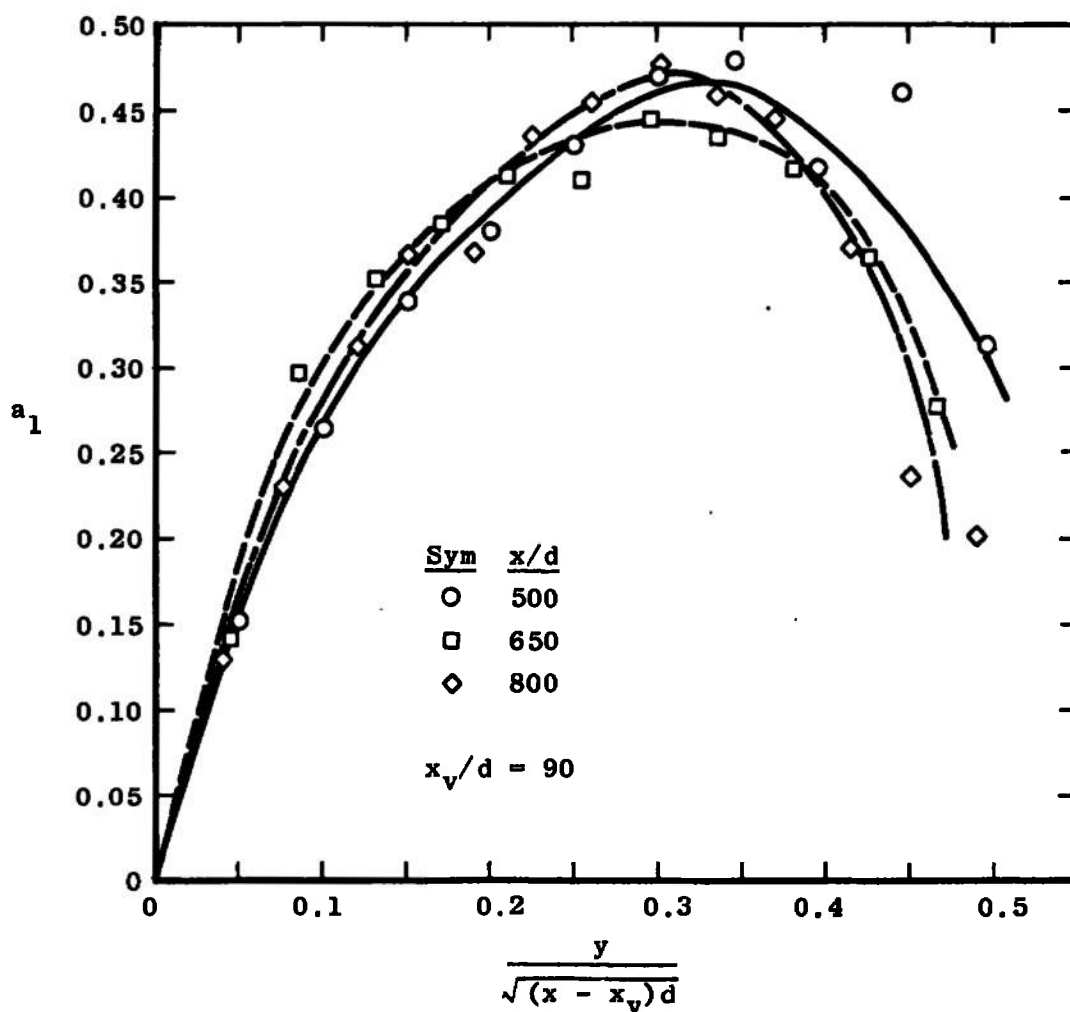


Figure 3.30. Ratio of turbulent shear stress to turbulent kinetic energy, two-dimensional wake, data of Townsend ([5] and [50]).

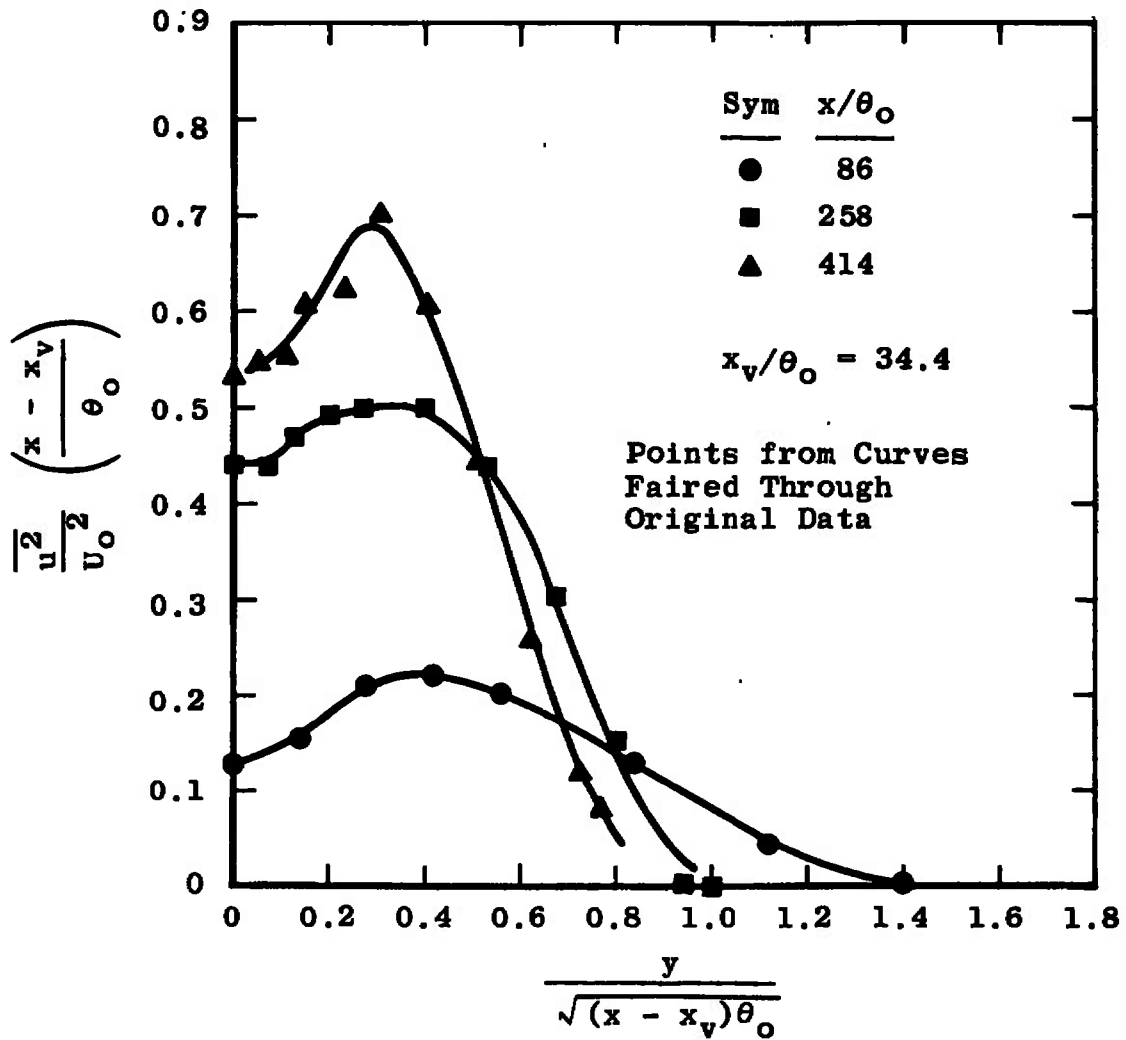


Figure 3.31. Test for self-preservation of turbulent intensity, Chevray and Kovasznay [52], 2D wake.

Figure 3.32. Figure 3.31 shows the axial component of the turbulent intensity from Chevray and Kovasznay's [52] data plotted in similarity variables, while Figure 3.32 shows the turbulent shear stress plotted the same way. Clearly these profiles do not reduce to one curve, and self-preservation is not achieved.

Chevray and Kovasznay's data [52] incorporates a number of closely spaced profiles, from which, as shown in Figure 3.33, a very interesting picture of the development of the parameter a_1 can be obtained. In Figure 3.33, this parameter can be seen evolving rather rapidly from a profile quite like the boundary-layer profiles of this parameter shown by Bradshaw, et al., [55] to a profile characteristic of a free mixing process, and in particular, to a profile qualitatively quite similar to the self-preserving profiles seen in Figure 3.30. This of course is the sort of process that the flow must undergo as it changes in character from a boundary-layer to a free-mixing flow.

Axisymmetric Wakes

Axisymmetric wakes are formed by two types of bodies, either circular or square disks, the latter in the far field, or axisymmetric solid bodies, immersed in a uniform stream. The disks are mounted perpendicular to the mean flow direction. Axisymmetric bodies, if they are not spherical, are mounted with their longer axis parallel to the mean flow direction. As for the two-dimensional wake,

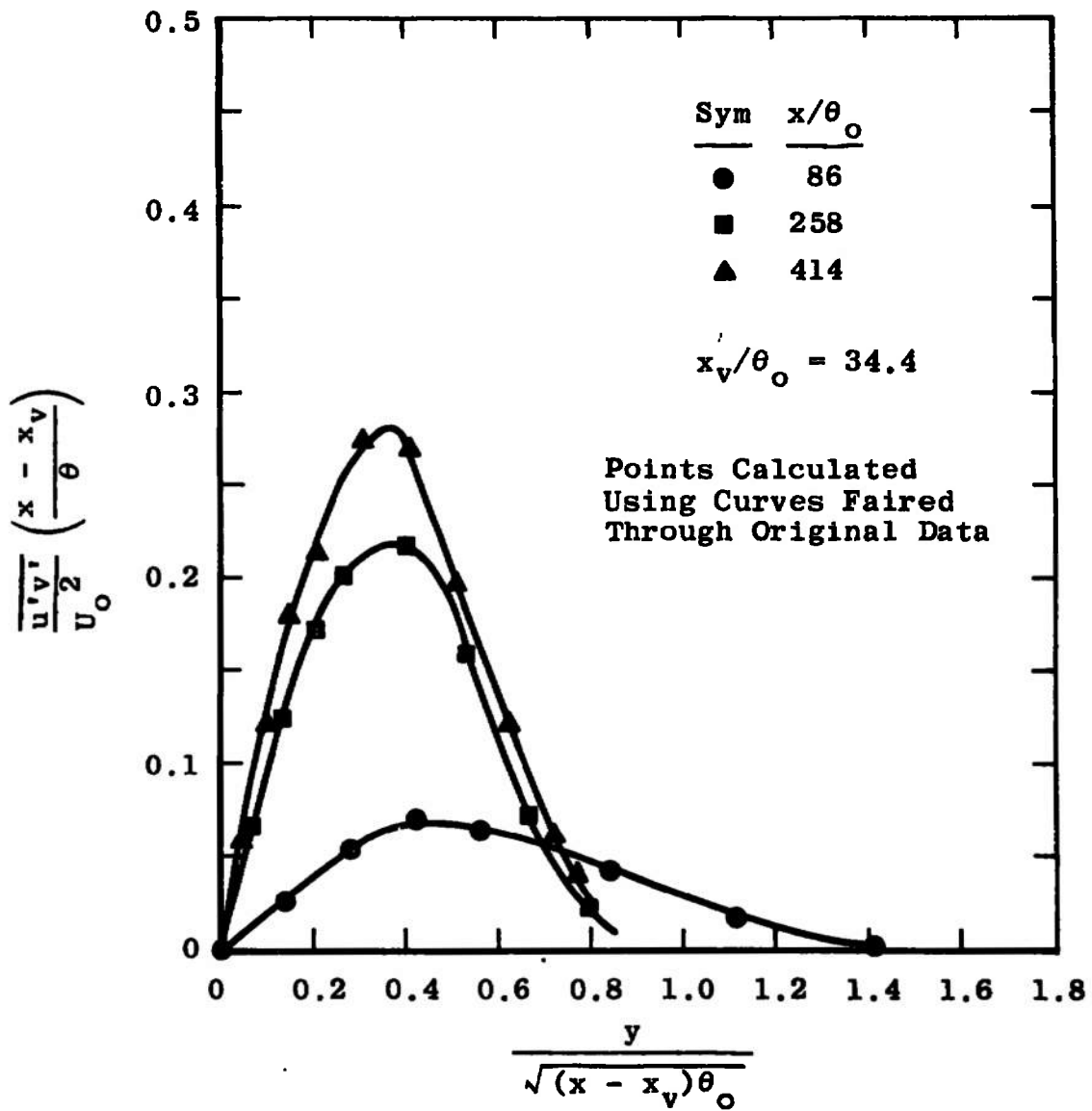


Figure 3.32. Test for self-preservation: turbulent shear stress profiles. Chevray and Kovaszny [52], 2D wake.

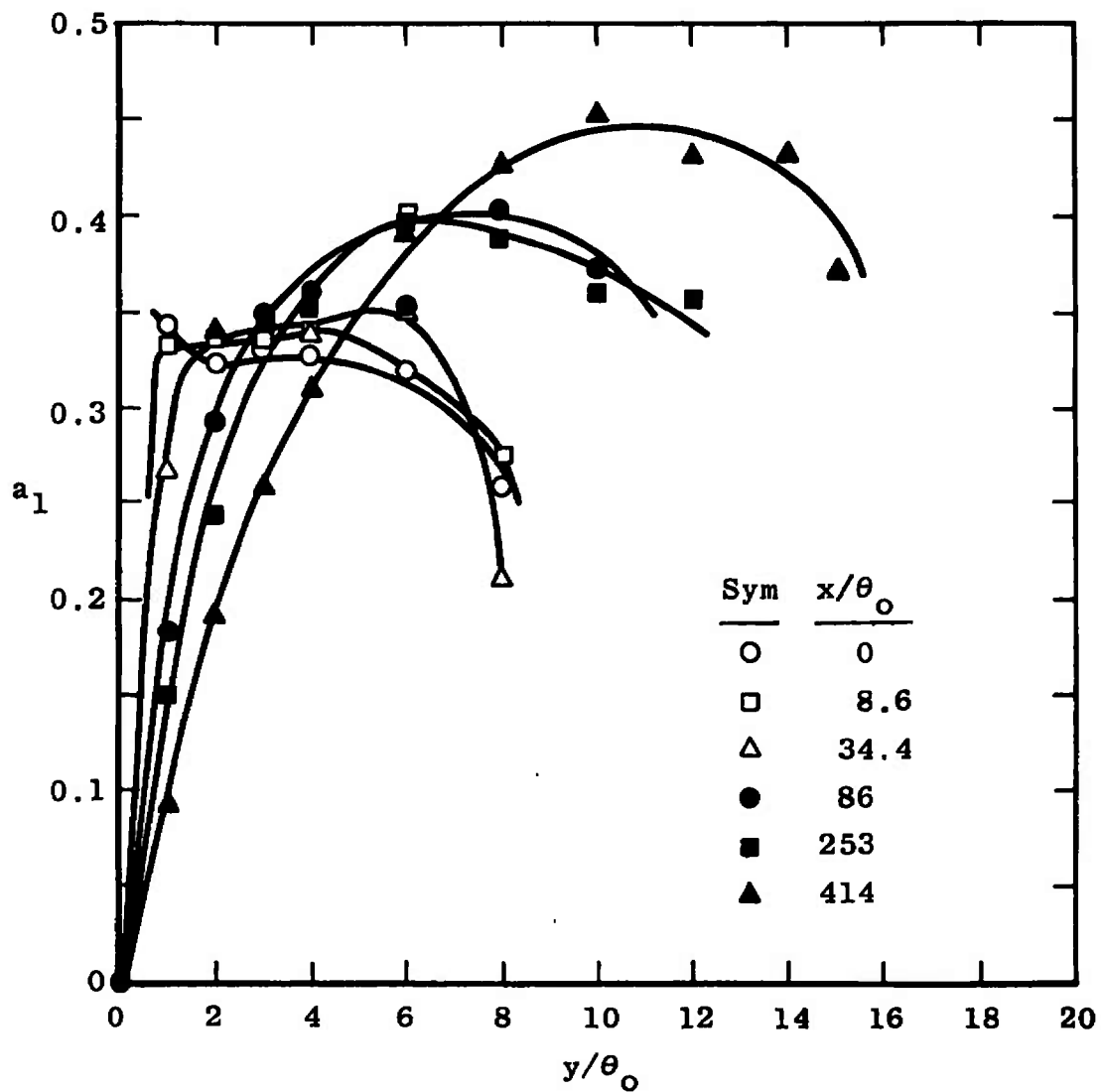


Figure 3.33. Evolution of the ratio of the turbulent shear stress to the turbulent kinetic energy in a two-dimensional wake. Data of Chevray and Kovasznay [52].

if the characteristic Reynolds number $U_0 d/\nu$, where d is here a characteristic dimension such as the diameter of a circular disk or sphere, the length of the short axis of an ellipsoid of revolution, or the edge length of a square disk, is large enough, the axisymmetric wake will be turbulent.

The principal characteristics of the wakes to be considered in this section are listed in Table 3.4. Not included in Table 3.4 is the axisymmetric wake experiment reported by Hwang and Baldwin [60]. This paper is not included as it deals solely with some details of the structure of turbulence, without reporting any of the details of the flow necessary for this study.

There is only one axisymmetric wake experiment, that of Cooper and Lutzky [56], which is carried far enough downstream to investigate the existence of self-preservation. Like the two-dimensional wake, self-preservation for an axisymmetric wake exists only in an approximate sense, when $(U_0 - U_c)/U_0 \ll 1$. This restricts self-preservation to large x/D , where the velocity deficit has been reduced to the point that $(U_0 - U)/U_0 \approx u'/U_0$ where u' is the axial component of the turbulent intensity. For such a case, Newman ([3], Appendix C) shows that the mean flow velocity deficit profiles should collapse when plotted as $(1 - U/U_0)[(x - x_v)/b]^{2/3}$ versus $y/[(x - x_v)b^2]^{1/3}$ where x_v

TABLE 3.4
AXISYMMETRIC WAKES

Investigator	Ref.	Year	Dia. (in.)	U_1 (ft/sec)	Reynolds No. $U_j D/\nu \times 10^{-4}$	Coeff. Drag C_D (Meas.)	Momentum Check, Percent ^a	Type
Cooper and Lutzky	56	1955	0.2	35-140	0.362-1.485	-	-	Disk
			0.2 ^b	80-140	0.85 -1.485	1.40	10	Square
			0.2 ^b	80-140	0.85 -1.485	-	-	$\ell/D=3$
			0.2 ^b	80-140	0.85 -1.485	-	-	$\ell/D=5$
			0.2 ^b	80-140	0.85 -1.485	-	-	$\ell/D=10$
Carmody	57	1964	2.0	75	7.0		13 ^c	
			6.0	25	7.0	1.14	3 ^d	Disk
			0.9	75	3.2			
Chevray	58	1968	10.0	90	275.0	0.06	10	Aerodynamic Body, $\ell/D=6$
Gibson, Chen, and Lin	59	1968	1.5	0.13-13.1	0.10-10	-	-	Sphere

^aMaximum deviation from average.

^bWidth.

^cAt $x/D = 2$.

^dFor $x/D \geq 6$.

is the distance from the physical origin of the wake to the virtual origin, and b is a characteristic body dimension.

Figure 3.34 shows that self-preservation is not achieved by the wake data of Cooper and Lutzky [56] at least up to $x/b = 381$, and only marginally, if at all, by $x/b = 681$. In this particular case the wake was produced by a square disk, and b is the length of an edge of the disk. It should however be noted that considerable error is likely to be inherent in obtaining the data shown in Figure 3.34 from the data of Reference [56], so that firm conclusions regarding the onset of self-preservation for this data cannot be drawn.

Self-preservation also requires that $(U_o - U_c)/U_o$ be proportional to $(x/d)^{-2/3}$ ([3], Appendix C). Figure 3.35 compares the centerline velocity decay data for three of the experiments considered, with a line representing an $(x/d)^{-2/3}$ decay. The data can be seen to approach such a decay, with the approximation becoming considerably better as x/D increases. The deviation of the data of Chevray [58] from the majority of the other data may represent the same sort of Reynolds number shift as observed in other configurations; however, the situation is somewhat clouded by the differences in the type of bodies used to generate the wake.

Both Carmody [57] and Cooper and Lutzky [56] used bluff bodies, thin in the dimension parallel to the flow, to

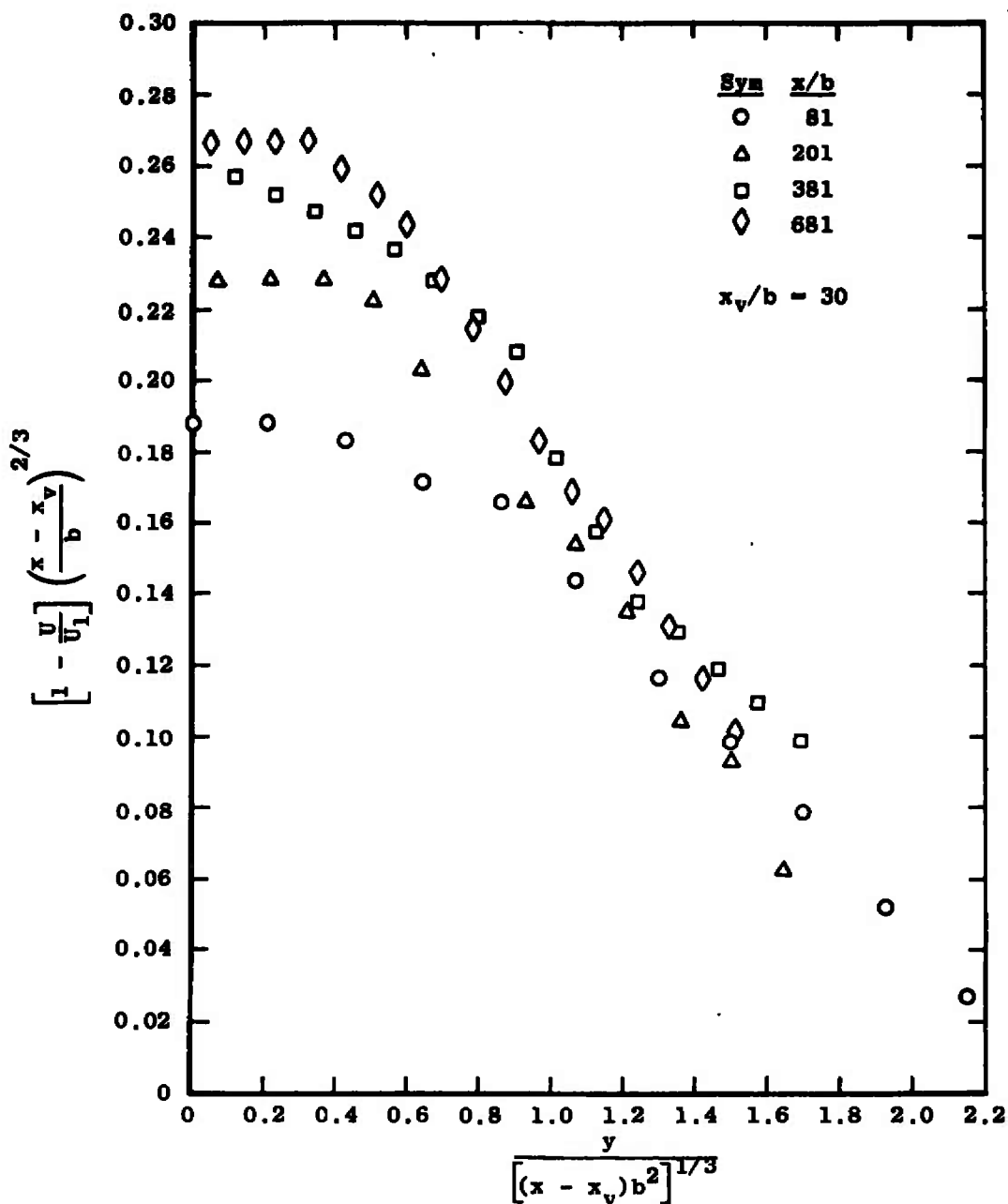


Figure 3.34. Test for self-preservation, axisymmetric wake of a square plate 0.2 in. on a side ($b = 0.2$ in.), data of Cooper and Lutzky [56].

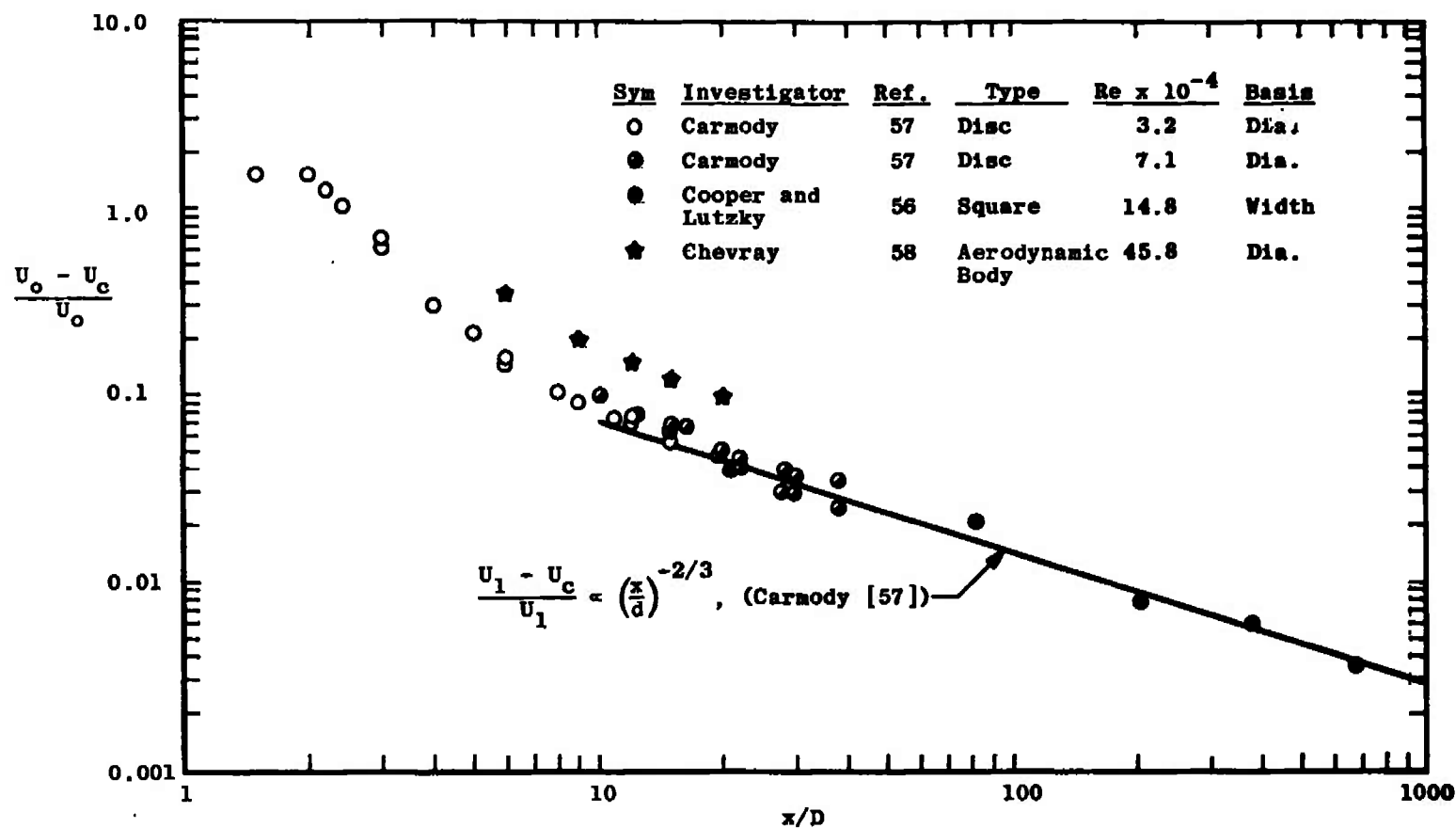


Figure 3.35. Comparison of centerline velocity decays, axisymmetric wake.

generate their wakes, while Chevray [58] used an aerodynamic body. Thus, there are fundamental differences in the manner in which the wake is formed. In the case of a bluff body, the wake is generated from the vortices which emerge from the edge of the disk; initial boundary layers are negligible. On the other hand the wake of a symmetric body of revolution such as Chevray's is formed from the large turbulent, viscous region created by the separation of the boundary layer from the surface of the body of revolution. In Chevray's case this separation always occurred upstream of the end of the body. Hence the basic mechanism for the formation of the wake is different in the two cases. If the same sort of effect of initial conditions observed for other configurations is to be expected in this case, then a shift of the decay curves such as observed in Figure 3.35 may be due primarily to the change in wake formation mechanism.

Carmody [57], Chevray [58], and Gibson, et al., [59] all investigated in some detail the turbulence structure of the axisymmetric wake. The last mentioned investigation was primarily aimed at measurement of the dissipation rate of turbulent kinetic energy by viscosity, and of "thermal variance by conduction." To this end measurements were made in the middle region of the wake of a sphere in a water tunnel. Both dissipation rates were found to decrease with streamwise distance approximately as $x^{-2.4}$

for up to 60 diameters. No details of the turbulence structure other than these measurements of kinetic energy dissipation rate were presented.

Both Carmody [57] and Chevray [58] made detailed measurements of turbulent intensity and turbulent shear stress in the early region of the wake, in the former case the wake of a bluff disk and in the latter of a body of revolution. Carmody found that his mean flow profiles became geometrically similar at $x/D = 20$ while Chevray's became geometrically similar much earlier, at $x/D = 10$. Both Carmody and Chevray noted discrepancies between their hot-wire turbulent shear measurements and those obtainable from integration of the mean velocity profiles; neither reported the lower frequency limit of their hot-wire equipment.

The ratio of turbulent shear stress to turbulent kinetic energy for both of these wakes agrees well with the linear relationship, as for other flows: Figure 3.36. Figure 3.37 depicts the evolution of the lateral profiles of the parameter a_1 in the middle region of Carmody's axisymmetric wake; the early region is not included because of the recirculating flows and complex velocity field involved. However, the velocity fields involved in Chevray's experiments were somewhat less complex and the evolution of the parameter a_1 is shown in Figures 3.38 and 3.39 from an axial position upstream of the end of the wake-producing body to a

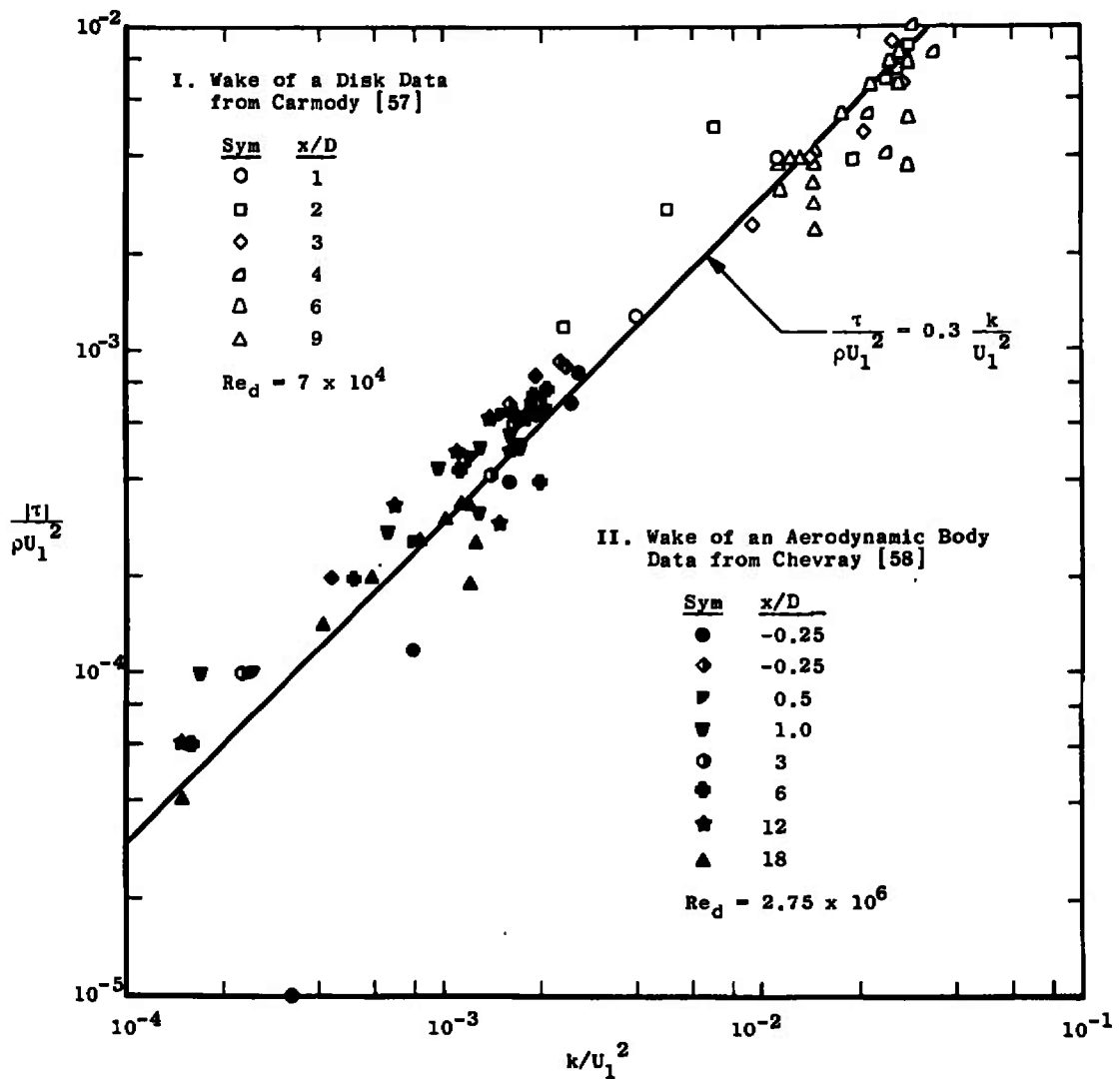


Figure 3.36. Relation between turbulent shear stress and turbulent kinetic energy, axisymmetric wakes.

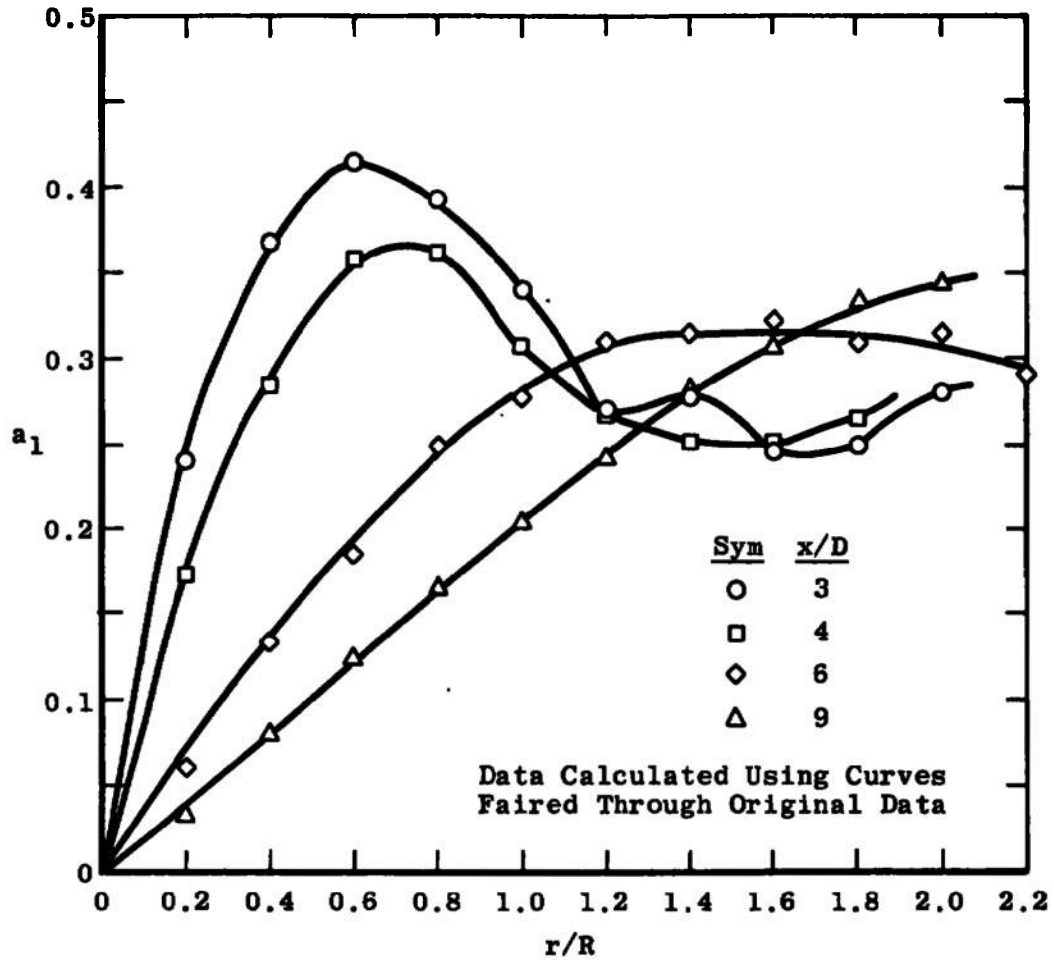


Figure 3.37. Evolution of the parameter a_1 in the middle region of the axisymmetric wake of a disk. Data from Carmody [57].

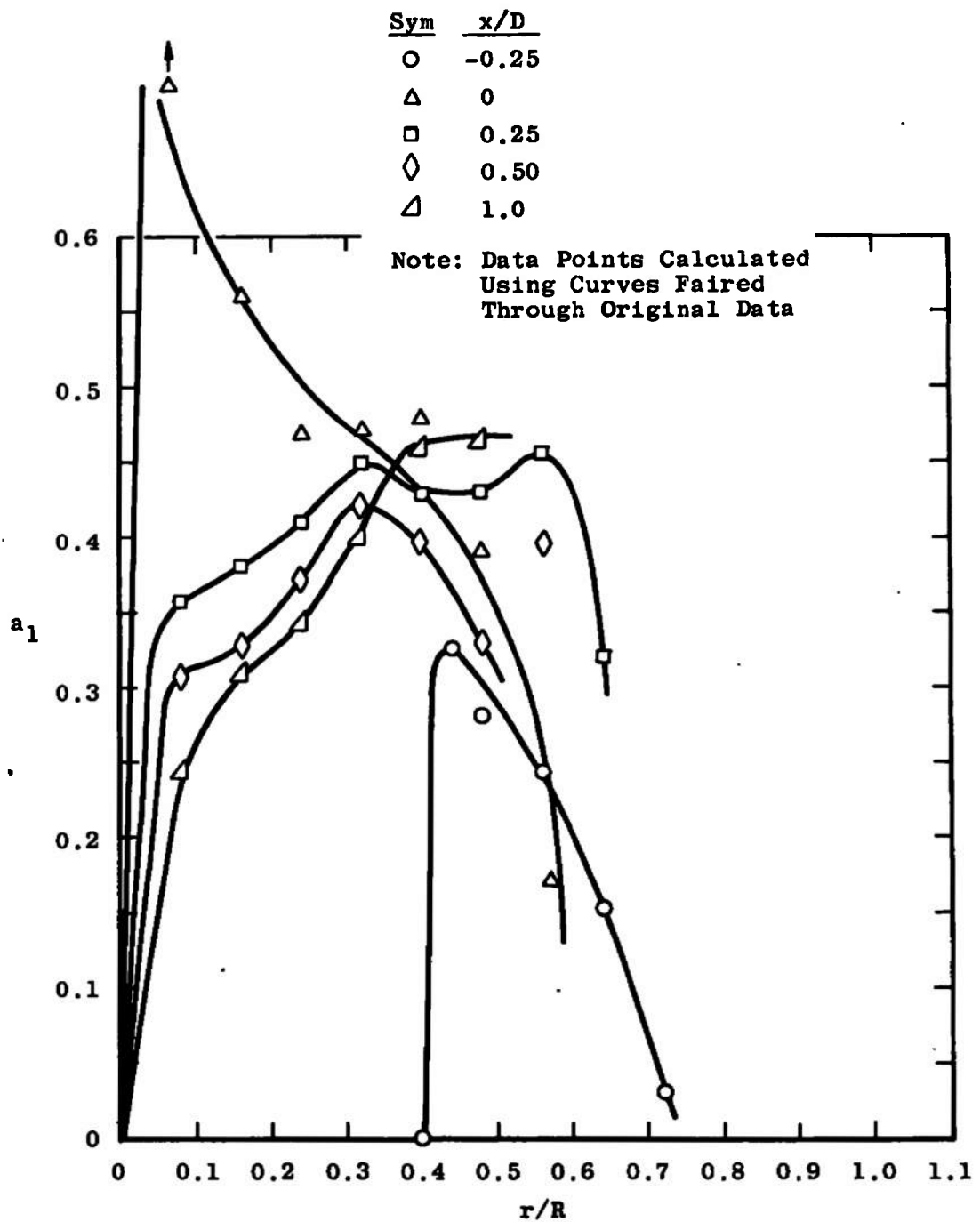


Figure 3.38. Evolution of the parameter a_1 in the early region of the axisymmetric wake of an aerodynamic body, data from Chevray [58].

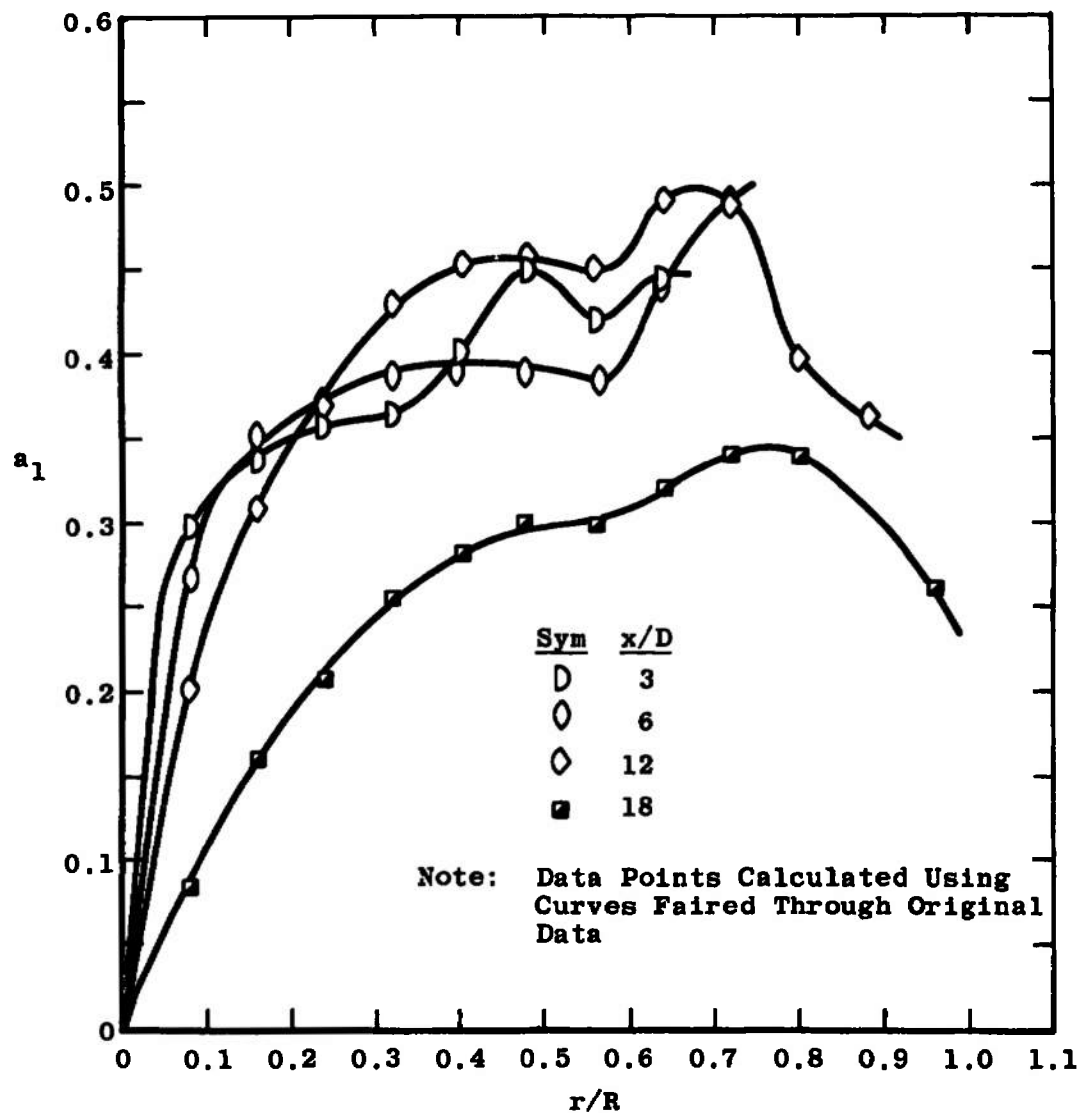


Figure 3.39. Evolution of the parameter a_1 in the middle region of the axisymmetric wake of an aerodynamic body. Data from Chevray [58].

position well downstream of the body. As observed in the two-dimensional wake, the parameter a_1 evolves rapidly from values and profiles characteristic of the separating boundary layer on the body to profiles characteristic of a free shear layer. Especially interesting is the extreme peak of the parameter a_1 at $x/D = 0$, resulting from very high turbulent shear stresses near the centerline; it is apparently this sudden jump in turbulent shear stress level that is responsible for the initial very rapid changes in mean flow velocity. Also of interest is the fact, observed here as in the two-dimensional wake [52] that the peak value of a_1 decreases from $x/D = 0$ to $x/D = 1.0$ and then increases to $x/D = 12$; it decreases again for the axisymmetric wake at $x/D = 18$. This last profile is generally similar to profiles measured by Carmody [57] at $x/D = 6$ and $x/D = 9$.

One further experiment of interest which is not included here because of its specialized nature is the axisymmetric wake investigated by Naudascher [61]. By flowing a jet through the center of a wake-producing disk and carefully balancing the momentum flux, Naudascher was able to approximate the wake of a self-propelled body. This was done in order to generate a shear field that changes into a shear-free field, in order that the approximations used in isotropic turbulence can be expected to hold. However, the interest in the present work is primarily in

relatively strong-shear fields, so the wake of a self-propelled body will not be pursued further.

Two-Stream Two-Dimensional Mixing Layers

The single stream two-dimensional layer, as described in Chapter 2, is formed when a two-dimensional stream mixes with a fluid at rest. The two-stream two-dimensional layer, on the other hand, forms between two streams when they merge after an initial separation. When the two streams are at the same velocity, the resulting mixing layer is a two-dimensional wake, such as those investigated by Chevray and Kovasznay [52] and by Lee [51]. When the two streams are of different velocities, the result is a two-dimensional two-stream mixing layer. As in the case of the two-dimensional two-stream jet, the primary reason for investigating this particular flow is that the existence of a finite level of mean velocity everywhere in the flow makes hot-wire measurements of turbulent fluctuations easier.

The two-stream two-dimensional mixing layer was investigated by Lee [51] and Watt [62]. Both investigators measured the turbulence intensities and turbulent shear stresses; in addition, Watt [62] measured the various terms of the turbulent energy equation. Lee's measurements were made in the initial region of the formation of a mixing layer from the boundary layers on the sides of the divider. Figure 3.40 shows the development of the mean velocity

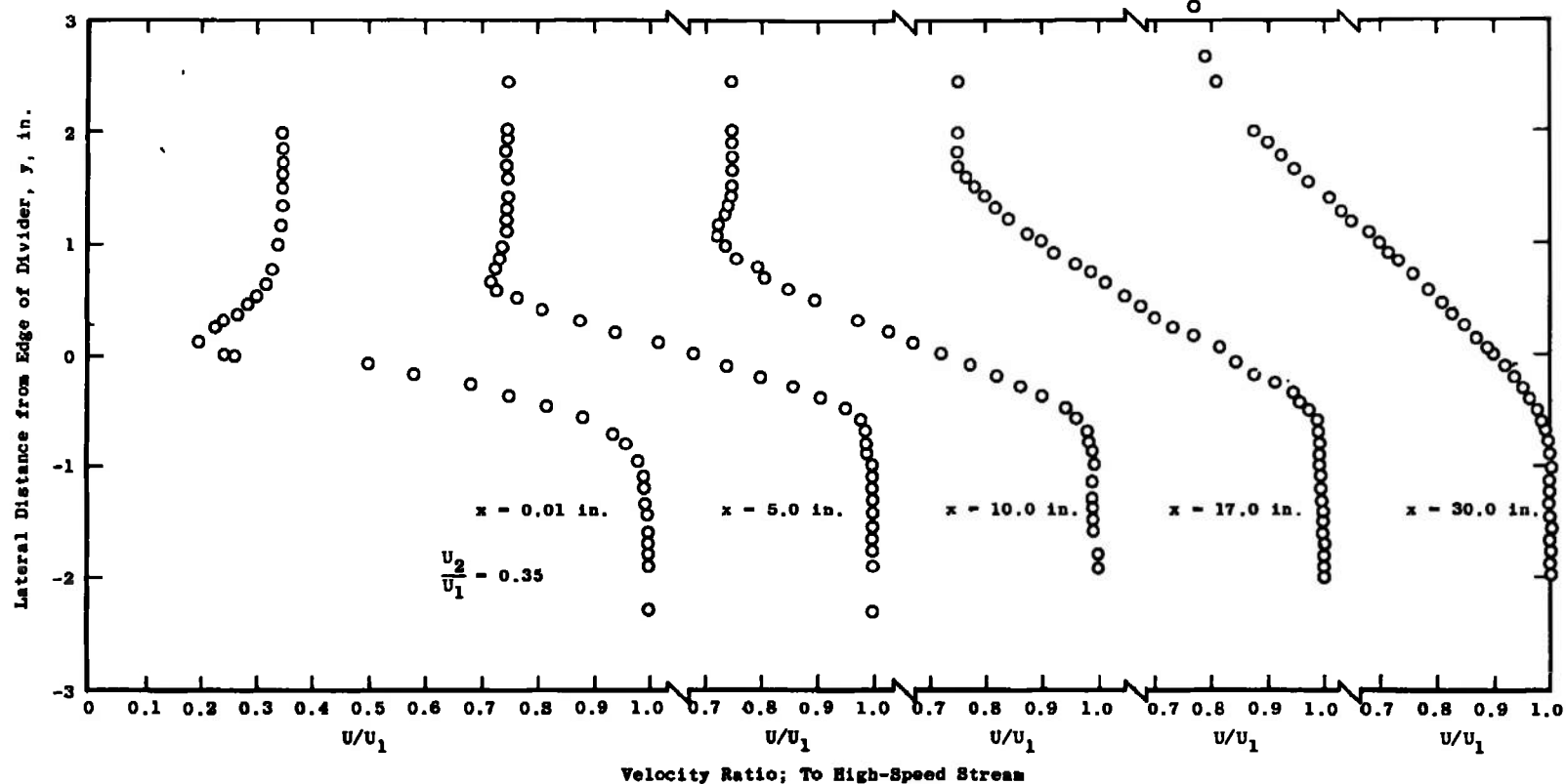


Figure 3.40. Velocity profiles in initial region of mixing between two different velocity streams with initial boundary layers. Data from Lee [51].

profile from one characteristic of that created by the merging of two boundary layers to one characteristic of a turbulent two-stream two-dimensional mixing layer. Watt [62] on the other hand made his measurements in the fully-developed region. His Reynolds number (based on axial distance x and the velocity of the high-speed stream) ranged from 5.6×10^5 to 1.73×10^6 , while Lee's ranged to 1.6×10^6 . Watt shows that his velocity profiles exhibit geometric similarity for $Re_x > 5.6 \times 10^5$, which agrees with the observations made by Leipmann and Laufer [17] in a single-stream two-dimensional mixing layer. Lee's measurements, on the other hand, do not exhibit geometric similarity, even for $Re_x = 1.6 \times 10^6$ as is shown by Figure 3.41, despite the great difference in velocity between the two streams. This deviation from geometric similarity may be caused by the rather large initial boundary layers obtained by Lee, as well as by the initial angularity of the flow--the streams are separated by a 10 degree included angle wedge. Because of this angularity, it is also possible that the initial region of this flow is not at constant pressure. Figures 3.42 and 3.43 indicate that in Watt's experiment, both the turbulent kinetic energy and the turbulent shear stress are geometrically similar to a reasonable degree.

The linear relationship between the turbulent shear stress and the turbulent kinetic energy observed in

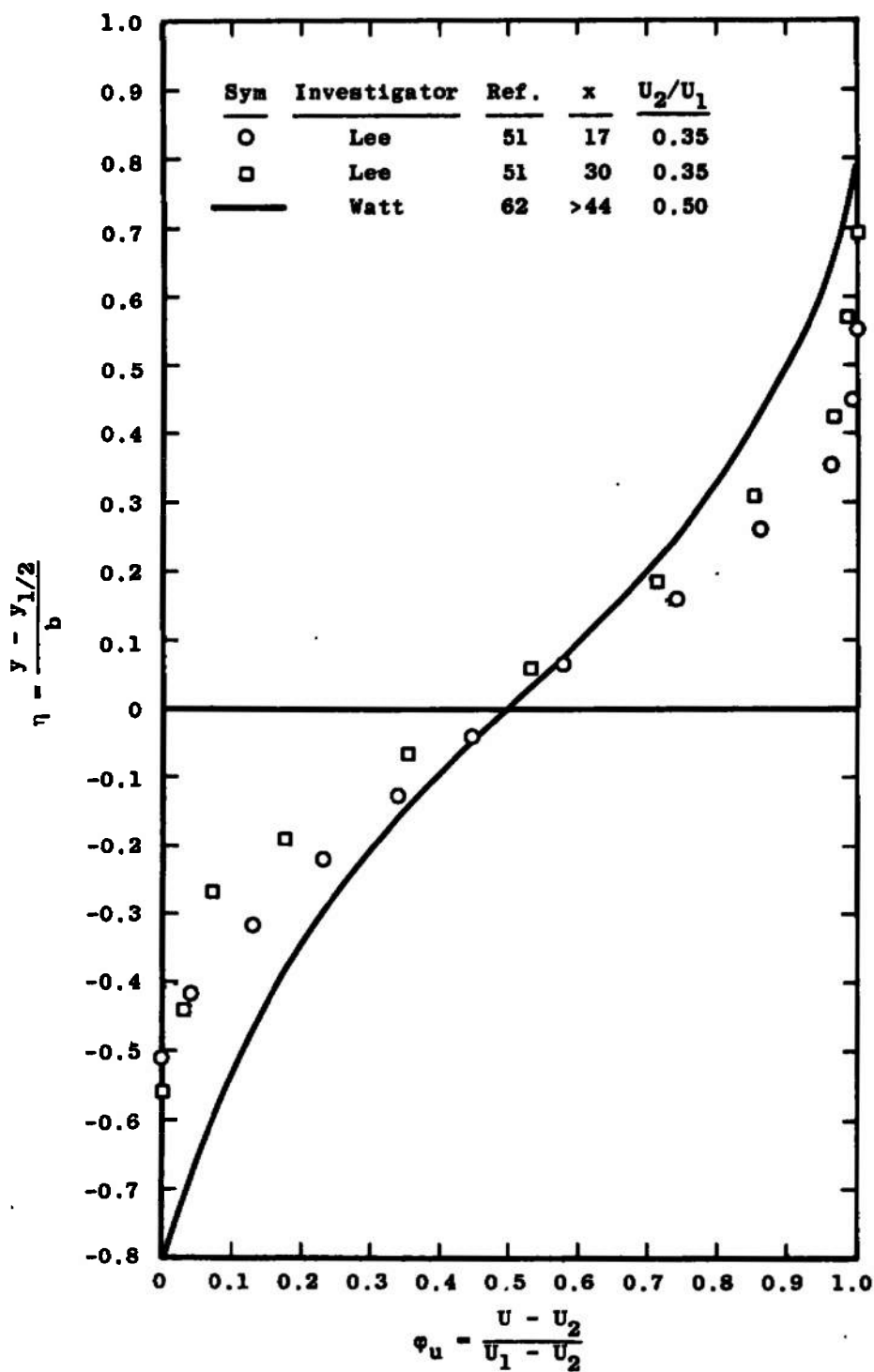


Figure 3.41: Test for similarity, two-stream mixing, Lee data, Reference [51].

Sym	x, in.	Re _x
○—	44	5.6×10^5
△—	76	1.73×10^6

Notes:

1. For $x = 44$ in., $k = 1/2 [u'^2 + 2 \cdot v'^2]$
2. For $x = 76$ in., $k = 1/2 [u'^2 + v'^2 + w'^2]$
3. Points Represent Data Obtained from Curves
Faired Through Original Data

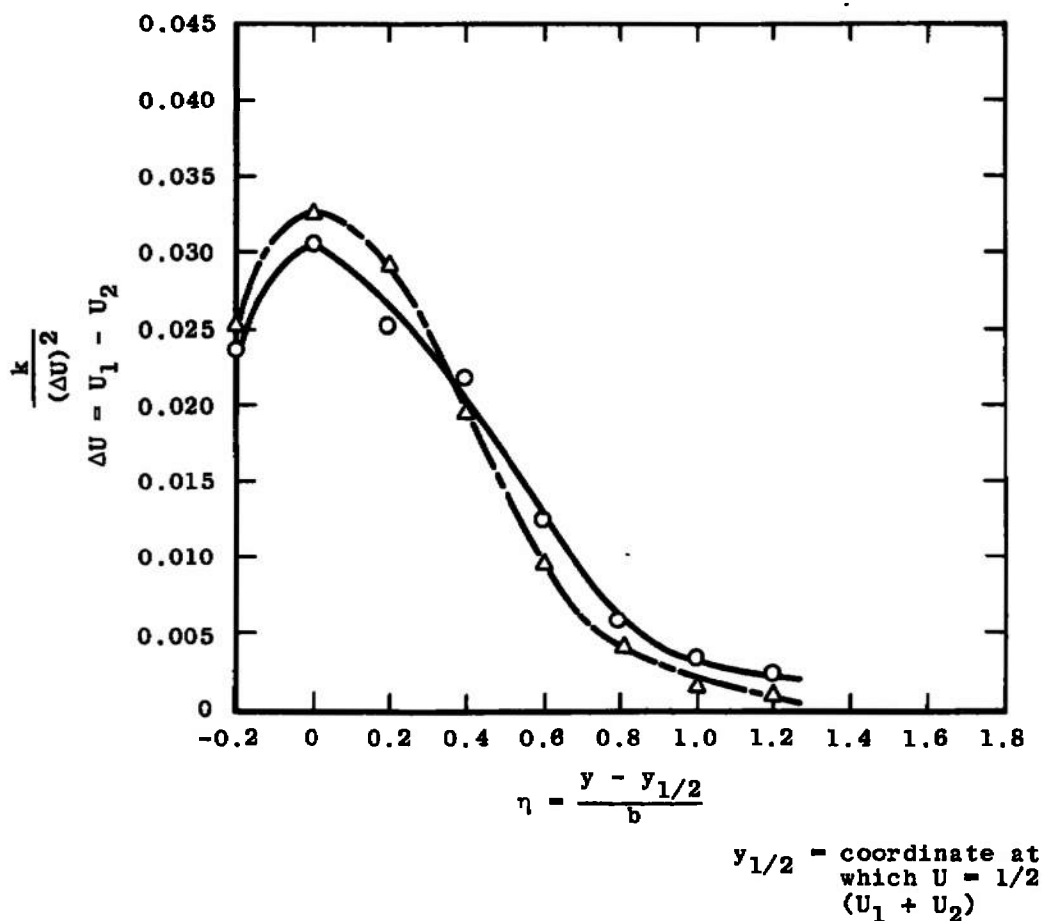


Figure 3.42. Similarity plot of kinetic energy measurements from Watt [62].

Sym	x, in.	Re _x
—○—	44	5.6×10^5
—△—	76	1.73×10^6

Notes:

1. For $x = 44$ in., $\frac{\overline{uv}}{\Delta U^2} = \frac{\overline{uv}}{u'v'} \cdot \frac{u'}{\Delta U} \cdot \frac{v'}{\Delta U}$

2. Points Taken from Data Obtained from Curves Faired Through Original Data

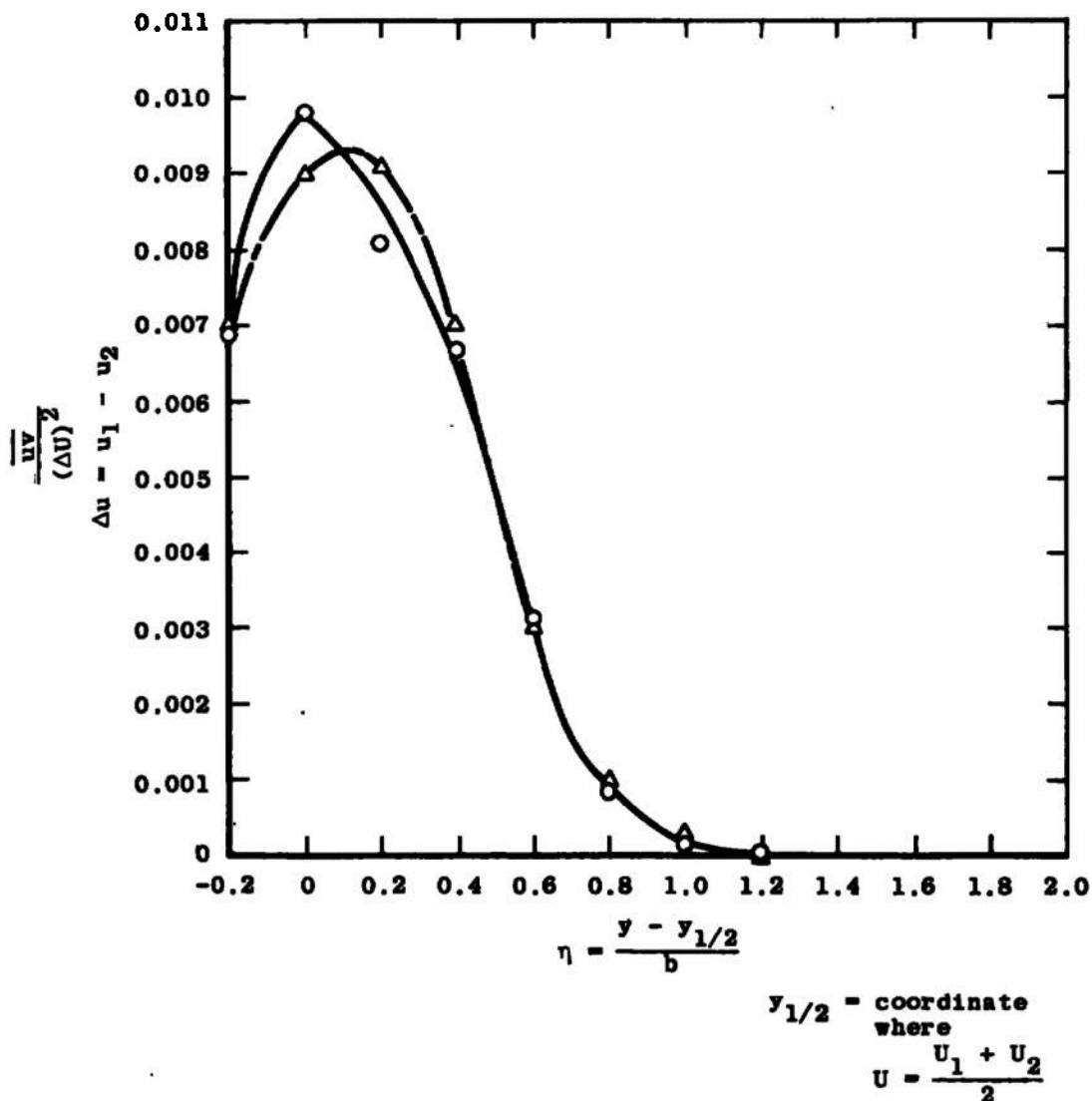


Figure 3.43. Similarity plot of shear stress measurements from Watt [62].

many other flows is also found satisfactory for this type of mixing layer. Figure 3.44 includes both Lee's [51] and Watt's [62] data; the relationship can be seen to hold both in the initial region and in the region of geometric similarity. For these calculations it was assumed for Lee's data that $w' = v'$, as w' was not measured by Lee; this assumption was also made for Watt's data at $x = 44$ inches.

The lateral variation of the parameter a_1 for the two-stream two-dimensional mixing layer in the fully-developed regime is quite similar to that observed for the single-stream two-dimensional mixing layer in the fully-developed regime, as Figure 3.45 demonstrates. In the initial region the lateral behavior of a_1 shows considerable scatter, as seen in Figure 3.46. However, a trend toward a development from a boundary layer profile such as was found by Chevray and Kovasznay [52] can be discerned on Figure 3.45, with a little imagination. Comparison of Figure 3.46 with Figure 3.33, page 163, is helpful in this regard.

Summary

In the two-dimensional, two-stream jet, self-preservation can exist only in an approximate sense ([3], Appendix C) for $U_o/U_j \ll 1.0$. If self-preservation exists, the velocity, turbulent intensity, and turbulent shear stress profiles will be functions only of the parameter $y/b(x)$, $b(x)$ will vary as (x/h) , and $(U_c = U_o)/U_j - U_o$ will vary as $(x/h)^{-1/2}$. For flows that satisfy the condition

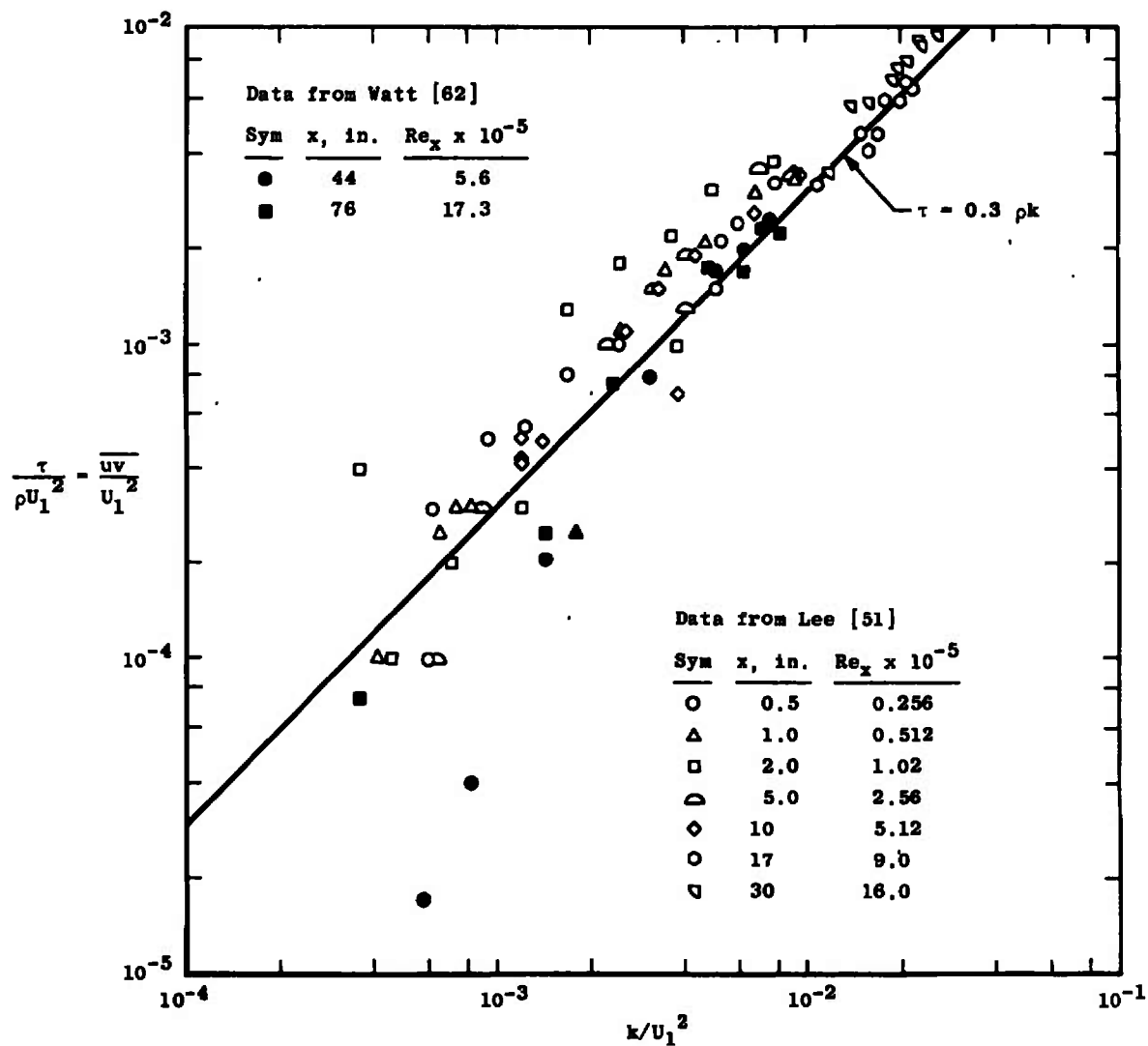


Figure 3.44. Relation between turbulent shear stress and turbulent kinetic energy for two-dimensional two-stream mixing layers.

Sym	Investigator	Ref.	$Re_x \times 10^{-5}$
●	Watt	62	5.6
▲	Watt	62	17.3
□	Liepmann and Laufer	17	3.73
◇			6.75
▽			9.37

Note: Data Points Calculated from
Curves Faired Through Original
Data

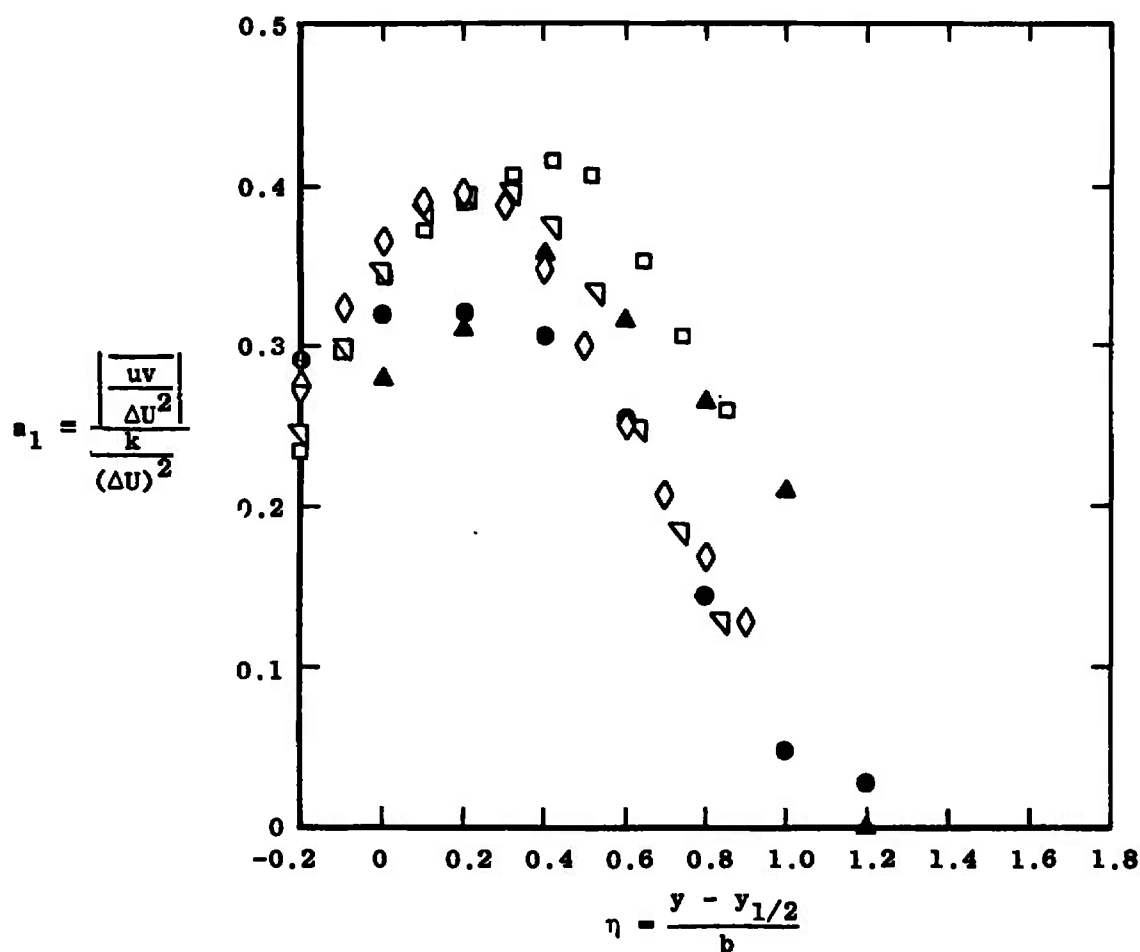


Figure 3.45. Comparison of data--single-stream and two-stream mixing layers.

Sym	Investigator	Ref.	x, in.	$Re_x \times 10^{-5}$
○	Lee ↓	51 ↓	5	2.56
△			10	5.12
□			17	9.0
◇			30	15.4
—	Watt	62	124	17.3

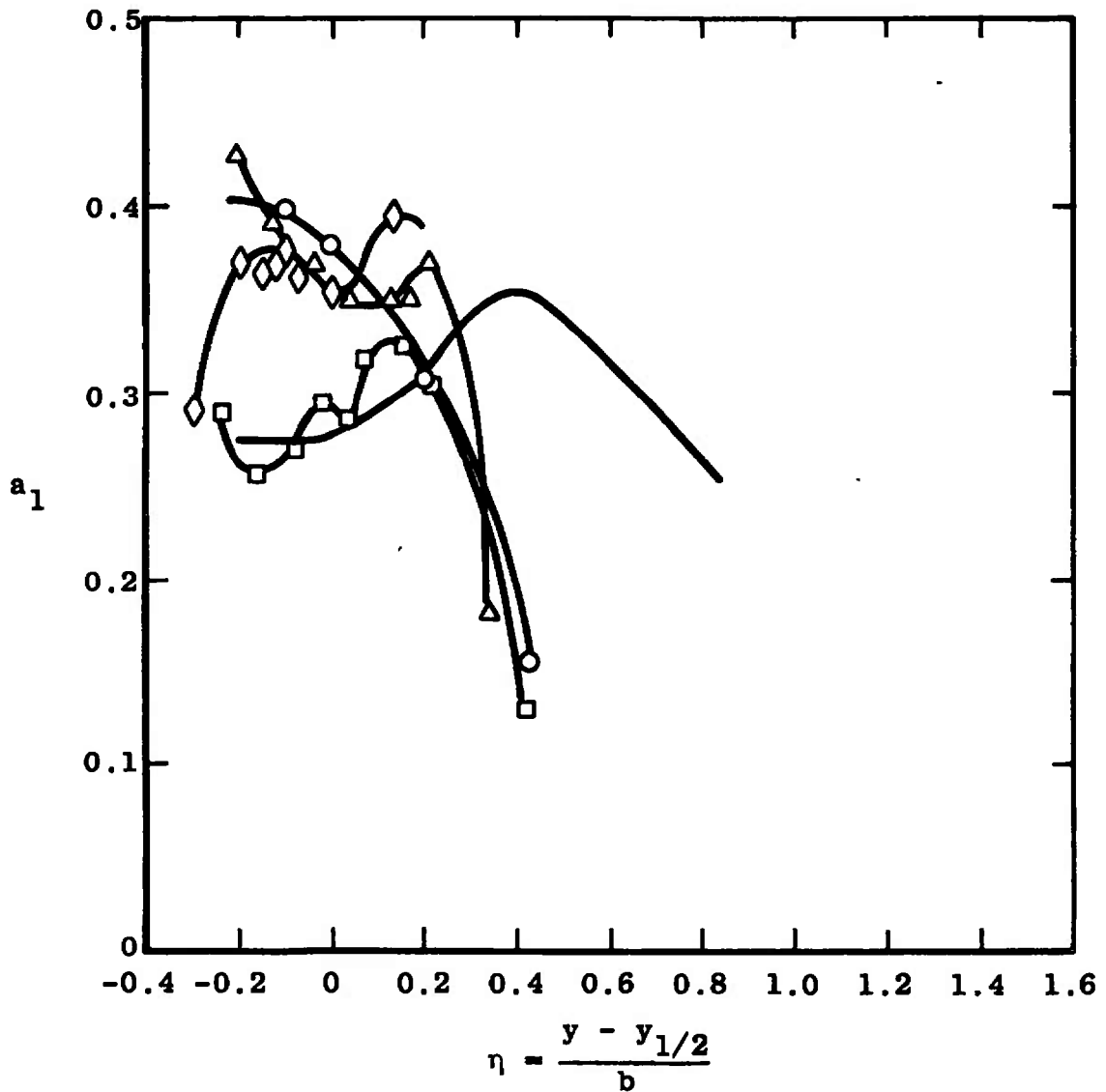


Figure 3.46. Development of the lateral variation of the parameter a_1 in the initial region of a two-dimensional two-stream mixing layer.

that $U_o/U_j \ll 1.0$, self-preservation is achieved for $x/h > 30$ [37]. But even for flows that do not satisfy this condition, the axial variation of the centerline velocity appears to decay as $(x/h)^{-1/2}$ [36, 37] as shown on Figure 3.4, page 110. For $x/h > 15$, geometric similarity of velocity profiles appears to be achieved [36], where for geometric similarity $(U - U_o)/(U_c - U_o) = f(y/b_{1/2})$; $b_{1/2}$ is the value of y for which $U = U_o + (U_c - U_o)/2$. This is shown by Figure 3.6, page 113. Figure 3.4 also demonstrates that the length of the velocity potential core increases as the ratio U_o/U_j increases towards unity. There is not sufficient data available to evaluate any Reynolds number shift in these decay curves that may exist.

For two-dimensional two-stream jets, Bradbury [39] gives the semi-empirical relations (based on similarity considerations and conservation of momentum)

$$\frac{U_c - U_o}{U_j - U_o} = 2.5 \sqrt{\frac{\lambda}{\lambda-1}} \left(\frac{x}{h}\right)^{-1/2}$$

$$\frac{b_{1/2}}{h} = 0.109 \frac{x}{h} \left[1 + \frac{0.55}{\sqrt{\lambda(\lambda-1)}} \sqrt{\frac{x}{h}}\right]^{-1}$$

where

$$\lambda = U_j/U_o$$

The expression for centerline velocity decay gives fairly

good results for $\lambda > 2$ and $x/h > 10$, and improves for increasing λ . As with all relations based on similarity considerations, these should be used with caution.

Self-preservation for coaxial mixing, as for two-dimensional two-stream mixing, only exists in an approximate sense for $U_o/U_j \ll 1$ ([3], Appendix C); for this case self-preservation involves profiles which are functions only of r/x and axial decays $(U_c - U_o)/(U_j - U_o)$ proportional to $(x/D)^{-1}$. Geometric similarity involves velocity profiles that are functions only of $r/r_{1/2}$, where $r_{1/2}$ is the value of r for which $U = U_o + (U_c - U_o)/2$. Figure 3.12, page 124, indicates that geometric similarity exists when Figure 3.13, page 125, shows true self-preservation does not. However, as Figure 3.14, page 129, shows, axial decays approximately proportional to $(x/D)^{-1}$ are commonly achieved. Also from Figure 3.14 it can be seen that as for the two-dimensional two-stream jet, the coaxial jet shows an increase in the length of the potential core with increase of the velocity ratio U_o/U_j toward 1.0. Unlike the two-dimensional two-stream jet, there is evidence for a shift in the position of the axial decay of centerline velocity curves with jet Reynolds number for this configuration. Part of this evidence comes from a comparison of the results of Forstall [40] and of Landis and Shapiro [43], shown on Figure 3.15, page 130. This figure indicates a definite increase in potential core length with primary jet Reynolds number for

jets with the same primary-to-secondary velocity ratio. Additional evidence for the effects of initial conditions is presented by the centerline composition results of Fejer, et al., [45] at a velocity ratio U_o/U_j of 1.0: Figure 3.18, page 136. Unfortunately the trend of these data runs counter to the trend exhibited by the comparison of Figure 3.16, page 132. The reason for this anomaly is not known; there may have been effects of laminar to turbulent transition involved.

As for the two-dimensional case, Bradbury [39] has obtained algebraic relations for velocity decay and width increase for coaxial jets. Again, these are limited to large values of λ and $x/D > 10$; they are

$$\frac{U_c - U_o}{U_j - U_o} = 6.82 \sqrt{\frac{\lambda}{\lambda-1}} \left(\frac{x}{D}\right)^{-1}$$

$$\frac{r_{1/2}}{D} = 0.089 \frac{x}{D} \left[1 + \frac{0.27}{\sqrt{\lambda(\lambda-1)}} \frac{x}{D}\right]^{-1/2}$$

Turbulence results for both the two-dimensional two-stream jet [37] and coaxial jets [44, 35] indicate average values of the parameter a_1 for all cases of about 0.30. Other experimental results for the diffusion of trace gases [40, 41], and temperature [42, 43] in essentially constant density coaxial flows indicate Schmidt numbers of approximately 0.7 and Prandtl numbers ranging from 0.5 [43]

to 0.7 [42]. It should be noted that spatial distributions of the turbulent Prandtl number are presented by Paulk [42]; such distributions are not available in the other works.

There are two possible experimental methods of developing two-dimensional wakes in the laboratory--either through the use of a cylindrical obstacle [50] or an aerodynamic body [51, 52]. In the latter case, both a flat-plate [52] and a wedge-shaped body [51] have been used. Both of these experiments show finite levels of velocity on the centerline as near as can be measured to the edge of the wake-producing body, indicating an extremely rapid energization of the boundary layer on the edges of the body. Calculations of the parameter a_1 for these data indicate an average value of 0.3 in the early region of the wake [51, 52] rising to 0.4 in the self-preserving region [50]. Self-preservation is shown in [50] to occur for $x/D > 500$. The initial region is of course not self-preserving. Detailed measurements of shear stress and kinetic energy show a fairly rapid change from profiles of the parameter a_1 characteristic of a boundary layer, where a_1 is about constant [55], to profiles characteristic of free mixing layers (Figure 3.33, page 163).

Axisymmetric wakes may also be formed in two ways--either by a disk-shaped obstacle [56, 57] or by an axisymmetric aerodynamic body [58]. The different approaches lead to different initial conditions for the two

types of flow, as in the latter case thick boundary layers may be built up, and the wake develops from the separation of these boundary layers from the body. Again self-preservation can exist only in an approximate sense ([3], Appendix C). For the axisymmetric wake the data [56] do not indicate that a self-preserving state has been reached prior to $x/D = 600$, but this value may be in doubt. Self-preservation leads to an axial decay of centerline velocity ratio $(U_o - U_c)/U_o$ proportional to $(x/D)^{-2/3}$; Figure 3.35, page 168, indicates that beyond $x/D = 10$ such a decay curve is followed fairly well. Both the wakes of a disk [57] and of an aerodynamic body [58] produce values of the parameter a_1 of about 0.3. The rapid increase in the value of a_1 near the trailing edge of an aerodynamic body as measured by Chevray [58], Figure 3.38, page 173, is noteworthy.

For the two-stream mixing layer, Watt [62] finds that self-preserving velocity profiles are attained at $Re_x = 5.6 \times 10^5$, which agrees well with the single stream value of $Re_x = 3.7 \times 10^5$ shown by Liepmann and Laufer [17] for the achievement of self-preservation. Self-preservation is not achieved in the experiments of Lee [52], probably because of initial condition effects. Again 0.3 appears to be a good value for the parameter a_1 .

Table 3.1, page 109, lists the two-stream, two-dimensional constant-density flows considered in this Chapter. All of these flows are in satisfactory agreement

with the momentum flux criterion. The range of parameter values (U_o/U_j , Re_h) considered is quite limited, but the coverage is probably adequate considering the somewhat academic nature of the flow. Of the three experiments listed, Weinstein, Osterle, and Forstall [36] is restricted to mean-flow measurements, while Bradbury [37] and Bradbury and Riley [38] include turbulent structure measurements. The latter work is presented only in similarity variables; however, the mean-flow data of [39] appear to be from the same experiments.

Coaxial mixing of constant-density streams is one of the more important free-mixing phenomena. Table 3.2, page 126, shows that the experimental coverage of this phenomena is fairly broad, with velocity ratios U_o/U_j ranging from 0.125 to 39.5 and Reynolds numbers (of the primary jet) ranging from 6.9×10^2 to 2.12×10^5 . Of the data listed, that of Paulk [42] is the only set in which the outer stream was not ducted, although the ducts used by Fejer, et al., [45] and Zawacki and Weinstein [35] appear to be large enough not to affect the flow. The same cannot be said of the work of Forstall [40, 41] particularly at the higher values of U_o/U_j . Here the effect of the walls appears to have shown up in the momentum integral for the $U_o/U_j = 0.5$ case.

Initial velocity profiles are presented only by Forstall [40, not 41] and Zawacki and Weinstein [35]. Shear

stress profiles are presented by Curtet and Ricou [44], Zawacki and Weinstein [35] (both obtained from hot-wire measurements), and by Paulk [42], obtained from integration of the mean flow profiles. Fejer, et al., [45] also present radial profiles of the eddy viscosity for $1 \leq x/D \leq 15$, for velocity ratio $U_o/U_j = 0.25$; in the range $2 \leq x/D \leq 15$ for $U_o/U_j = 0.33$, and in the range $2 \leq x/D \leq 24.5$ for $U_o/U_j = 0.20$. However, they do not report corresponding velocity profiles. The Zawacki and Weinstein data were obtained at very high values of the ratio U_o/U_j , with center jets that were, in all but the $U_o/U_j = 3.4$ case, laminar, and these data suffer from effects introduced by the recirculation phenomena that have been shown to exist [47] in these flows. Further, the Curtet and Ricou data [44] were obtained in a duct with a measurable axial pressure gradient. Since free mixing analyses generally take the axial pressure gradient to be zero, they cannot be used for direct comparison with these data.

Because of the importance of the coaxial jet configuration, some data for this configuration should be selected for comparison with theoretical predictions. Because the initial profiles are reported in Forstall's thesis [40], the $U_o/U_j = 0.20$ and $U_o/U_j = 0.25$ cases from these data will be used. For comparison with theoretical approaches which need initial shear stress profiles, the data of Paulk [42] will be used. This situation is clearly

not very satisfactory, as only a relatively small range of U_o/U_j can be investigated (0.2 to 0.477). Some higher velocity ratio data has been obtained by Paulk [42] and Fejer, et al., [45]; however, further experimental work is clearly needed for jets with velocity ratios in the range 0.5 to 1.0. But it is in this region that the effects of the initial condition for such flows be carefully measured and carefully documented. This indeed is true for any free-mixing experiment. All theoretical treatments depend to some extent on the initial conditions that are assumed, and it is to be expected that the better theories will demand more detail in the initial conditions. The detail now available is at best fragmentary and at worst nonexistent. A clear need for more experimental research exists in this area.

Although there are not many experiments on two-dimensional wakes, as Table 3.3, page 151, shows, those that exist are very detailed and provide a wealth of information about the flow. The experiments of Townsend [5, 50] are well known, and those of Lee [51] and Chevray and Kovasznay [52] provide needed detail on the initial development. Because the initial development of a wake-flow from the turbulent boundary layer flow is a technically interesting flow, which is also of great value to the understanding of turbulent free-mixing layers, the data of Chevray and

Kovaszny [52] has been selected for use in comparison with theoretical predictions.

The development of an axisymmetric wake is also of great technical interest. Although there are a number of experiments available for the incompressible axisymmetric wake, the majority of them either concern wakes of disks [56, 57] or do not contain sufficient information for comparison with calculations [59]. The wake of a disk in general includes a large recirculation region immediately behind the disk, which is not easily amenable to analysis. However, the wake of the aerodynamic body investigated by Chevray [58] includes only a small recirculation region, which may be (to a first approximation) ignored. Thus, this experiment also has been selected for comparison with theoretical predictions.

CHAPTER 4

VARIABLE-DENSITY SINGLE-STREAM FLOWS:

EXPERIMENTAL DATA

Flows with density variations are probably more common in practical engineering applications than the constant density flows considered in the previous two Chapters. The density variations involved may be produced by virtue of compressibility effects, if the flow velocity (and Mach number) are sufficiently high, or they may be produced in low-speed flows by variations in temperature between a flow and its surroundings, or by the use of different gases. In the most complex cases, compressibility, temperature, and concentration effects may combine.

Because of the variation in density, the vast majority of experiments in this area involve only mean-flow measurements. The heat transfer rate from a hot-wire depends not only on its temperature, but also on the thermodynamic properties of the gas. If the gas composition (for two gases), temperature (for a heated single gas system), or density (in a compressible flow, as well as in the preceding two cases) has a fluctuating component, the interpretation of the results of a hot-wire measurement in terms of the fluctuating velocity components becomes exceedingly difficult. Those measurements which have been made, such as

in a two-gas system by Zawacki and Weinstein [35] and in a heated single-gas system by Corrsin and Uberoi [25] have been of the simplest components of turbulence, such as the axial fluctuation u' and the temperature-velocity correlation $\overline{u\theta}$.

Even mean-flow measurements are more complicated in a variable-density flow; measurements of additional quantities, such as the gas composition and temperature, need to be made, and corrections applied, such as those for the pitot pressure in a supersonic flow. For this reason the range of parameters to be determined in a given experiment is greater, which leads to increased complication in evaluation of the experiment and comparison of it with other experiments.

The Compressible Circular Jet

One of the simplest of the variable density flows to achieve experimentally, the supersonic jet into quiescent surroundings, has been the most exhaustively studied. Even so, the state of knowledge about this flow does not compare with that for the constant-density jet into still surroundings. Both two-dimensional and circular supersonic jet experiments exist, but the two-dimensional jets [63, 64] are of such low aspect ratio as to be more likely three-dimensional in character than two-dimensional. Thus, primary attention will be paid to the circular supersonic jet. A schematic of the circular supersonic jet is shown in

Figure 4.1. As in the constant density jet, the mixing can be divided into two distinct regions, one in which the turbulent mixing layer is expanding into both the quiescent surroundings and the essentially nonturbulent potential core of the jet, called regime I, and the other in which turbulent mixing extends from the outer edge of the jet to its centerline, called regime II. Providing that the potential core of the jet is shock-free, the length of the potential core, x_{core} , will be greater in a supersonic jet than in a low-speed jet of the same gas; a linear increase in potential core length with Mach number has been often observed, e.g., Broer and Rietdijk [65] and Anderson and Johns [66].

To obtain a disturbance-free, uniform, parallel flow at the jet exit, the nozzle must be properly designed and operated fully-expanded, i.e., so that $P_e = P_a$ on

Figure 4.1. The only jets to be considered here are those that are fully expanded and shock-free. The effects on the mixing phenomena of the wave phenomena that occur in improperly expanded nozzles are not clear. Two investigations have looked at this problem in detail. In one, Donaldson and Gray [67], neither over- or under-expansion was found to have a "first-order" effect on the mixing phenomena. Johannesen [68] on the other hand, experimenting with nozzles having fairly strong shock waves in the core of the jet found that jets with a given exit Mach number and

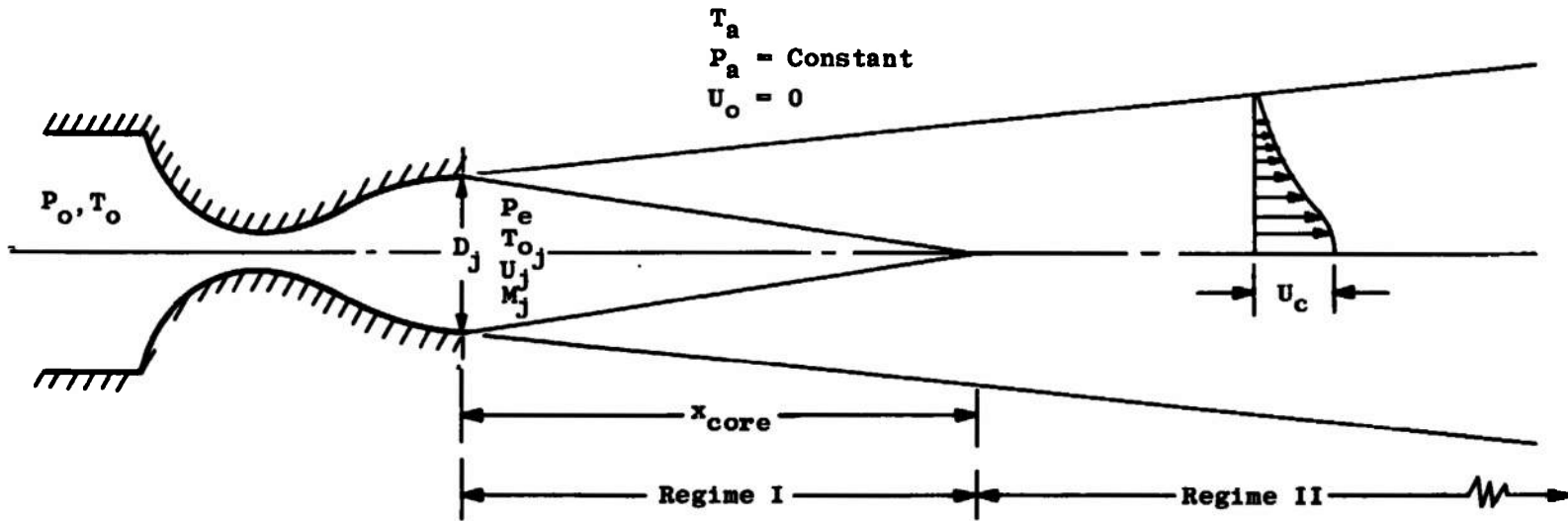


Figure 4.1. Supersonic jet into quiescent surroundings.

strong shocks spread very much more rapidly than jets with the same exit Mach number and no shocks. The jet with strong shocks was also unsteady; Donaldson and Gray note that their conclusion applies only when the shock structure "does not flap."

Table 4.1 presents the important parameters for the single-jet flows considered in this section. As mentioned above, both Gooderum, Wood, and Brevoort [63] and Bershader and Pai [64] performed experiments on flows which probably suffer from three-dimensional effects. Gooderum, et al., reported geometric similarity (based on a local width scale) for their velocity profiles. The Bershader and Pai data [64] in addition to being probably three-dimensional, suffers somewhat from extreme nondimensionalization: the data presented are shifted both axially (by use of a virtual origin) and laterally, and are further multiplied by a scale factor.

Warren's work [70] represents an extensive investigation of the supersonic jet, at four Mach numbers and three ratios (for the subsonic Mach numbers) of jet total (or stagnation) temperature to ambient temperature, T_{O_j}/T_a (see Figure 4.1). The portions of Warren's work considered in this section involve jets for which $T_{O_j}/T_a = 1$; those for $T_{O_j}/T_a \neq 1$ will be considered in the following section.

TABLE 4.1
COMPRESSIBLE JET INTO QUIESCENT AIR

Investigator	Ref.	Year	Type	M_j	D_j (in.)	Re_D $\times 10^{-5a}$	Largest x/D	Momentum Check, Percent of Avg.	Range of Momentum Check
Gooderum, Wood, and Brevoort	63	1949	2D	1.6	3x3	-	2.5	-	-
Bershader and Pai	64	1950	2D	1.7	0.394 $\times 0.788$	-	-	-	-
Warren	70	1957	Circ.	0.69	2.554	16.3	25	4	$4 < x/D < 15$
				0.97	2.554	23.5	30	4	$4 < x/D < 20$
				1.51	2.526	41.5	-	-	b
				2.60	2.554	90.5	20	4	$10 \leq x/D \leq 20$
Pitkin and Glassman	71	1958	Circ.	2.60	-	-	20	-	-
Broer and Rietdijk	65	1960	Circ.	1.74	0.704	13.2	25	30	$x/D = 21.4^c$
Johnnesen	68	1962	Circ.	1.40	0.75	10.7	93.5	4 ^d	$x/D \leq 53.5$
	69								
Eggers	72	1966	Circ.	2.22	1.007	26.5	75	6	$x/D \leq 45$

^aReynolds number estimated assuming $T_{O_j} = T_a = 530^\circ R$ if not specified.

^bNo velocity profiles presented.

^cJet shows marked change in decay at $x/D = 20$.

^dAuthor's measurement.

Jets with $T_{O_j}/T_a = 1$, as all of those in this section, are commonly considered to be isoenergetic, i.e., $T_O = T_{O_j}$ everywhere in the flow. This assumption is made by Warren [70], Pitkin and Glassman [71], Johannesen [68, 69], and Eggers [72]; however, it has been questioned by Broer and Rietdijk [65] who measured a five percent axial variation in T_O in their experiment on a $M = 1.74$ jet. The error that a five percent deviation of total temperature introduces in a velocity calculation is easily estimated. For a perfect gas

$$U = \sqrt{\gamma g R} \sqrt{T} M \quad (4.1)$$

where

$$\sqrt{T} = \frac{\sqrt{T_O}}{[1 + \frac{\gamma-1}{2} M^2]^{1/2}} \quad (4.2)$$

so that

$$U = \ln(\sqrt{\gamma g R}) + \ln\left(\frac{M}{[1 + \frac{\gamma-1}{2} M^2]^{1/2}}\right) + \frac{1}{2} \ln T_O \quad (4.3)$$

from which the error in the determination of U is obtained by standard techniques (assuming that γ , g , and R are known exactly)

$$\frac{\Delta U}{U} = \frac{\Delta \left[\frac{M}{(1 + \frac{\gamma-1}{2} M^2)^{1/2}} \right]}{\frac{M}{(1 + \frac{\gamma-1}{2} M^2)^{1/2}}} + \frac{1}{2} \frac{\Delta T_o}{T_o} = \frac{\Delta f(M)}{f(M)} + \frac{1}{2} \frac{\Delta T_o}{T_o}$$

Assuming for the purposes of this discussion that the Mach number is known exactly, $\Delta f(M) = 0$ and

$$\frac{\Delta U}{U} = \frac{1}{2} \frac{\Delta T_o}{T_o} \quad (4.5)$$

so that a five percent error in T_o leads to a 2.5 percent error in the determination of U . Thus taking the total temperature to be a constant would appear to introduce only a small error in the calculation of velocity.

All of the investigators in this section assume that the static pressure is constant and equal to the ambient pressure throughout the flow field. The static pressure field was measured by Warren [70, 73], who found that the static pressure is not constant either axially or laterally. The variation in static pressure appears to increase with jet Mach number; at $M = 2.6$ the variation along the jet axis is four percent, with a ten percent lateral variation at $x/D = 15$. One can here perform an exercise, similar to that performed above to investigate the effect of total temperature variation, to investigate the effect of static pressure variation on the determination of Mach number. Then, starting with

$$\frac{P_0}{P} = \left(1 + \frac{\gamma-1}{2} M^2\right)^{\frac{\gamma-1}{\gamma}} \quad (4.6)$$

one gets, assuming that P_0 is accurate

$$\frac{\Delta \left[1 + \frac{\gamma-1}{2} M^2\right]}{1 + \frac{\gamma-1}{2} M^2} = \frac{1-\gamma}{\gamma} \frac{\Delta P}{P} \quad (4.7)$$

which leads to

$$(\gamma-1) M \Delta M = \frac{1-\gamma}{\gamma} \left(1 + \frac{\gamma-1}{2} M^2\right) \frac{\Delta P}{P} \quad (4.8)$$

or

$$\left| \frac{\Delta M}{M} \right| = \frac{1 + \frac{\gamma-1}{2} M^2}{\gamma M^2} \frac{\Delta P}{P} \quad (4.9)$$

Warren [70, 73] indicates that $\Delta P/P \approx 0.10$ at $x/D = 15$.

From Reference [70], at $x/D = 15$, $M_c = 2.3$ and

$$\left| \frac{\Delta M}{M} \right| = 0.28 \frac{\Delta P}{P} = 0.028$$

indicating a three percent error in Mach number due to the static pressure variation. Warren [70, page 59] concluded that the static pressure variations

. . . although they provide information concerning the jet structure, do not have a large effect upon the velocity calculations. . . . Therefore, for calculation of the jet velocity characteristics,

the static pressure was assumed to be constant in the subsonic cases. In the $M_j = 2.60$ series, the static pressure variations were included for velocity calculations.

Since all other jets considered were at Mach numbers less than 2.60, the assumption of constant pressure commonly used by the other investigators is probably justified.

The question of a turbulence correction to the total and static pressure measurements used in these experiments is considered by both Warren [70] and Johannesen [69]. As for the constant-density jet discussed in Chapter 2, the approach to making the correction is unclear; in the variable-density case it is complicated further by density fluctuation effects. Thus, no corrections have been applied to any of the measurements considered.

The turbulent Prandtl number is evaluated for this configuration by Broer and Rietdijk [65] who report $Pr_t = 0.7$. Warren [70] concludes that the turbulent Prandtl number is not unity, but his method of evaluation of the turbulent Prandtl number is such that he is unable to establish a meaningful numerical value for it. In considering the work of Broer and Rietdijk, it should be noted that the momentum integral for this work could only be evaluated at $x/D > 20$, a region where the axial decay curve begins to deviate strongly from the slope established upstream. Thus the value listed for the deviation of the momentum integral from a constant value for this data is probably worse than the actual overall deviation.

A note should be added regarding the evaluation of the momentum integral. The requirement is, from Appendix A, that

$$\int_0^{\infty} \rho U^2 r dr = \text{constant} \quad (4.10)$$

Except for Eggers [72] who presented profiles of ρU^2 , this was evaluated through use of the perfect gas law, $P = \rho RT$, thus:

$$\rho U^2 = \frac{P}{RT} U^2 = \gamma g P_a \frac{U^2}{\gamma g RT} = \gamma g P_a M^2$$

where P has been taken as constant and equal to P_a . Thus, the conservation of momentum requirement for this flow becomes

$$\int_0^{\infty} M^2 r dr = \text{constant} \quad (4.11)$$

The Mach number was evaluated from the velocity profiles available assuming constant total temperature: thus for the centerline Mach number

$$M_c = \frac{U_c}{49.1 \sqrt{T_c}} \quad (4.12)$$

$$T_c = \frac{T_{0c}}{1 + \frac{\gamma-1}{2} M_c^2} \quad (4.13)$$

so that

$$M_c = \frac{U_c}{[(49.1)^2 T_o - \frac{\gamma-1}{2} U_c^2]^{1/2}} \quad (4.14)$$

and similarly at any axial station

$$M = \frac{U/U_c}{\left\{ \frac{1}{M_c^2} + \frac{\gamma-1}{2} \left[1 - \left(\frac{U}{U_c} \right)^2 \right] \right\}^{1/2}} \quad (4.15)$$

Figure 4.2 shows a comparison of the centerline axial velocity decay curves for the compressible flow experiments of Warren [70] and two of the jets measured by Alexander, et al., [27]. Over the relatively short axial distances involved, Warren's data can be seen to follow the $U_c/U_j \propto (x/D)^{-1}$ decay rate established for the incompressible jet relatively well. The length of the potential core, as defined by the intercept of the $(x/D)^{-1}$ line characteristic of a given set of data and the line $U_c/U_j = 1.0$, can be seen to increase with Mach number. If these core lengths, as well as those from other experiments at different jet Mach numbers are plotted, as in Figure 4.3, they can be seen to group along two lines with the break between groups occurring at about $M_j = 1.0$.

Figure 4.4 shows the axial decay of centerline velocity for several experiments with Mach numbers ranging from 1.40 to 2.60. As was discussed above, calculations of

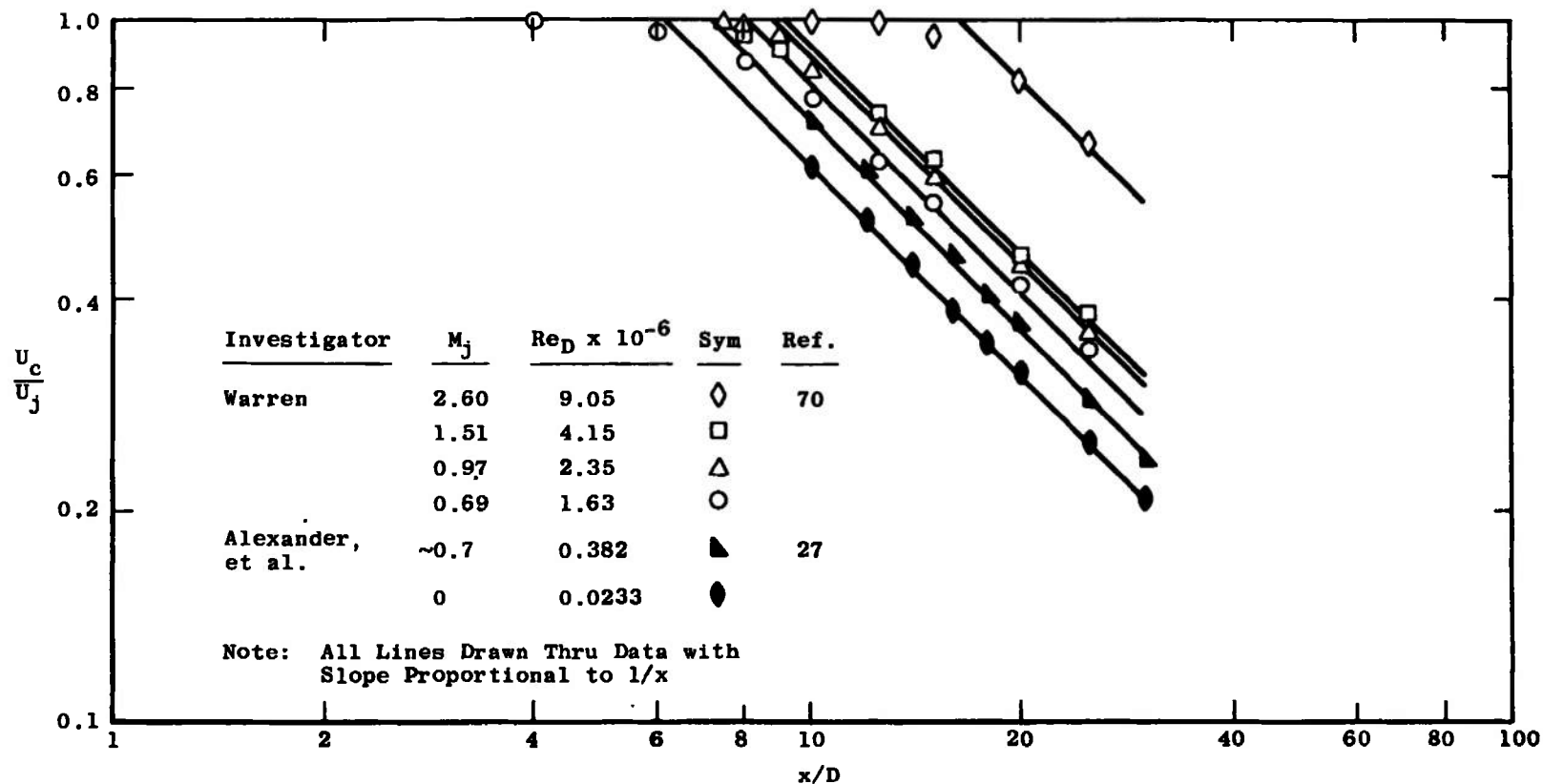


Figure 4.2. Comparison of compressible free jet data with effectively incompressible data; decay of centerline velocity.

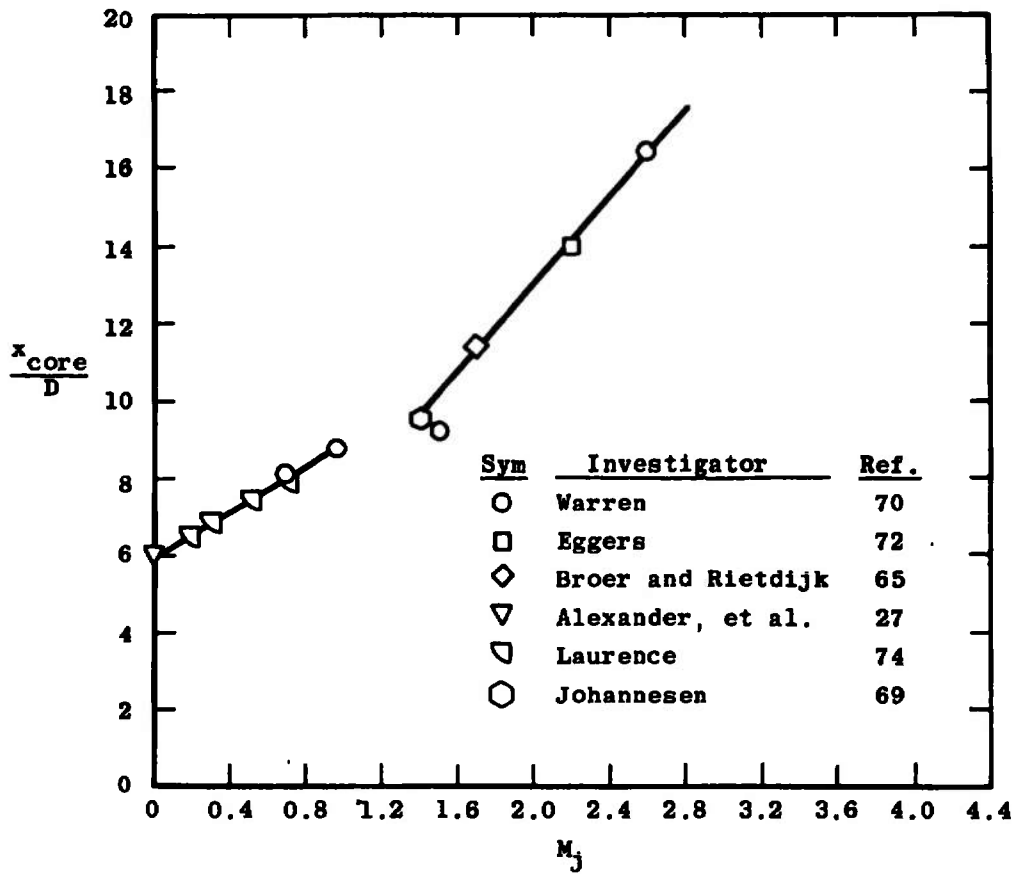


Figure 4.3. Variation of core length with Mach number, compressible jet-into-still-air.

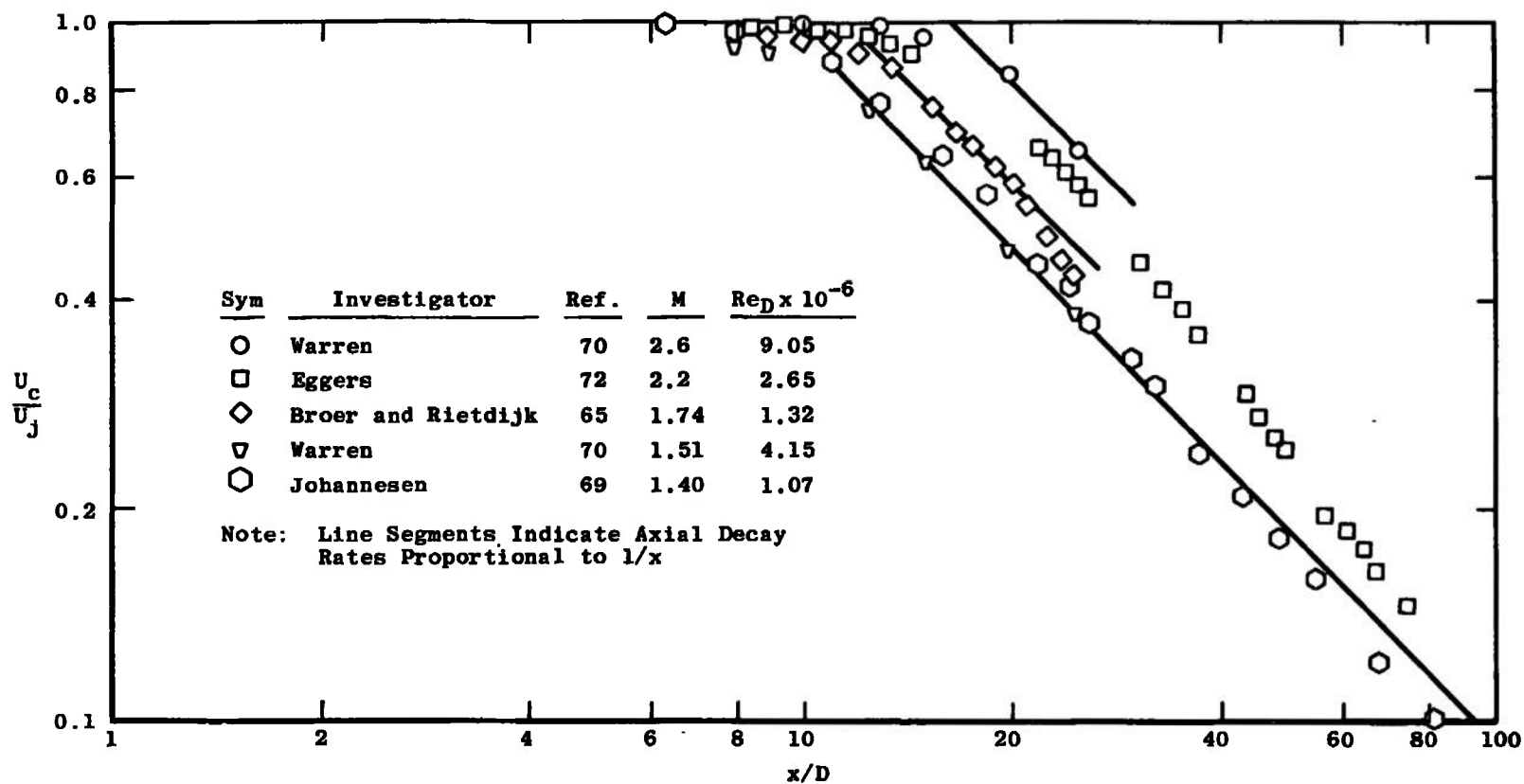


Figure 4.4. Axial decay of centerline velocity;
compressible jet-into-still-air.

the momentum integral for the data of Broer and Rietdijk [65] indicate that its value deviates quite strongly from a constant value for $x/D > 20$; this behavior is borne out by the strong deviation from the upstream decay behavior shown on Figure 4.4 for $x/D > 20$. On the other hand, Johannesen's data [69] follows a straight line decay (on a log-log plot) quite well, except for very large x/D .

The behavior of Egger's data [72] is somewhat different. As can be seen from Figure 4.4, the data cannot be fit by a line segment of the form $U_c/U_j \propto (x/D)^{-1}$, although each segment of the data can be, the line segments used being different for each data segment. Reference to Table 4.1, page 198, shows that Egger's data satisfies the momentum integral criterion to about the same degree as does Johannesen's, for about the same axial distance. Two reasons for the decay behavior of Egger's data are possible--either the data should be fit by an x^{-1} line, which would indicate an origin shift between each set of data, or the data should not be fit by an x^{-1} line, but by a line having a different slope. The first possibility seems unlikely for two reasons--first the relatively good agreement with the momentum integral requirement, and secondly, by the fact that with a supersonic nozzle flow such as this, the only parameter that can conceivably change between runs is the jet total temperature. Increase of the jet total temperature to ambient air temperature ratio could cause a shift in

the decay curves, at least for subsonic flow, as will be seen in the following section, but whether the same effect occurs to the same extent in a supersonic flow has not been determined. Eggers [72] does not report whether or not all the data were taken in a single test, so the question of whether or not a change occurred in jet stagnation conditions, and the effect this might have had on the velocity decay curves cannot be answered.

The $U_c/U_j \propto (x/D)^{-1}$ curve is found universally in the constant density low speed jet. When coupled with a spreading rate proportional to x/D , and velocity profiles which are functions of the parameter r/x , this indicates, for the axisymmetric jet, that self-preservation has been achieved. Because of the effect of density gradients, it is not possible to define self-preservation in a compressible jet in the same manner. One might expect an approach to self-preserving behavior far enough downstream, as the centerline Mach number approaches zero. But from Johannesen's observations [69]

. . . the results presented in the present paper suggest that full self-preservation may never in practice be reached at measurable velocities. Put another way, it may not be reached until the velocities are so low that they are of the same order as the random velocity fluctuations in the "still" air into which the jet is issuing.

In the incompressible jet, axial velocity decays inversely proportional to x/D are obtained, as well as geometric similarity of the profiles, before true self-preservation is

reached. As can be seen from Figure 4.5, geometric similarity is adequately obtained for the compressible jet into still air, with velocity profiles well fit by an equation of the form

$$\frac{U}{U_c} = \exp[-0.6932 \left(\frac{r}{r_{1/2}}\right)^2] \quad (4.16)$$

However, the fairly limited information available suggests that for Mach numbers greater than about two, axial velocity decays inversely proportional to x/D should not be expected, and that any eventual transition to behavior such as found for the constant density jet-into-still-air may occur so far downstream as to be not in practice measurable.

Circular Jets with Density Differences Caused by Temperature and Composition Differences

The jets to be considered in this section are generally low speed flows, but with significant density differences caused by heating the jet or by using a jet of a different gas from that of the surroundings. There are numerous practical applications of such jets, one of the more interesting being the orchard heater as discussed by Cleaves and Boelter [75].

Table 4.2 lists the important parameters for the experiments considered in this section. As mentioned above, the experiments of Cleaves and Boelter [75] were designed to investigate the flow field of a configuration representing an

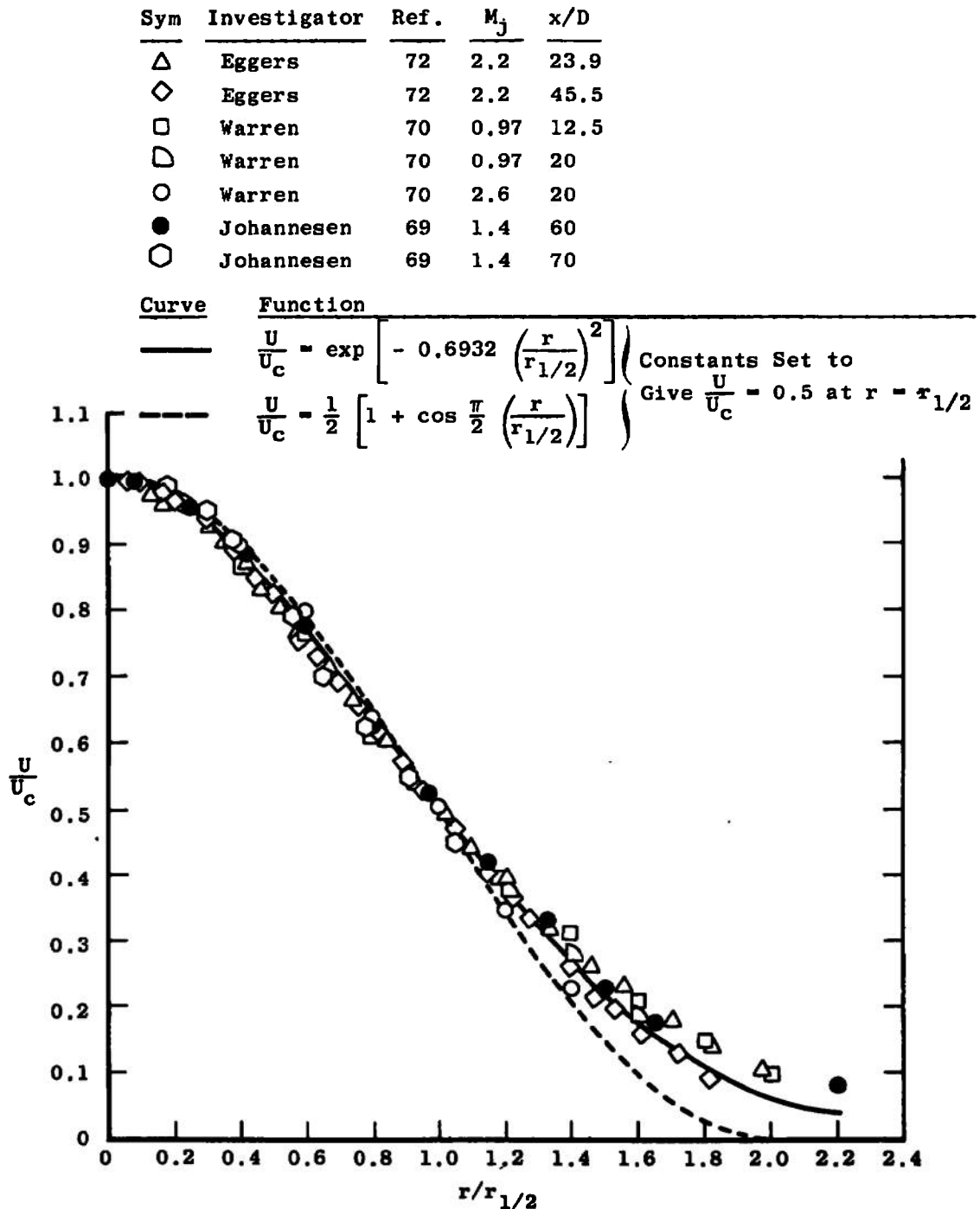


Figure 4.5. Similarity plot, jet-into-still-air ($T_{O_j}/T_a = 1.0$) and comparison with commonly used profiles.

TABLE 4.2

CIRCULAR JETS INTO QUIESCENT AIR WITH TEMPERATURE
OR CONCENTRATION DIFFERENCES

Investigator	Ref.	Year	U_j (M_j) ^a	Jet Gas	T_{Oj}/T_a (H_{Oj}/H_a)	Largest x/D	Momentum Check Percent of Average
Cleeves and Boelter	75	1947	21.6	Air	1.0	41.0	-
			21.6	Air	3.09	15.2	-
Keagy and Weller	76	1949	400	He	-	48 ⁴	+60, -38, 16 < x/D < 48
			400	N ₂	-	48	7, 8 < x/D < 42
			400	CO ₂	-	48	10, 8 < x/D < 43
Corrsin and Uberoi	25	1950	65-115	Air	1.47	27	-
					1.91	24	-
Warren	70	1957	(0.69)	Air	1.242	25	Not Calculated
			(0.68)	Air	1.429	20	Not Calculated
			(0.967)	Air	1.240	20	Not Calculated
			(0.97)	Air	1.428	25	Not Calculated
Donaldson and Gray	67	1966	(0.75)	Methane	(1.702)	17	-
				N ₂	(0.871)	34	-
				CO ₂	(0.699)	31	-
O'Connor, Comfort, and Cass	77	1966	(0.782)	N ₂ (8% dissoc.)	19.45	21	10 ^b

^aft/sec.^bAuthor's measurement.

orchard heater, so that very high temperature ratios and low jet velocities were used, giving rise to significant buoyancy effects.

Keagy and Weller [76] on the other hand investigated the effects of density gradients on free mixing of single jets with quiescent surroundings, and chose a jet velocity such as to minimize the buoyancy effects. In their analysis they give the integral momentum equation including the buoyancy term as (the jet issues vertically; x is measured axially)

$$\int_0^{\infty} \rho U^2 r dr = g \int_0^x \int_0^{\infty} (\rho_0 - \rho) r dr dx + \text{constant} \quad (4.17)$$

where

$$\rho = \rho_0 + (\rho_j - \rho_0)c \quad (4.18)$$

and c represents concentration of jet gas. Following their analysis, the importance of the buoyancy term may be assessed as follows. Using (4.18) in the buoyancy term

$$g \int_0^x \int_0^{\infty} (\rho_0 - \rho) r dr dx = -g(\rho_j - \rho_0) \int_0^x \int_0^{\infty} c r dr dx \quad (4.19)$$

Following Keagy and Weller (4.10), assume

$$\left. \begin{aligned} \eta &= y/x \\ c &= c_c e^{-\mu k \eta^2} \\ c_c &= kD/x \end{aligned} \right\} \quad (4.20)$$

and

$$U = U_c e^{-k \eta^2}$$

which, after some algebra gives for the buoyancy term B

$$\begin{aligned} B &= -g(\rho_j - \rho_o) \int_0^x \int_0^\infty c r dr dx \\ &= -gkD(\rho_j - \rho_o) \frac{x^2}{2} \int_0^\infty \eta e^{-\mu k \eta^2} d\eta \end{aligned} \quad (4.21)$$

Now

$$\int_0^\infty \rho U^2 r dr = \rho_o \int_0^\infty U^2 r dr + (\rho_j - \rho_o) \int_0^\infty U^2 c r dr \quad (4.22)$$

which, using Equation (4.20) becomes

$$\begin{aligned} \int_0^\infty \rho U^2 r dr &= \rho_o U_c^2 x^2 \int_0^\infty \left(\frac{U}{U_c}\right)^2 \eta d\eta + \\ &\quad + (\rho_j - \rho_o) c_c U_c^2 x^2 \int_0^\infty \left(\frac{U}{U_c}\right)^2 \frac{c}{c_c} \eta d\eta \\ &= \rho_o U_c^2 x^2 \int_0^\infty \eta e^{-k \eta^2} d\eta + \\ &\quad + (\rho_j - \rho_o) c_c^2 U_c^2 x^2 \int_0^\infty \eta e^{-(1+\mu)k \eta^2} d\eta \end{aligned} \quad (4.23)$$

so that the ratio of the momentum flux term to the buoyancy term, R , is, noting that

$$\int_0^{\infty} n e^{-\alpha n^2} dn = \frac{1}{2\alpha}$$

$$R = \frac{\rho_o U_c^2 x^2 + (\rho_j - \rho_o) \frac{k^2 D^2 U_c^2}{1+\mu}}{gD(\rho_j - \rho_o) \frac{x^2}{2\mu}}$$

or

$$\begin{aligned} R &= \frac{2\mu U_c^2}{g} \left[\left(\frac{\rho_o}{\rho_o - \rho_j} \right) \frac{1}{D} + \frac{k^2 D}{(1+\mu)x^2} \right] \\ &= \frac{2\mu U_c^2}{gD} \left[\frac{\rho_o}{\rho_o - \rho_j} + \frac{k^2}{1+\mu} \left(\frac{D}{x} \right)^2 \right] \end{aligned} \quad (4.24)$$

The buoyancy effect should be greatest for the helium jet.

From Keagy and Weller [76], for this case

$$k = 57$$

$$\mu = 0.50$$

$$\rho_o = 0.076 \text{ lbm/ft}^3$$

$$\rho_j = 0.011 \text{ lbm/ft}^3$$

$$D = 0.0106 \text{ ft}$$

and, evaluating (4.24)

$$R = 484$$

which indicates that the buoyancy effect is indeed negligible. The momentum integral was evaluated incorporating the buoyancy term for these data, using Equations (4.17) and (4.20), and the results indicate that even with the inclusion of this term, the experimental results of Keagy and Weller using helium fail to satisfy constancy of momentum by a wide margin. This difficulty is most probably caused by inaccuracies in the low pitot pressures involved with helium jets at the relatively low velocities used here.

The experiments of Corrsin and Uberoi [25] are some of the few experiments in non-constant-density flows in which some details of the turbulence structure were measured. Thus they provide one of the few available measures of the effect of a fluctuating temperature (or density) field on a fluctuating velocity field. Figure 4.6, taken from the data of Reference [25], shows that at a given axial station, the intensity of the axial velocity fluctuation is decreased in a hot jet compared to a cold jet at substantially the same nozzle exit velocity. For the particular case shown here, the centerline velocity ratio U_c/U_j at $x/D = 20$ was 0.30 for the hot jet as compared to 0.33 for the cold jet. The linear relationship between turbulent shear stress and turbulent kinetic energy

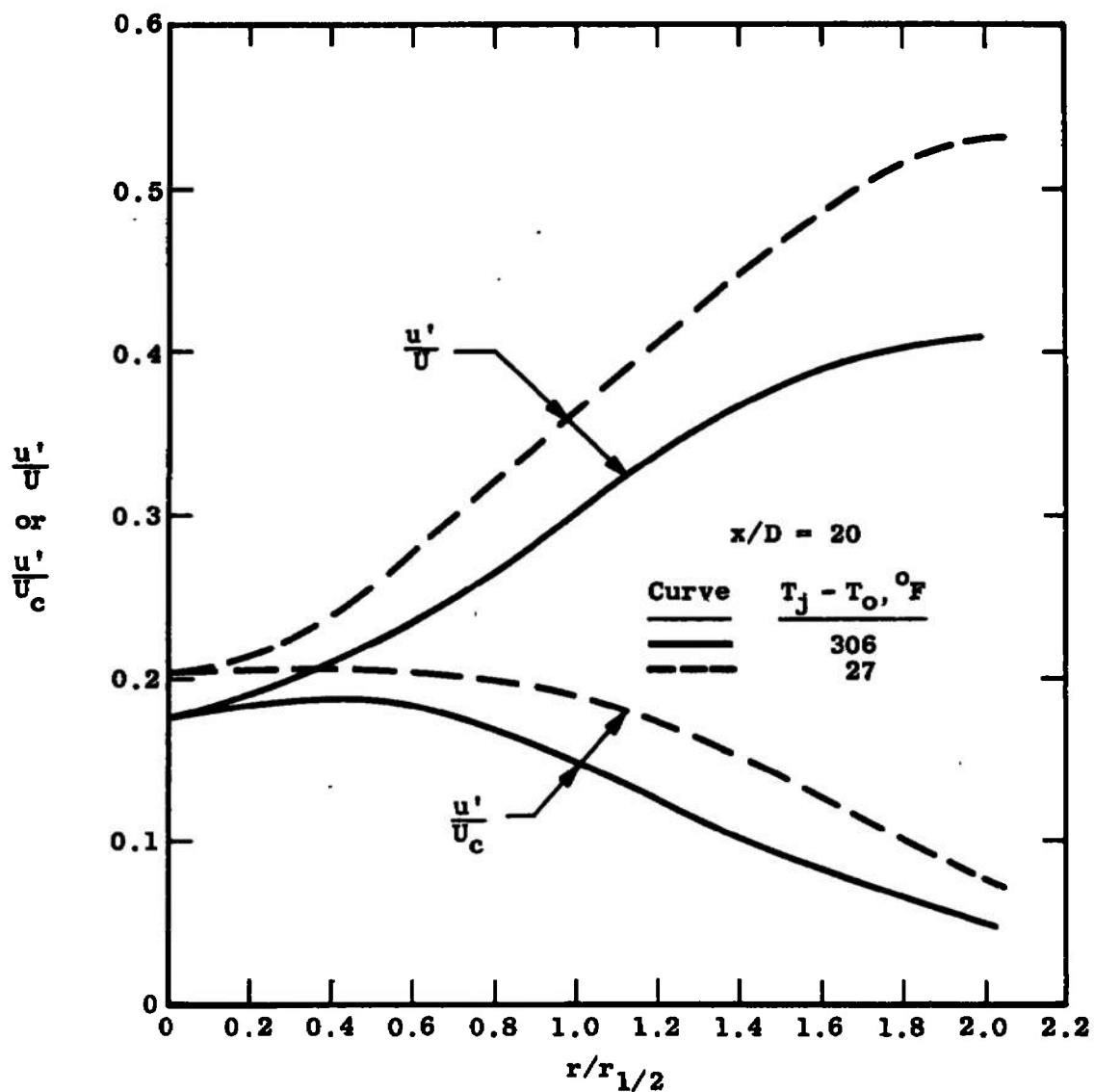


Figure 4.6. Comparison of axial component of turbulent velocity, hot and cold jets. Data from Corrsin and Uberoi [25].

established in constant-density flow is followed satisfactorily by these data, as shown by Figure 4.7, although the constant a_1 , which was seen to have an average value of about 0.3 in the constant-density case, here appears to be 0.25. There is not, however, sufficient data to completely establish the particular average value of a_1 for this flow. Figure 4.8 shows that the lateral distribution of the parameter a_1 agrees favorably with the constant density data of Sami [29], especially when it is remembered from Chapter 2 that the peak value of a_1 tends to decrease slowly with axial distance.

Warren's data [70] are a continuation of the experimental work discussed in the preceding section and thus do not need to be reintroduced. Donaldson and Gray [67] carried out measurements similar to those made by Keagy and Weller [76], at somewhat higher velocities, and at different temperature ratios (although no temperature ratios are reported by Keagy and Weller). However, no velocity profiles are reported by Donaldson and Gray, so that no momentum check can be made. Finally, O'Connor, et al., [77] carried out an extensive investigation of a high-enthalpy jet of partially dissociated nitrogen, measuring axial and lateral profiles of velocity, total enthalpy, and concentration.

Figure 4.9, incorporating data from Cleeves and Boelter [75] and Corrsin and Uberoi [25] illustrates the

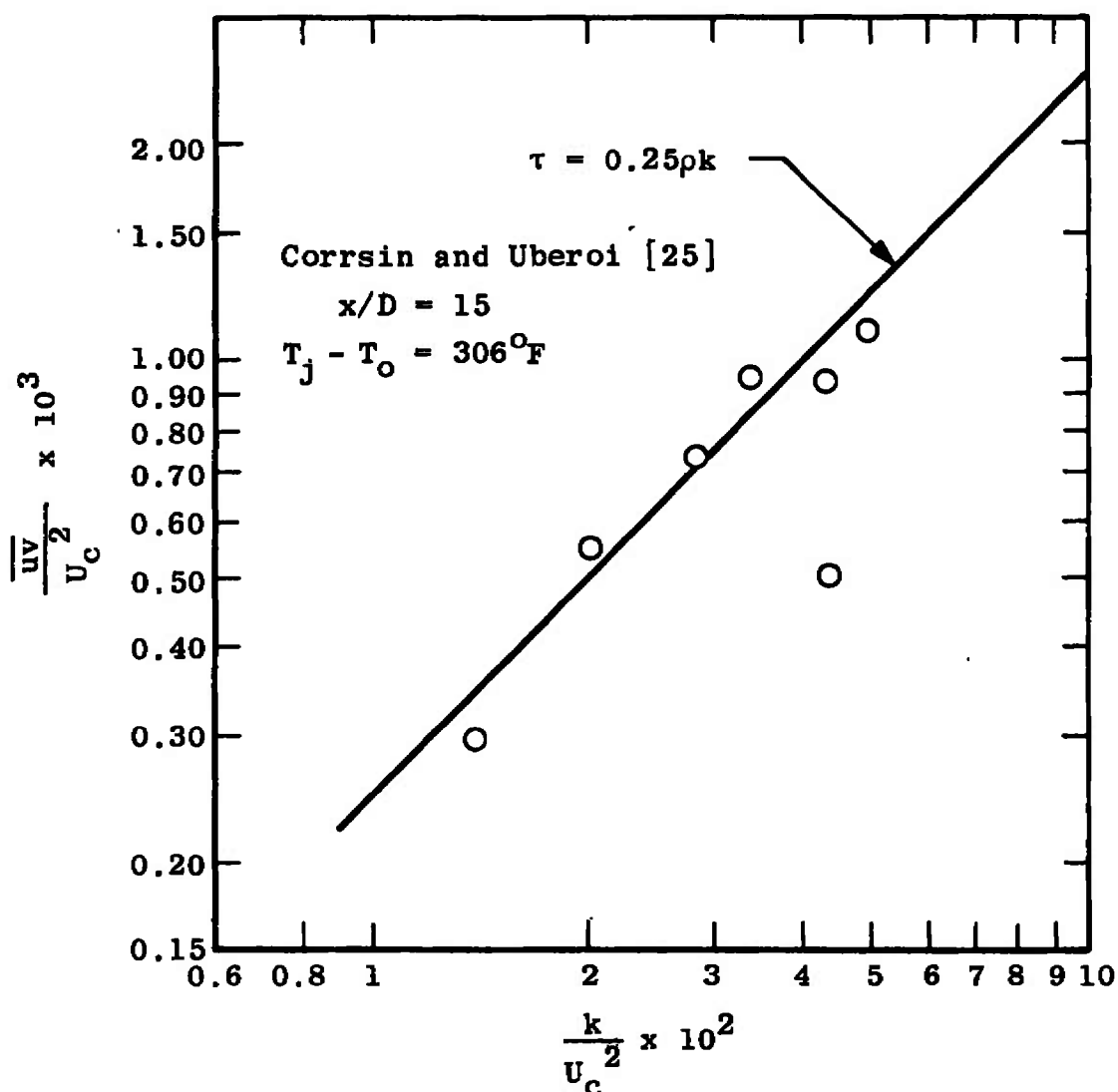


Figure 4.7. Relation between turbulent shear stress and turbulent kinetic energy, hot jet.

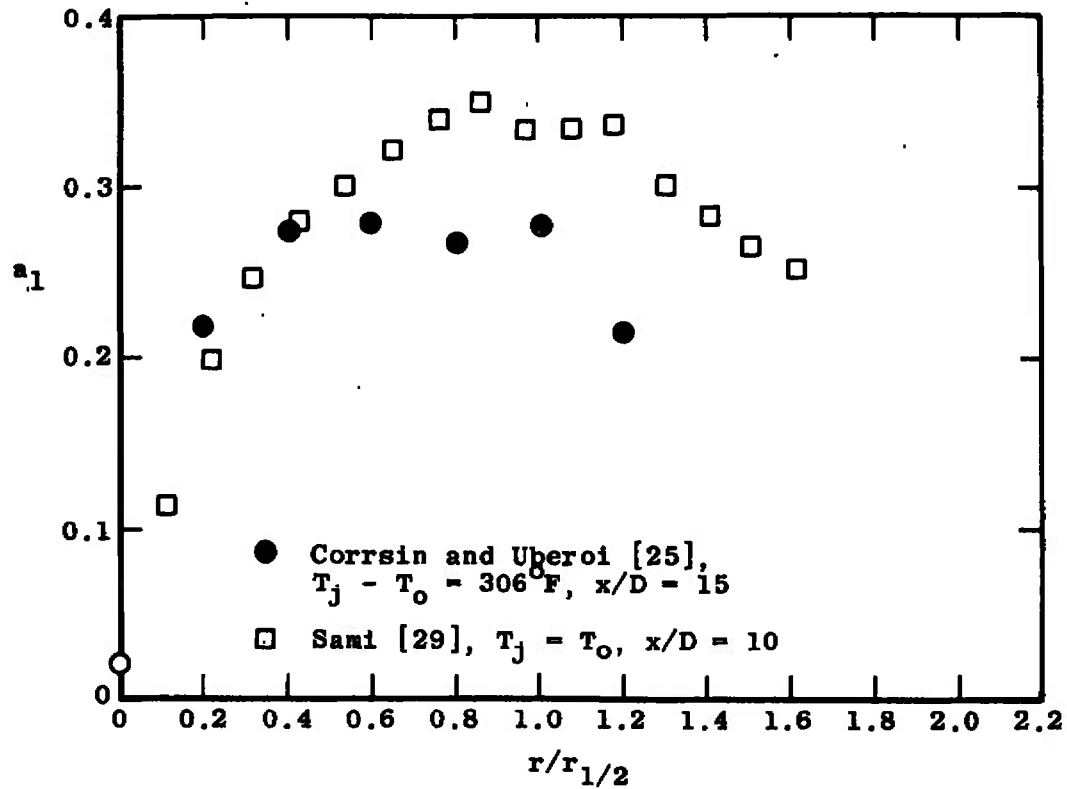


Figure 4.8. Comparison of ratio of turbulent shear stress to turbulent kinetic energy, hot and cold jets.

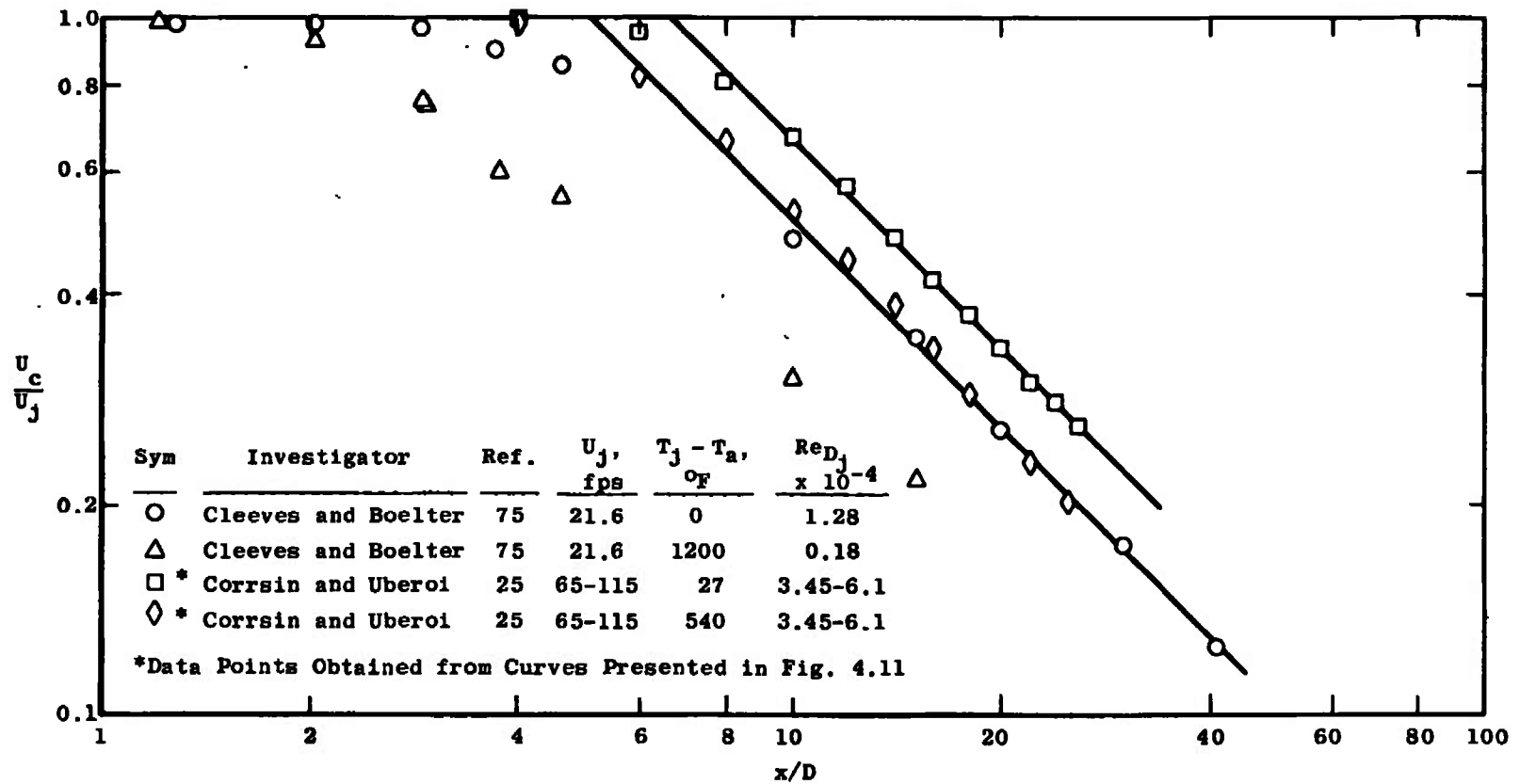


Figure 4.9. Comparison of axial decay of centerline velocity, isothermal and nonisothermal jets.

effect of initial temperature differences on the axial decay of centerline velocity. It can easily be seen that increasing the ratio of jet temperature to the temperature of the surroundings decreases the length of the potential core, while except for the high-temperature-ratio, Cleaves and Boelter data, which is probably strongly affected by buoyancy, the velocity data all exhibit a decay inversely proportional to x/D . It can also be noted from Figure 4.9 that the Corrsin and Uberoi near-isothermal data are shifted compared to the Cleaves and Boelter data, as would be expected from the discussion of Reynolds number effects in Chapter 2.

Corrsin and Uberoi [25] report that the temperature field spreads faster than the velocity field. Figure 4.10 demonstrates that the centerline temperature ratio also decays faster than the centerline velocity. In this case the best fit to the data not affected by buoyancy appears to be a line for which $T_c - T_o / T_j - T_o \propto (x/D)^{-5/4}$.

When the velocity half-radius (defined as the radius at which $U/U_c = 0.5$) is used as a non-dimensionalizing parameter, the lateral temperature ratio distributions do not appear to exhibit geometric similarity, as seen from Figure 4.11. If on the other hand, a new half radius, $r_{1/2T}$, is defined--as the radius at which $(T - T_o)/(T_c - T_o) = 0.5$ --and this radius is used as a non-dimensionalizing factor, Figure 4.12 shows that the data

Sym	Investigator	Ref.	U_j , fps	ΔT , °F	$Re_j \times 10^{-4}$
○	Corrsin and Uberoi	25	65-115	27	3.45-6.1
□	Corrsin and Uberoi	25	65-115	540	3.45-6.1
◻	Cleeves and Boelter	75	56	1200	0.47
◇	Cleeves and Boelter	75	21.6	1200	0.18

Notes: 1. Corrsin and Uberoi Data Points Taken from Curves Presented in Ref.
 2. Lines Faired Thru Data Have Slopes Proportional to $(x/D)^{-5/4}$

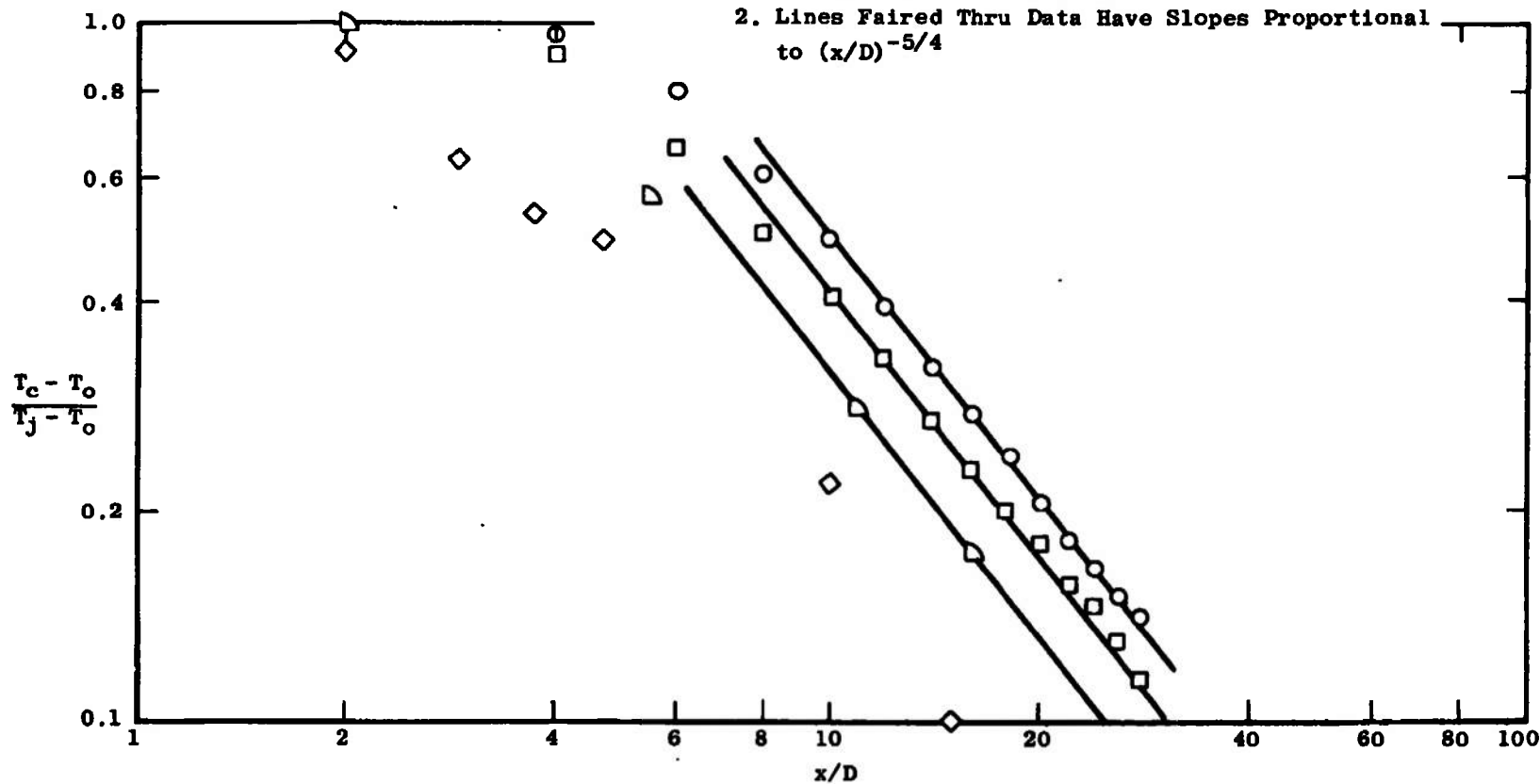


Figure 4.10. Axial decay of centerline temperature ratio.

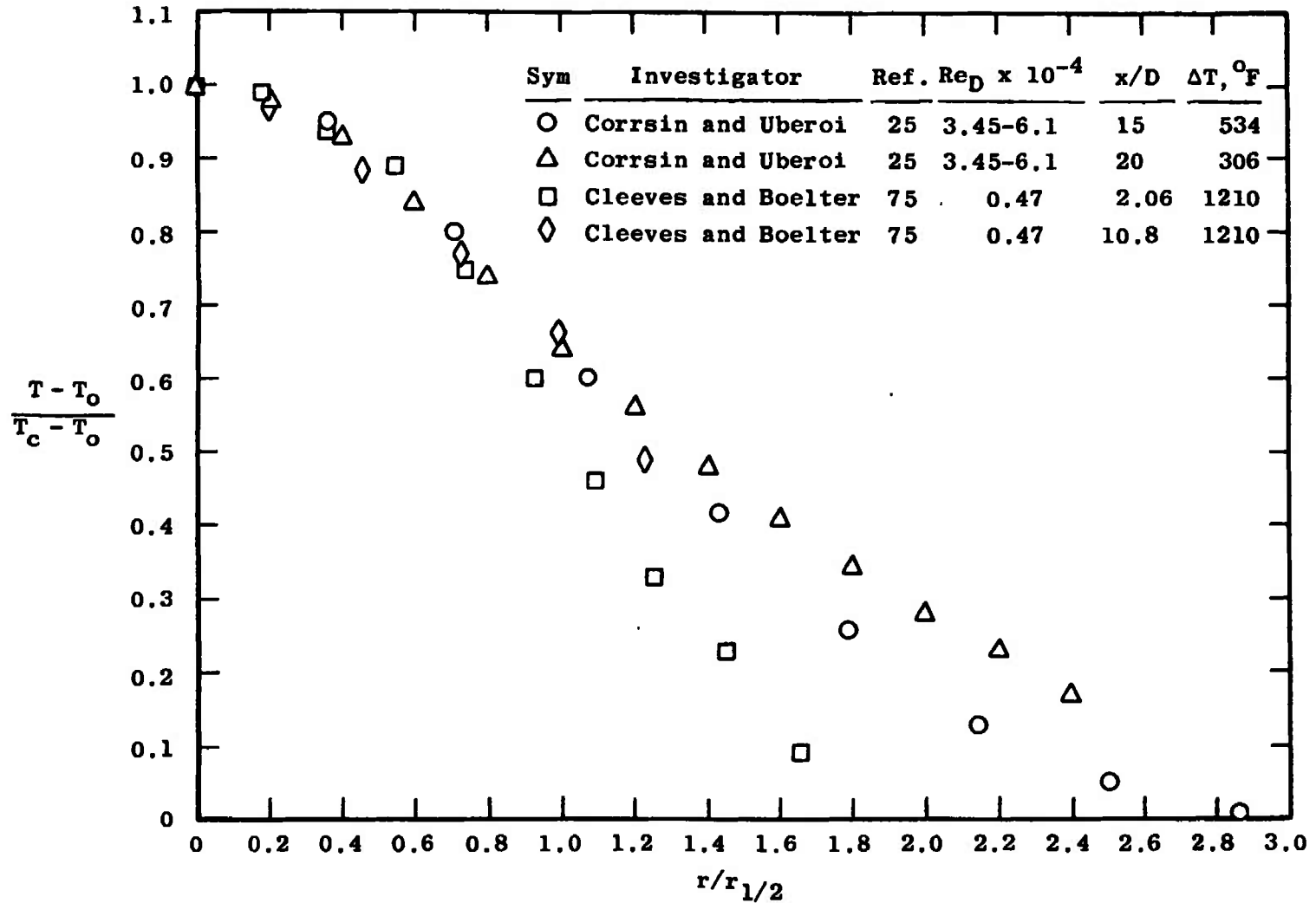


Figure 4.11. Radial temperature distribution $(T - T_o) / (T_c - T_o)$ versus $r/r_{1/2}$, where $r_{1/2} = r$ for $U/U_c = 0.5$.

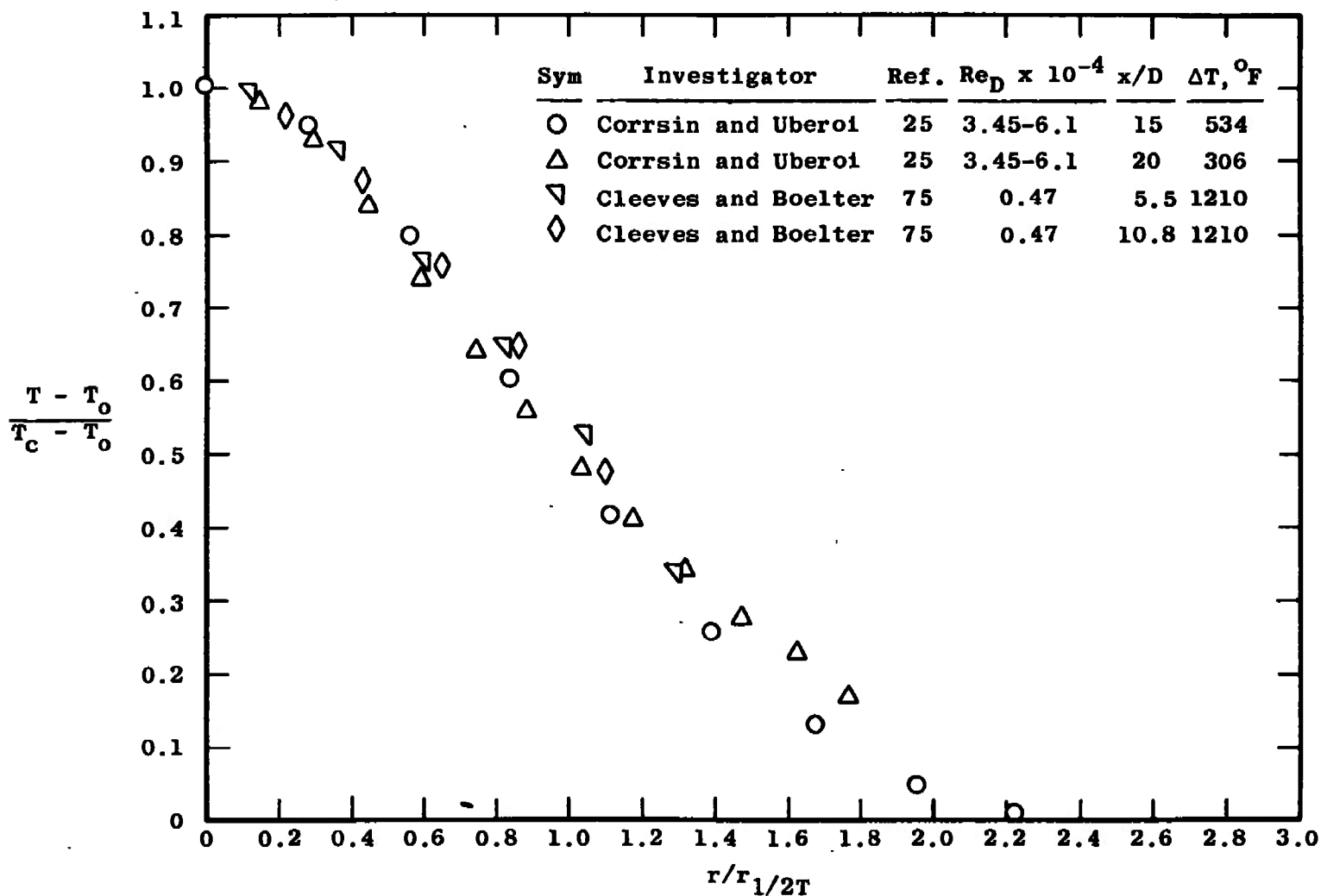


Figure 4.12. Radial temperature distribution $(T - T_o) / (T_c - T_o)$ versus $r / r_{1/2T}$, where $r_{1/2T} = r$ for $(T - T_o) / (T_c - T_o)$.

collapse together reasonably well, especially so considering the limited range of axial distance.

A comparison of Warren's [70] $M_j = 0.69$ data at various jet-stagnation to ambient temperature ratios indicates, as in Figure 4.13, that a nonunity temperature ratio does not affect the existence of local geometric similarity. The data of O'Connor, et al., [77] for the very high enthalpy jet indicates, Figure 4.14, that even in this extreme case, geometric similarity of the velocity profiles is a reasonably good assumption. However, the axial decay of centerline velocity measured by O'Connor, et al., does not follow a line of $U_c/U_j \propto (x/D)^{-1}$. This is shown by Figure 4.15. Such behavior might be expected given the apparent deviation from such a line shown by the axial decay data of Eggers [72] (Figure 4.4, page 209) for the supersonic jet, which could be taken to indicate that such deviations in that case increase with the jet Mach number. Figure 4.15 also shows that the centerline enthalpy for these data appear to decay the same rate as the centerline velocity, while the centerline composition of jet gas follows a different rate, approximately inversely proportional to x/D . This disagrees with lower-temperature experiments which commonly show that the rates for total enthalpy and composition are equal. The composition results here may have been affected by the existence of partial dissociation at the high temperatures involved. Comparison

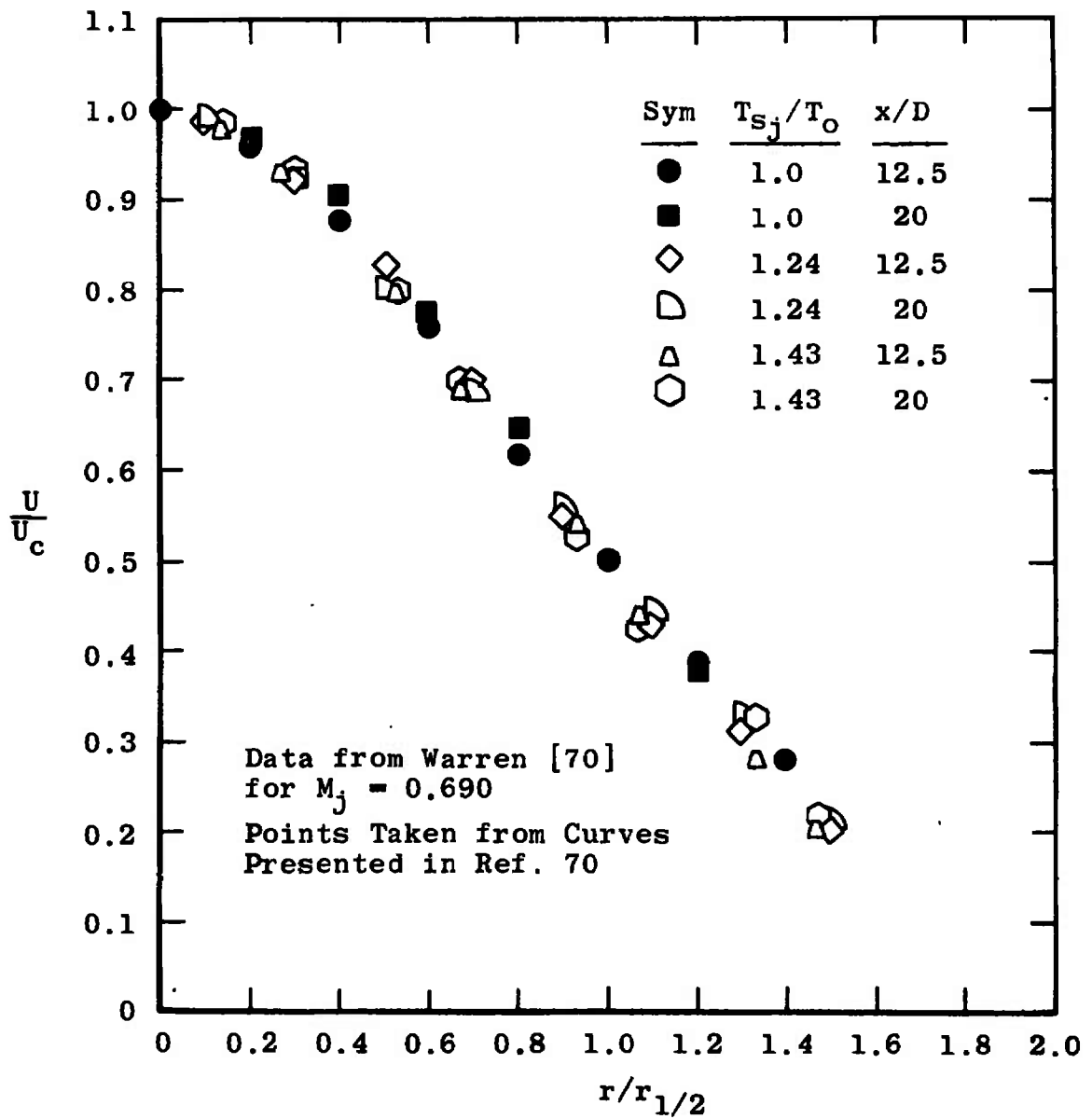


Figure 4.13. Effect of nonunity temperature ratio on velocity profile, compressible jet-into-still-air.

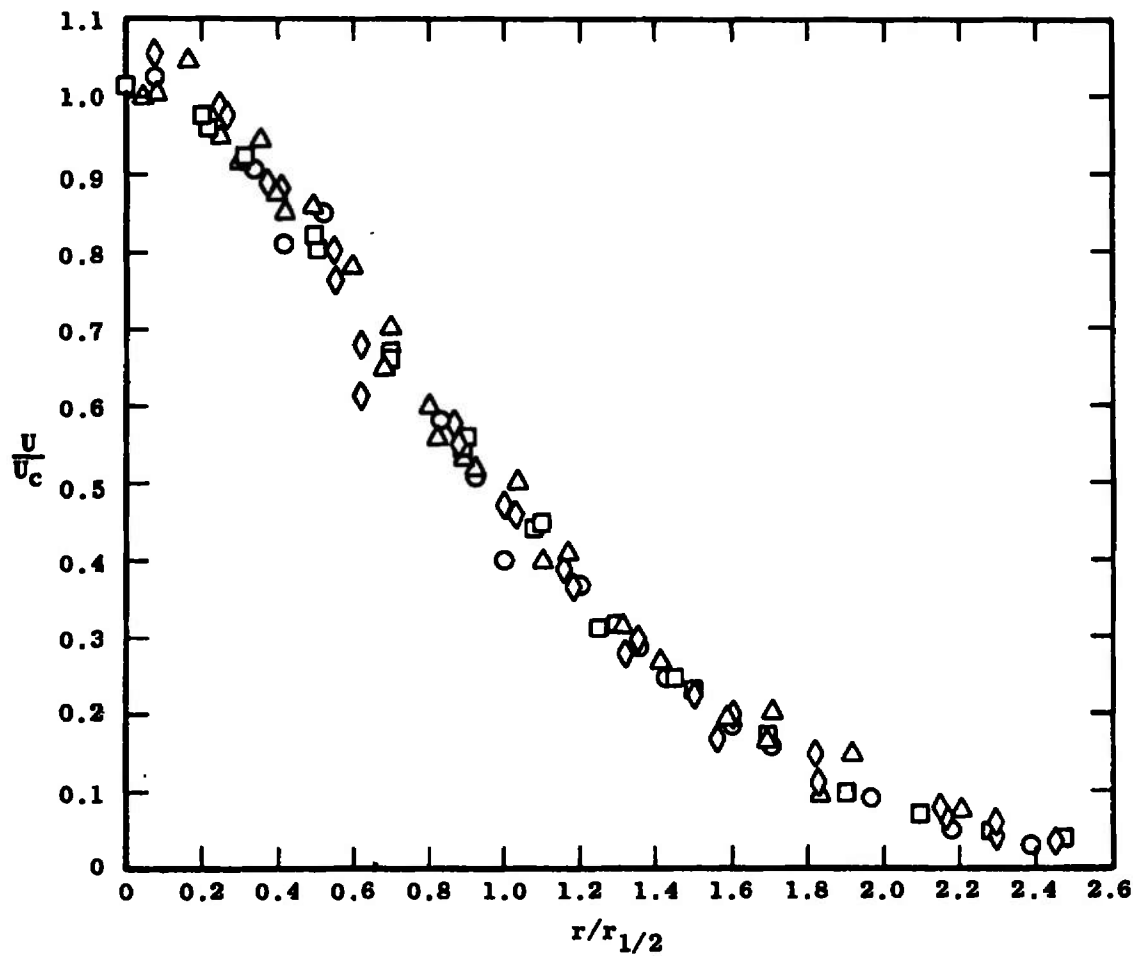


Figure 4.14. Test for geometric similarity--high enthalpy N_2 jet-into-still-air--Reference [77].

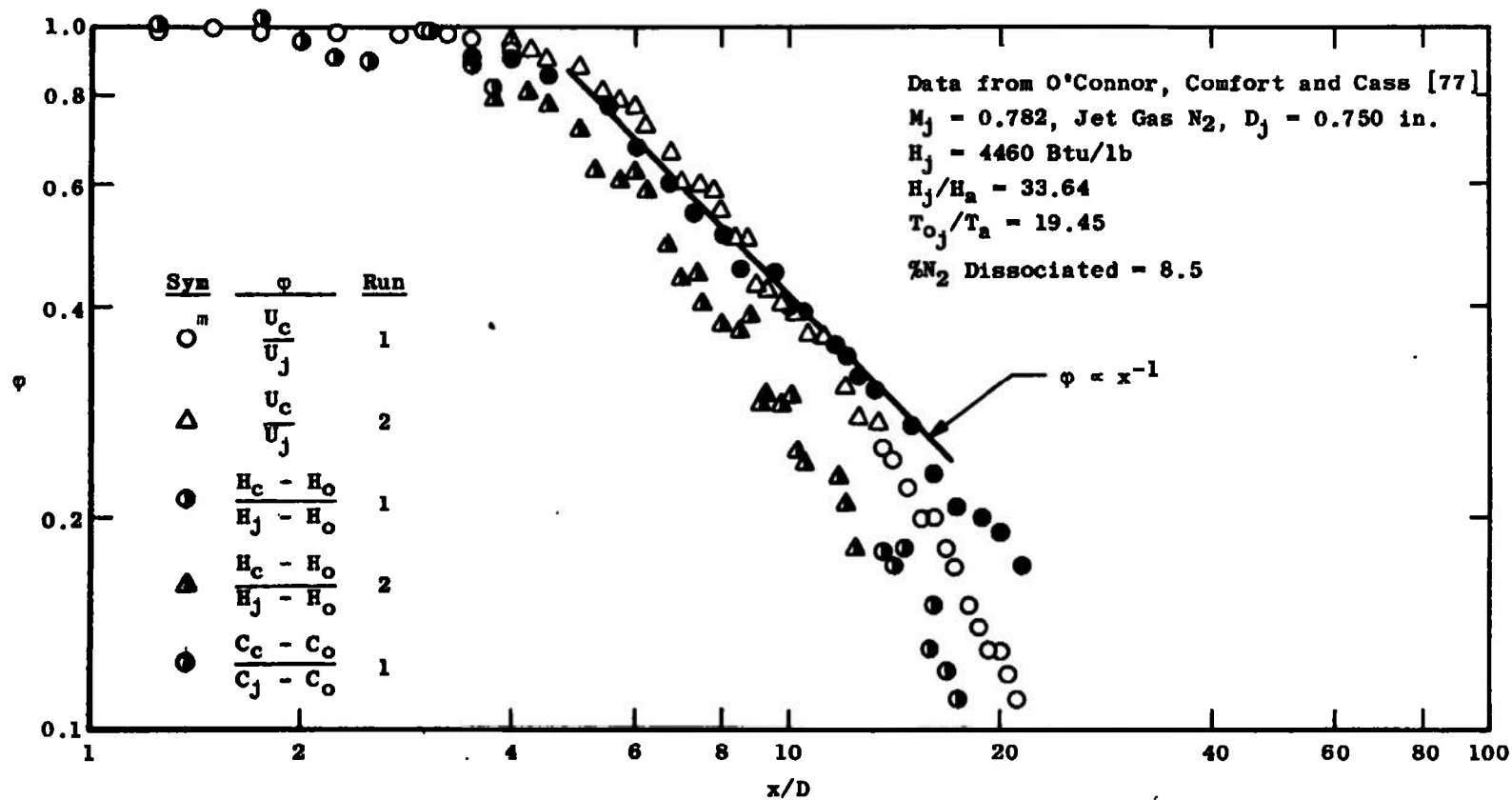


Figure 4.15. Centerline decay of velocity, stagnation enthalpy, and concentration, high temperature jet-into-still-air.

of the centerline velocity ratio decay data of Warren [70] with that of O'Connor, et al., [77], Figure 4.16, shows as expected that the length of the potential core decreases with an increasing ratio of the jet stagnation temperature to the ambient temperature, T_{O_j}/T_a . Further, for the very high temperature ratio case, the slope of the velocity curve changes from the $U_c/U_j \propto (x/D)^{-1}$ character observed by Warren to a greater slope. Figure 4.17 illustrates that the same sort of comparison holds true for the centerline enthalpy ratio decay. Warren's data is at low enough temperatures for the assumption of constant specific heat to be valid, and thus $(T_{O_c} - T_a)/(T_{O_j} - T_a) = (H_c - H_o)/(H_j - H_o)$ for Warren's data.

For low speed jets of different gases, the data of Keagy and Weller [76] exhibit an increase in potential core length with an increase in jet molecular weight (or jet density). In this case, as in all others in this section, the surrounding gas is air. This is in agreement with the results for a heated jet, which indicate that the length of the potential core increases as the jet-to-surroundings temperature ratio decreases (and thus the jet-to-surroundings density ratio increases). Figure 4.18 illustrates this fact, as well as showing that except for the helium jet, the results for which are questionable (see Table 4.2, page 214), the axial velocity decay is again inversely proportional to x/D . The centerline composition

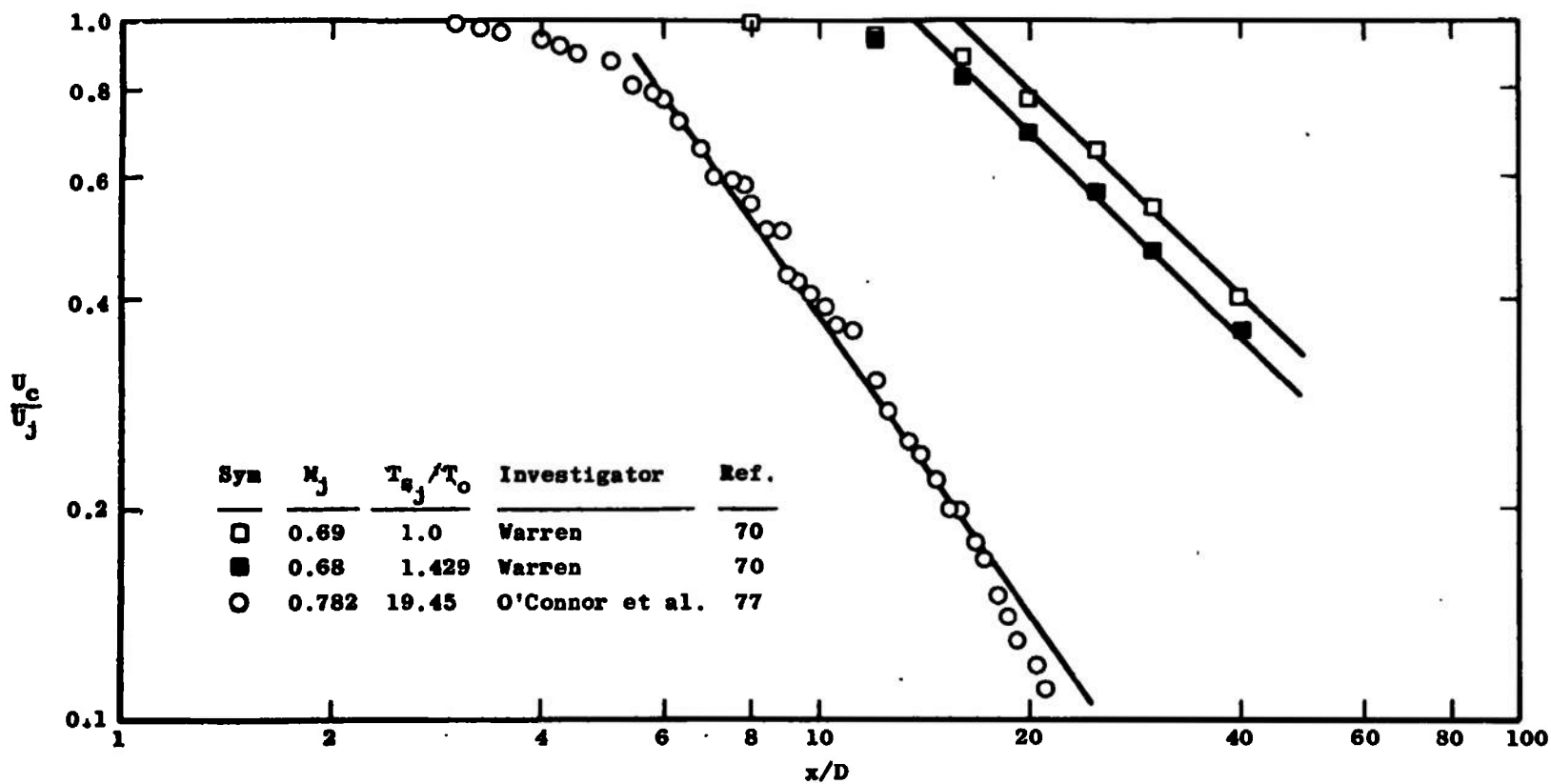


Figure 4.16. Effect of initial temperature ratio on centerline velocity decay.

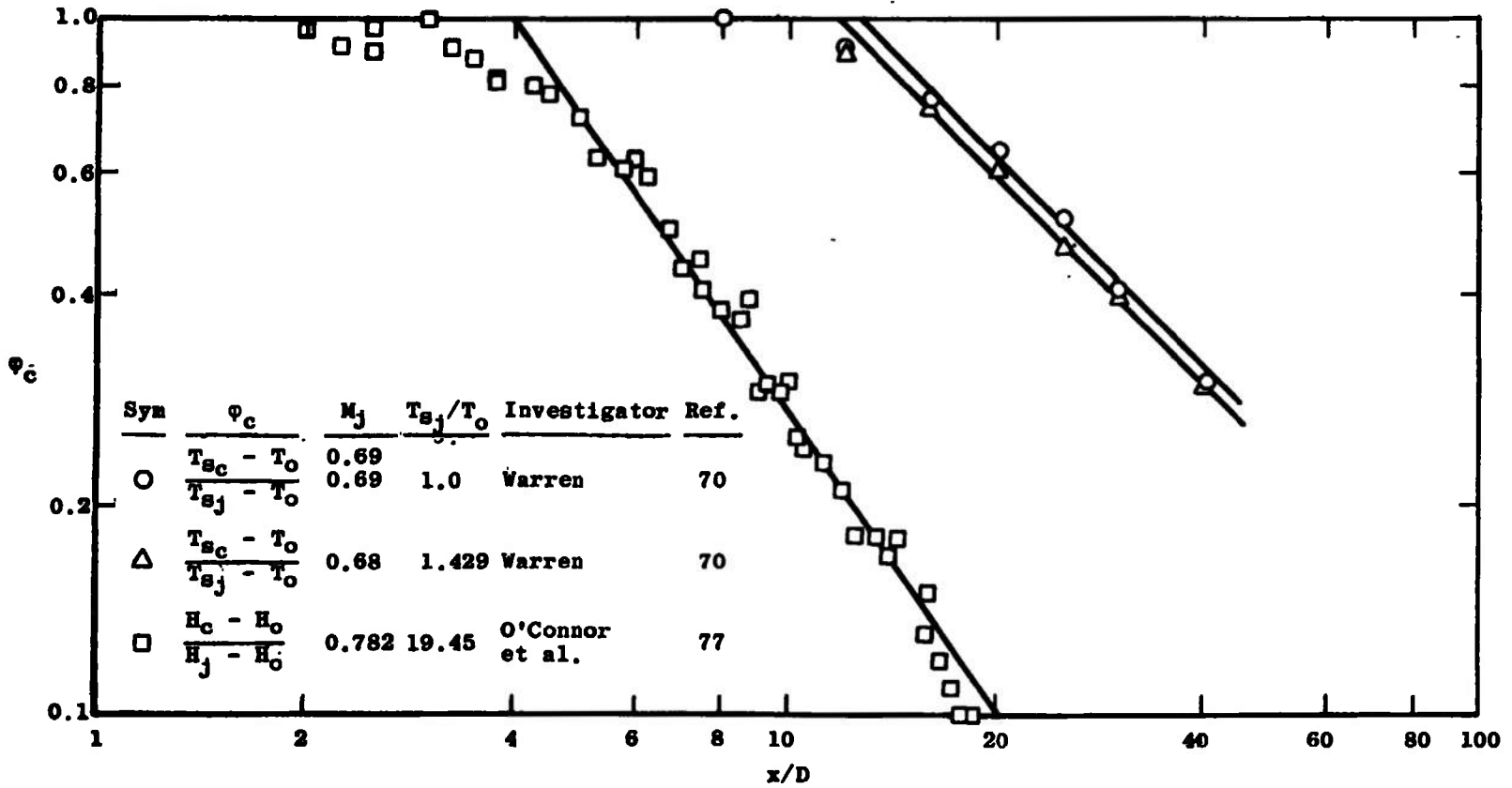


Figure 4.17. Effect of initial temperature ratio on centerline decay of total enthalpy.

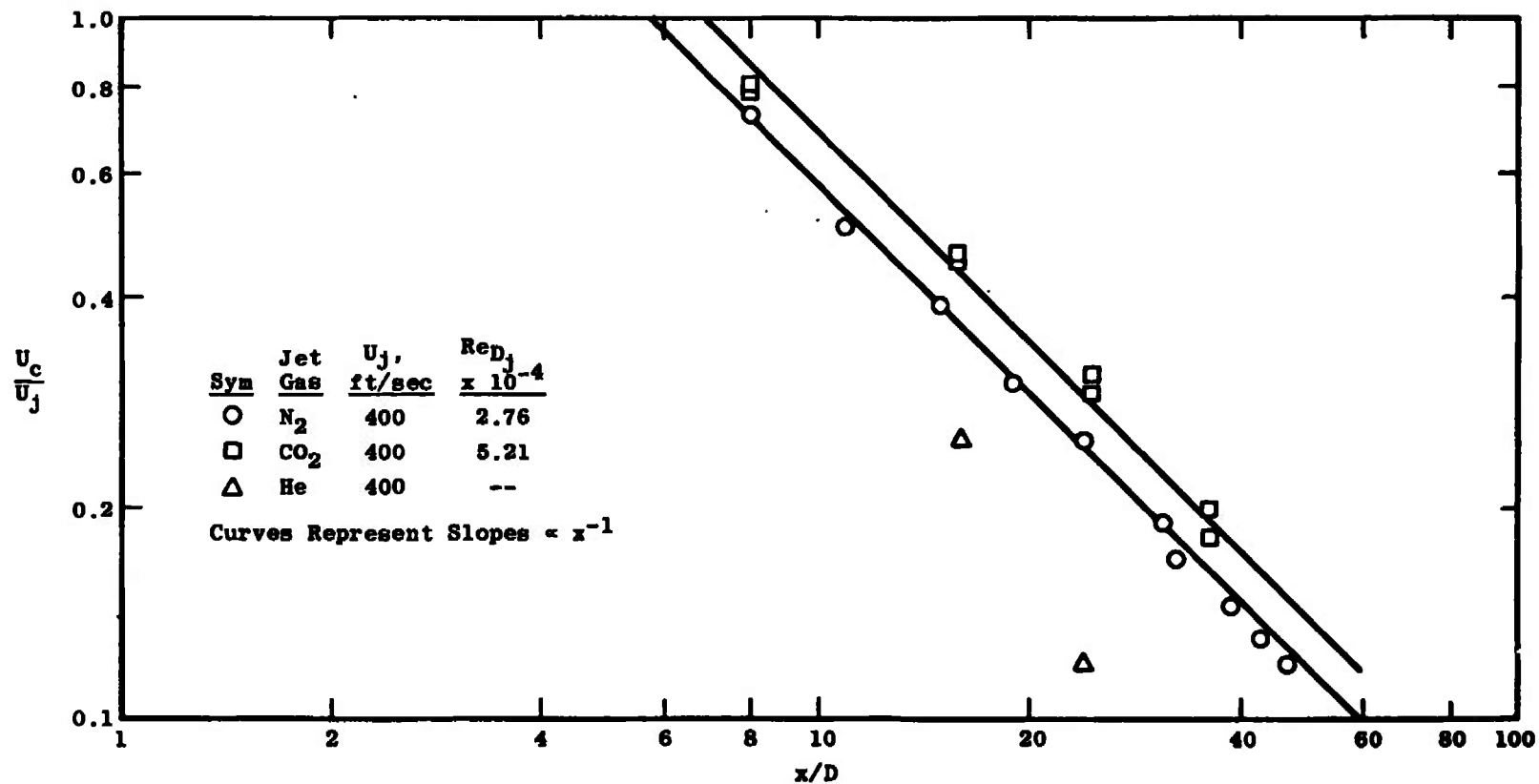


Figure 4.18. Axial decay of centerline velocity, circular jets of various gases into air, Keagy and Weller [76].

decay results are somewhat different as Figure 4.19 shows. In this case there is a behavior that is the reverse of that observed for the velocity decay; the centerline composition of jet gas curves show that at a given axial station the value of the ratio C_c/C_j (where $C_j = 1$ by definition) is greater the lower the molecular weight of the gas. This would imply concentration potential core lengths that decrease with increasing jet gas molecular weight. The reasons for this anomalous behavior are not clear.

The behavior of the centerline velocity decay curves measured by Keagy and Weller [76] is substantiated by the results of Donaldson and Gray [67]. Here, too, the length of the velocity potential core increases with increasing jet gas molecular weight. This is shown in Figure 4.20. Further, these results, at higher jet Mach numbers than those of Keagy and Weller, show longer core lengths than Keagy and Weller's data, as would be expected.

Other Flows

A number of experiments have been made in variable-density flows with zero secondary-stream velocity that do not conveniently fit into the categories discussed above. Such flows include the circular jet formed by the exhaust of a rocket nozzle, and two-dimensional cavity flows and mixing layers. The special nature of these flows makes the calculation of the momentum integral difficult; because of this difficulty and the relatively specific nature of the

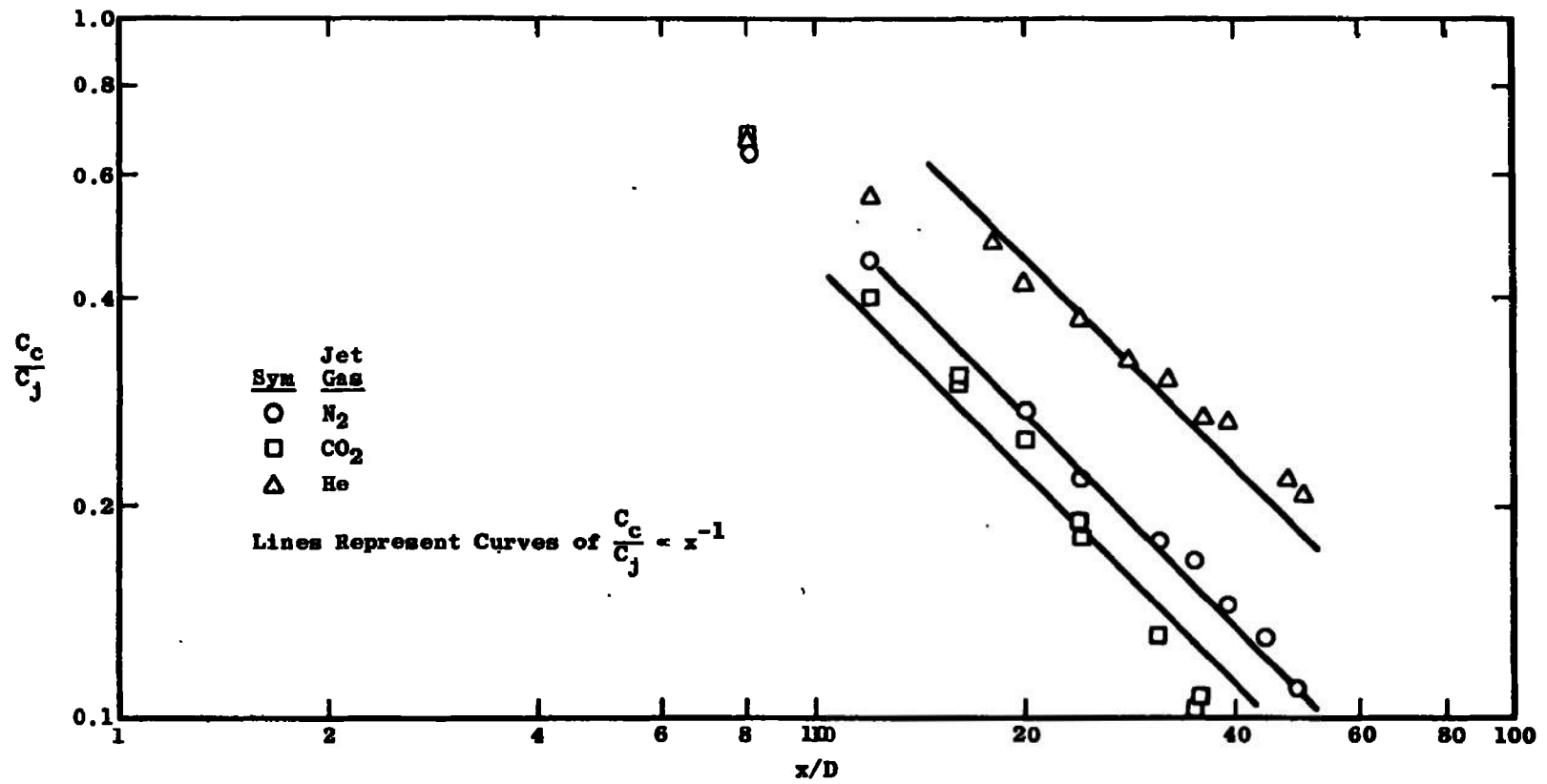


Figure 4.19. Axial decay of centerline composition, circular jets of various gases into air, Keagy and Weller [76].

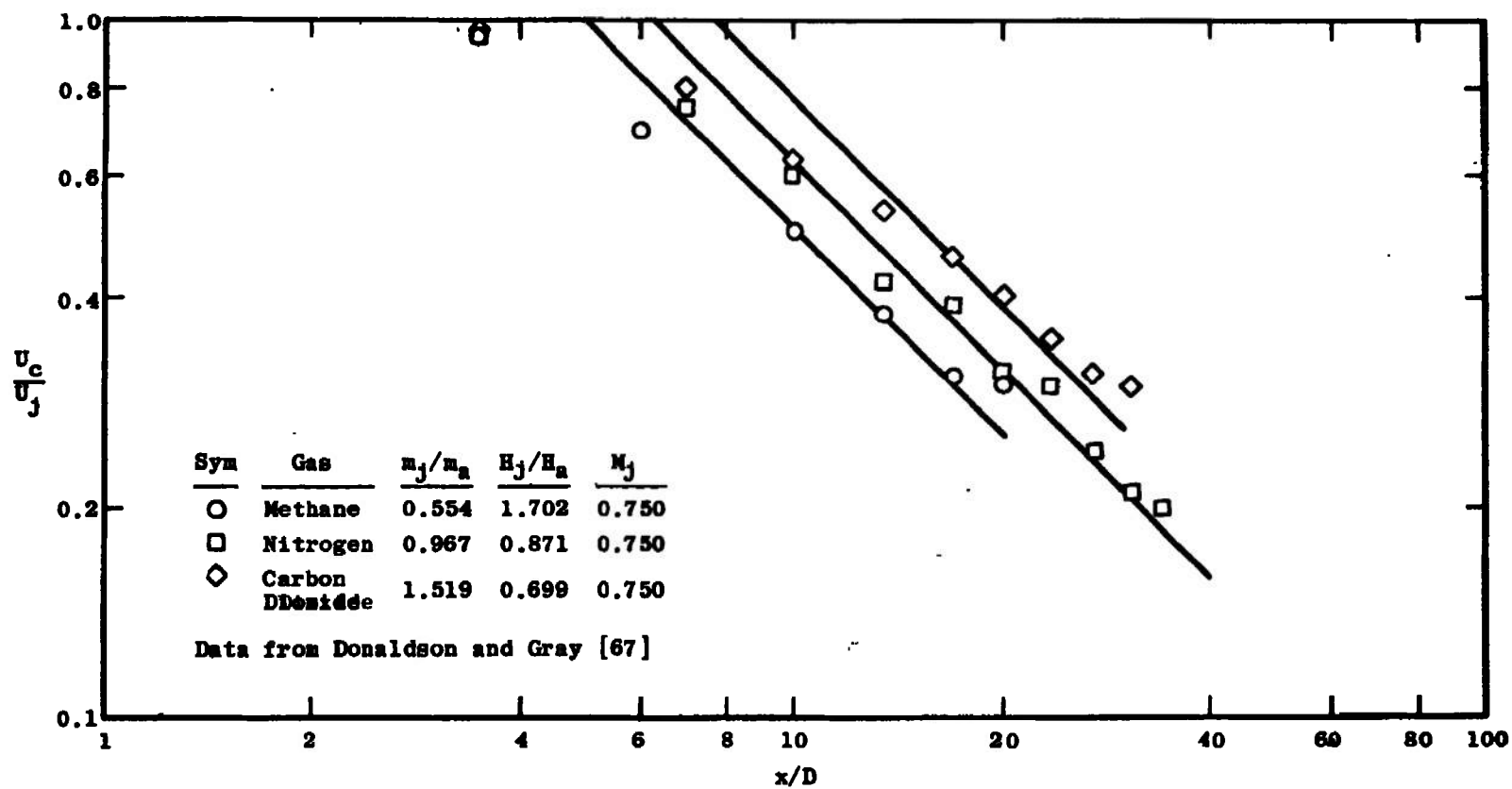


Figure 4.20. Effect of initial molecular weight ratio on centerline decay of axial velocity.

individual experiments, the momentum integral has not been evaluated for these flows and they will not be discussed in detail.

Table 4.3 lists the important characteristics of the flows considered. Anderson and Johns [66] made the most fundamental investigation of this group, using for their experiments two air jets, one at $M = 1.4$ and $T_0 = 1960^\circ\text{R}$ and the other at $M = 1.84$ and $T_0 = 1960^\circ\text{R}$. In addition, experiments were made using three solid propellant rockets, with exit Mach numbers of 2.82, 3.42, and 3.53, and chamber temperatures of the order of 4000°R . No details are given as to the composition of the exhaust product.

Anderson and Johns [66] present radial profiles of pressure and temperature for the similarity region for all five jets, observing geometric similarity in all cases. Because their theoretical analysis can handle only subsonic flows, they break the air jets, which are the most extensively investigated, down into two parts, defining the "supersonic core" to be the distance until the centerline Mach number drops to unity. They find that, to a good approximation, the length of this "supersonic core" for all of the jets considered increases linearly with jet (exit) Mach number. Axial decay results are presented for the centerline velocity for the two air jets. However, these results are nondimensionalized with respect to the

TABLE 4.3
OTHER VARIABLE-DENSITY FLOWS WITH ZERO SECONDARY VELOCITY

Investigator	Ref.	Year	Type of Flow	M_j	Jet Gas	$T_{o,j}/T_a$ ($H_{o,j}/H_a$)	Largest x/δ	Momentum Check, ^a Percent
Anderson and Johns	66	1955	Circular Jet	1.40	Air	3.73	n.a. ^b	Not Calculated
				1.84	Air	3.73	n.a. ^b	
			Rocket Exhaust	2.82	n.a. ^b	7.55	n.a. ^b	
				3.42	n.a. ^b		n.a. ^b	
				3.43	n.a. ^b		n.a. ^b	
Frauenberger and Forbister	78	1961	Rocket Exhaust	2.69	Specified Mixture	8.35	40	
Maydew and Reed	79	1963	First Regime of Jet	0.7	Air	n.a. ^b	3.84	
				0.85	Air	n.a. ^b	3.84	
				0.95	Air	n.a. ^b	3.84	
				1.49	Air	n.a. ^b	3.84	
				1.96	Air	n.a. ^b	3.84	
Hill and Nicholson	80	1964	2D Mixing Layer	1.48	N ₂ , He	n.a. ^b	-	
				2.61	N ₂ , He, SF ₆	n.a. ^b	-	
				4.04	N ₂ , He, SF ₆	n.a. ^b	-	
				6.07	N ₂ , He, SF ₆	n.a. ^b	-	
				9.63	N ₂	n.a. ^b	-	
Hill	81	1968	Cavity	2.1	Air	n.a. ^b	5.7 ^c	
				3.2	Air	n.a. ^b		
				3.5	Air	n.a. ^b		
				3.7	Air	n.a. ^b		
Rom	82	1968	Circular Jet	n.a. ^b	N ₂ +Air	15-20	10	
			3D Jet	n.a. ^b	N ₂ +Air	15-20	10 ^d	

^aPercent of average.

^bIndicates data unavailable.

^c x/δ where δ = initial boundary layer thickness.

^d x/h where h = jet width.

"effective diameter at the $M = 1$ point;" the writer does not understand Anderson and Johns' explanation of how to obtain this quantity.

Frauenberger and Forbister [78] made an extensive experimental investigation of a supersonic jet emerging from a solid propellant rocket motor into air at rest. The exit Mach number was 2.69 and the jet was underexpanded. The mixture composition was specified by Frauenberger and Forbister, and the chamber conditions were $P_0 = 70$ atm. and $T_0 = 4500^\circ\text{R}$. Measurements included the distribution of total pressure and stagnation temperature in the subsonic region.

Maydew and Reed [79] investigated the mixing layer formed in the first regime of a supersonic jet into still air. This experiment is thus analogous to the incompressible-flow work of A. J. Chapman [16] discussed in Chapter 2; it was designed to investigate the variation of the parameter σ , which occurs in the similarity analysis of two-dimensional mixing layers, with Mach number. To do this, experimental velocity profiles in the first regime were measured at Mach numbers of 0.7, 0.85, 0.95, 1.49, and 1.96, and the best fit of the function $U/U_j = f(\sigma y/x)$ to these profiles was obtained by varying the value of σ . From this method, Maydew and Reed found that at $M = 0.7, 0.85, 0.95, 1.49, \text{ and } 1.96$, $\sigma = 10.5, 10.8, 11.0, 15.0, \text{ and } 20$, respectively.

An alternate approach, involving the relationship of the growth of the mixing layer to the amount of fluid entrained by the mixing layer, was used by Hill and Nicholson [80] to investigate the variation of σ with Mach number. Using a number of different gases at several Mach numbers ranging from 1.48 to 0.63, they find

$$\sigma = 9.1 \left(\frac{T_{O_C}}{T_C} \right)^{0.29} \quad (4.25)$$

where T_{O_C} is the stagnation temperature at the high velocity edge of the mixing layer, and T_C the static temperature.

The parameter σ in Equation (4.25) is related to the incompressible-flow velocity profile, as is σ in the work of Maydew and Reed. Figure 4.21 shows a comparison of this function with Maydew and Reed's experimental results (4.16). The calculations are based on the isentropic relation

$$\frac{T_{O_C}}{T} = 1 + \frac{\gamma-1}{2} M^2 \quad (4.26)$$

for $\gamma = 1.4$. Figure 4.21 clearly shows that the results of Hill and Nicholson [80] fall well below those of Maydew and Reed [80].

W. G. Hill [81] investigated the development of the free shear layer formed by the flow over a cavity at Mach numbers from 2.1 to 3.7 (see Table 4.3, page 238). The

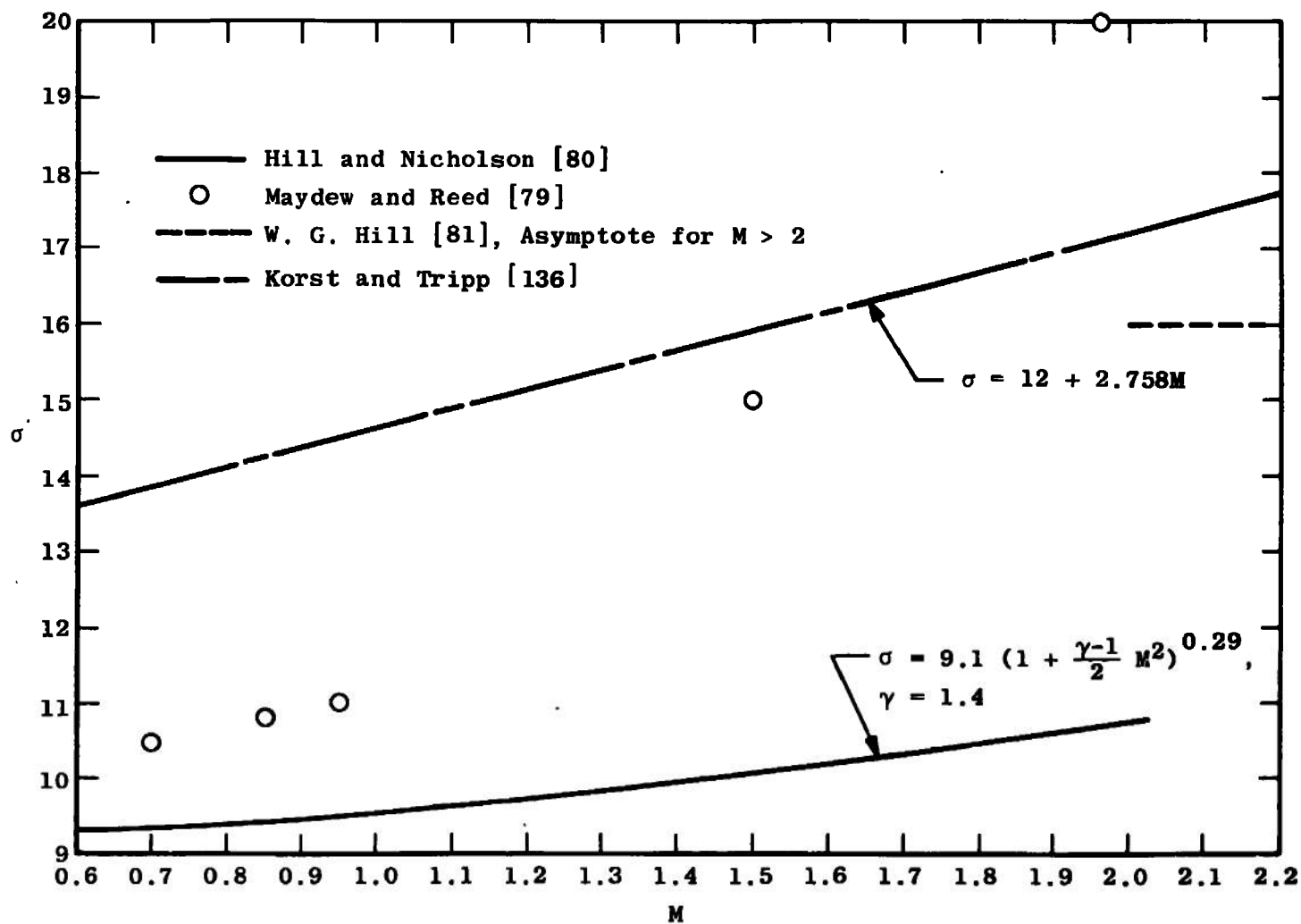


Figure 4.21. Comparison of determinations of variation of σ with Mach number.

boundary layer at the cavity edge had a momentum thickness of 0.30 in. and a velocity profile of the form

$$\frac{U}{U_o} = \left(\frac{y}{\delta_b}\right)^{1/8}$$

where δ_b is the physical boundary layer thickness, which was found to be independent of Mach number. Hill's results indicate that $\sigma = 16$ for $M > 2$. However, as at $M = 3.5$, $x/\delta_b = 5.7$, the mixing zone width was 2.4 in. in a 4 x 4 in. wind tunnel, these results may suffer somewhat from three-dimensional effects.⁴

The final entry in Table 4.3, page 238, concerns the jet-mixing experiments reported by Rom [82]. This work involved jets from a high temperature arc source, in both circular and three-dimensional (square and low aspect ratio rectangular) cross-section. Under the assumption that the nondimensional density and velocity profiles can both be expressed in similarity form, i.e., as functions of $\eta = y/x$, Rom finds that assuming that $U_c \propto x^{-(K+1)/2}$, the centerline Mach number $M_c \propto x^{-(K+1)/4}$ in the near jet and $M_c \propto x^{-(K+1)/2}$ in the far jet. $K = 1$ for axisymmetric flow and 0 for two-dimensional flow. These assumptions are somewhat questionable, and Rom's results [82], given in terms of the Mach number, are not in good agreement with his analysis.

⁴An empirical relationship, $\sigma = 12 + 2.758M$ has been given by Korst and Tripp [138].

Summary

Practically all of the circular jet experiments investigated have shown that geometric similarity of the velocity profiles, defined by a relation of the form

$$\frac{U}{U_c} = f\left(\frac{r}{r_{1/2}}\right)$$

is achieved in the variable-density jet into still air within five diameters of the end of the potential core [67, 70, 71, 73, 79]. For the supersonic jet, Figure 4.5, page 219, shows that the velocity data are very well fit by the function

$$f\left(\frac{r}{r_{1/2}}\right) = \exp\left[-0.6932\left(\frac{r}{r_{1/2}}\right)^2\right]$$

which also provides a fairly good representation of the very high enthalpy data of Reference [79], Figure 4.14, page 230. Temperature profiles also exhibit geometric similarity within about five diameters of the end of the potential core, provided that the half radius $r_{1/2T}$ is used where $r_{1/2T}$ is defined as the radius at which $T - T_o/T_c - T_o = 0.5$, rather than $r_{1/2}$, which is defined as the radius at which $U/U_c = 0.5$. Figures 4.11, page 226, and 4.12, page 227, illustrate this. For concentration profiles, Keagy and Weller show that the profile of C/C_c is a function only of $\eta = y/x$ for $x/D = 16$. This is a more stringent requirement

than the usual definition of (local) geometric similarity, as this requirement demands that $r_{1/2} \propto x$. Geometric similarity of composition and total enthalpy profiles is observed for the high-enthalpy jet [77] as well as for rocket exhausts [66, 78].

Similar profiles are also found in the first regime of supersonic jets. In this region the profiles can be fit with a function of the form [79, 80]

$$\frac{U}{U_j} = g\left(\frac{\sigma y}{x}\right)$$

where the parameter σ varies with the Mach number. The variation of this parameter with Mach number has been fairly extensively investigated [79, 80, 81] but the form of its variation is still not well known.

For subsonic and low supersonic Mach numbers, the centerline velocity ratio U_c/U_j appears to vary as $1/x$. This is observed in Reference [70] as shown in Figure 4.2, page 207. For Mach numbers greater than about 2.0 this variation no longer seems to hold [72]--see Figure 4.4, page 209, while the decay of centerline velocity seems to be faster than the $1/x$ function predicts for subsonic high-enthalpy jets as well [77]; see Figure 4.15, page 231.

Self-preservation can be defined as the state in which the profiles of the dependent variables are functions only of a variable $\eta = r/b(x)$, when nondimensionalized by

their centerline values. Thus

$$U = U_c(x)f(\eta)$$

$$T - T_o = [T_c(x) - T_o]g(\eta)$$

$$C = C_c(x)h(\eta)$$

etc. For the incompressible jet-into-still-air, it was shown further that under self-preservation $U_c \propto 1/x$ and $b \propto x$ (Reference [3], also Appendix C). Self-preservation has not been observed in the supersonic jet-into-still-air, and the indications are that it may not be reached within practical distances [69]. For subsonic jets with jet-to-surroundings temperature or concentration differences, insufficient information is as yet available to evaluate the approach to self-preservation.

The effect of decreasing the jet-to-surroundings density ratio whether by temperature differences or differences in gas composition seems always to be to reduce the length of the potential core. This effect can be observed in Figures 4.9, 4.16, 4.18, and 4.20, pages 223, 233, 235, and 238. In the case of extreme temperature differences, the slope of the decay curve is also increased, as Figure 4.15, page 231, shows. The potential core length is defined here as the axial distance to the intersection of the line representing the axial decay of centerline velocity with the $U_c/U_j = 1.0$ line on a log-log plot.

Since the turbulent Prandtl number is not generally 1.0 for the supersonic jet [65] and for subsonic compressible jets [70], being 0.7 in the former case, the potential core length for temperature will not in general be the same as that for velocity. No measurements of the turbulent Schmidt number are available for the jet-into-still-air, but evidence in coaxial mixing which will be discussed below, and some evidence with effectively constant-density flows with trace gases indicates that it, too, is not unity, so that the concentration core length will also in general be different from the velocity core length.

The length of the velocity potential core increases with Mach number, as shown on Figure 4.2, page 207, using the data of Reference [70]. Comparison of these data with other data indicates, as shown by Figure 4.3, page 208, that the variation in core length is linear with Mach number, with one relationship holding for $M < 1.0$ and a second for $M > 1.0$.

There is very little data on turbulent fluctuations in a variable density flow. The only experiment in which u' , v' , and \overline{uv} have been measured in such a flow is the heated jet of Corrsin and Uberoi [25]. Investigation of these data--Figures 4.8 through 4.10, pages 222, 223, and 225--does not show any substantial differences in behavior between these results and those of a similar constant density experiment.

There are a number of valuable experiments which are concerned with the variable density jet-into-still-air, but because of experimental difficulties the coverage of the phenomenon is not nearly as complete as it is for the constant-density jet-into-still-air. Warren [70] has investigated the broadest range of Mach numbers and temperature ratios (Tables 4.1 and 4.2, pages 203 and 214). His experimental results satisfy the momentum integral requirement quite well. Warren's results include jet-exit velocity and temperature profiles, but no shear stress profiles are given. The axial range is limited to a maximum of thirty diameters.

The work of Broer and Rietdijk [65] does not satisfy the momentum integral requirement. However, their presented profiles (of $M\sqrt{T}/(M\sqrt{T})_c$) are sketchy at best, and so the evaluation of the momentum integral is possibly overly pessimistic. As in all other supersonic jet experiments, Broer and Rietdijk do not present profiles of velocity ratio (here $M\sqrt{T}$ ratio) below a value of ~ 0.1 for large x/D , presumably due to experimental difficulties. To evaluate the momentum integral for these flows, the profiles presented have been extrapolated to $U/U_c \approx 0$, which is assumed to occur at $r/r_{1/2} \approx 2.5$.

Both Johannesen [69] and Eggers [72] present axial and radial velocity profiles to large x/D , and both sets of results agree favorably with the momentum integral criterion.

In these cases, there exists an axial distance beyond which velocity profiles are only incompletely presented; that is, velocity ratios U/U_c below 0.1 are not measured. The momentum check has been carried as far as this axial distance. Both Johannesen and Eggers investigate one particular facet of the flow in particular detail. Johannesen [69] presents his measured velocity and static pressure profiles in detail from $x/D = 0$ to $x/D = 10.67$. Eggers [72] presents eddy viscosity distributions, where the eddy viscosity is defined by

$$\epsilon = \frac{\tau/\rho}{\partial u/\partial r}$$

at six axial locations downstream of the end of the potential core. Because these data are at high Mach number, include tabulated velocity profiles, and include these eddy viscosity distributions, from which the shear stress profiles may be evaluated, Eggers' data [72] have been selected for use in the confrontation between theory and experiment.

The only data on turbulent fluctuations for a heated jet into still air is that of Corrsin and Uberoi [25]. This is clearly an area requiring considerable additional study. Because no mean velocity profiles are presented by Corrsin and Uberoi [25] for their heated jet, no evaluation of the momentum integral can be made.

However, on the assumption of geometric similarity the momentum integral can be evaluated for the cold-jet, incompressible flow; this has been done in Chapter 2 and the results, presented in Table 2.3, page 65, indicate that the cold jet satisfies the momentum criterion within 10 percent.

For flows in which the jet gas is different from the surroundings, data are presented by Keagy and Weller [76] and by Donaldson and Gray [67]. The latter work includes only axial velocity profiles for subsonic jets, so that no momentum check can be made, and the utility of the data is seriously limited. Keagy and Weller [76] present considerably more detail, but their radial profiles (of velocity and concentration) are available for only two stations. All of Keagy and Weller's data are limited to the second regime of mixing. As Table 4.2, page 214, shows, both the N_2 and CO_2 results of Keagy and Weller are in good agreement with the momentum criterion; however, their He results seem to be too far out of agreement to be of any practical use.

Finally, O'Connor, Comfort, and Cass [77] have provided a very detailed investigation of a high enthalpy jet. Their results include profiles in physical coordinates as well as in similarity coordinates, which is commendable. However, no initial conditions are included, which hampers confrontation of theory and experiment, and the behavior of

the centerline concentration profiles does not agree with other experiments at lower temperatures.

CHAPTER 5

VARIABLE-DENSITY TWO-STREAM FLOWS:

EXPERIMENTAL DATA

The most complex flows to be considered in this study are the variable-density two-stream flows: two-dimensional and axisymmetric coaxial jets, and two-dimensional and axisymmetric wakes. The density variations are caused, as in the single-stream flow cases, by temperature or composition variations between the streams, or by compressibility effects, or by combinations of these phenomena.

Because of the complexity of the flow systems involved (and the severity of the environments in which such flows are produced), the experimental data for flows in this section is not very detailed. There is only one experiment [35] in which turbulence intensities have been measured in a two-gas coaxial stream flow, and even in this experiment the only measurement is of the axial component of the turbulent intensity, u' . Clearly the subject of turbulent structure in a variable-density flow remains to be explored, but this must await the development of more sophisticated instrumentation.

The author has not encountered any experimental work in the literature on variable density two-dimensional

two-stream flows--the coaxial configuration is both easier to achieve experimentally and more practical. The same situation appears to exist for the variable-density wake. Thus the first section of this Chapter will cover variable-density coaxial free mixing, and the second the axisymmetric variable-density wake.

Coaxial Jets

As Table 5.1 shows, a number of variable-density coaxial jet mixing experiments have been reported in recent years. There is only one [43] appearing in Table 5.1 which was reported prior to 1962. The experiments listed in Table 5.1 may conveniently be broken down into three groups, which are: (a) the mixing of two streams of air, possibly with a temperature tracer or trace gas, (b) the mixing of two streams of different gases, with both streams subsonic, and (c) the mixing of two streams of different gases, with one stream supersonic and the other stream subsonic. Category (a) includes mixing in which both streams are subsonic, but with a substantial amount of trace gas in one stream (sufficient to produce a relatively large density ratio) [43], mixing in which both streams are subsonic but at a relatively high Mach number so that compressibility effects may enter [91], and mixing in which one air stream is supersonic and the other subsonic [87, 91].

Past the end of the potential core, the center-line velocity decay curves for compressible coaxial air-air

TABLE 5.1
VARIABLE-DENSITY COAXIAL MIXING

Investigator	Ref.	Year	Configuration	ρ_o/ρ_j	U_o/U_j	$\frac{\rho_o U_o}{\rho_j U_j}$	Profiles	Axial Decay	Momentum Check
Landis and Shapiro	43	1950	1 ^a , air	1.3	0.25	0.325	similar	yes	no
				1.3	0.50	0.650			
				1.19	0.50	0.595			
				1.19	0.50	0.595			
				1.19	0.50	0.595			
Ferri, Libby, and Zakkay	83	1962	2, H ₂	n.a. ^b	2.78	n.a.	at x/D=16.2	C ^c only	no
					1.43				
					1.0				
					0.75				
Alpinieri	84	1964	2, H ₂	16.7	1.51	25.2	C at x/D=10.5,	C only	no
				16.8	1.05	17.65	15, 20		
				16.9	0.80	13.50	C, U at	C, U	<1%
			2, CO ₂	0.72	2.13	1.52	x/D=15,		<1%
				0.68	1.54	1.05	20, 25		<2%
				0.67	1.28	0.85			
Zakkay and Krause	85	1964	2, H ₂	8.15	0.88	7.15	no	C	no
				8.12	1.32	10.65			
				8.10	2.38	19.25			
				9.10	5.0	45.5			
				19.10	2.38	45.5			
				3.85	5.0	19.25			

TABLE 5.1 (continued)

Investigator	Ref.	Year	Configuration	ρ_o/ρ_j	U_o/U_j	$\frac{\rho_o U_o}{\rho_j U_j}$	Profiles	Axial Decay	Momentum Check
Zakkay, Krause, and Woo	86	1964	2, H ₂	7.2	1.3	9.35	no C ^e	no U,C vs x/x _C ^f	no
				31.05	0.69	21.30			
				23.5	0.59	13.90			
				19.45	0.41	8.05			
			2, He	2.96	2.20	6.5	no	no	
				3.82	0.91	3.47			
				10.7	0.91	9.72			
				9.05	0.60	5.41			
			2, A	0.36	5.54	2.01	U, C ^e	U,C vs x/x _C ^f	
				0.29	3.23	0.94			
			3, A	0.23	2.31	0.54			
				0.17	1.94	0.34			
			2, A	0.90	1.89	1.70			
				0.71	1.78	1.27			
				0.63	1.62	1.03			
Bluston	87	1965	2, air	0.44	2.28	1.01	yes	yes	no
Forde	88	1965	3, CO ₂	0.76	1.32	1.0	yes	no	no
Ragsdale and Edwards	89	1965	1, Br ₂	0.18 ^g	1.25	0.23	no	yes	no
					0.97	0.18			
					0.83	0.15			

TABLE 5.1 (continued)

Investigator	Ref.	Year	Configuration	ρ_o/ρ_j	U_o/U_j	$\frac{\rho_o U_o}{\rho_j U_j}$	Profiles	Axial Decay	Momentum Check
Chriss	90	1968	1, H ₂	11.1	0.16	1.79	U,	U,	13 ^h
				11.1	0.23	2.57	C,	C,	7.3
				12.5	0.26	3.12	H,	also	5
				12.5	0.33	4.16	τ	τ	10
				12.5	0.42	5.25			-
				7.1	0.22	1.61			9
				7.7	0.31	2.44			17 ⁱ
				8.3	0.40	3.33			10
Zawacki and Weinstein	35	1968	1, Freon	0.25	20.3	5.1	U,	yes ^j	40
					11.6	2.9	ρ		13
					9.2	2.3			23
					5.6	1.4			15
					5.4	1.35			-
					7.6	1.9			-
				0.14	3.6	0.9			-
					11.5	1.64	U,		-
					5.8	0.83	ρ		-
				0.25	8.9	1.27			12
					36.8	9.2			-
					26.5	6.63			-
					9.3	2.33			-
					5.4	1.35			-
Eggers and Torrence	91	1969	2, air	1.13 ^k	1.36	1.54 ^k	U, C	U, C	no ^l
				1.17	1.54	1.80			
			1, air	1.02	1.21	1.24			

TABLE 5.1 (continued)

Investigator	Ref.	Year	Configuration	ρ_o/ρ_j	U_o/U_j	$\frac{\rho_o U_o}{\rho_j U_j}$	Profiles	Axial Decay	Momentum Check
Fejer, et al.	92	1969	1, Freon-air	1.0	0.26	0.26	no	U, C	no
				0.67	0.26	0.13	U, C		
				1.0	0.18	0.18	no		
				1.0	0.18	0.18			
				1.0	0.13	0.13			
				0.51	0.25	0.13			
				0.69	1.0	0.69			
				1.0	1.0	1.0			

^aCodes: 1 - subsonic primary, subsonic secondary; 2 - subsonic/supersonic; 3 - supersonic/supersonic. Gas is listed for primary jet, secondary is in all cases air.

^bIndicates data unavailable.

^cC - concentration; U - velocity; ρ - density; H - enthalpy; τ - turbulent shear stress.

^dMaximum percent deviation from average value (range for Alpinieri data: $7.5 < x/D < 12.5$).

^ePresented nondimensionalized in terms of unstated parameters.

^f x_c is core length, obtainable from other results.

TABLE 5.1 (continued)

^gEstimated.

^hRange for all of Chriss' data: $4.5 \leq x/D \leq 16$.

ⁱData shift apparent for these results.

^jObtainable from profiles presented.

^kDerived value.

^lLack of density profiles makes calculation impossible.

mixing all appear to follow a $(U_c - U_o)/(U_j - U_o) \propto (x/D)^{-1}$ line fairly well, as shown by Figure 5.1, despite the wide variation in Mach numbers involved. However, the behavior of the results of Eggers and Torrence [91] in the region upstream of the beginning of this " x^{-1} " decay is somewhat unusual. The configuration used by Eggers and Torrence involves a coaxial two-stream mixing system in which the outer stream is at a greater velocity than the inner. Thus the decay curves shown on Figure 5.1 indicate that the centerline velocity for the central jet decreases for some distance downstream after it leaves the nozzle, despite the greater free-stream velocity, and then after some distance begins to reaccelerate towards the free stream velocity. This behavior has been observed in very low-speed flows by Zawacki and Weinstein [35], and was investigated in detail by Rozenmann [47] in a low speed flow. In this case it was found that the apparent decrease in centerline velocity was brought about by the existence of a recirculation pattern in the jet. However, this effect was not observed to occur below a velocity ratio U_o/U_j of 13; Eggers and Torrence do not report velocity ratios greater than 1.56.

In this case the effect apparent in Figure 5.1 appears to be related to the persistence of the initial boundary layer profiles. The deceleration of the jet centerline velocity caused by the existence of the initial thick boundary layers appears to be initially a more

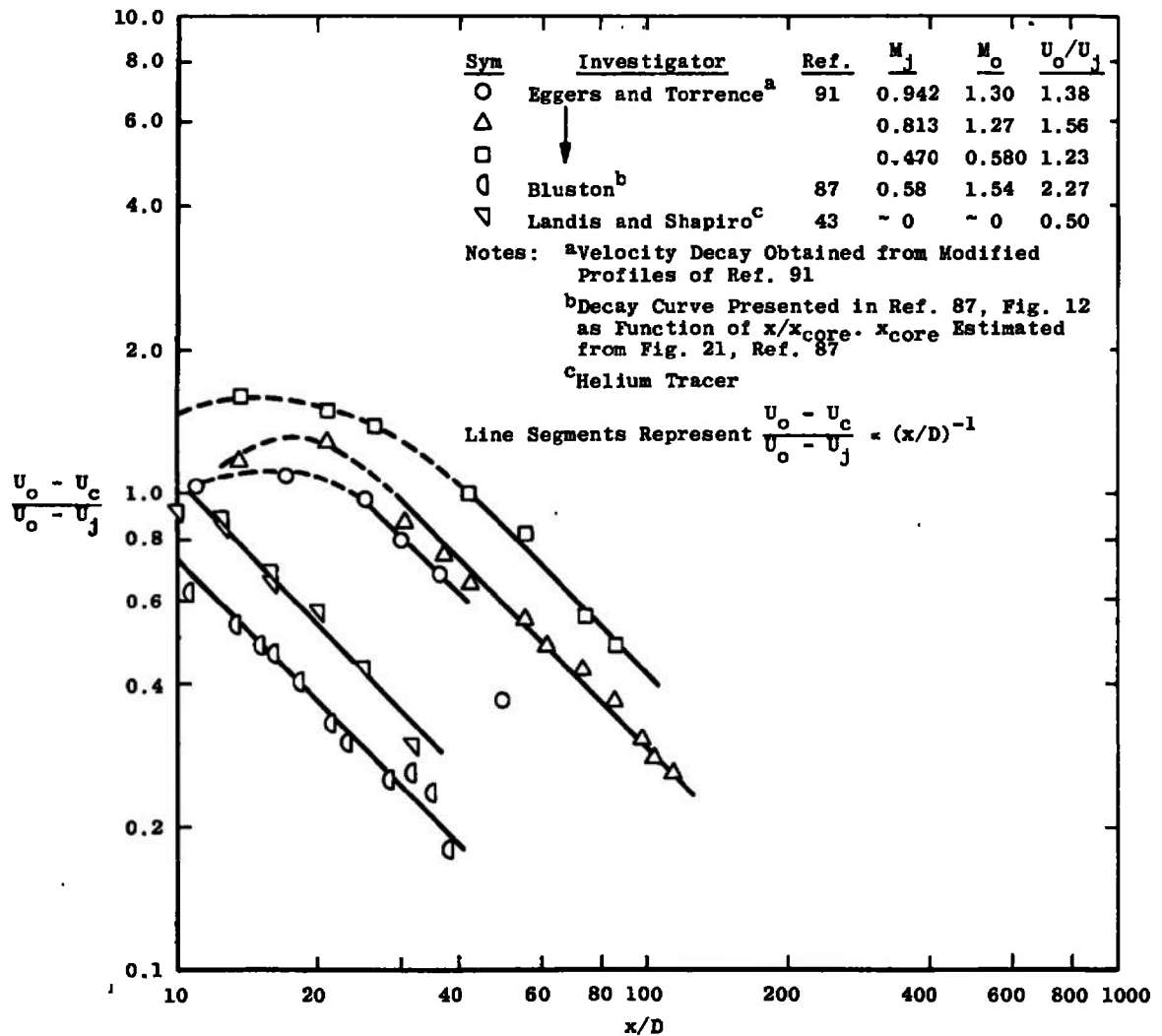


Figure 5.1. Axial decay of centerline velocity, compressible coaxial (air-air) jets.

important phenomenon than the acceleration of the boundary layers by the higher-velocity outer flow. Bluston's work [87], which is the only directly comparable work, does not include centerline velocity measurements in the potential core region. His results for centerline velocity decay are in fact given in terms of the parameter x/x_{core} ; an "estimated" potential core length which Bluston reports ([87], Figure 21) has been used in constructing Figure 5.1.

As Figure 5.2 shows, despite the anomalous behavior of the centerline velocity in the potential core region, the velocity data reported in Reference [91] fits a local similarity plot fairly well. Although detailed velocity (and trace-gas composition) profiles are given in Reference [91], no density profiles or temperature profiles are available and so the momentum integral has not been evaluated. Eggers and Torrence report a mass-flow check on their data; the results are not conclusive. Further work on coaxial air-air systems with supersonic outer streams would appear to be necessary.

Coaxial mixing of two subsonic streams, with temperature or concentration differences between the streams has been investigated by Landis and Shapiro [43] who studied the mixing of coaxial low-velocity streams with a temperature difference between the streams, Zawacki and Weinstein [35] and Fejer, et al., [92] who studied coaxial mixing of low velocity Freon-air streams, and by Alpinieri [84] and

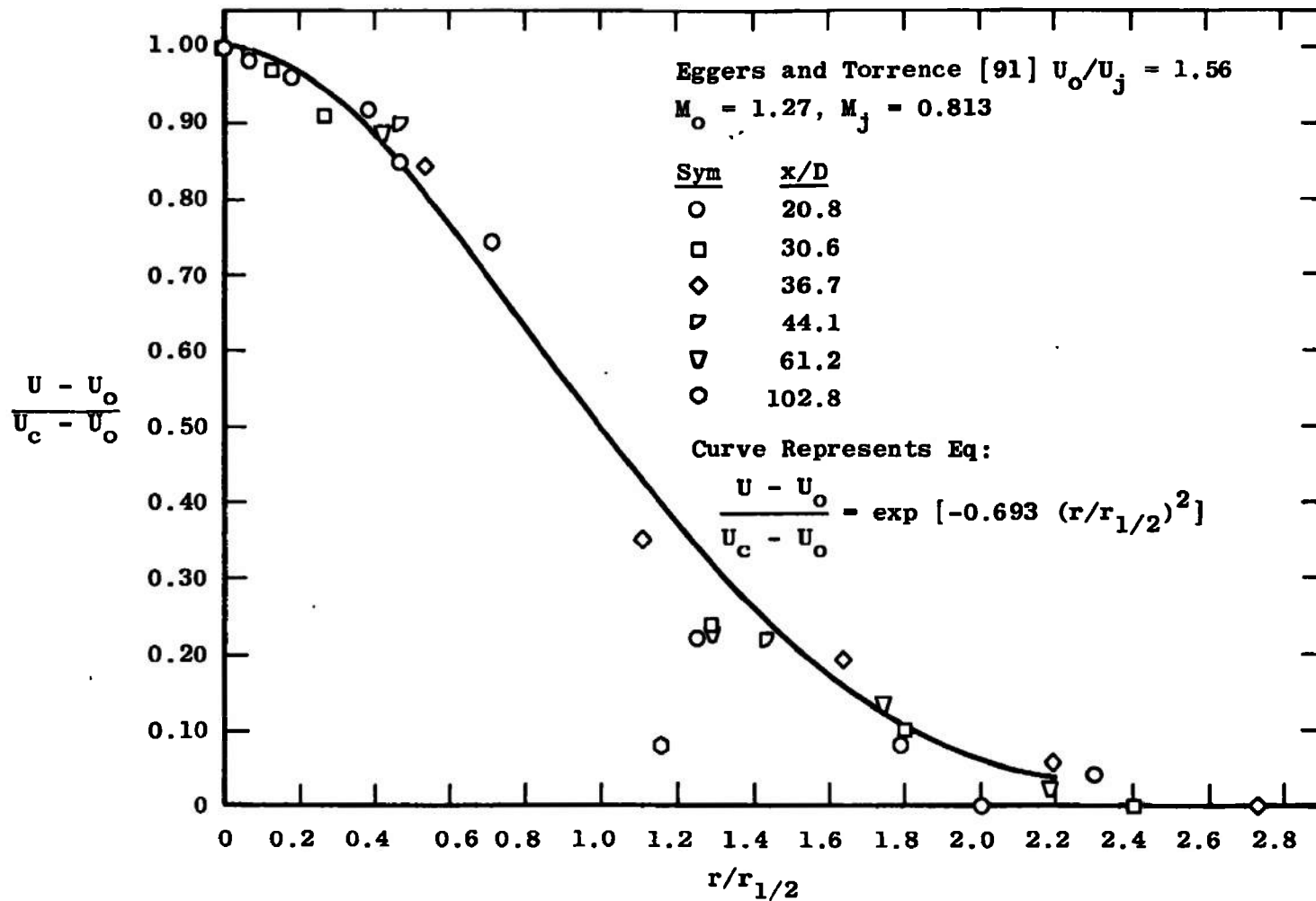


Figure 5.2. Similarity plot for velocity ratio, compressible coaxial jets.

Chriss [90] who studied relatively high velocity coaxial mixing between hydrogen and air. Alpinieri [84] also studied carbon-dioxide-air mixing, and bromine-air mixing was studied by Ragsdale and Edwards [88].

Axial decays of centerline velocity ratio and centerline temperature ratio for the data of Landis and Shapiro [43] are shown in Figure 5.3; axial decays of centerline velocity, temperature, and composition ratio are shown in Figure 5.4. The apparatus used by Landis and Shapiro [43] has already been described in Chapter 3; briefly, it comprises a 1/2-inch diameter nozzle and a 4-inch duct. The jet velocity in all cases reported here was 200 ft/sec. It can be seen from Figures 5.3 and 5.4 that the axial decays of velocity, temperature, and concentration are all fit reasonably well by lines of $\phi \propto (x/D)^{-1}$, where ϕ represents the particular ratio in question. Readers familiar with the work of Landis and Shapiro may recall that these authors report various different slopes for the different curves--thus in Reference [43] they give, if n is defined as the exponent in the expression $\phi \propto (x/D)^{-n}$, $n = 1.04$ for both velocity and temperature for the $U_o/U_j = 0.25$ case, $n = 1.03$ for velocity and $n = 1.08$ for temperature for the $U_o/U_j = 0.50$ case (Figure 5.3), and $n = 1.22$ for velocity, temperature, and composition for the $U_o/U_j = 0.50$, $\rho_o U_o / \rho_j U_j = 0.515$ (Figure 5.4) case. In each case these exponents have been obtained

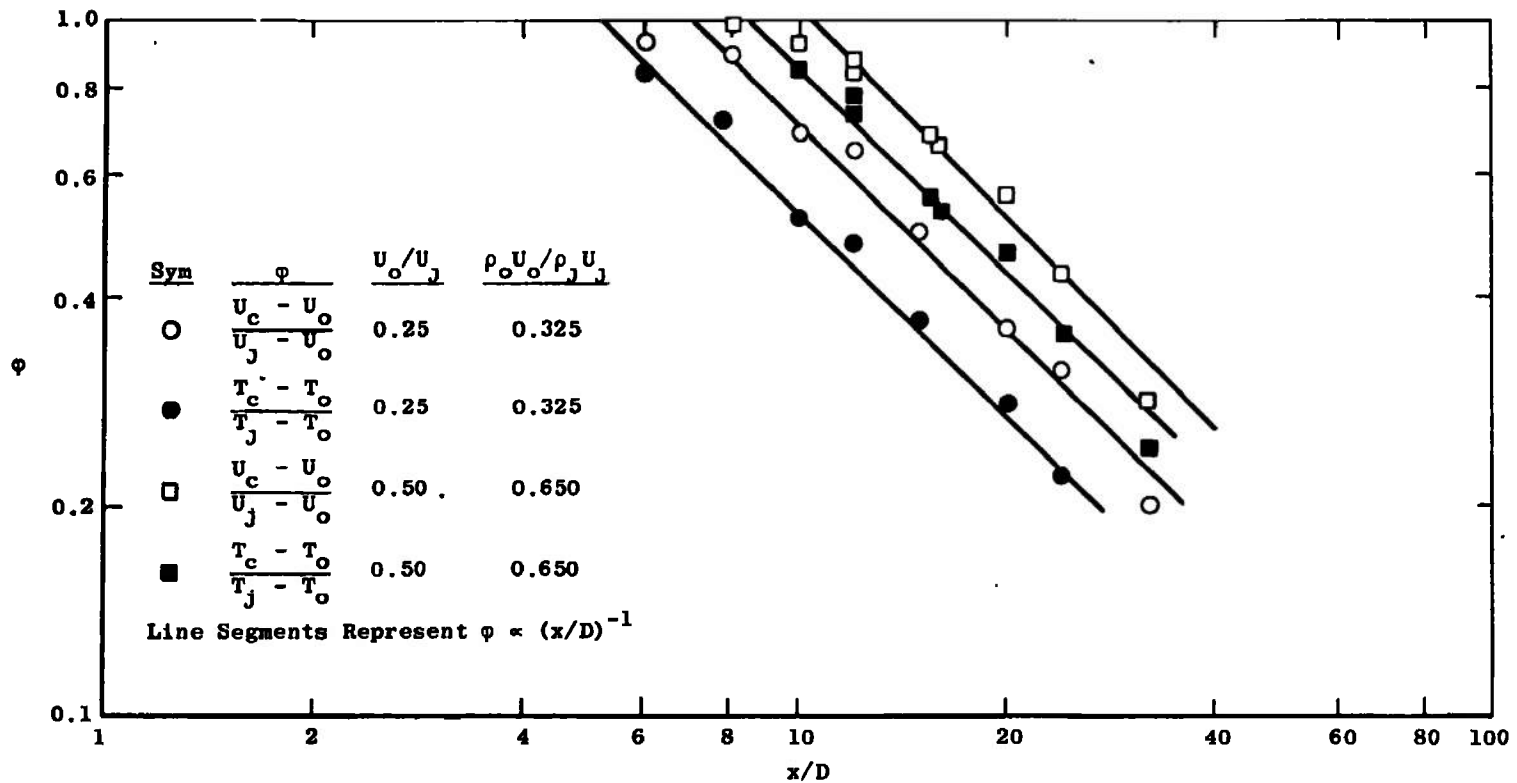


Figure 5.3. Axial decay of centerline velocity and temperature ratio, subsonic/subsonic coaxial jets. Data from Landis and Shapiro [43].

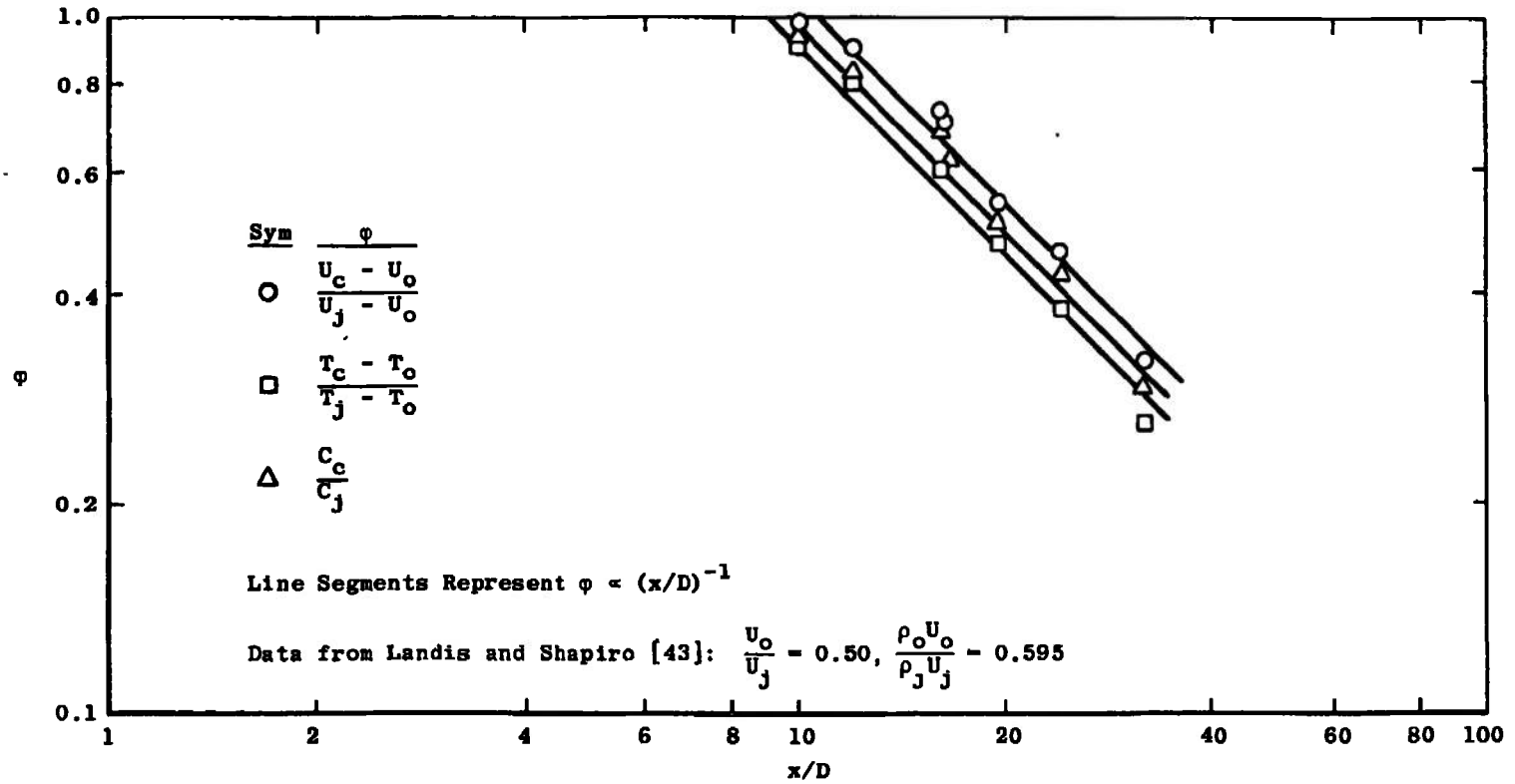


Figure 5.4. Axial decay of centerline velocity, temperature and composition, coaxial subsonic/subsonic mixing.

by Landis and Shapiro by taking the best-fit curve to all of their data. It is the author's experience that this is in general not a good practice for the velocity decay curves, as evaluation of the momentum integral for a number of configurations has shown that the apparent error for the velocity measurement in general increases with axial distance. This is particularly true with the kind of apparatus used by both Forstall [40, 41] and Landis and Shapiro [43], as was discussed in Chapter 3. It will be seen from Figures 5.3 and 5.4 that curves of $\phi \propto (x/D)^{-1}$ adequately describe the data, particularly if the last points (at $x/D = 32$) are discounted. The author does not believe that attempts at fitting the data any more closely are justified.

Landis and Shapiro [43] demonstrate that as for coaxial air-air mixing, the velocity profiles can be shown to be geometrically similar, when $(U - U_o)/(U_c - U_o)$ is plotted versus $r/r_{1/2}$, where $r_{1/2}$ is the value of r for which $U = U_o + (U_c - U_o)/2$. Further, the temperature profiles are also geometrically similar, when $(T - T_o)/(T_c - T_o)$ is plotted versus $r/r_{1/2T}$, where $r_{1/2T}$ is the value of r for which $T = T_o + (T_c - T_o)/2$. This is shown in Figure 4 of Reference [43]. Because the velocity profiles are presented only as data bands on normalized plots, no momentum check can be made on these data. However, sufficient information was given in Reference [43] for

a momentum check to be made on a coaxial air-air mixing case; this check showed that the momentum integral was satisfied within 10 percent, and the cases considered here are probably similar.

Freon-air mixing, in a coaxial subsonic-stream configuration has been studied by Zawacki and Weinstein [35] and Fejer, et al., [92]. The apparatus used by the former investigators was described in Chapter 3; it consists of a 0.712 inch diameter jet in an 8 x 8 inch square surrounding stream. Fejer, et al., [92] used a one inch inside diameter jet in a six inch diameter duct. Both experiments thus could involve pressure gradients, although it does not appear that they were carried out to a large enough number of diameters for these to be important. No measurements of static pressure distribution are reported.

Figures 5.5 and 5.6 show the axial decay of centerline velocity measured in selected experiments from Reference [35] and in the experiments of Reference [93], respectively. The major point of difference between the two sets of experiments lies in the mass-flow-per-unit-area ratio, $\rho_o U_o / \rho_j U_j$. The experiments of Reference [35] had a sufficiently large ratio of free-stream to jet velocity U_o / U_j so that even though the jet was denser than the secondary stream, the mass flow per unit area ratio (which will be called simply the "mass flux ratio" in the following) remained greater than 1.0. On the other hand, the work of

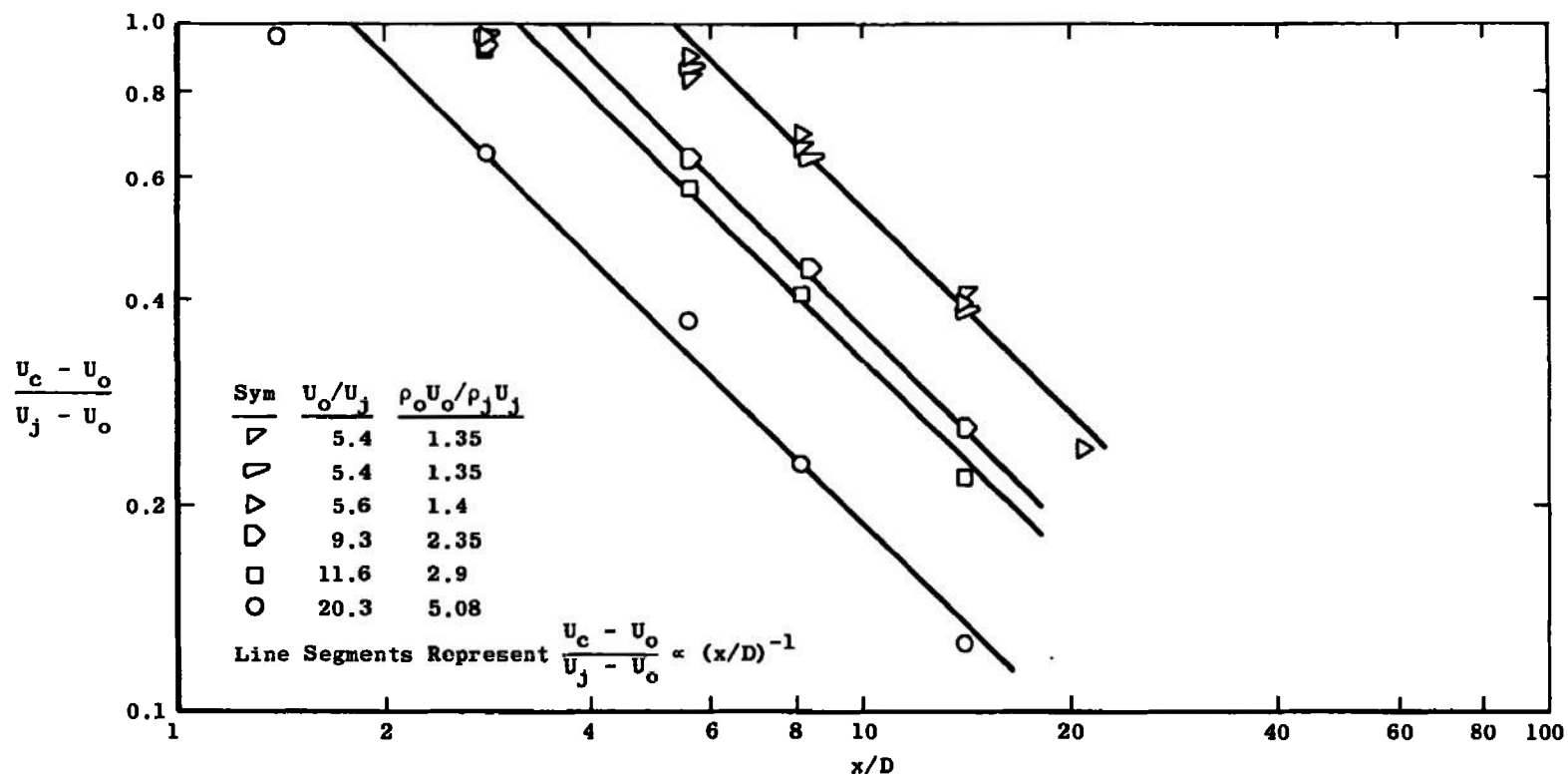


Figure 5.5. Axial decay of centerline velocity, Freon-air mixing, Reference [35]. $\rho_o U_o / \rho_j U_j > 1.0$, $U_o/U_j > 1.0$.

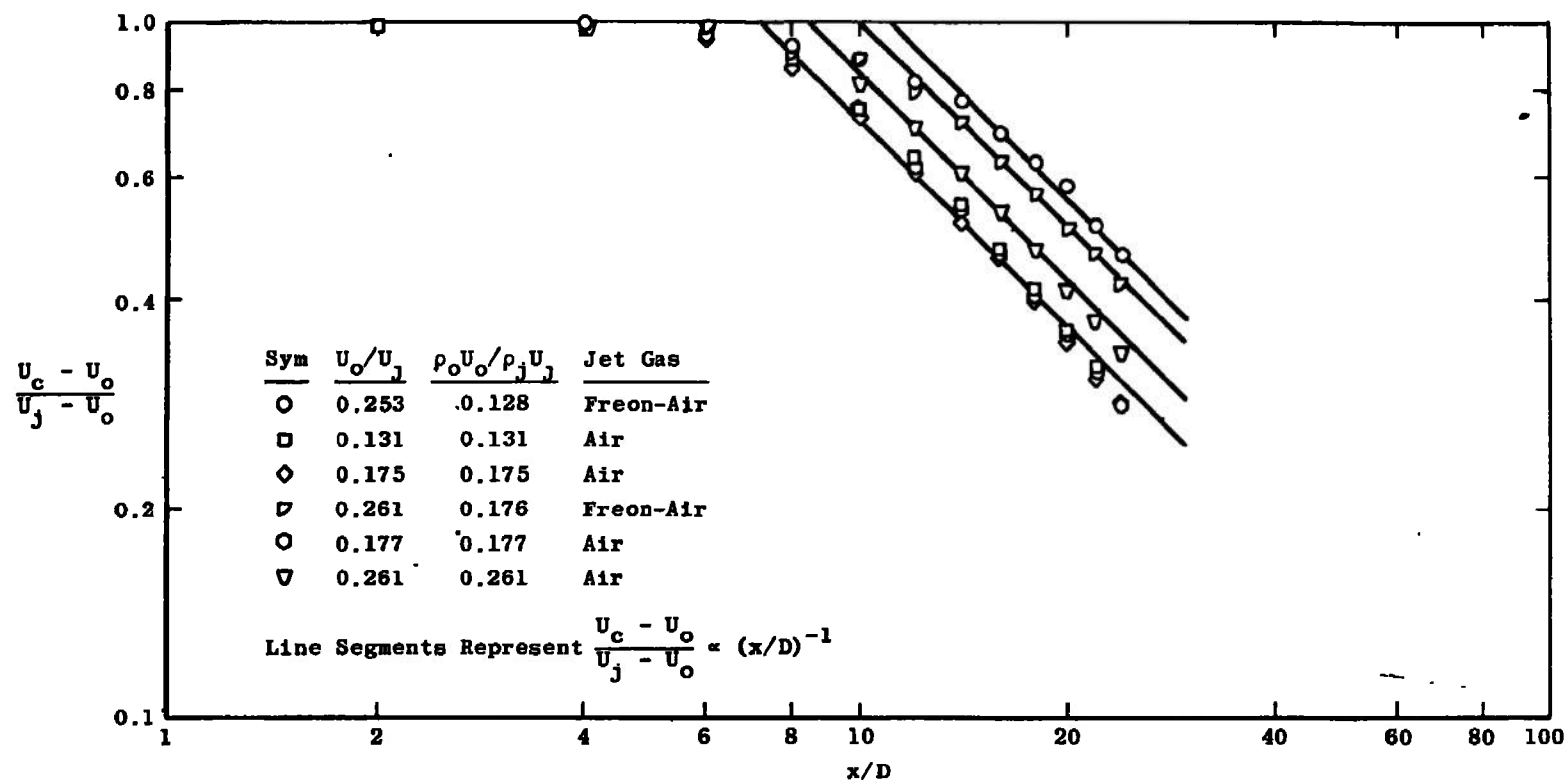


Figure 5.6. Axial decay of centerline velocity ratio, air-air and Freon-air coaxial mixing. Data from Reference [92].

Fejer, et al., with jet velocities greater than that of the surrounding stream, produces mass flux ratios always less than one.

As Figures 5.5 and 5.6 show, the axial decay of centerline velocity is in every case well represented by a line of the form $(U_c - U_o)/(U_j - U_o) \propto (x/D)^{-1}$. Figure 5.5 also shows that the length of the velocity potential core decreases as the mass flux ratio $\rho_o U_o / \rho_j U_j$ (or alternately, because the density ratio is constant, the velocity ratio U_o/U_j) increases from 1.0. The actual length of the velocity potential core for these data may, however, be somewhat doubtful; see the discussion of recirculation in this flow in Chapter 3.

Figure 5.6 also illustrates a decreasing velocity potential core length with increasing mass flux ratio, for the Freon-air data, but the air-air data show an increasing velocity potential core length as the mass flux ratio increases towards 1.0. Further, the Freon-air data at a mass flux ratio of 0.128 shows a considerably longer potential core than the air-air data at $\rho_o U_o / \rho_j U_j = 0.131$. As the behavior of the air-air data--increasing potential core length with increasing U_o/U_j --is consistent with that observed in Chapter 3, and the behavior of the Freon-air data is consistent both with that of the data of Zawacki and Weinstein [35], Figure 5.5, and Landis and Shapiro [43],

Figure 5.3, page 265, it would appear that the addition of Freon to an air jet decreased the mixing.

Figure 5.7 illustrates the axial decay of centerline concentration for the data of Fejer, et al., [92]. Again a line of the form $(C_c/C_j) \propto (x/D)^{-1}$ is a good approximation to most of the data, except for $\rho_o U_o / \rho_j U_j = 1.0$. The effect of changing mass flux ratio is not nearly so apparent on the concentration profiles as it is on the velocity profiles.

Hydrogen-air mixing, with two subsonic coaxial streams, has been investigated by Chriss [90] and by Alpinieri [84]. The investigation performed by Chriss was quite extensive, covering eight mass flux ratios in the range 1.61 to 5.25 with a 0.5-inch diameter primary jet and a 3.5-inch diameter secondary jet. The outer stream in this flow was not ducted. Because of the very low density of hydrogen, it is quite difficult to obtain a mass flux ratio $\rho_o U_o / \rho_j U_j$ of less than one in a coaxial hydrogen air system even with $U_j > U_o$. Figure 5.8 shows the axial decay of centerline velocity ratio for these data. Except for the $U_o/U_j = 0.4$, $\rho_o U_o / \rho_j U_j = 3.33$ case, all of these data can be fit reasonably well by lines of the form $(U_c - U_o)/(U_j - U_o) \propto (x/D)^{-2}$, although if the last points of a given set are discounted, the exponent may be somewhat less than two. Further, it can be seen that, except for one case, the length of the velocity potential core decreases as

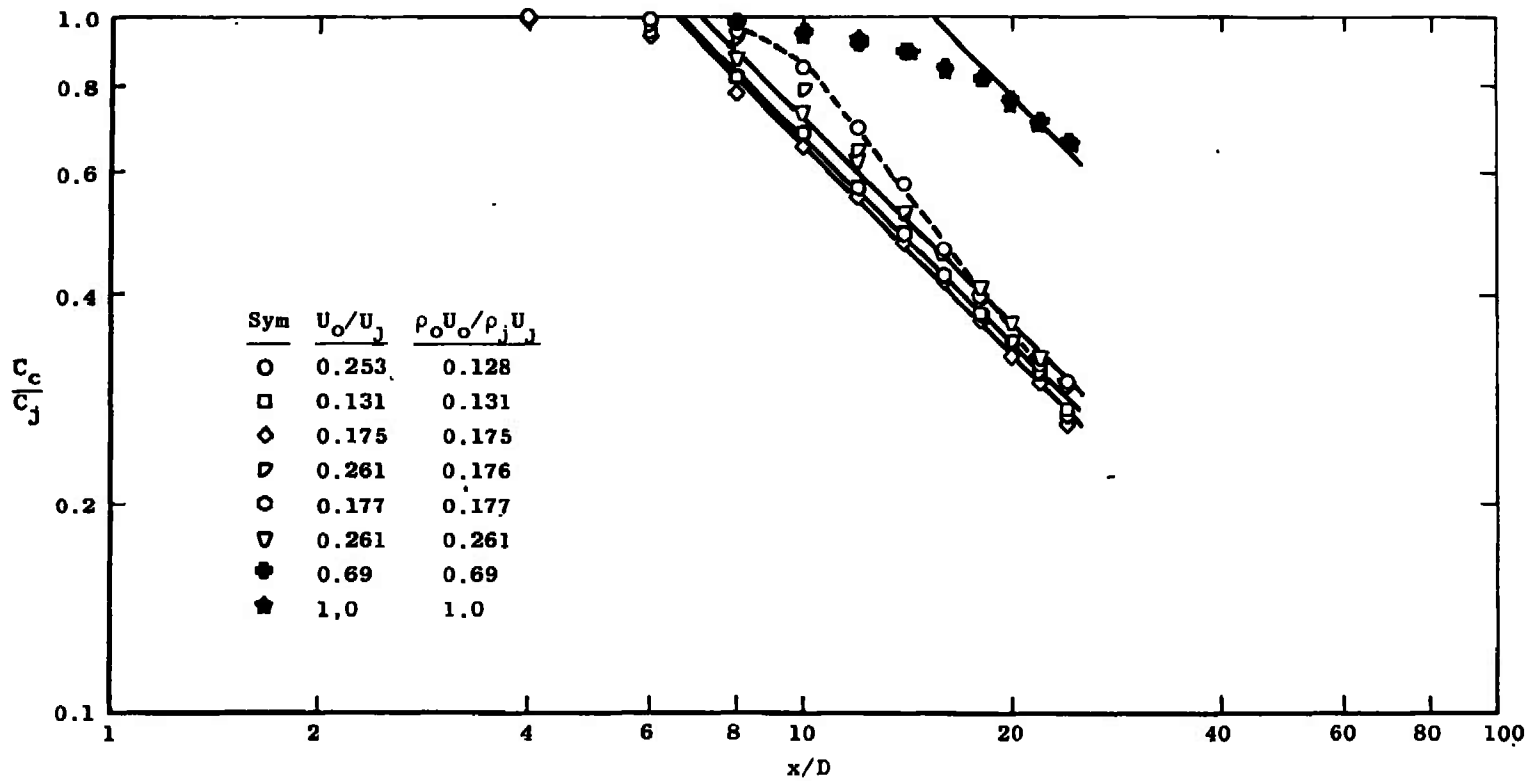


Figure 5.7. Axial decay of centerline concentration, air-air and Freon-air coaxial mixing. Data from Fejer, et al., [92].

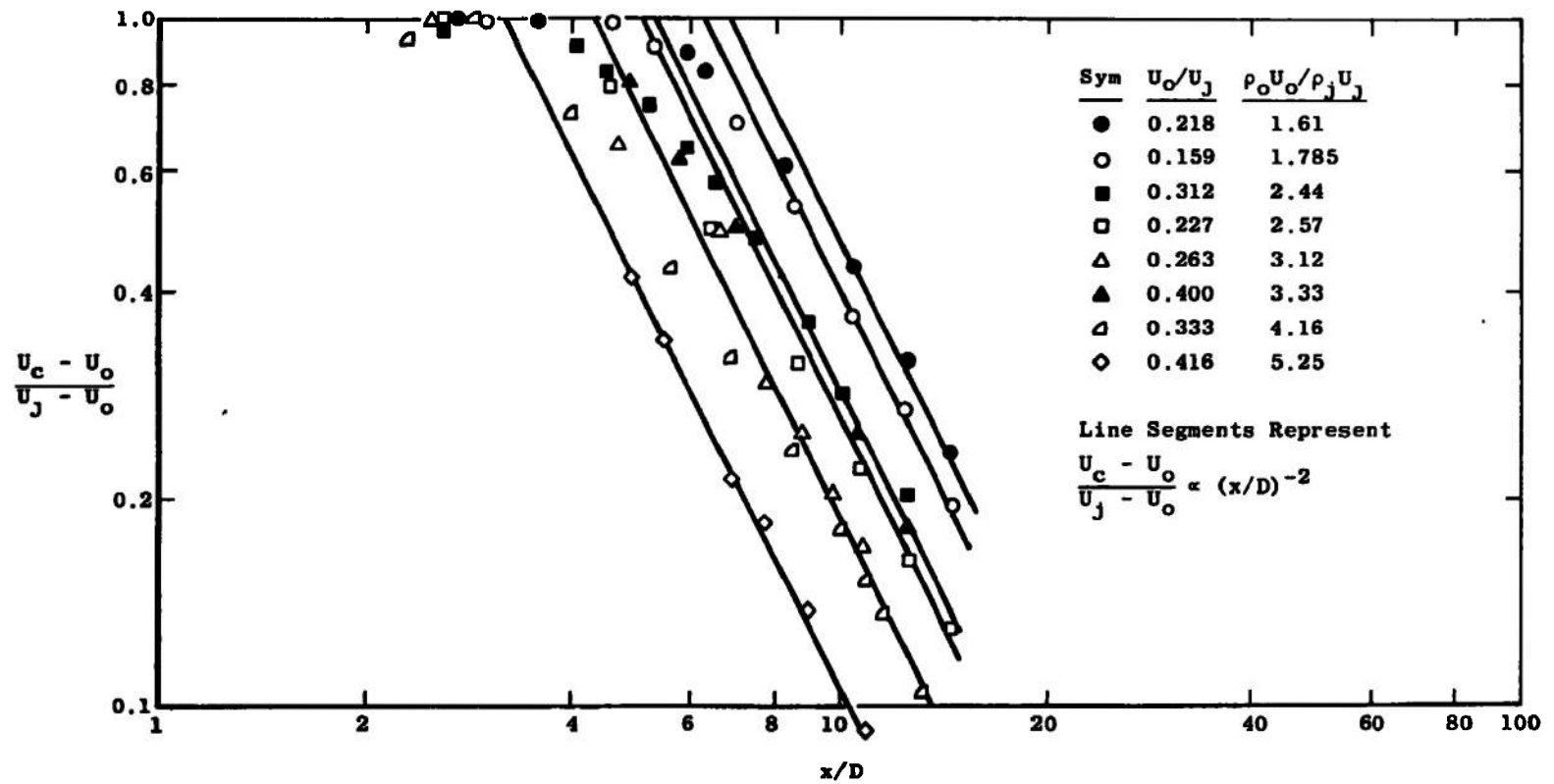


Figure 5.8. Axial decay of centerline velocity ratio, H_2 -Air mixing. $\rho_o U_o / \rho_j U_j > 1.0$, $U_o/U_j < 1.0$. Data from Chriss [90].

the mass flux ratio $\rho_o U_o / \rho_j U_j$ increases from 1.0; no such correlation is possible with the velocity ratio U_o / U_j alone.⁵ This trend agrees well with the data of Zawacki and Weinstein [35] for Freon-air mixing.

Figure 5.9 shows the axial decay of centerline composition for the coaxial mixing experiment of Chriss [90]. Again the concentration data are reasonably well fitted by a line of the form $C_c / C_j \propto (x/D)^{-2}$, and the data show a decreasing potential core length (for concentration) with increasing mass flux ratio $\rho_o U_o / \rho_j U_j$.

Figures 5.10 through 5.12 show radial profile data obtained from the experiments of Chriss [90]. Figure 5.10 shows that for axial stations downstream from the end of the potential core, the experimental data for hydrogen-air mixing shows good profile similarity. For this case, the "cosine function"

$$\frac{U - U_o}{U_c - U_o} = \frac{1}{2}[1 + \cos \frac{\pi}{2}(r/r_{1/2})] \quad (5.1)$$

provides a good representation of the data. A cosine function can also be used in the first regime, as is shown by Figure 5.11. In this figure, $r_{0.9}$ represents the radius

⁵The one case that does not fit well for these data may be taken as indicating that it may not be possible to completely characterize such flows with any simple parameter.

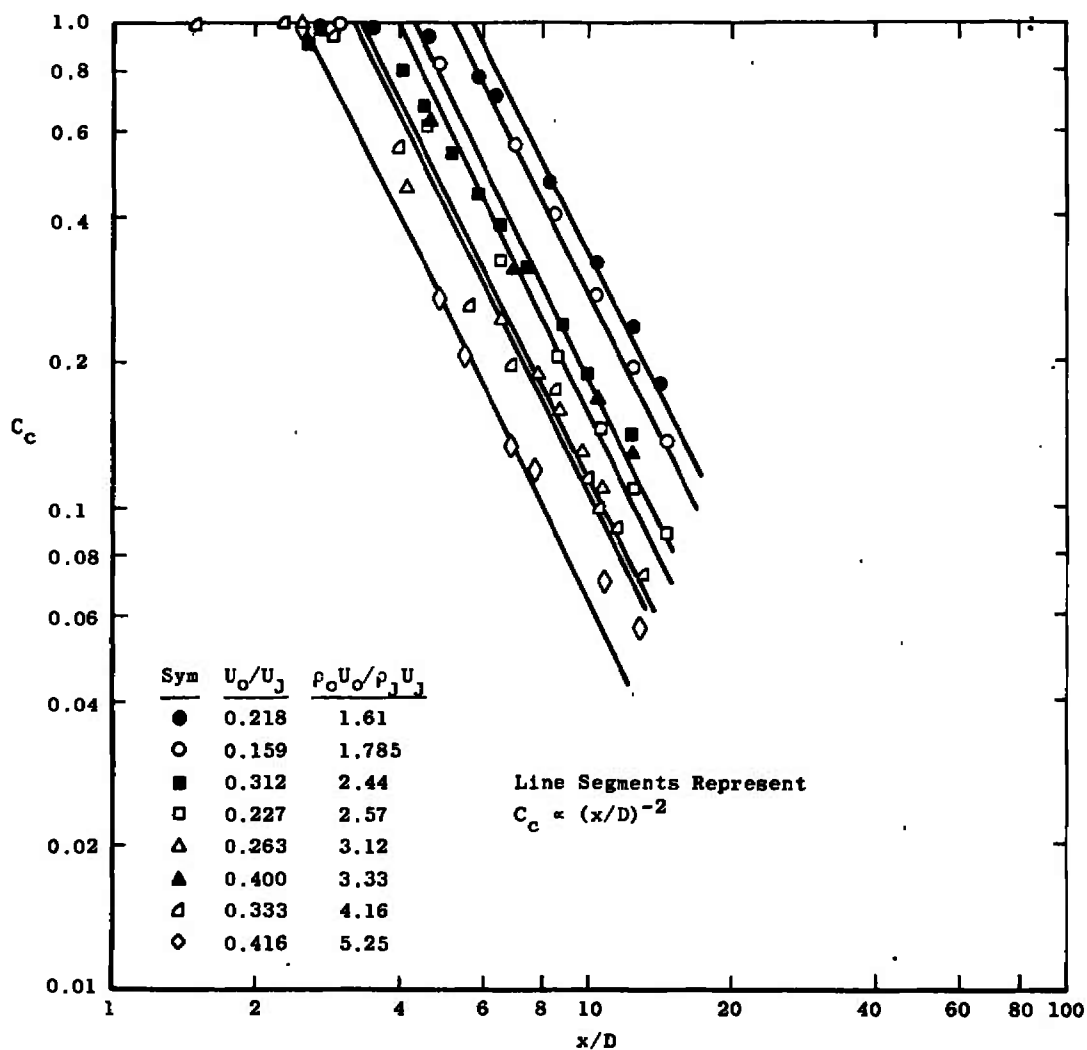


Figure 5.9. Axial decay of centerline composition, coaxial hydrogen-air mixing. Data of Chriss [90].

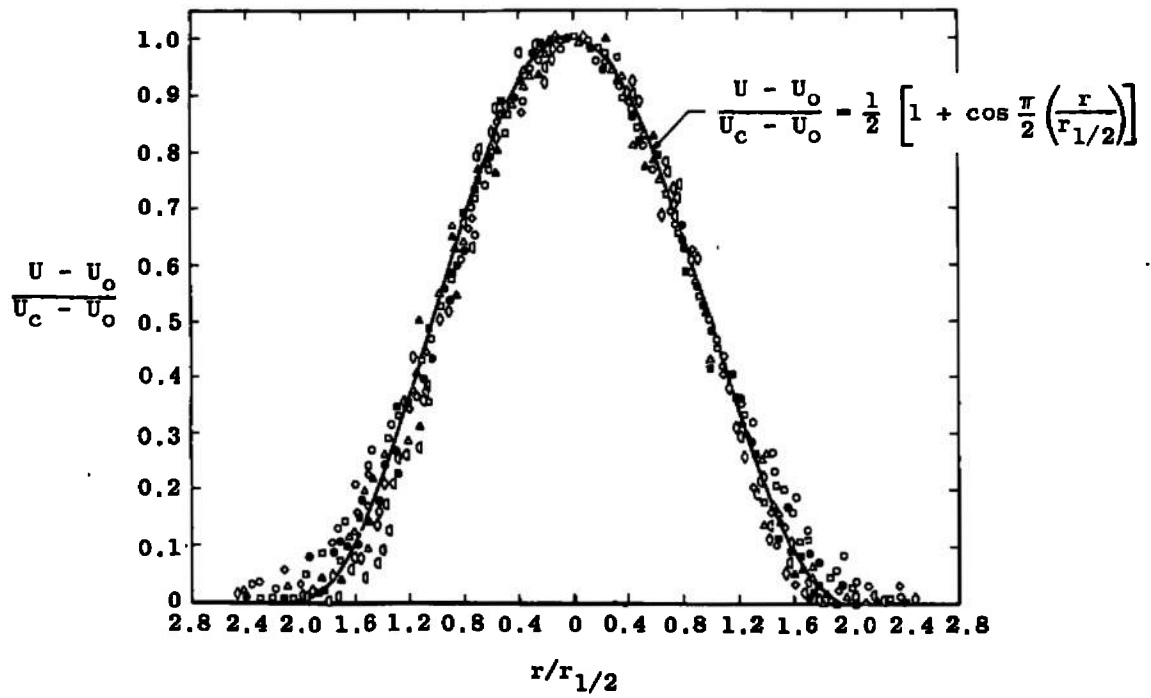


Figure 5.10. Radial velocity profile. Data of Chriss [90].

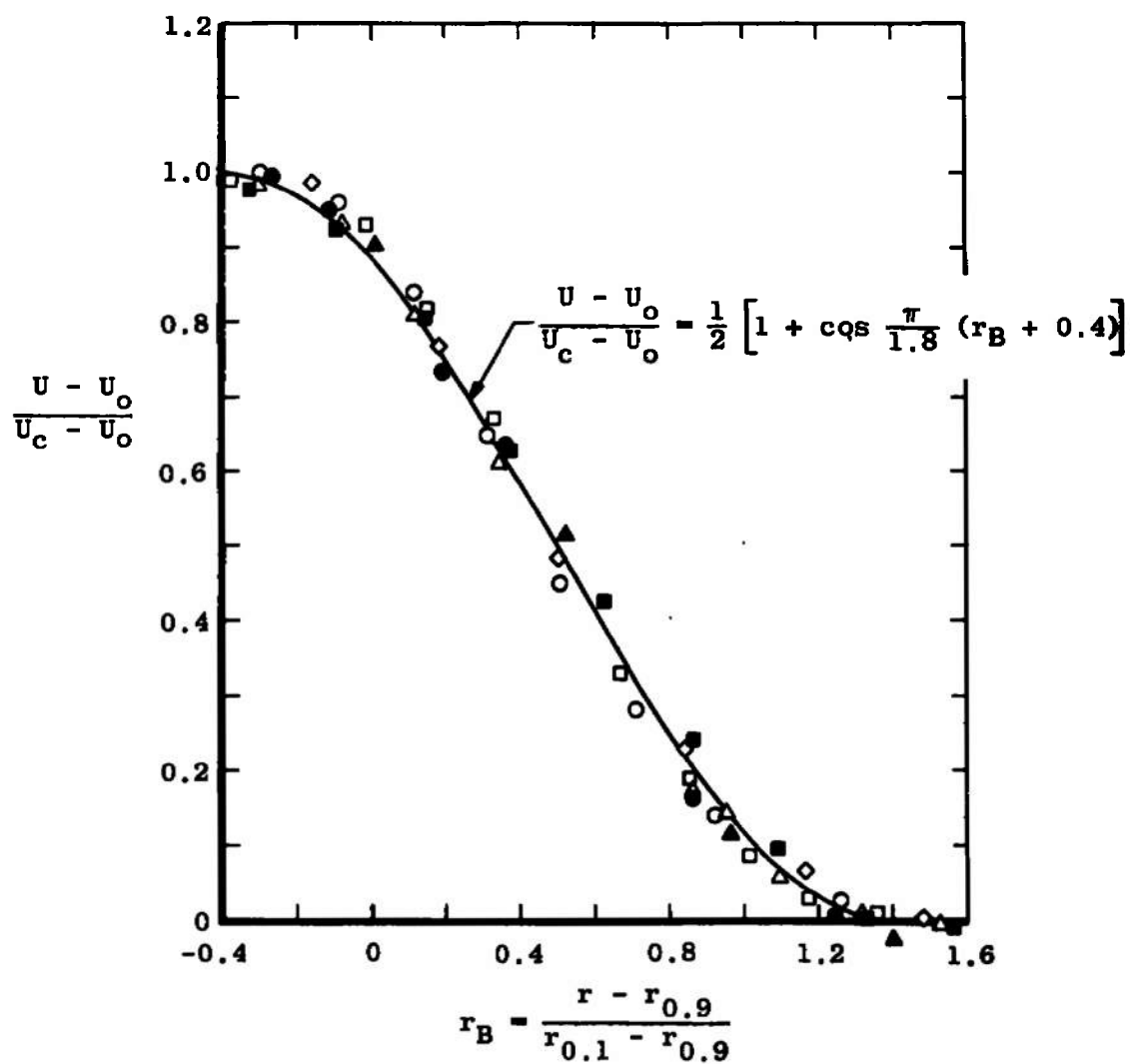


Figure 5.11. First regime radial velocity profile. Data of Chriss [90].

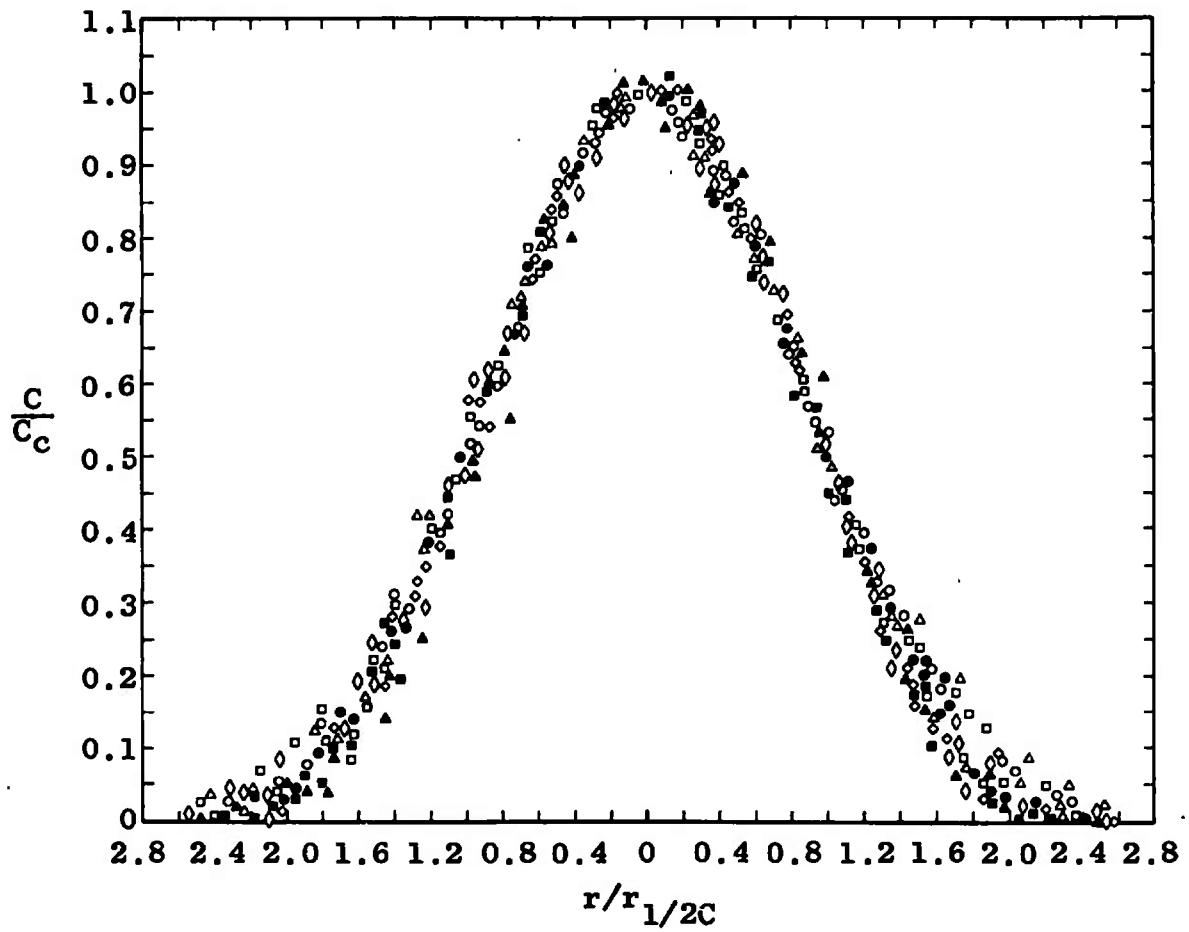


Figure 5.12. Radial composition profile. Data of Chriss [90].

for which $U = 0.9 (U_c - U_o)$. Geometric similarity for the composition profiles in the second regime is demonstrated by Figure 5.12. If the Prandtl number, which is the ratio of the transport coefficients for momentum and energy, is unity, then the nondimensional velocity profile

$\phi_U = (U - U_o)/(U_c - U_o)$ should at every point be equal to the nondimensional enthalpy profile $\phi_H = (H - H_o)/(H_c - H_o)$. That this is not in general the case is shown by Figure 5.13. From this figure, an empirical relationship

$$\phi_H = \phi_U^{(1+\phi_U)} \quad (5.2)$$

was developed by Chriss [90] for hydrogen-air mixing.

As well as hydrogen-air mixing, Alpinieri [84] also studied carbon-dioxide-air mixing. He does not present axial velocity decay for his hydrogen-air mixing experiments; however, it is presented for CO₂-air mixing. As can be seen from Figure 5.14, these experiments, which involve a 2-inch diameter inner jet and an 8-inch diameter duct, indicate a centerline velocity decay proportional to $(x/D)^{-1}$. Further, the velocity potential core length can be seen to decrease with increasing mass flux ratio, $\rho_o U_o / \rho_j U_j$.

Centerline concentration decays from both the CO₂-air and H₂-air experiments of Alpinieri are presented in Figure 5.15. Again, it may be seen that $C_c \propto (x/D)^{-2}$, and that the length of the concentration potential core

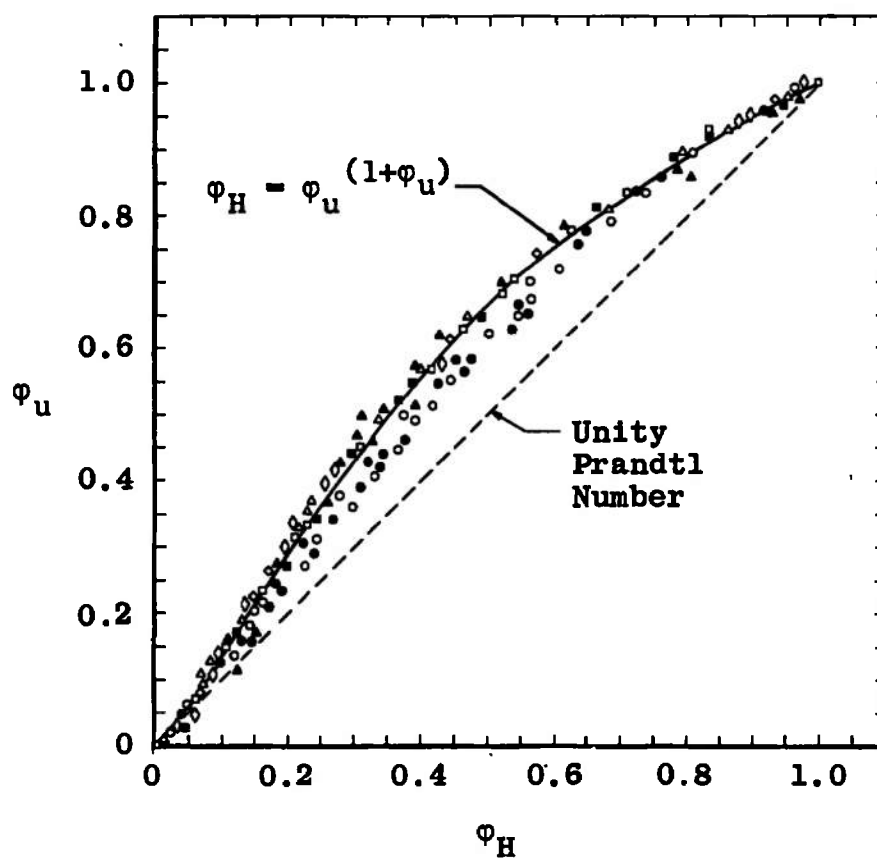


Figure 5.13. Velocity-enthalpy relationship for hydrogen-air tests. Data of Chriss [90].

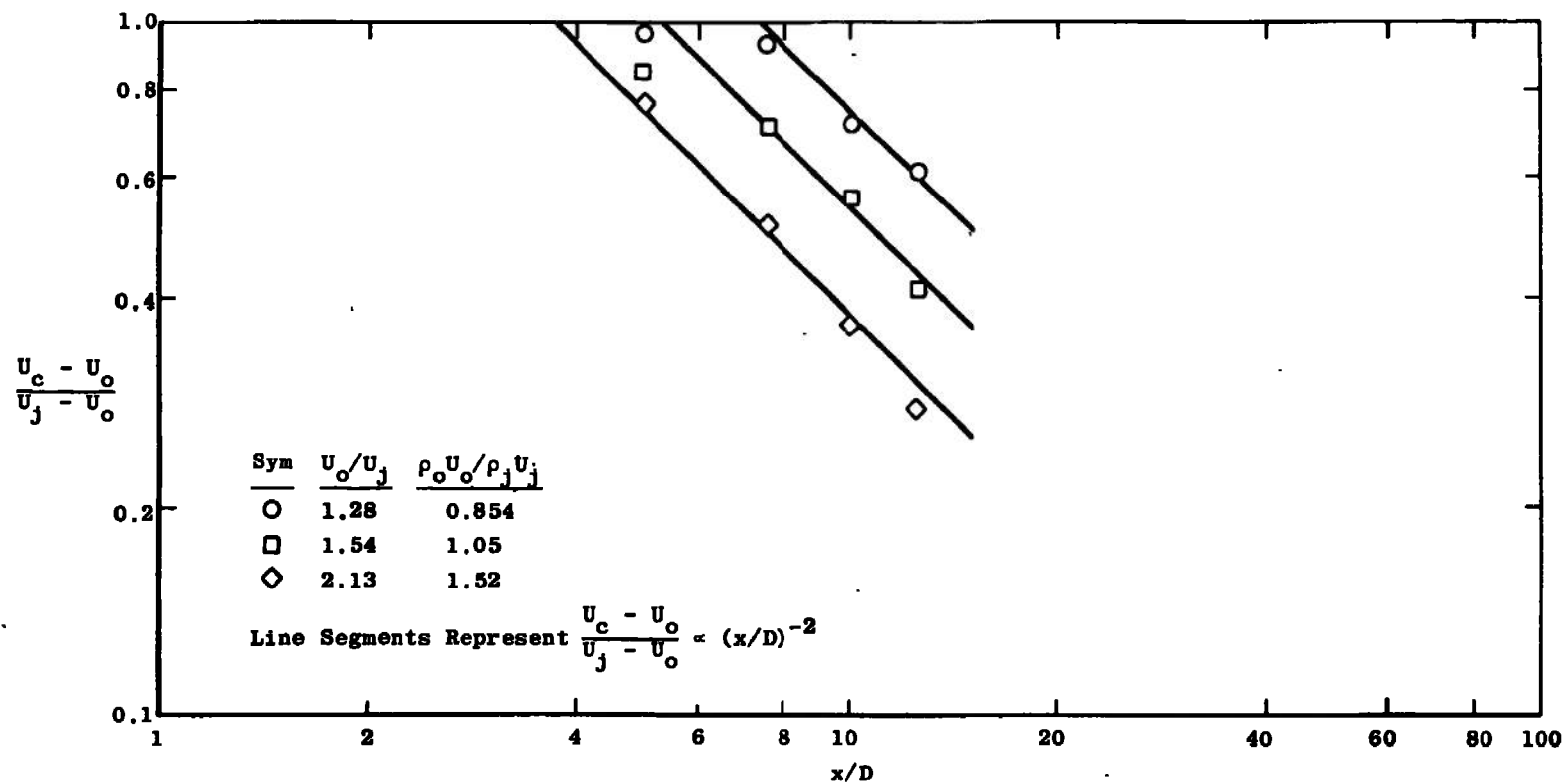


Figure 5.14. Axial decay of centerline velocity ratio, coaxial mixing of CO_2 and air. Data from Alpinieri [84].

Sym	U_o/U_j	$\rho_o U_o / \rho_j U_j$	Gas
○	1.28	0.854	CO ₂
□	1.54	1.05	CO ₂
△	2.13	1.52	CO ₂
●	0.80	13.5	H ₂
■	1.05	17.65	H ₂
◆	1.51	25.2	H ₂

Line Segments Represent $C_c \propto (x/D)^{-2}$

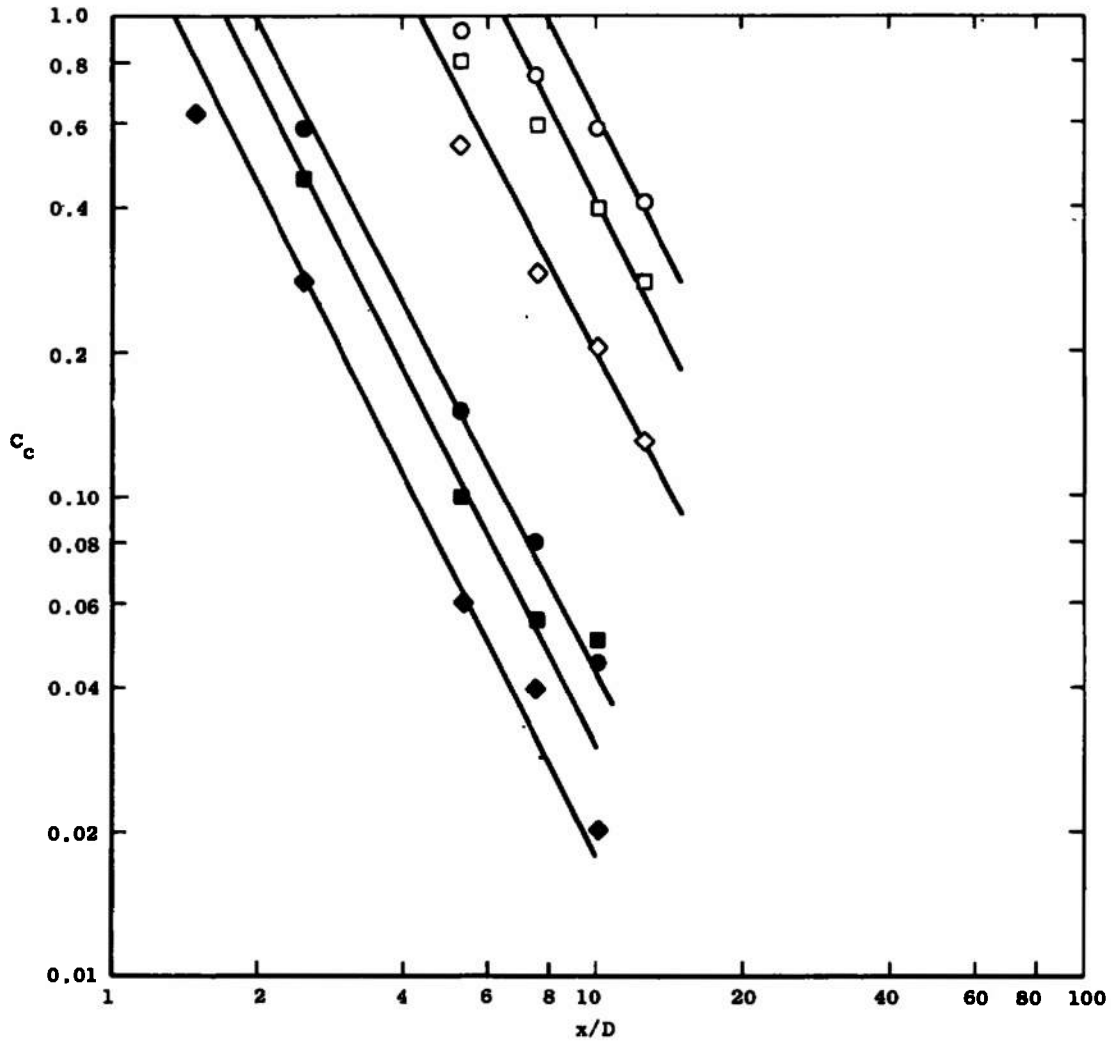


Figure 5.15. Centerline concentration decay, coaxial subsonic/subsonic mixing. Data from Alpinieri [84].

decreases with increasing mass flux ratio. The very short potential cores of the hydrogen-air experiments are, however, worthy of some comment. It will be noted from Figure 5.15 that the mass flux ratios for the hydrogen-air experiments of Alpinieri [84] range from 13.5 to 25.2. It will be recalled from the discussion of Chapter 3 that in the Freon-air configuration of Zawacki and Weinstein [35], Rozenmann [47] found that recirculation occurred for a velocity ratio U_o/U_j greater than 26 (which implies a mass flux ratio $\rho_o U_o / \rho_j U_j$ of the order of 10); for air-air this was observed to occur for U_o/U_j greater than 13. The mass flux ratios involved in Alpinieri's hydrogen-air experiments [84] are in every case greater than either of these numbers. A second piece of evidence can be obtained from Figure 9 of Reference [84], reproduced here as Figure 5.16. From this figure it can be seen that although in every case the velocity ratio U_c/U_j at $x/D = 2.5$ is approximately 1.0 on the centerline, the centerline value of composition ratio C_c/C_j is nowhere greater than 0.6. Taken together, these pieces of evidence seem to the author to clearly indicate the likelihood of recirculation phenomena in Alpinieri's hydrogen-air experiments.

One other subsonic/subsonic coaxial mixing of dissimilar gases experiment is listed in Table 5.1, pages 255-259. This is the bromine-air mixing experiment of

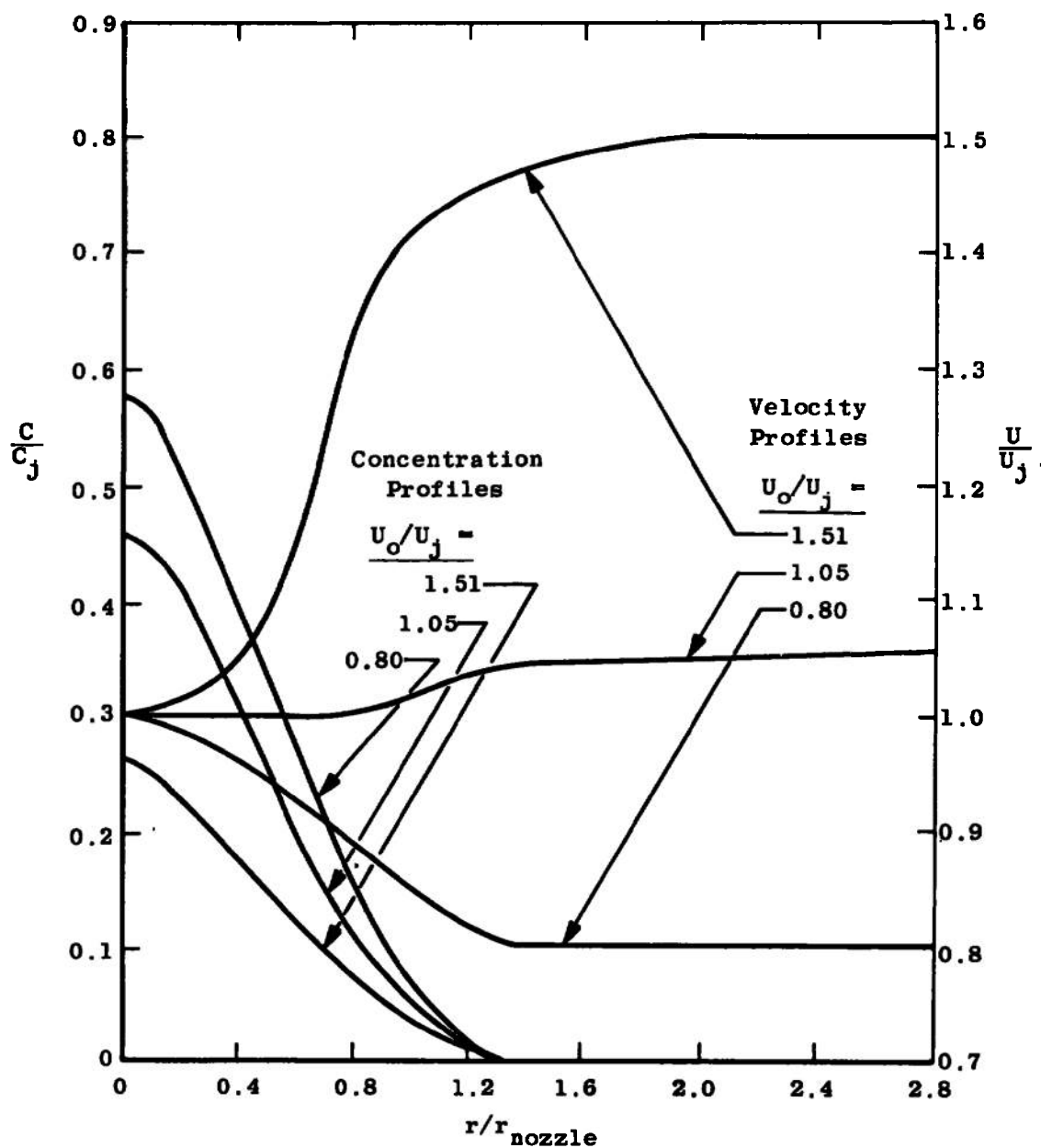


Figure 5.16. Initial profiles of concentration and velocity at $X/D = 2.5$. Hydrogen-air mixing. Reproduced from Reference [84].

Ragsdale and Edwards [89]. However, as can be seen from Figure 5.17, the limited data presented is too scattered to draw any conclusions from it.

There are a number of different experiments on turbulent coaxial mixing in which one or both of the streams are supersonic, but despite the number of experiments the available data are very limited. This is because little information is given in the reports listed. The experiment discussed in Ferri, et al., [83] involved a subsonic hydrogen jet exhausting into a surrounding $M = 3$ airstream, the entire flow contained within a duct. No dimensions are given for the apparatus in Reference [83]. Axial distribution of centerline composition for four velocity ratios are given in Reference [83], as well as radial concentration profiles for $x/D = 16.2$. However, comparison of these two figures (III-8 and III-9 of [83]) will show that there is a discrepancy between the centerline compositions shown on III-8 of [83] at $x/D = 16.2$ and the value of the composition at $r = 0$ from III-9 of [83].

The hydrogen-air mixing data of Zakkay and Krause [85] is somewhat more detailed. Here the primary subsonic jet nozzle diameter is given as 0.6 inch, and the outer $M = 1.55$ nozzle diameter as 3.44 inches. Both jets exhaust into a 12 inch diameter tube. The only measurements reported in Reference [85] are of the axial decay of centerline composition. These data are shown in Figure 5.18,

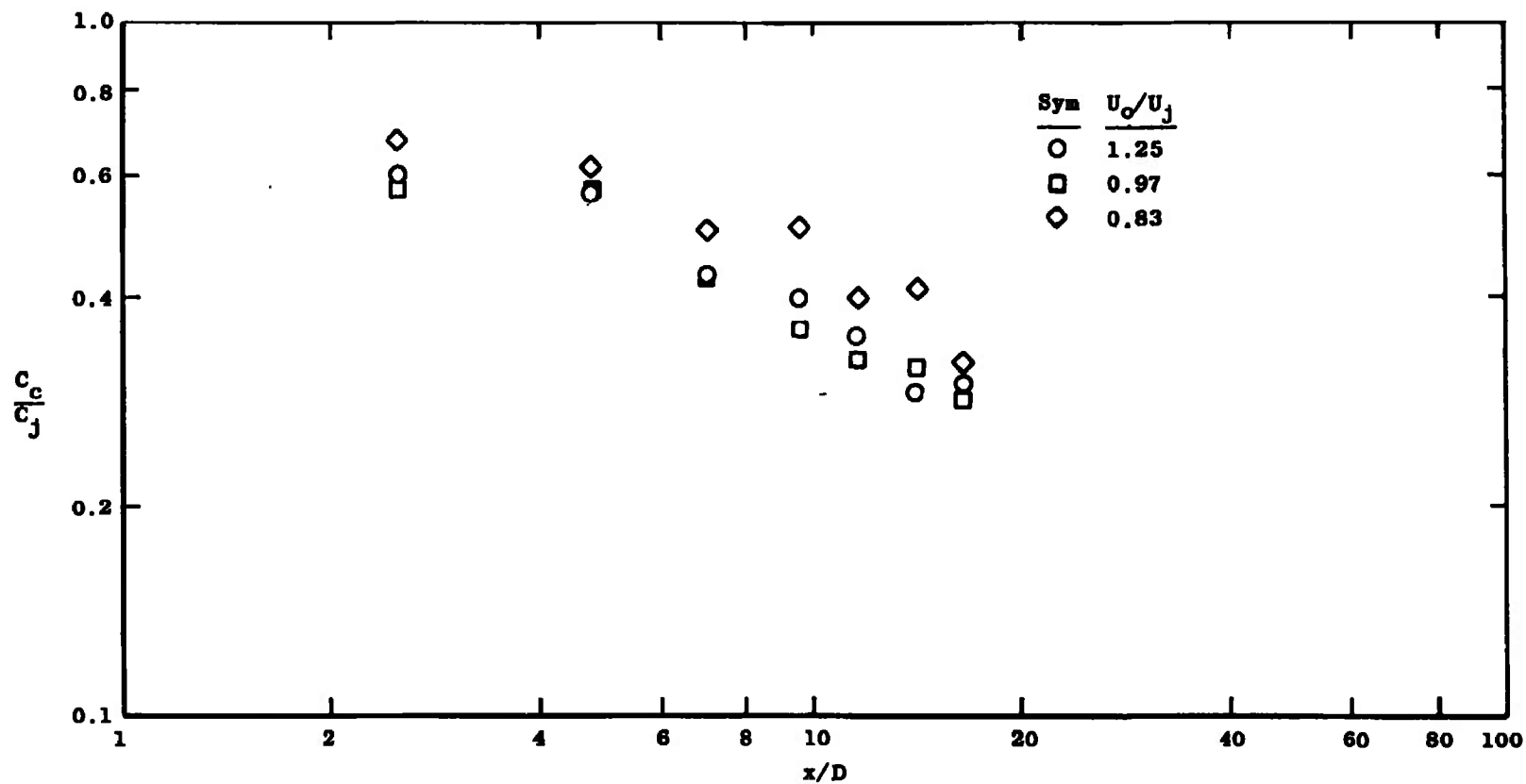


Figure 5.17. Centerline composition decay, coaxial bromine-air mixing [89].

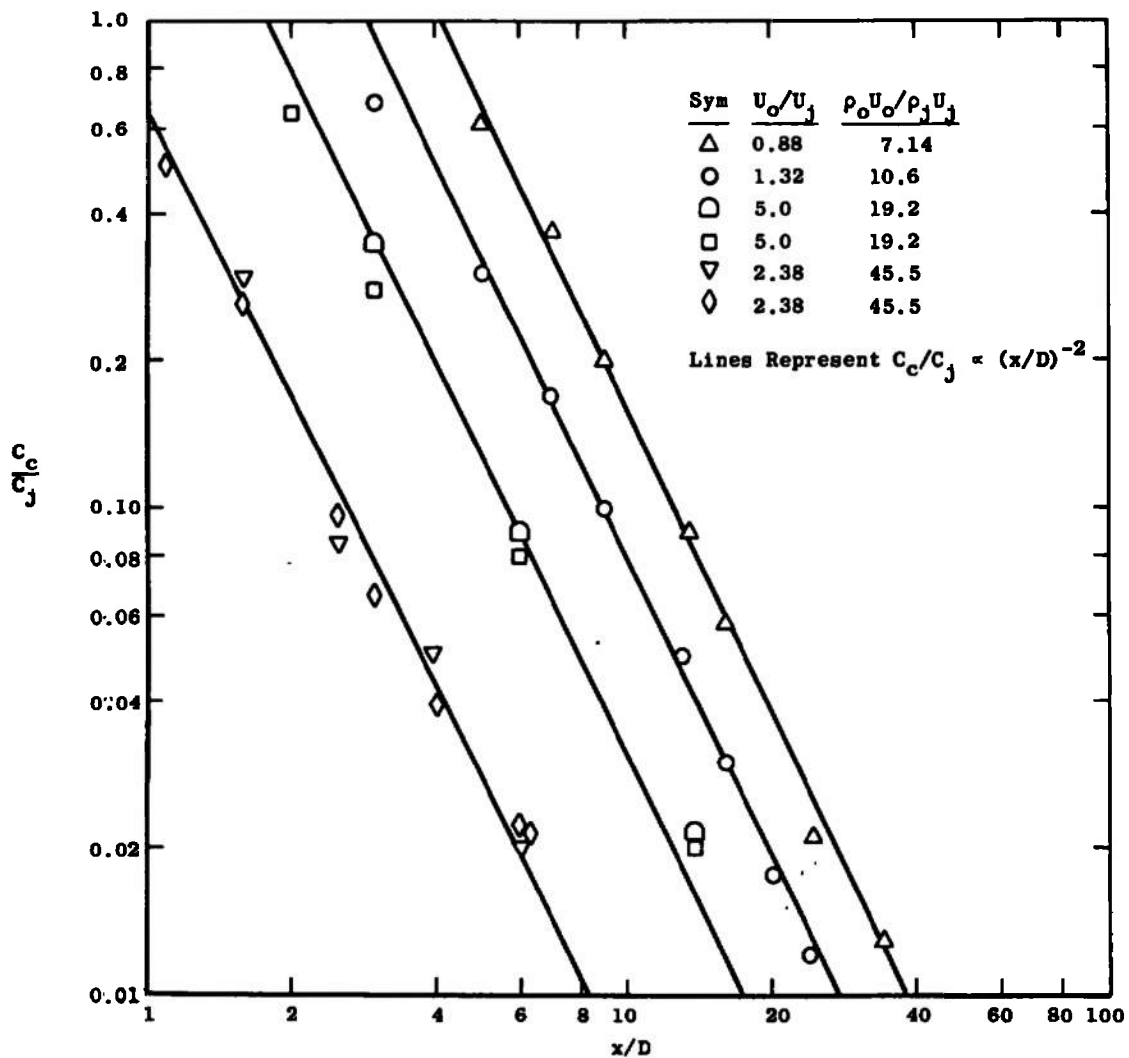


Figure 5.18. Axial decay of centerline composition, subsonic/supersonic coaxial mixing. Data of Zakkay and Krause [85].

from which it can be seen that the centerline composition decay for these tests follows a line proportional to $(x/D)^{-2}$, as for the hydrogen-air data of Chriss [90]. Also, as was previously observed, the length of the potential core (for composition) can be seen to decrease with increasing values of $\rho_o U_o / \rho_j U_j$. Figure 5.18 shows some particularly short composition potential cores. In the light of the discussion of recirculation phenomena above, it would appear likely that some sort of recirculation phenomenon or a substantial deflection of outer-flow streamlines toward the centerline is responsible for the very short composition potential core lengths shown in Figure 5.18.

Much the same comment can probably be made about at least a part of the hydrogen-air mixing data presented in Zakkay, et al., [93], and shown in Figure 5.19. Reference [94] reports some results of both subsonic/supersonic and supersonic/supersonic mixing experiments, carried out with several primary stream gases. The primary jet diameter was 0.3 inch; it exhausted into a $M = 1.6$ secondary stream flowing through a 3.44 inch diameter duct. As can be seen from Figure 5.19, all of the decay of centerline composition curves appear to fit a $(x/D)^{-2}$ decay line fairly well.

The data shown in Figure 5.19 as well as additional data are also presented by Zakkay, et al., in another reference [86]. A number of conclusions are reached in Reference [86] that are worthy of some discussion. The

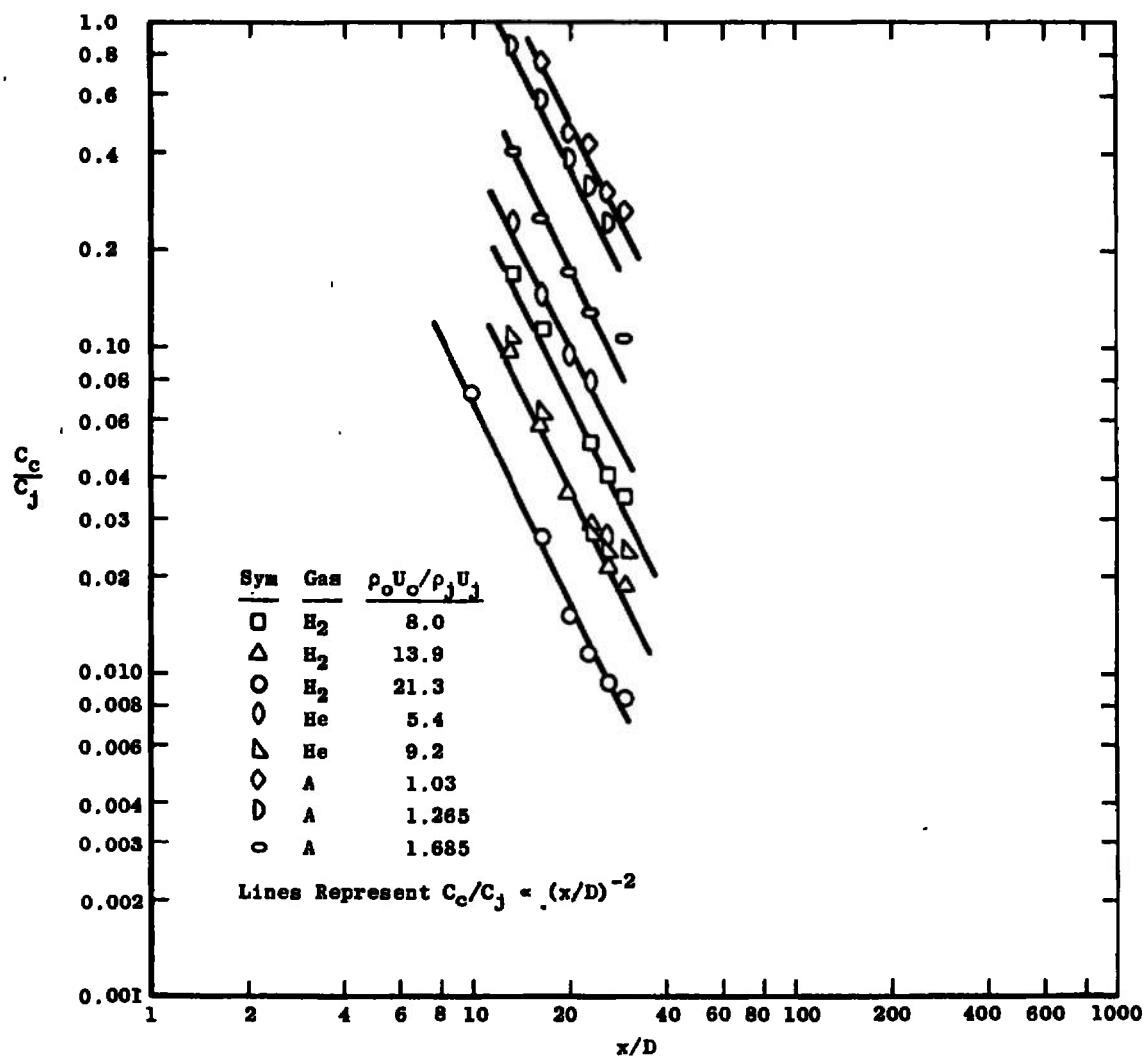


Figure 5.19. Axial decay of centerline composition, subsonic/supersonic and supersonic/supersonic jets. Data from Zakkay, et al., [93].

first is that centerline composition decays as $(x/D)^{-2}$. This conclusion seems to be well supported by subsonic/supersonic and supersonic/supersonic jet data (Figure 5.20, also Figure 5.19, and Figure 5.18, page 288). However, all of these data are for $\rho_o U_o / \rho_j U_j > 1.0$. For subsonic/supersonic data, the conclusion is supported by Alpinieri [84] for $\rho_o U_o / \rho_j U_j > 1.0$, and by Chriss [90] for $\rho_o U_o / \rho_j U_j > 1.0$, as shown by Figure 5.21, and also by Figures 5.14, page 282, and 5.9, page 276. However, for $\rho_o U_o / \rho_j U_j < 1.0$, the data of Landis and Shapiro [43], Figure 5.22, do not support this relation. Further, the data of Fejer, et al., [92], Figure 5.7, page 273, also do not support this relation; these latter two experiments both display curves of the form $C_c/C_j \propto (x/D)^{-1}$. From the data observed in this Chapter, it appears that in the mixing of two subsonic streams, the centerline concentration ratio C_c/C_j is proportional to $(x/D)^{-1}$ for $\rho_o U_o / \rho_j U_j < 1.0$, and C_c/C_j is proportional to $(x/D)^{-2}$ for $\rho_o U_o / \rho_j U_j > 1.0$. For supersonic/subsonic or supersonic/supersonic data, the centerline composition ratio appears always to be proportional to $(x/D)^{-2}$.

Zakkay, et al., [86] note that the centerline composition data for a number of tests (all supersonic/supersonic or supersonic/subsonic--primary jet/secondary jet) all collapse together on a single line if plotted versus x/x_c . This is not particularly surprising, as it is shown

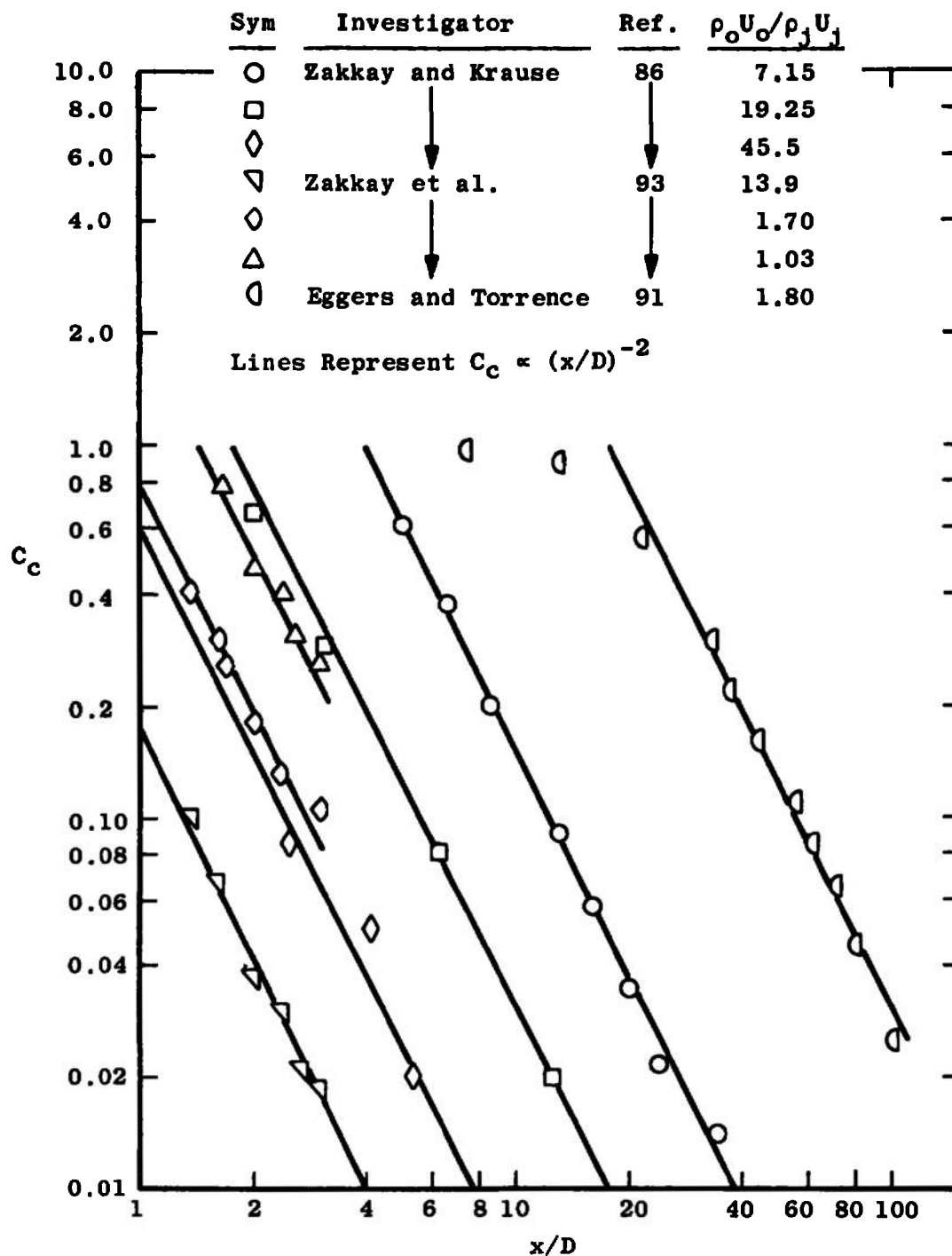


Figure 5.20. Axial decay of centerline composition, subsonic/supersonic coaxial jets. Mass flow ratio $\rho_o U_o / \rho_j U_j > 1.0$.

Sym	Investigator	Ref.	U_o/U_j	$\rho_o U_o / \rho_j U_j$	Jet Gas
○	Alpinieri	84	1.51	25.2	H ₂
◇	↓	↓	1.54	1.05	CO ₂
□	↓	↓	0.80	13.5	H ₂
▽	Chriss	90	0.26	3.12	↓
○	↓	↓	0.33	4.16	↓
▽	↓	↓	0.42	5.25	↓
△	↓	↓	0.31	2.44	↓

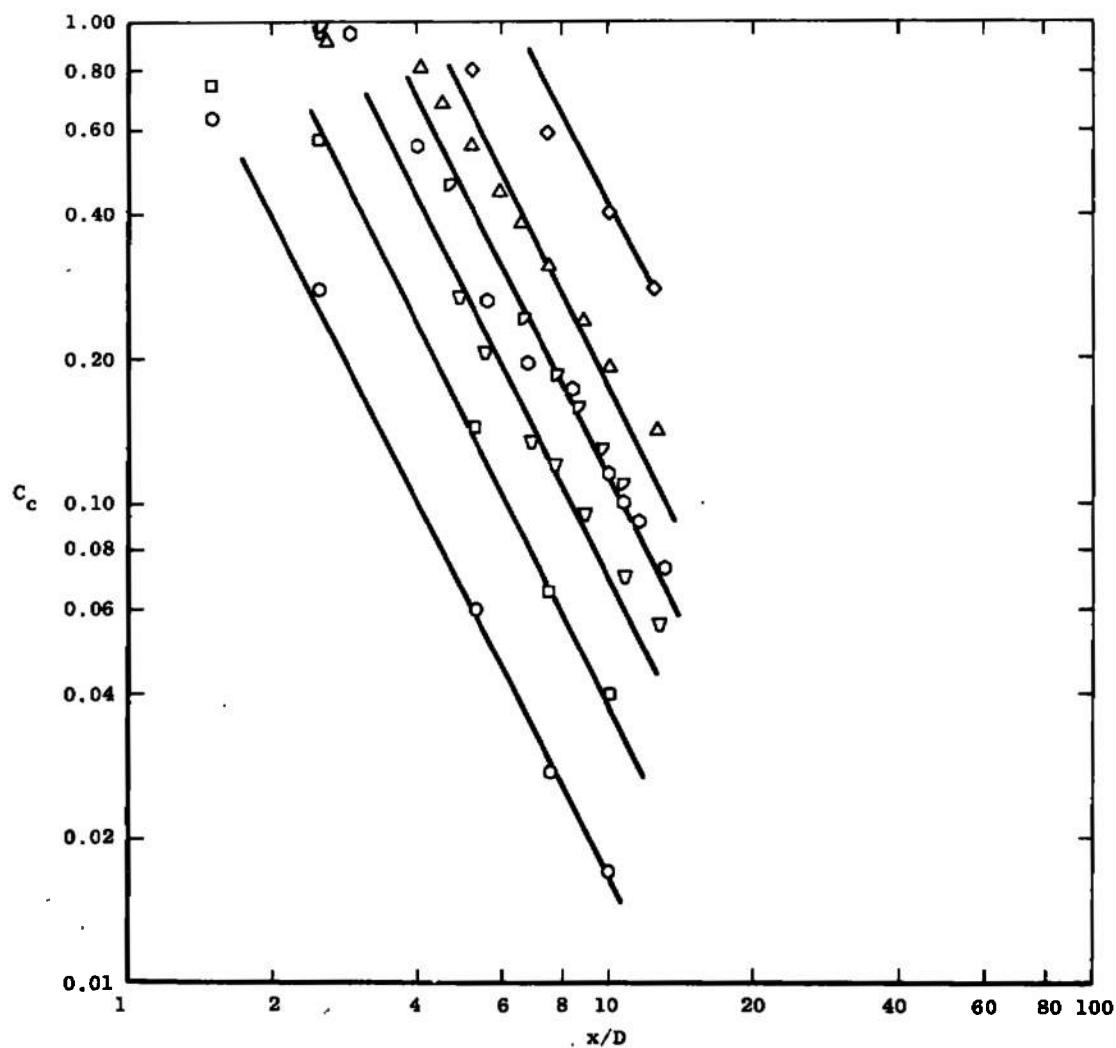


Figure 5.21. Axial decay of centerline composition.
Subsonic/subsonic coaxial jets, mass-flow ratio > 1.0.

Sym	Investigator	Ref.	U_o/U_j	$\rho_o U_o/\rho_j U_j$	ϕ
○	Landis and Shapiro	43	0.25	0.325	$\frac{T_c - T_o}{T_j - T_o}$
□	Landis and Shapiro	43	0.50	0.650	$\frac{T_c - T_o}{T_j - T_o}$
◇	Alpinieri	84	1.28	0.854	C_c/C_j
▽	Ragsdale and Edwards	89	1.25	0.226	C_c/C_j

Lines Represent Curves of $\phi \propto x^{-1}$

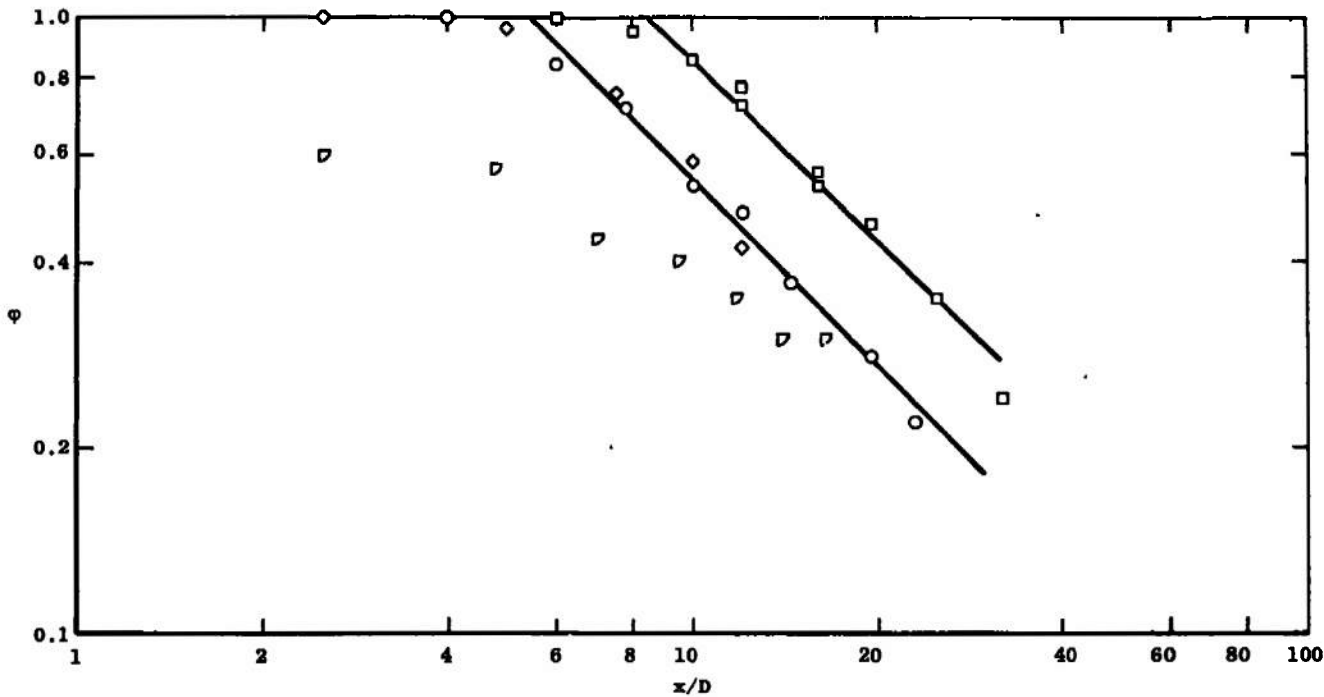


Figure 5.22. Axial decay of centerline composition (or temperature ratio), subsonic/subsonic coaxial jets, mass-flow ratio < 1.0.

in Appendix B that in simple flows under some somewhat restrictive assumptions, the sole parameter in a coaxial free mixing flow is the core length ratio x_c/D . Since there is no composition boundary layer (the initial condition for the composition is a step function), the composition mixing problem treated independently of the momentum mixing problem can be considered as such a simple flow. However, knowing the value of C_c/C_j as a function of x/x_c is of little use unless x_c is known as well.

Recognizing this problem, Zakkay, et al., set out to find an empirical expression for the core length as a function of some quantity known a priori. The expression that they settled on was

$$\frac{x_c}{D} = 11\sqrt{\lambda} \quad (5.2)$$

where

$$\lambda = \rho_j U_j / \rho_o U_o$$

This expression was obtained by plotting the concentration potential core length for a number of coaxial subsonic/subsonic, supersonic/subsonic, or supersonic/supersonic tests as a function of λ . The concentration potential core length is obtained from the intersection of the line through the decay data with the $C_c/C_j = 1.0$ line.

The author has obtained these core lengths for a number of flows, including those investigated by Zakkay, et al., and incorporating some which were not. The results are shown on Figure 5.23, from which it can be seen that the line given by Equation (5.2) is in error for all but a few points. The magnitude of the errors involved are given in Table 5.2 for a few cases.

It should also be noted that a combination of Equation (5.2) and the assumed expression for axial decay of centerline composition

$$\frac{C_c}{C_j} = \left(\frac{x}{x_c}\right)^{-2} \quad (5.3)$$

leads to a general expression for concentration decay

$$\left. \begin{aligned} \frac{C_c}{C_j} &= 1 \frac{x}{D} < 11\sqrt{\lambda} \\ \frac{C_c}{C_j} &= 121 \lambda \left(\frac{x}{D}\right)^{-2} \frac{x}{D} > 11\sqrt{\lambda} \end{aligned} \right\} \quad (5.4)$$

Figure 5.24 shows a comparison between the results of Equation (5.4) and some of the data of Reference [90]. From Table 5.2 and Figure 5.24, it can be seen that this correlation cannot be recommended for general engineering use.

The data of Reference [86] also shows a variation in the turbulent Schmidt number ranging from 0.3 to 2.3, and

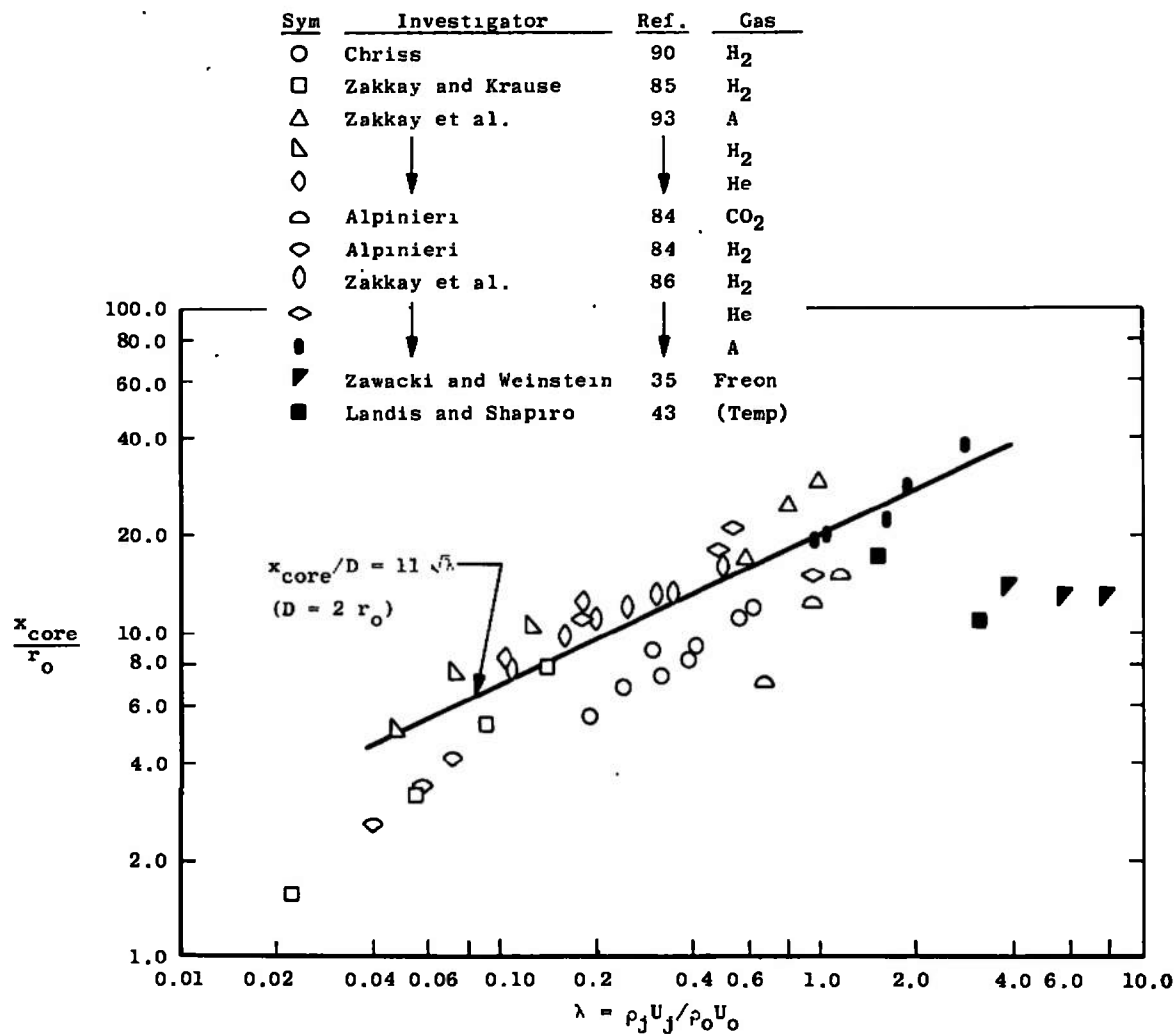


Figure 5.23. Core-length correlation, variable-density coaxial mixing.

TABLE 5.2

COMPARISON OF MEASURED CONCENTRATION POTENTIAL
CORE LENGTHS WITH THOSE PREDICTED
BY EQUATION (5.2)

Investigator	Ref.	λ	$(x_c/D)_m$ Meas.	$(x_c/D)_p$ Equation (5.2)	Percent Error ^a
Chriss	90	0.19	2.5	4.79	91.6
		0.30	4.0	6.05	50.6
		0.57	5.2	8.3	59.5
Zakkay, et al.	93	0.072	3.85	2.45	23.4
		0.185	6.3	4.8	31.2
Alpinieri	84	0.04	1.3	2.2	69.4
		0.66	4.05	8.9	120.0
		1.17	7.5	11.9	58.7

$$^a \{ [(x_c/D)_p - (x_c/D)_m] / (x_c/D)_m \} \times 100.$$

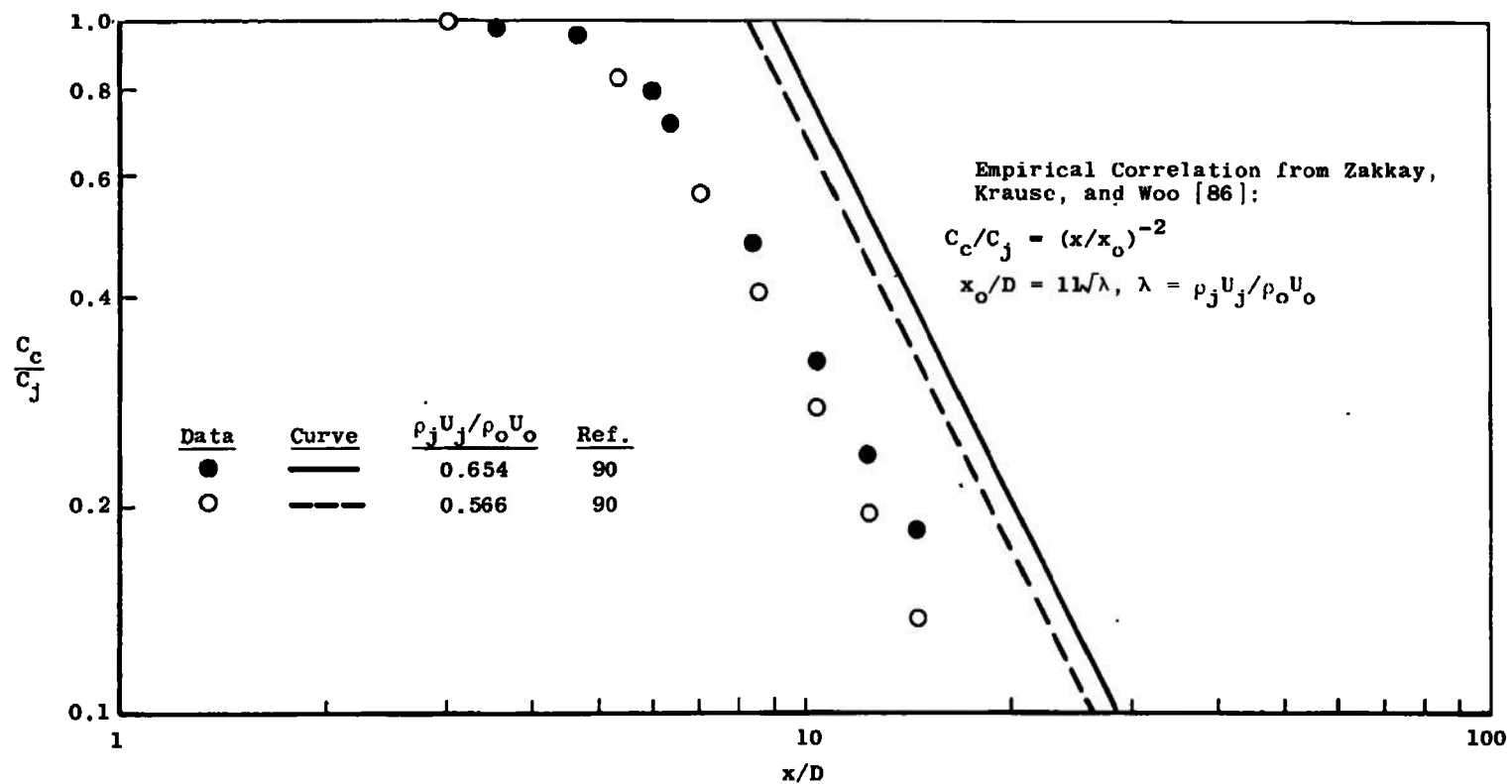


Figure 5.24. Comparison of experimental data with empirical prediction.

that the turbulent Lewis number ranges from 0.4 to 1.0. Reference [94] reports values of both the turbulent Prandtl number and the turbulent Schmidt number of about 0.85 for hydrogen-air mixing with the turbulent Lewis number being 1.0.

Zakkay and Krause [95] present further results obtained from the data partially reported in [86], in this case reporting the radial variation of the eddy viscosity in the flow. The profiles of velocity used are fitted with a cosine profile, and experimental values for the half-radius $r_{1/2}$ and the centerline decay of velocity ratio as functions of x/D are used. As was pointed out by Fejer, et al., [45] the axial decay curve and the specification of the cosine profile automatically determine the axial variation of the half-velocity radius. Thus the problem as established by Zakkay and Krause is overspecified. The results of Reference [95] show $\epsilon \rightarrow \infty$ as $r/r_{1/2} \rightarrow 2$; this behavior is due to the overspecification referred to.

The final piece of experimental work referred to in Table 5.1, pages 255-259, is the supersonic/supersonic CO_2 -air mixing experiment carried out by Forde [88]. As listed in Table 5.1, this work includes some measurements of radial profiles of mean flow quantities and of spread rates; however, no axial decay curves are presented.

Axisymmetric Wakes

One of the most complex of free mixing flows is the axisymmetric compressible wake. The complexity of the flow involves primarily its formation; since a compressible wake is in general formed behind a body traveling at supersonic speed, the initial part of such a wake involves the interaction between inviscid flow shock phenomena and the viscous turbulent mixing flow. This complex interaction is, however, outside the scope of this study. In this work attention will primarily be focused on the mixing characteristics of such wakes.

As can be seen from Table 5.3, the study of compressible axisymmetric wakes began only fairly recently, and to the present time the most extensive investigations have been of wakes of relatively high supersonic Mach numbers. The work of Zakkay and Fox [96] involves the wake behind a flat-faced cylindrical body mounted by wire supports in a Mach 11.3 wind tunnel. The body L/D was 24; measurements of the axial decay of centerline Mach number difference ratio for this flow are shown in Figure 5.25. This figure shows an initial slow period of decay followed by a more rapid (and linear on a log-log plot) period, which undergoes transition to another slower decay region.

The only other experiment which goes to relatively large x/D is that of Demetriades [99]. As shown on Figure 5.26 the velocity ratio decay data for this experiment--at

TABLE 5.3
AXISYMMETRIC COMPRESSIBLE WAKES

Investigator	Ref.	Year	M _o	Re _o /ft x10 ⁵	D in.	Radial Profiles		Axial Distributions					ρ
						M	T _s	U	M	T _s	U	P _s	
Zakkay and Fox	96	1966	11.8	4.5	0.25								
					0.50	x	x	x	x				
					1.0								
					2.0								
					1.4	x			x			x	
Demetriades	97	1967	3.0	15.25 ^a	0.156 ^a		x ^b	x ^b					
Fox, Zakkay, and Sinha	98	1967	3 ^a				x	x	x				
			4			x			x				
			5				x	x	x				
			12			x	x	x	x	x			
Demetriades	99	1968	3.0	15.25	0.156		x	x		x	x		x
Sinha and Zakkay	100	1968	3.92	385.0	1.4				x	x	x	x	

^aObtained from Reference [99].

^bNormalized profiles only.

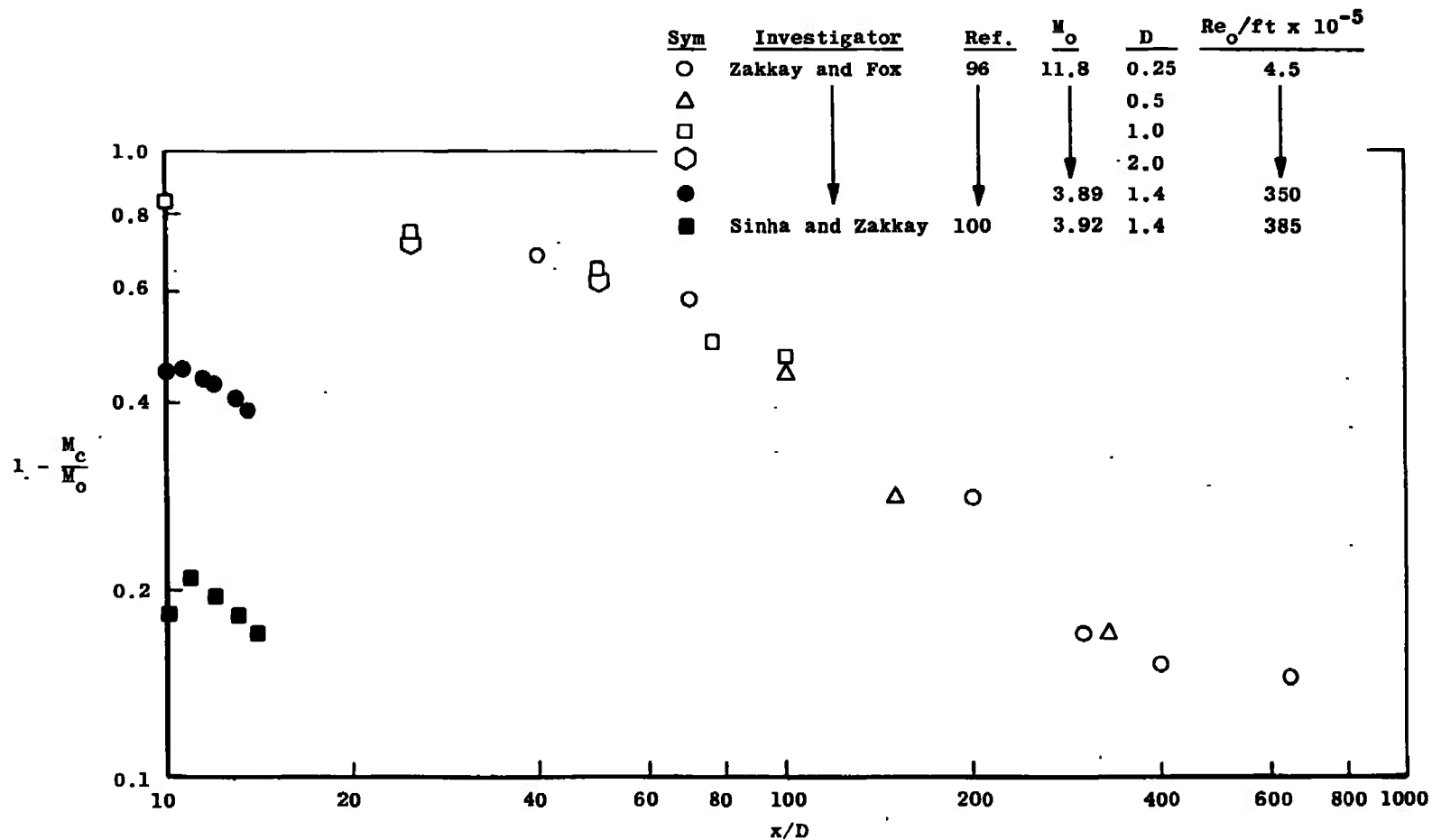


Figure 5.25. Axial increase of centerline Mach number, axisymmetric supersonic wakes.

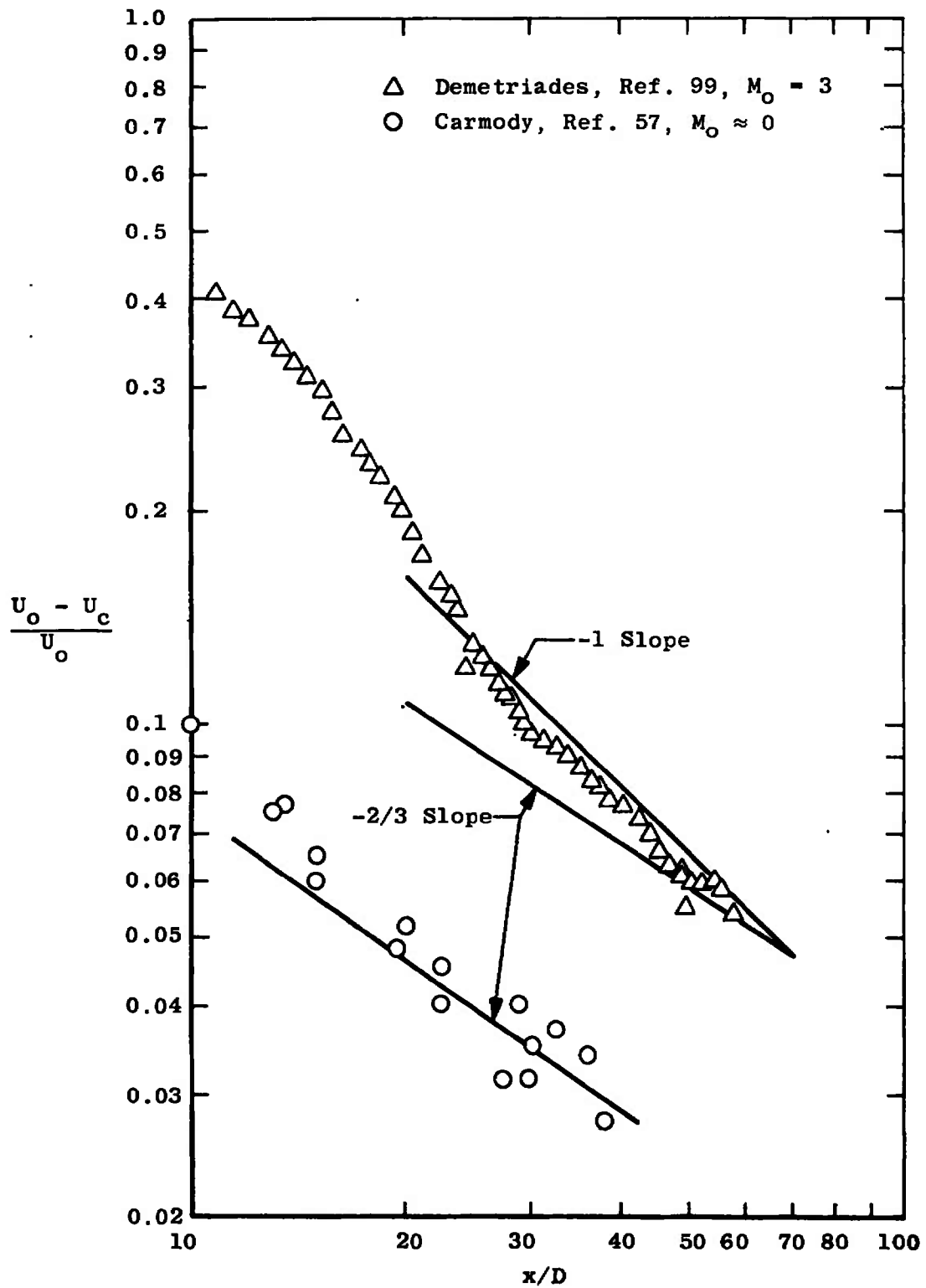


Figure 5.26. Comparison of centerline velocity decay rates, axisymmetric wakes.

very much lower free-stream Mach number ($M_0 = 3$) and higher free-stream Reynolds number/foot (15.25×10^5 compared to 4.5×10^5 for Reference [96])--also show a steepening of the decay curve followed by (possibly) a gradual decrease in slope. Figure 5.26 compares the data of Demetriades [99] with that of Carmody [57] for a subsonic wake. The $x^{-2/3}$ slope required for self-preservation does not seem to be overwhelmingly supported by either data. However, a better check for approximation to self-preservation relations is to plot the data using as axial coordinate the parameter $(x - x_v)/D$, where x_v is the virtual origin. This is especially important in the near- and mid-ranges, where x_v may be a significant fraction of x . The approach of the axial velocity profiles measured by Demetriades to a decay proportional to $[(x - x_v)/D]^{-2/3}$ is shown in Figure 5.27; the fit is somewhat better. Figure 5.27 also shows that the axial decay of centerline temperature ratio is apparently approaching an $[(x - x_v)/D]^{-2/3}$ decay, while the centerline density ratio is not.

At first glance it may seem as if the centerline density ratio should decay at the same rate as the centerline temperature ratio. However, a simple development using the perfect gas equation of state will show that this is not so, for if

$$\rho = P/RT$$

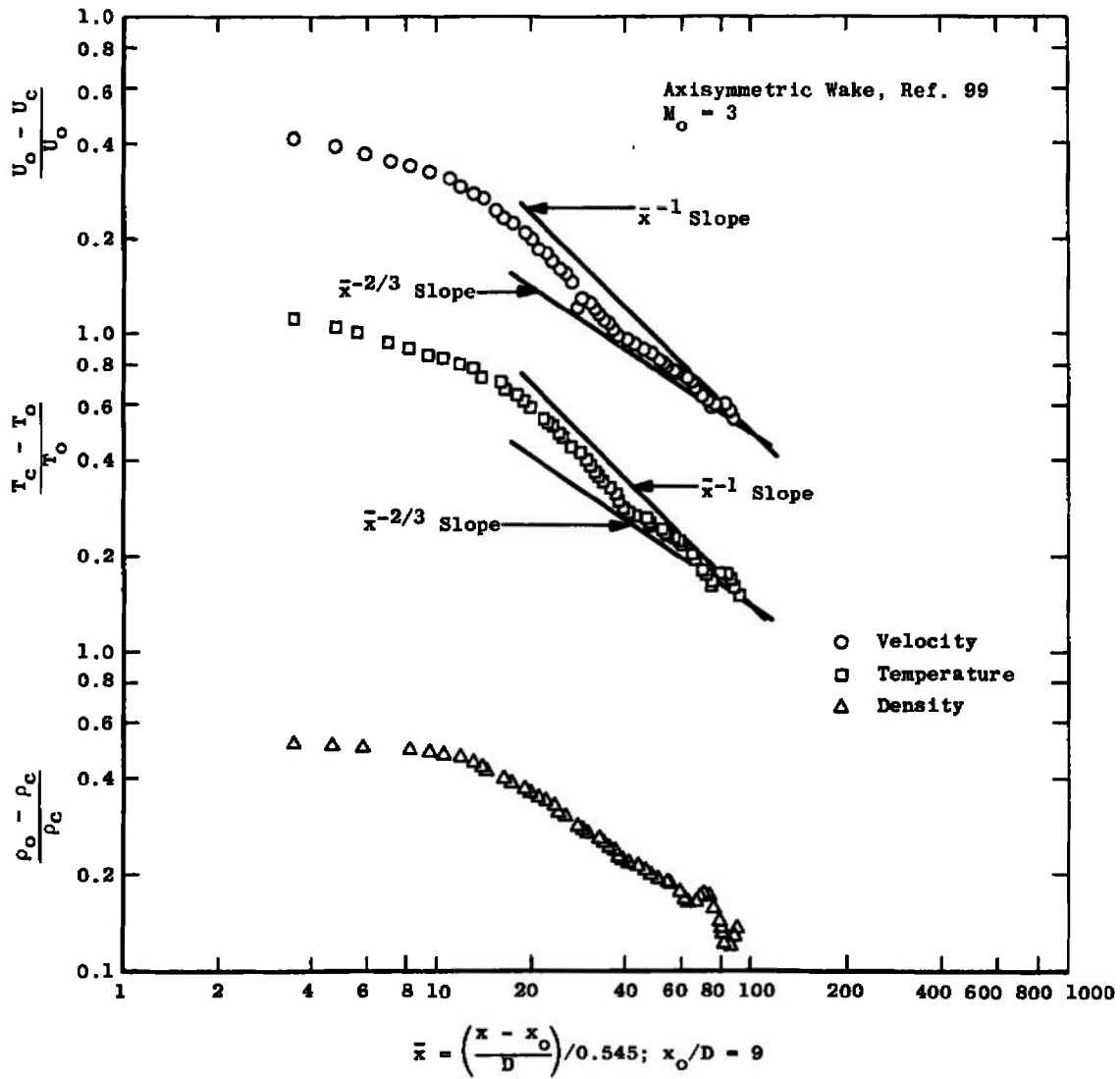


Figure 5.27. Axial decay curves in self-preserving coordinates. Data of Demetriades [99].

then

$$\frac{\rho_o - \rho_c}{\rho_o} = \frac{\frac{P_o}{RT_o} - \frac{P_c}{RT_c}}{\frac{P_o}{RT_o}}$$

assuming constant pressure and gas molecular weight, then

$$\begin{aligned} \frac{\rho_o - \rho_c}{\rho_o} &= \frac{\frac{1}{T_o} - \frac{1}{T_c}}{\frac{1}{T_o}} = \frac{T_c - T_o}{T_c} = \\ &= \left(\frac{T_c - T_o}{T_o} \right) \left(\frac{T_o}{T_c} \right) \end{aligned} \quad (5.5)$$

Thus Equation (5.5) shows that the centerline density ratio decay will behave as the centerline temperature ratio only for $T_o/T_c \approx 1.0$, thus at large x/D .

Demetriades [97] presents fully-normalized lateral velocity ratio and lateral temperature ratio data for a $M_o = 3$ axisymmetric wake for the range $17 \leq x/D < 68.3$. These data are reproduced schematically in Figure 5.28. From this figure it appears that geometric similarity for the temperature profiles is achieved rather quickly while the velocity profiles exhibit considerably more scatter.

The initial region of a compressible wake has been investigated by Zakkay and Fox [96] at $M_o = 3.89$ and by Sinha and Zakkay [100] at $M_o = 3.92$; centerline Mach number data from these investigators is shown in Figure 5.29.

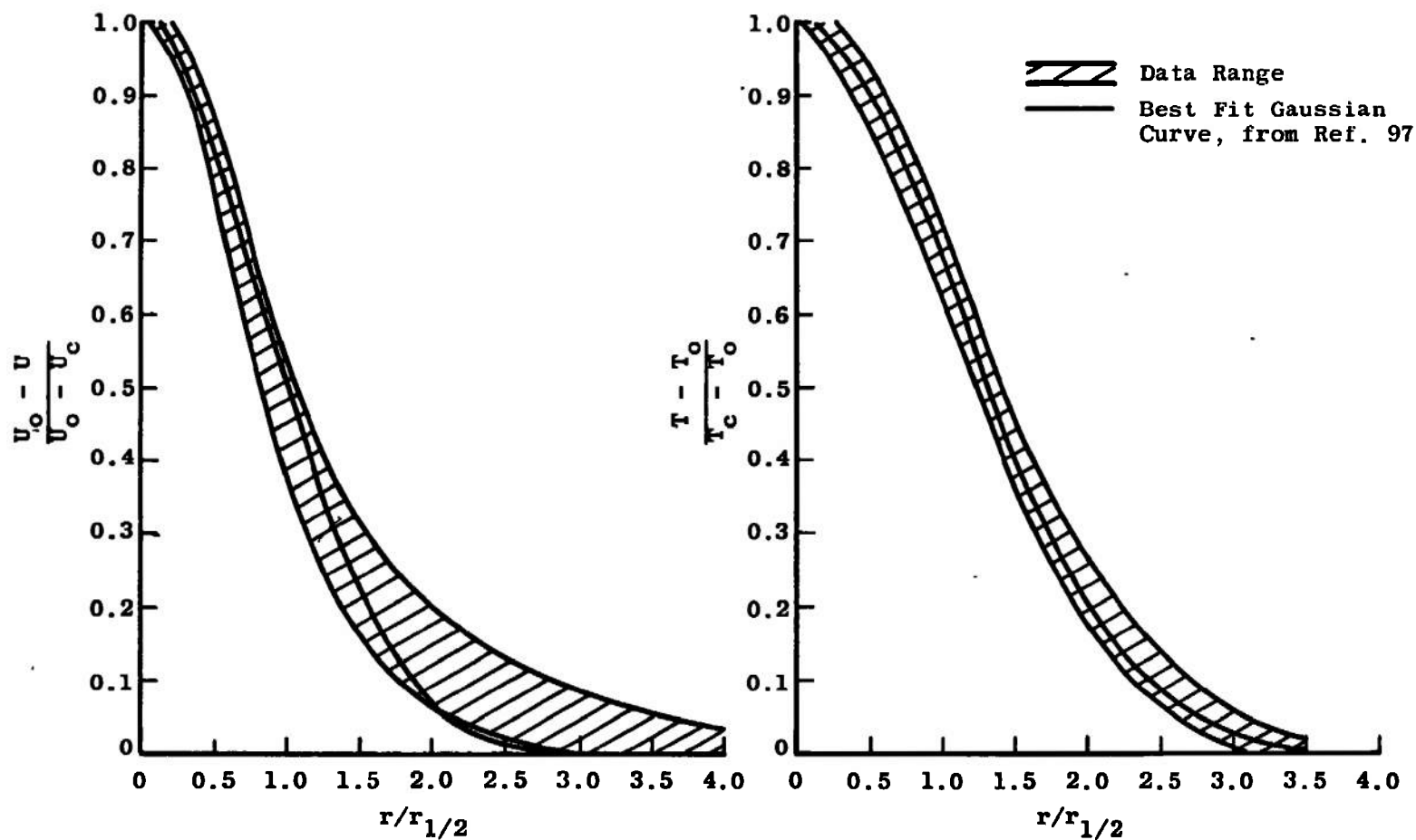


Figure 5.28. Normalized axial velocity and temperature profiles. $M_o = 3$. Axisymmetric wake data from Reference [97], $x/D = 17.00$ to 68.28 .

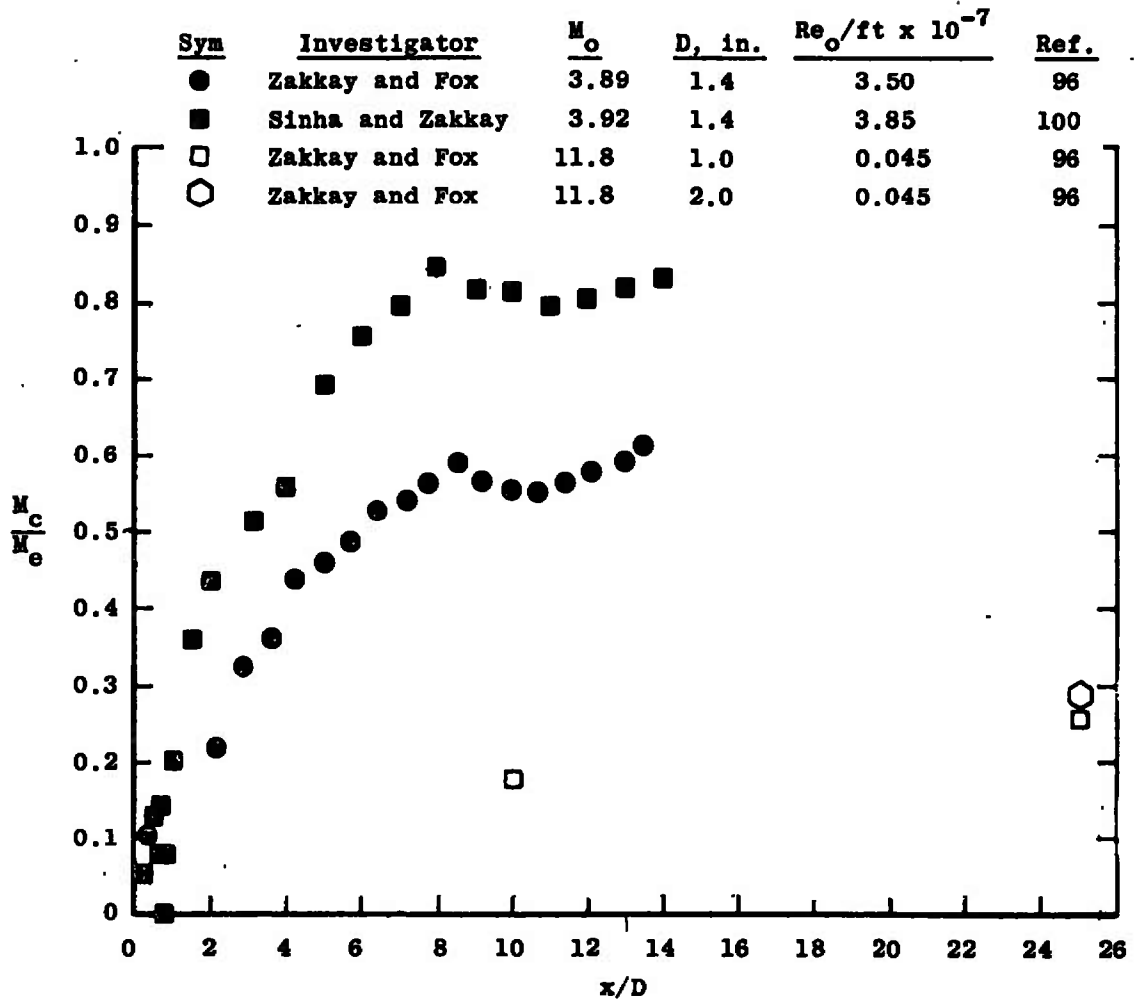


Figure 5.29. Axial increase of centerline Mach number, axisymmetric supersonic wakes.

Sinha and Zakray [100] also report that the centerline velocity ratio decays as x^{-2} in the initial region. Their data are shown on Figure 5.30, along with that of Demetriades [99] for comparison. If it is concluded from Figure 5.30 that the mid-region of the Demetriades data supports an x^{-2} decay of centerline velocity ratio, then Figure 5.30 would also imply that the mixing for Demetriades' data [99] was very much slower than that shown by the data of Sinha and Zakray [100]. This is supported by the increase in free-stream Reynolds number between the two sets of data; an increase in free-stream Reynolds number implies a greater value of the velocity difference $U_o - U_c$ so that the faster mixing indicated by these decay curves seems reasonable.

Summary

Although in many cases the closest to practical configurations, variable-density two-stream flows have not been extensively studied. In large part, this is due to the complexity of the flows involved, which gives rise to the need for complex and sophisticated instrumentation, while on the other hand the sheer number of variable parameters makes it impossible, or at least highly unlikely, to cover the complete range of possible flow conditions.

Again, basically because of its complexity, this category of flows has only been extensively studied in recent years, as the entries in Table 5.1, pages 255-259,

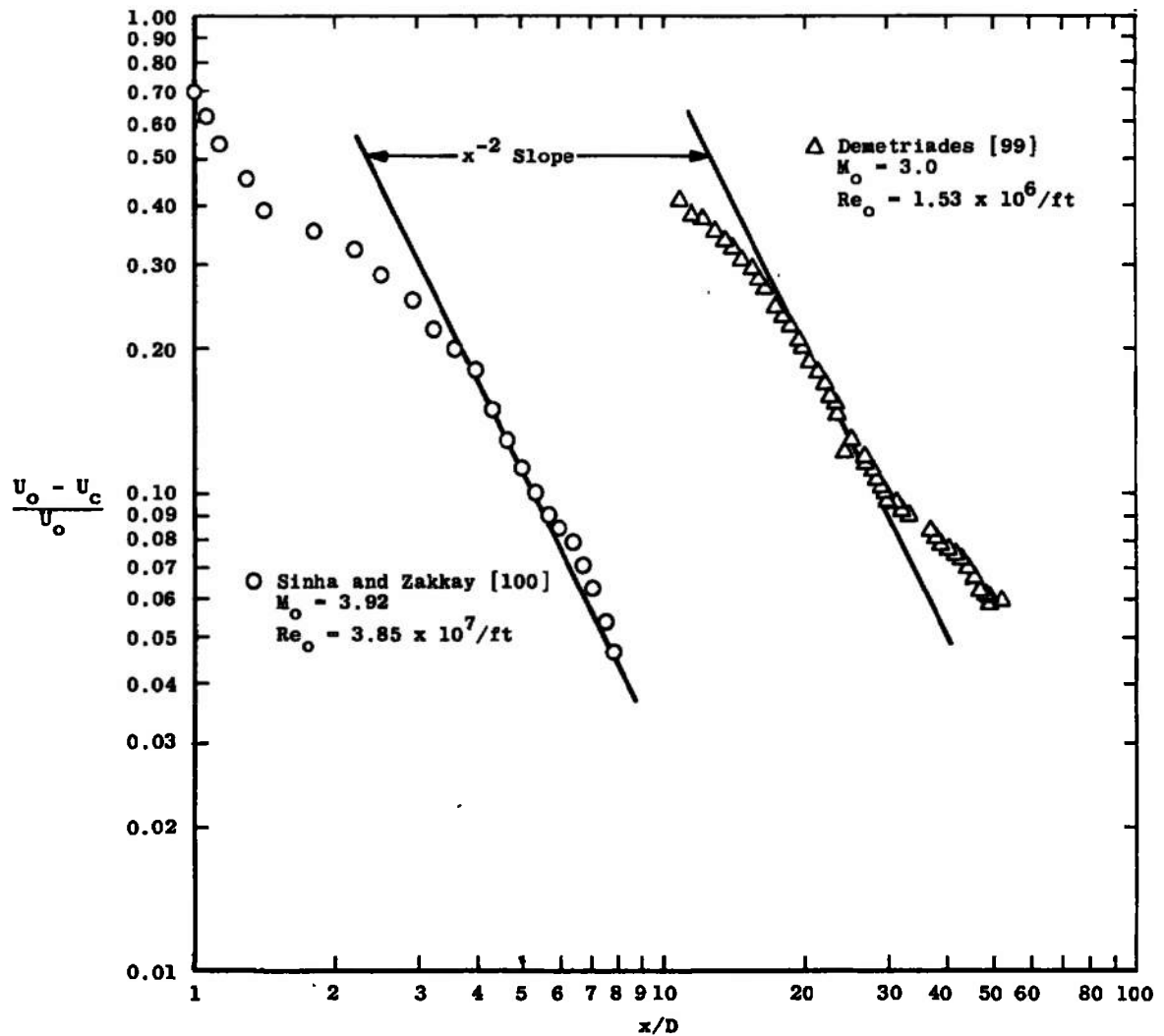


Figure 5.30. Comparison of initial decay curves with x^{-2} decay, axisymmetric compressible wakes.

and Table 5.3, page 302, show. The jet flows listed in Table 5.1, pages 255-259, include supersonic coaxial air jets (one or both streams supersonic) supersonic and subsonic coaxial jets of different gases, and subsonic jets with relatively large gaseous or temperature tracers. The results for the air-air mixing case indicate that for velocity ratios U_o/U_j both greater than and less than 1.0, the centerline velocity ratio $(U_c - U_o)/(U_j - U_o)$ is, outside the potential core, proportional to $(x/D)^{-1}$ [87, 91, 43]--see Figure 5.1, page 261. As there are only two experiments available on compressible coaxial air-air mixing, in both cases with a subsonic jet and a supersonic outer stream, further experimentation would seem to be indicated. There is no available work in which the inner stream is supersonic and the outer stream subsonic, and this lack would seem to require immediate attention.

Experiments on subsonic coaxial streams with temperature or concentration differences between streams, or with both temperature and composition different, have been reported by many investigators [35, 43, 84, 89, 90, 92]. For low speed flows these experiments show that the centerline velocity and temperature ratios both decay as $(x/D)^{-1}$, and that both velocity and temperature profiles show geometric similarity [43]. In cases with large density differences between streams the controlling parameter seems to be the mass flux parameter $\rho_o U_o / \rho_j U_j$; see for example,

Figures 5.8 and 5.9, pages 274 and 276. For low subsonic speeds, both centerline concentration and centerline velocity ratio decay as $(x/D)^{-1}$ (Figures 5.5 through 5.7, pages 269, 270, 275) for $\rho_o U_o / \rho_j U_j < 1$; velocity ratio goes as $(x/D)^{-1}$ for $\rho_o U_o / \rho_j U_j > 1$ also. For coaxial air-air mixing at low speeds, it was seen in Chapter 3 that the length of the velocity potential core increased as the ratio U_o / U_j approached 1.0 from below. In these flows $U_o / U_j = \rho_o U_o / \rho_j U_j$. But for Freon-Air flows, Figure 5.6, page 270, shows a decrease in the length of the potential core as $\rho_o U_o / \rho_j U_j$ increases towards 1.0. Figure 5.8, page 274, shows that for hydrogen-air flow with $\rho_o U_o / \rho_j U_j > 1.0$, the length of the velocity potential core decreases as $\rho_o U_o / \rho_j U_j$ increases. This, however, is consistent with the air-air result, as one might expect the greatest core length for $\rho_o U_o = \rho_j U_j$.

For hydrogen-air the velocity ratio decay is proportional to $(x/D)^{-2}$ --Figure 5.8. Figure 5.9 shows that this is also true for composition. Also for this case [90] radial profiles of velocity and composition show geometric similiarity (Figures 5.10, page 277 and 5.12, page 279). The axial decay of velocity and concentration for CO_2 [84], for $\rho_o U_o / \rho_j U_j > 1.0$, is also proportional to $(x/D)^{-2}$.

Coaxial mixing of two air streams, one subsonic and one supersonic, has been investigated by Eggers and Torrence [91] and by Bluston [87]. Unfortunately, both

experiments have substantial flaws. The behavior of the flow in the potential core region in the investigation of Eggers and Torrence [91] is somewhat strange--the centerline velocity, which is initially lower than the outer stream velocity, at first decreases and then begins to increase. Possibly this phenomenon is a manifestation of something not too unlike the recirculation phenomena discussed before. Another possibility was thought to be expansion of the outer stream caused by an underexpansion of the outer jet in the nozzle, however, as the effect encountered seems to be largest when the outer stream is subsonic, this must be ruled out. Blustøn's experiment [87] suffers from the presentation of the data in terms only of the parameter x/x_c ; the problems with this formulation have been pointed out in the text.

Mixing of two subsonic streams with temperature or composition differences (or both) was studied by Landis and Shapiro [43], temperature differences and trace gas addition; Zawacki and Weinstein [35], Freon-air; Fejer, et al., [92], Freon-air; Alpinieri [84], H_2 -air and CO_2 -air; Chriss [90], H_2 -air; and Ragsdale and Edwards [89], bromine-air. Initial conditions are completely reported only by Zawacki and Weinstein [35] and even in this case the recirculation phenomena discussed in the text cloud the results somewhat. Landis and Shapiro [43] used essentially the same apparatus as did Forstall [40, 41], but avoided some of the problems

involving the duct used evident in Forstall's experiments by limiting the axial traverse to 35 diameters. Fejer, et al., [92] only report complete axial and radial profile data for one condition, while Alpinieri [84] does not present any lateral profiles for his H_2 -air results. Chriss' results [90] are the most complete, including tabulated axial and radial profiles of enthalpy, velocity, and concentration; as well as calculated profiles of turbulent shear stress and eddy viscosity. However, Chriss was unable to get good profile definition in the potential core region.

Coaxial two-gas mixing with one or both streams supersonic was investigated by Zakkay, Krause, and Woo [86], Ferri, Libby, and Zakkay [83], and Zakkay and Krause [85]. The report by Ferri, et al., [83] presents too little data to be of great use, and as is explained in the text, the data that is presented is inconsistent. Somewhat more detail is given by Zakkay and Krause [85], but here only axial decays of centerline composition are given. However, it must in fairness be pointed out that the presentation of mixing data in both References [83] and [85] is incidental to the main purpose of each of these papers.

Considerable data and data correlation is presented by Zakkay, et al., [86]. These results include experiments with several gases, as described in the text. No initial condition data are given, and the results are presented in general in nondimensional form. One of the

conclusions of Zakkay, et al., is that the centerline composition is proportional to $(x/D)^{-2}$. The results of this Chapter show that this is indeed true in all cases for flows with subsonic primary stream and supersonic secondary stream, and for supersonic/supersonic flows. For subsonic/subsonic flows, $C_c \propto (x/D)^{-2}$ appears to be valid for $\rho_o U_o / \rho_j U_j > 1.0$, but for $\rho_o U_o / \rho_j U_j < 1.0$, $C_c \propto (x/D)^{-1}$ (Figures 5.7, page 273 and 5.22, page 294).

Zakkay, et al., [86] also develop a relation for the potential core length (for composition), x_c , as a function of $\rho_o U_o / \rho_j U_j$. As shown in the text, this relationship is not in general satisfactory.

The compressible axisymmetric wake has only been investigated in recent years (Table 5.3, page 302); these investigations have been carried out by Zakkay and Fox [96], Demetriades [97, 99], Fox, Zakkay, and Sinha [98], and Sinha and Zakkay [100], at free stream Mach numbers from 3 to 12. Apart from the evidence presented by Sinha and Zakkay [100] for a velocity decay proportional to $(x/D)^{-2}$ in the initial region of the wake, and the evidence presented by Demetriades [97, 99] for approximate geometric similarity of velocity and temperature profiles, the information on axisymmetric compressible wakes as free mixing flows remains somewhat sketchy.

Compressible coaxial flows are of sufficient importance that a flow of this type should be selected as a

test case for comparison with the predictions of calculation methods. As discussed above, the only experiment for which initial conditions are reported is the Zawacki and Weinstein [35] Freon-air experiment, but this experiment does not include initial shear stress profiles. In any event, it is a sufficiently unusual flow to mitigate against its being used for this study.

The most completely reported two-gas mixing experiment is by far that of Chriss [90] which includes data for eight different mass flux ratios. As this experiment includes shear stress profiles, as well as profiles of velocity, enthalpy, concentration, and other derived parameters, it has been chosen as the coaxial two-gas mixing experiment with which to compare the results of various calculation methods.

CHAPTER 6

LOCALLY-DEPENDENT THEORETICAL MODELS IN
CONSTANT DENSITY FLOWIntroduction

Ever since the derivation of the momentum equation for turbulent flow by Reynolds (see Reference [30], pages 13-24), the fundamental problem of the analysis of turbulent flow has been that of closing the system of governing equations. This is caused by the fact that even in its simplest form the turbulent flow momentum equation contains a "Reynolds stress" term made up of a correlation of the fluctuating components of the turbulent velocity field which acts as an apparent stress. Since the momentum equation is the governing equation for the mean velocity field, the presence of this apparent stress term introduces additional unknowns into the problem, and any equation derived without further assumptions to characterize these unknown quantities will in turn introduce other unknown quantities. One method of closing the system of equations is to formulate models for the turbulent shear stress in terms of already known (or knowable) quantities. This formulation of models can be handled in one of two ways--either some model can be postulated for the turbulent shear stress itself, or, in analogy to a laminar flow, the turbulent shear stress can be

assumed to be given by some effective viscosity multiplied by a local velocity gradient. In practice, models have been developed in both ways, and since an effective viscosity can always be defined as the local shear stress divided by the local velocity gradient, such models can often be used interchangeably.

Both the mixing-length theory of Prandtl, described by Schlichting ([101], page 477) and the vorticity-transport theory of Taylor ([102] and [101], page 482) are attempts to relate the turbulent shear stress directly to the mean flow velocity gradient. By contrast, in Reichardt's inductive hypothesis [103], a direct model for the turbulent shear stress in incompressible flow, \overline{uv} , is avoided by choosing a model for the term $\overline{UV} = (\overline{U}\overline{V} + uv)$. The model used is chosen so as to lead to a form of the governing equation known to have solutions which agree with experimentally measured velocity profiles. Other approaches to the theory of free turbulence involve relating the turbulent shear stress to the kinetic energy. The turbulent kinetic energy, and thus the turbulent shear stress, is then solved for simultaneously with the mean velocity field, using the transport equation for the turbulent kinetic energy. These approaches will be discussed in Chapter 8.

The alternate approach is to relate the turbulent shear stress to the mean velocity gradient through the medium of an effective, or eddy, viscosity. This then

requires some formulation for the eddy viscosity. Such an approach was first described by Boussinesq (see [101], page 475); models for the eddy viscosity itself have been proposed by many investigators. Commonly, the eddy viscosity is taken to be a function of the axial coordinate only, so that the momentum equation takes a form similar to that used in laminar boundary layer analyses. The eddy viscosity may be taken as a locally-dependent quantity, i.e., it may be evaluated at given points in the flow from already-known mean flow quantities. Such locally-dependent eddy viscosity models are discussed in this and the following chapters. Alternately, as is discussed in Chapter 8, a transport equation may be written for the eddy viscosity, to be solved along with other equations describing the flow. However, this equation is an artificial one, while the turbulent kinetic energy equation may be derived from physical principles.

Mixing Length Theory

One of the earliest formulations for the turbulent shear stress is the mixing-length theory developed by Prandtl in 1925. The development of this theory (which is somewhat analogous to the development of simple kinetic theory of gases) is described in detail in many texts, as for example, Schlichting ([101], page 477). Thus only a brief description will be given here.

The fundamental idea of mixing length theory is that turbulent mixing can be thought of as taking place between discrete "lumps" of turbulent fluid. These "lumps" are envisaged as leaving a region of the flow with a velocity (and therefore momentum) characteristic of that region, and then moving a certain lateral distance, called the mixing length, as a discrete particle before suddenly mixing with other fluid of different velocity. The actual mathematical development of this idea is gone into in detail by Alexander, et al., [27] who show that necessary assumptions in the development are that the turbulence intensity and mixing length are isotropic. Since a turbulent shear flow is of course anisotropic, this is a rather crude assumption; it can, however, be rationalized by assuming that the differences between the fluctuating coefficients are of second-order effect compared to the degree of correlation of the shear stress [27].

In its final form, which strictly is valid only for two-dimensional or axisymmetric flow [27], the Prandtl mixing length theory gives the relation

$$\tau = \rho \ell^2 \left| \frac{\partial U}{\partial y} \right| \frac{\partial U}{\partial y} \quad (6.1)$$

where

$$\ell = c.b \quad (6.2)$$

The term ℓ represents the mixing length, c is an empirical constant, and b is a measure of the width of the mixing region. Equation (6.1) has been used in the calculation of a variety of flows, using a number of analytical methods.

Taking for example the jet-into-still-air, if self preservation of the flow is assumed, then all parameters become functions of the variable $\eta = y/x$, and the partial differential equations of motion reduce to ordinary differential equations which may then be solved using analytical or numerical techniques. An approximate analytical solution technique assuming self-preservation was described by Tollmein for the circular jet into still surroundings ([101], page 607), the two-dimensional jet into still surroundings ([101], page 605), and the two-dimensional two stream mixing layer ([101], page 598). Prandtl's mixing length theory was used to evaluate the turbulent shear stress. The two-dimensional wake was handled in the same fashion by Schlichting ([101], page 600), with $c = 0.18$, and the axisymmetric wake by Swain [104] with c left to be empirically evaluated. Acharya [105] recalculated Tollmein's results, for the two-dimensional and axisymmetric cases, using a simplified analysis. Kuethe [106] extended Tollmein's mixing layer solution to the case where the two streams have different velocities, using $\ell = cx$ and $c = 0.0174$.

An alternate approach to the solution of a given free mixing problem is to assume local similarity, i.e., that the dependent variables are functions only of the variable $\zeta = y/b(x)$,⁶ and solve the integrated form of the equation of motion written in terms of ζ . This was done by Kuethe [106] for the initial region of the circular jet into still surroundings, and by Squire and Trouncer [48] for axisymmetric coaxial jets. Kuethe [106] used $c = 0.0705$ (and $\ell = c b$) while Squire and Trouncer [48] chose $c = 0.082$.

Vorticity Transport Theory

As in the mixing length, or "momentum transport" theory, the vorticity transport theory envisages discrete "lumps" of turbulent fluid. However, in the vorticity transport theory these lumps are thought of as transporting vorticity, whereas in the mixing length theory they are considered to transport momentum. This is the key supposition of Taylor's theory [102] which, in its "modified" form also supposes that the vorticity is conserved over a certain mixing length ℓ_T before it is mixed with fluid in a region of different vorticity [107].

A number of the assumptions which underlie the Taylor vorticity transport theory have been brought out by various writers. First, it is assumed that the motion is in

⁶Clearly the assumption of self preservation involves postulating a functional relationship for $b(x)$, while the assumption of local similarity does not.

two dimensions [102] which means ([101], page 483) that all of the vortices in the stream have axes normal to the main flow direction. Then it is assumed that the fluctuating components of the vorticity are isotropic [27]. According to Reference [27], in order to write the turbulent shear stress in terms of a mixing length, it is necessary also to assume that the turbulence intensity is isotropic. The mathematical development of the vorticity transport theory is given in References [101] and [102], and in greater detail in Reference [27]; the result is the expression

$$\tau = \rho \ell_T^2 \left| \frac{\partial U}{\partial y} \right| \frac{\partial U}{\partial y} \quad (6.3)$$

where

$$\ell_T = \sqrt{2} \ell \quad (6.4)$$

(ℓ being the Prandtl mixing length).

The Taylor theory has been used in the solution (in self-preserving coordinates) of the momentum equation for the circular jet by Tomotika [108], for the plane and circular jet by Howarth [109], and it has also been used by Grodzovskiy [110] for coaxial axisymmetric jets.

Both the momentum transport theory of Prandtl and Taylor's vorticity transport theory share the objection raised by Squire [111] that the mixing length, assumed small in the development of the model, is found in the course of

calculation not to be small. In addition, the number of assumptions involved in these models is, especially in the case of Taylor's model, somewhat intimidating. Such considerations have led to interest in other approaches.

The Inductive Hypothesis

The turbulent shear stress model proposed by Reichardt [103] is obtained in an entirely different manner from the models described above; like Taylor's theory (see Reference [101], page 485) it is applicable only to free turbulence. The development of Reichardt's model begins with the observation that the "momentum" profiles $(\overline{\rho U^2})$ observed in free mixing take the form of exponential functions, such as the error function. Thus, he reasons, the partial differential equation describing the free mixing process must have the form of a heat conduction equation, i.e.,

$$\frac{\partial \phi}{\partial x} = K(x) \frac{\partial^2 \phi}{\partial y^2} \quad (6.5)$$

In order that the momentum equation take this form, it is necessary that

$$\overline{UV} = - \Lambda \frac{\partial \overline{U^2}}{\partial y} \quad (6.6)$$

where

$$\begin{aligned}
 \overline{UV} &= \overline{(\bar{U} + u)(\bar{V} + v)} \\
 &= \overline{\bar{U}\bar{V} + u\bar{V} + v\bar{U} + uv} \\
 &= \bar{U}\bar{V} + \overline{uv}
 \end{aligned} \tag{6.7}$$

Note that in this hypothesis no direct model has been used for the turbulent Reynolds stress \overline{uv} . Equation (6.6) is obtained as the form of \overline{UV} necessary to put the time average of the x-momentum equation (neglecting viscosity):

$$\frac{\partial}{\partial x} \left(\frac{P}{\rho} + \overline{U^2} \right) + \frac{\partial}{\partial y} (\overline{UV}) = 0 \tag{6.8}$$

(for constant pressure) into the form of Equation (6.5) as an equation for the parameter $\overline{U^2}$.

A number of calculations of various free mixing flows have been made using Reichardt's inductive hypothesis. Alexander, et al., [27] have used it in the calculation of an axisymmetric jet into still surroundings, Weinstein, et al., [36] for concurrent plane jets, and Vulis, et al., [112] have used the hypothesis in a number of different flows. Recently, its use was reposed by Sforza, et al., [113]. However, the Reichardt hypothesis has been objected to by Prandtl [114] on the grounds that Equation (6.5) overemphasizes the axial variation in the flow at the expense of the lateral variation.

Constant Exchange Coefficient Models

The exchange coefficient models can all be traced back to the original Boussinesq concept mentioned in the introduction to this chapter. The concept of an exchange coefficient is based on the expression for the shear stress in a laminar flow,

$$\tau_L = \rho \nu \frac{\partial U}{\partial y} \quad (6.9)$$

and it is postulated that the turbulent shear stress can be written in terms of an effective exchange coefficient or eddy viscosity so that in a turbulent flow

$$\tau = \rho \epsilon \frac{\partial U}{\partial y} \quad (6.10)$$

The most commonly used eddy viscosity formulation is the model proposed by Prandtl [114] which may be written

$$\epsilon = K_p b |U_{\max} - U_{\min}| \quad (6.11)$$

Here K_p is a constant, b a measure of the width of the mixing region, and U_{\max} and U_{\min} the maximum and minimum values, respectively, of the axial component of the mean velocity. Note that in this formulation, $\epsilon = \epsilon(x)$ only.

The first use of Equation (6.11) in the calculation of free mixing flows was the work of Gortler, described by Schlichting [101]. Gortler's calculations,

based on the assumption of self-preservation, included the two-dimensional free jet boundary ([101], page 598) for which $K_p = 0.014$, with b defined as the width between the point where the velocity is 0.1 of the stream velocity and that where it is 0.9 of the stream velocity, and the two-dimensional jet ([101], page 605), with $K_p = 0.037$, and b the half-velocity width; i.e., the width from the centerline to the point where $U = 1/2 U_c$. He further assumed a linear growth rate, i.e., $b = c.x$. A similar analysis of the circular jet, with $K_p = 0.0256$, is also reported by Schlichting ([101], page 608).

Later calculations using the constant-exchange-coefficient model of Prandtl include the coaxial jet calculations of Szablewski [115] ($K_p = 0.01$) and Weinstein and Todd [116] ($K_p = 0.0047$). Szablewski's analysis assumes local similarity and uses the integral form of the equations of motion while Weinstein and Todd report a numerical solution of the governing partial differential equations. A numerical solution of the governing equations for the mixing of a round cold-air jet with ambient hot air at rest is also performed in a later work by Szablewski [117] in which K_p is taken to be 0.0082 in the first regime and 0.0085 in the second. The papers listed here do not by any means cover the entire range of reports of calculations using the Prandtl eddy viscosity model; they are, however, representative.

Other constant-exchange coefficients models have been proposed. One such is that proposed by Pai and used by Chapman and Korst [118], in which the eddy viscosity is written as

$$\epsilon = \epsilon_0 \left(\frac{x}{L}\right)^n \quad (6.12)$$

where ϵ_0 is a constant and L a length scale. In their analysis, Chapman and Korst [118] find that for a two-dimensional shear layer, in the range $1 < x/\delta_0 < 10$ (δ_0 being the initial boundary layer thickness), $n = 0.7$. However, ϵ_0 is found to depend on the initial conditions.

Summary

Of the shear stress and eddy viscosity models proposed for use in incompressible flow calculations, the two credited to Prandtl are by far the most commonly used. These are the mixing length theory, Equation (6.1), and the Prandtl eddy viscosity model, Equation (6.11). Taylor's vorticity transport theory, Equation (6.13) as Alexander, et al., [27] point out, requires many more assumptions than the Prandtl mixing length model without any apparent increase in validity.

Reichardt's inductive hypothesis, Equation (6.3), is no longer as attractive as it once was, as the availability of large scale computing machines removes the advantages of using a heat-conduction type equation.

Further, Equation (6.6) involving as it does an empirical relationship for both the Reynolds stress \overline{uv} and the cross velocity product \overline{UV} seems to the author to be suspect. This, and the fact that the consistent use of the Reichardt hypothesis involves the use of a heat-conduction equation rather than the boundary-layer form of the momentum equation used elsewhere in this work, rule out the use of the Reichardt hypothesis in this study. Pai's model, from the work of Chapman and Korst [118], does not seem to the author to be of a generally useful nature.

Thus the mixing length theory and the Prandtl eddy viscosity model will be used in this study. As the discussions above have shown, the values of the constants used in these models vary from investigator to investigator. One of the ground rules of this study is that the same constants must be used in all calculations, and it might seem that the choice of constant would be difficult to make. In actual fact, however, the choice is not very critical, since a wide enough range of experimental conditions is being used to give each model selected a good chance of representing the experimental results for some flow. The constant selected for use with the Prandtl mixing length, Equation (6.1), is $c = 0.082$, as was obtained by Squire and Trouncer [48] from an experiment on a circular jet into still surroundings, and used in their calculations of coaxial mixing.

For use with the Prandtl eddy viscosity model, the set of constants used by Peters [119] will be used here. Thus, for regime I, $K_p = 0.007$ while in regime II, $K_p = 0.011$. It is worth noting that for the cosine profiles that Peters [119] used in his integral analysis in the second regime of mixing, the constant $K_p = 0.011$ used with the Prandtl eddy viscosity model predicts the same value of τ at the half-velocity point as does the constant $c = 0.082$ used in the Prandtl mixing length model.

CHAPTER 7

LOCALLY-DEPENDENT THEORETICAL MODELS IN
VARIABLE DENSITY FLOWIntroduction

As problems in which turbulent mixing occurs between two streams of different densities are of great practical importance, the development of shear stress and eddy viscosity models for use in a variable density flow has been of considerable interest. The most obvious approach is to take one of the models described in Chapter 6 and simply apply it directly, perhaps with a change in constant, to a variable density flow. This method has not been very successful, which has led to the investigation of other models.

There are four approaches that can be taken to the establishment of shear stress models in a variable-density flow. The direct one is to attempt to develop a model for variable-density flows by correlating variable-density flow experimental data. Such an approach has been used by Ferri, et al., [83], Alpinieri [84], and Zakkay, et al., [86]. In each case the result is a modification to a constant-density model, which reduces to the appropriate form for constant density flow. Another approach is to attempt to derive a model in such a manner that the effects of variable-density

are included, so that both constant-density and variable-density flows can be calculated. The displacement thickness model developed by Schetz [120, 121] falls into this class. The empirical constant established in this model is evaluated in an incompressible flow and it is expected to apply to variable-density flow as well.

In the third approach to models for the eddy viscosity in a variable-density flow an incompressible eddy viscosity model is made applicable to a compressible flow by the use of an empirical correction factor, commonly related to some characteristic Mach number. Examples of such correction factors and their use are given by Warren [70], Donaldson and Gray [67], and Peters [119].

The fourth approach is to attempt to find a transformation of the compressible-flow governing equations that will convert them to the appropriate constant-density form. The transformed equations can, in principle, then be solved using an eddy viscosity model developed for constant-density flow, and the results transferred back into physical coordinates. Commonly the time-averaged equations of motion are transformed into an incompressible form using the Howarth transformation [122], but it has been suggested [123] that the transformation be applied to the instantaneous equations and the resulting equation time-averaged. Solutions using such transformations have been obtained by Channapragada and Wooley [124] and Libby [125] among others.

Ferri Eddy Viscosity Model

The development of the Ferri model for the eddy viscosity proceeds from the realization that the Prandtl eddy viscosity model, Equation (6.11), predicts that no mixing will take place when the streams are of equal velocity, even if substantial temperature or density differences exist between the streams. Quoting Reference [83], "this is not consistent with the fact that in these cases a dissipative mechanism still exists due to heat conduction or concentration changes that would sustain turbulence." To circumvent this problem, Ferri, et al., [83] propose the modified model

$$\rho \epsilon = (\rho \epsilon)_c = K_F r_{1/2} |\rho_o U_o - \rho_c U_c| \quad (7.1)$$

where $r_{1/2}$ is the radial location at which

$$\rho U = \frac{1}{2} [\rho_c U_c + \rho_o U_o] \quad (7.2)$$

Ferri, et al., recommended for K_F a value of 0.025. Note from Equation (7.1) that the Ferri model requires that $\rho \epsilon = \text{constant}$ laterally; i.e., that the product $\rho \epsilon = \rho \epsilon(x)$ only.

Alpinieri Eddy Viscosity Model

In his experiments, Alpinieri [84] established a flow in which the ratio $\rho_o U_o / \rho_c U_c$ was near unity. For this

case, the Ferri model, Equation (7.1) predicts a vanishing eddy viscosity coefficient, yet Alpinieri's experiment indicated substantial mixing. Since both the Prandtl model, Equation (6.11), and the Ferri model, Equation (7.1), were known to give reasonably good results for some flows, Alpinieri reached the conclusion that the proper eddy viscosity formulation must contain a term that becomes important when $U_o = U_c$ and $\rho_o U_o = \rho_c U_c$. This reasoning, coupled with a correlation of his experimental results, led Alpinieri to an eddy viscosity formulation given by the equation:

$$\rho \epsilon = (\rho \epsilon)_c = K_A r_{1/2} \rho_o (U_c + \frac{U_o^2}{U_j}) \quad (7.3)$$

where U_j is the primary jet velocity and $r_{1/2}$ is the radius at which $U = 1/2 (U_c + U_o)$. Alpinieri reported a value for K_A of 0.025. Again note that the formulation implies that the product $\rho \epsilon$ is a function only of x .

Zakkay Eddy Viscosity Model

Zakkay, et al., [86] obtained an asymptotic form for the eddy viscosity through use of an asymptotic, linearized solution of the transformed governing equations with turbulent Prandtl and Lewis numbers of unity. The solution used was that obtained by Libby [125]; one of the necessary assumptions of this solution is that $\epsilon = \epsilon(x)$ (in

the incompressible, transformed plane). This asymptotic solution and the requirement that the potential core length x_c/r_j , be given by the expression

$$x_c/r_j = K[\rho_j U_j / \rho_o U_o]^{1/2} \quad (7.4)$$

led to an asymptotic eddy viscosity form

$$\epsilon = K_z r_{1/2} U_c \quad (7.5)$$

where $r_{1/2}$ is the half velocity radius, and $K_z = 0.011$ [86]. Two things ought to be mentioned in regard to Equations (7.4) and (7.5): first, that the potential core x_c is the concentration potential core length which is equal to the velocity potential core length only under the assumption that the turbulent Prandtl and Lewis numbers are unity; secondly, Equation (7.4) itself is not entirely accurate--see the discussion of this relationship in Chapter 5. It should also be noted that Equation (7.5) indicates $\epsilon = \text{constant laterally; i.e., } \epsilon = \epsilon(x)$.⁷

Schetz Displacement Thickness Model

Taking a different approach than those described

⁷To be strictly accurate, Equation (7.5) is obtained in Reference [86] using an analysis which evaluates the eddy viscosity only along the centerline. No restriction on Equation (7.5) is stated in Reference [86], and it has been assumed herein that it can be used throughout the flow field.

above, Schetz [120, 121] sets up a model that incorporates the effect of density variations in a more fundamental manner. After noting that for a planar flow, the Prandtl model, Equation (6.11), and the Clauser model

$$\epsilon = 0.018 U_o \delta^* \quad (7.6)$$

where δ^* is the displacement thickness

$$\delta^* = \int_{-\infty}^{\infty} \left| 1 - \frac{U}{U_o} \right| dy \quad (7.7)$$

are equivalent, Schetz proposes an extension of the Clauser model to a compressible flow simply through an extension of the definition of the displacement thickness, which becomes

$$\delta^* = \int_{-\infty}^{\infty} \left| 1 - \frac{\rho U}{\rho_o U_o} \right| dy \quad (7.8)$$

and so

$$\rho \epsilon = K_c \rho_o U_o \delta^* \quad (7.9)$$

That the incompressible Clauser model is equivalent to the Prandtl eddy viscosity for a planar flow is easily shown. Consider for example a planar wake. It is shown in Chapter 3 that for such a wake, the velocity profiles may be written

$$\frac{U_o - U}{U_o - U_c} = f(\eta)$$

where

$$\eta = y/b(x)$$

Then

$$\begin{aligned} \delta^* &= b(x) \int_{-\infty}^{\infty} \left| 1 - \frac{U}{U_o} \right| d\eta = b(x) \int_{-\infty}^{\infty} \left| \frac{U_o - U}{U_o} \right| d\eta \\ &= b(x) \left| \frac{U_o - U_c}{U_o} \right| \int_{-\infty}^{\infty} f(\eta) d\eta \\ &= K_b \left| \frac{U_o - U_c}{U_o} \right| \end{aligned}$$

so that from the Clauser model

$$\epsilon = K_2 b |U_o - U_c| \quad (7.10)$$

which is formally the equivalent of the Prandtl model, Equation (6.11).

All this, however, suffices only for planar flow. For axisymmetric flow the compressible displacement thickness must be redefined. This Schetz does, defining a new displacement thickness by the equation

$$\pi \rho_o U_o \delta_r^{*2} = \int_0^{\infty} |\rho_o U_o - \rho U| 2\pi y dy \quad (7.11)$$

and the new eddy viscosity model becomes

$$\mu_T(x) = \rho \varepsilon = \frac{K_S}{r_j} (\rho_o U_o \pi \delta_r^{*2}) \quad (7.12)$$

for $K_S \pi$, Schetz gives the value 0.018.

One objection to this can immediately be raised, which is that the definition of δ_r^{*2} is (as it must be) indeterminate for the jet-into-still-air. Moreover, if one assumes similar profiles of the form

$$\frac{U-U_o}{U_c-U_o} = f(\eta)$$

where (7.13)

$$\eta = y/b(x)$$

then (7.11) becomes for incompressible flow

$$\begin{aligned} \pi U_o \delta_r^{*2} &= |U_c - U_o| \int_0^{\infty} \left| \frac{U - U_o}{U_c - U_o} \right| 2\pi y dy \\ &= |U_c - U_o| b^2 \int_0^{\infty} f(\eta) 2\eta d\eta \\ &= K_3 |U_c - U_o| b^2 \end{aligned}$$

so that

$$\mu_T(x) = \rho \epsilon = \frac{K_S K_3}{r_j} \rho b^2 |U_C - U_O|$$

which, for a given flow, implies

$$\epsilon = c_1 b^2 |U_C - U_O| \quad (7.14)$$

whereas the Prandtl model, Equation (6.11), states

$$\epsilon = K_P b |U_C - U_O| \quad (7.15)$$

Thus, for $U_O \rightarrow 0$, where models such as Equation (7.15) are known to provide good results, Equation (7.12) will clearly predict an eddy viscosity which will increase too rapidly as the mixing zone thickness increases.

Compressibility Corrections

The "compressibility correction" approach to the problem of obtaining an eddy viscosity model valid for a variable-density flow assumes that the influence of variable density in the mixing layer can be accounted for by correcting the empirical constant in an incompressible eddy viscosity model. This correction--to the constant K_P in the Prandtl eddy viscosity model--was evaluated by Donaldson and Gray [67]; their evaluation was extended by Peters [119]. Donaldson and Gray found that the influence of variable

density in the mixing layer could be generalized if the constant K_p was taken to be a function of the Mach number at the half-velocity radius, M_m . Peters [119] extended the correlation and found a curve-fit for it: if K_{p_0} is the value of the constant in the Prandtl eddy viscosity model for constant-density flow, then

$$\frac{K_p}{K_{p_0}} = 0.66 + 0.34 \exp(-3.42 M_m^2) \quad (7.16)$$

Compressibility Transforms

For Prandtl number of unity and for viscosity variation proportional to temperature, it is well known that the laminar, compressible boundary layer form of the equation of motion for zero pressure gradient can be transformed to the incompressible form by defining a new lateral coordinate Y by the equation

$$Y = \int_0^y \rho/\rho_0 dy \quad (7.17)$$

where y represents the physical lateral coordinate. This is the Howarth transformation for a laminar boundary layer.

Although the application of the Howarth transformation directly to the instantaneous equation of motion has been proposed by Snyder [123], in general the application of the Howarth transformation to turbulent flow has followed

the approach of Mager [122] in which it is applied to the time-averaged equations, coupled with some assumptions regarding the invariance of the shear stress.

Application of the Howarth transformation leads to equations for the transformation of the eddy viscosity which are different for two-dimensional or axisymmetric flows. These expressions, which were first developed by Ting and Libby [126], are derived in Appendix D. The results are:

Two-Dimensional Flow

$$\rho^2 \epsilon = \rho_o^2 \epsilon^* \quad (7.18)$$

where the asterisk refers to the incompressible eddy viscosity and ρ_o is a reference density, and

Axisymmetric Flow

$$r^2 \rho^2 \epsilon = 2 \rho_o^2 \epsilon^* \int_0^r \left(\frac{\rho}{\rho_o} \right) r' dr' \quad (7.19)$$

where the asterisk and ρ_o have the same meanings as above. In both cases, r , ρ and ϵ refer to the radius, density, and eddy viscosity in the compressible flow. Both Equation (7.18) and (7.19) involve the definition of a reference density. The choice of this reference density is one of the more important problems of the transformation theory, as the lateral and axial variation of the transformation depends on the definition. Unfortunately, theory gives no guidance for the choice.

A two-dimensional compressible flow solution using Equation (7.18) has been performed by Channapragada and Woolley [124]. In two-dimensional flow, Deverall and Channapragada [127] have shown that the assumption regarding the invariancy of the shear stress under the transformation (see Appendix D) is superfluous, as under the Howarth transformation the shear stress

$$\tau = \int_0^y [\rho U \frac{\partial U}{\partial x} + \rho V \frac{\partial U}{\partial y}] dy + A_0(x)$$

is invariant across any axial section.

The Ting and Libby form of the eddy viscosity for axisymmetric flow has been used by Libby [125] in a linearized analysis of free mixing processes. It has also been used by Kleinstein [128] in a similar analysis.

Summary

It is interesting to note that the five models proposed in this section for the calculation of a variable density flow (discounting for the moment the Donaldson and Gray correction) incorporate three different expressions for the variation of ϵ . Thus, the Ferri model [83] and the Alpinieri model [84] require that the product $\rho\epsilon$ be constant laterally while the Zakkay model [86] implies that ϵ is constant laterally. The Schetz model again requires that $\rho\epsilon$ be constant laterally, but the two-dimensional Ting-Libby transform says that given $\epsilon = \epsilon(x)$ in the incompressible

flow, then $\rho^2 \epsilon$ is constant laterally for the compressible flow. This prescription does not hold for axisymmetric flow under the Ting-Libby transform, as Equation (7.19) shows. It seems curious that the axisymmetric Ting-Libby transform does not reduce to the two-dimensional transform. However, as shown in Appendix D, different assumptions are required in the derivation of each version.

Since the practical effects of the various eddy viscosity formulations are of interest in this study, the Ferri model, Equation (7.1), the Alpinieri model, Equation (7.3), the Zakkay model, Equation (7.5), and the Schetz model, Equation (7.9) will all be compared in detail to the range of selected experiments. The Donaldson and Gray correction [67] is primarily of interest at higher Mach numbers than are included in this study; however, calculations for a few flows were made using this correction.

Libby [125] gives a solution in terms of tabulated functions for a general coaxial mixing flow using the Prandtl eddy viscosity model, through use of the Ting-Libby eddy viscosity transformation under the assumption that the Prandtl and Lewis numbers are both unity. The solution is in the transformed plane; to get back to the compressible plane the transform must be inverted using the parameters of the particular experiment in question. As part of this study, a computer program has been written to perform this inversion. The mathematical details of the program follow

Libby [125]. The results of these calculations for several of the hydrogen-air experiments of Chriss [90] will be compared with the results obtained through use of other eddy viscosity models.

CHAPTER 8

HISTORY-DEPENDENT THEORETICAL APPROACHES

Introduction

In recent years methods of calculating turbulent flows which involve the consideration of the physical mechanism by which the turbulent shear stress is created have become of interest. The reason for this interest has been well put by Bradshaw [129] with reference to boundary layer flow; his statement also holds true for free mixing flows:

No great advance in boundary-layer prediction can be made without in some way considering the mechanism by which turbulent shear stress is produced, and in particular allowing for the fact that the shear stress at a point depends on the upstream history of the flow and not only the local mean flow, because the lifetime of the stress-producing eddies may be many times the boundary layer thickness.

Two ways of including the history of the flow in computing its development have been described to date. One method, described by Nee and Kovasznay [130], involves the development of a rate equation for the turbulent eddy viscosity. This rate equation is then solved simultaneously with the other equations describing the flow. The other approach is to use the turbulent kinetic energy equation as a means of obtaining the turbulent shear stress. The

rationale for this approach is also described by Bradshaw [129]:

The shear stress is almost a by-product of the turbulent fluctuations and it seems inevitable that to derive the shear stress we require some knowledge of the processes which determine the turbulent intensity together with a relation between the intensity and the shear stress. The chief merit of examining the turbulent intensity rather than the shear stress is that turbulent intensity amounts to a kinetic energy per unit mass of the fluctuation and obeys a conservation equation which is more tractable than the related Reynolds equation for the shear stress. . . .

This method clearly requires that a relationship exist between the turbulent shear stress and the turbulent kinetic energy. The data described in Chapters 2 and 3 show that a relation does exist between these two quantities; other evidence is to be found in References [12], [55], and [132]. The existence of such a relationship and the availability of high-speed computing machines have stimulated interest in this approach, as is evidenced by the work of Bradshaw, et al., [55] on boundary layer flows, and Laster [131] and Lee and Harsha [132] on free mixing flow.

Eddy Viscosity Rate Equation

As will be discussed in the following section, the formulation of the turbulent kinetic energy equation as developed by Bradshaw, et al., [55] and Laster [131] requires the specification of three empirical relationships, one for the diffusion of turbulent kinetic energy, one for the dissipation of turbulent kinetic energy, and one for

the relationship between the turbulent shear stress and the turbulent kinetic energy. The approach used by Lee and Harsha [132] specifies the form of the diffusion function, but this method then requires the specification of a diffusion coefficient for the turbulent kinetic energy. Nee and Kovaszny [130] devise a rate equation for the turbulent eddy viscosity which involves only two empirical constants, but which, like the turbulent kinetic energy approach, includes the past history of the flow, through the medium of a convective term.

Nee and Kovaszny start by defining a turbulent eddy viscosity using the expression

$$\epsilon = \frac{\overline{uv}}{\partial U / \partial y} \quad (8.1)$$

In this formulation ϵ is a scalar quantity. They next note that in general, any transportable scalar quantity F subject to the conservation laws is transported according to the equation

$$\frac{\partial F}{\partial t} + (\underline{U} \cdot \underline{\nabla}) F = \underline{\nabla} \cdot \phi_F + \text{production} - \text{decay} \quad (8.2)$$

where the underscore indicates a vector quantity and the term ϕ_F represents the flux of F due to diffusion. Assuming that the total turbulent viscosity $n = \epsilon + \nu$ is also a transportable scalar quantity that obeys the conservation

laws and that the turbulent motion diffuses by itself, so that the diffusion coefficient for n is n , then Equation (8.2) becomes

$$\frac{\partial n}{\partial T} + (\tilde{U} \cdot \tilde{\nabla}) n = \tilde{\nabla} \cdot (n \tilde{\nabla} n) + G - D \quad (8.3)$$

Expressions for the production term G and the decay term D are also devised by Nee and Kovaszny. The chosen expressions are

$$\left. \begin{aligned} G &= A(n-v) \left| \frac{\partial U}{\partial y} \right| \\ D &= \frac{B}{L^2} n(n-v) \end{aligned} \right\} \quad (8.4)$$

where A and B are universal constants and L is a length scale which depends on the flow. The resulting system of equations solved by Nee and Kovaszny [130] are

$$U \frac{\partial U}{\partial x} + V \frac{\partial U}{\partial y} = - \frac{1}{\rho} \frac{dP}{dx} + \frac{\partial}{\partial y} \left(n \frac{\partial U}{\partial y} \right) \quad (8.5)$$

$$\frac{\partial U}{\partial x} + \frac{\partial V}{\partial y} = 0 \quad (8.6)$$

$$\begin{aligned} U \frac{\partial n}{\partial x} + V \frac{\partial n}{\partial y} &= \frac{\partial}{\partial y} \left(n \frac{\partial n}{\partial y} \right) + A(n-v) \left| \frac{\partial U}{\partial y} \right| - \\ &\quad - \frac{B}{L^2} n(n-v) \end{aligned} \quad (8.7)$$

which embody the assumption of two-dimensional steady quasi-parallel flow.

Solutions of Equations (8.5) and (8.6) were obtained in Reference [130] for several turbulent boundary layer flows, with reasonable results. However, at the recent Stanford Symposium [133] the Nee and Kovasznay approach did not compare favorably with other approaches--including the kinetic energy calculations of Bradshaw, et al., [55]. In fairness, the unfavorable rating given this method was primarily a result of excessive computing time, which may be correctable.

A more fundamental objection to the Nee and Kovasznay method is that it is essentially a sophisticated technique for obtaining an imaginary quantity. The production and dissipation terms cannot be based on physical arguments, as they can, at least in principle, when the turbulent kinetic energy equation is used to evaluate the turbulent shear stress, for the turbulent eddy viscosity is an imaginary quantity. Thus, the economy of having only two empirical constants seems to the author to be offset somewhat by the lack of any real physical knowledge of two of the terms of the governing equation. Again in fairness, however, it will be seen below that the terms of the kinetic energy equation are themselves only loosely related to the physics of the flow.

The Turbulent Kinetic Energy Approach

In order to use the turbulent kinetic energy equation to calculate the turbulent shear stress in a free mixing problem, it is necessary that there exist a relationship between the turbulent shear stress and the turbulent kinetic energy. One such relation was proposed by Glushko [134] and by Patankar and Spalding [135]; it involves defining an eddy viscosity by the equation:

$$\mu_T = \ell_k \rho \bar{k}^{1/2} \quad (8.8)$$

where $k = 1/2[u^2 + v^2 + w^2]$, and ℓ_k is a length scale for the turbulent kinetic energy. The overscore represents a time average. The turbulent shear stress is then given by

$$\tau = \ell_k \rho \bar{k}^{1/2} \frac{\partial U}{\partial y} \quad (8.9)$$

A more direct relation was described by Dryden [136] in discussing the work of Nevzgljadov. This relationship, which relates the shear stress directly to the turbulent kinetic energy,

$$\tau = a_1 \rho \bar{k} \quad (8.10)$$

where a_1 may be a function of the lateral coordinate, has been used by Bradshaw, et al., [55], Laster [131], and Lee and Harsha [132]. A correlation of this relationship with

available experimental data has been carried out by Harsha and Lee [12]. This correlation shows that (1) a_1 can be considered to be constant over a significant lateral region in any given flow, and that (2) in the region where it can be considered constant, a value of 0.3 is appropriate. As implied by (1) and (2) above, there is a lateral variation of a_1 . Equation (8.10) implies that the shear stress is always of the same sign as the kinetic energy. However, it is known that at the centerline of a symmetric flow the turbulent shear stress is zero, while the turbulent kinetic energy is not, and that there exist flows, such as jets, in which the turbulent shear stress is negative while the kinetic energy is positive. The modification of Equation (8.10) to account for these regions has been handled differently by different investigators. Thus, Bradshaw, et al., [55], being concerned with a boundary layer flow in which the shear stress is positive and drops to zero only where the kinetic energy does also, were able to assume a constant value of a_1 , equal to 0.3, with the definition of a_1 used here. Laster [131] and Lee and Harsha [132] on the other hand were both faced with both regions of zero shear stress and nonzero kinetic energy and with regions of negative shear. Laster [131] chose to handle the former problem with an empirical (polynomial) fit for the radial variation of a_1 , so that

$$a_1 = \text{constant} \cdot f\left(\frac{r}{b}\right) \quad (8.11)$$

where $f(r/b) = 0$ for $r = 0$. Laster did not consider problems in which the sign of the shear stress changed; thus he was able to arbitrarily establish the sign of a_1 before starting a calculation. Lee and Harsha [132], on the other hand, chose to give the turbulent shear stress the same sign as the velocity gradient, and to model the radial variation of a_1 in terms of the velocity gradient so that, for axisymmetric flow

$$\left. \begin{aligned} a_1 &= 0.3 \frac{\partial U}{\partial r} / \left| \frac{\partial U}{\partial r} \right|_{\max} & 0 \leq r \leq r_m \\ a_1 &= 0.3 \frac{\partial U}{\partial r} / \left| \frac{\partial U}{\partial r} \right| & r_m < r \end{aligned} \right\} \quad (8.12)$$

where $\left| \partial U / \partial r \right|_{\max}$ is the maximum value of the velocity gradient in a profile and r_m is the radial location of this maximum. For planar flow, the correction was applied only near maxima or minima within the profile where $\partial U / \partial y \approx 0$, so that

$$\left. \begin{aligned} a_1 &= 0.3 \frac{\partial U}{\partial y} / \left| \frac{\partial U}{\partial y} \right|_{\max} & \frac{\partial U}{\partial y} \approx 0 \\ a_1 &= 0.3 \frac{\partial U}{\partial y} / \left| \frac{\partial U}{\partial y} \right| & \text{elsewhere} \end{aligned} \right\} \quad (8.13)$$

The region in which the correction was applied ordinarily encompassed of the order of 5% of the total mass flow of the stream.

Given some relationship between the turbulent shear stress and the turbulent kinetic energy, the problem becomes one of establishing the appropriate form of the turbulent kinetic energy equation. Using the turbulent kinetic energy equation to evaluate the Reynolds stress term of the momentum equation does not itself solve the turbulent closure problem. Indeed, the turbulent kinetic energy equation incorporates two terms involving unknown quantities and their derivatives. In block diagram form the turbulent kinetic energy equation can be written, for steady flow, as

$$\begin{aligned} \text{CONVECTION} = \text{DIFFUSION} + \text{PRODUCTION} - \\ - \text{DISSIPATION} \end{aligned} \quad (8.14)$$

or, in words, the net convection of turbulent kinetic energy through a volume element in the fluid is equal to the diffusion of turbulent kinetic energy into the volume plus the production of turbulent kinetic energy in the volume minus the amount of turbulent kinetic energy dissipated (by viscosity, into heat) within the volume. The formal representation of the terms of Equation (8.14) can be obtained from the time-averaged turbulent momentum equation in a rigorous manner. Thus, Hinze [30] shows that (using Cartesian tensor notation)

$$\text{CONVECTION} = U_i \partial \bar{k} / \partial x_i$$

$$\text{DIFFUSION} = - \frac{\partial}{\partial x_i} \left[\overline{u_i \left(\frac{P}{\rho} + k \right)} \right] + \nu \frac{\partial^2 \bar{k}}{\partial x_i \partial x_i} \quad (8.15)$$

$$\text{PRODUCTION} = - \overline{u_i u_j} \frac{\partial u_j}{\partial x_i}$$

$$\text{DISSIPATION} \approx \nu \overline{\frac{\partial u_j}{\partial x_i} \frac{\partial u_j}{\partial x_i}}$$

where the last term is strictly equal to the dissipation only for an isotropic flow. The lower case letters refer to turbulent fluctuations, while upper case indicates mean flow values. The convection and production terms give no problems, as they are both defined in terms of known (or knowable) quantities. However, some approximations must be made for the diffusion and dissipation terms to get them into a form suitable for computation.

All approaches to date that use the turbulent kinetic energy equation have used essentially the same form for the term representing the dissipation of turbulent kinetic energy. This term, which is recommended by Patankar and Spalding [135] as "in accordance with dimensional analysis," is:

$$\text{DISSIPATION} = \frac{a_2 \rho \bar{k}^{3/2}}{\ell_k} \quad (8.16)$$

where a_2 is a parameter which may vary spatially and ℓ_k is a

"mixing length" for turbulent kinetic energy. Bradshaw, et al., [55] define a parameter L by the relation

$$L \equiv \left(\frac{\tau}{\rho}\right)^{3/2} / \epsilon \quad (8.17)$$

where $\tau = a_1 \rho \bar{k}$; this parameter is then modeled as a function of the lateral coordinate using experimental data for a flat plate boundary layer. Lee and Harsha [132] took the parameter a_2 in Equation (8.16) as a constant, which was determined by trial and error in the calculation process; the value obtained was 1.5. This is equivalent to setting L in Equation (8.17) equal to a_2 / ℓ_k where ℓ_k was taken as the width of the mixing region b .

In contrast to the formulation of the dissipation term, considerable controversy surrounds the choice of a diffusion term. As the rigorous expression for the diffusion term in Equation (8.15) shows, the diffusion of turbulent kinetic energy contains both a convective diffusion term $\overline{u_i k}$ and a gradient term $\partial \bar{k} / \partial x_i$. The gradient diffusion term is commonly considered to be small in comparison to the convective diffusion term. These two modes of diffusion can also be thought of in relation to the turbulent eddies in the flow. Thus if diffusive processes are carried out by the action of the large eddies, mixing fluid on a large scale, the diffusion ought to be convective in nature while if the diffusion is carried out within the

smaller eddies in the flow, then it should appear to be a gradient diffusion process. Some observations of turbulent flows favor the hypothesis that the turbulent energy is distributed by the large eddies--see, for example, Grant [53]--but some of the other limited evidence available on the relative importance of the two terms, e.g., Watt [62], seems to favor gradient diffusion.

The entire controversy might be somewhat moot were it not that the choice of diffusion function leads to two quite different formulations of the mathematics of the free mixing problem. If one chooses a convective diffusion model, which relates the diffusion of kinetic energy to a "diffusion velocity," Ω , one is led, as shown by Bradshaw, et al., [55] and Laster [131] to a system of equations--continuity, momentum, and kinetic energy--which is hyperbolic. If, on the other hand, one chooses a gradient diffusion model, i.e., one in which the diffusion of turbulent kinetic energy is proportional to the kinetic energy gradient,

$$\text{DIFFUSION} \propto \frac{\partial \bar{k}}{\partial y} \quad (8.18)$$

the resulting system of equations can be made parabolic.

In the hyperbolic formulation, Bradshaw, et al., [131] neglect the term

$$v \frac{\partial^2 \bar{k}}{\partial x_i \partial x_i}$$

in Equation (8.15) and use as the diffusion term:

DIFFUSION = $\rho k \Omega$. They establish the convection velocity Ω by relating it to the maximum shear stress across a layer, i.e.,

$$\Omega = \left(\frac{\tau_{\max}}{\rho} \right)^{1/2} G(y/\delta) \quad (8.19)$$

where $G(y/\delta)$ is modeled from experimental data for the ratio

$$G = \frac{\overline{\left(\frac{P}{\rho} + \nu k \right)}}{\left(\frac{\tau_{\max}}{\rho} \right)^{1/2}} \frac{\tau}{\rho} \quad (8.20)$$

This formulation has been used by Laster [131] in a free mixing system, with fairly good results. Laster [131] extended the work of Bradshaw, et al., to compressible flow, as well as extending it to a free-mixing flow. The details of this calculation are described in Reference [131] and will not be repeated here.

The greatest disadvantage of the hyperbolic formulation of the problem is that it becomes exceedingly complex when applied to a complex problem, which requires the solution of the energy and/or species equations as well as the momentum, continuity, and kinetic energy equations. This is because in a hyperbolic formulation each new dependent variable introduces an additional characteristic direction. Thus a problem with five dependent variables-- axial and lateral velocity components, U and V , turbulent kinetic energy k , total enthalpy H , and jet species

concentration c --involves five characteristic directions, and the numerical problem of searching for the intersection of the five characteristic lines involved becomes formidable. For this reason the writer feels that the parabolic approach has greater overall promise than the hyperbolic approach. As an example, the author has successfully used the parabolic turbulent kinetic energy formulation in the calculation of a number of turbulent, coaxial, hydrogen-air mixing flows with nonunity Prandtl and Schmidt numbers, for which the continuity, momentum, total (mean-flow) energy, species, and kinetic energy equations are solved simultaneously. As of yet, this has not been attempted using the hyperbolic formulation. Because of its greater flexibility, and in the author's opinion, greater promise, the parabolic formulation of the turbulent kinetic energy solution of a turbulent free mixing problem will be described in detail.

Like the approach of Nee and Kovaszny [130], the parabolic formulation of the turbulent kinetic energy problem proceeds from the definition of a parameter

$$\epsilon = \frac{-\overline{uv}}{\partial U / \partial y} = \frac{\tau / \rho}{\partial U / \partial y} \quad (8.21)$$

In analogy to the formulation of the conservation equations for the mean flow, the diffusion term for the turbulent kinetic energy, for two-dimensional or axisymmetric flow, is defined as

$$\text{DIFFUSION: } - \frac{1}{y^\alpha} \frac{\partial}{\partial y} \left[\rho \frac{y^\alpha \epsilon}{Pr_k} \frac{\partial \bar{k}}{\partial y} \right] \quad (8.22)$$

where $\alpha = 0$ for plane flow and $\alpha = 1$ for axisymmetric flow. The term Pr_k in the diffusion expression plays the same role for the kinetic energy of turbulence as does the turbulent Prandtl number in the mean flow energy equation. It too is a ratio of the turbulent eddy viscosity to a coefficient for energy transfer. Thus, Pr_k is termed a "Prandtl number" for turbulent kinetic energy.

With this expression for the diffusion term, the conservation equation for turbulent kinetic energy becomes

$$\begin{aligned} \rho U \frac{\partial \bar{k}}{\partial x} + \rho V \frac{\partial \bar{k}}{\partial y} = & \frac{1}{y^\alpha} \frac{\partial}{\partial y} \left[\rho \frac{y^\alpha \epsilon}{Pr_k} \frac{\partial \bar{k}}{\partial y} \right] + \\ & + \rho \epsilon \left(\frac{\partial U}{\partial y} \right)^2 - a_2 \rho \frac{\bar{k}^{3/2}}{\ell_k} \end{aligned} \quad (8.23)$$

when (8.16) is used for the dissipation term and (8.21) for the production term. The primary reason for formulating the turbulent kinetic energy equation as a parabolic equation is to enable it to be solved simultaneously with the other parabolic equations governing the flow. Under the boundary layer assumptions, and further assuming that the gas mixture is at most two gases, and that there are no chemical reactions occurring, the remaining equations are

Continuity

$$\frac{\partial}{\partial x}(\rho U) + \frac{1}{y^\alpha} \frac{\partial}{\partial y}(\rho v y^\alpha) = 0 \quad (8.24)$$

Momentum

$$\rho U \frac{\partial U}{\partial x} + \rho v \frac{\partial U}{\partial y} = \frac{1}{y^\alpha} \frac{\partial}{\partial y} [\rho y^\alpha \epsilon \frac{\partial U}{\partial y}] \quad (8.25)$$

Total (Mean-Flow) Energy

$$\begin{aligned} \rho U \frac{\partial H}{\partial x} + \rho v \frac{\partial H}{\partial y} = \frac{1}{y^\alpha} \frac{\partial}{\partial y} \{ & \frac{\rho y^\alpha \epsilon}{Pr} [\frac{\partial H}{\partial y} + \\ & + (\frac{Pr}{Pr_k} - 1) \frac{\partial k}{\partial y} + (Pr-1) \frac{\partial}{\partial y} (\frac{U^2}{2})] \} \end{aligned} \quad (8.26)$$

Species

$$\rho U \frac{\partial C}{\partial x} + \rho v \frac{\partial C}{\partial y} = \frac{1}{y^\alpha} \frac{\partial}{\partial y} [\frac{\rho y^\alpha \epsilon}{Sc} \frac{\partial C}{\partial y}] \quad (8.27)$$

where

U, V - components of mean-flow velocity

H - total enthalpy

C - mass fraction of jet gas

and

Pr - turbulent Prandtl number = $\rho C_p \epsilon / \kappa$

where

C_p - specific heat

and

κ - thermal conductivity

Sc - turbulent Schmidt number = ϵ/D

With the additional relations

$$\epsilon = \frac{\tau/\rho}{\partial U/\partial y}$$

and

$$\tau = a_1 \rho \bar{k} f\left(\frac{\partial U}{\partial y}\right)$$

and incorporating the modifications given by Equations (8.12) and (8.13), Equations (8.23) through (8.27) represent a system of five equations in five unknowns, U , V , H , C , and \bar{k} . The solution to this system is obtained using a modified and extended version of a program written by Patankar [135] for the solution of an arbitrary number of simultaneous parabolic partial differential equations. This numerical procedure has also been used to make all other calculations described in this study with the exception of the inversion of the Libby solution [125] described in Chapter 7. The details of the numerical procedure are given in Appendix E.

It should be noted that the formulation of the turbulent kinetic energy equation, Equation (8.23), is strictly valid only for an incompressible flow. Laster

[131] has derived the appropriate equation for a compressible flow, including density fluctuations, and has shown that the effect of these density terms is to add another term to Equation (8.23). His calculations, however, showed that this term was very small, and hence the formulation given by Equation (8.23) would appear to be adequate for a compressible flow.

Summary

The realization that a promising line of approach to the calculation of turbulent flows is opened by the inclusion of the history of the turbulent structure in the shear stress formulation has led to the development of two types of methods of including flow history. The first method is the rate equation formulation of Nee and Kovaszny [130] in which an equation is devised describing the conservation of the total turbulent viscosity $n = \epsilon + \nu$. This equation is obtained from consideration of the general form of the equation of conservation for a transportable scalar quantity and from consideration of reasonable forms for terms describing the production and dissipation of the turbulent eddy viscosity. The resulting equation is then solved simultaneously with the momentum and continuity equation to obtain the velocity field.

This method has been used in the computation of turbulent boundary layer flows [130] and [133], but to the writer's knowledge it has not been applied to free turbulent

mixing. Further, this approach seems to the author to have been overtaken by the development of the turbulent kinetic energy approach, for this latter approach can be looked on as utilizing a rate equation for the turbulent shear stress, one which can be derived on a somewhat more rigorous physical basis.

The turbulent kinetic energy approach involves the use of an empirical (and apparently quite general) relationship between the turbulent shear stress and the turbulent kinetic energy. Given such a relationship, the turbulent kinetic energy equation can be used to provide a rate equation (in Nee and Kovaszny's terms) for the turbulent shear stress. This formulation does not of course solve the familiar closure problem, as the turbulent kinetic energy equation itself involves unknown correlations of the fluctuating velocity components and their derivatives. Some recent work has been done on obtaining approximate relations for these unknown terms in a semi-rigorous manner [137], but calculation methods using the turbulent kinetic energy equation have to date all used empirical approximations.

Approximations are necessary for both the diffusion and dissipation terms of the turbulent kinetic energy equation. All calculations made to date have used essentially the same formulation for the viscous dissipation of turbulent kinetic energy. The diffusion term has, however, been modeled in two ways. If one assumes that the

diffusion process is primarily carried on by the large eddies of the flow, one is led to a convective formulation of the diffusion term. This approach was followed by Bradshaw, et al., [55] and by Laster [131]. On the other hand, one can assume that diffusion is carried on by the smallest eddies, and thus that the diffusion process itself is a gradient diffusion process. Such an assumption has been used by Lee and Harsha [132].

The difference between the two assumptions is primarily mathematical--convective diffusion leads to a hyperbolic system of equations and gradient diffusion to a parabolic system. For a simple flow the hyperbolic system of equations allows the use of an efficient computational technique, the method of characteristics. However, the simplest flow involves three characteristics (one normal, as in boundary layer flows the static pressure is assumed constant laterally), and thus consideration of flows with variable temperature and concentration can become exceedingly difficult. The parabolic system on the other hand, is easily extended to the computation of more complex flows. Thus, this approach, described in Reference [132] for a simple flow, has been extended in this study to the calculation of more complex flows involving temperature and concentration gradients. Calculations have been made of all of the flows considered, ranging from two-dimensional wakes to coaxial variable density jets. These calculations,

together with those based on other transport models, will be described in the following Chapter.

CHAPTER 9

CONFRONTATION OF THE THEORETICAL MODELS WITH
THE EXPERIMENTAL DATAResume of the Selected Experiments

The experimental data with which the predictions of the various shear stress models will be compared can be put into six categories. The first of these is the circular jet-into-still-air. To confront the theoretical models with a more complex but still relatively simple flow, two-stream air-air coaxial mixing has been chosen. The effect of density differences on the predictions made by the various models in a coaxial mixing system is investigated using a hydrogen-air coaxial mixing experiment, while compressibility effects are represented by an experiment on a supersonic jet-into-still-air. Finally, two examples of wake flows have been chosen, one axisymmetric and the other two-dimensional. Table 9.1 presents the important parameters for the experiments selected for use in this confrontation.

The incompressible circular jet-into-still-air is the most widely investigated flow configuration, as was seen in Chapter 2. Thus, there exists a large body of data, including both mean flow and hot-wire (turbulence structure) measurements. Although there is a scale effect of the

TABLE 9.1
CHARACTERISTICS OF THE SELECTED EXPERIMENTS

Investigator	Ref.	Type	U_j ft/sec	U_o/U_j	$\frac{\rho_o U_o}{\rho_o U_j}$	Re $\times 10^{-4}$	Basis of Re	Initial Profiles				Location
								U	H	C	τ	
Bradshaw, et al.	18	Circular Jet	(M= 0.03)	-	-	35.0	U_j, D_j	x			x	x/D= 2.0
Paulk	42	Coaxial Jet	412	0.371	0.417	10.9	U_j, D_j	x	x		x	x/D= 8.5
			405	0.125	0.138	10.75		x	x		x	x/D= 6.8
Forstall	40	Coaxial Jet	225	0.20	0.217	2.98	U_j, D_j	x				x/D= 0
			120	0.25	0.272	1.59						x/D= 0
Chriss	90	Coaxial Jet	3300	0.158	1.785	11.65	U_j, D_j	x	x	x	x	x/D= 5.4
			3200	0.227	2.57	11.30		x	x	x	x	x/D= 4.6
			3050	0.263	3.12	10.75		x	x	x	x	x/D= 4.6
			2400	0.333	4.16	8.48		x	x	x	x	x/D= 4.0
			1900	0.416	5.25	6.71		x	x	x	x	x/D= 4.8
			3100	0.218	1.61	10.95		x	x	x	x	x/D= 5.9
			2450	0.312	2.44	8.65		x	x	x	x	x/D= 5.3
			1950	0.400	3.33	6.89		x	x	x	x	x/D= 4.8
Eggers	72	Circular Jet	1765	-	-	265.0	U_j, D_j	x	x		x	x/D=14.5
Chevray and Kovasznay	52	2D Wake	-	-	-	0.16	U_j, θ_o^a	x			x	x= 0
Chevray	57	Circular Wake	90	-	-	275.0	U_o, D	x			x	x= 0

^a θ_o = momentum thickness at x = 0.

nozzle exit Reynolds number, as was described in Chapter 2, all of the data available for the circular jet-into-still-air fall into a relatively narrow band of U_c/U_j versus x/D . The mean flow profiles are commonly found to exhibit geometric similarity a short distance from the end of the velocity potential core. There are a number of experiments available in which the turbulence structure of the near field was investigated, and a number of other experiments in which the mean flow profiles were investigated far from the origin. However, there is no single experiment which covers the whole range from very near to very far field. Thus, the following approach was decided upon: a specific detailed near-field experiment, which included turbulent shear stress measurements, would be chosen to start the calculations, and a composite of the far-field experiments would be used to compare with the resulting far-field prediction. The initial condition is taken from the experiment of Bradshaw, Ferris, and Johnson [18]; this paper presents profiles of the mean velocity U and the turbulent fluctuations u' , v' , and w' at $x/D = 2.0$. From these latter quantities the profiles of the turbulent kinetic energy per unit mass k can be calculated. The profiles at $x/D = 2$ are used for all calculations made comparing the predictions of the various models with the jet-into-still-air data; the k profile is of course suppressed when eddy viscosity models are used.

The coaxial air-air mixing system is the next simplest system and it is thus a logical next step in the confrontation of theory and experiment. While at first glance there would seem to be a number of experimental results available for a fairly wide variety of outer-to-inner stream velocity ratios, closer inspection, as in Chapter 3, shows that experiments with U_o/U_j of 0.5 and above are generally not reliable. The reliable data seem, with some exceptions, to be limited to $U_o/U_j \leq 0.5$. Turbulent structure data is available for two coaxial air-air mixing flows. However, as was discussed in Chapter 3, both of these experiments involve phenomena which make them unsuitable for use in this study. Except for the data of Paulk [42], all of the coaxial flows available have been ducted. Paulk's is an unducted free mixing flow but has only a very short second regime. On the other hand, the velocity ratio $U_o/U_j = 0.2$ and 0.25 data of Forstall [40] both exhibit long second regimes, and do not seem to be substantially affected by any pressure gradient within the duct. However, Forstall's data are limited to profiles of the velocity and trace-gas composition, while Paulk's include both turbulent shear stress, velocity, and total enthalpy profiles, the latter because the outer stream was slightly heated. Both Paulk's and Forstall's experiments have been selected for use in this confrontation. Calculations for the Forstall case are started at the nozzle

exit, $x/D = 0$, using the velocity boundary layer thickness shown in Forstall's thesis [40] and an assumed $1/7$ power law profile for all but the kinetic energy calculations. These are begun at $x/D = 0$ using the measured velocity profiles and shear stress profiles obtained from these velocity profiles using the Prandtl eddy viscosity model, with $K_p = 0.007$. The flow in all cases is assumed to be incompressible without a trace gas; i.e., $\rho_j/\rho_o = 1.0$. Eddy viscosity calculations (and the mixing-length model) for the data of Paulk are begun with a $1/7$ power law profile for the velocity and a $2/7$ power law profile for the total enthalpy. The mixing layer thickness is assumed to be 0.0015 ft on a 0.0416 ft diameter nozzle. Although the density ratio for this flow is not much different from one, this density ratio is preserved in order to bring out whatever effect this might have on the predictions made by the various models. The kinetic energy calculations for Paulk's experiment start downstream from $x/D = 0$ (but still within the potential core region). This is done to allow these calculations to begin with a reasonably accurate measured turbulent shear stress profile. The turbulent Prandtl number was assumed to be 0.60 for all calculations.

In order to test the effects that the hypotheses for the variation of the parameter $\rho\epsilon$ that are inherent in various models for ϵ (or $\rho\epsilon$) have on the predictions made by these models, a series of coaxial hydrogen-air mixing

experiments are used. Although there are a number of coaxial hydrogen-air mixing experiments available, as well as experiments involving other gases, such as CO_2 or Freon and air, none is nearly as detailed as the hydrogen-air mixing work of Chriss [90], which includes profiles of mean velocity, hydrogen concentration, and total enthalpy. Turbulent shear stress data from these experiments are reported in Reference [94]. All eight cases from these data are used in this study, encompassing a range of the mass flux parameter $\rho_o U_o / \rho_j U_j$ of 1.61 to 5.25. Although no data at $x/D = 0$ are reported by Chriss (except for a limited boundary layer survey which indicates that the boundary layers were "thin") eddy viscosity (and mixing length) calculations are started at $x/D = 0$, assuming 1/7 power law profiles for U , 2/7 power law profiles for H , and linear profiles for C , ranging from one at $y = 0$ to zero at the maximum value of y . The mixing layer thickness is assumed to be 0.0013 ft (on a 0.0416 ft diameter nozzle). This assumption is based on the limited initial boundary layer data presented in Reference [90]. Kinetic energy calculations are started downstream of the potential core to insure reliable initial shear stress profiles; the measured profiles of the velocity, concentration, total enthalpy, and turbulent shear stress are used. All calculations of this hydrogen-air data have assumed that the turbulent Prandtl

number is 0.85 and the turbulent Lewis number equals 1.0. These values are consistent with the experimental data.

The available data on compressible flows is relatively limited, but an experiment involving a compressible flow is needed to test both compressibility corrections and the eddy viscosity models expected to apply to a compressible flow. Since one of the latter is the kinetic energy theory, such an experiment should include measured shear stresses. There is only one available experiment from which experimental shear stresses can be obtained--this is the $M_j = 2.22$ jet-into-still-air experiment of Eggers [72]. This experiment is quite completely reported, including profiles of U , ρU , $\rho \epsilon (= \tau / \partial U / \partial y)$ and ϵ . The values of ϵ were obtained by Eggers by integrating the mean flow momentum equation to various control surfaces, smoothing curves through the resulting shear stress data, and differentiating the results. This is essentially the same technique used by Paulk [42] and Chriss (described in Reference [94]), but Eggers [72] gives no details of how the smoothing was carried out. To check Eggers' results, a version of the Patankar program used in this study (see Appendix E) which uses an arbitrary spatial distribution of eddy viscosity in tabular form rather than an eddy viscosity model was run using Eggers' measured eddy viscosities and starting with his measured velocity and total enthalpy profiles at the first axial station ($x/D = 14.5$) for which

an eddy viscosity profile is available. The results reproduced the experimental distributions of velocity satisfactorily, indicating that Eggers' eddy viscosities are consistent, within the experimental accuracy, with the remainder of his data. This method of recomputation has also been applied to the data of Paulk [42] and of Chriss [90]; the results in every case have been satisfactory.

Calculations using locally-dependent models were started using measured velocity and total enthalpy profiles at $x/D = 0$. Kinetic energy calculations were begun at $x/D = 14.5$, using the measured eddy viscosity, velocity, and total enthalpy profiles at this station. A turbulent Prandtl number value of 0.6 was used in all calculations.

Incompressible wake flows are of considerable academic and practical interest. Because of this, two types of wakes have been selected. Both wakes are incompressible, and both experiments involve the initial region of the wake, in which the centerline velocity ratio U_c/U_0 ranges from zero to 0.90. The axisymmetric wake is represented by the data of Chevray [57] and the two-dimensional wake by the data of Chevray and Kovasznay [52]. Both experiments include detailed (hot-wire) turbulent shear stress profiles, and calculations of both of these flows are begun at $x = 0$ using measured velocity and, where necessary, shear stress profiles.

Resume of the Selected Theoretical Models

The theoretical models for the turbulent shear stress that are considered in this study have been described in detail in Chapters 6, 7, and 8. Table 9.2 summarizes the models that will be used. The parameter b appearing in Table 9.2 is the width of the mixing layer, which is ordinarily defined as the distance from the point where the axial mean velocity ratio equals 0.1 to the point where the velocity ratio equals 0.9. The term $r_{1/2}$ is the half-velocity width, defined as the value of the lateral coordinate for which $U - U_o = 1/2(U_c - U_o)$.

The first model listed in Table 9.2 is the classical Prandtl mixing length model, the expression for which is given in Schlichting [101]. In calculations made with this model, the same expression is used for both the first regime (potential core) and the second regime. The constants chosen for use in this study are those reported by Squire and Trouncer [48]. This choice allows a comparison to be made between the predictions made by the finite difference program used in this study and the similar-profile, integral analysis used by Squire and Trouncer. Figure 9.1 shows the results of this comparison. The most important points of comparison are the asymptotic slopes of the predicted decay curves; these should agree irrespective of the predicted potential core length. From Figure 9.1 it can be seen that this is indeed the case. It can also be

TABLE 9.2

THEORETICAL MODELS FOR THE TURBULENT SHEAR STRESS

Model	Ref.	Expression for Eddy Viscosity	Expression for Turbulent Shear Stress	Width Core	Parameter Regime II	Value of Constant Core	Constant Regime II	Ref. for Constant
Mixing Length	101	-	$\tau = \rho C^2 l^2 \left \frac{\partial u}{\partial y} \right \frac{\partial u}{\partial y}$	$l=b$	$l=2r_{1/2}$	0.082	0.082	48
Prandtl Eddy Viscosity	114	$\epsilon = K_p l (U_{\max} - U_{\min})$	$\tau = \rho \epsilon \frac{\partial u}{\partial y}$	$l=b$	$l=2r_{1/2}$	0.007	0.011	119
Schetz "Unified Theory" ^a	121	$\rho \epsilon = K_S \pi (\rho_o U_o \delta_r^{*2}) / r_o$	$\tau = \rho \epsilon \frac{\partial u}{\partial y}$					121
Ferri	83	$\rho \epsilon = K_F l \rho_o U_o - \rho_c U_c $	$\tau = \rho \epsilon \frac{\partial u}{\partial y}$	$l=b/2$	$l=r_{1/2} \rho U^b$	0.025	0.025	83
Zakkay	86	$\epsilon = K_Z l U_c$	$\tau = \rho \epsilon \frac{\partial u}{\partial y}$	$l=b/2$	$l=r_{1/2}$	0.011	0.011	86
Alpinieri	84	$\rho \epsilon = K_A l \rho_o (U_c + U_o^2 / U_j)$	$\tau = \rho \epsilon \frac{\partial u}{\partial y}$	$l=b/2$	$l=r_{1/2}$	0.025	0.025	84
Kinetic Energy	132	-	$\tau = a_1 \rho k F \left(\frac{\partial u}{\partial y} \right)$					132, Present Study

^aIn this study, mixing length used for core.

^b $r_{1/2} \rho U = r$ for which $\rho U = (\rho_c U_c + \rho_o U_o) / 2$.

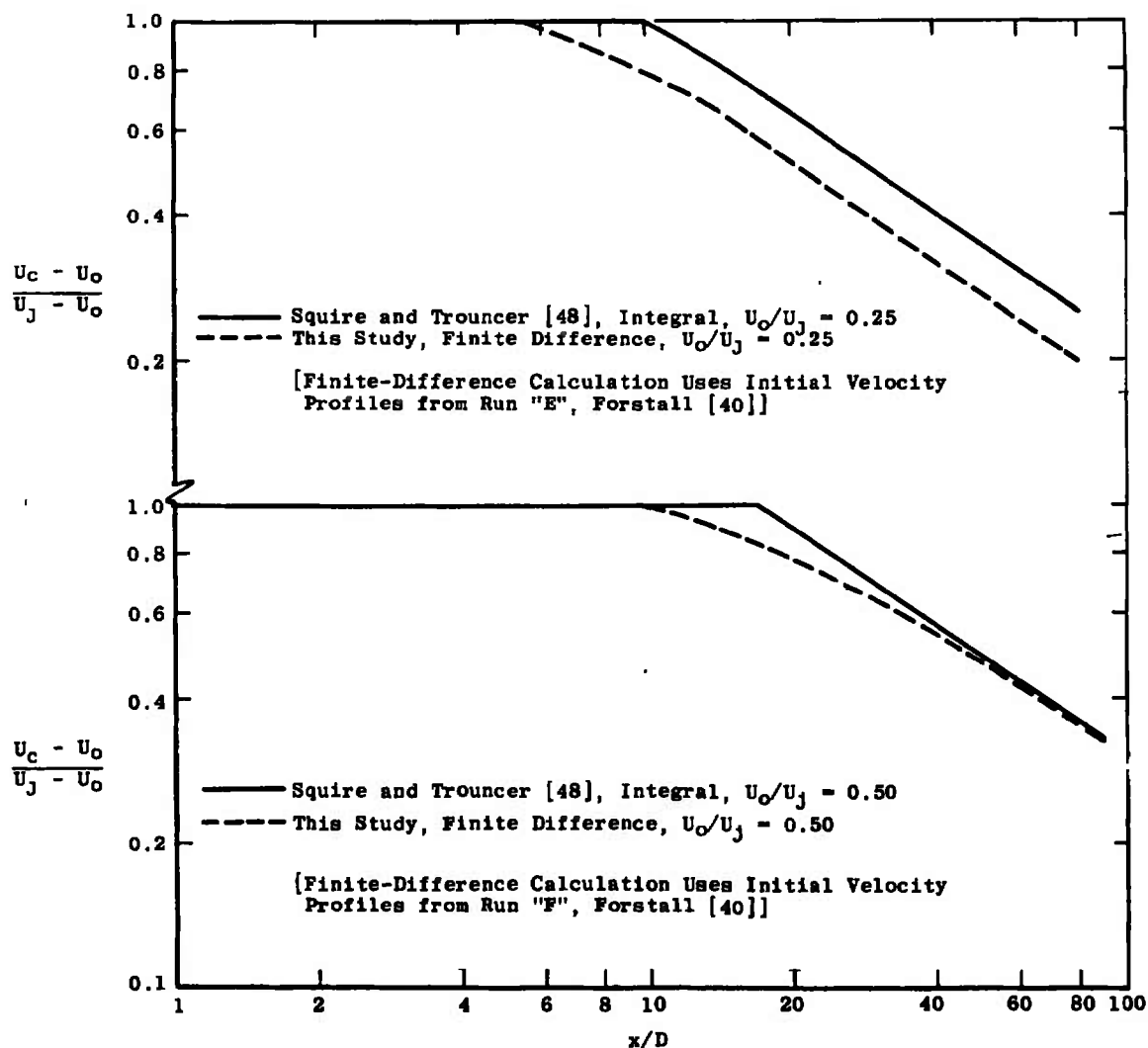


Figure 9.1. Comparison of predicted axial decay of center-line velocity using Prandtl mixing length: integral analysis and finite-difference analysis.

seen from Figure 9.1 that the finite difference approach (which starts with a finite initial boundary layer thickness) predicts shorter potential core than the integral approach; it also is capable of predicting a gradual transition from the potential core region to the second regime, which the integral technique cannot, because of its reliance on geometrically similar profiles.

Prandtl's eddy viscosity model, the second model listed in Table 9.2, is probably the most widely used eddy viscosity model. The form listed in Table 9.2 is that given by Prandtl [114]. Two constants are used for this model, one for the potential core region and one for the second regime. This approach was suggested by Peters [119] who also suggested the values of the constants listed in the table.

The displacement thickness model proposed by Schetz [120, 121] is of recent origin and thus has not been widely used. It has been developed in order to incorporate density differences between mixing streams in a somewhat more rational manner than is possible for other eddy viscosity models, and is based on an eddy viscosity model used in two-dimensional boundary layer work.

Schetz [121] has shown that this model is equivalent to the Prandtl eddy viscosity model for a two-dimensional mixing layer and he used it for both the first and second regimes of mixing. However, in the present study

the Prandtl mixing length theory was used for the core region.⁸ The effects of this difference on the predictions made by the Schetz model are shown in Figure 9.2, which compares calculations made in this study with those presented by Schetz [121]. As for the comparison of the calculation of the present study with those of Squire and Trouncer using the mixing length model, it is to be expected that the trends of the axial decay of centerline velocity curves will be similar. For the air-air calculation, with $U_o/U_j = 0.50$, a small difference in the predicted slopes is evident. The reason for this difference is unknown, but it does not appear to be significant. On the other hand, the slope agreement for the hydrogen-air calculation also shown on Figure 9.2 is quite good. Schetz' work described in Reference [121] did not include a calculation of the potential core region for this flow.

The Ferri [83], Alpinieri [84], and Zakkay [86] models are all efforts to generalize the Prandtl eddy viscosity model to a variable density flow. However, they differ from each other in a number of details. The Ferri model is a relatively straightforward adaptation of the Prandtl model: the mass flux difference $|\rho_c U_c - \rho_o U_o|$ is substituted for the velocity difference $|U_c - U_o|$. In

⁸This was done because Schetz, in Reference [120], did not make clear the application of his model to the first regime of mixing. His work in Reference [121] has since clarified this point.

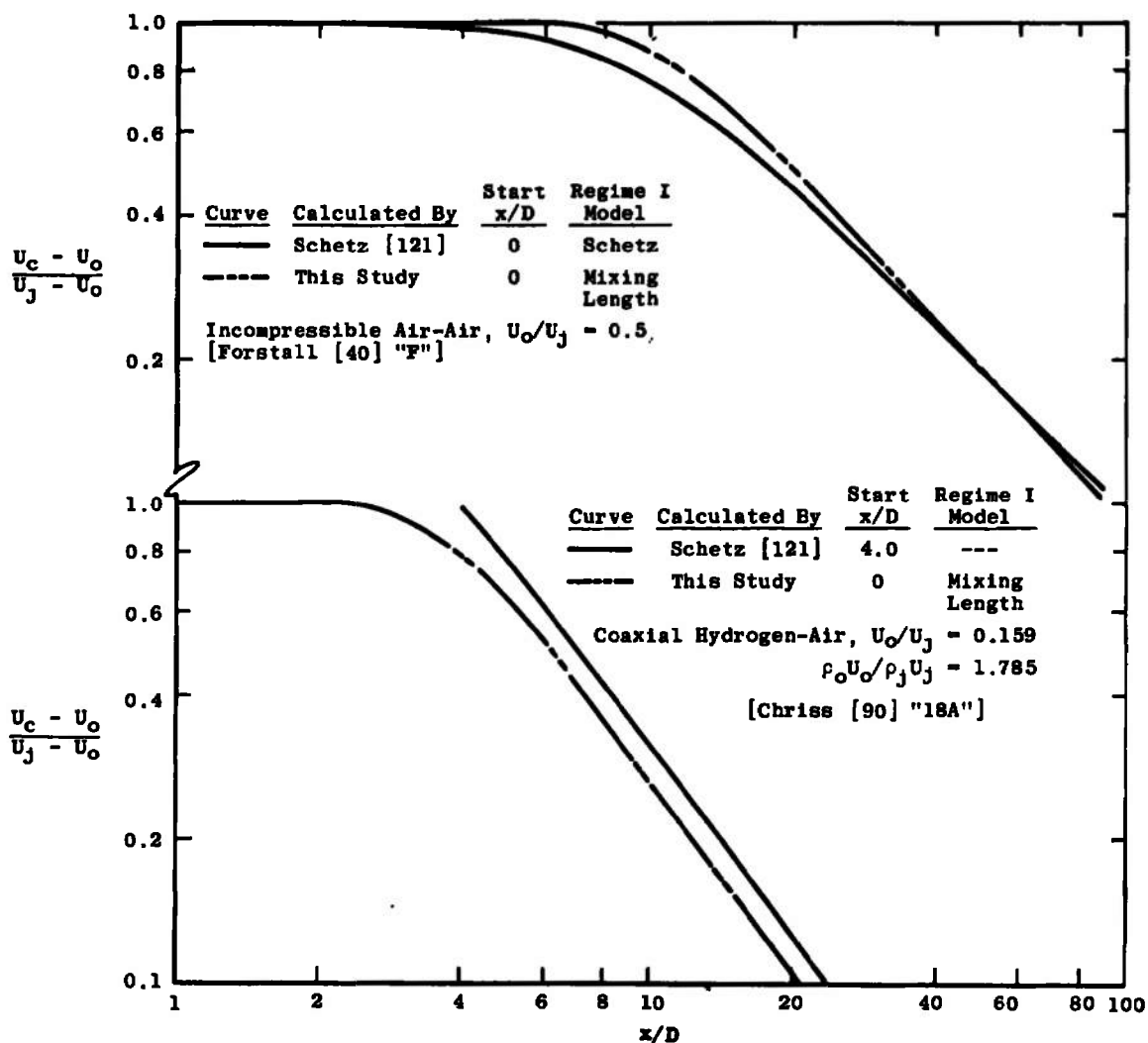


Figure 9.2. Comparison of calculated velocity decay using Schetz theory: Schetz calculation [121] and present study.

keeping with this substitution, the half-radius is defined as the lateral coordinate at which $\rho U = 1/2[\rho_c U_c + \rho_o U_o]$ rather than the usual half-radius definition. This evaluation of the half-radius is unique to this model. The Zakkay model [86] was obtained from asymptotic expressions for the far-downstream velocity profile and thus in this model the velocity difference $|U_c - U_o|$ is replaced by the centerline velocity U_c alone. Alpinieri [84] derived his model to match experiments in which, as is discussed in Chapter 5, the flow may have been more like a wake in character than a jet. Thus it is not to be expected that this model will agree well with experiments in which this is not the case.

The kinetic energy theory is conceptually quite different from any of the eddy viscosity models previously discussed. Instead of evaluating the shear stress or eddy viscosity based on some locally-dependent quantity such as the mean-velocity gradient, the kinetic energy theory relates the turbulent shear stress to the turbulent kinetic energy per unit mass. This method has been discussed in detail in Chapter 8; briefly, it rests upon a relationship between the turbulent shear stress and the turbulent kinetic energy which has been shown from experimental data to be quite general [12]. Given this relationship, the turbulent shear stress is solved for simultaneously with the other dependent variables in the flow field using the turbulent kinetic energy equation in parabolic form. However, using

this equation involves developing expressions for certain of its terms, as has been described in Chapter 8. In an alternate form, the turbulent kinetic energy method has been applied to boundary layers by Bradshaw, et al., [55] and to free mixing flows by Laster [131]. An application of the method used here to two simple flows has also been reported [132]. However, none of the calculations reported in this study have been previously reported.

In this section the prediction of the Ting-Libby eddy viscosity transform [126] as used by Libby [125] will be compared with selected hydrogen-air mixing experiments. The Donaldson and Gray compressibility correction [67] as modified by Peters [119] will also be used in conjunction with the Prandtl eddy viscosity model in comparison with selected hydrogen-air experiments and the compressible jet experiment.

The comparison which follow will primarily be made on the basis of curves of the predicted axial decay of centerline velocity. The reasons for using such a comparison have been discussed in Chapter 1; here some further comments are made. Figure 9.3 shows a comparison of fully-normalized radial profiles predicted by all of the models considered herein for one of the coaxial air-air mixing experiments of Forstall [40]. It can be seen that when the profiles are presented in this manner, there is little to choose between them as far as accuracy is

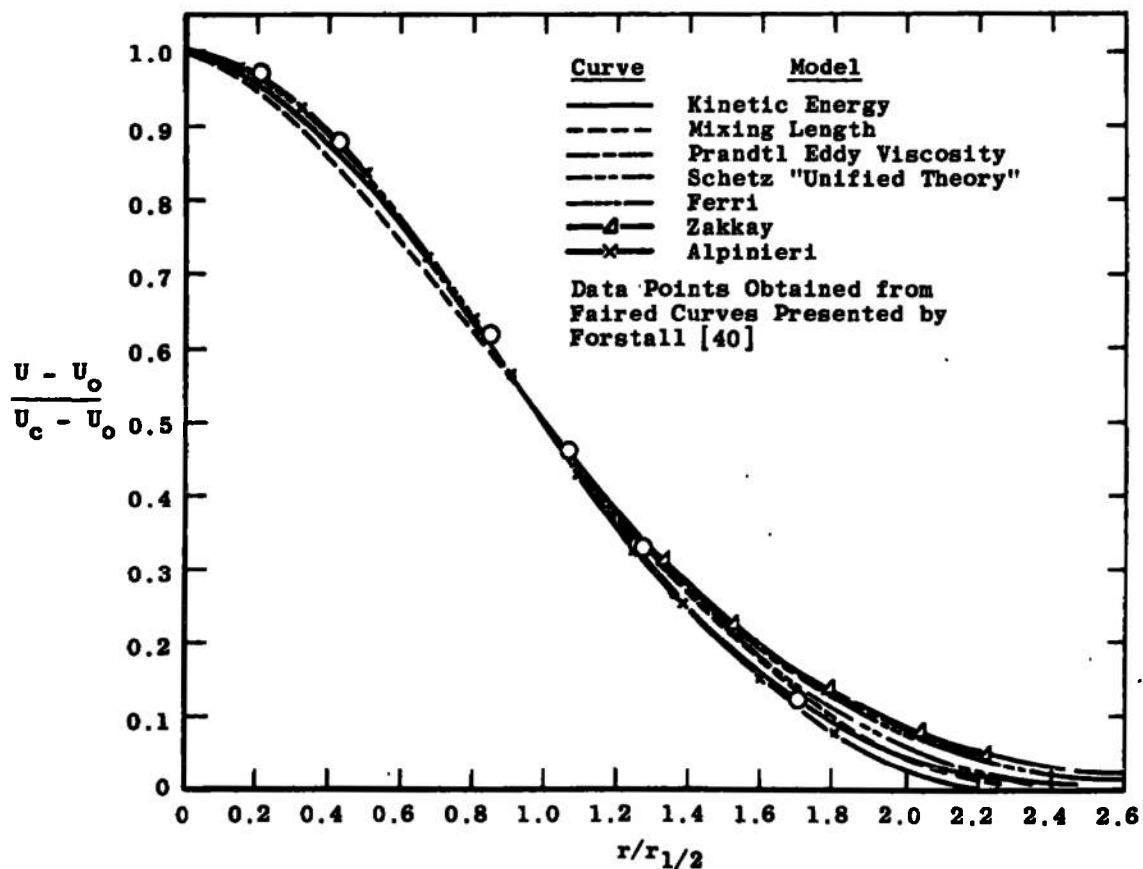


Figure 9.3. Comparison of fully-normalized profiles predicted by various models with coaxial air-air mixing data. Data from Forstall [40], $U_o/U_j = 0.2$, $x/D = 24$.

concerned. If, on the other hand, semi-normalized radial profiles such as those shown in Figure 9.4 are used for the same data, incorrect conclusions can be drawn. This can be explained as follows: if a given calculation satisfies the requirement that the value of the momentum integral remain constant, and if the calculations result as they normally do in geometrically similar profiles, then the axial decay of centerline velocity and the axial variation of the velocity half-width $r_{1/2}$ cannot be specified independently. If the axial decay is predicted to occur at too great a rate, so that at a given axial station the predicted centerline velocity is too low, then the half-width at the same station must appear to be too large in order that the momentum requirement be satisfied. Thus either the centerline velocity or the half-width distribution would in principle serve for purposes of comparison, but the centerline velocity is more commonly reported.

Centerline velocity decay curves are unequivocal; they do not depend on the definition of any other quantity. Further, as was described in Chapter 1, in logarithmic form they indicate not only the error at a given axial station, but also the trend of the error. For these reasons, centerline axial decay of velocity curves are used in the following confrontation; there will, however, also be a brief presentation of some pertinent profile data.

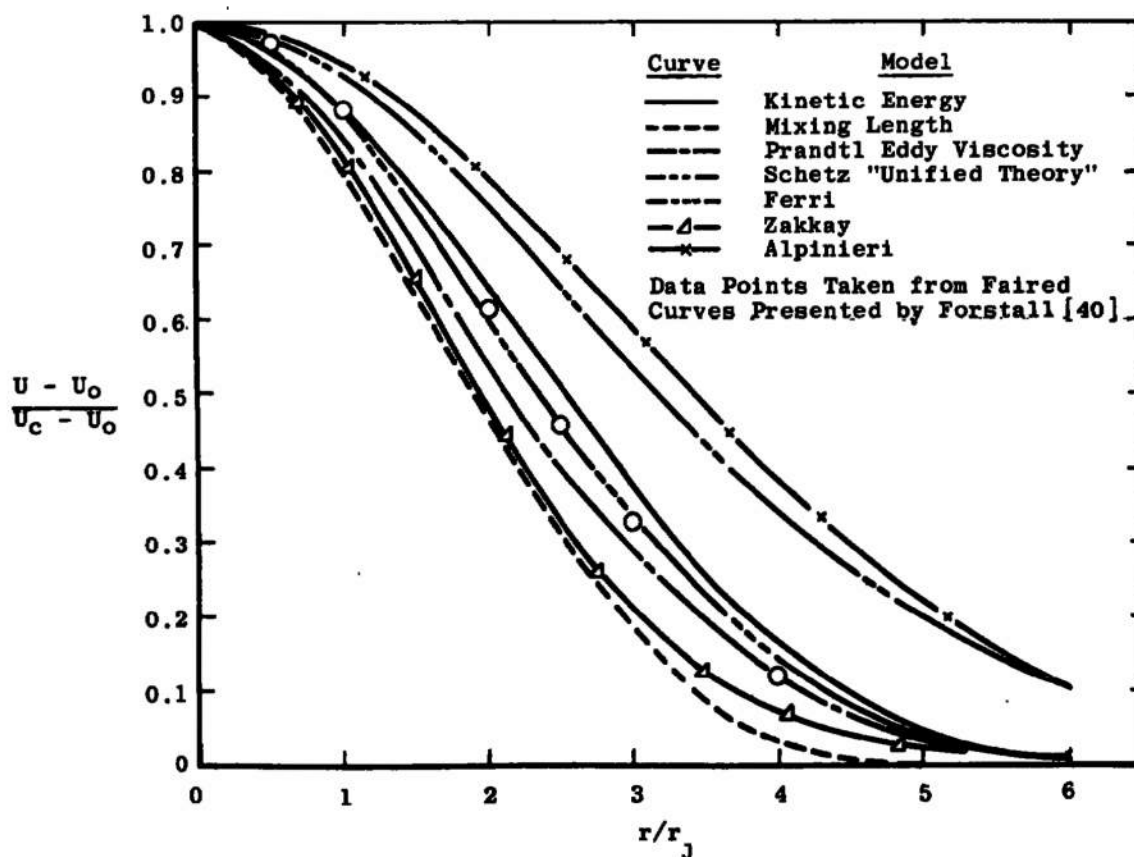


Figure 9.4. Comparison of semi-normalized velocity profiles predicted by various methods with coaxial air-air mixing data of Forstall [40]: $U_o/U_j = 0.2$, $x/D = 24$.

The system of equations solved in this study is given by Equations (8.24) through (8.27), page 361. These equations are derived under the standard boundary layer assumptions, and further assume a two-gas mixture (for the dissimilar-gas calculations), and that no chemical reactions occur. The various turbulent shear stress models are incorporated into this system through the eddy viscosity, ϵ , except in the case of the turbulent kinetic energy method. In this case, Equation (8.23), page 360, is solved simultaneously with Equations (8.24) through (8.27). The numerical technique used is described in Appendix E.

Confrontation I: The Mixing Length Theory

Despite the widespread use that the Prandtl mixing length theory has seen, when it is applied to a variety of flows with a single constant for all calculations its predictions are poor. This conclusion is not particularly surprising, for it has long been known that good results with the Prandtl mixing length theory can only be achieved through a judicious juggling of constants.

As shown by Figure 9.5, the asymptotic slope of the decay curve predicted by mixing length theory is inaccurate for both incompressible and compressible jet-into-still-air flows. With a constant of 0.082, the prediction of the core length is fairly good for the incompressible case, but inaccurate for the compressible flow. The situation is much the same for coaxial air-air

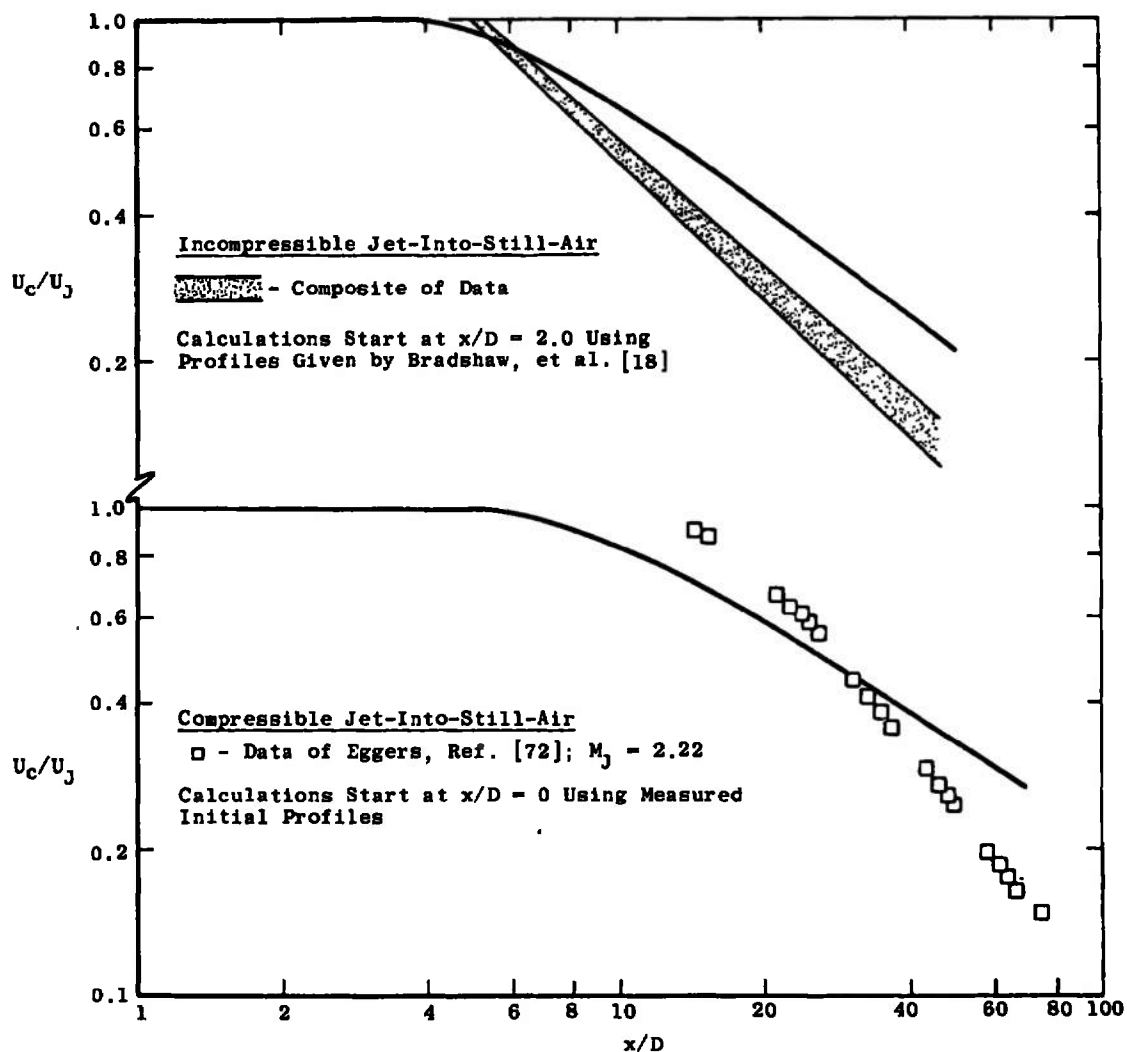


Figure 9.5. Comparison of prediction of mixing length theory with jet-into-still-air data.

mixing, as can be seen from Figures 9.6 and 9.7. Here again the slope is too low, but a reasonably good prediction of the velocity potential core length is made.

For hydrogen-air coaxial mixing, the mixing length theory still underpredicts the rate of decay by a substantial amount, and this underprediction increases as the ratio $\rho_o U_o / \rho_j U_j$ increases from 1.0. This is shown by Figure 9.8, which also shows that the previously good record this model has shown for the prediction of the velocity potential core length is spoiled by the data for $\rho_o U_o / \rho_j U_j > 2$. Overall, the level of agreement for the hydrogen-air data, as for the air-air data, is unsatisfactory.

On the other hand, the mixing length model does rather well in predicting the early velocity increase on the centerline of a wake. This is shown by Figures 9.9 and 9.10, for an axisymmetric and a two-dimensional wake, respectively.⁹ Note, however, that the downstream predictions of the mixing length theory deteriorate for both two-dimensional and axisymmetric wakes. As for two-stream jets, the asymptotic trend of the prediction is wrong.

Confrontation II: Prandtl Eddy Viscosity Model

The Prandtl eddy viscosity model is probably the single most widely used eddy viscosity model. But just as

⁹Note that δ_o on Figure 9.10 is the boundary layer thickness at the edge of the flat plate forming the wake.

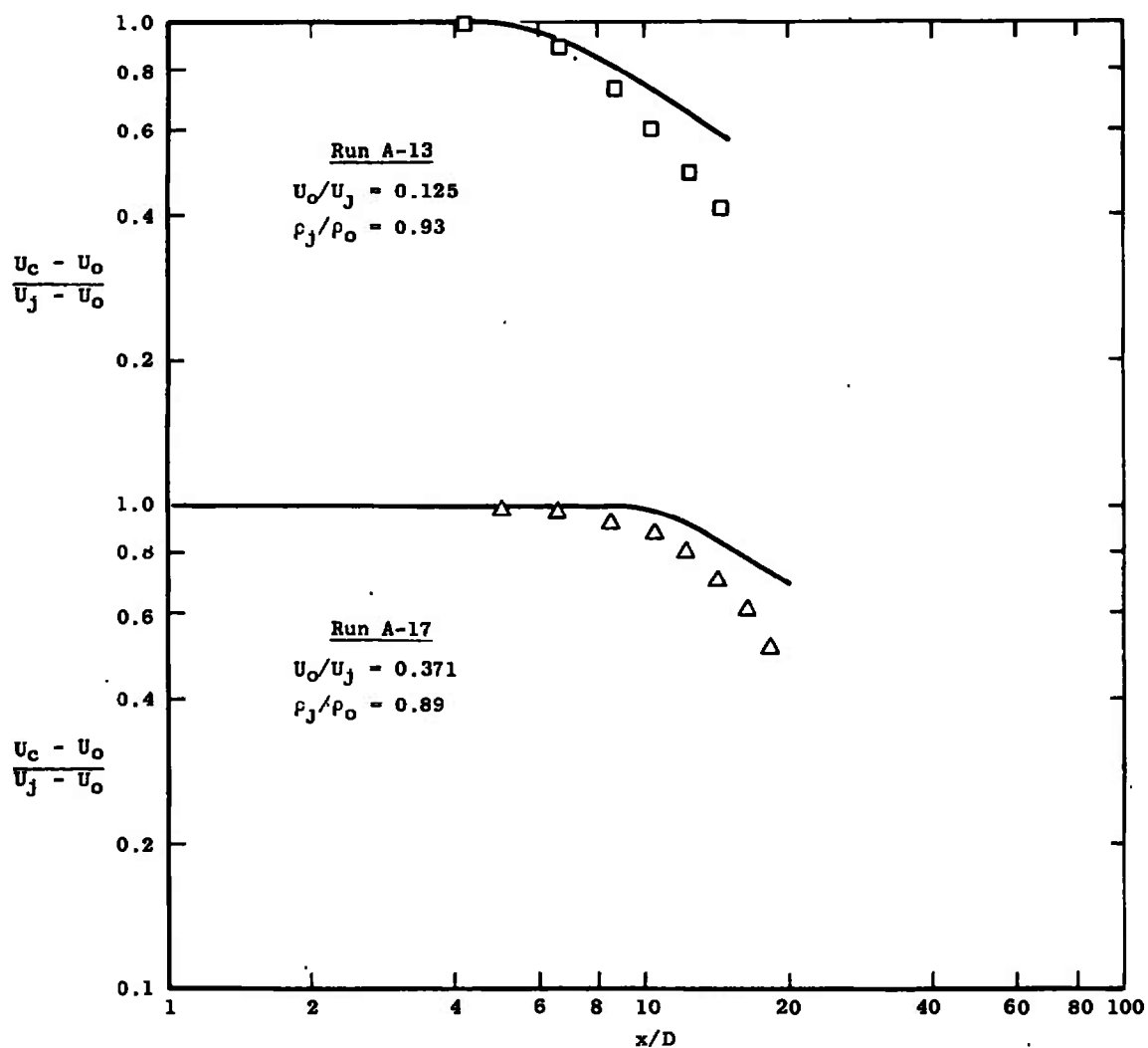


Figure 9.6. Comparison of predictions of mixing length theory with coaxial air-air data of Paulk [42].

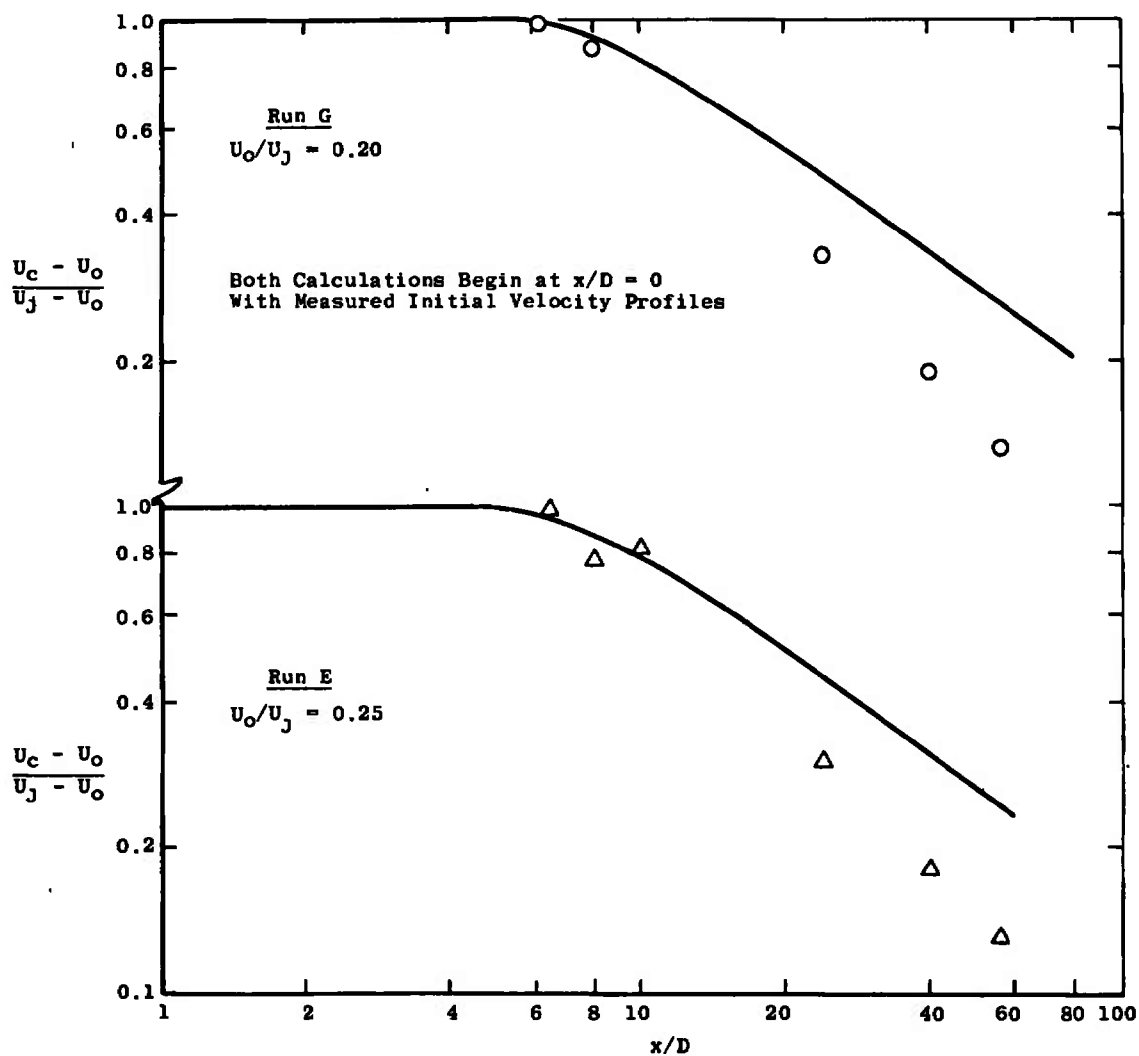


Figure 9.7. Comparison of prediction of mixing length theory with coaxial air-air mixing data. Data of Forstall [40].

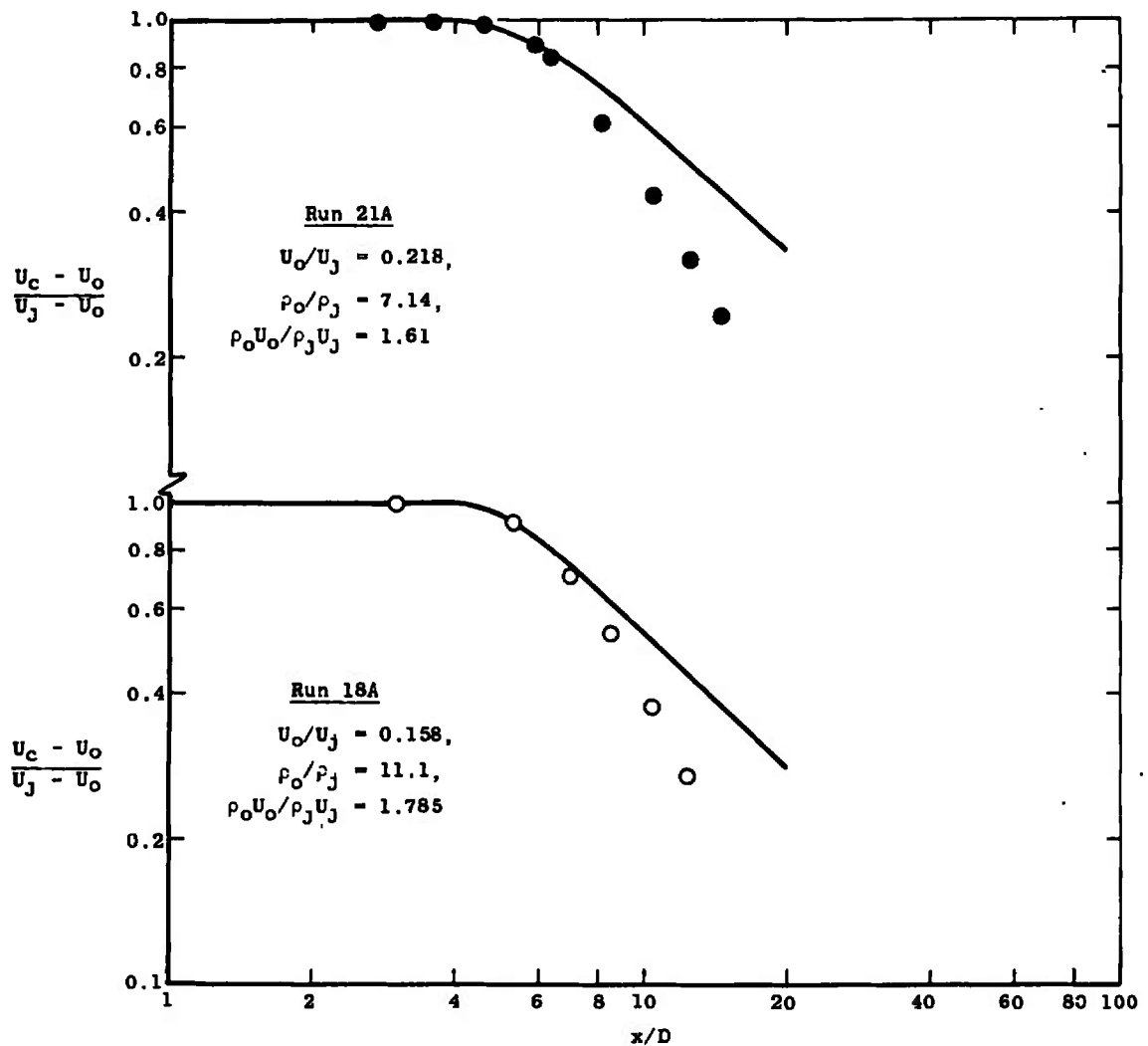


Figure 9.8. Comparison of prediction of mixing length theory with coaxial H_2 -air mixing data of Chriss [90].

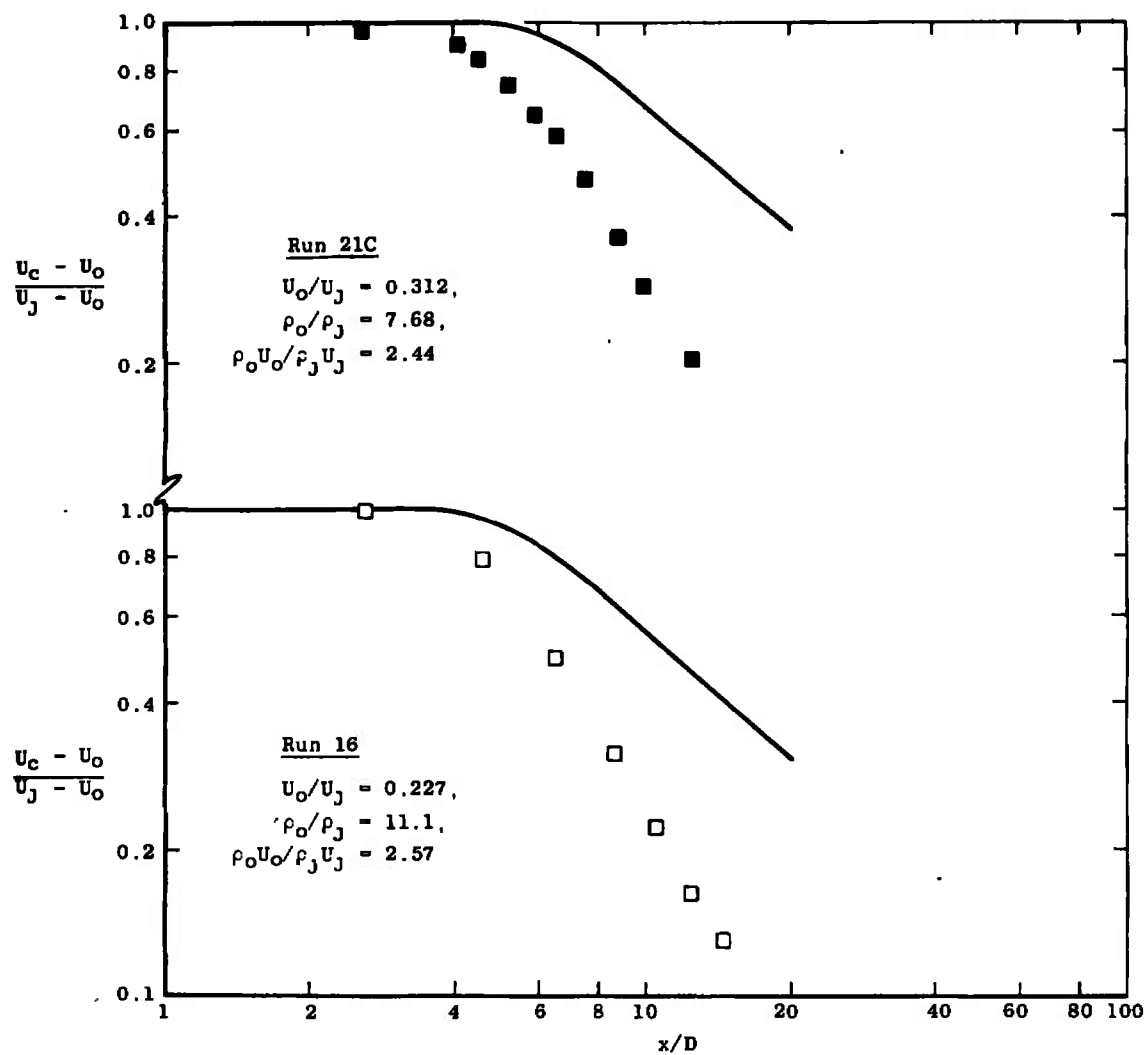


Figure 9.8. (continued)

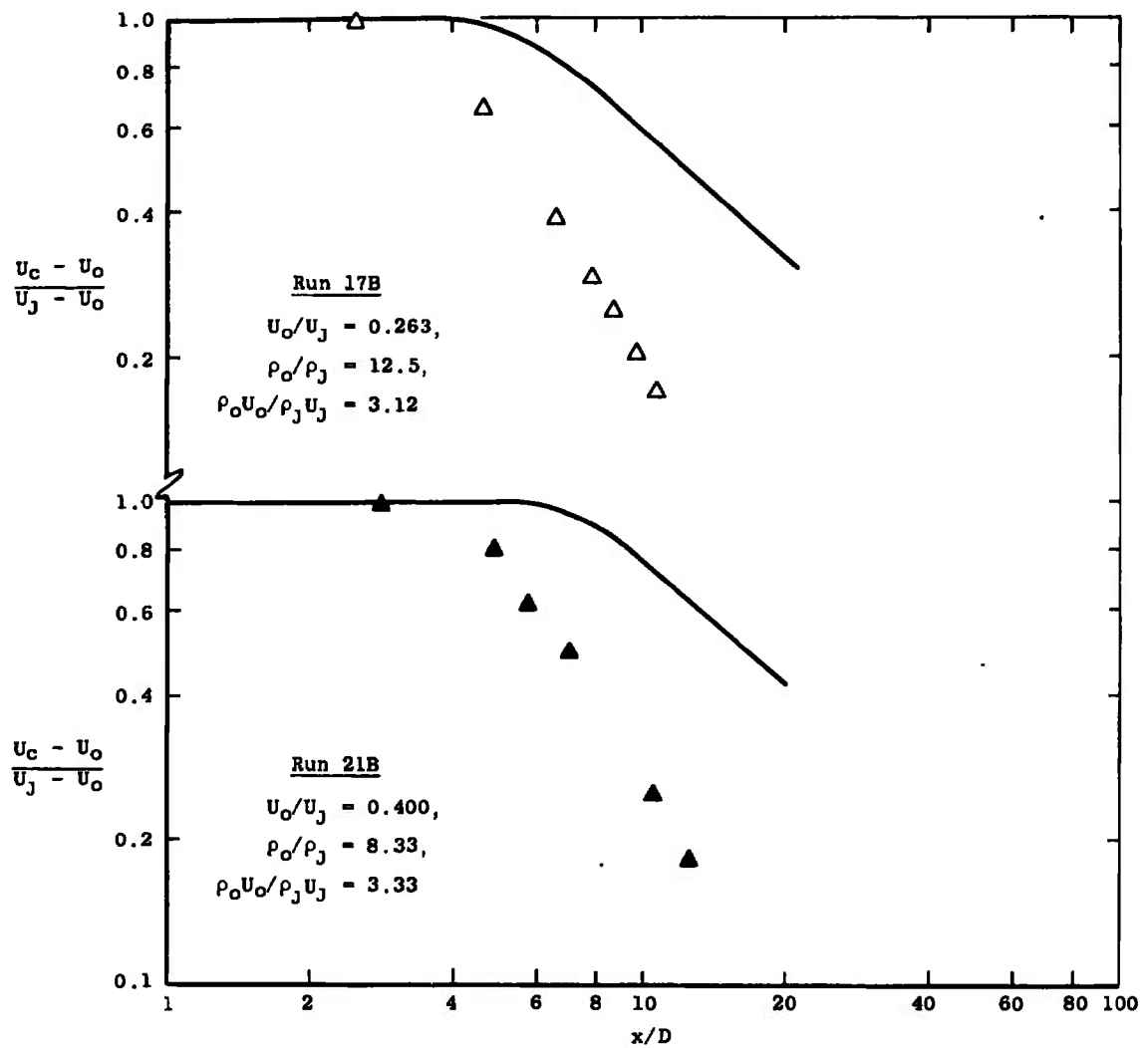


Figure 9.8. (continued)

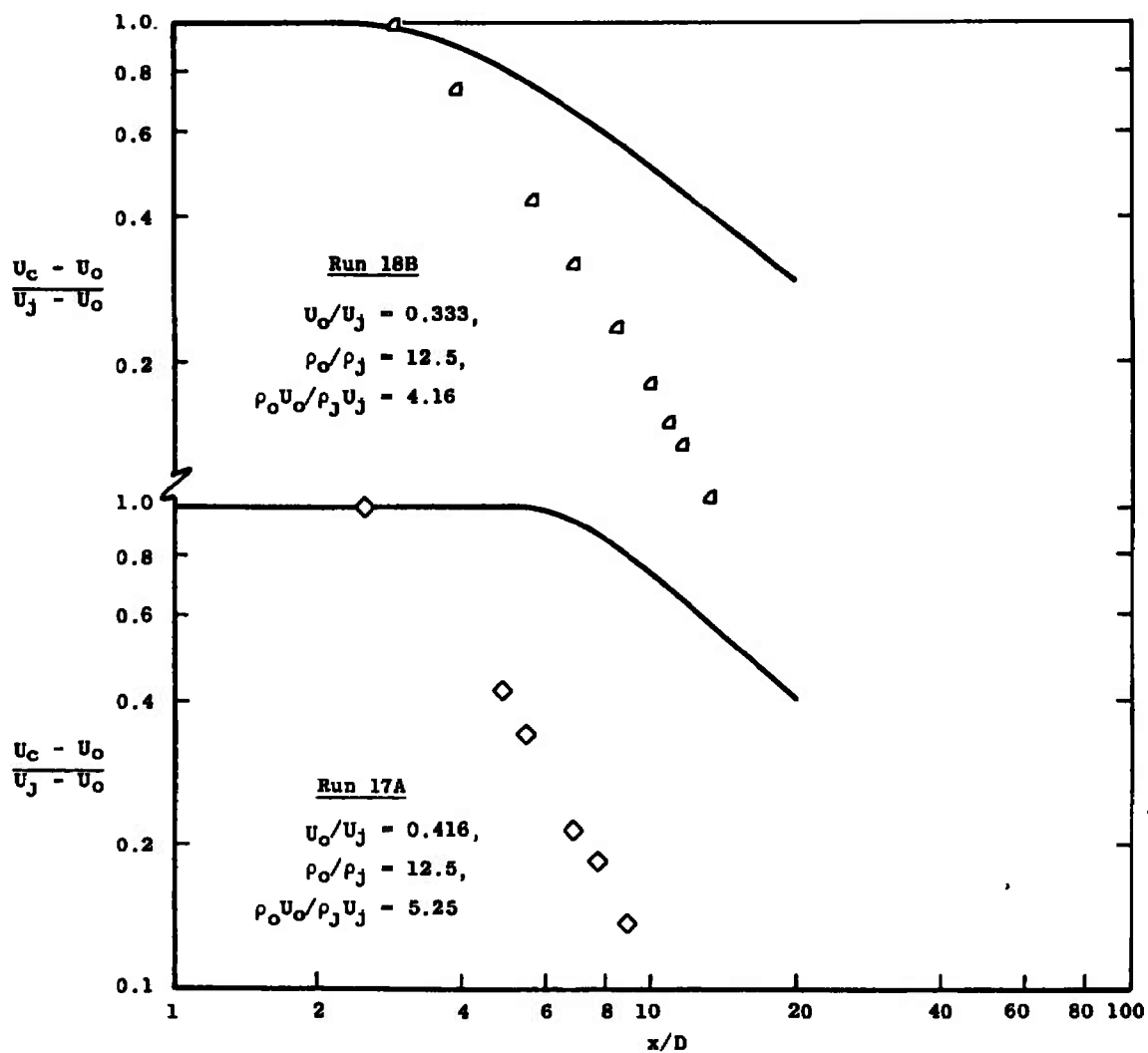


Figure 9.8. (continued)

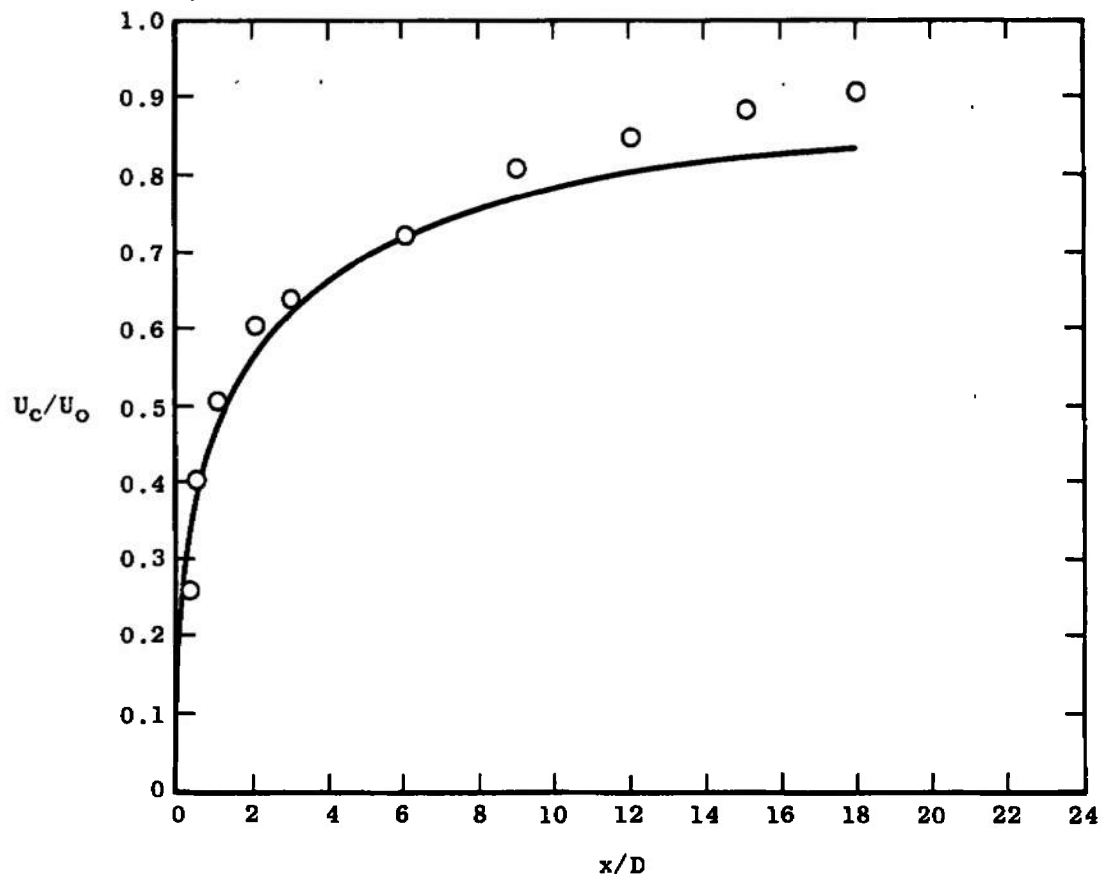


Figure 9.9. Comparison of prediction of mixing length theory with data for the initial region of an axisymmetric wake. Data of Chevray [58].

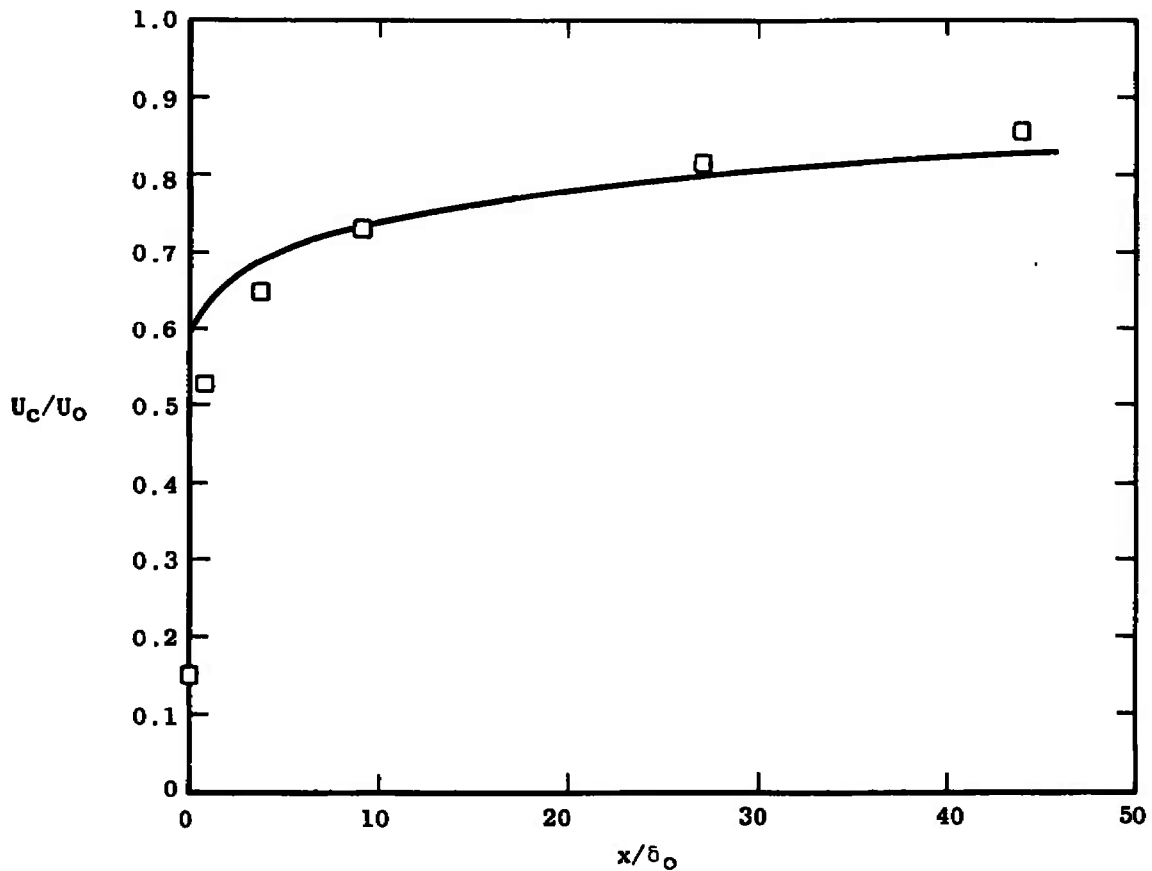


Figure 9.10. Comparison of prediction of mixing length theory with data for the initial region of a two-dimensional wake. Data of Chevray and Kovasznay [52].

the mixing length theory, it is commonly used with constants selected in such a way as to properly predict a given flow; these constants are different from investigator to investigator, and even for different configurations in a given study.

Figure 9.11 illustrates the performance of the Prandtl eddy viscosity model with the constants chosen for use in this study in predicting the two jet-into-still-air experiments selected. It can be seen that the prediction in the incompressible case is reasonably good, with a good prediction of the potential core length and a fair level of agreement with the asymptotic slope of the decay data. Clearly the trend is to underpredict the rate of decay. The situation is not as good in the compressible case, also on Figure 9.11; here both the core length and the rate of decay predicted by the Prandtl eddy viscosity model are clearly considerably in error.

Again as for the mixing length model, the predictions made by the Prandtl eddy viscosity model for the velocity potential core length in coaxial air-air mixing are reasonably good. This is shown by Figures 9.12 and 9.13. The slope prediction made by the present model is considerably better than that made by the mixing length theory for these flows, but the rate of mixing as measured by the decrease in centerline velocity is still underpredicted.

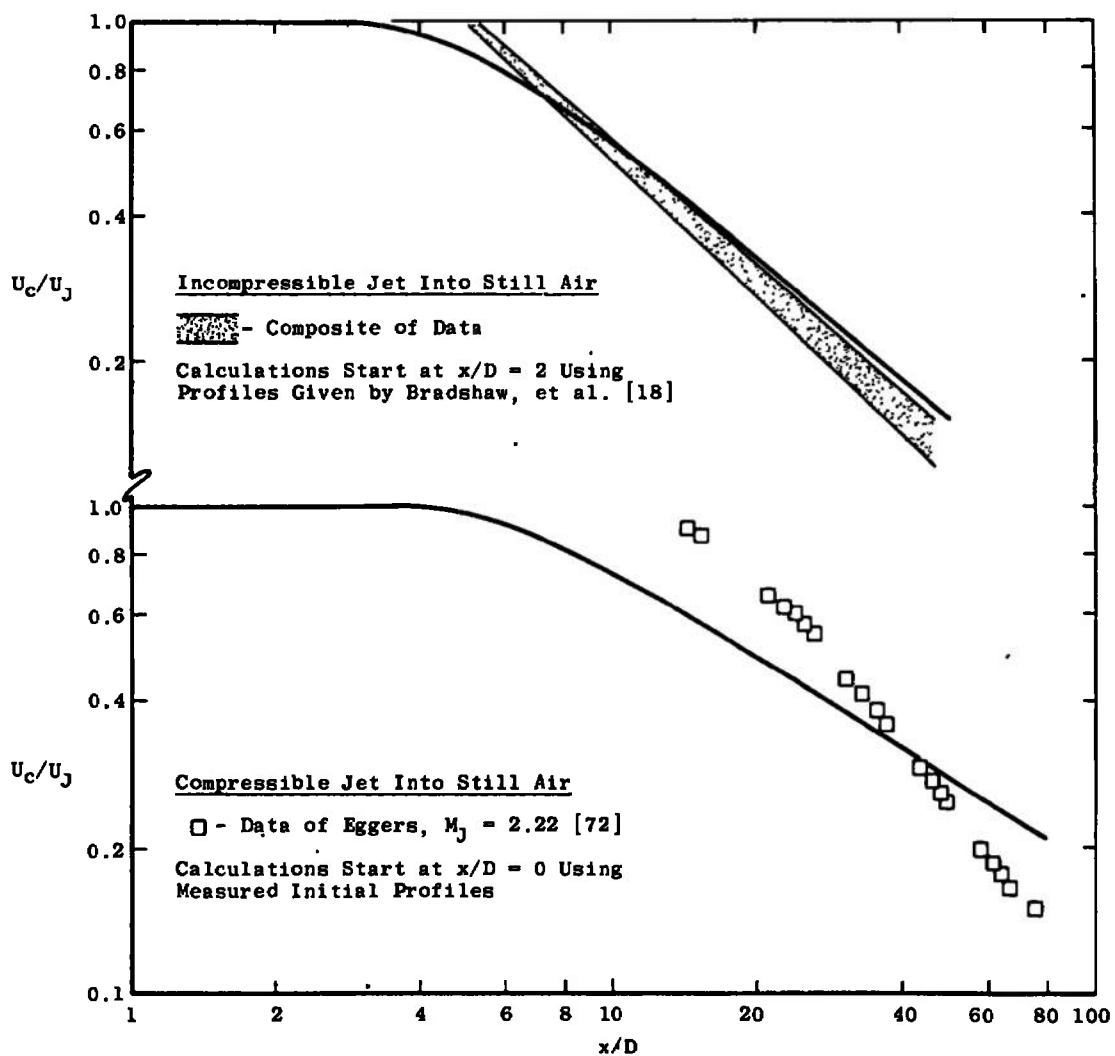


Figure 9.11. Comparison of predictions of Prandtl eddy viscosity theory with jet-into-still-air data.

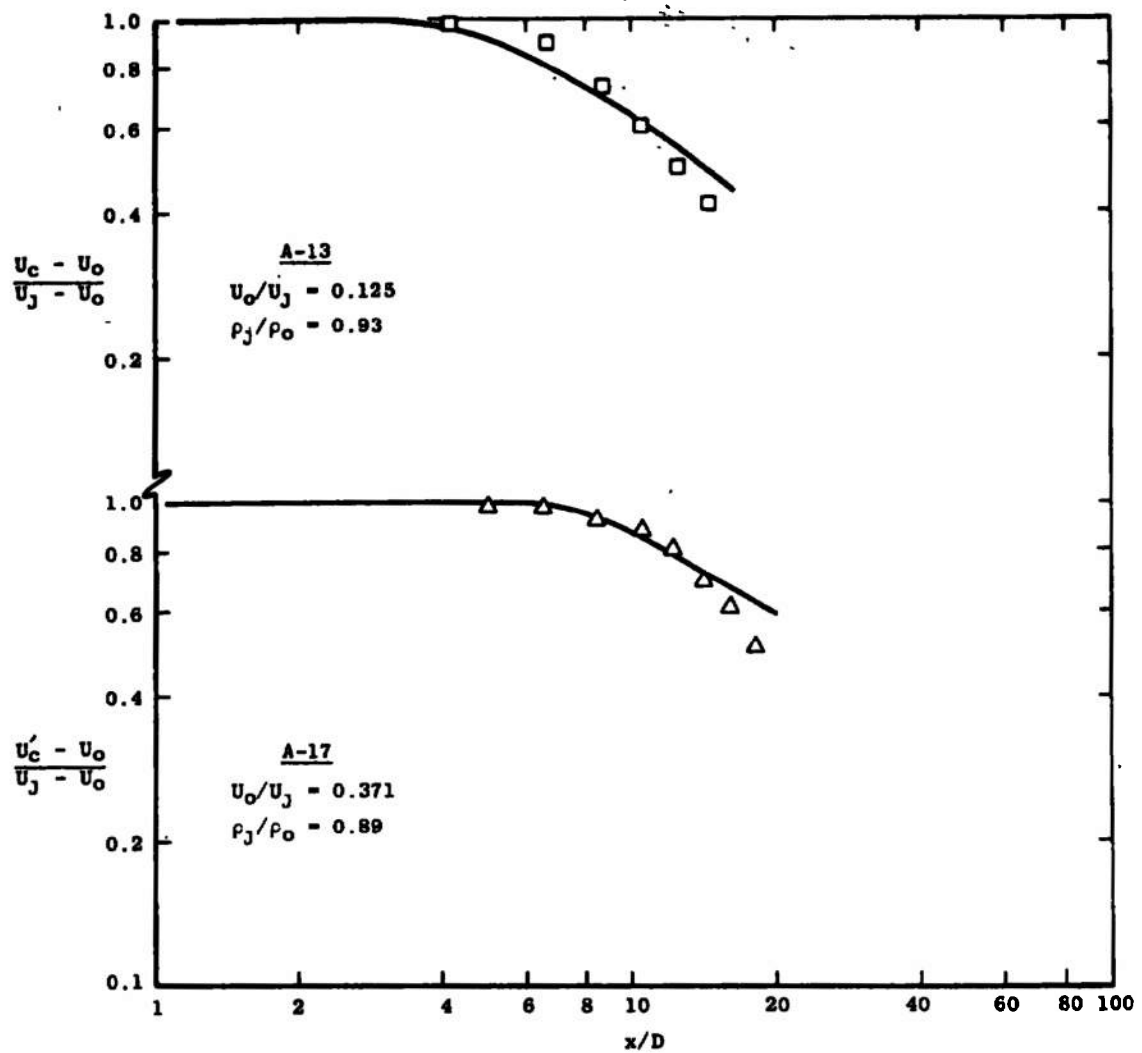


Figure 9.12. Comparison of predictions of Prandtl eddy viscosity theory with coaxial air-air data of Paulk [42].

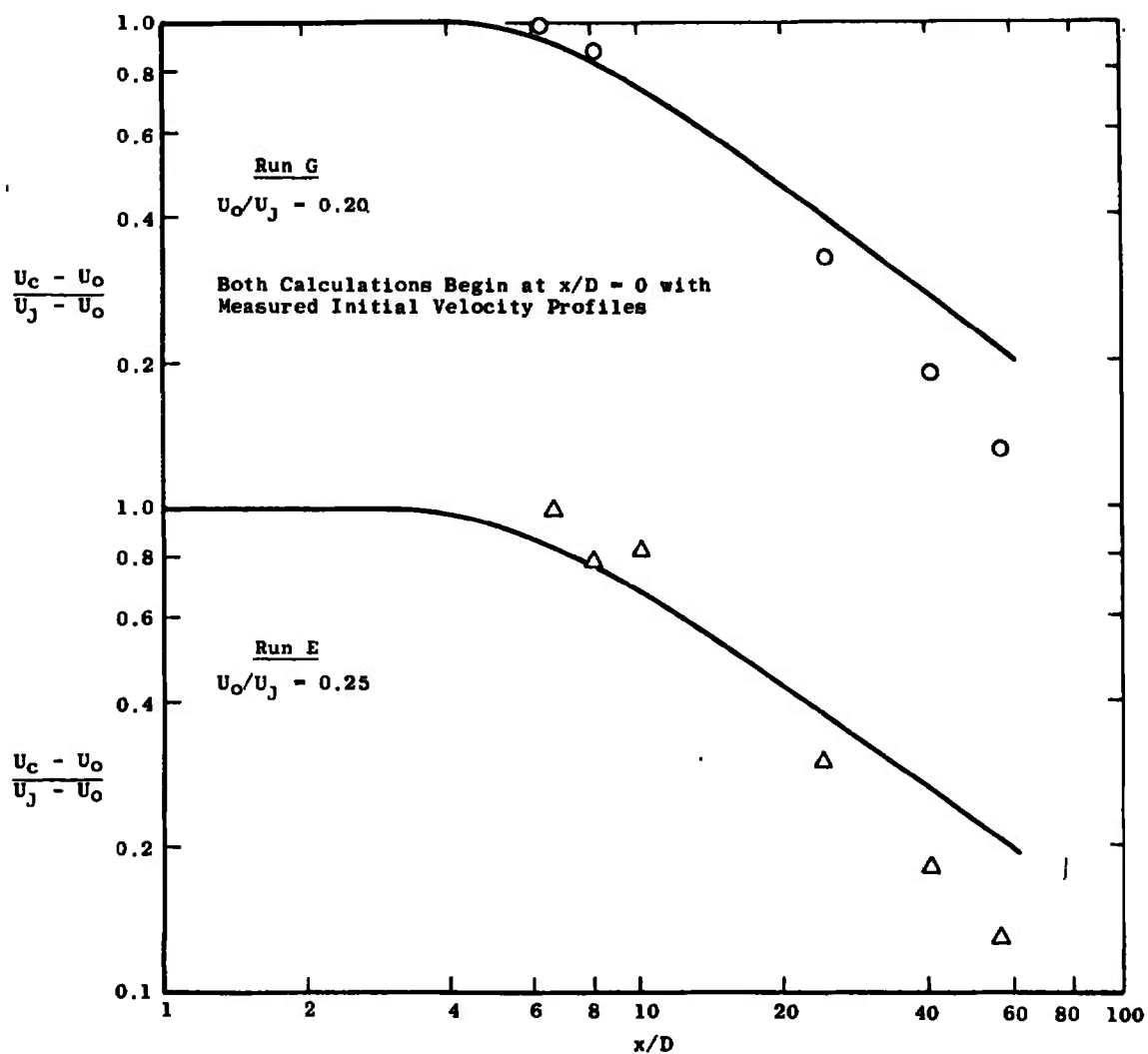


Figure 9.13. Comparison of predictions of Prandtl eddy viscosity theory with coaxial air-air mixing data. Data of Forstall [40].

Note also that the core length prediction for the Forstall "run E" case (Figure 9.13) is not quite as good as that of the mixing length theory.

The prediction of mixing made by the Prandtl eddy viscosity model for a coaxial hydrogen-air system is not satisfactory, and it becomes more unsatisfactory as the mass flux ratio $\rho_o U_o / \rho_j U_j$ increases from unity. This is depicted in Figure 9.14. The theory predicts that as the ratio $\rho_o U_o / \rho_j U_j$ increases, the length of the velocity potential core increases, while the rate of decay remains essentially the same. The data, on the other hand, indicates a decreasing core length with increasing mass flux ratio, and an increasing rate of decay of centerline velocity with increasing $\rho_o U_o / \rho_j U_j$. The prediction of the axisymmetric and two-dimensional wake data made by the Prandtl eddy viscosity model is quite similar to the prediction made by the mixing length theory. Figures 9.15 and 9.16 illustrate the predictions of the Prandtl eddy viscosity model for these flows.

Confrontation III: Schetz "Unified Theory"

The displacement thickness model proposed by Schetz [120, 121] is one of the very few recently proposed models for the eddy viscosity for a free turbulent flow which is not merely a restatement of the Prandtl eddy viscosity model, although some of the ideas behind the Prandtl eddy viscosity model are inherent in this model

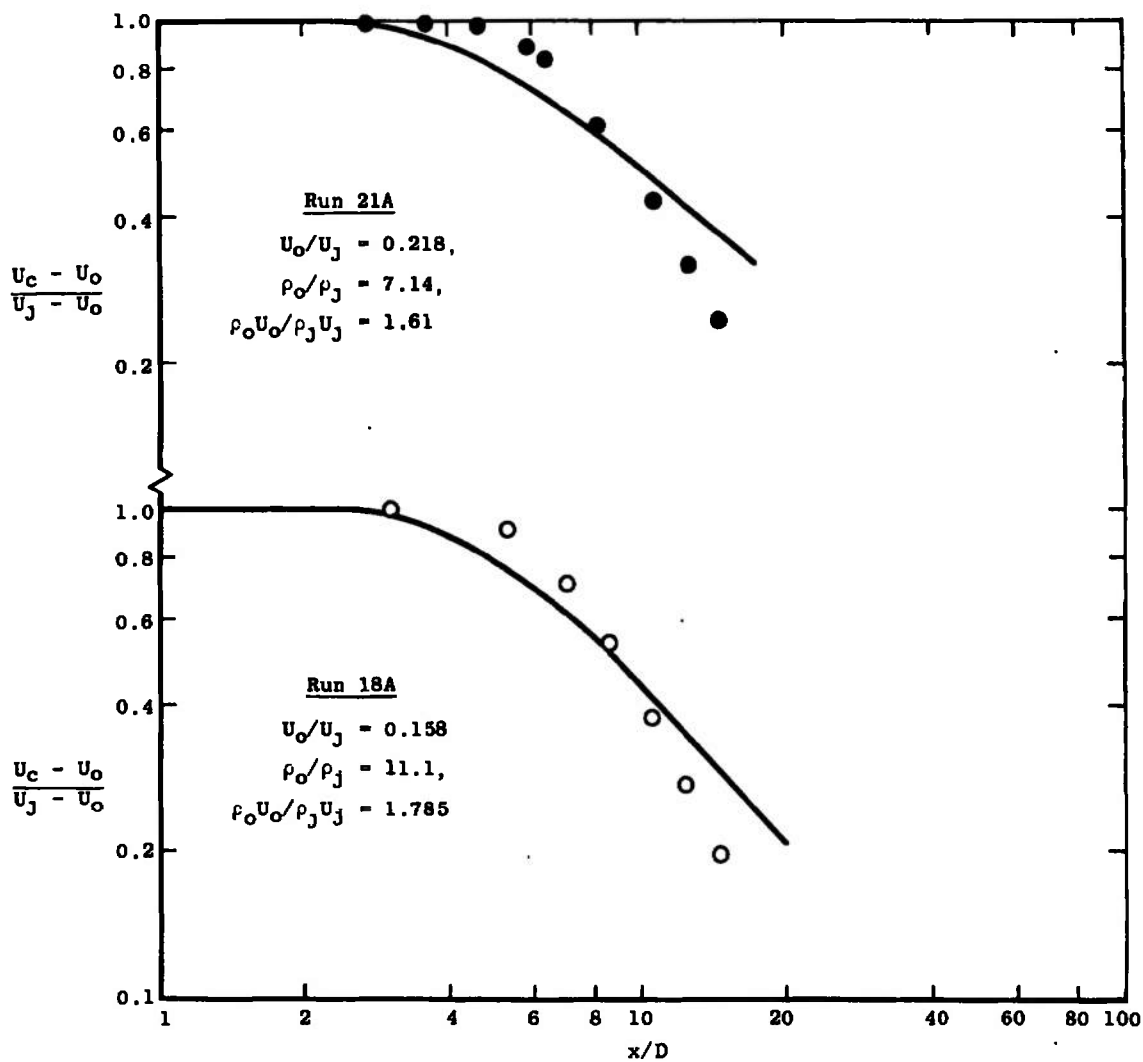


Figure 9.14. Comparison of Prandtl eddy viscosity theory with coaxial H₂-air mixing data of Chriss [90].

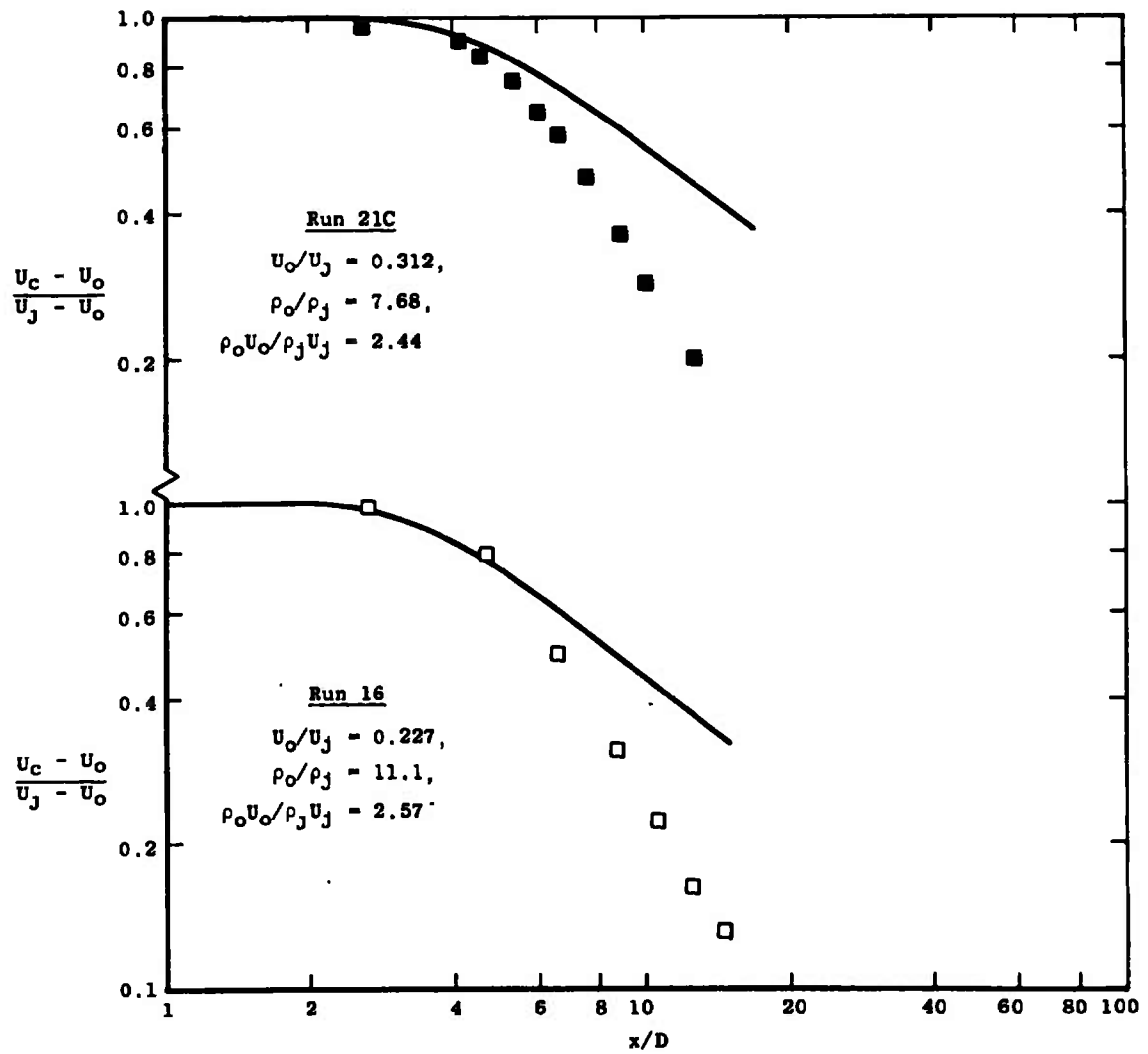


Figure 9.14. (continued)

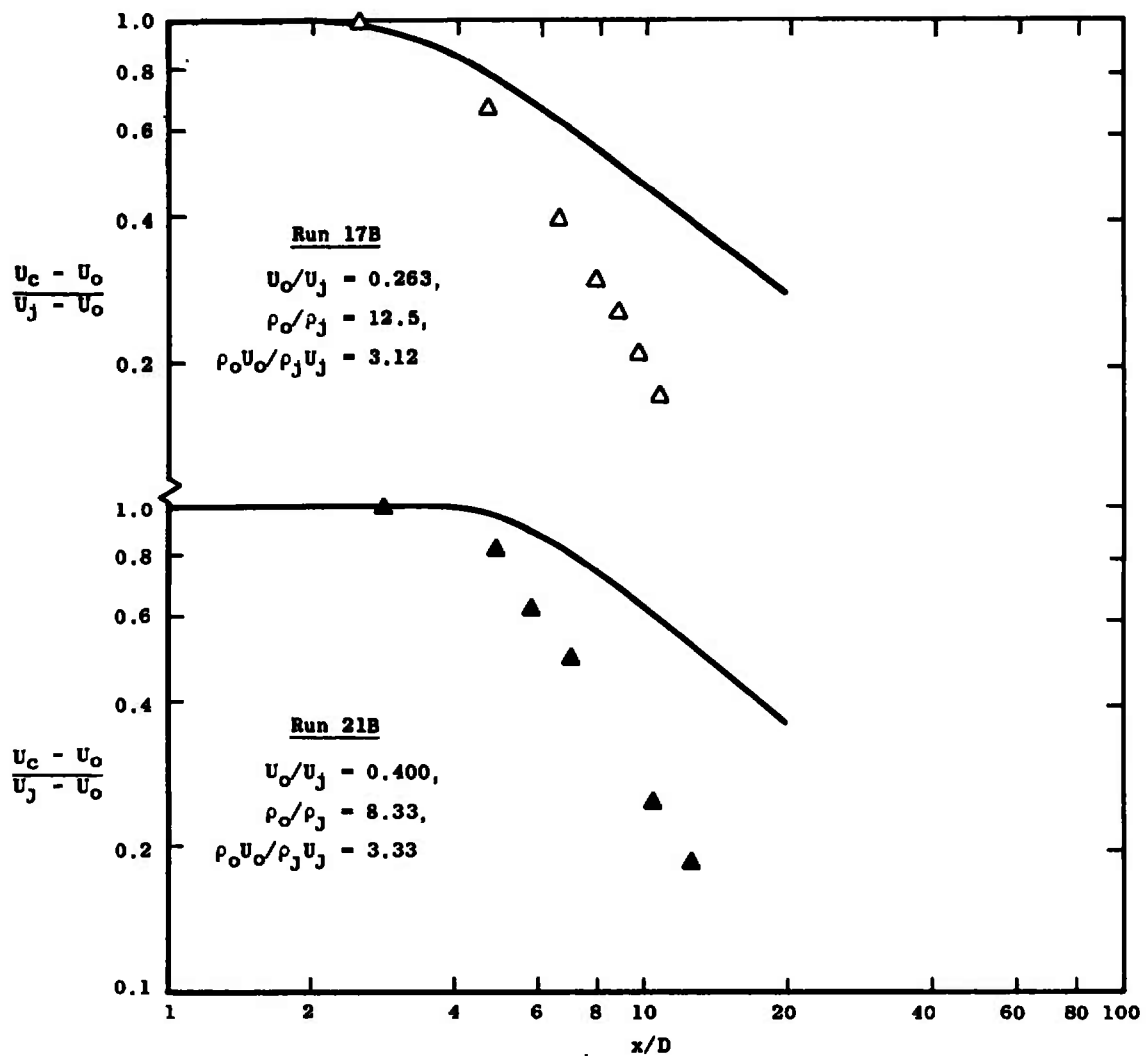


Figure 9.14. (continued)

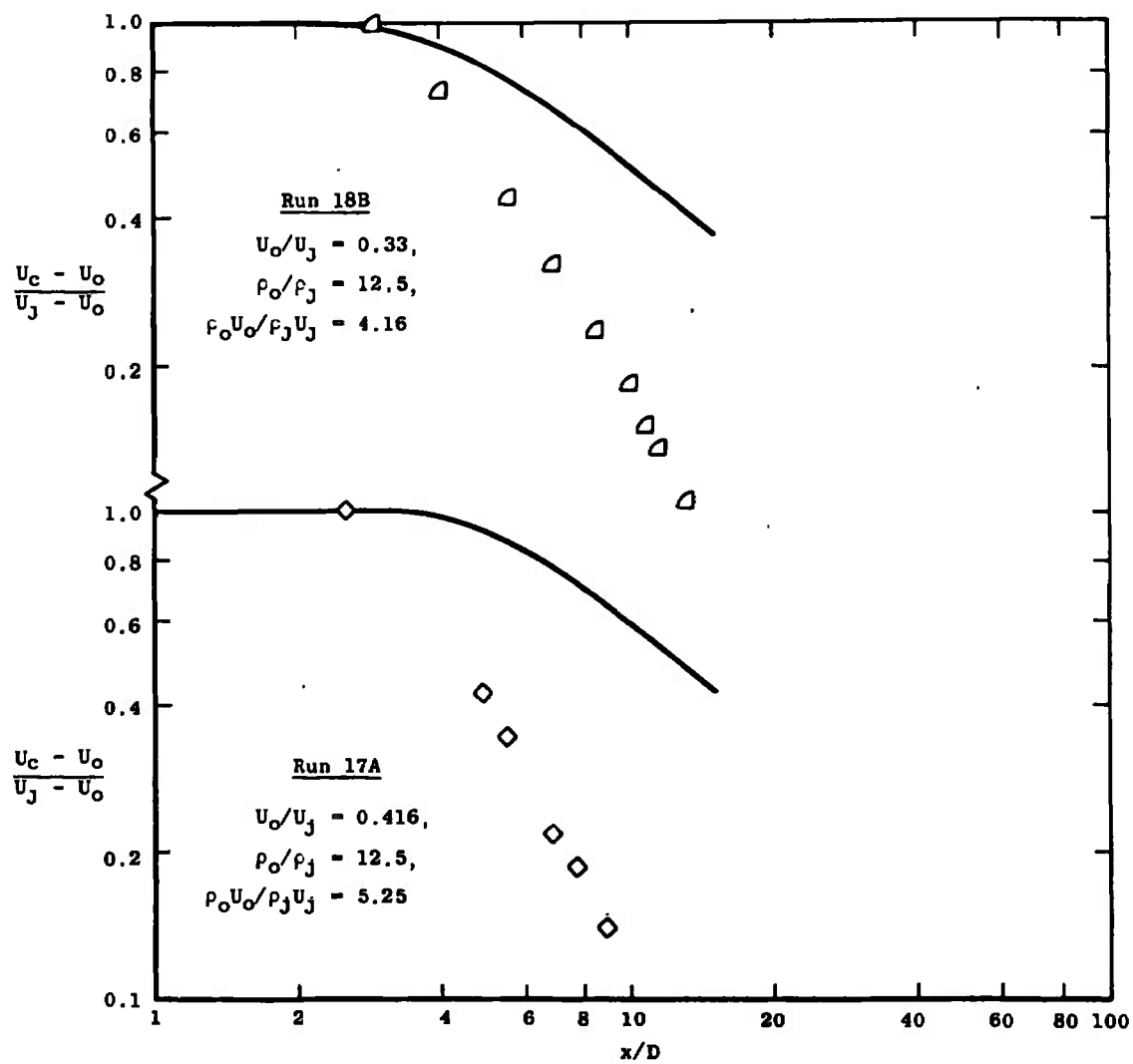


Figure 9.14. (continued)

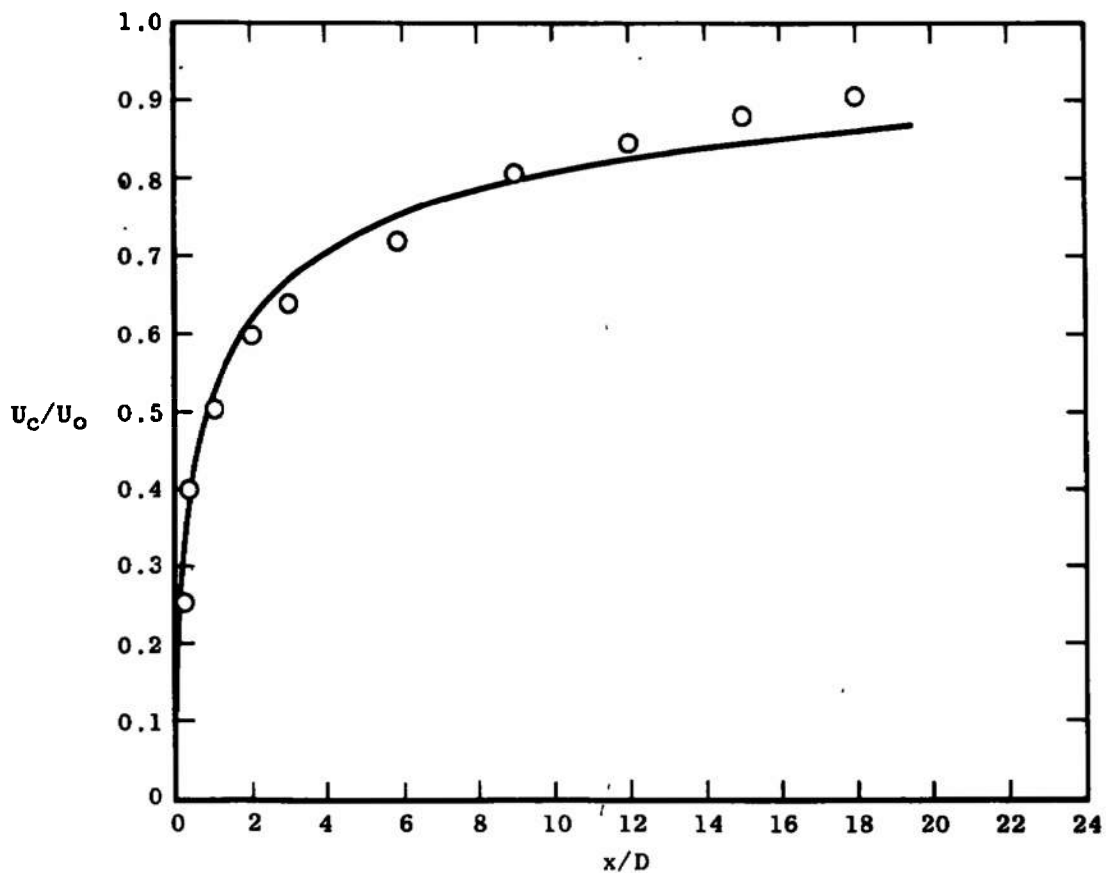


Figure 9.15. Comparison of prediction of Prandtl eddy viscosity theory with data for the initial region of an axisymmetric wake. Data of Chevray [58].

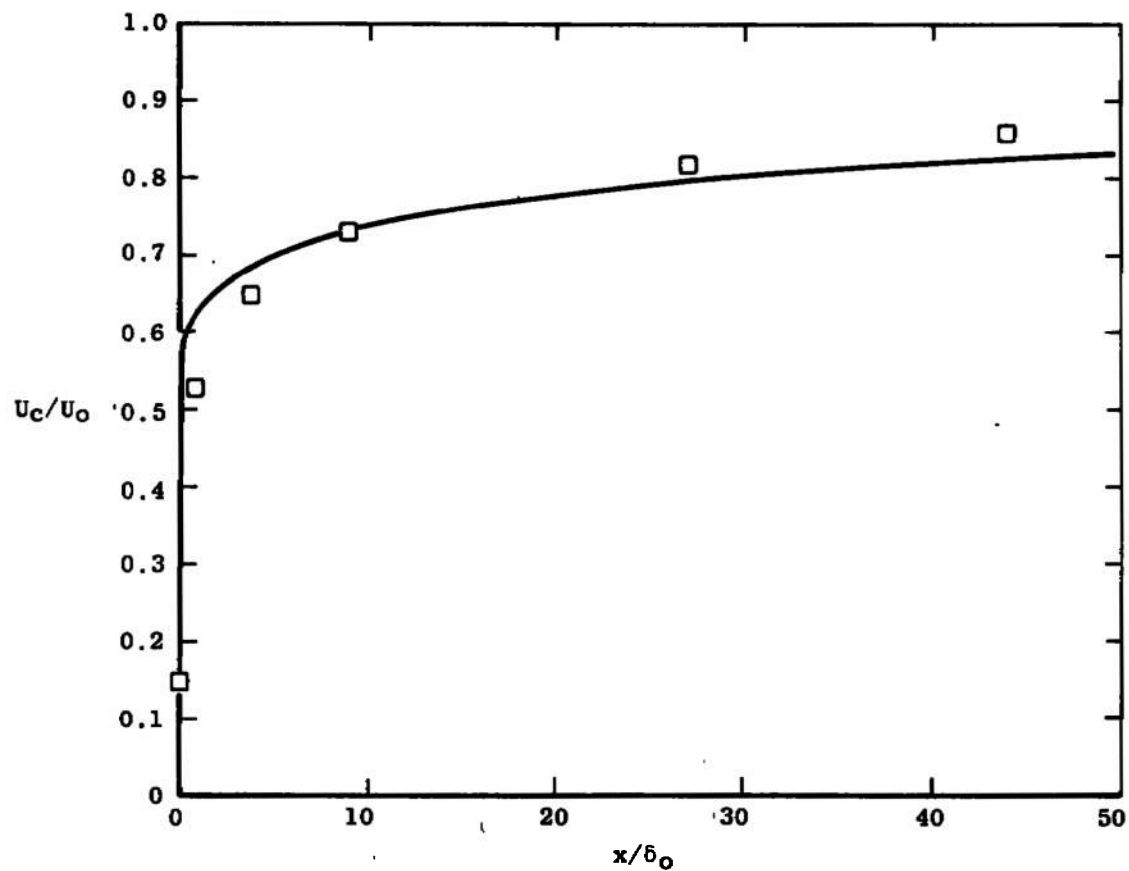


Figure 9.16. Comparison of prediction of Prandtl eddy viscosity theory with data for the initial region of a two-dimensional wake. Data of Chevray and Kovasznay [52].

also. Unlike most other locally dependent models, Schetz has formulated his model incorporating a single and hopefully universal constant.

Application of the Schetz model to the jet-into-still-air case is not really fair, since the displacement thickness is not readily defined in this case. However, since finite-difference calculations of free mixing flows often approximate a single-stream flow by incorporating a small but finite velocity at the outer edge of the mixing layer (as does the technique used in this study) it is of interest to observe the behavior of the model as U_o approaches zero. Figure 9.17 illustrates this behavior. As was pointed out in Chapter 7, for the case $U_o \rightarrow 0$, the Schetz model behaves like the Prandtl model with the width scale b replaced by b^2/r_j . This explains the drastic drop of the centerline velocity curve and the extreme overprediction of the mixing at any given axial station apparent in Figure 9.17. Because this calculation, like all of the others made in this study, conserves momentum and predicts geometrically similar profiles, the predicted jet width at $x/D = 20$ is huge compared to the predictions of other models. Figure 9.18 illustrates this fact well; even for $r/r_j = 15$, the local velocity ratio U/U_c is still equal to 0.8. Returning to Figure 9.17, the prediction of the Schetz model for the compressible jet-into-still-air can be seen to also be very inaccurate. The slope is not as wrong as for

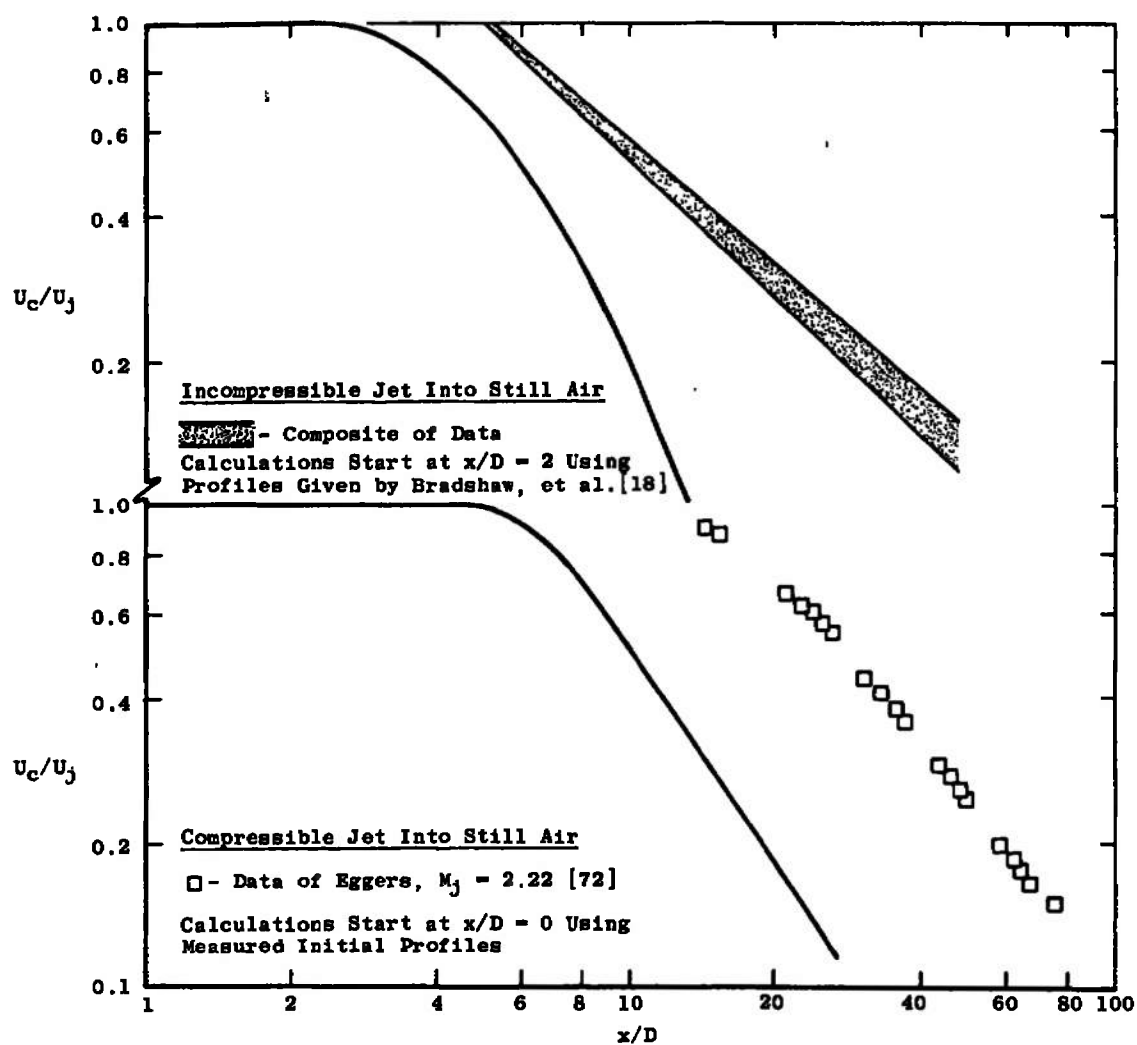


Figure 9.17. Comparison of predictions of Schetz "Unified Theory" with jet-into-still-air data.

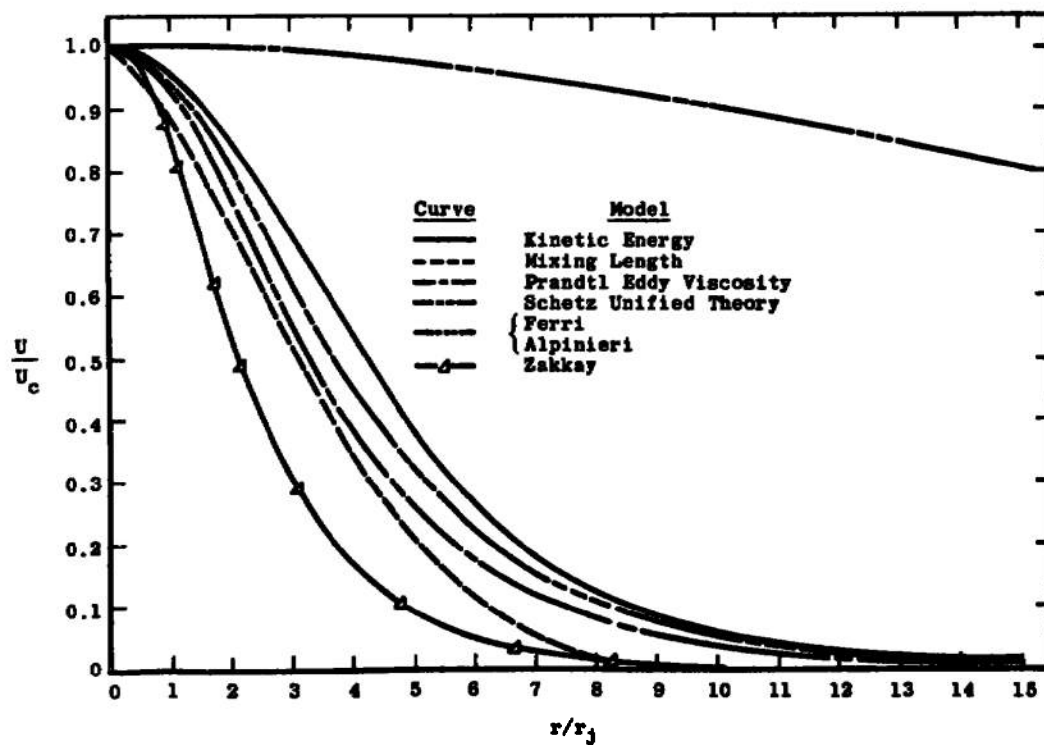


Figure 9.18. Comparison of semi-normalized velocity profiles predicted by various theoretical models for the jet-into-still-air at $x/D = 20$.

the incompressible jet. However, this apparent improvement may be an artifice of the calculation procedure. In the case of the incompressible jet, the chosen ratio of jet centerline velocity to the edge velocity was 0.01, while for the compressible jet this ratio, U_o/U_j was taken to be 0.07, as this was the lower-velocity limit of the data presented in Reference [72]. At $x/D = 15$ for the incompressible jet, U_c/U_o is still equal to 9. But for the compressible jet at $x/D = 20$, the ratio $U_c/U_o = 2.6$. This is because the jet velocity $U_j = 1785$ fps, so $U_o = 0.07 U_j = 125$ fps. Thus by $x/D = 20$, or earlier, the compressible jet calculation may be behaving like a coaxial mixing calculation.

The Schetz model (used here only in the first regime) performs much better for coaxial air-air mixing systems than for the jet-into-still-air case. Figures 9.19 and 9.20 illustrate this. However, the predicted asymptotic slope of the decay curve is, in all but one case, too large. The case for which the slope prediction appears to be good is the $U_o/U_j = 0.371$ data of Paulk [42], Figure 4.19, page 237. The constant in the Schetz model was evaluated by Schetz [120, 121] from considerations of the best fit with Forstall's $U_o/U_j = 0.5$ data. While these data have not been used in this confrontation because of their lack of agreement with the momentum integral criterion, and because of problems related to their initial conditions, it seems quite

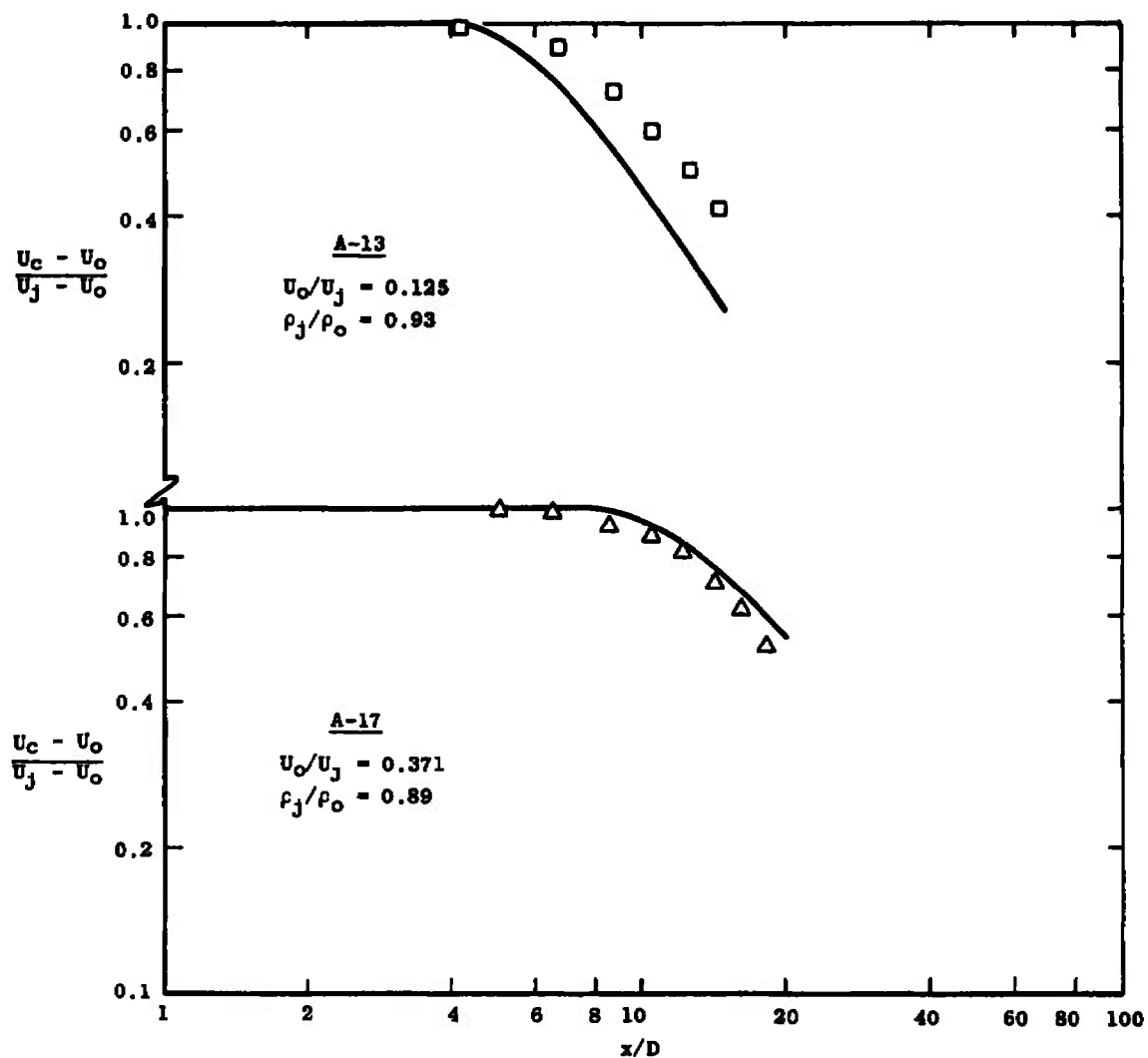


Figure 9.19. Comparison of predictions of Schetz "Unified Theory" with coaxial air-air data of Paulk [42].

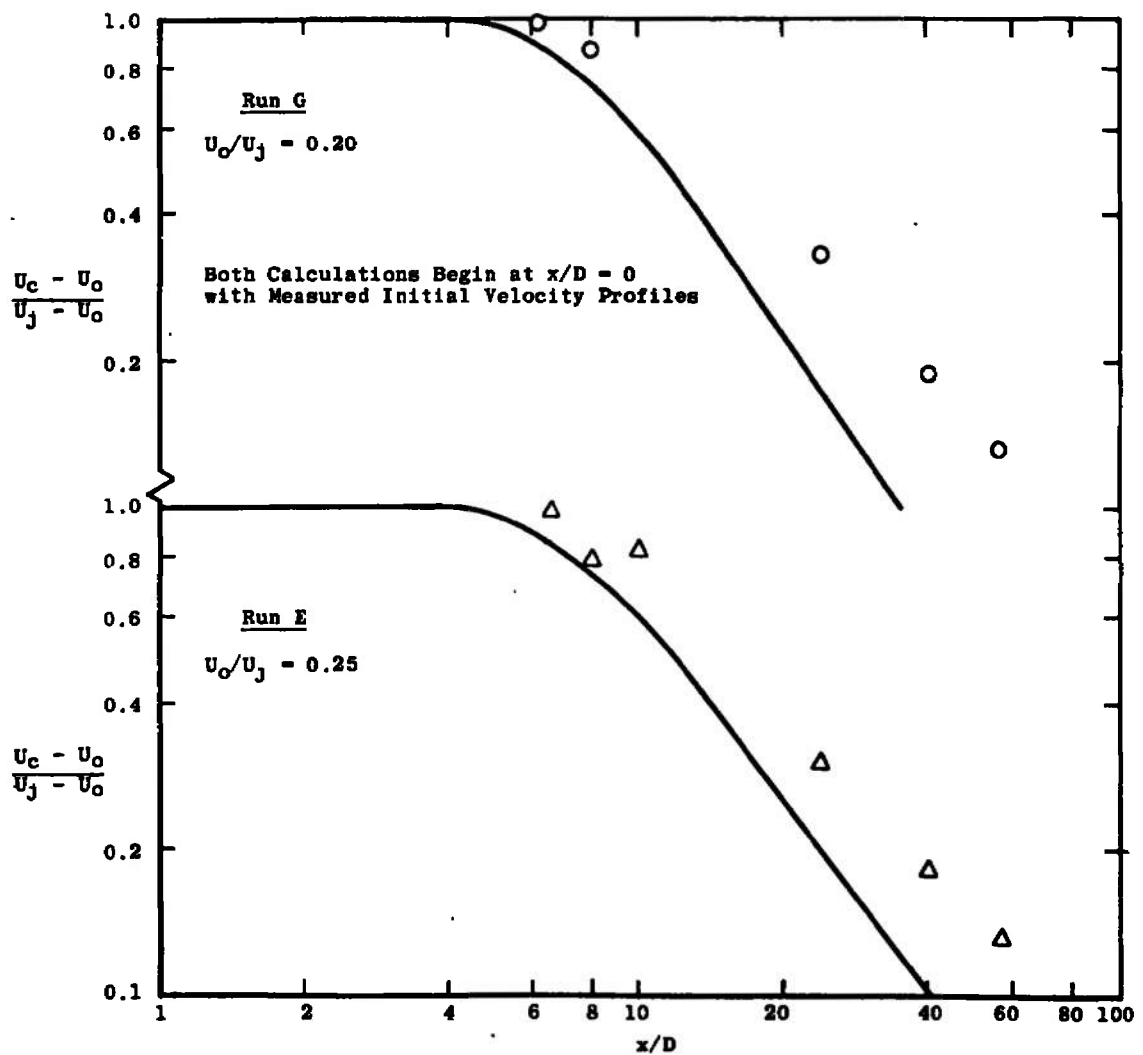


Figure 9.20. Comparison of predictions of Schetz "Unified Theory" with coaxial air-air mixing data. Data of Forstall [40].

possible that the Schetz model will agree best in the coaxial air-air mixing case when the velocity ratio is in the neighborhood of 0.5.

The Schetz model provides a better prediction of the hydrogen-air mixing data used in this study than any other locally-dependent eddy viscosity model. It is also the only locally-dependent model which predicts an increasing centerline velocity decay rate as the ratio $\rho_o U_o / \rho_j U_j$ increases from 1.0, which may indicate that the method which Schetz uses to include the effect of density differences is fundamentally more sound than that used in the other eddy viscosity models. Figure 9.21 illustrates the behavior of the Schetz model in comparison with experimental data. It can be seen from Figure 9.21 that the axial decay curve slope predicted by the Schetz model is in all cases reasonably close to the slope experimentally measured. The deviations in the velocity potential core length from the experimental values seen in Figure 9.21 cannot be charged to the Schetz model as Prandtl mixing length was used for the core region in all of these calculations. In his comparison with some of these same data [121], Schetz does not start the calculations at $x = 0$ but rather begins them using experimental profiles downstream of the end of the experimental velocity potential core.

From Figure 9.21 it can be seen that there is a progressive change in the character of the axial decay

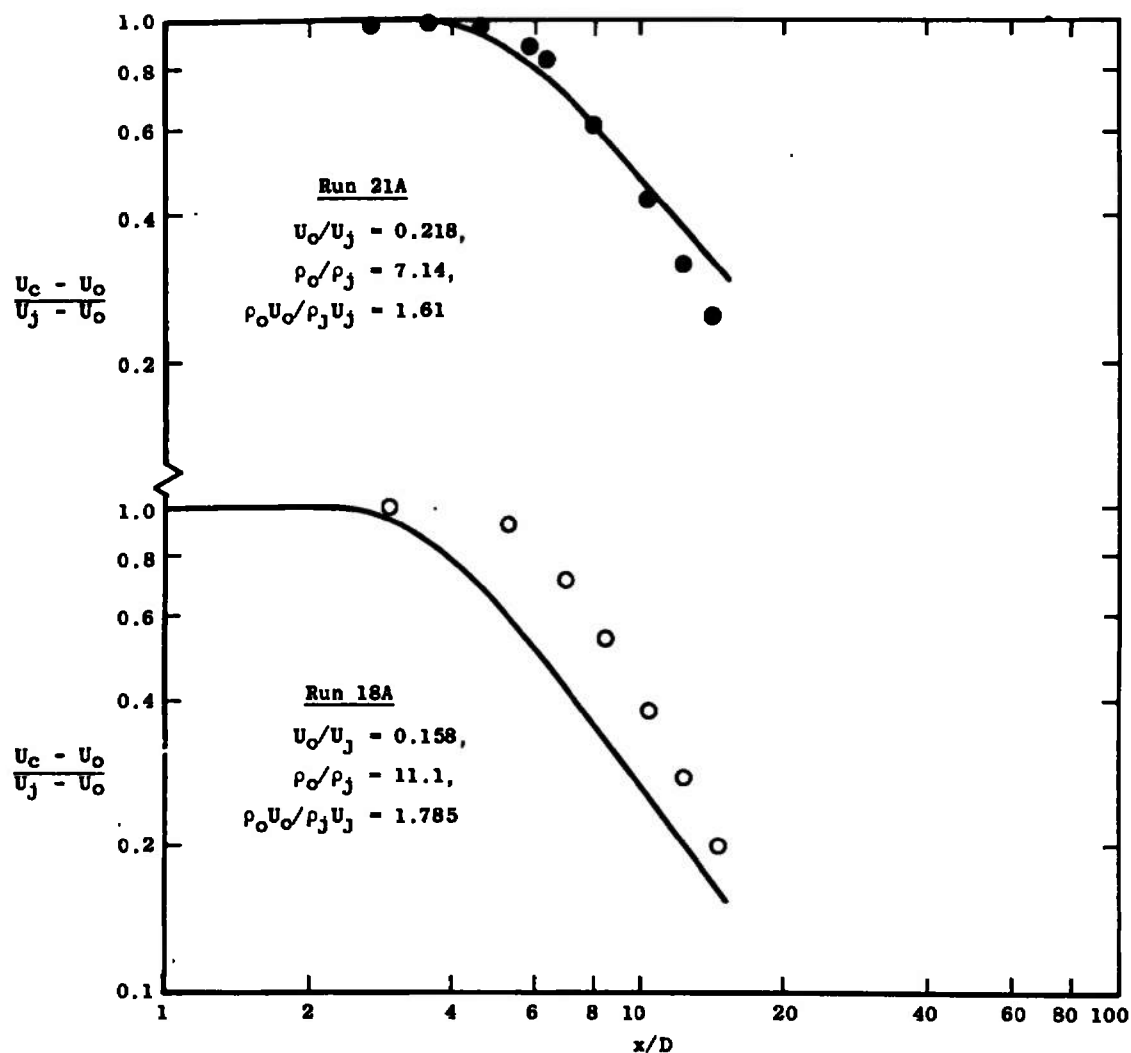


Figure 9.21. Comparison of Schetz "Unified Theory" with coaxial H₂-air mixing data of Chriss [90].

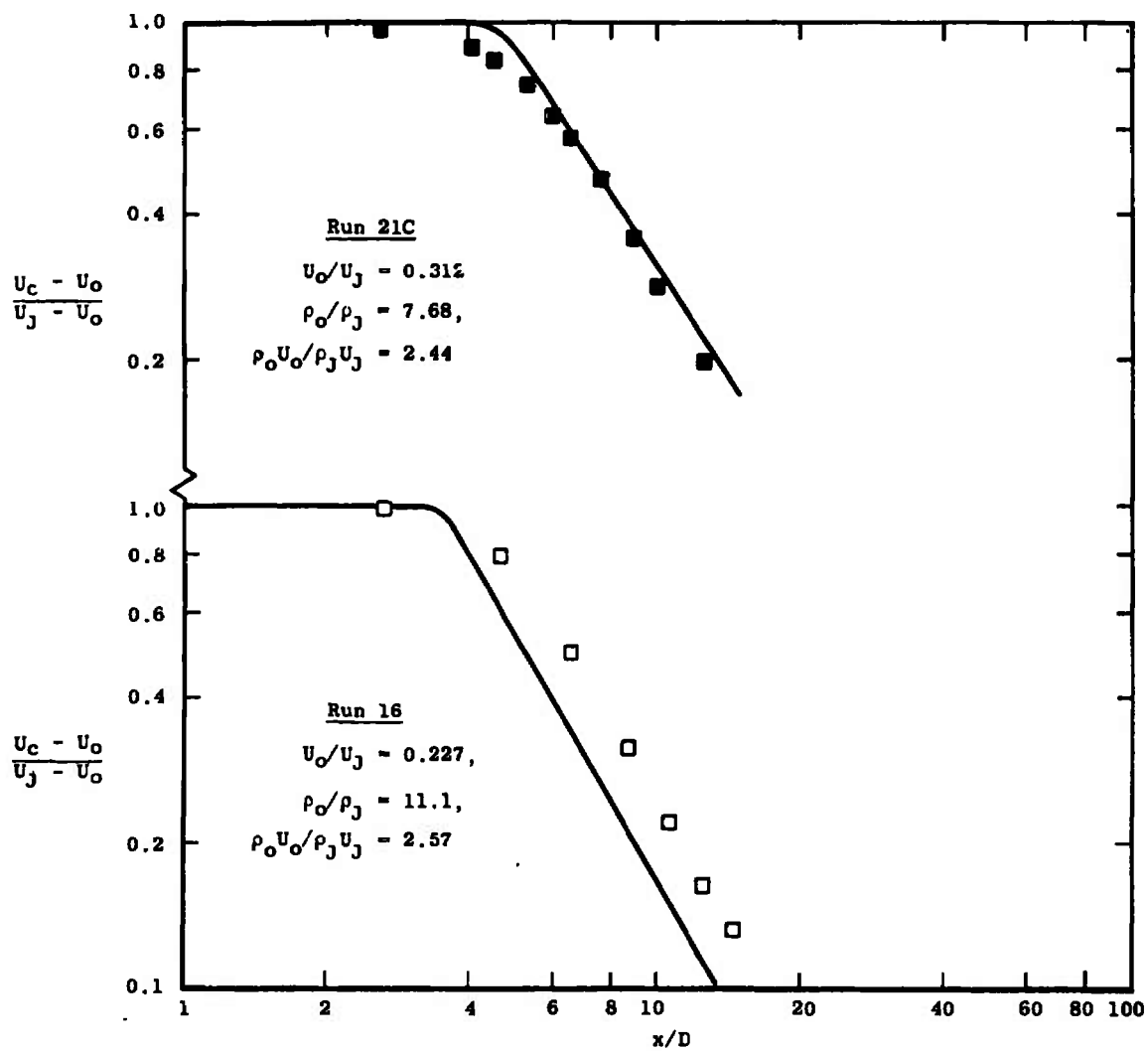


Figure 9.21. (continued)

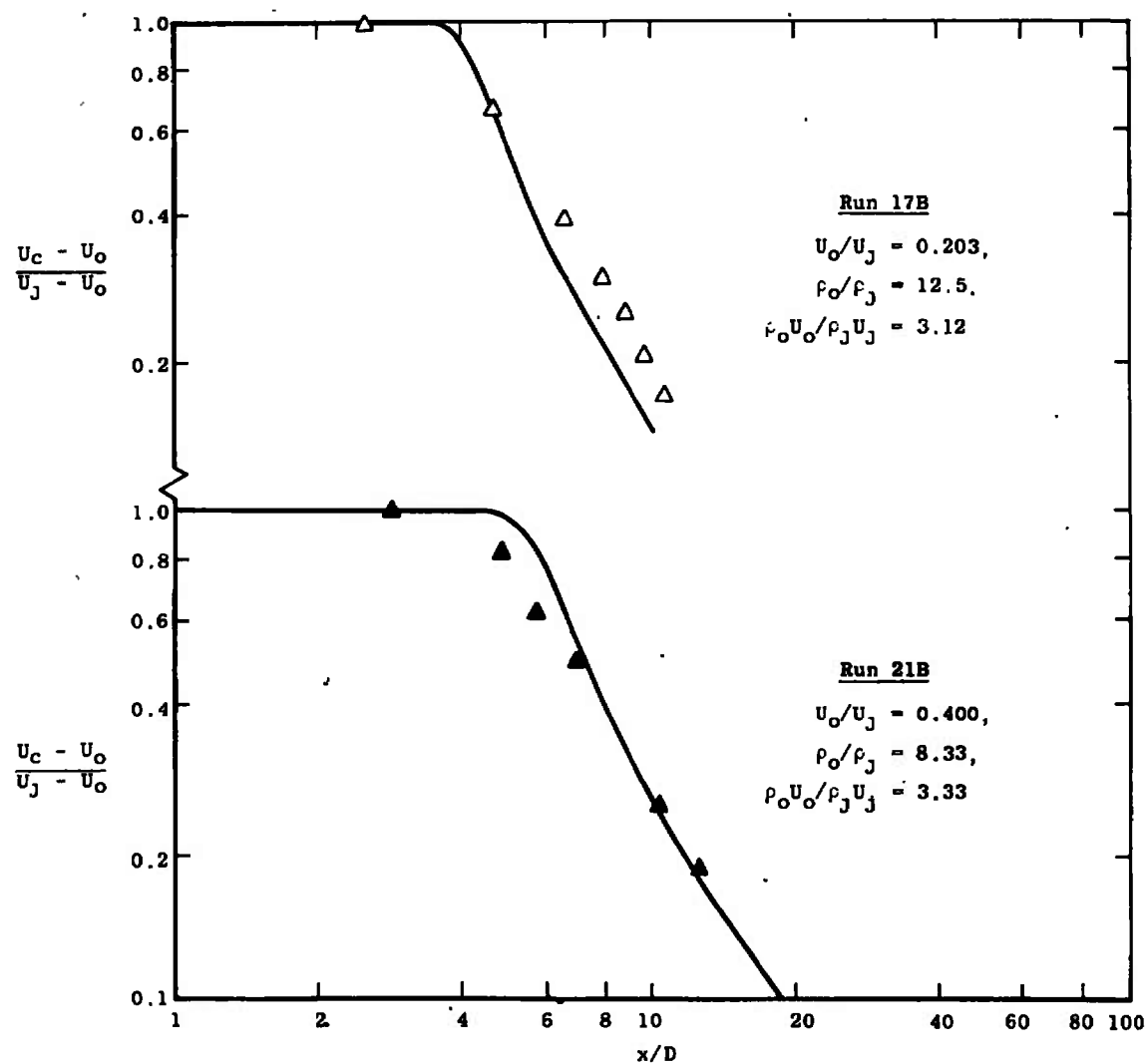


Figure 9.21. (continued)

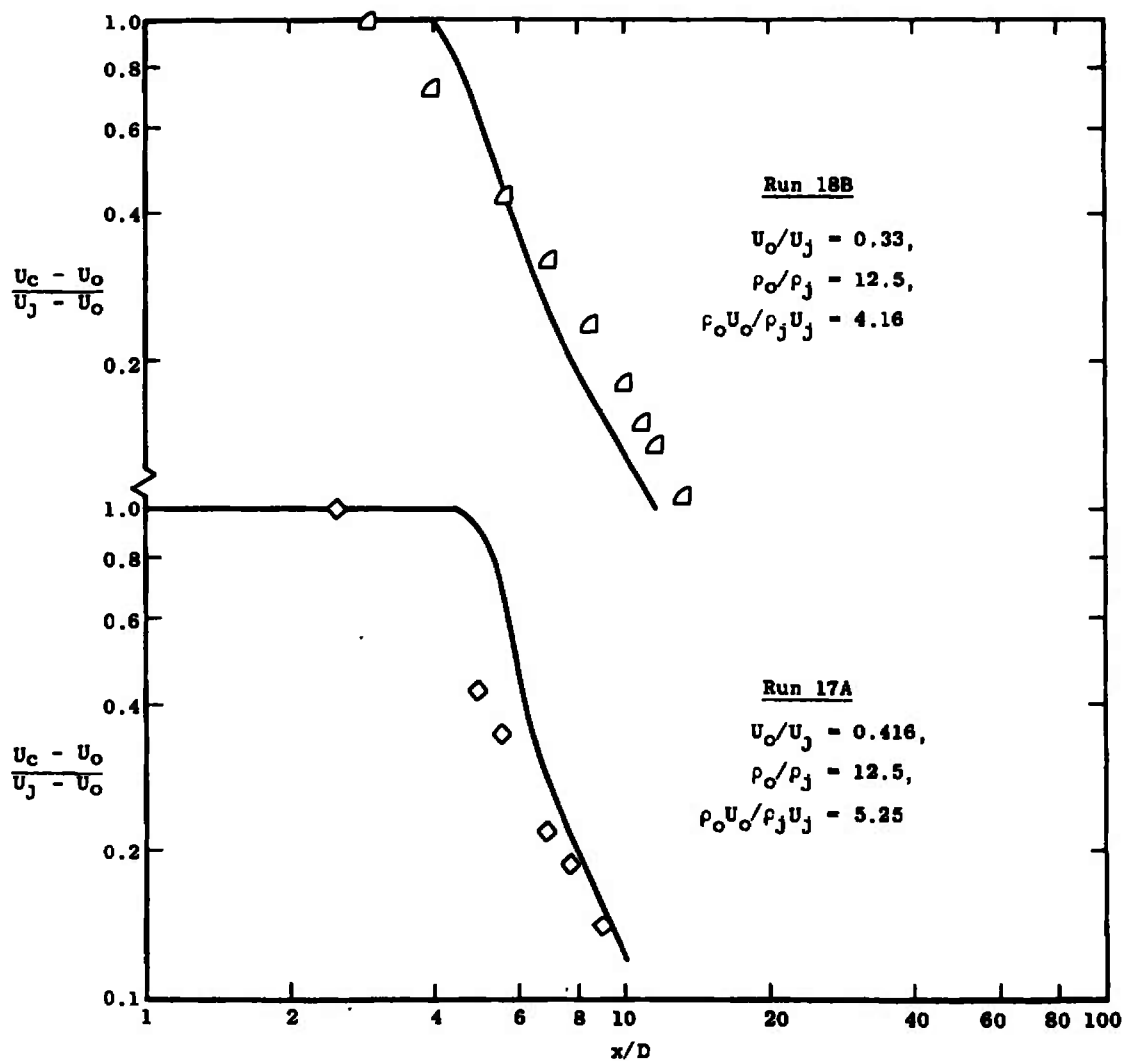


Figure 9.21. (continued)

curves of the Schetz model from the linear (on a log-log plot) character at low values of $\rho_o U_o / \rho_j U_j$ which is also characteristic of other models at all values of this parameter--to a shallow s-curve shape which becomes quite pronounced at larger $\rho_o U_o / \rho_j U_j$ values. Figure 9.22 shows the fully-normalized velocity and shear stress radial profiles calculated at two axial stations for the data of Chriss, run 17A, which had the most pronounced change in slope. The calculations, which of course use the Schetz model, show that there is no pronounced change in the velocity profiles between the two stations, although the farther downstream station shows a quicker velocity profile cutoff. Since the fully-normalized velocity profiles were shown in Chapter 5 to follow a "cosine" velocity profile, which gives $(U - U_o) / (U_c - U_o) = 0$ at $r = 2r_{1/2}$, the cutoff shown for the $x/D = 12.8$ profile on Figure 9.22 represents an inaccuracy; the cutoff is also reflected in the shear stress profiles (τ / τ_{max}) also shown on the figure. However, experience has shown that these effects at the calculated edge of the mixing layer do not exert a substantial effect on the calculations, leading to the conclusion that the s-curve shape shown in Figure 9.21, pages 415-418, reflects a change both in velocity decay slope and in half-width growth. The reasons for this change remain obscure.

Figures 9.23 and 9.24 depict the performance of the Schetz model as compared to data for the increase of

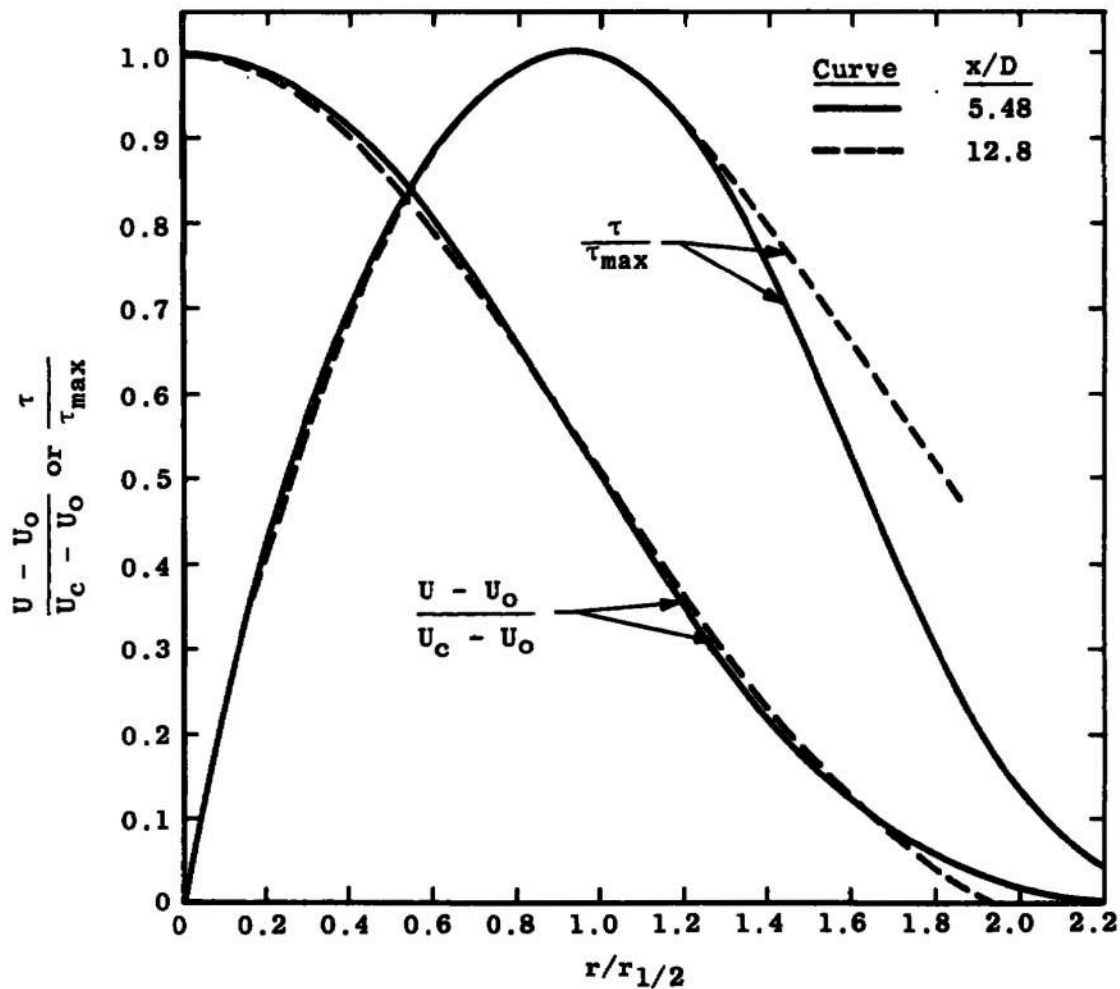


Figure 9.22. Comparison of calculated velocity and shear stress profiles at two axial stations: coaxial H₂-air mixing, Schetz model.

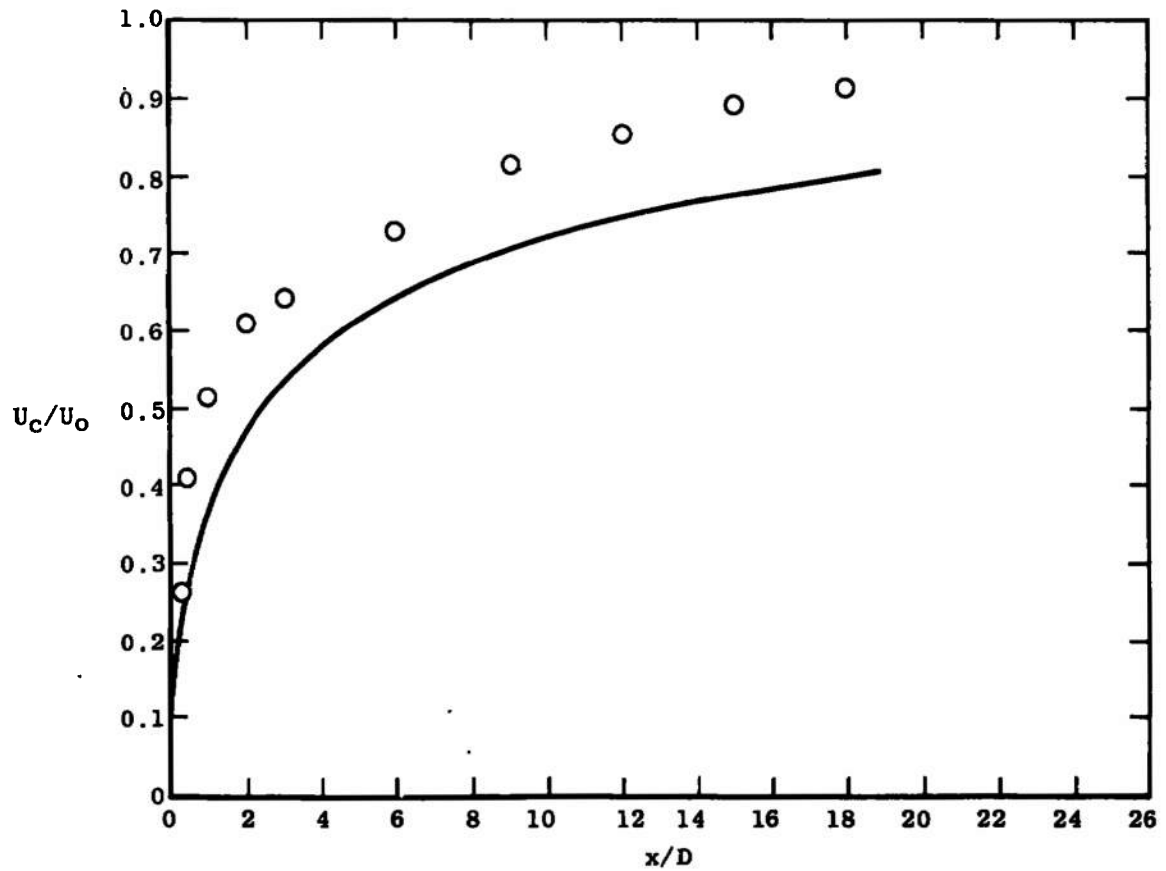


Figure 9.23. Comparison of prediction of Schetz "Unified Theory" with data for the initial region of an axisymmetric wake. Data of Chevray [58].

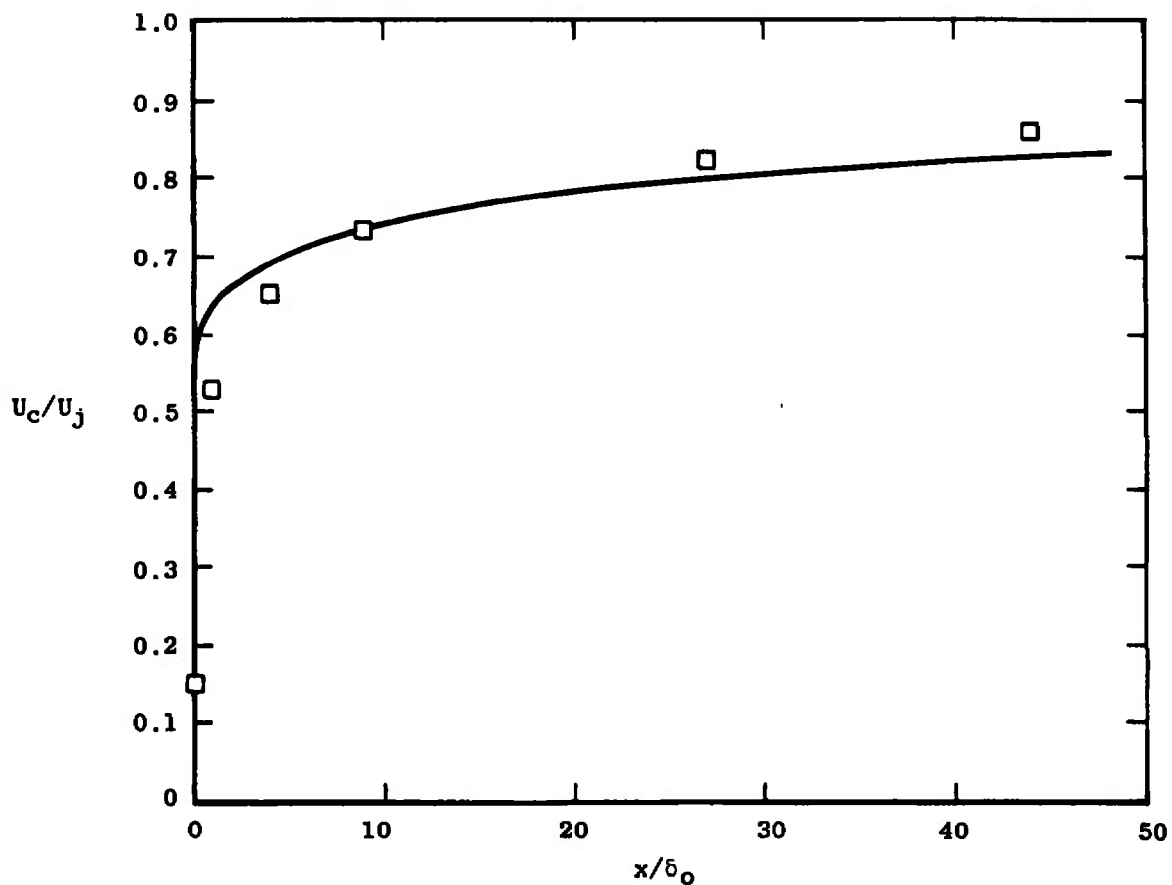


Figure 9.24. Comparison of prediction of Schetz "Unified Theory" with data for the initial region of a two-dimensional wake. Data of Chevray and Kovasznay [52].

centerline velocity in axisymmetric and two-dimensional turbulent wakes. Interestingly, the behavior of the calculations is different for the two wakes, with the initial increase in velocity being overpredicted for the two-dimensional wake and underpredicted for the axisymmetric wake. Schetz [121] points out that in a two-dimensional flow his model reduces to the Prandtl eddy viscosity model, which gives a similar prediction. This is not the case for the axisymmetric flow, and this difference may explain the observed difference in the calculations.

The two-dimensional wake provides a good test of the conclusion reached by Schetz [121] that in a two-dimensional flow the predictions made by this model and that of the Prandtl eddy viscosity model are similar. Figure 9.25 illustrates a comparison of these two predictions for this data; also included is the mixing length theory which, as has been shown above, shows a similar behavior to that of the Prandtl eddy viscosity model for this flow. Figure 9.25 shows that the predictions of all three models are virtually identical for the two-dimensional wake.

Confrontation IV: Ferri Model

The eddy viscosity model proposed by Ferri [83] is a first-cut try at modifying the Prandtl eddy viscosity model already discussed so that it will apply to a variable-density flow. To make this modification, Ferri simply substituted the mass-flux difference $|\rho_c U_c - \rho_o U_o|$ for the

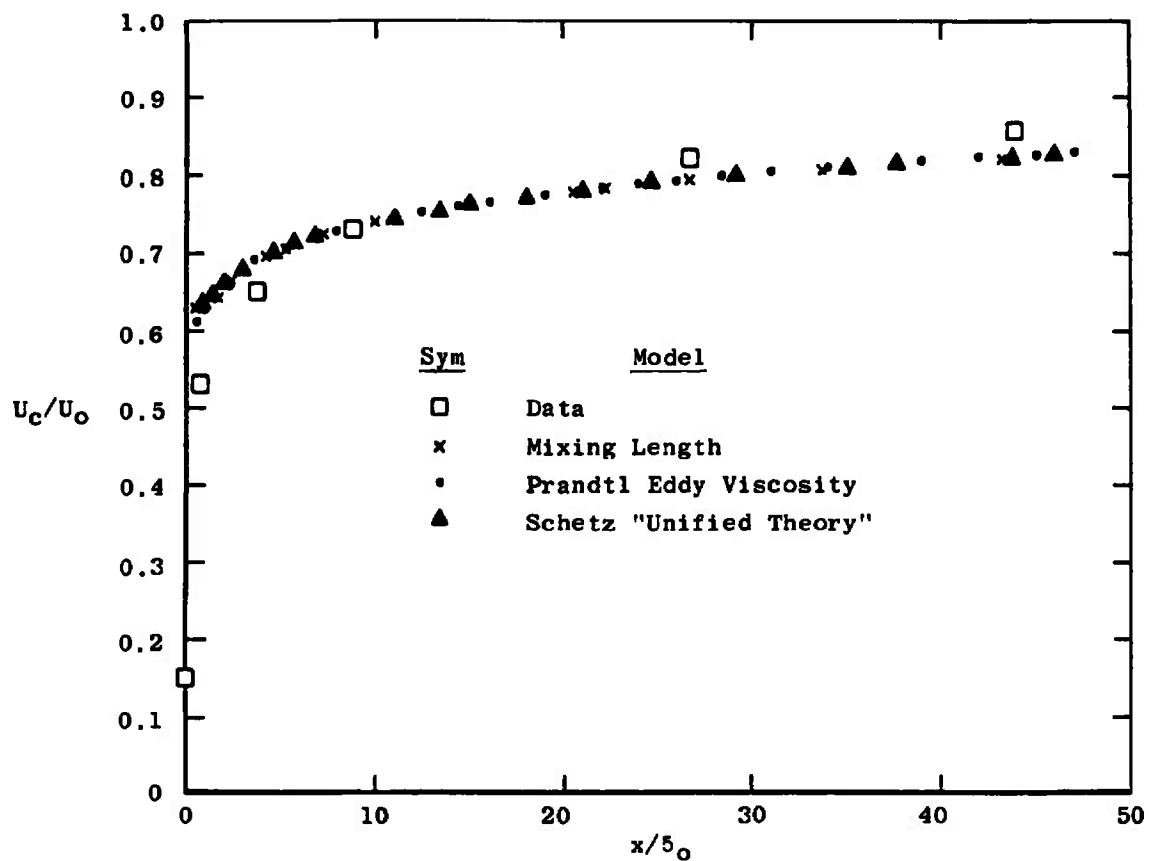


Figure 9.25. Comparison of predictions of three models for the two-dimensional wake data of Chevray and Kovaszny [52].

equivalent expression $\rho |U_c - U_o|$ in the Prandtl model. This change has the implication that the product $\rho \epsilon$ is constant across a lateral profile, rather than ϵ , for comparing expressions one has for the Ferri model

$$\rho \epsilon = K_F r_{1/2} |\rho_c U_c - \rho_o U_o| \quad (9.1)$$

and for the Prandtl model

$$\rho \epsilon = K_P r_{1/2} \rho |U_c - U_o| \quad (9.2)$$

Two additional changes were introduced by Ferri: first, the parameter $r_{1/2}$ is defined as the radius for which $\rho U = 1/2[\rho_c U_c + \rho_o U_o]$ rather than the radius for which $U = 1/2[U_c + U_o]$; second, the value of the constant K_F was changed.

The constant K_F was chosen by Ferri, et al., [83] as 0.025 in order to agree with experimental data for the incompressible jet-into-still-air. Here of course the Ferri model reduces to the Prandtl eddy viscosity model. Because the constant was so chosen, it is not surprising that the agreement of this model with the data is quite good, as shown on Figure 9.26; however, the slope is still not quite correct as compared with the mean of the data. It is in fact identical to the slope predicted by the Prandtl model.

Since the Ferri model reduces to the Prandtl eddy viscosity model for an incompressible flow, a comparison of

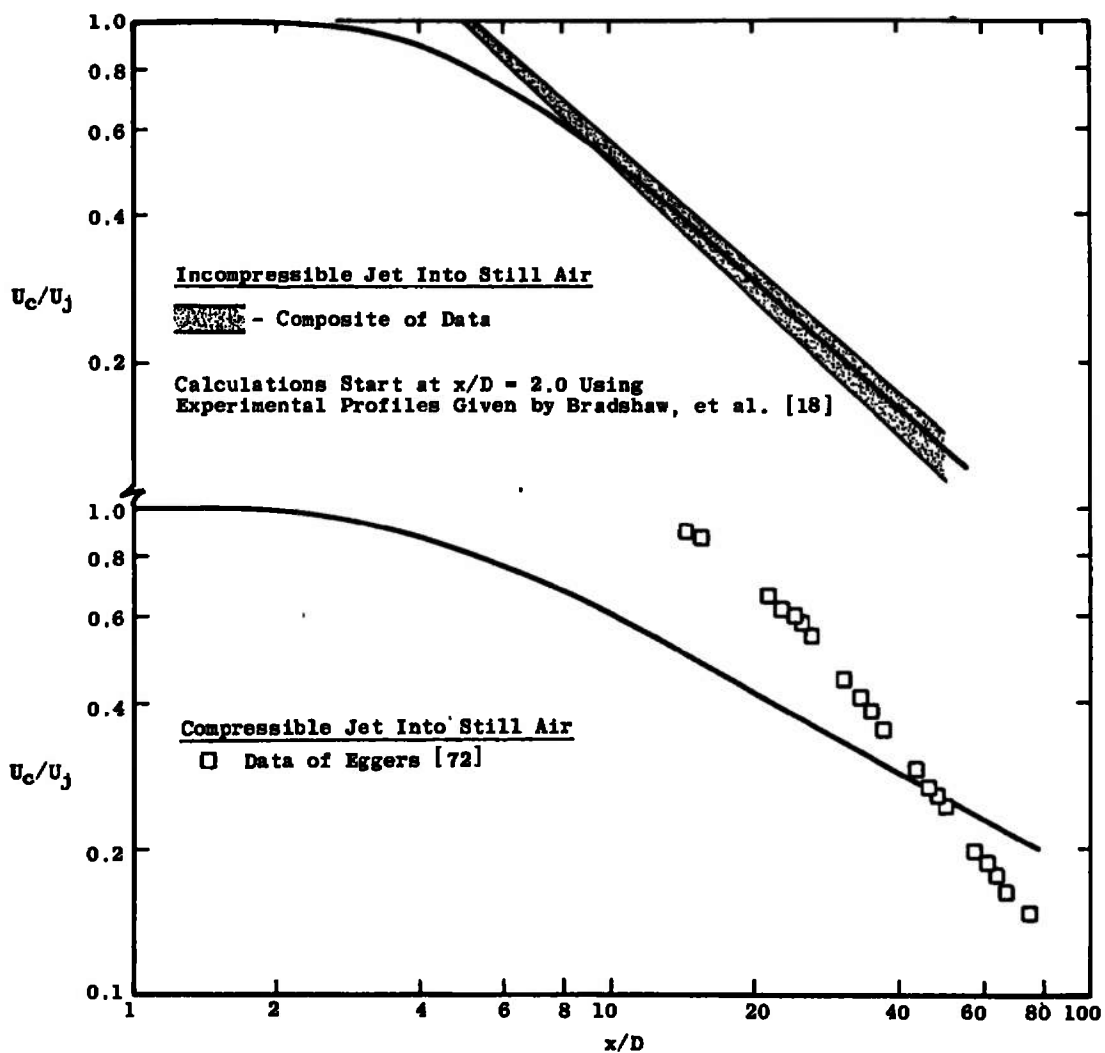


Figure 9.26. Comparison of predictions of Ferri model with jet-into-still-air data.

calculations made with these two models will indicate the effect of changing the constant on the Prandtl model. The constant used in the Ferri model is 0.025; it will be recalled that the Prandtl model as used here has $K_p = 0.007$ in the first regime and 0.011 in the second. Figure 9.27 presents a comparison of the calculations, from which it is easily seen that for both single-stream and coaxial mixing the effect of the change in constant (which of course represents a change in shear stress) is to change the predicted length of the velocity potential core while preserving the predicted slope of the decay curve.

Returning to Figure 9.26, it can be seen that the prediction made by the Ferri model for the compressible jet-into-still-air is poor, with a highly underpredicted core length and asymptotic decay curve slope. This characteristic, which causes the predictions of the Ferri model to intersect the experimental data rather than paralleling it, will be seen to be characteristic.

Figures 9.28 and 9.29 illustrate the behavior of the Ferri model when it is applied to coaxial air-air mixing problems. As was discussed just above, the predicted slope of the axial decay of the centerline velocity curve is the same as that of the Prandtl eddy viscosity model, but the predicted velocity potential core length is smaller. This combination improves the level of accuracy of the prediction somewhat in the range of axial distance considered, since

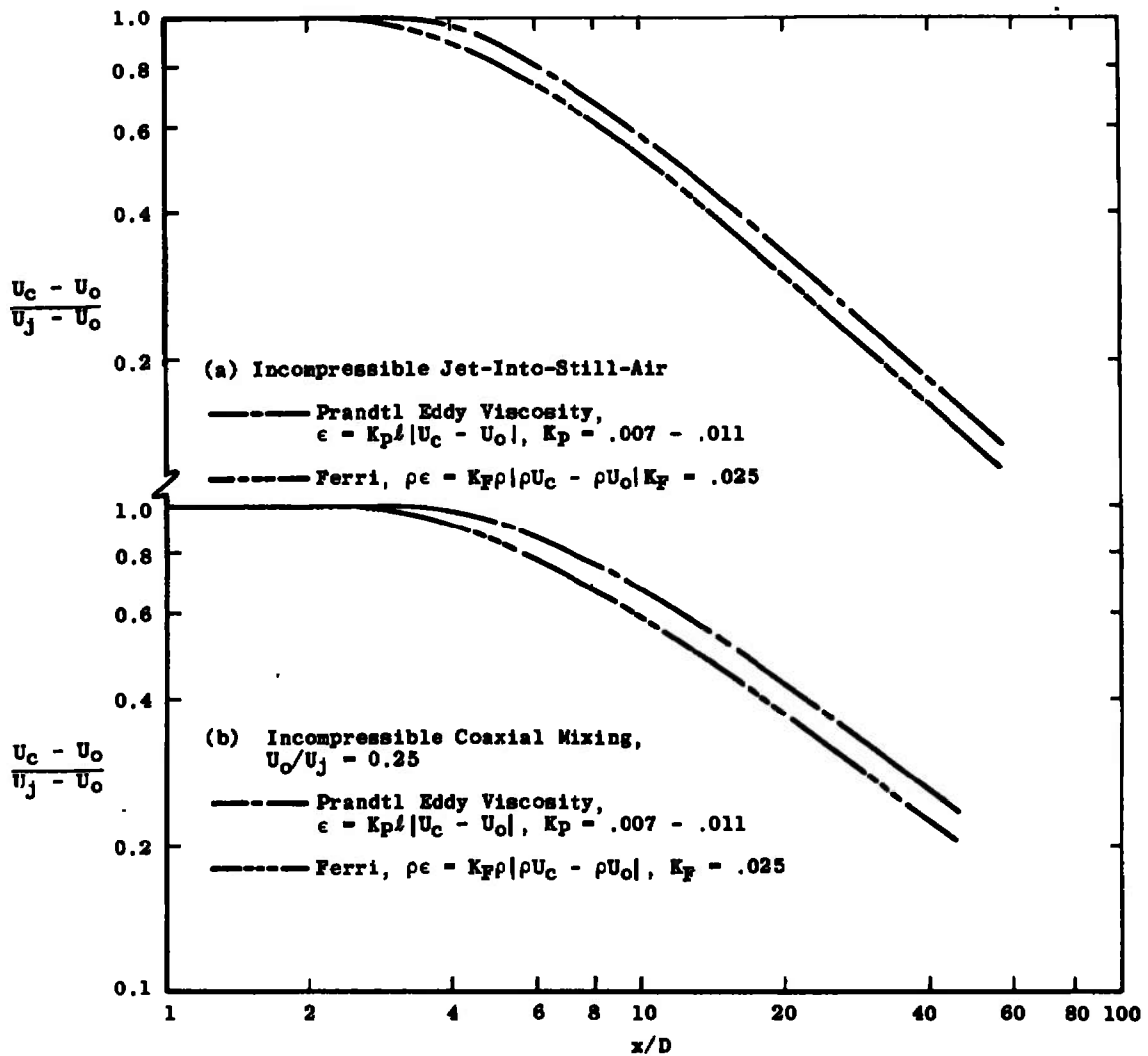


Figure 9.27. Effect of change of constant in the Prandtl eddy viscosity model.

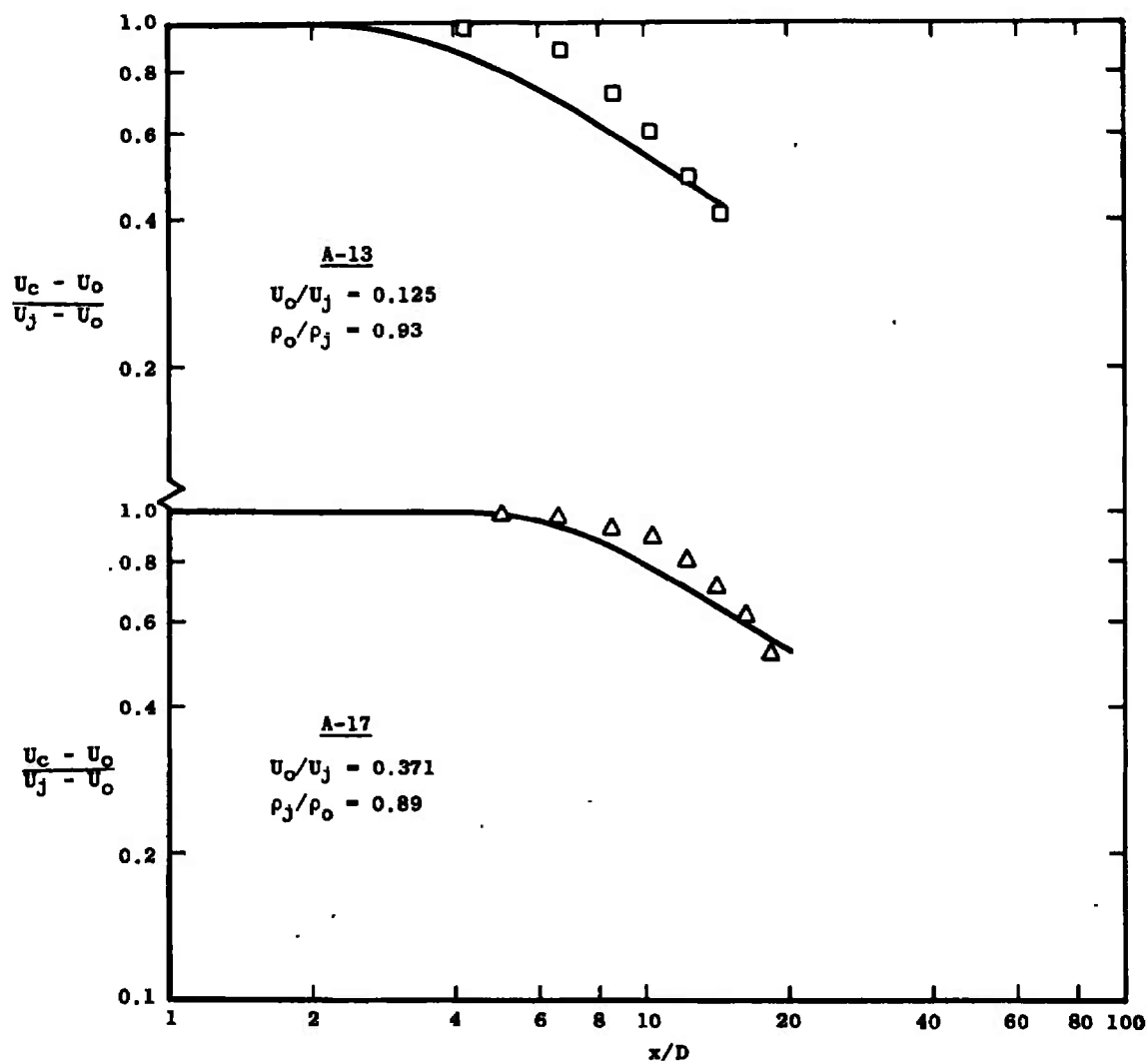


Figure 9.28. Comparison of predictions of Ferri model with coaxial air-air data of Paulk [42].

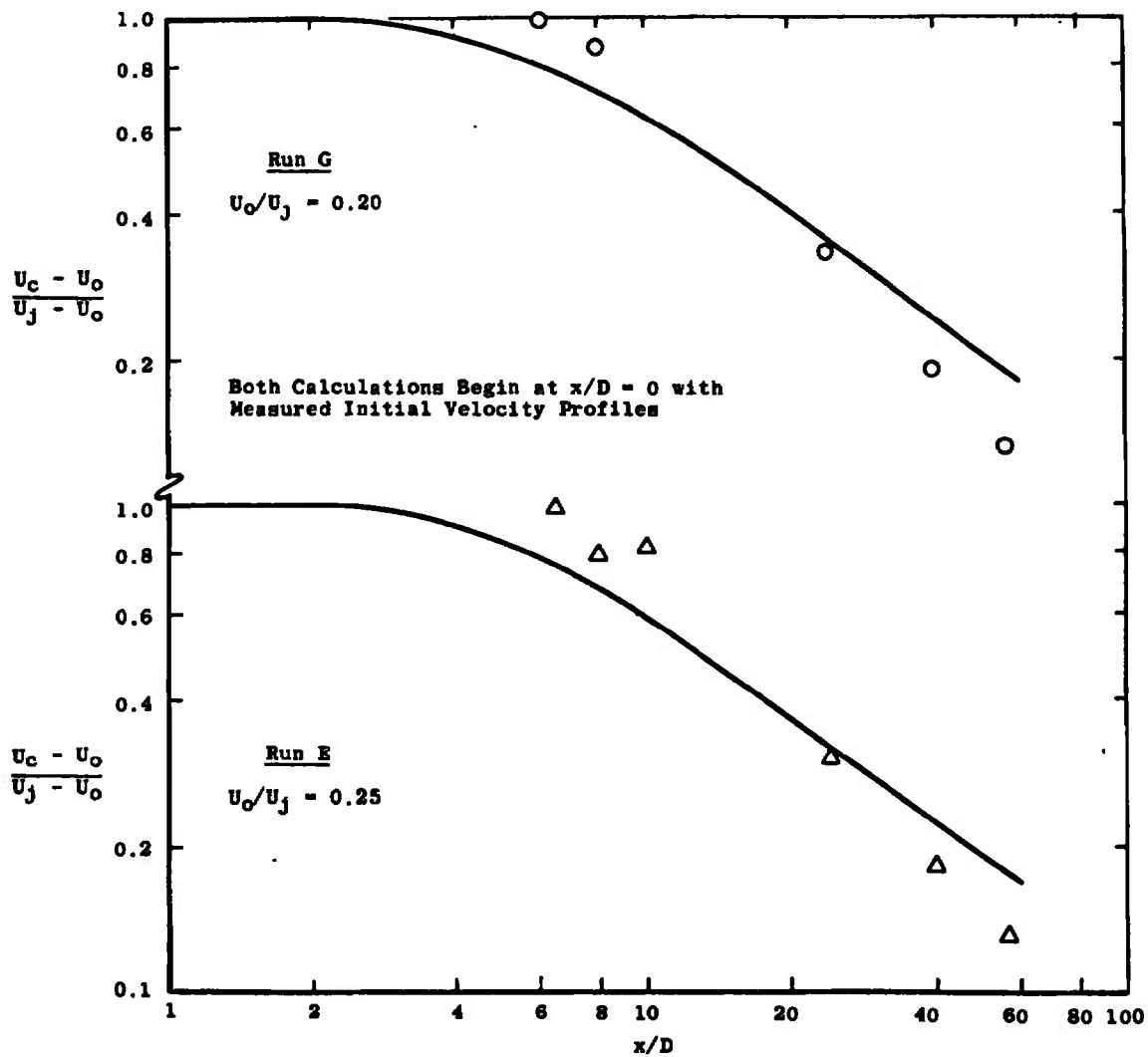


Figure 9.29. Comparison of predictions of Ferri model with coaxial air-air mixing data. Data from Forstall [40].

the decay curves now intersect the data. However, it is clear that as for the Prandtl eddy viscosity model, the trend of the prediction is wrong.

The same characteristics appear in the Ferri model predictions of hydrogen-air coaxial mixing as shown on Figure 9.30. The velocity potential core length is underpredicted, in the high $\rho_o U_o / \rho_j U_j$ cases grossly so. The slope of the decay curve is also underpredicted, so that as described above the prediction intersects the data curve at some point. Since a change in the constant would only change the predicted velocity potential core length and not the asymptotic slope of the decay curve, it is clear that the density-variation modification proposed by Ferri is fundamentally unsound.

The Ferri model will again reduce to the Prandtl model for the two wakes considered in this study, with a different eddy viscosity constant. The behavior of the calculation will be thus similar to that using the Prandtl model. Figures 9.31 and 9.32 indicate that this is the case, and that the increased constant improves, in the axisymmetric case, the initial velocity rise prediction and, in the two-dimensional case, the middle-range velocity prediction. But once again (and of course like the Prandtl model) the trend of the prediction is wrong (too small a rate of increase of centerline decay is predicted) and it is

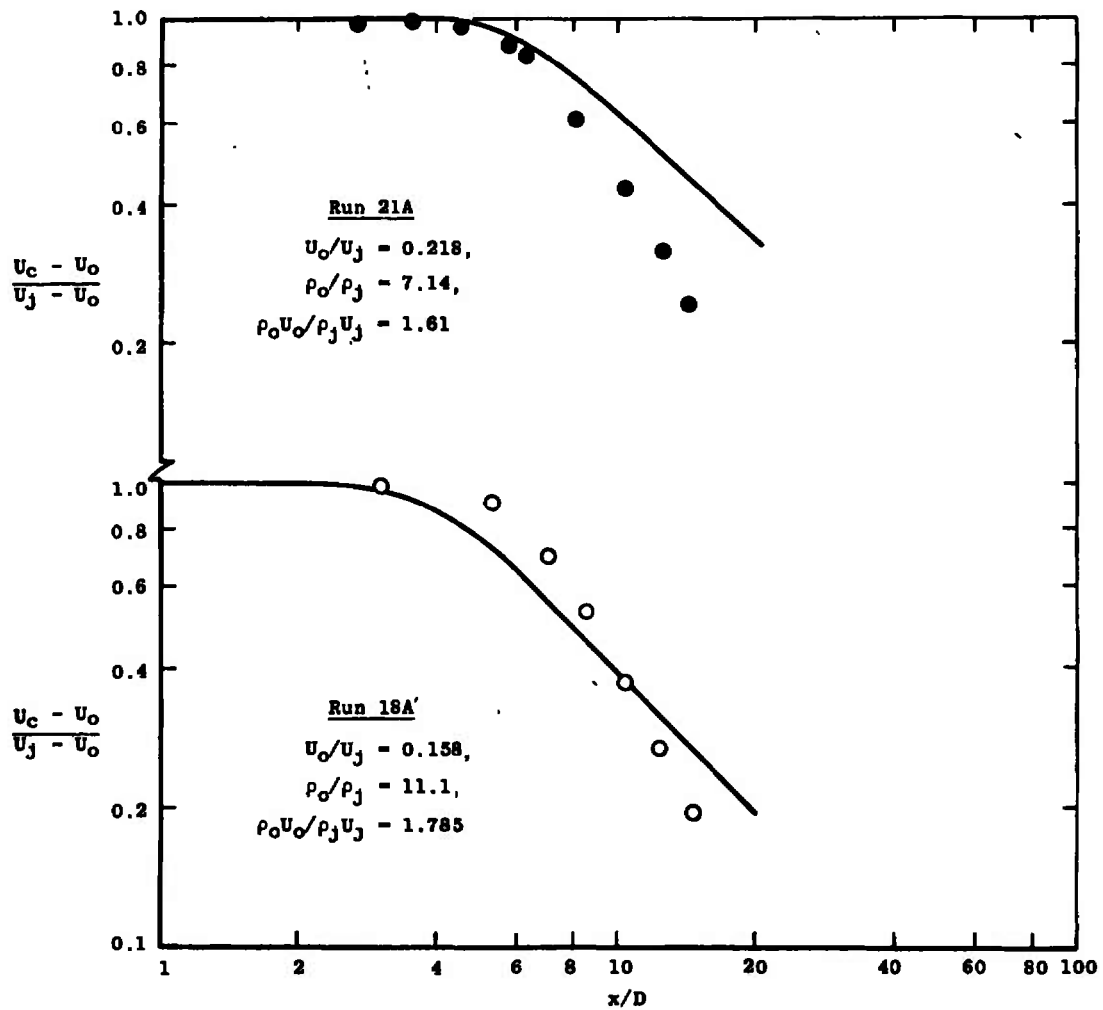


Figure 9.30. Comparison of predictions of Ferri model with coaxial H_2 -air mixing data of Chriss [90].

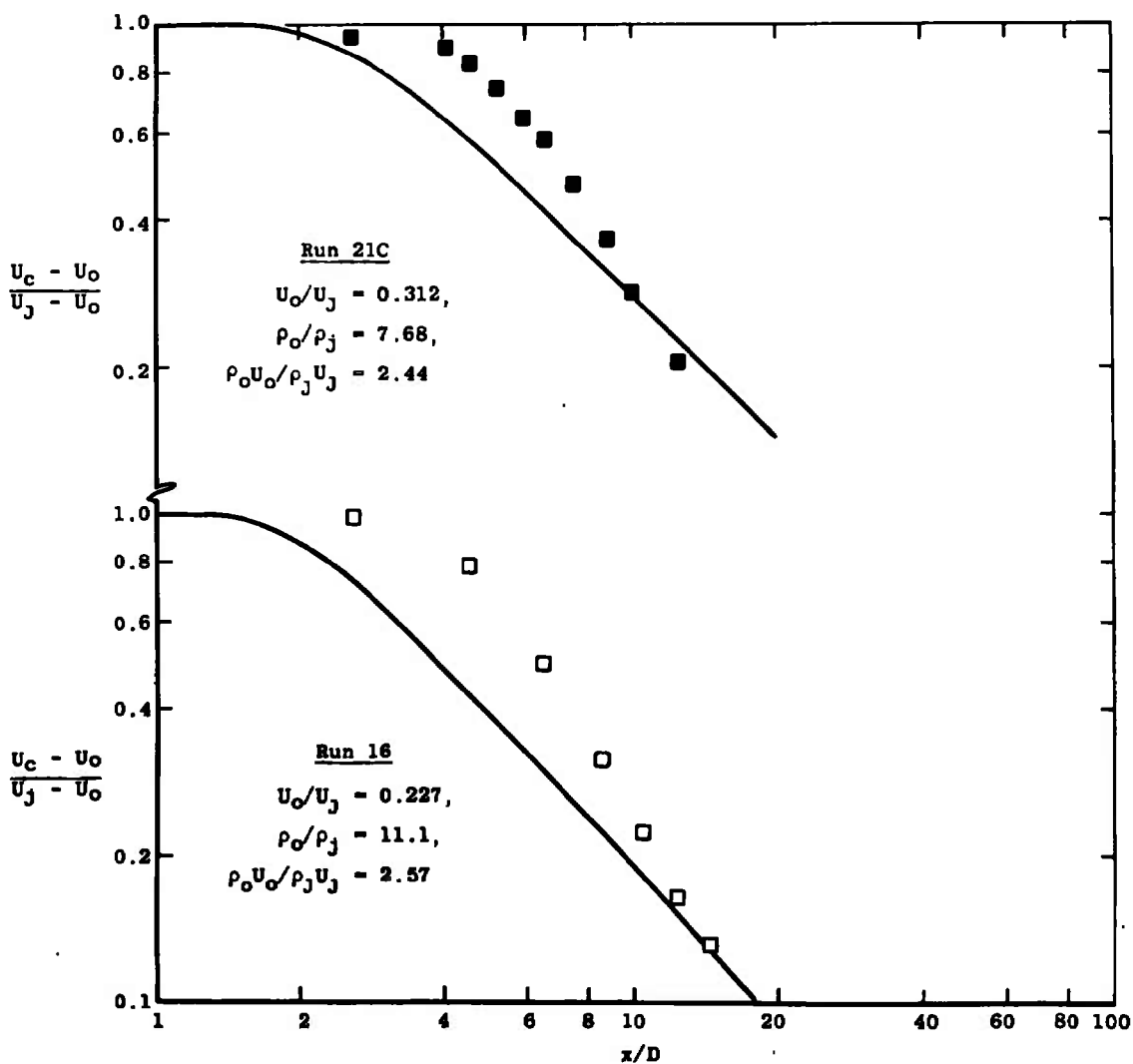


Figure 9.30. (continued)

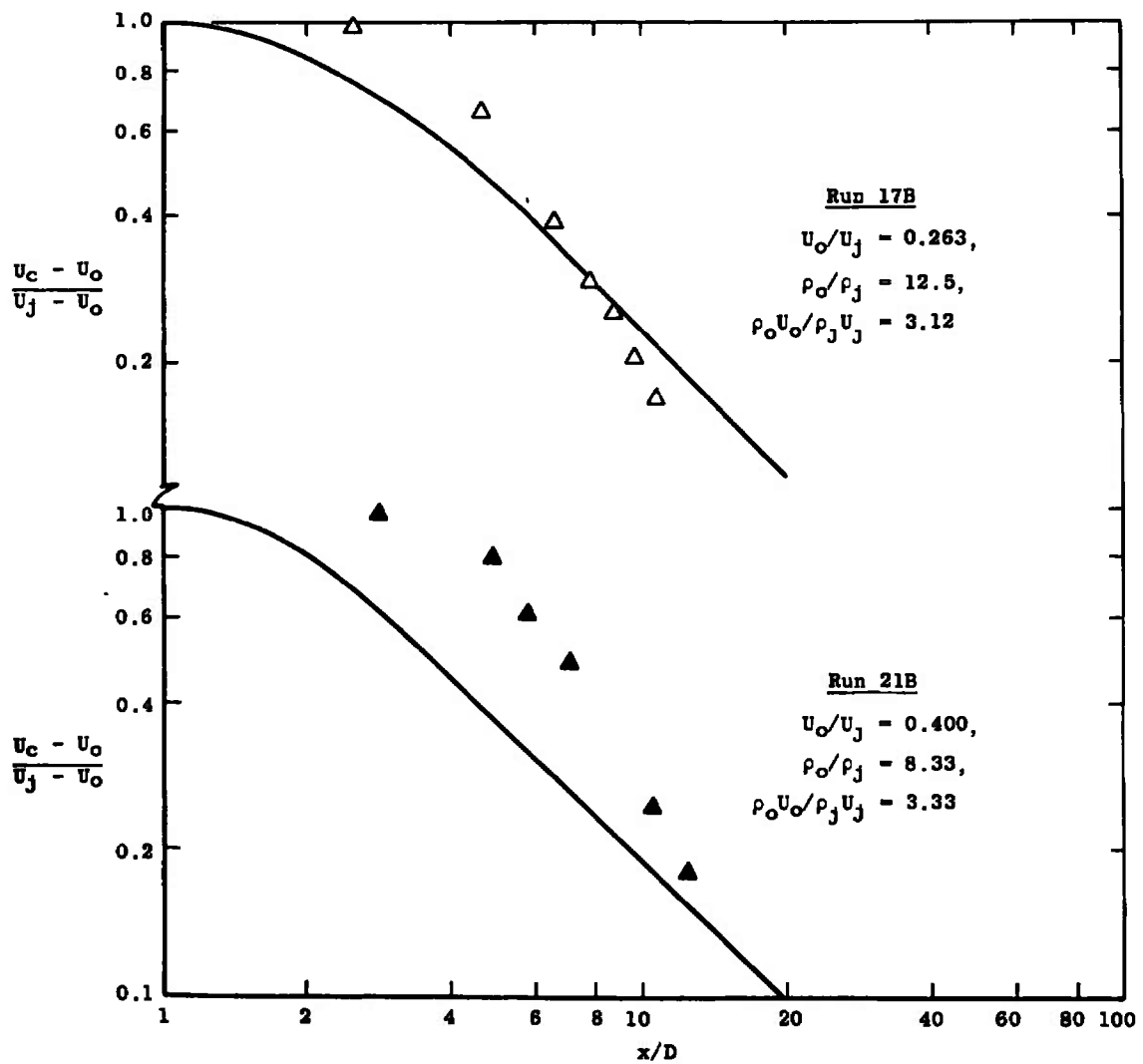


Figure 9.30. (continued)

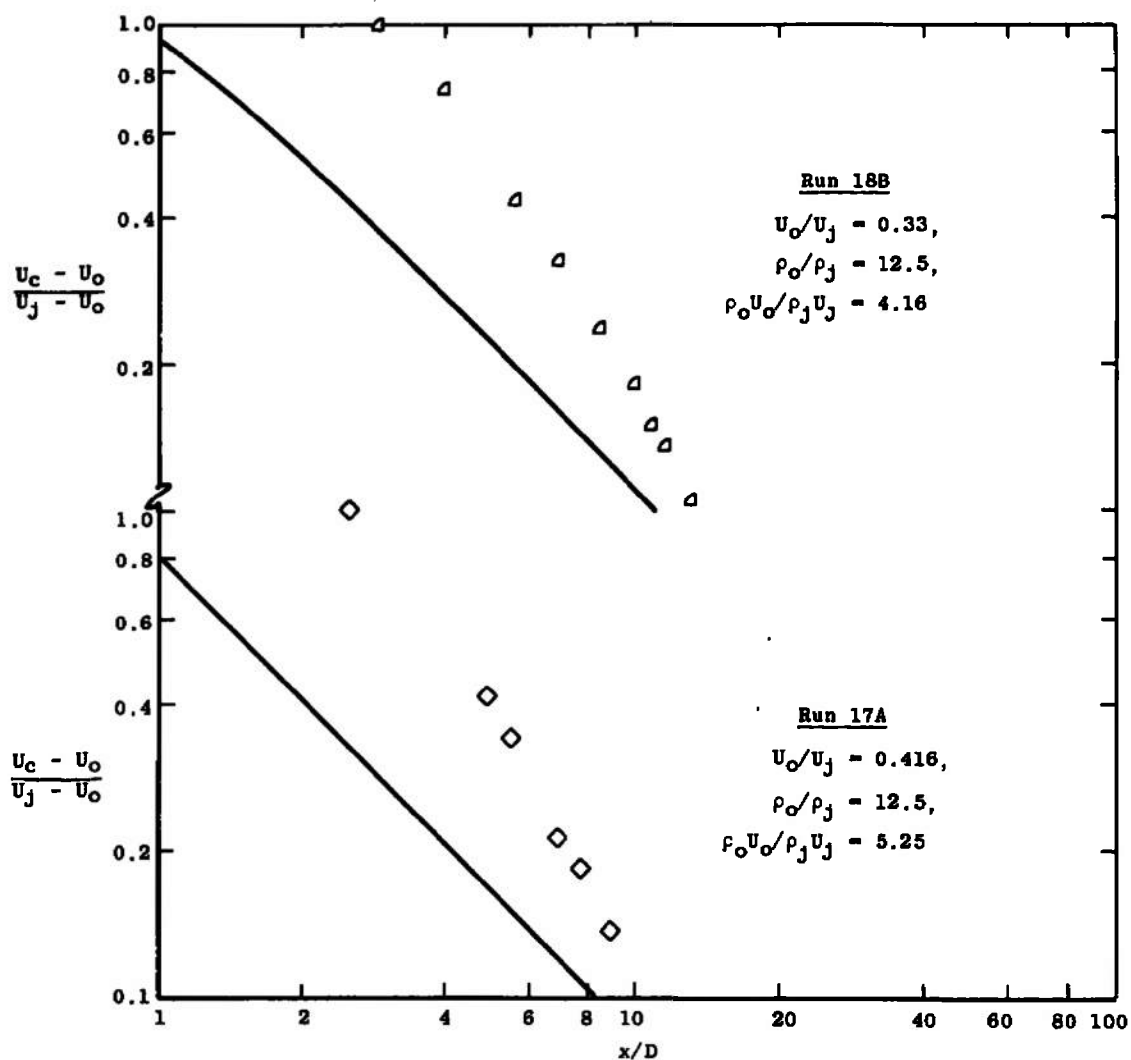


Figure 9.30. (continued)

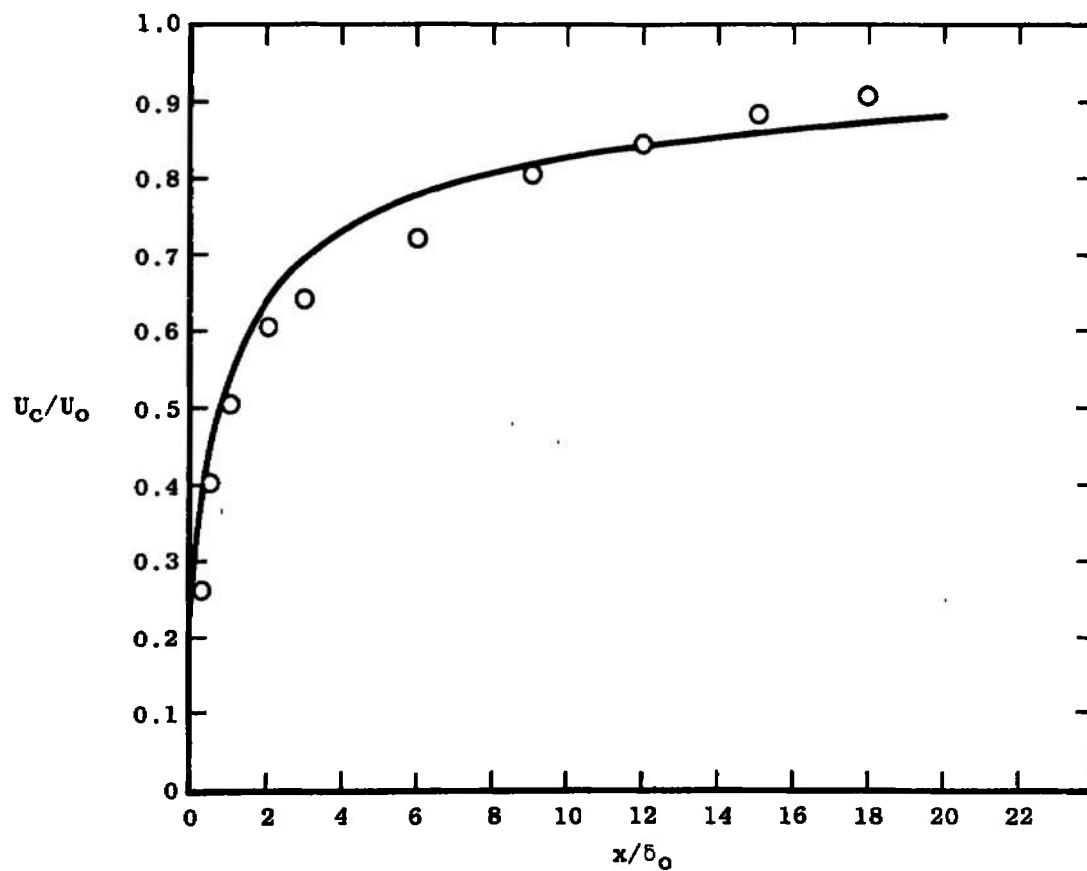


Figure 9.31. Comparison of prediction of Ferri model with experimental data for the initial region of an axisymmetric wake. Data of Chevray [58].

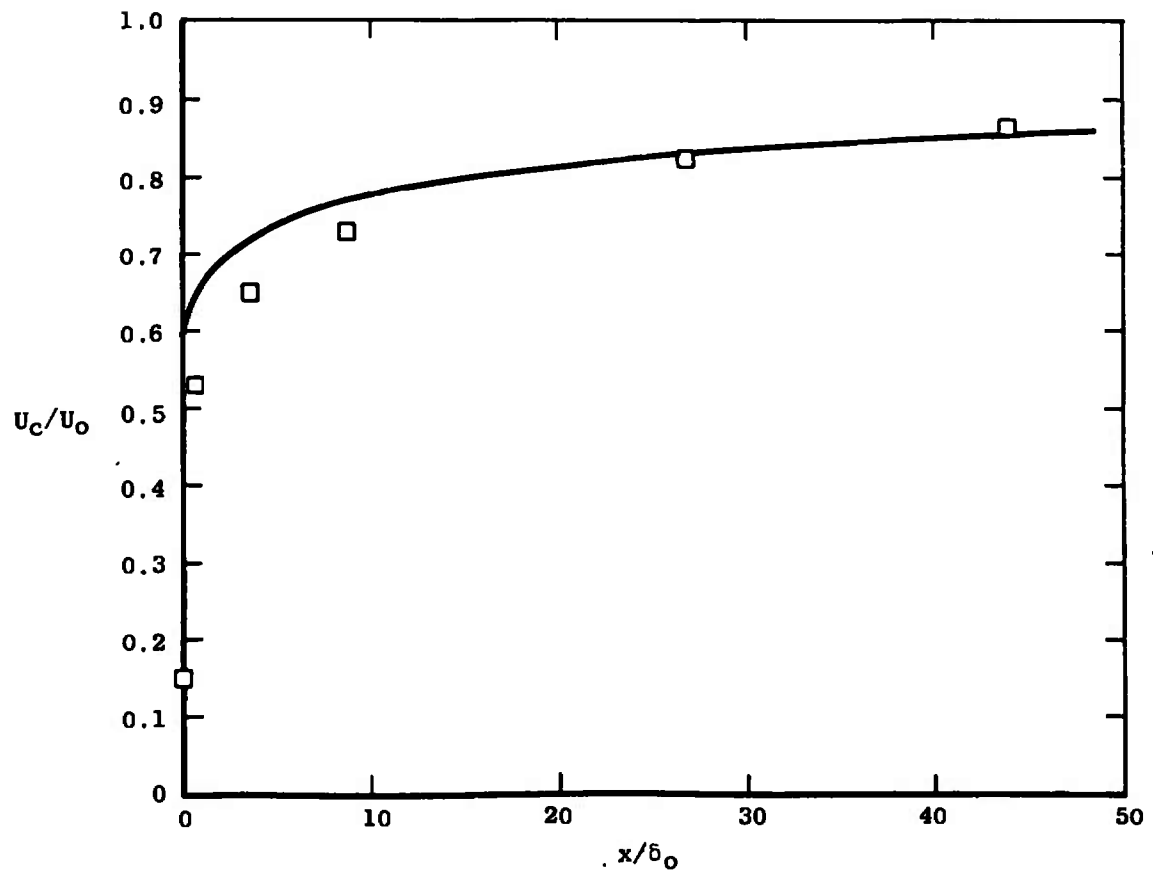


Figure 9.32. Comparison of prediction of Ferri model with data for the initial region of a two-dimensional wake. Data of Chevray and Kovasznay [52].

not possible to correct this merely by a reasonable change in the constant selected.

Confrontation V: Zakkay Model

As was described at the beginning of this Chapter, the model here called the "Zakkay Model," reported by Zakkay, Krause, and Woo [86], was obtained from considerations of the asymptotic behavior of coaxial jets. The Zakkay model was also designed to satisfy the empirical observation made in Reference [86] that the axial decay of concentration along the centerline of coaxial two-gas jets decays as x^{-2} ; this conclusion has been discussed in Chapter 5 in which it has been shown that under some circumstances the decay is actually proportional to x^{-1} .

For the jet-into-still-air, the Zakkay model is identical to the Prandtl eddy viscosity model. However, as the width as defined for the Zakkay model is one-half of the width definition used in the Prandtl model, the effective value of the eddy viscosity at any point is lower in the Zakkay model than it is in the Prandtl eddy viscosity model, despite the larger numerical value of the constant used in the first regime. Figure 9.33 illustrates the effects of this change in constant for both the incompressible and the compressible jet-into-still-air. As would be expected, the reduction in eddy viscosity (and thus the turbulent shear stress) compared with the Prandtl model results in a lengthened velocity potential core region. Comparison of

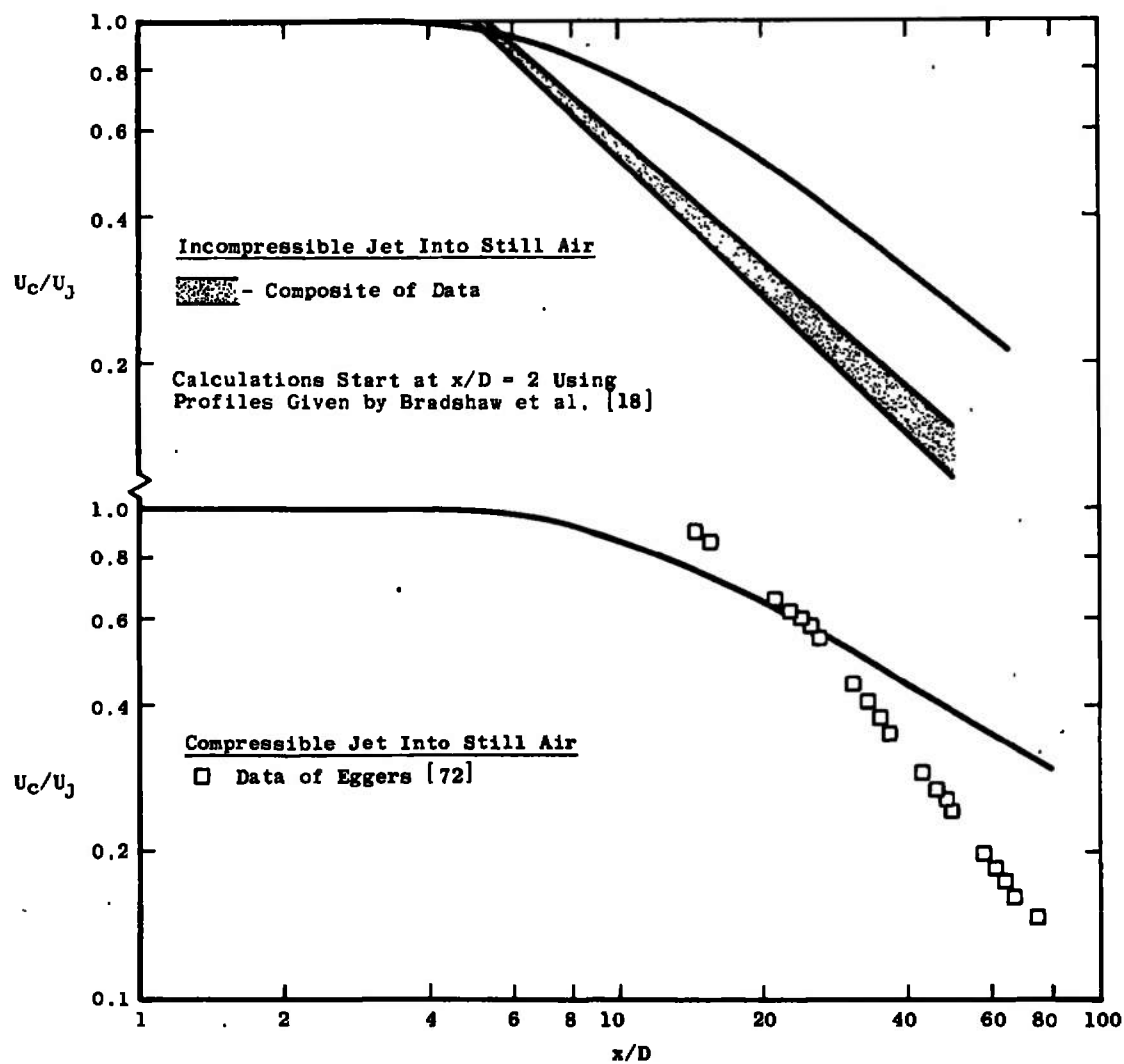


Figure 9.33. Comparison of predictions of Zakkay model with jet-into-still-air data.

the Zakkay model calculation of the incompressible jet-into-still-air with that of the Prandtl eddy viscosity and Ferri model (Figure 9.27, page 428) shows that this calculation predicts the same asymptotic slope as both the other models, as would be expected from the discussion of the previous section. This is true also for the compressible jet case.

With the exception of one case, the level of agreement of the Zakkay calculation with the coaxial air-air mixing data is relatively poor, as shown by Figures 9.34 and 9.35. The exception is the $U_o/U_j = 0.371$ case represented on Figure 9.34. However, the velocity potential core length prediction of the Zakkay model is relatively good for these data.

Since the Zakkay model was designed to handle coaxial hydrogen-air mixing, its performance when compared with the hydrogen-air mixing data used in this study is of interest. As shown on Figure 9.36, the performance of this model in comparison with these data is unsatisfactory. One major failing, common however to the other eddy viscosity models similar to this model, is that the Zakkay model fails to predict the increase in decay rate observed with increasing $\rho_o U_o / \rho_j U_j$ ratio observed for these data. It is of interest that despite the apparently substantial differences in the formulation of the Zakkay eddy viscosity model as compared to the Prandtl eddy viscosity model, the behavior of the predictions of the former model is quite

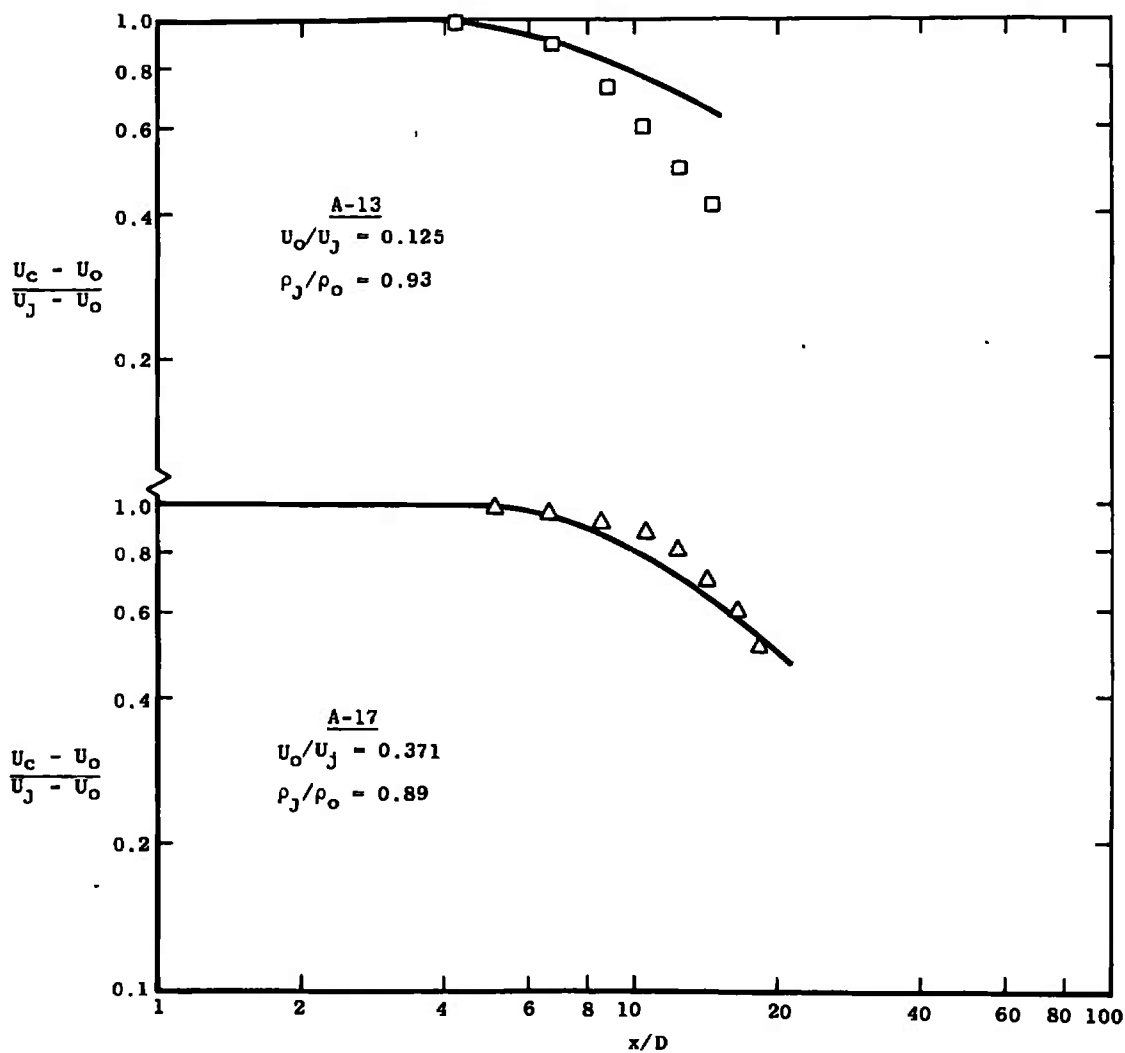


Figure 9.34. Comparison of predictions of Zakkay model with coaxial air-air mixing data of Paulk [42].

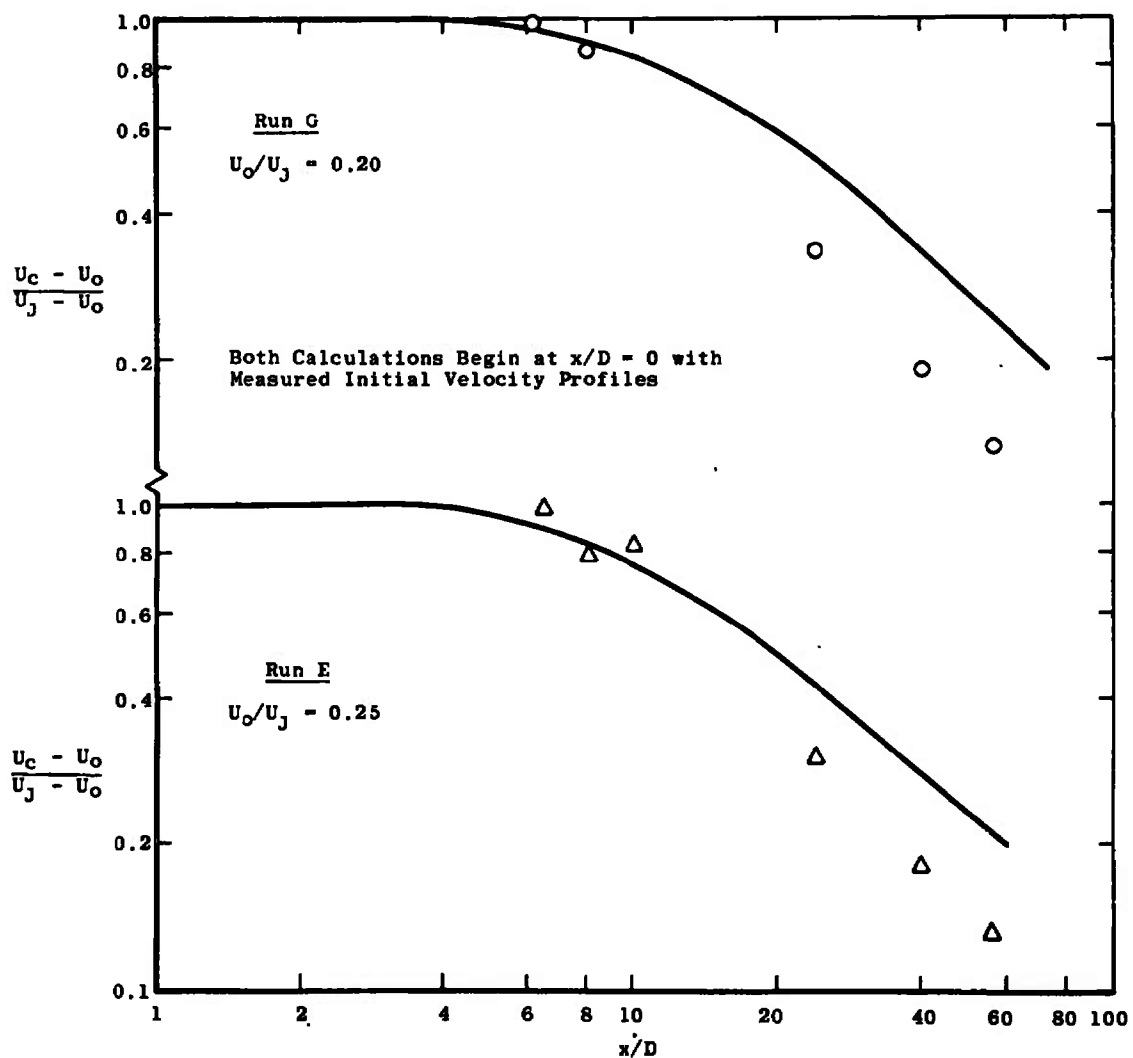


Figure 9.35. Comparison of predictions of Zakkay model with coaxial air-air mixing data. Data from Forstall [40].

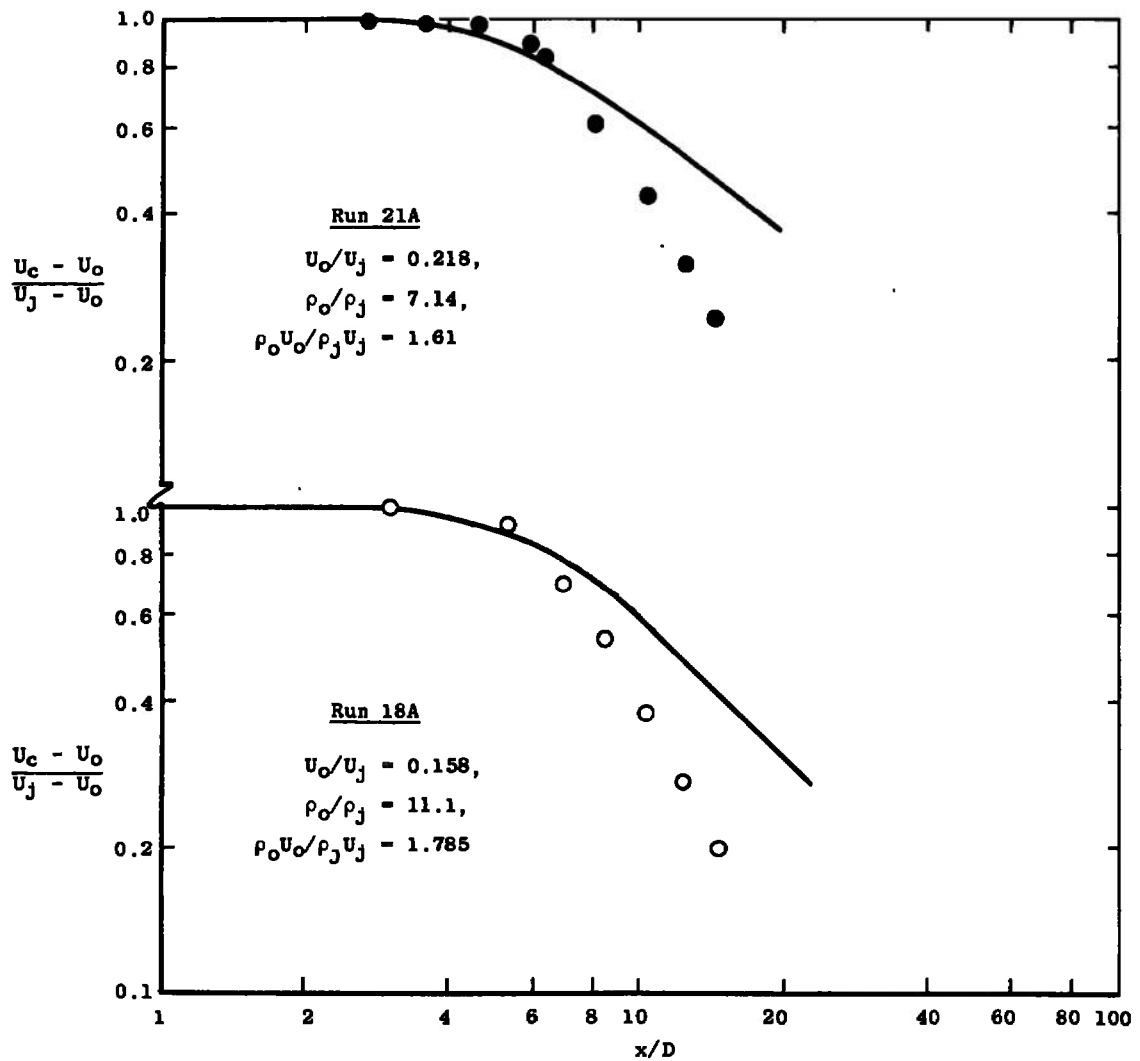


Figure 9.36. Comparison of predictions of Zakkay model with coaxial hydrogen-air mixing data of Chriss [90].

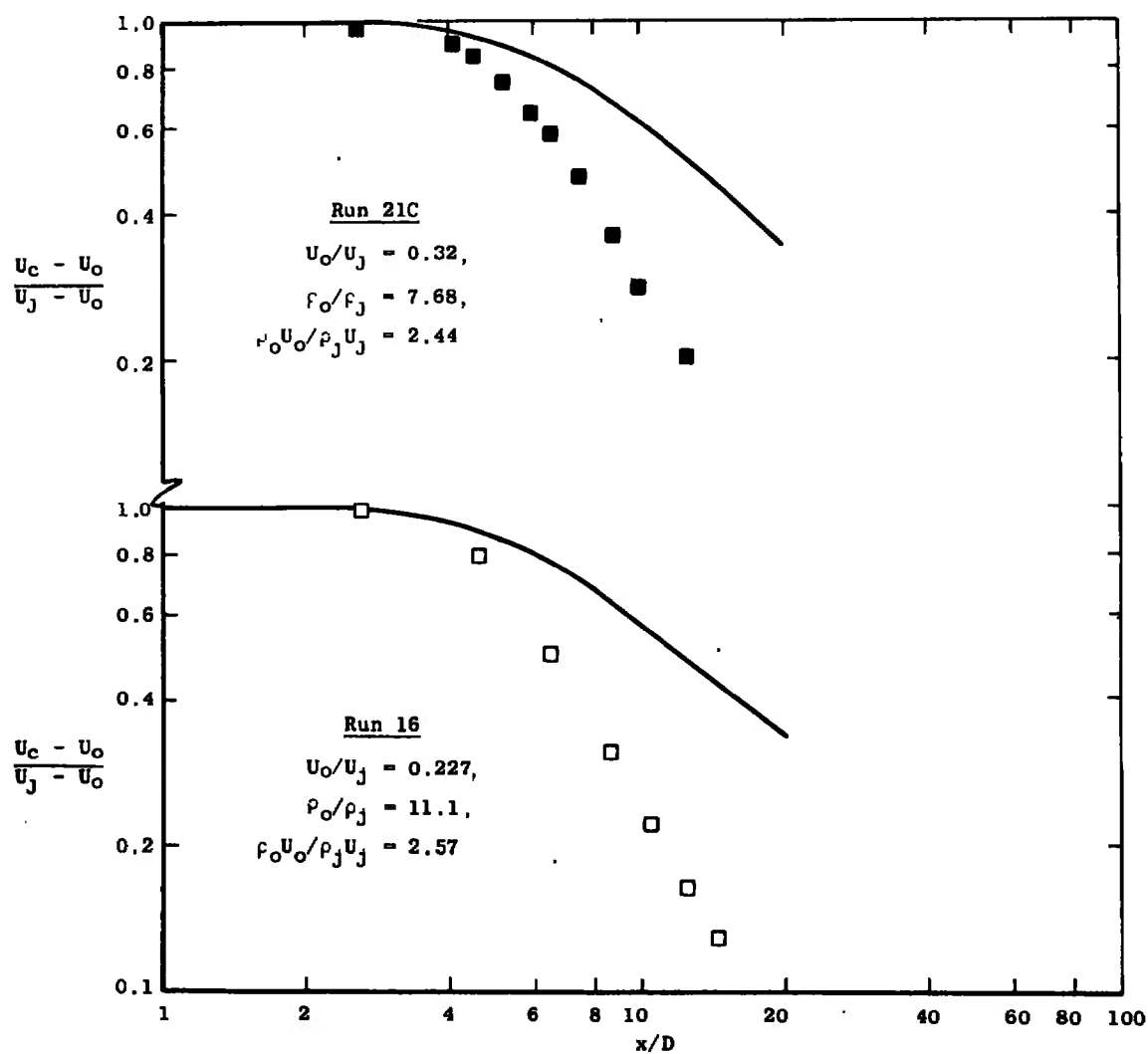


Figure 9.36. (continued)

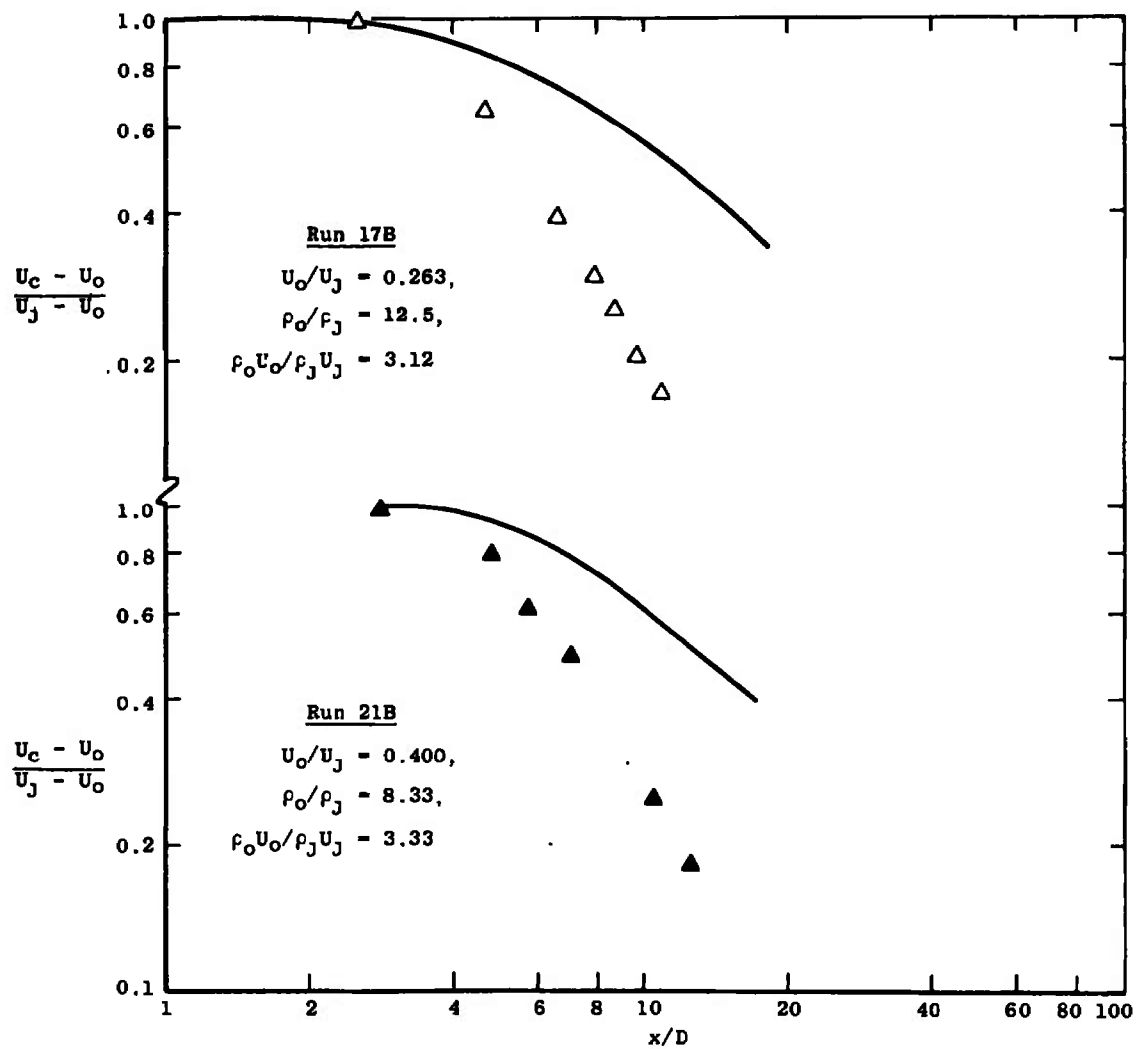


Figure 9.36. (continued)

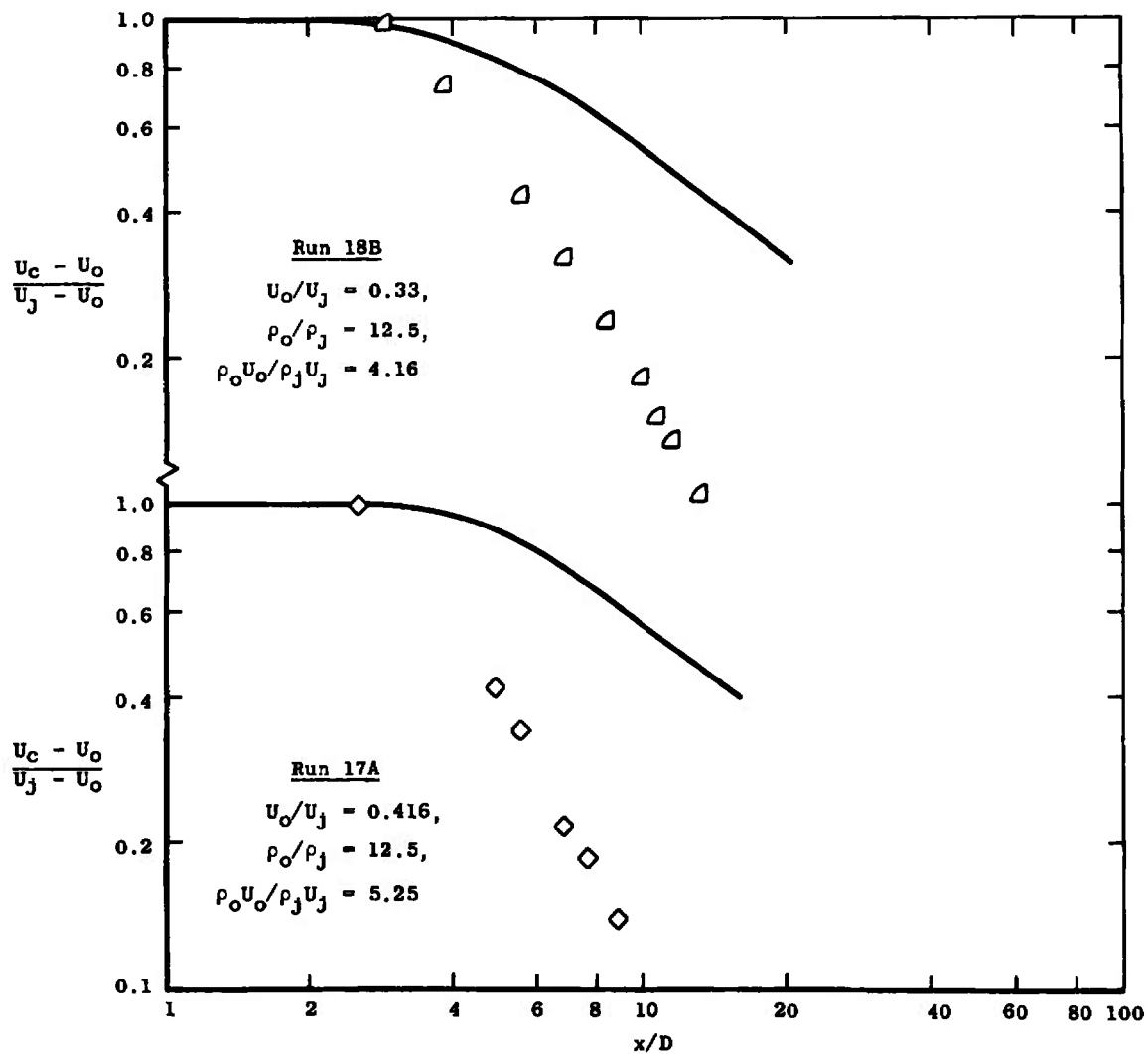


Figure 9.36. (continued)

similar to that of the latter, as comparisons of Figure 9.36 with Figure 9.14, pages 402-405, will show.

Figures 9.37 and 9.38 show the predictions of the Zakkay model as compared to the data for an axisymmetric wake and a two-dimensional wake. The Zakkay model predicts $\epsilon = 0$ at $x = 0$ where $U_c = 0$, and if the Zakkay model prediction is compared to the Prandtl model one finds that

$$\frac{\epsilon_P}{\epsilon_Z} = 2 \left| \frac{U_o - U_c}{U_c} \right| \quad (9.3)$$

so that when $U_c = U_o/2$, both models predict the same eddy viscosity value. As U_c increases, the Prandtl model predicts that as $U_c \rightarrow U_o$, $\epsilon \rightarrow 0$, while the Zakkay model predicts that as $U_c \rightarrow U_o$, $\epsilon \rightarrow \text{constant}$. Thus the Zakkay model will underpredict the rate of increase of centerline velocity in the very early region of the wake, compared to the Prandtl model. However, in the asymptotic region, since experimental data show that $\epsilon \rightarrow \text{constant}$ is a proper assumption, one would expect the Zakkay model to exhibit the proper trend. Figures 9.37 and 9.38 show that this is indeed the case; the agreement for the case of the two-dimensional wake being quite good.

Confrontation VI: Alpinieri Model

The Alpinieri model [84] was devised to produce predictions agreeing with coaxial hydrogen-air mixing

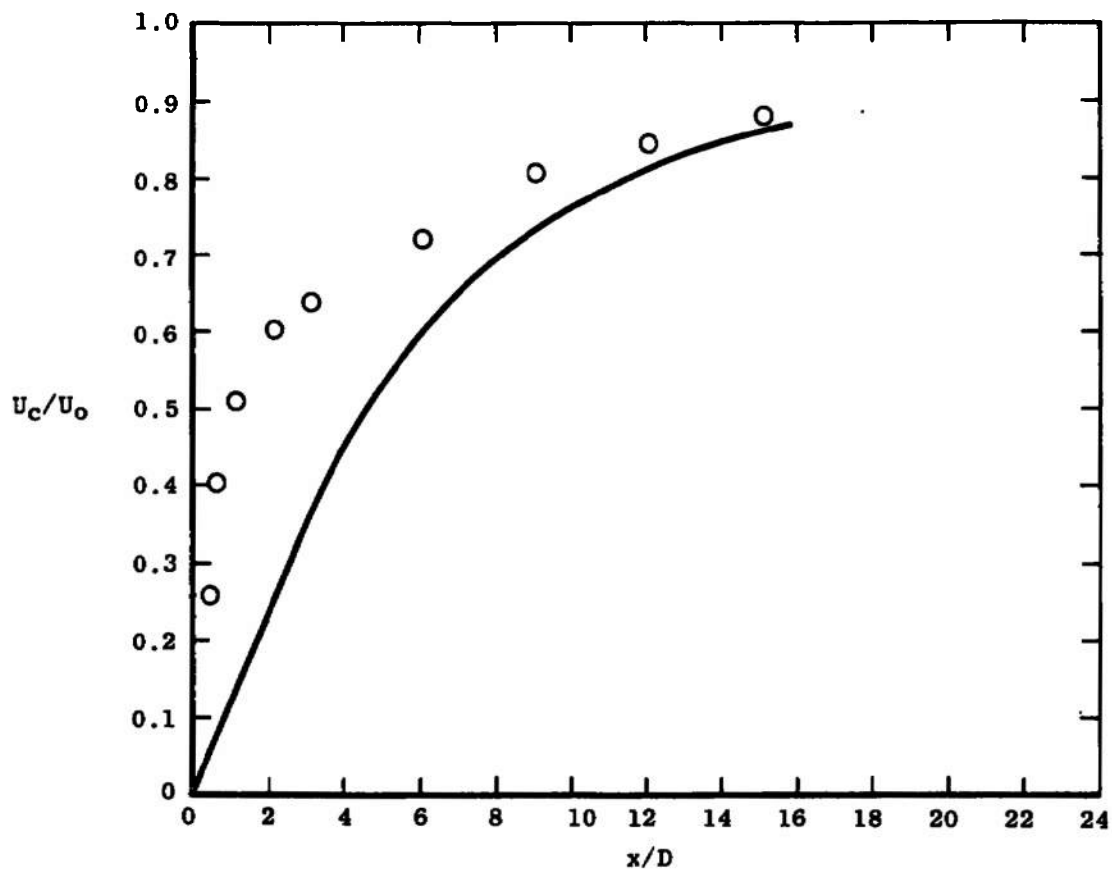


Figure 9.37. Comparison of prediction of Zakkay model with experimental data for the initial region of an axisymmetric wake. Data of Chevray [58].

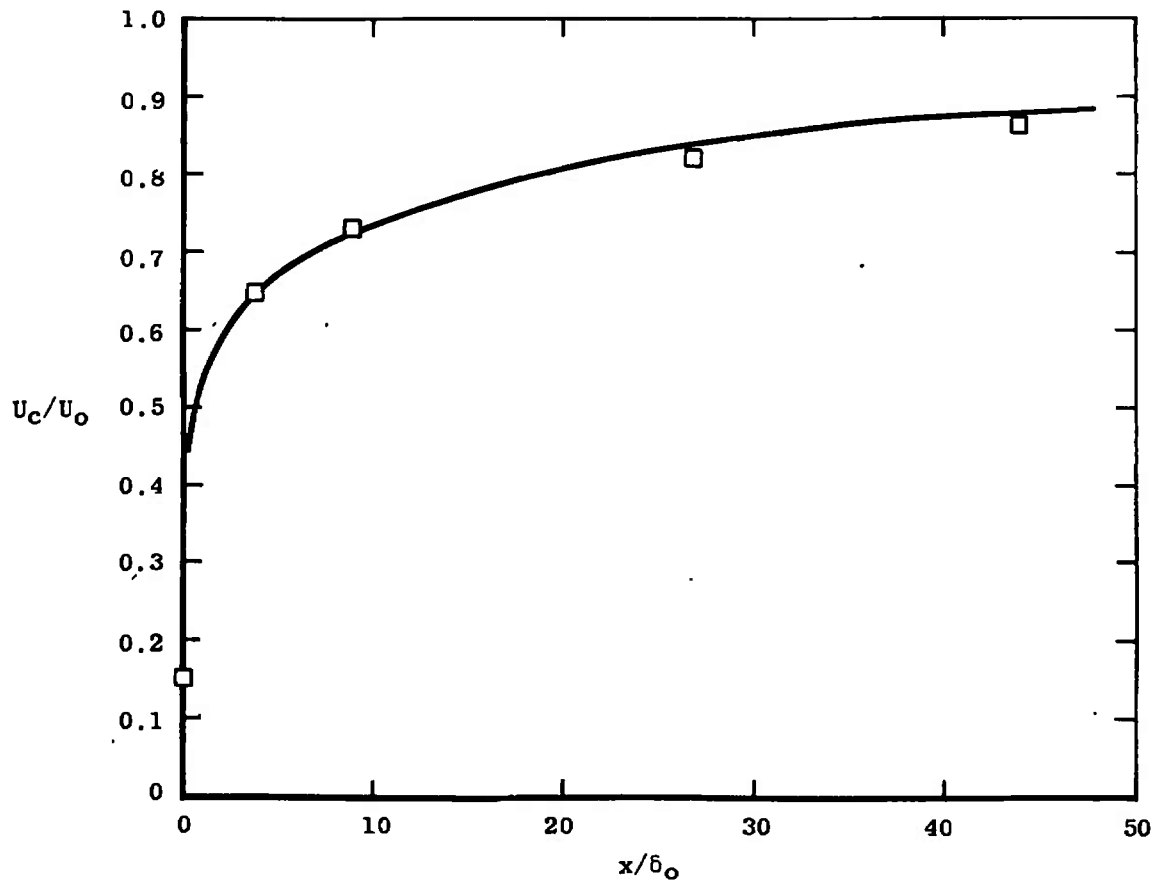


Figure 9.38. Comparison of prediction of Zakkay model with data for the initial region of a two-dimensional wake. Data of Chevray and Kovasznay [58].

experiments which as described in Chapter 5 had a strongly wake-like character. This character manifested itself in a very rapid decrease of centerline velocity, and in particular centerline composition, when compared to other coaxial hydrogen-air mixing experiments. To produce agreement with these experiments, Alpinieri had to devise a model which indicates a level of eddy viscosity which is several times larger than other models would predict. For example, consider the Alpinieri model and the Ferri model applied to a hydrogen-air system with $U_o/U_j = 0.33$ and $\rho_j/\rho_o = 0.08$. The ratio of the two eddy viscosity models is

$$\begin{aligned}
 \frac{(\rho\varepsilon)_{\text{Alpinieri}}}{(\rho\varepsilon)_{\text{Ferri}}} &= \frac{\rho_o (U_c + U_o^2/U_j)}{|\rho_o U_o - \rho_c U_c|} \\
 &= \frac{U_c + U_o^2/U_j}{|U_o - \rho_c U_c/\rho_o|} \\
 &= \frac{U_c/U_j + (U_o/U_j)^2}{|U_o/U_j - \rho_c U_c/\rho_o U_j|} \quad (9.5)
 \end{aligned}$$

Now consider an x-station at the end of the potential core, where $U_c = U_j$. Then

$$\frac{(\rho\varepsilon)_{\text{Alpinieri}}}{(\rho\varepsilon)_{\text{Ferri}}} = \frac{1 + (U_o/U_j)^2}{|U_o/U_j - \rho_j/\rho_o|} \quad (9.6)$$

so that for the example cited

$$\frac{(\rho\epsilon)_{\text{Alpinieri}}}{(\rho\epsilon)_{\text{Ferri}}} = \frac{1.11}{0.25} = 4.44 \quad (9.7)$$

For an air-air mixing case, with $\rho_j = \rho_o$ and $U_o/U_j = 0.2$,

$$\frac{(\epsilon)_{\text{Alpinieri}}}{(\epsilon)_{\text{Ferri}}} = \frac{1.04}{0.8} = 1.3 \quad (9.8)$$

while for the incompressible jet-into-still-air,

$\rho_j = \rho_o$, $U_o = 0$, and

$$\frac{(\epsilon)_{\text{Alpinieri}}}{(\epsilon)_{\text{Ferri}}} = 1.0 \quad (9.9)$$

Note also that for a wake, $U_j = 0$ and the Alpinieri model yields infinite eddy viscosity.

As has just been shown, for the incompressible jet-into-still-air the Alpinieri model is identical to the Ferri model, and thus predicts the same potential core length and centerline velocity decay. This is shown in Figure 9.39. For the compressible jet-into-still-air the Alpinieri model, because of its treatment of the density variation, predicts a slightly greater eddy viscosity in the ratio

$$\frac{(\rho\epsilon)_{\text{Alpinieri}}}{(\rho\epsilon)_{\text{Ferri}}} = \frac{\rho_o}{\rho_c} \quad (9.10)$$

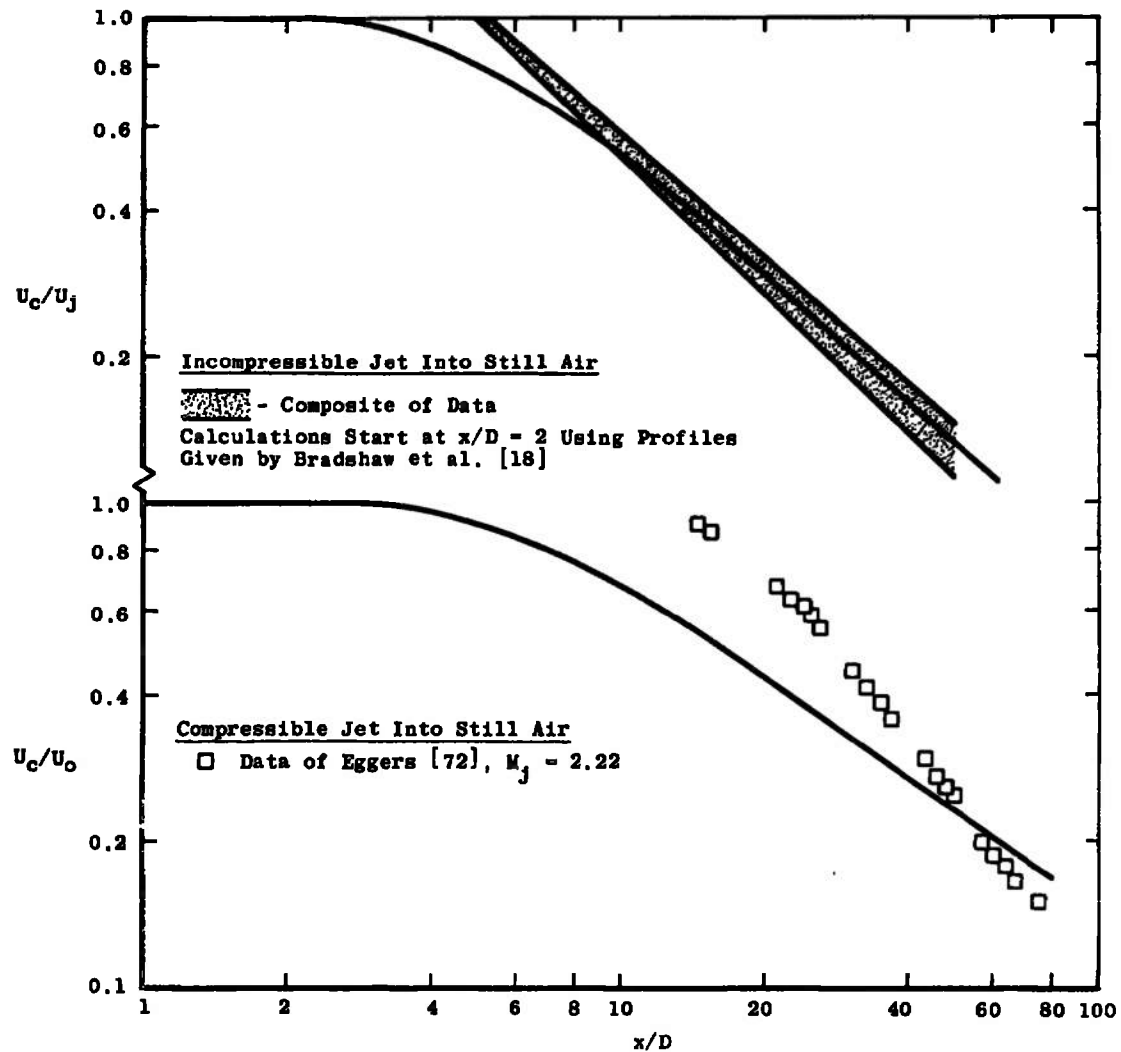


Figure 9.39. Comparison of predictions of Alpinieri model with jet-into-still-air data.

and so, as shown on Figure 9.39, the Alpinieri model indicates a shorter potential core length and greater velocity decay than the Ferri model. As was shown above (Equation (9.11)) the eddy viscosity predicted by the Alpinieri model is greater than that predicted by the Ferri (or Prandtl eddy viscosity) models, and this has the expected influence on the velocity potential core length predictions and on the centerline velocity decay for both sets of coaxial air-air mixing data used in this study. Figures 9.40 and 9.41 show this. In no case is the prediction of the Alpinieri model satisfactory.

The great overprediction of the eddy viscosity by the Alpinieri model for the hydrogen-air mixing data used in this study is apparent in the prediction shown in Figure 9.42. The Alpinieri model is completely unable to predict these data. Interestingly, the model does predict in a general manner the decrease in potential core length with increasing mass flux ratio observed for these data; however, the trend predicted by the Alpinieri model is not simply a decrease with increasing $\rho_o U_o / \rho_j U_j$ but appears to be more complexly related to the parameters ρ_o / ρ_j and U_o / U_j .

As was described above, the Alpinieri model predicts an infinite eddy viscosity for a wake calculation, for which $U_j = 0$. Thus, no comparisons with turbulent wake data will be shown.

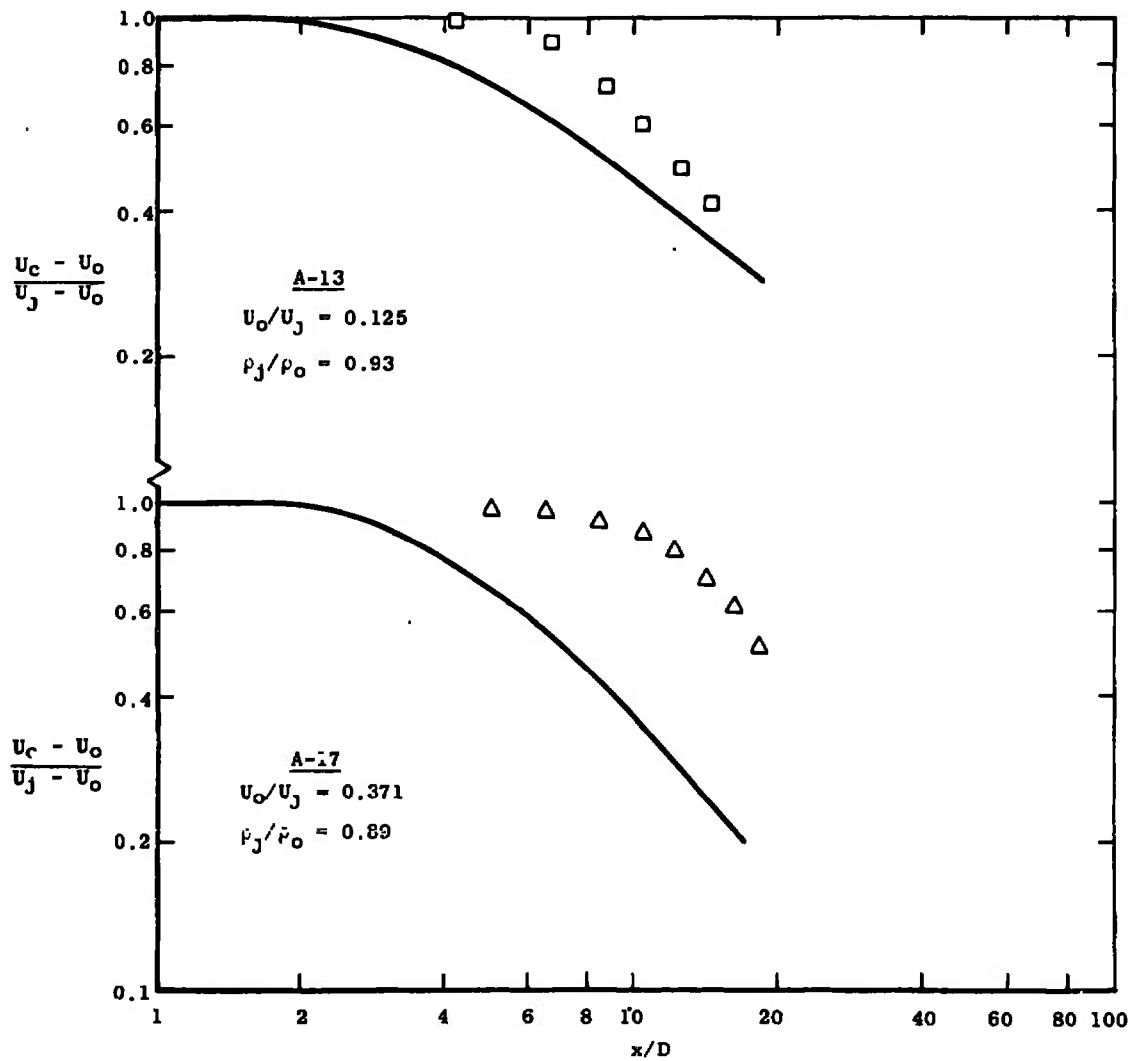


Figure 9.40. Comparison of predictions of Alpinieri model with coaxial air-air data of Paulk [42].

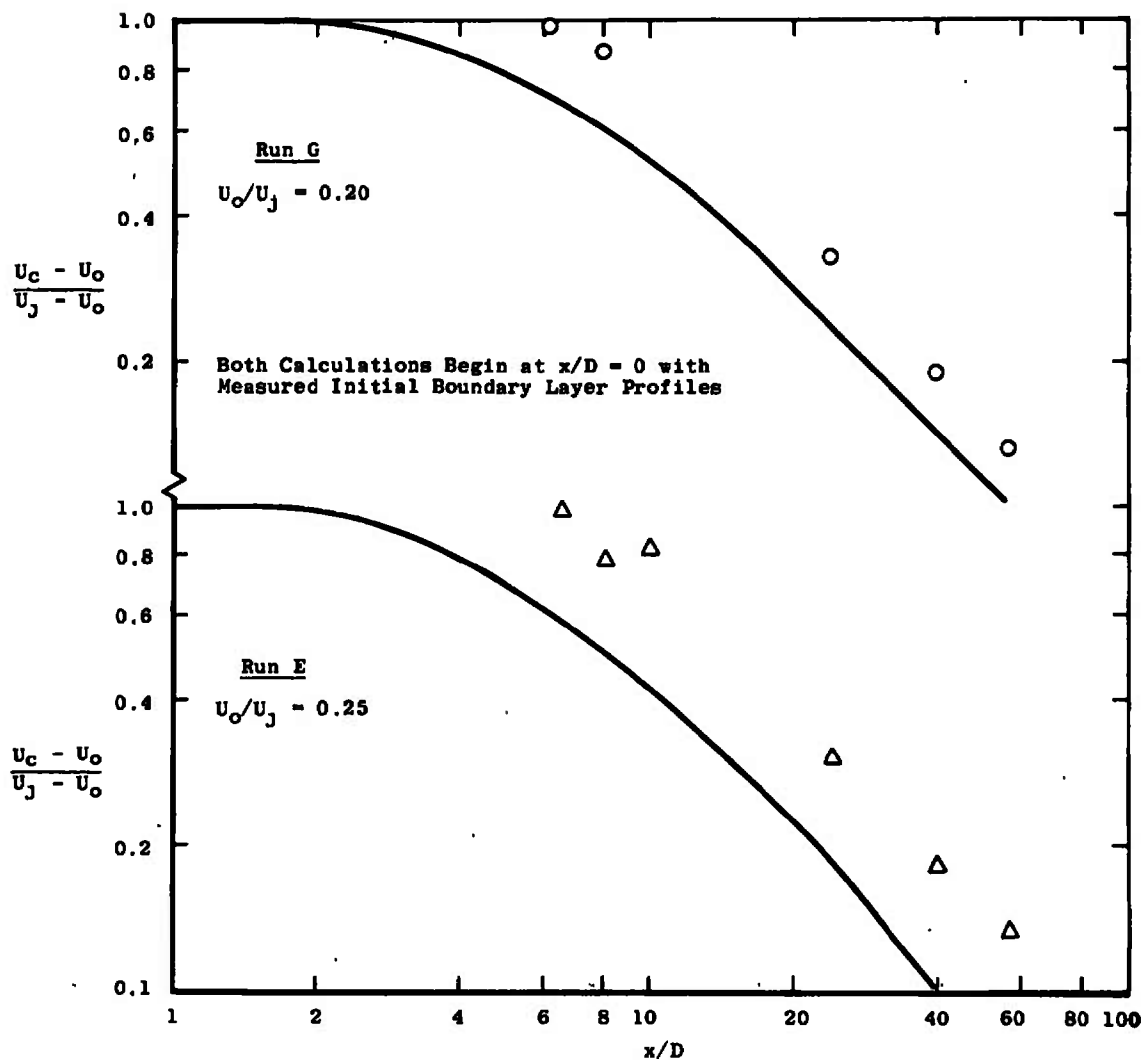


Figure 9.41. Comparison of predictions of Alpinieri model with coaxial air-air mixing data. Data from Forstall [40].

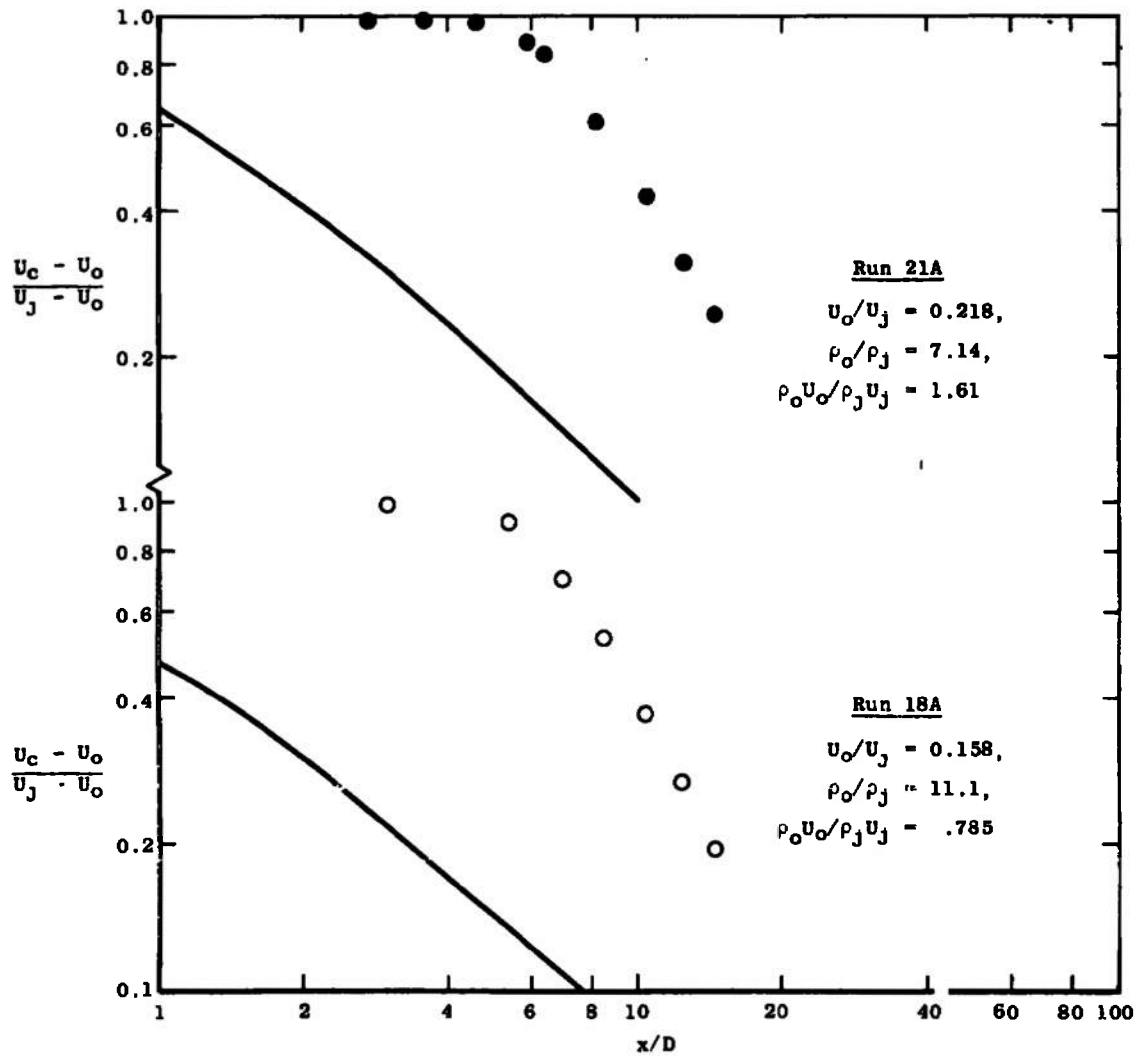


Figure 9.42. Comparison of predictions of Alpinieri model with coaxial H₂-air mixing data of Chriss [90].

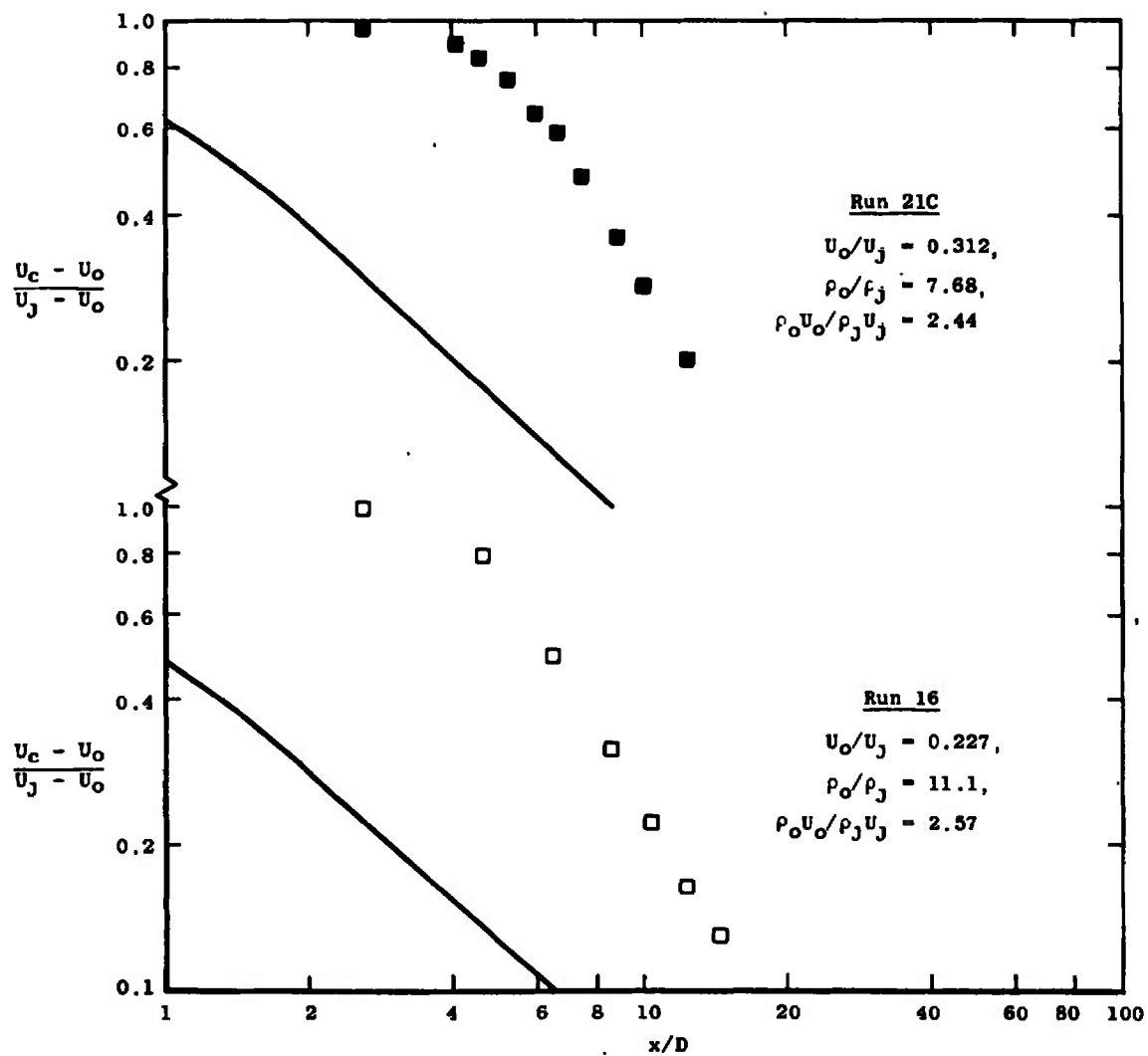


Figure 9.42. (continued)

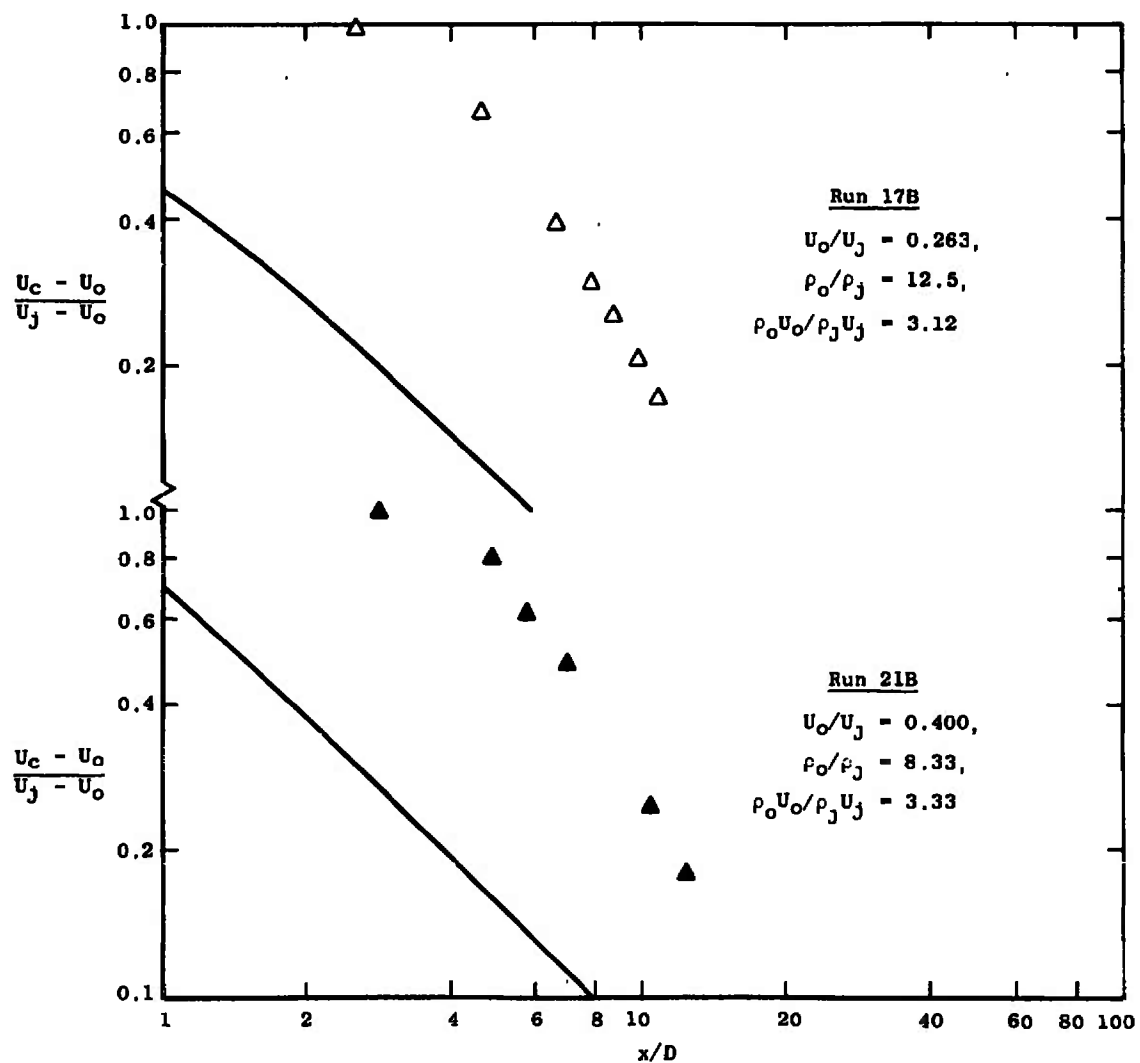


Figure 9.42. (continued)

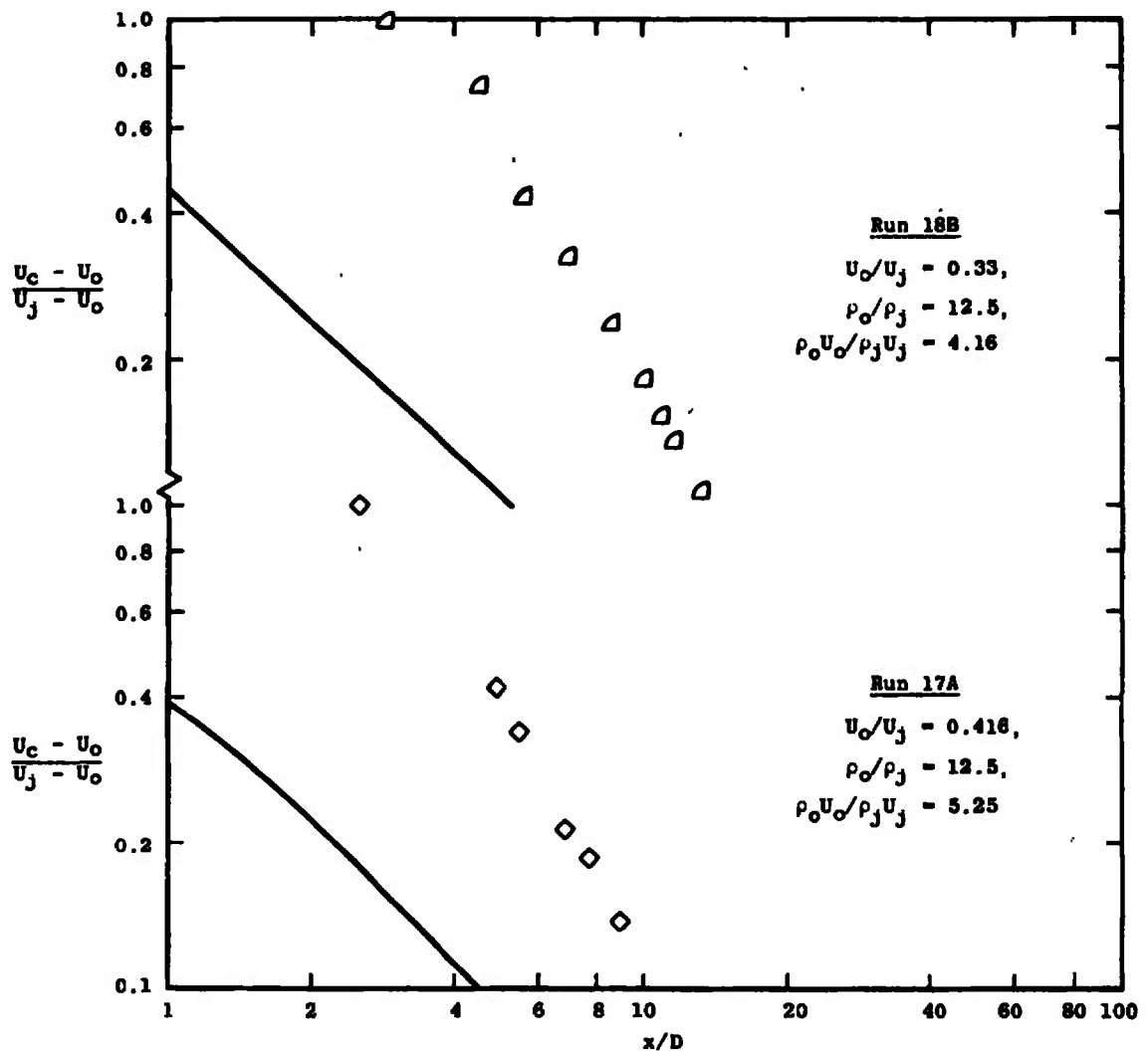


Figure 9.42. (continued)

Confrontation VII: Turbulent Kinetic Energy

Because it attempts to include more of the actual physics of the flow in the modeling of the turbulent shear stress, the turbulent kinetic energy approach is more complex both in concept and in application than any of the eddy viscosity models described above. In addition to requiring the solution of an additional simultaneous partial differential equation, the method also involves the specification of three parameters. As was described in Chapter 8, one of these parameters involves the ratio of the turbulent shear stress to the turbulent kinetic energy per unit mass, another is used in the model chosen for the dissipation of turbulent kinetic energy, and the third represents a Prandtl number for the turbulent kinetic energy, i.e., a ratio of the transport coefficient for turbulent kinetic energy to that for momentum. But since these parameters relate to more fundamental turbulence structure quantities than the mean-flow velocity and density gradients, there is some hope that the constants chosen may prove to be universal.

One of the ground rules for this study has been that the constants used in the various models not be changed from calculation to calculation. Thus for the kinetic energy model, the constants chosen are $a_1 = 0.3$ for the ratio of turbulent shear stress to turbulent kinetic energy, $a_2 = 1.5$ for the dissipation constant, and a value of the

turbulent kinetic energy Prandtl number Pr_k of 0.70. As described in Chapter 8, the modeling of the turbulent shear stress involves a parameter based on the local velocity gradient both to give the turbulent shear stress the proper sign (the turbulent kinetic energy is always positive) and to approximate the observed variation of the ratio of turbulent shear stress to the turbulent kinetic energy in regions where the turbulent shear stress approaches zero while the turbulent kinetic energy does not. Thus, for two-dimensional flow, in regions where $(\partial U / \partial y) \approx 0$

$$\tau = 0.3 \rho k \frac{\partial U / \partial y}{|\partial U / \partial y|_{\max}} \quad (9.11)$$

where $(\partial U / \partial y)_{\max}$ is the absolute value of the local maximum value (at the given cross-section) of the mean velocity gradient, and

$$\tau = 0.3 \rho k \frac{\partial U / \partial y}{|\partial U / \partial y|} \quad (9.12)$$

elsewhere; for axisymmetric flow

$$\tau = 0.3 \rho k \frac{\partial U / \partial r}{|\partial U / \partial r|_{\max}} \quad (9.13)$$

from the centerline to the value of r for which

$$\partial U / \partial r = (\partial U / \partial r)_{\max} \text{ and}$$

$$\tau = 0.3 \rho k \frac{\partial U / \partial r}{|\partial U / \partial r|} \quad (9.14)$$

elsewhere.

Whereas techniques which use locally dependent models require velocity profiles and if necessary enthalpy and species concentration profiles to begin a finite-difference calculation such as is used here, the kinetic energy method must also have a turbulent kinetic energy or turbulent shear stress profile. As was described in the introduction to this Chapter, these profiles have been obtained in a number of ways. The particular method used for a given calculation will be described when the calculation in question is discussed.

The incompressible jet-into-still-air calculations made using the kinetic energy method begin using turbulent kinetic energy profiles measured by Bradshaw, et al., [18] at $x/D = 2$, while the compressible jet-into-still-air calculations begin at $x/D = 14.5$ using turbulent shear stress profiles generated from the velocity and eddy viscosity profiles presented by Eggers [72]. The results of these calculations are given in Figure 9.43. The agreement with the data is reasonably good. For the incompressible jet case the agreement is not as good as the best locally-dependent model (the Ferri model), but it is not as bad as

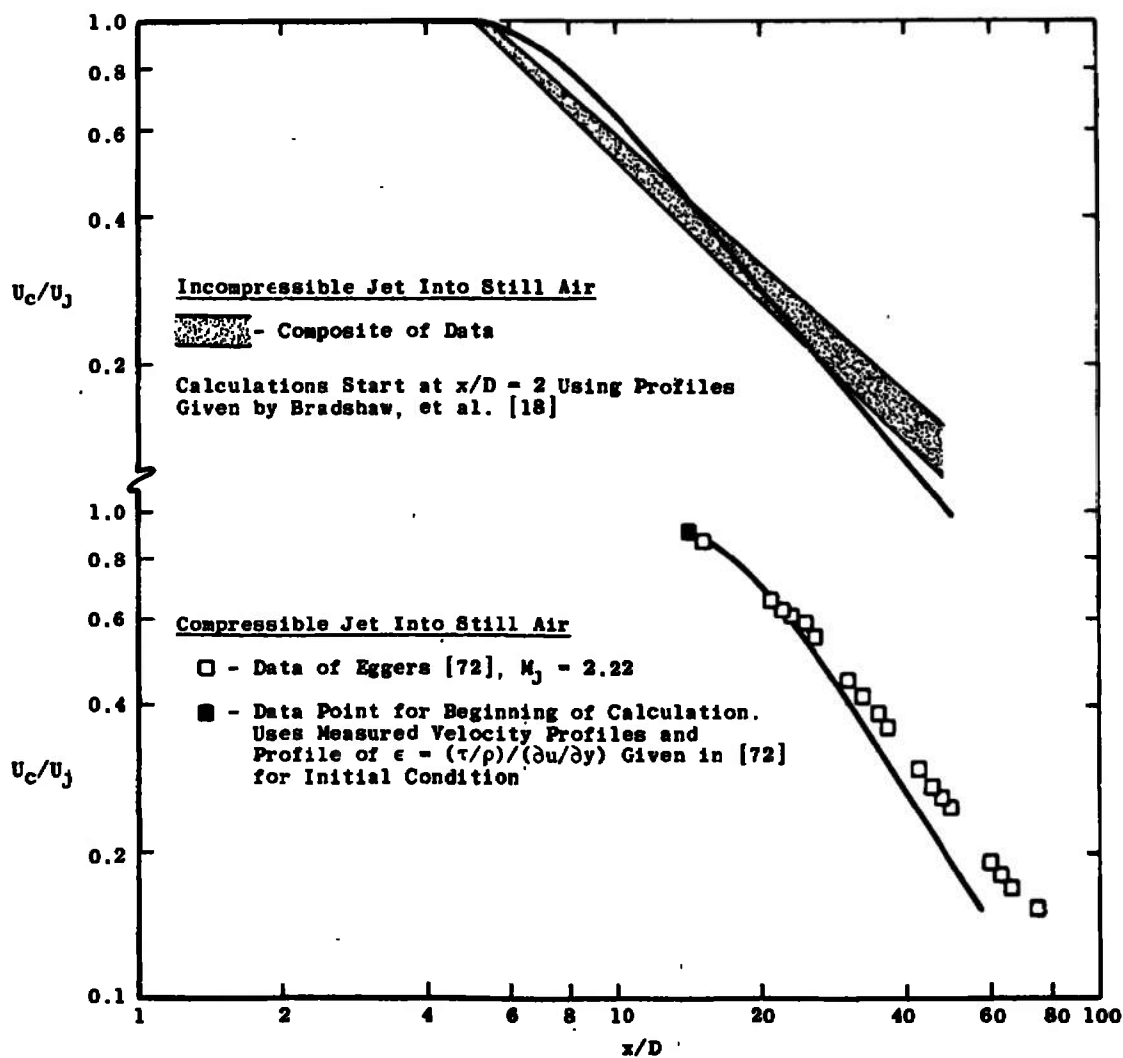


Figure 9.43. Comparison of predictions of kinetic energy theory with jet-into-still-air data.

the worst (the Schetz model); for the compressible jet-into-still-air case the agreement is better than that shown by any other model.

Calculations of the coaxial air-air mixing data of Paulk [42] using the kinetic energy method were begun at the first station for which reliable shear stress profiles were available. In this case, the shear stress profiles were obtained by Paulk through integration of the mean flow momentum equation. The results of the kinetic-energy model calculations are shown on Figure 9.44 from which it can be seen that the agreement with the experimental data is excellent for both velocity ratios used over the limited axial distance for which data is available.

Figure 9.45 shows the results of calculations of the air-air coaxial mixing data of Forstall made with the kinetic energy method. In this case a different technique was used to generate the initial shear stress profiles: the velocity profiles presented in Forstall's thesis [40] were used in conjunction with the Prandtl eddy viscosity model (with $K_p = 0.007$) to establish the initial shear stress profiles. As can be seen from the figure, the results of the calculation are in excellent agreement with the experimental data, even to $x/D = 56$. It must be emphasized, however, that there is no a priori justification for believing that this method of establishing the initial shear

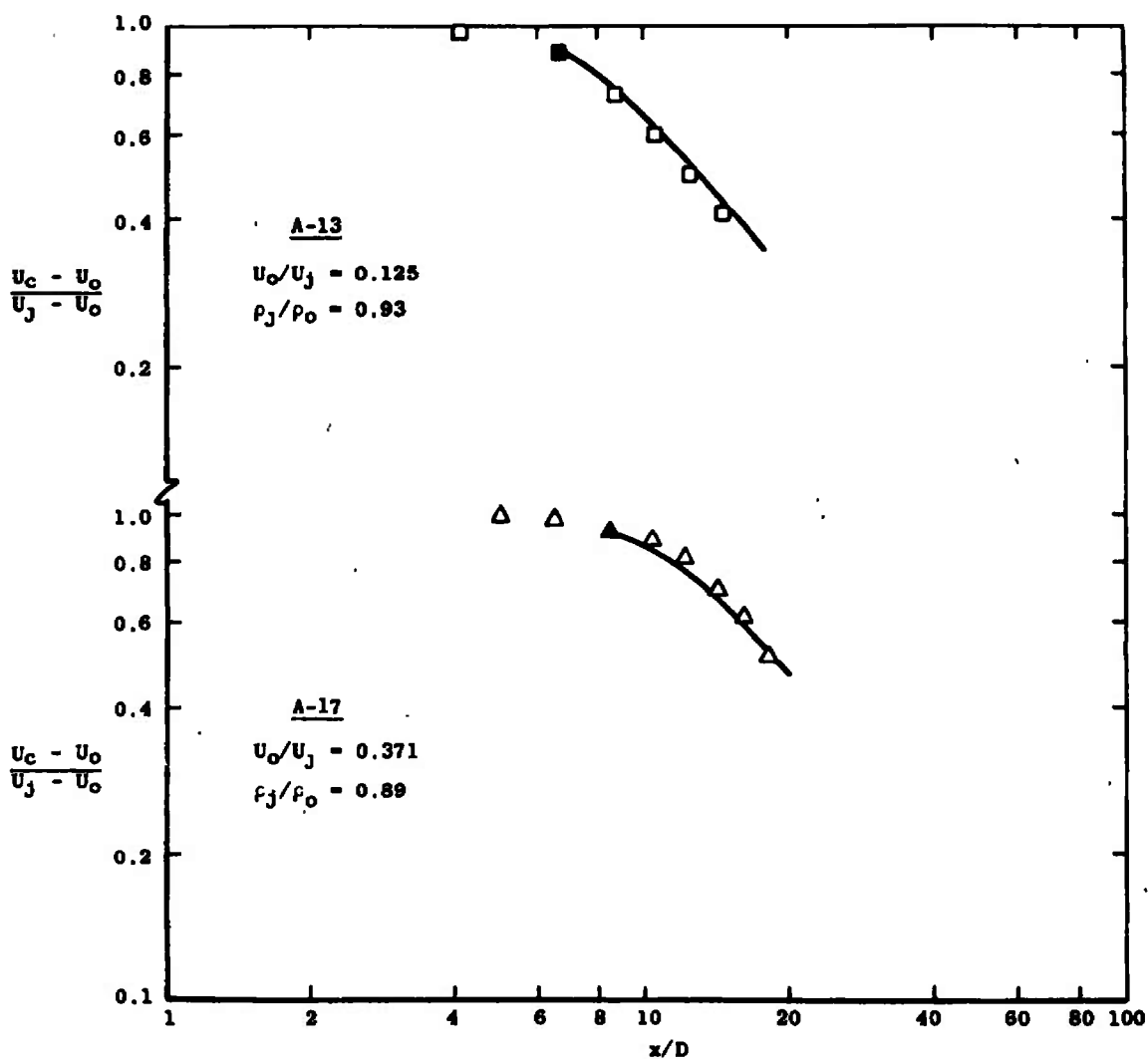


Figure 9.44. Comparison of predictions of kinetic energy theory with coaxial air-air mixing data of Paulk [42].

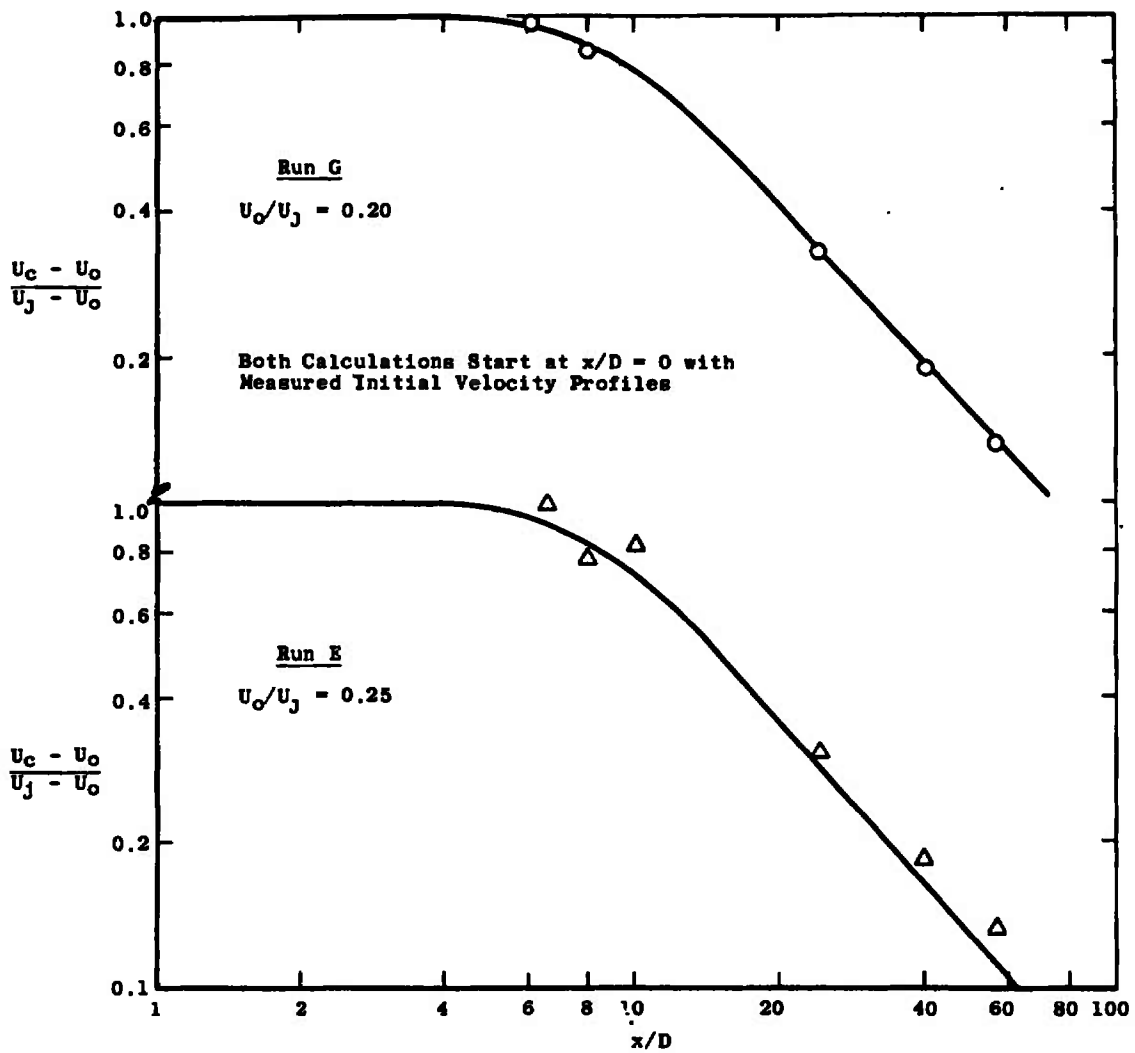


Figure 9.45. Comparison of predictions of kinetic energy theory with coaxial air-air mixing data. Data of Forstall [40].

stress profiles will work in other cases. Indeed, in the course of this study the same technique was attempted for the coaxial hydrogen-air mixing experimental data, with wholly unsatisfactory results. What Figure 9.45 does demonstrate is that such an approach can work, if some rational technique for obtaining a shear stress profile can be devised.

Figure 9.46 demonstrates the performance of the turbulent kinetic energy method when compared to coaxial hydrogen-air mixing data. In all cases the calculations shown in this figure were started at a station downstream of the end of the velocity potential core at which an accurate shear stress profile was available. As in the case of the coaxial air-air data of Paulk [42], the shear stress profile was obtained by integration of the mean flow momentum equation. The point at which the calculation was started is signaled on Figure 9.46 in one of two ways: if open symbols are used the initial condition is shown cross-hatched, while if closed symbols are used for the data the initial condition is shown as a flagged symbol.

In general the results of these calculations are extremely good. The calculation for "Run 21A" of the data of Chriss [90] shows a curious discontinuity in slope between $x/D = 5$ and $x/D = 8$; the reason for this is not known to the author, although it may be related to an initial overprediction of the shear stress level. This

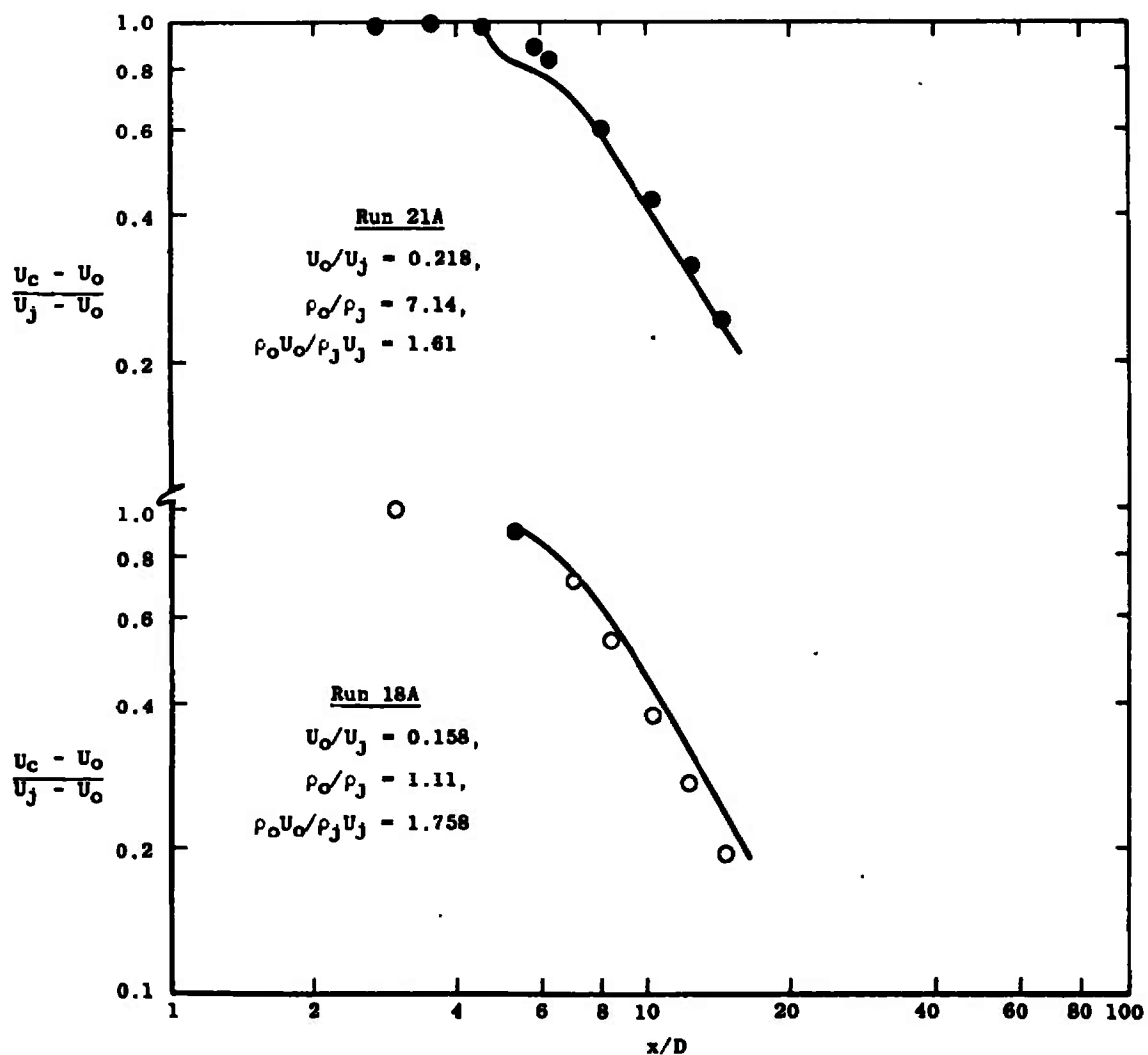


Figure 9.46. Comparison of predictions of kinetic energy theory with coaxial H₂-air mixing data of Chriss [90].

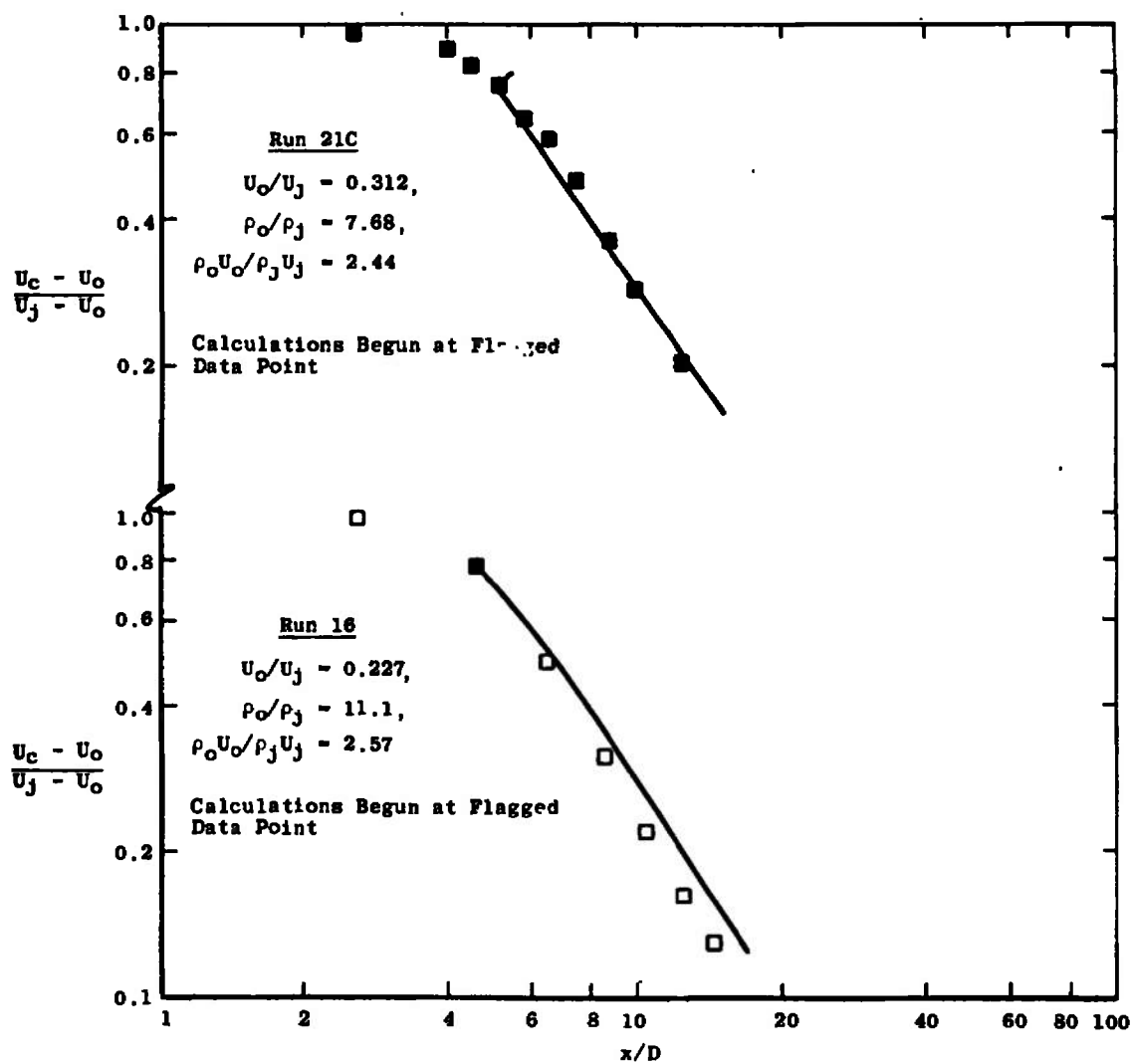


Figure 9.46. (continued)

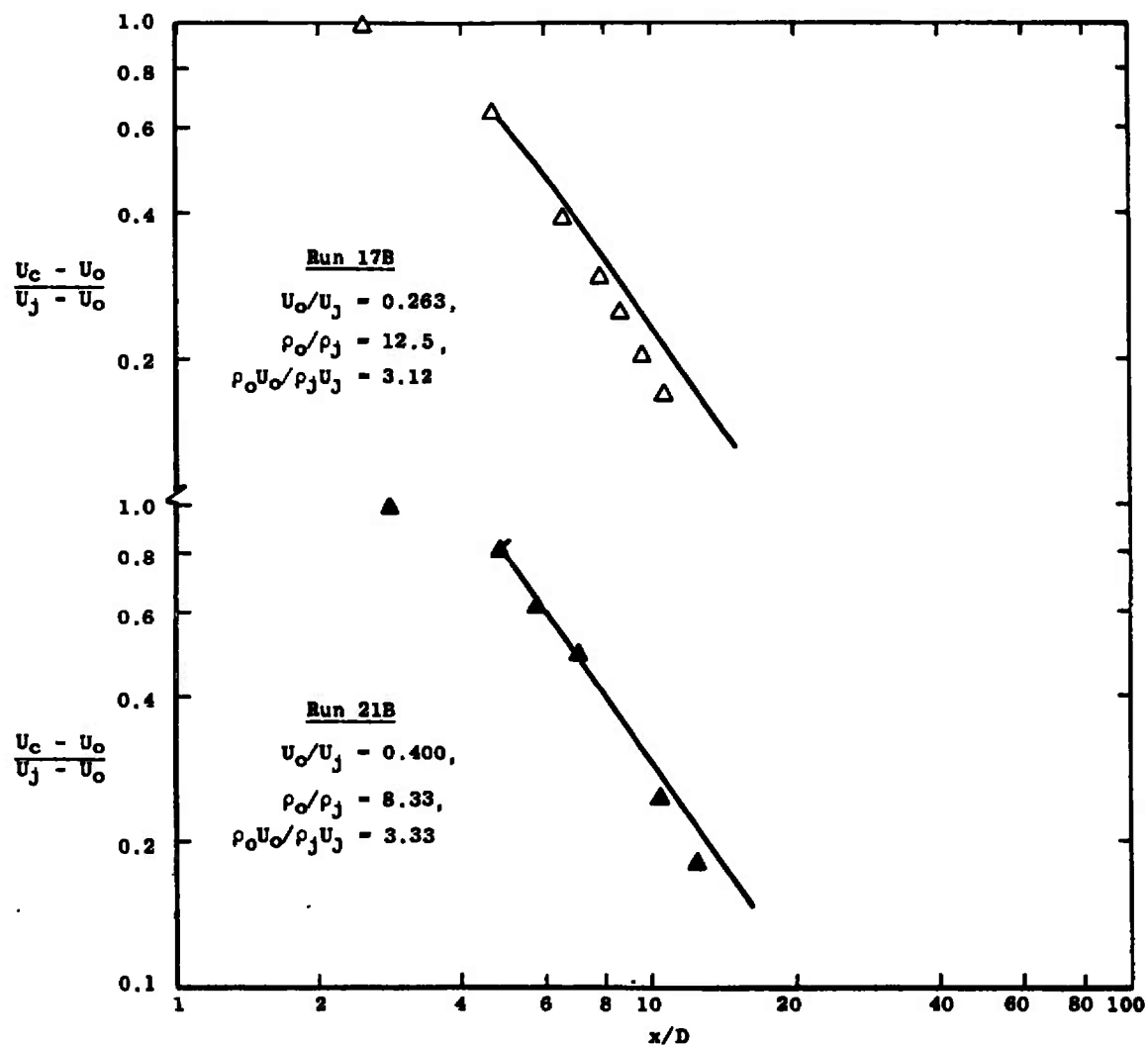


Figure 9.46. (continued)

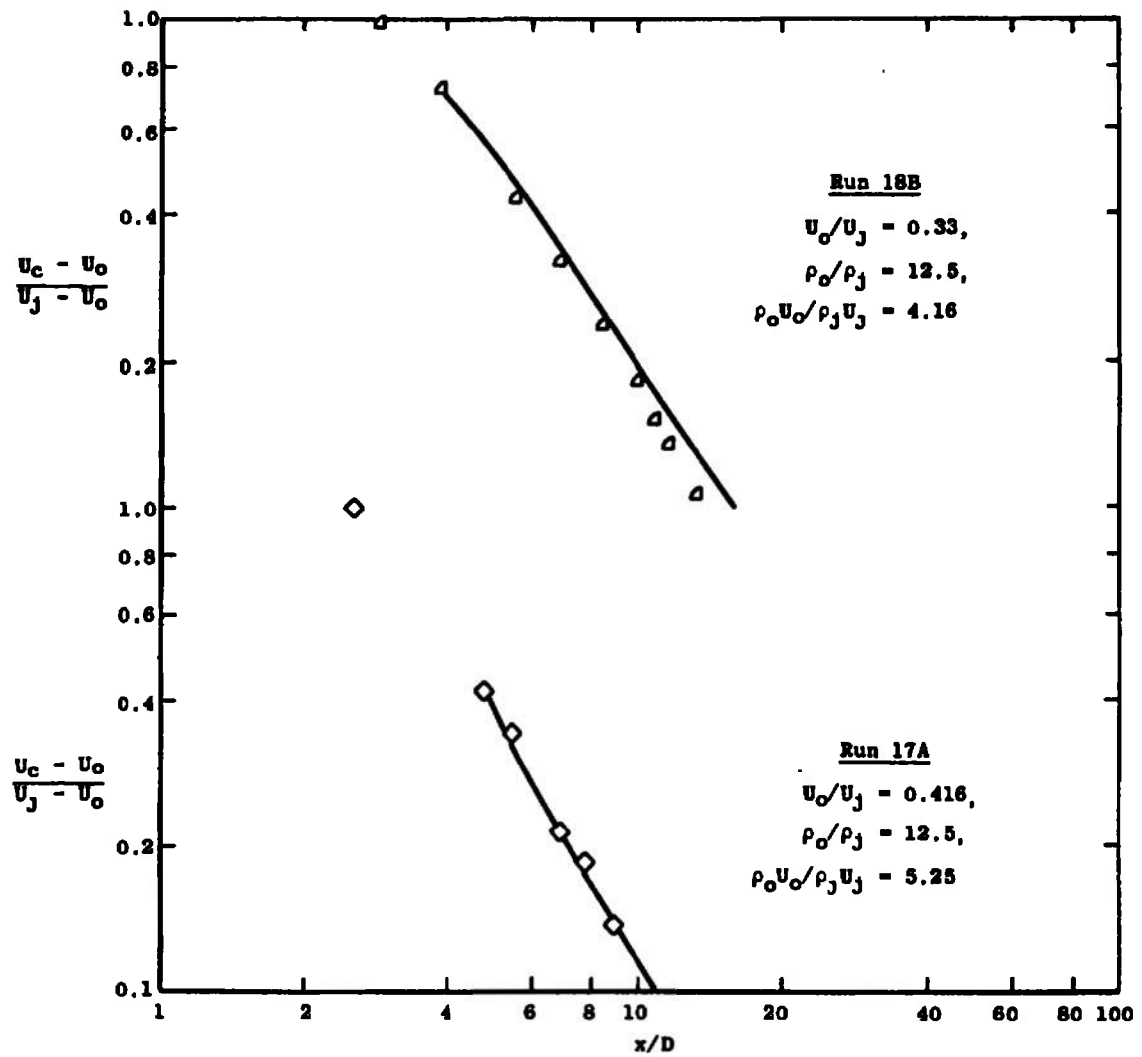


Figure 9.46. (continued)

slope discontinuity appears also on axial profiles of the composition decay and the half radius growth which are not shown here, but which will be discussed in Chapter 10 following. One fact worthy of note from Figure 9.46 is that these kinetic energy theory calculations (all made with the same set of constants) predict the centerline velocity decay equally well irrespective of the value of velocity ratio, density ratio, or mass flux ratio.

The performance of the kinetic energy theory in predicting the centerline velocity increase in the initial period of an axisymmetric wake is shown in Figure 9.47. These calculations were begun using profiles of the turbulent shear stress measured with hot-wire equipment at $x = 0$. At this location, the velocity profiles from Reference [58] showed the presence of a small recirculation region; this region has been ignored in making these calculations. Especially to be noted in Figure 9.47 is the apparent good agreement of the asymptotic trend of the kinetic energy calculation ($x/D \geq 16$) with that of the data. Although several of the locally-dependent models have produced a better level of agreement for $(x/D) < 16$, none, with the possible exception of the Zakkay model, has shown a better level of asymptotic agreement, and the kinetic energy prediction for $(x/D) < 16$ is considerably better than the Zakkay predictions.

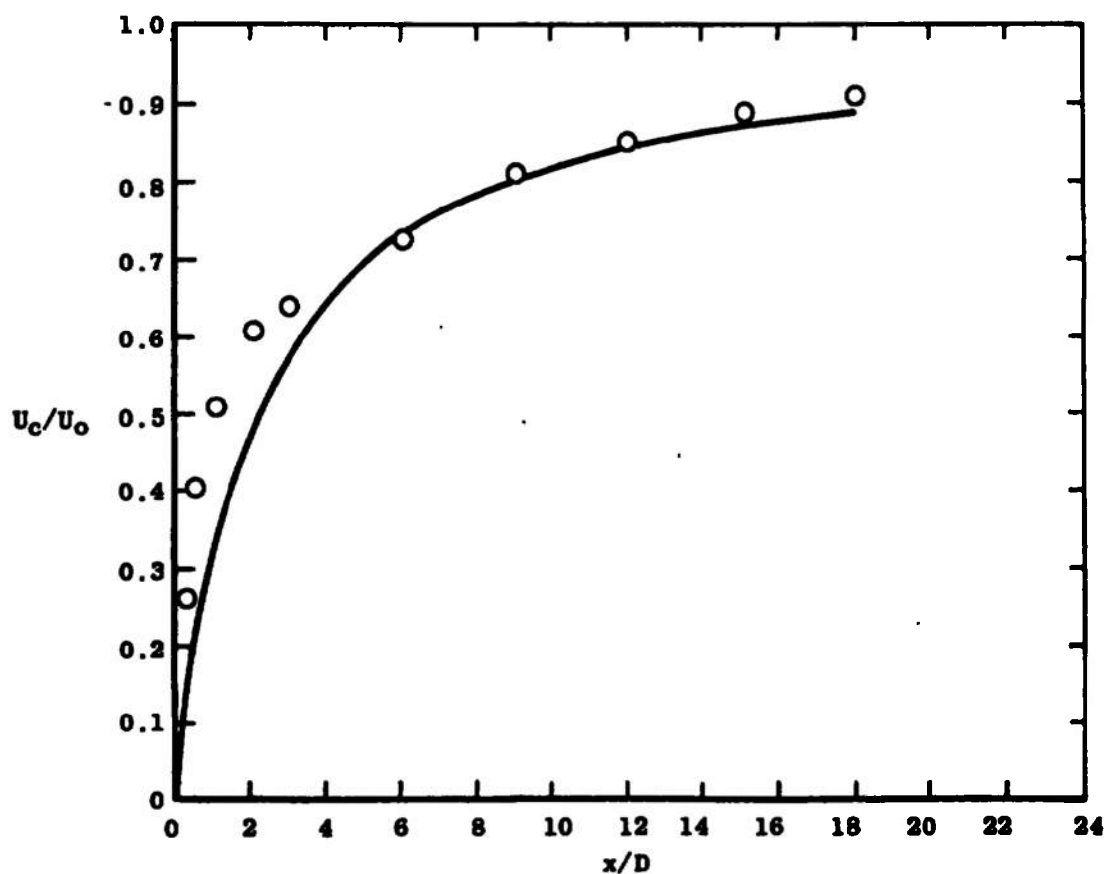


Figure 9.47. Comparison of prediction of kinetic energy theory with experimental data for the initial region of an axisymmetric wake. Data of Chevray [58].

The results of a kinetic energy calculation of the two-dimensional wake data of Chevray and Kovasznay [52] is shown on Figure 9.48. The level of agreement, both for the early period and the asymptotic behavior, is very good. These calculations were begun at $x = 0$ using the turbulent shear stress profiles measured at this point by Chevray and Kovasznay. As was shown in Chapter 3, the shear stress profile at this point shows a large peak, apparently related to the energization of the inner region of the boundary layer which has just left the plate at this point. It is the high level of shear stress here which causes the rapid centerline velocity increase shown, and the fidelity of the kinetic energy approach in reflecting both this early rapid rise and the later asymptotic behavior is remarkable.

Confrontation VIII: Compressibility Correction

Several of the eddy viscosity models described above are attempts to generalize an incompressible eddy viscosity model to a compressible flow by developing a model for the parameter $\rho\varepsilon$ rather than the eddy viscosity ε . An alternate approach is to assume that the parameter ε can be modeled in a compressible flow by using the incompressible model multiplied by a compressibility correction. Such an approach was taken by Donaldson and Gray [67] who evaluated the magnitude of the correction for a number of flows, all of them jets with still surroundings. This evaluation was

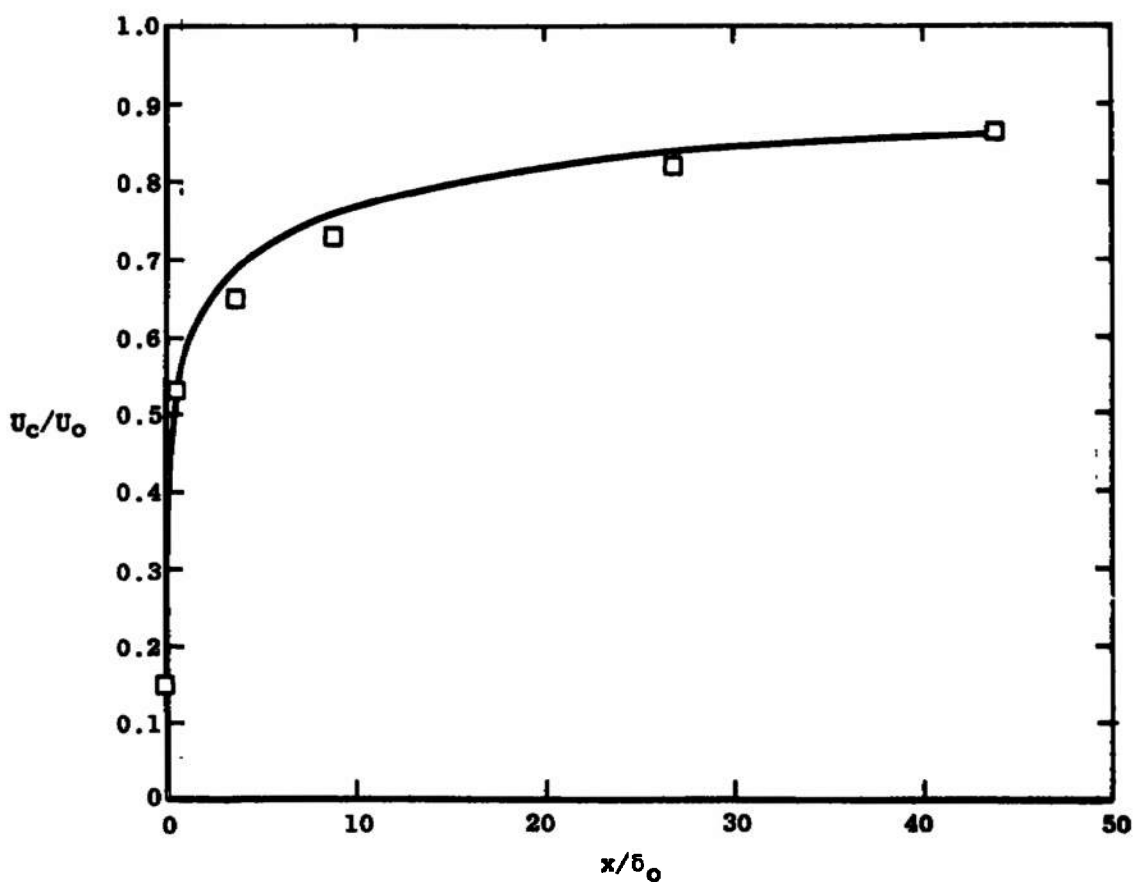


Figure 9.48. Comparison of prediction of kinetic energy theory with data for the initial region of a two-dimensional wake. Data from Chevray and Kovasznay [52].

extended to higher half-velocity Mach numbers by Peters [119], who also established an analytical relation, Equation (7.16), for the correction.

Calculations using this correction have been made for several flows in this study. The eddy viscosity model used was the Prandtl eddy viscosity model, with $K_p = 0.007$ in the first regime and $K_p = 0.011$ in the second. As a check case, a clearly incompressible flow was calculated. The case chosen was the incompressible coaxial mixing experiment of Forstall [40] for which $U_o/U_j = 0.25$. As Figure 9.49 shows, the correction for this flow is negligible, had no effect on the calculation. The expression for the correction is

$$\frac{K_p}{K_{p_o}} = 0.66 + 0.34 \exp(-3.42 M_m^2)$$

where K_{p_o} is the incompressible value of the constant in the Prandtl eddy viscosity model and K_p is the value for a compressible flow; M_m is the Mach number at the half-velocity radius. Thus for this flow, $M_m \approx 0$, and $K_p = K_{p_o}$.

The next set of calculations was made of the coaxial hydrogen-air mixing data of Chriss [90]. Two cases were chosen, one at each extreme of the variation of $\rho_o U_o / \rho_j U_j$ he investigated. The results of these calculations are shown on Figure 9.50 compared to the predictions made with the uncorrected eddy viscosity model taken from

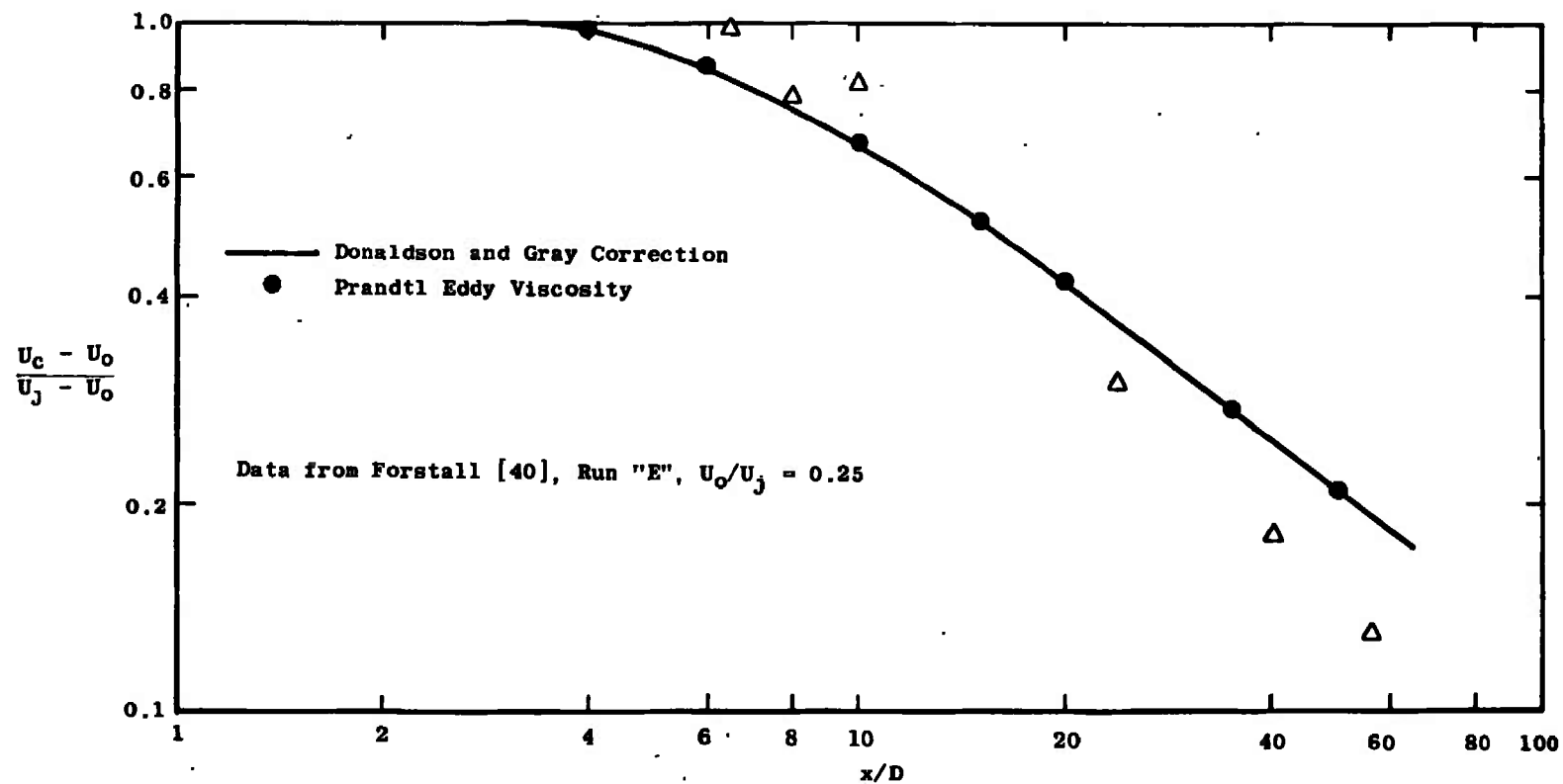


Figure 9.49. Comparison of calculations of centerline velocity decay for incompressible coaxial mixing.

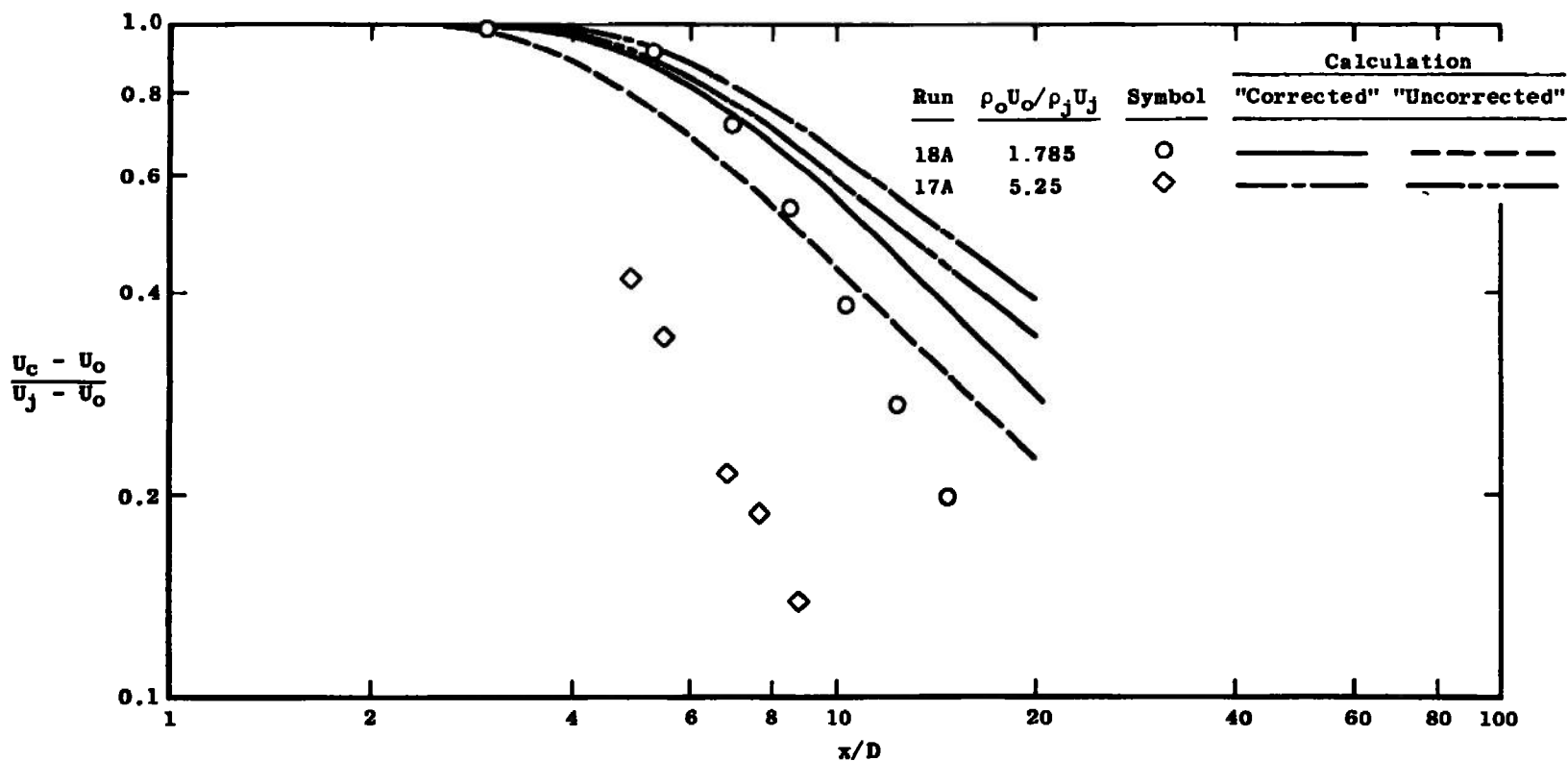


Figure 9.50. Comparison of predictions of Prandtl eddy viscosity model for coaxial hydrogen-air mixing with and without Donaldson and Gray correction.

Figure 9.14, pages 402-405. The uncorrected Prandtl eddy viscosity model underpredicts the rate of decay of the centerline velocity data. As can be seen from the equation above, the effect of the Donaldson and Gray correction is to reduce the value of the constant in the eddy viscosity model as the half-radius Mach number increases. It would be expected that this correction would have the effect of increasing the predicted value of the centerline velocity ratio at any given axial station, and Figure 9.50 shows that this is indeed the case. Because the uncorrected Prandtl model itself overpredicts the centerline velocity ratio, the Donaldson and Gray correction does not in this case improve the level of agreement.

Figure 9.51 compares the performance of the Prandtl model with and without the Donaldson and Gray correction for the supersonic jet-into-still-air data of Eggers [72]. Again the effect of the correction is to reduce the predicted centerline velocity ratio value. In this case, however, there appears to be a slight increase in the calculated rate of decay using the correction as opposed to that obtained without a correction; the other data, at lower half-radius Mach numbers, does not show this effect. It should be noted that there appears to be an improvement in the prediction of the velocity potential core length using this correction.

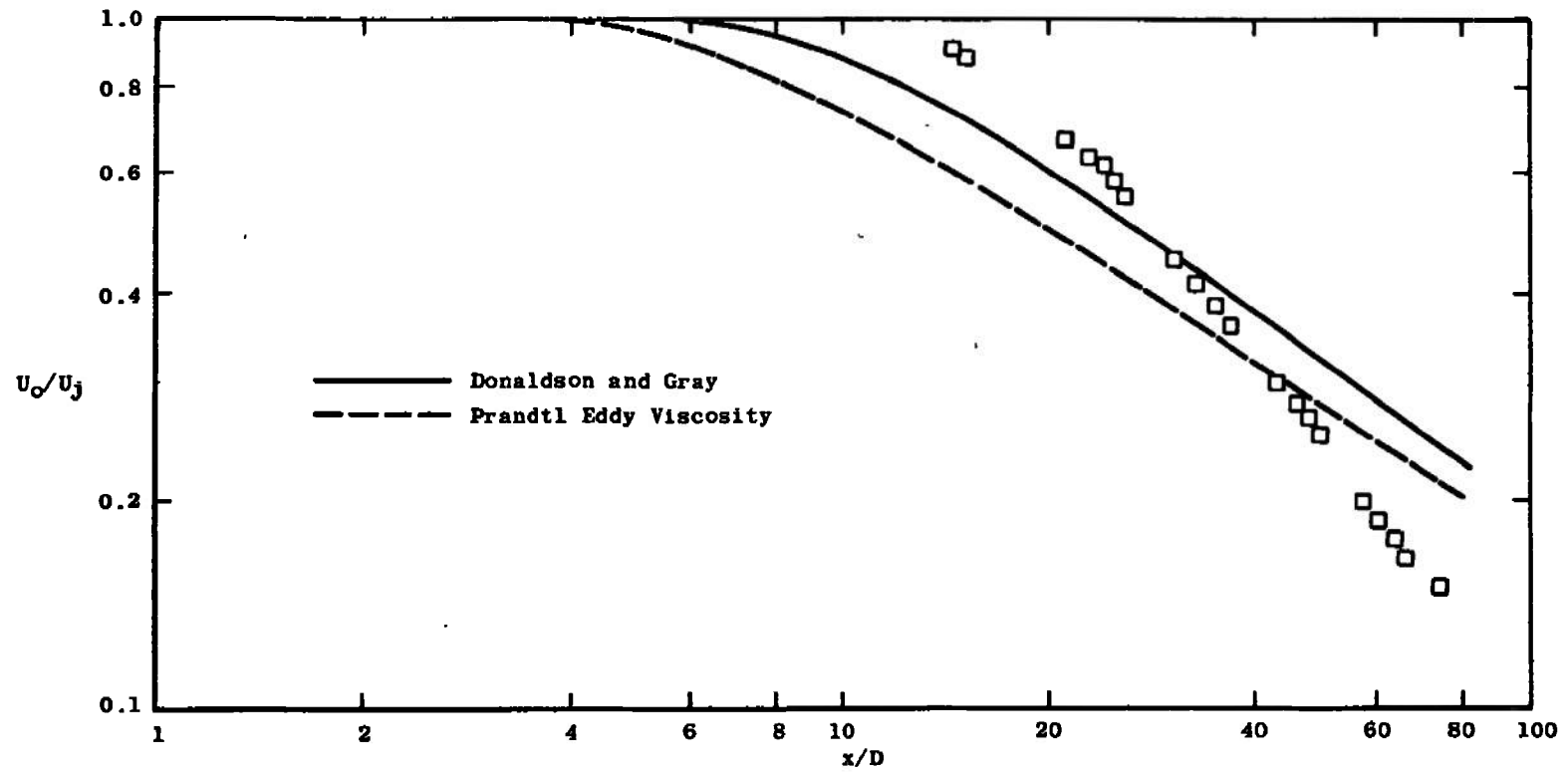


Figure 9.51. Comparison of prediction of Prandtl eddy viscosity model with and without Donaldson and Gray correction, for supersonic jet-into-still-air, data from Eggers [72].

Confrontation IX: Compressibility Transforms

In the discussion of the various compressibility transforms in Chapter 7, it was pointed out that the basic idea of the compressibility transform is to avoid the problem of specifying a compressible eddy viscosity model by transforming the mathematical statement of the compressible flow problem into a coordinate system in which the density is no longer a variable. However, in practice such transformations are highly complex and can usually only be performed under rather restrictive assumptions. In this section the results of one such transformation, that proposed by Libby [125] will be explored for a limited number of flows. The predictions will be compared to those made in the same flow situation by the Donaldson and Gray model just discussed and by the incompressible Prandtl eddy viscosity model, upon which both the Donaldson and Gray correction and the Libby transform are based.

Using the eddy viscosity transformation developed by Ting and Libby ([126], see Appendix D), and with the assumptions that the turbulent Prandtl and Lewis numbers are both unity and that the eddy viscosity is a function of the axial coordinate only, Libby [125] obtains a closed form solution for the compressible coaxial turbulent mixing problem in terms of a grouping of Bessel functions described by Libby as the ". . . so called offset circular probability function P" An additional assumption which

basically bears on the radial variation of the compressible eddy viscosity is necessary to obtain this solution, but it is not of great importance to this study; the reader is referred to Equation (10) of Reference [125]. In order to return from the transformed coordinates to the physical coordinates, it is necessary to specify the incompressible eddy viscosity, which in turn requires the value of the parameter Ψ_j , where

$$\Psi_j = r_j (\rho_j U_j / \rho_o U_o)^{1/2} \quad (9.15)$$

and to specify the value of ξ_c , the transformed x-coordinate at which the potential core ends. Libby uses the Prandtl eddy viscosity with $K_p = 0.0125$ in the form used in this study (i.e., for $b = 2r_{1/2}$). Libby takes for this last parameter $\xi_c = 0.05 \Psi_j$; this and the coordinate transformation expression

$$\xi = \int_0^x \left(\frac{\rho_c}{\rho_o} \frac{\epsilon}{U_o \Psi_j} \right) dx \quad (9.16)$$

specify x_c as a function of the velocity ratio U_j/U_o . Consider, from Equation (9.16)

$$\xi_c = \int_0^{x_c} \frac{\rho_c}{\rho_o} \frac{\epsilon}{U_o \Psi_j} \quad (9.17)$$

For $0 \leq x \leq x_c$, $\rho_c = \rho_j = \text{constant}$, and ρ_o and U_o are constant for free mixing. Thus

$$\xi_c = \frac{\rho_j}{\rho_o} \frac{1}{U_o \psi_j} \int_0^{x_c} \epsilon \, dx \quad (9.18)$$

For the first regime, Libby ([125], Equation (18)) specifies

$$\epsilon = 0.00137 \times |U_o - U_j| \quad (9.19)$$

so that, substituting (9.19) into (9.18), and noting that $\psi_j^2 = r_j^2 (\rho_j U_j / \rho_o U_o)$, one gets for the potential core length x_c

$$\frac{x_c}{r_o} = \frac{2x_c}{D} = \frac{U_j/U_o}{0.0137 |1 - U_j/U_o|} \quad (9.20)$$

Note that Equation (9.20) specifies a core length variation independent of the density ratio.

In order to test the predictions of the Libby transform against some of the variable density data used in this study, a computer program was written to invert the Libby transform solution to real coordinates. Figure 9.52 shows the prediction of the Libby transform as compared to three of the coaxial hydrogen-air mixing experiments of Chris's. As can be seen, both the core length prediction and the downstream decay prediction are in each case erroneous. Further, the Libby transform predicts an increase in core

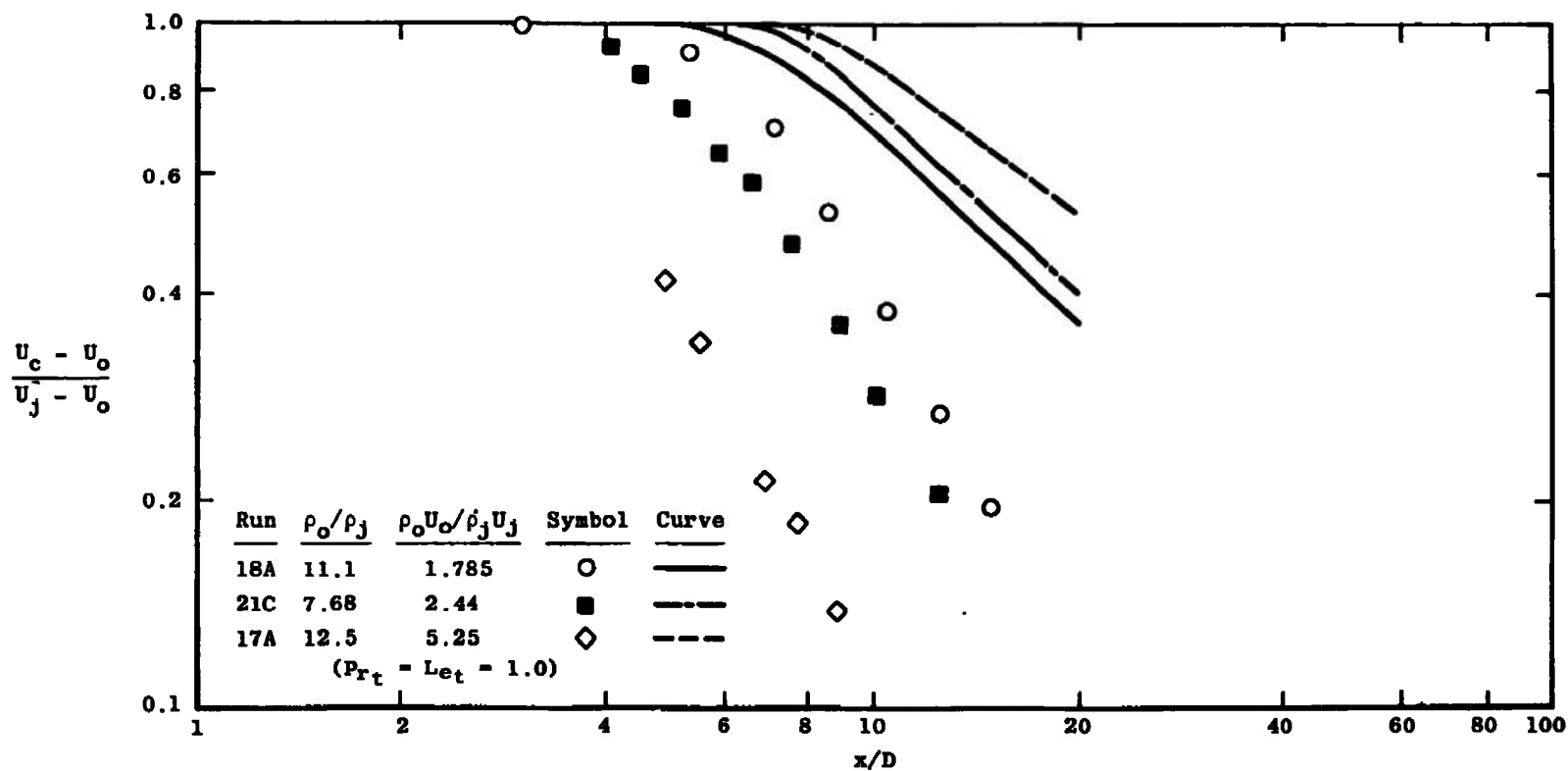


Figure 9.52. Comparison of predictions of the Libby transform with coaxial hydrogen-air mixing data. Data of Chriss [90].

length with increase of U_o/U_j , while the data indicate the opposite; the transform solution also predicts an increase in the rate of centerline velocity decay with a decrease in the parameter $\rho_o U_o / \rho_j U_j$ which is also opposite to the trend of the data.

Figure 9.53 compares the results predicted by the Libby transform for one of these coaxial hydrogen-air mixing cases with the Donaldson and Gray correction calculation made in this study for the same case, and with the Prandtl eddy viscosity calculation, also made in this study. As was pointed out above, in the notation of this study the constant K_p used by Libby in the second regime is 0.0125, while the Prandtl constant is 0.011 for the second regime; the Donaldson and Gray correction is perhaps approximately 0.7 for these data. Somewhat surprisingly, Figure 9.53 indicates that the unadorned Prandtl model gives the best fit to this to this particular data.

The Libby transform requires that the turbulent Prandtl and Lewis numbers be unity, while the experimental data of Chriss, described in Reference [94], indicates that the proper value of the turbulent Prandtl number is 0.85. The turbulent Lewis number was found to be 1.0 for the same data. Because it assumes $Pr_t = 1$, the Libby transform predicts the same decay for centerline jet species concentration as it does for centerline velocity. Figure 9.54

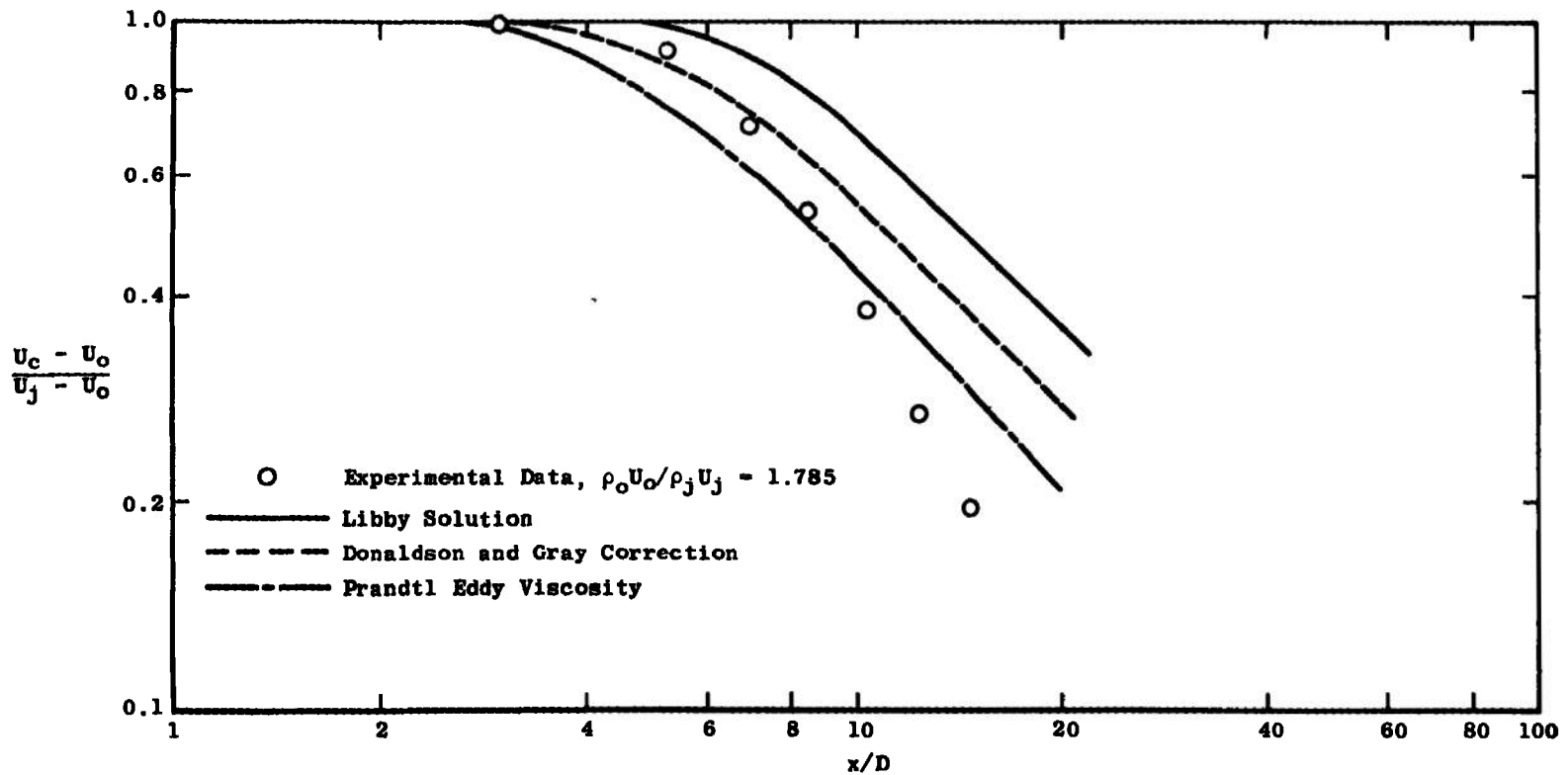


Figure 9.53. Comparison of predictions of centerline velocity decay by Libby transform and by Donaldson and Gray correction for coaxial hydrogen-air mixing. Experimental data from Chriss [90].

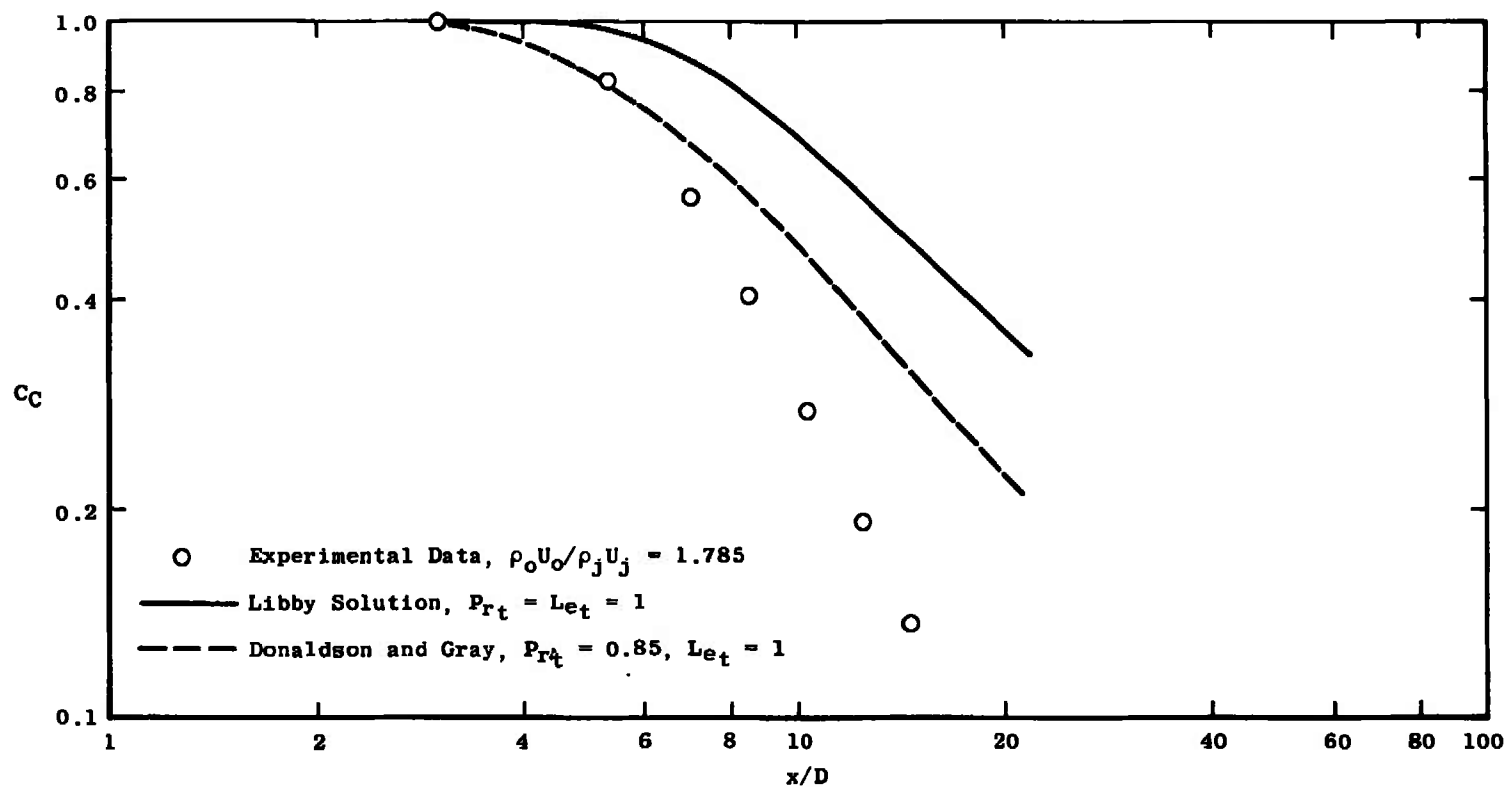


Figure 9.54. Comparison of predictions of centerline composition decay by Libby transform and by Donaldson and Gray correction, for coaxial hydrogen-air mixing. Experimental data from Chriss [90].

demonstrates the difference between the two predictions for centerline species concentration.

Because of the assumptions embodied in the use of Equation (9.20), the primary effect of the Libby transform on the velocity calculation is on the predicted potential core length, with only a small secondary effect on the decay rate. This is shown by Figure 9.55, which also again emphasizes the effect of the unity Prandtl number assumption.

Summary

From the experimental data examined in Chapters 2 through 5, six experiments have been selected. These experiments include the jet-into-still-air, coaxial air-air jets, coaxial hydrogen-air jets, the compressible jet-into-still-air, and two-dimensional and axisymmetric wakes. The important parameters for the selected experiments are given in Table 9.1, page 368.

A total of nine theoretical models for the turbulent shear stress are considered in this study. Seven of these are confronted with the entire range of experiments discussed above. The other two are of somewhat more limited applicability and have only been compared to a portion of the range of experimental flows. Table 9.2, page 376, lists the seven models that have been confronted with the entire range of experiments. These are the Prandtl mixing length [101], the Prandtl eddy viscosity theory [114], the displacement thickness model of Schetz [120, 121], the eddy

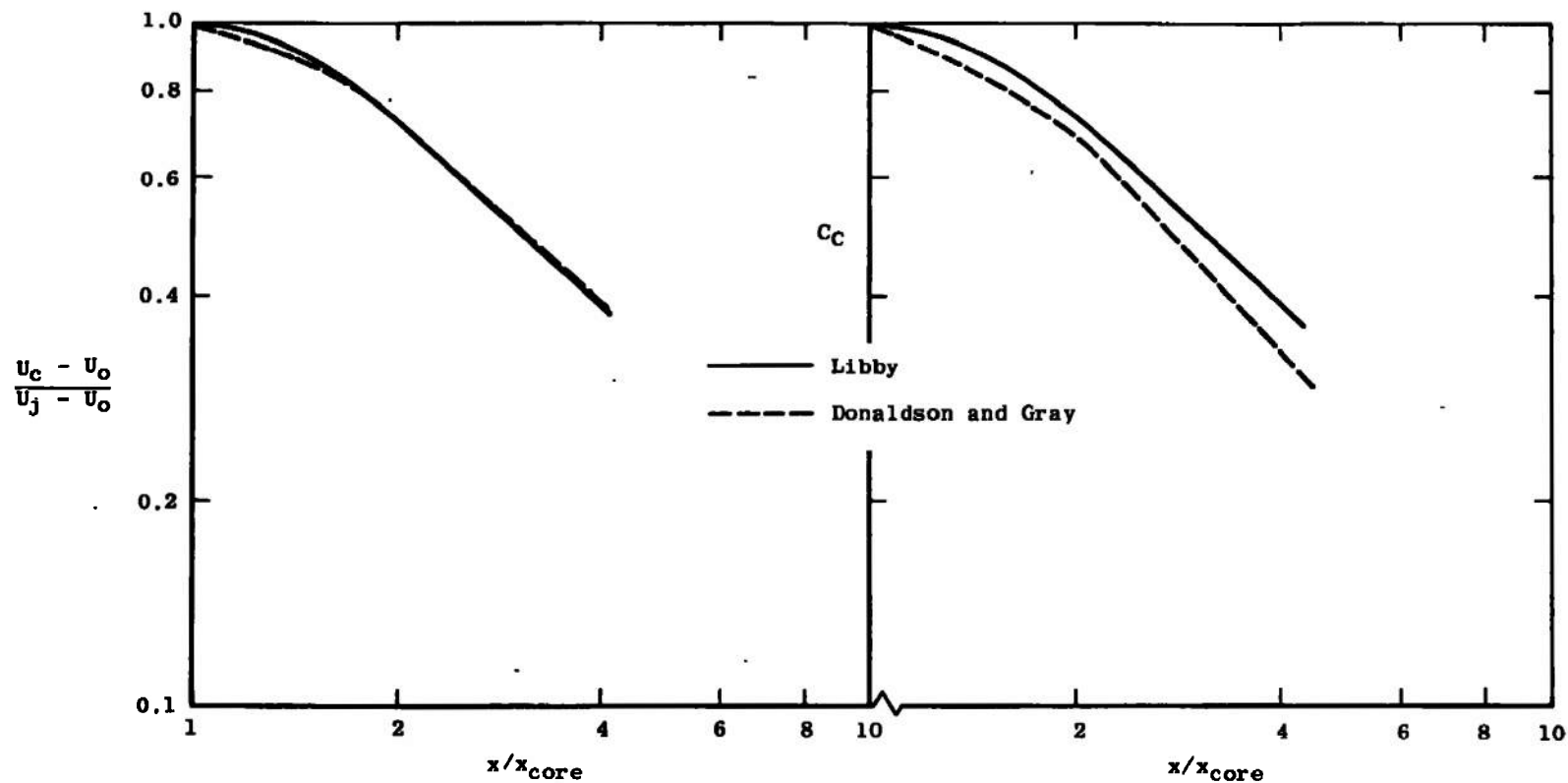


Figure 9.55. Comparison of centerline decay predictions normalized with respect to computed velocity potential core length; Libby transform and Donaldson and Gray correction.

viscosity models of Ferri [83], Alpinieri [84], and Zakkay [86], and the kinetic energy theory [131-133]. The values of the constants used with these models were obtained from several sources. Thus, the constants used with the mixing length theory were taken to be those given by Squire and Trouncer [48], while the constants used with the Prandtl eddy viscosity model were those given by Peters [119]. In the remainder of the cases listed, for the locally-dependent models, the constants used were those recommended by the developer of the model in question. In the case of the Schetz displacement thickness model or "Unified Theory" [121], the Prandtl mixing length was used for reasons of convenience to calculate the first regime of mixing for the jet-flows. This introduces only small differences in the results compared to those given by Schetz, and does not affect the conclusions drawn. In the case of the kinetic energy theory, the constants used were those given in Reference [133].

The remaining two models can both be considered in effect to be corrections to the Prandtl eddy viscosity theory. For the Donaldson and Gray Mach number correction [67], the constants used were those of Reference [119], while the constants used in the Libby transformation were given by Libby [125]. These two corrections were applied to only a limited number of flows; the Donaldson and Gray correction to coaxial air-air, coaxial hydrogen-air and the

compressible jet, and the Libby transform to only coaxial hydrogen-air mixing. The results of these confrontations, as well as the other more extensive ones are summarized in the remainder of this section.

Prandtl mixing length. For this model the conclusion of the confrontation must be that when it is applied to a variety of flows with a single "universal" constant, it performs poorly. In general, the mixing length theory underpredicts the rate of decay of centerline velocity quite substantially, for coaxial hydrogen-air mixing and the compressible jet-into-still-air. However, it does predict well the length of the velocity potential core for the incompressible jet-into-still-air and coaxial air-air mixing. The mixing length theory provides a good prediction of the initial centerline velocity increase for both two-dimensional and axisymmetric wakes, but it is not capable of predicting the asymptotic rate of increase of velocity in these flows. Thus the mixing length theory cannot be recommended except for the early portion of wakes, and for such flows there are other models that do as well or better.

Prandtl eddy viscosity. This model does a fairly good job on the incompressible jet-into-still-air, although the value of the slope of the centerline velocity decay curve is somewhat too low. The prediction of the

compressible jet is not satisfactory, as the slope here is much too low. The core length prediction of the Prandtl eddy viscosity model is good for the incompressible jet-into-still-air and also coaxial air-air mixing, but the rate of mixing is still underpredicted in this latter case. For hydrogen-air mixing the predictions are not satisfactory. The model predicts an increase in velocity potential core length for increasing mass flux ratio $\rho_o U_o / \rho_j U_j$ while the data indicate the opposite. Further, the Prandtl eddy viscosity model shows little or no change in the rate of centerline velocity decay with increasing $\rho_o U_o / \rho_j U_j$; the data show an increase. Use of the Prandtl eddy viscosity model cannot be recommended for these flows. The wake predictions of this model are quite similar to those of the mixing length theory; they are nearly identical for the two-dimensional wake. For the axisymmetric wake, the Prandtl eddy viscosity model predicts a better asymptotic behavior than the mixing length, but here as for the two-dimensional wake the trend is still to underpredict the velocity rise. Overall, the Prandtl model can be recommended for engineering use, with a change of constant (see the summary of the performance of the Ferri model below) for the jet-into-still-air, coaxial air-air mixing ($U_o/U_j \leq 0.5$) and for the axisymmetric wake. In all of these cases, use cannot be recommended in flows with large density gradients.

Schetz "unified theory". The Schetz model, as is described in this Chapter, cannot rigorously be used for the jet-into-still-air, as a displacement thickness cannot be defined. However, because calculations of such flows may be carried out assuming a small but finite velocity at the edge of the jet, it can conceivably be used for computational purposes in a jet-into-still-air calculation. Thus, its behavior in this case is of interest. As was pointed out in the text, for the jet-into-still-air the Schetz model can be shown to have the same behavior as the Prandtl eddy viscosity model with the width scale b replaced by b^2/r_j . Noting this, it is not surprising that the decay rate predictions of the Schetz model for the jet-into-still-air, both incompressible and compressible, are wholly inaccurate. For coaxial air-air calculations the Schetz model overpredicts the rate of centerline velocity decay, although the overprediction seems to lessen as the velocity ratio U_o/U_j increases. For comparison, the predictions of the Prandtl eddy viscosity model appear to diverge more greatly from the data as U_o/U_j increases toward 1.0. On the other hand, the predictions of the Schetz "unified theory" for coaxial hydrogen-air mixing are better than those of any other locally dependent model. In some cases the level of prediction is quite good; indeed it appears that the asymptotic slope prediction is improving with increasing $\rho_o U_o / \rho_j U_j$, and the Schetz model, unlike other locally

dependent models, shows an increase in the slope of the velocity decay curve with increasing $\rho_o U_o / \rho_j U_j$. The prediction for the axisymmetric wake is not particularly good, with the initial increase in velocity being underpredicted. For the two-dimensional wake, the Schetz model prediction is nearly identical to that of the Prandtl eddy viscosity and mixing length models.

Ferri eddy viscosity model. The Ferri eddy viscosity model reduces to the Prandtl eddy viscosity model, with a change in constant, for an incompressible flow. This change in constant improves the level of accuracy for these flows. Thus for the jet-into-still-air, the level of the prediction is quite good (although the asymptotic trend is to underpredict the centerline decay of velocity). Obviously the character of the Ferri model is to always intersect the data at some point. This character improves the Ferri prediction over the Prandtl eddy viscosity prediction for the coaxial air-air flows over part of the range of the data, but the asymptotic trend remains to underpredict the centerline velocity decay. Despite the fact that it was specifically developed for variable-density flows, the performance of the Ferri model for coaxial hydrogen-air mixing is unsatisfactory. Here the core is always underpredicted, as is the slope of the decay curve. The result is the character alluded to above. For the wake data, the behavior of the Ferri model is again like that of

the Prandtl eddy viscosity model, but the changed constant serves to improve the predictions. For the axisymmetric wake the Ferri model prediction is the best of the locally dependent eddy viscosity models. Again, no recommendation can be made for wakes with significant density gradients.

Zakkay eddy viscosity model. The Zakkay model cannot satisfactorily predict the behavior of the jet-into-still-air, either incompressible or compressible. For this case it overpredicts the velocity potential core length, but underpredicts the slope of the centerline velocity decay curve. For coaxial air-air mixing the velocity potential core prediction is reasonably good, but the slope prediction is still too low. The behavior of the Zakkay model for hydrogen-air mixing is also incorrect. Although the velocity potential core length prediction is fairly good, the downstream axial decay curve slope is underpredicted. Further, the Zakkay model does not predict an increase in this slope with increasing $\rho_o U_o / \rho_j U_j$. The axisymmetric wake prediction of this model is very poor--the initial increase in centerline velocity is underpredicted and the asymptotic trend seems to be to an eventual overprediction of the centerline velocity. But the Zakkay model prediction for the centerline velocity variation in the two-dimensional wake is the best of the locally dependent models.

Alpinieri eddy viscosity model. As described in the text, the Alpinieri model was designed to agree with coaxial hydrogen-air experiments which showed an extremely (and anomalously) high mixing rate. It was also designed to reduce to the Ferri (Prandtl eddy viscosity) model for the incompressible jet-into-still-air. Thus, it is not surprising that the prediction of the Alpinieri model for the incompressible jet-into-still-air is good. In all other jet flows the Alpinieri model grossly underpredicts the velocity potential core length and underpredicts the rate of decay of centerline velocity. This is essentially the behavior of the Ferri model, but in this case the core length is so underpredicted that the theoretical curve does not intersect the data anywhere in the region of interest. The Alpinieri model cannot be applied to the wake flows considered, as it predicts infinite eddy viscosity for zero jet velocity.

Kinetic energy theory. The kinetic energy theory in general appears to be capable of providing predictions that are as good as or better than those of any other model for all of the data considered here. The worst predictions of the kinetic energy theory are for the compressible and incompressible jets-into-still-air. In both cases the theory overpredicts the velocity decay slope, although in the latter case the prediction is still better than that provided for any other model. For all of the other jet

flows considered, air-air and hydrogen-air, the kinetic energy theory in general predicts the centerline velocity decay quite accurately, and usually better than any other model. For the two wakes considered the kinetic energy theory is the only model (except possibly for the Zakkay model in the case of the two-dimensional wake) capable of predicting both the initial velocity rise and the asymptotic trend. But this excellent agreement with a broad range of data is not bought without cost. Specifically, such results can only be obtained if accurate initial shear stress profiles are known. This has restricted the use of this theory to the region downstream of the end of the velocity potential core in some cases, which may have given the approach an unfair advantage in this confrontation when compared to other models. The need for an initial shear stress profile remains a serious barrier to routine use of this model.

Donaldson and Gray correction. The Donaldson and Gray correction to the Prandtl eddy viscosity model has been compared with coaxial hydrogen-air mixing data and with data for the incompressible jet-into-still-air. In general, the effect of this correction is to decrease the value of the constant in the Prandtl eddy viscosity model for Mach numbers greater than zero. This does not improve the level of the prediction of the downstream behavior; however, it does improve the near-field prediction for high Mach number jets.

Libby transform. While it in effect behaves like a compressibility correction to the Prandtl eddy viscosity model, the Libby transform solution arrives at the correction in a significantly different way. The equations of motion for a turbulent axisymmetric flow with $Pr_t = Le_t = 1$ are transformed using the Ting and Libby [126] eddy viscosity transformation (which requires $\epsilon = \epsilon(x)$). Then under a further assumption described in the text, a solution in closed form is obtained. Returning this solution to the physical plane requires the knowledge of the experimental parameters; i.e., the inversion is specific. Such an inversion has been performed for several of the coaxial hydrogen-air flows considered here. The results indicate that the effect of this transformation is, like the Donaldson and Gray correction to reduce the value of the constant in the Prandtl eddy viscosity model. This and the restriction to $Pr_t = Le_t = 1$ make the predictions of this model unsatisfactory.

CHAPTER 10

RESULTS AND RECOMMENDATIONS

The aim of this study has been to select from the available experimental literature a set of reliable experiments covering as wide a range of conditions as possible, and to then confront the predictions of the various available models for the turbulent shear stress with these experimental results. All of the calculations used in this confrontation, with a single exception, were made using the same computer program, effectively removing any program dependencies from the results. The behavior of the various models for the turbulent shear stress in the different flows has been discussed in Chapter 9. In this Chapter, the most appropriate model for a given class of flows will be selected, and recommendations for the use of various models and the further development of some will be made. The work performed in this study has exposed the need for further experimentation in some areas. Reversing the procedure followed in the earlier chapters, the theoretical models will be discussed first, followed by discussion and recommendations for the experimental work. This is done because certain things will become apparent in the discussion of the theoretical results which have great importance for the experimental recommendations.

Selection of Theoretical Models

As would perhaps be expected, there is no one locally-dependent theoretical model for the turbulent shear stress capable of producing satisfactory predictions for the entire range of free turbulent flows considered. Certain models do, however, perform fairly adequately over a limited range of experimental conditions, and these models and the appropriate limits for their use will be described here. Further, the history-dependent turbulent kinetic energy approach has shown that it can produce reasonably accurate predictions over the entire range of flows, but only when some knowledge of the initial turbulent shear stress is available.

Figure 10.1 illustrates the behavior of the Ferri model [83] (which is equivalent for this flow to the Prandtl eddy viscosity, Reference [114]) and the kinetic energy theory for the incompressible jet-into-still-air. These two models provide the best predictions for this flow. It can be seen from Figure 10.1 that the Ferri model predicts a relatively gradual transition region, but that beyond $x/D = 10$, the prediction follows the mean of the experimental data. The kinetic energy theory, on the other hand, appears to overpredict the velocity potential core length (although the core length portion of the data is not apparent on Figure 10.1) and to then overpredict the rate of decay, resulting in a prediction 15 percent high at $x/D = 8$.

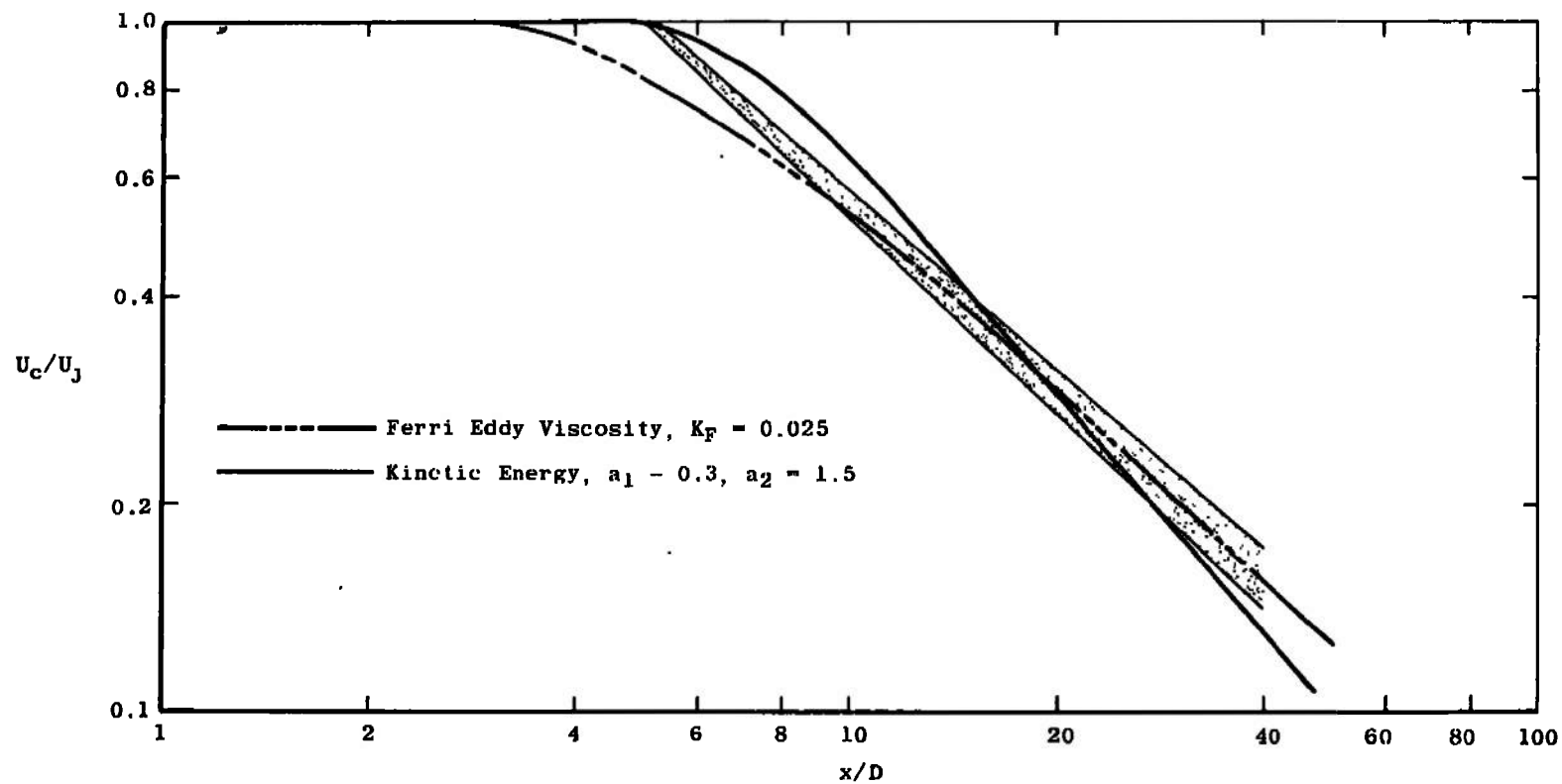


Figure 10.1. Comparison of best predictions with composite data for incompressible jet-into-still-air.

and 16 percent low at $x/D = 40$; these percentages are calculated from the mean of the experimental data.

On the other hand, the kinetic energy theory provides the only reasonable prediction for the compressible jet-into-still-air. Figure 10.2 shows this prediction as well as that for the Prandtl eddy viscosity model [114], which is one of the better eddy viscosity predictions. As was shown in Chapter 9, neither the Ferri model [83] nor the Donaldson and Gray correction [67] produces an improved prediction over the Prandtl eddy viscosity model. The kinetic energy calculations, however, could not be started before $x/D = 14.45$, because of a lack of shear stress profiles before this point. Even with a start at $x/D = 14.45$, as shown by Figure 10.2, the kinetic energy theory results in a centerline velocity prediction that is 24 percent low by $x/D = 60$. On the other hand, the Prandtl eddy viscosity prediction of the centerline velocity, is 35 percent low at $x/D = 15$ and 29 percent high at $x/D = 60$. Clearly the kinetic energy theory provides the better prediction.

The best predictions for the coaxial air-air mixing data shown in Figures 10.3 and 10.4 are made by the kinetic energy theory and, depending on the axial distance desired, the Prandtl eddy viscosity [114] or the Ferri eddy viscosity [83]. Taking the latter two first, it will be recalled that for incompressible flows, the Ferri model is

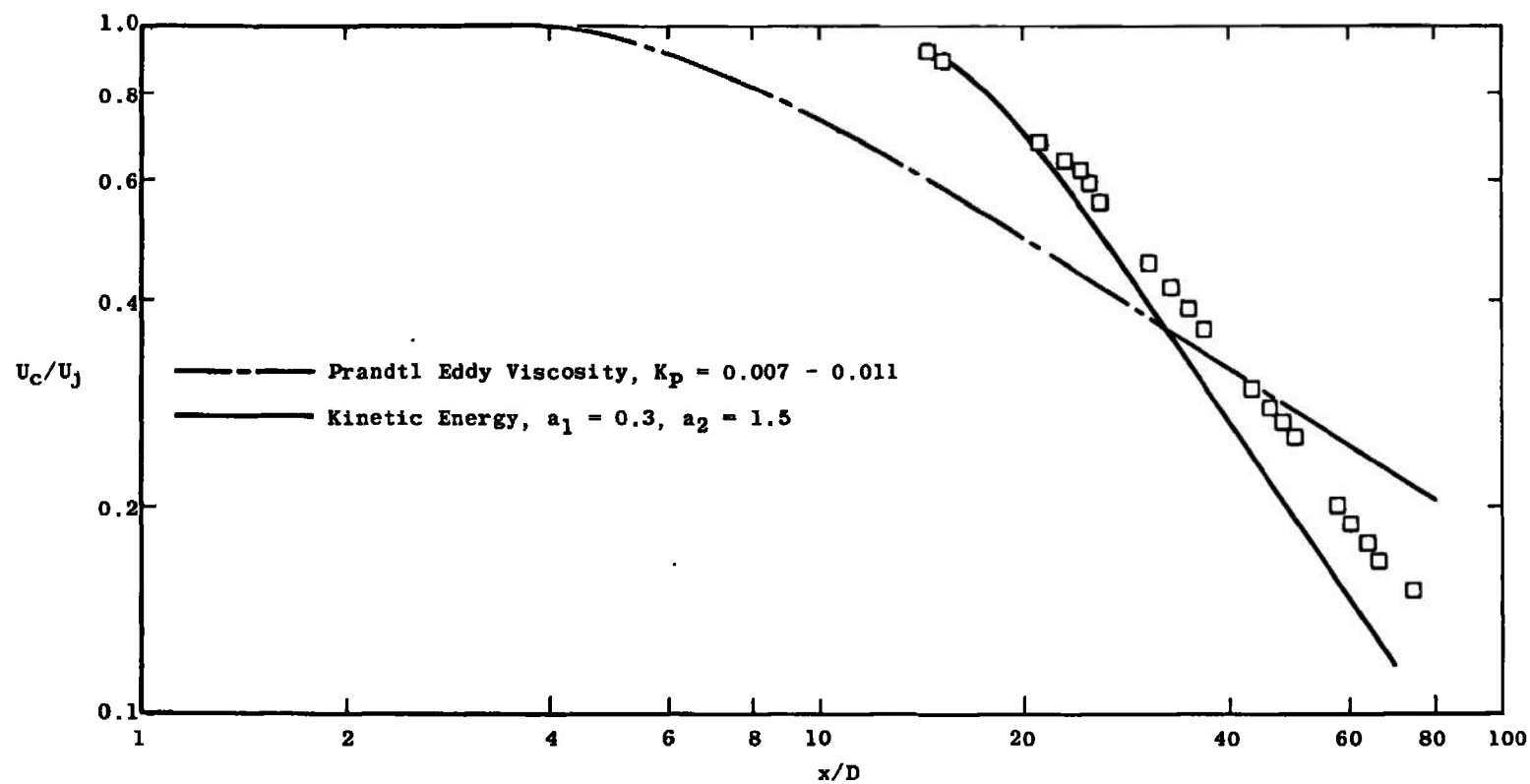


Figure 10.2. Comparison of best predictions with data for the compressible jet-into-still-air. Data from Eggers [7], $M_j = 2.22$.

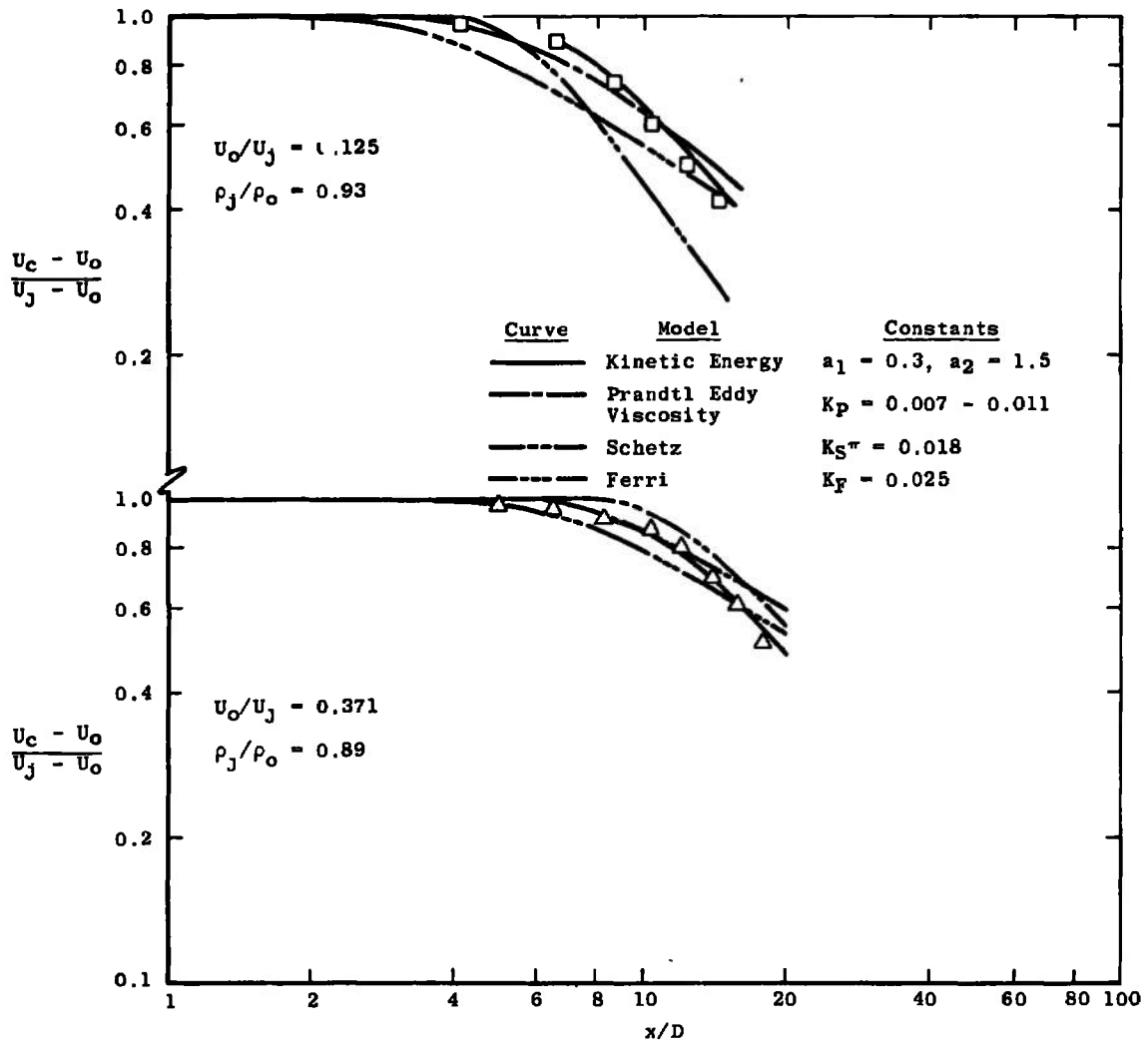


Figure 10.3. Comparison of best predictions with coaxial air-air mixing data of Paulk [42].

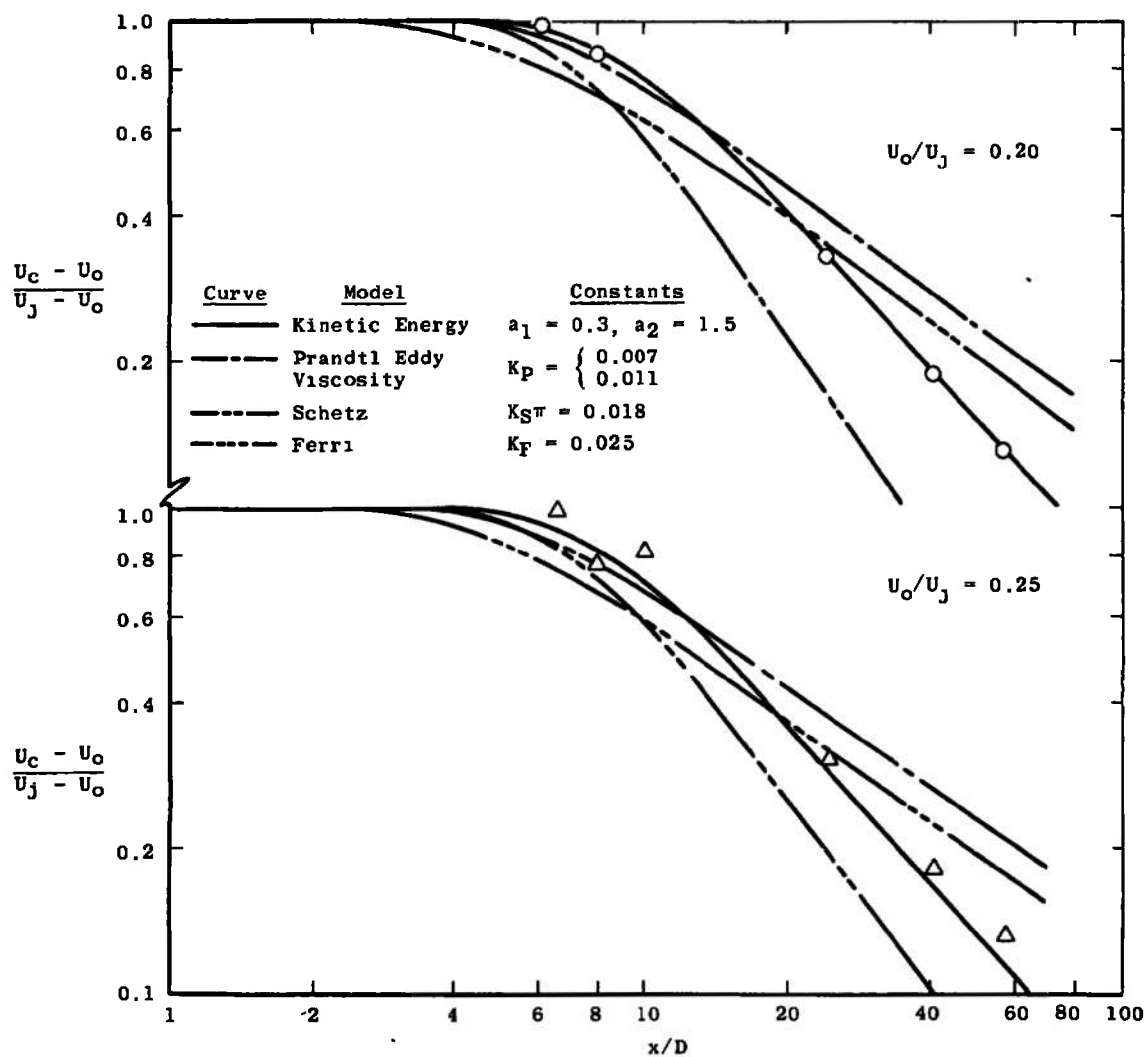


Figure 10.4. Comparison of best predictions with coaxial air-air mixing data of Forstall [40].

equivalent to the Prandtl model with a larger constant. Since both models predict the same slope of the axial decay of centerline velocity, and this predicted slope is smaller than the observed slope, both models tend to intersect the data. Because of its higher constant, the Ferri model predicts that velocity decay will begin sooner, and thus that the point of intersection will appear farther downstream. Hence, Figures 10.3 and 10.4 show that the Prandtl model provides a better prediction for $x/D < 20$.

The kinetic energy theory does quite well for these data. For the Paulk data [42], the calculations were begun at the first station at which a reliable turbulent shear stress profile was available. On the other hand, for the Forstall data [40], the calculations were begun at $x/D = 0$, using Forstall's measured boundary layer thickness, a one-seventh power law velocity profile, and a turbulent shear stress profile obtained from this velocity profile using the Prandtl eddy viscosity model with $K_p = 0.007$. No claim can be made for using this method to generate initial conditions; on the other hand, the good agreement with the data is indicative of the results obtainable with the kinetic energy theory when the proper initial conditions are used.

For the Paulk data, the Prandtl eddy viscosity model shows a maximum error of 16 percent at $x/D = 14$ for $U_o/U_j = 0.125$ and 26 percent at $x/D = 18$ for $U_o/U_j = 0.371$.

Both of these represent overpredictions of the experimental centerline velocity. For these same data, the Ferri model underpredicts the centerline velocity by 21 percent at $x/D = 6$ for the $U_o/U_j = 0.125$ case; the theoretical curve intersects the data at $x/D = 14.5$. For the $U_o/U_j = 0.371$ case, the Ferri model underpredicts the centerline velocity by 11.5 percent at $x/D = 10.5$, and intersects the data at $x/D = 16$. In both of these cases the error in the prediction of the kinetic energy theory is no more than 10 percent for the $U_o/U_j = 0.125$ case and 7 percent for the $U_o/U_j = 0.371$ case.

For the Forstall data (Figure 10.4, page 505), for $x/D > 20$, the prediction of the Ferri model is better than that of the Prandtl eddy viscosity model. For example, at $x/D = 56$, the Ferri model overpredicts the centerline velocity for $U_o/U_j = 0.2$ by 40 percent, while the Prandtl model overpredicts it by nearly 60 percent. The error in the prediction made by the kinetic energy theory is negligible. The results of the comparison for the $U_o/U_j = 0.25$ case are similar. Clearly the kinetic energy theory provides the best level of prediction, provided that some knowledge of the initial shear stress level is available. But since this is not always the case it would appear that when initial shear profiles are not available, the Prandtl eddy viscosity model formulation is adequate, with $K_p = 0.007$ in the first regime and $K_p = 0.011$ in the

second, when axial distances less than twenty diameters are of interest; for axial distances greater than twenty diameters the Ferri [83] choice of constant, 0.0125 in both regimes, seems to produce better results.

For hydrogen-air mixing there seem to be only two models which show the proper behavior. These are the kinetic energy theory and the Schetz displacement thickness model [121]. It will be recalled from Chapter 9 that there were two features of the hydrogen-air data used here which most turbulent shear stress models could not predict. These were the decrease in velocity potential core length with increasing outer-stream-to-jet mass flux ratio and the increase of slope of the decay curve also observed with increase of this ratio. Figure 10.5 illustrates the performance of the two recommended models. Both of these models exhibit an increase in velocity decay curve slope with increasing $\rho_o U_o / \rho_j U_j$. It is not possible to determine whether these models will also predict a decrease in velocity potential core length as $\rho_o U_o / \rho_j U_j$ increases, as the Schetz model as used here used the mixing length model for the core region, and it was not possible to start the kinetic energy calculations at $x/D = 0$.

Figure 10.5 illustrates that the level of agreement of the kinetic energy theory with the data is better than that of the Schetz theory, with the maximum deviation of the kinetic energy theory being of the order of 23 percent

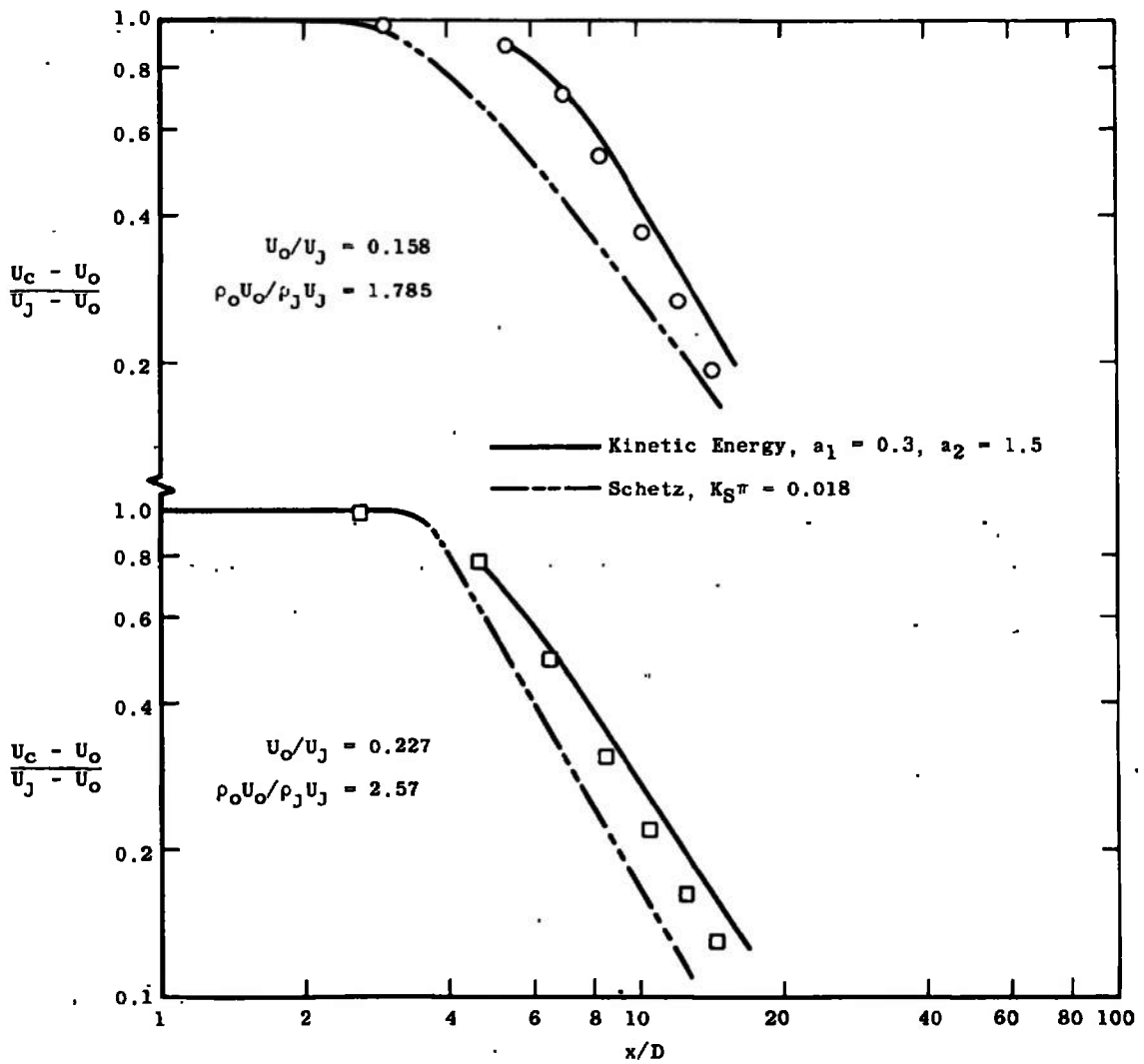


Figure 10.5. Comparison of best predictions with coaxial hydrogen-air mixing data of Chriss [90].

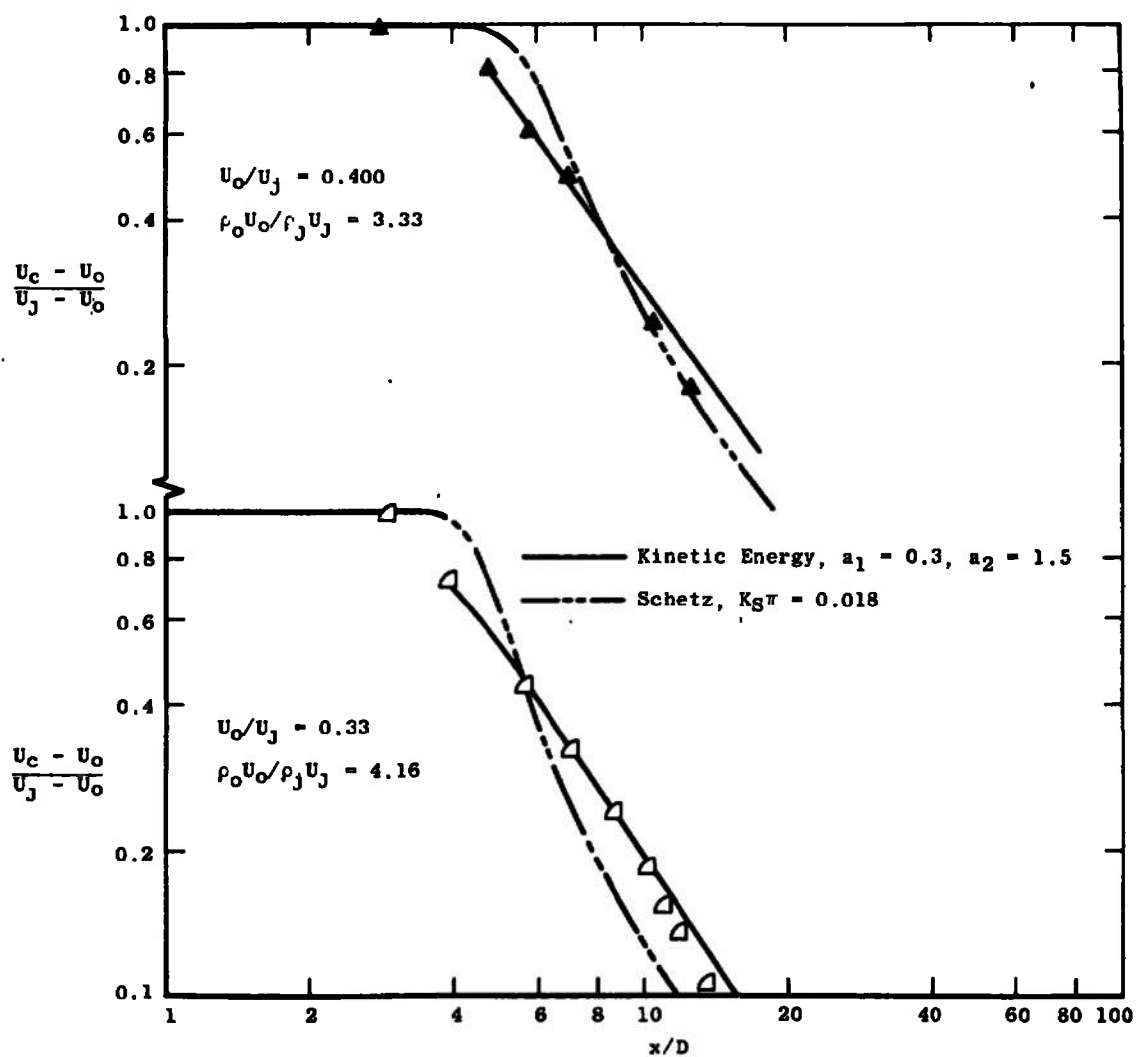


Figure 10.5. (continued)

at $x/D = 15$ (for the $\rho_o U_o / \rho_j U_j = 1.785$ case), representing an overprediction of the centerline velocity, while the Schetz model underpredicts the centerline velocity by a maximum of 40 percent at $x/D = 10.4$, also for

$\rho_o U_o / \rho_j U_j = 1.785$. Clearly substantial error is inherent in using the Schetz model (as compared to the kinetic energy theory), but the behavior of the model is such as to be recommended for further development. Also, as will be described below, there are certain anomalies in the comparison of these predictions which render difficult the interpretation of the actual magnitudes of the errors involved.

The predictions for the two wake flows are quite interesting as there are two points of comparison. In the early portion of the wake, the centerline velocity rises extremely rapidly. This rapid rise is followed by a portion in which the centerline velocity increases more gradually, eventually approaching an asymptote. Figures 10.6 and 10.7 depict the performance of the best performing models for these flows. It can be seen from these figures that the kinetic energy model again performs quite well for both the initial and asymptotic portions. For the axisymmetric wake, the Ferri version of the Prandtl eddy viscosity model provides a good prediction, although it appears that the asymptotic trend of this model is to underpredict the centerline velocity (note again the character of this model as it

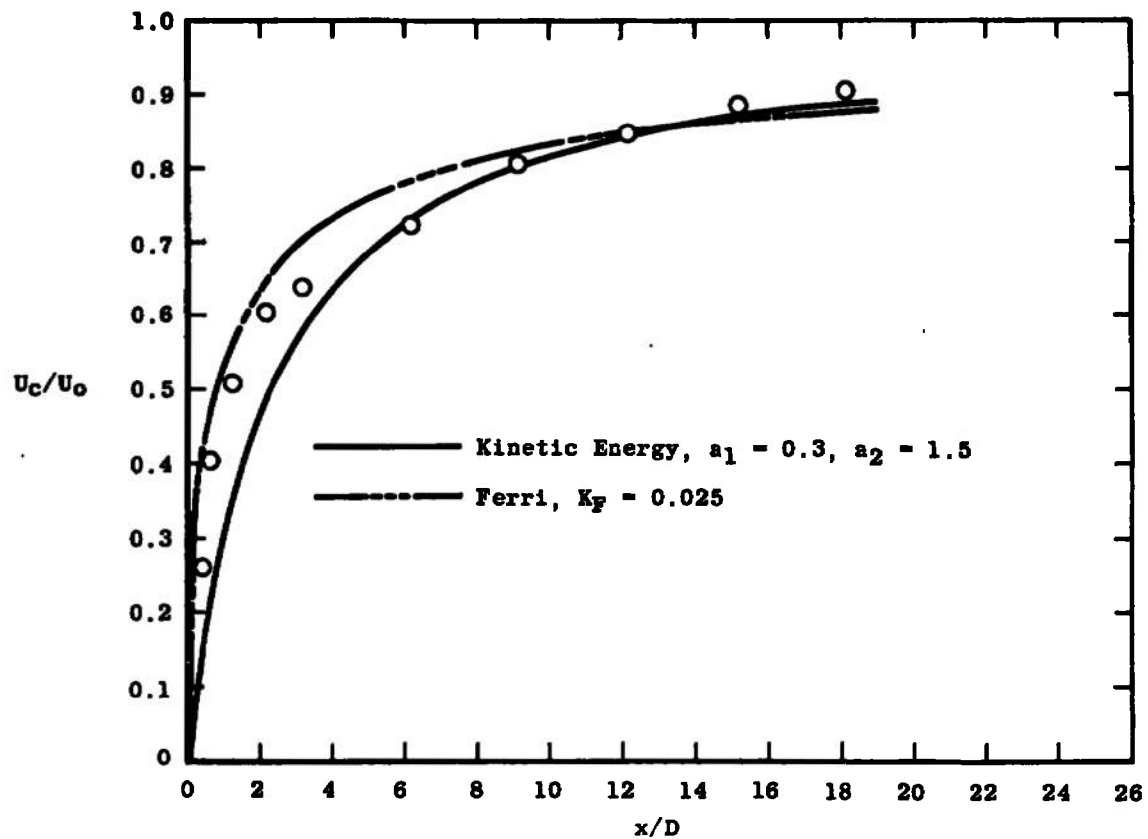


Figure 10.6. Comparison of best predictions with axisymmetric wake data of Chevray [58].

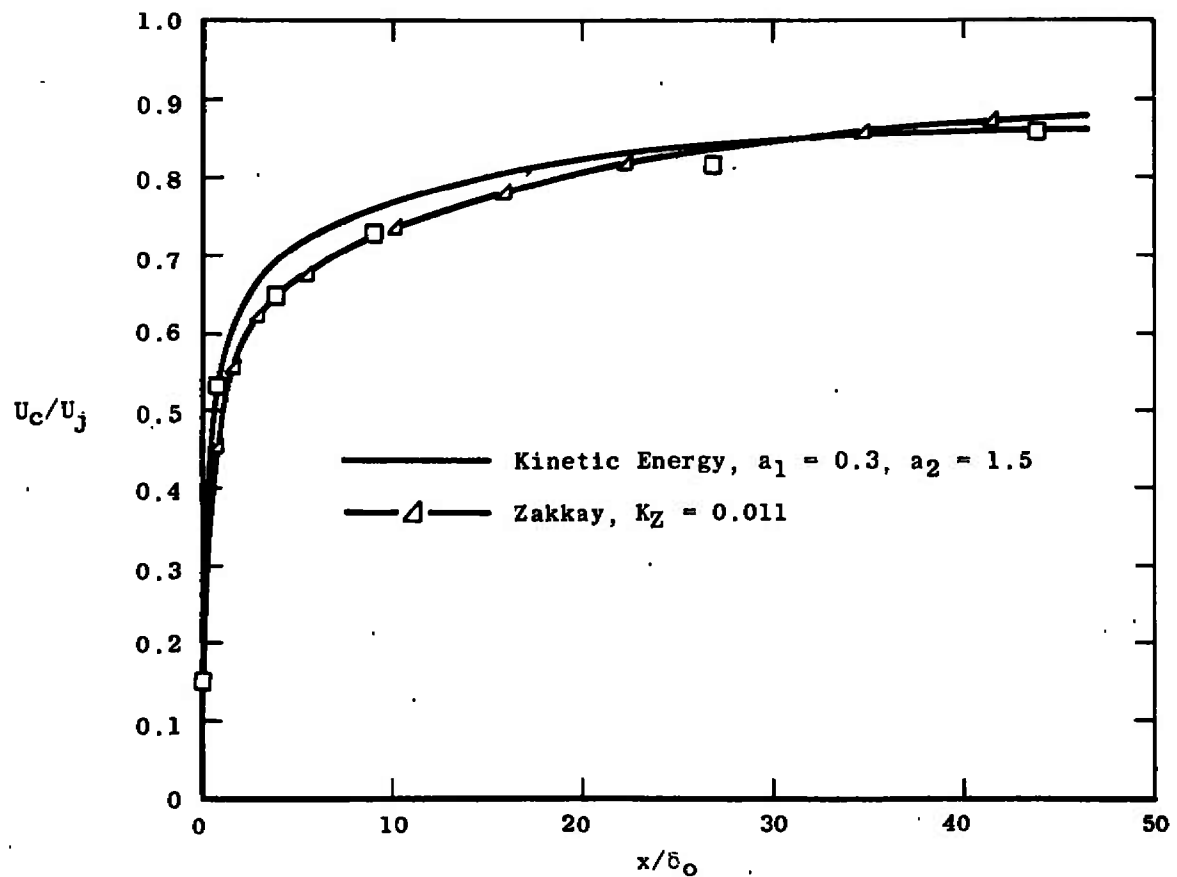


Figure 10.7. Comparison of best predictions with two-dimensional wake data of Chevray and Kovasznay [52].

intersects the data), while for the two-dimensional wake the Zakkay model [86] provides a good prediction--including an apparently good level of agreement with the asymptotic trend of the data.

Additional Results for Coaxial Hydrogen-Air Mixing

Typical velocity profiles for the various models are compared with some representative hydrogen-air data in Figure 10.8. Because these profiles are typical, it was considered more informative to look at other axial parameters for the hydrogen-air data. Figure 10.9 illustrates the velocity decay predictions of the Schetz model and kinetic energy theory for two cases of the hydrogen-air data of Chriss [90]. Figure 10.10 illustrates the centerline composition decay and half-radius growth for these same data. (C_c is the centerline mass fraction of hydrogen.) Returning to Figure 10.9, it can be seen that for the "Run 17B" case the kinetic energy theory overpredicts the centerline velocity for $x/D > 6$. It would be expected, as these calculations were made with $Pr_t = 0.85$ and $Le_t = 1.0$, that the kinetic energy theory would also overpredict the centerline concentration of jet species. Further, given profiles that normalize as Figure 10.8, i.e., as functions of $r/r_{1/2}$, it would be expected that the calculated half-radius would be smaller than the measured. Figure 10.10 shows that both of these expectations are confirmed. On the other hand, the centerline velocity for the same data is

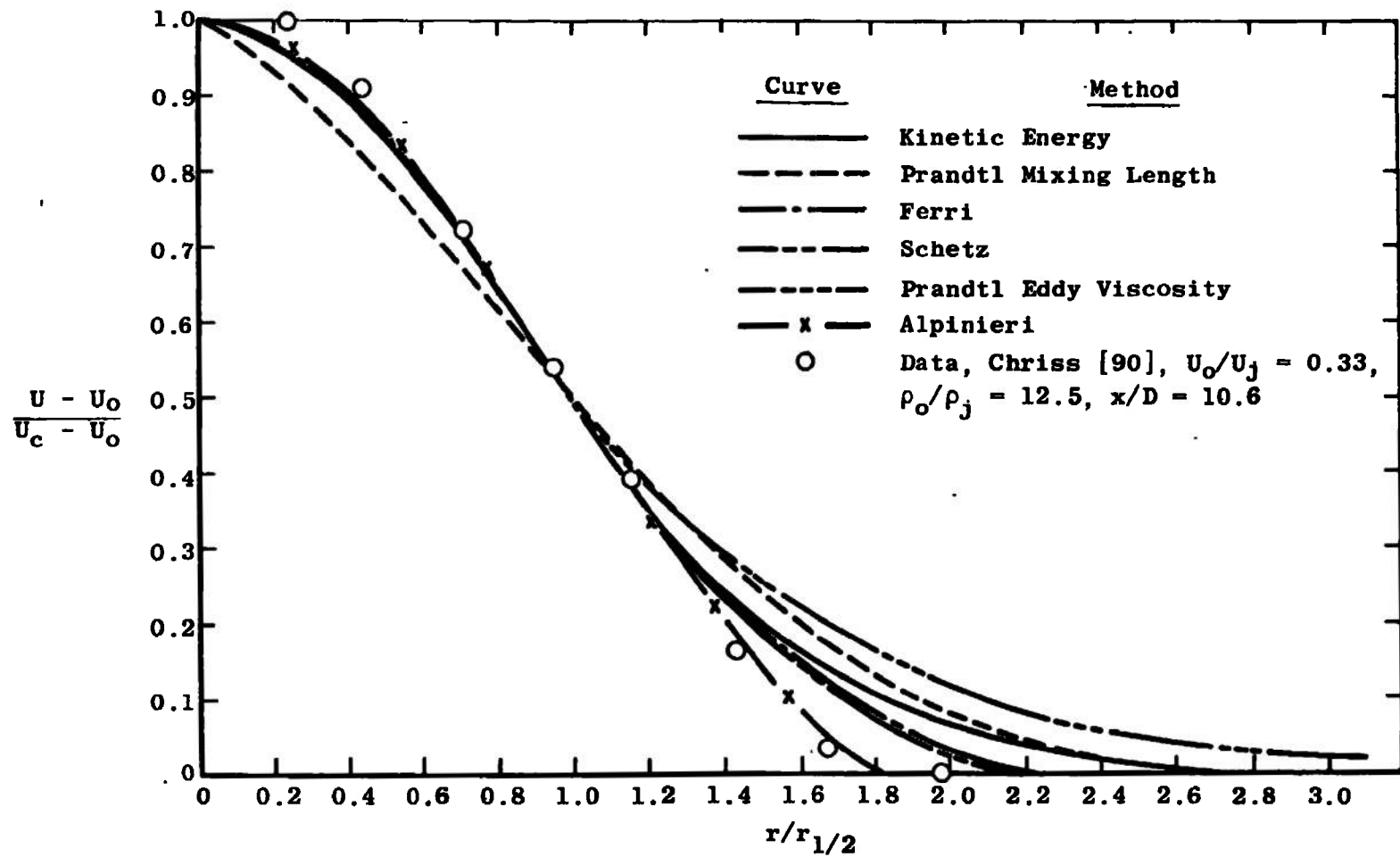


Figure 10.8. Comparison of velocity profile predictions of the various models with representative hydrogen-air data.

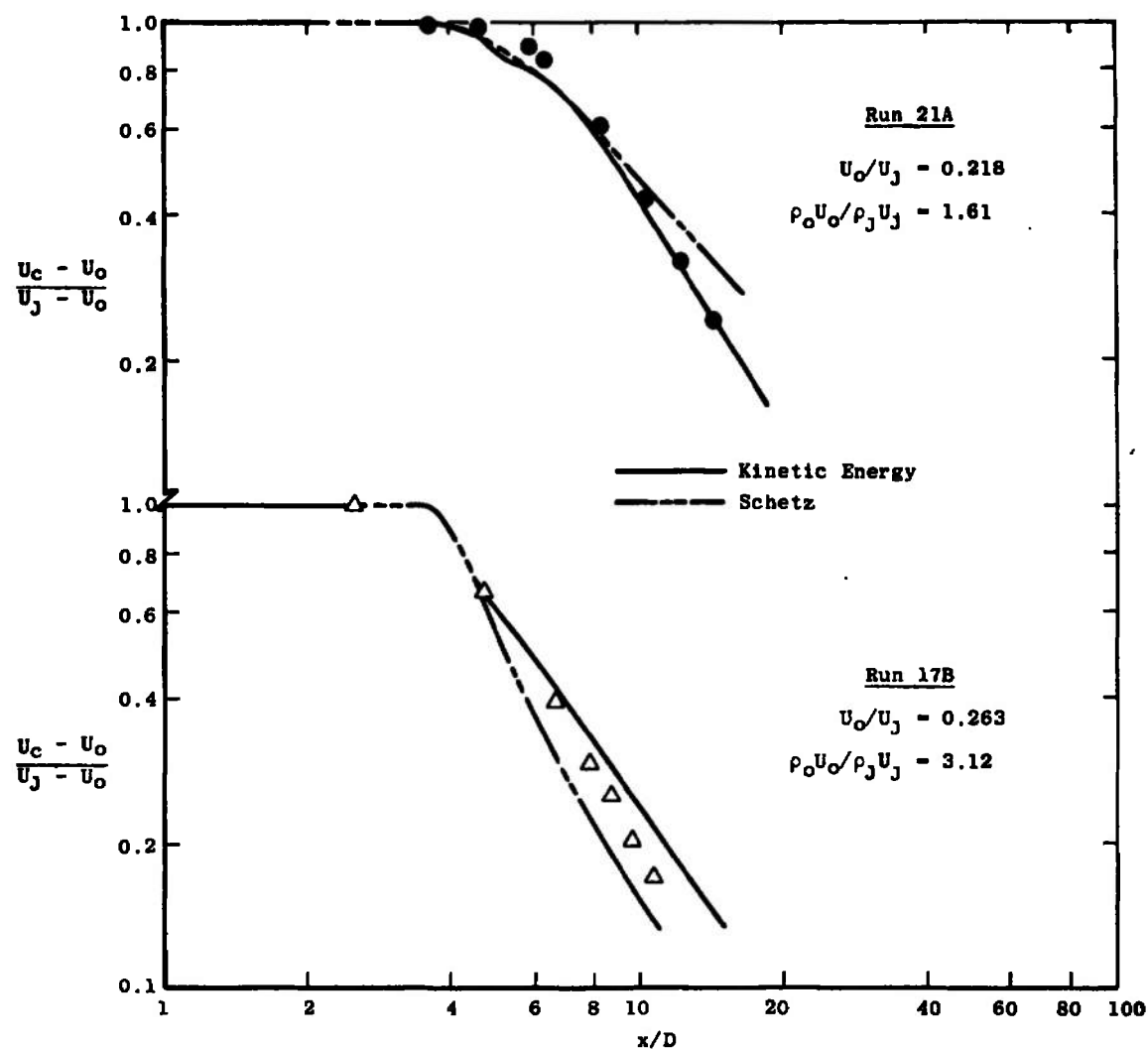


Figure 10.9. Velocity decay predictions for coaxial hydrogen-air mixing using Schetz model and kinetic energy theory. Data from Chriss [90].

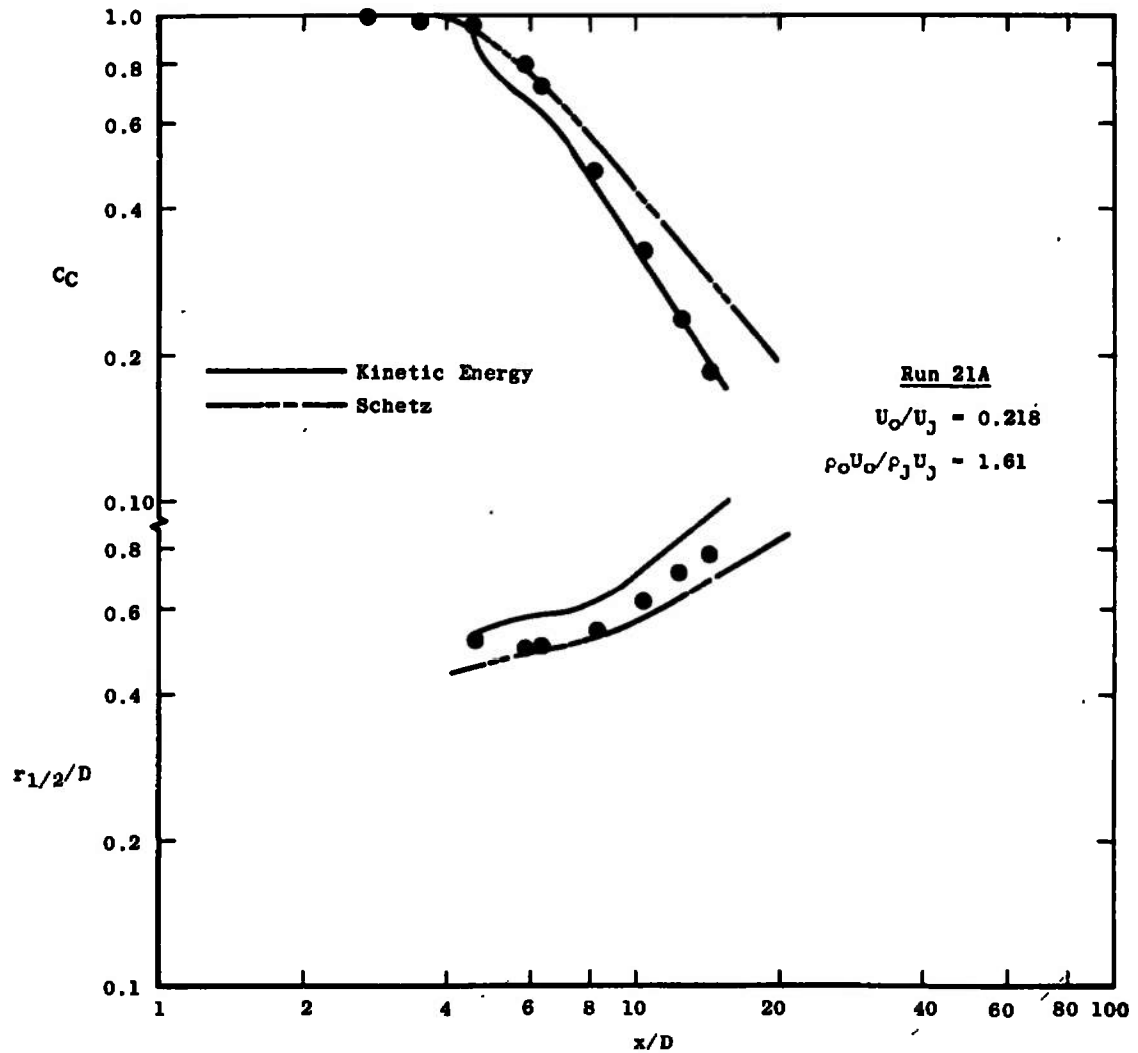


Figure 10.10. Comparison of centerline composition decay and half-radius growth predictions of Schetz model and kinetic energy theory with hydrogen-air data. Data from Chriss [90].

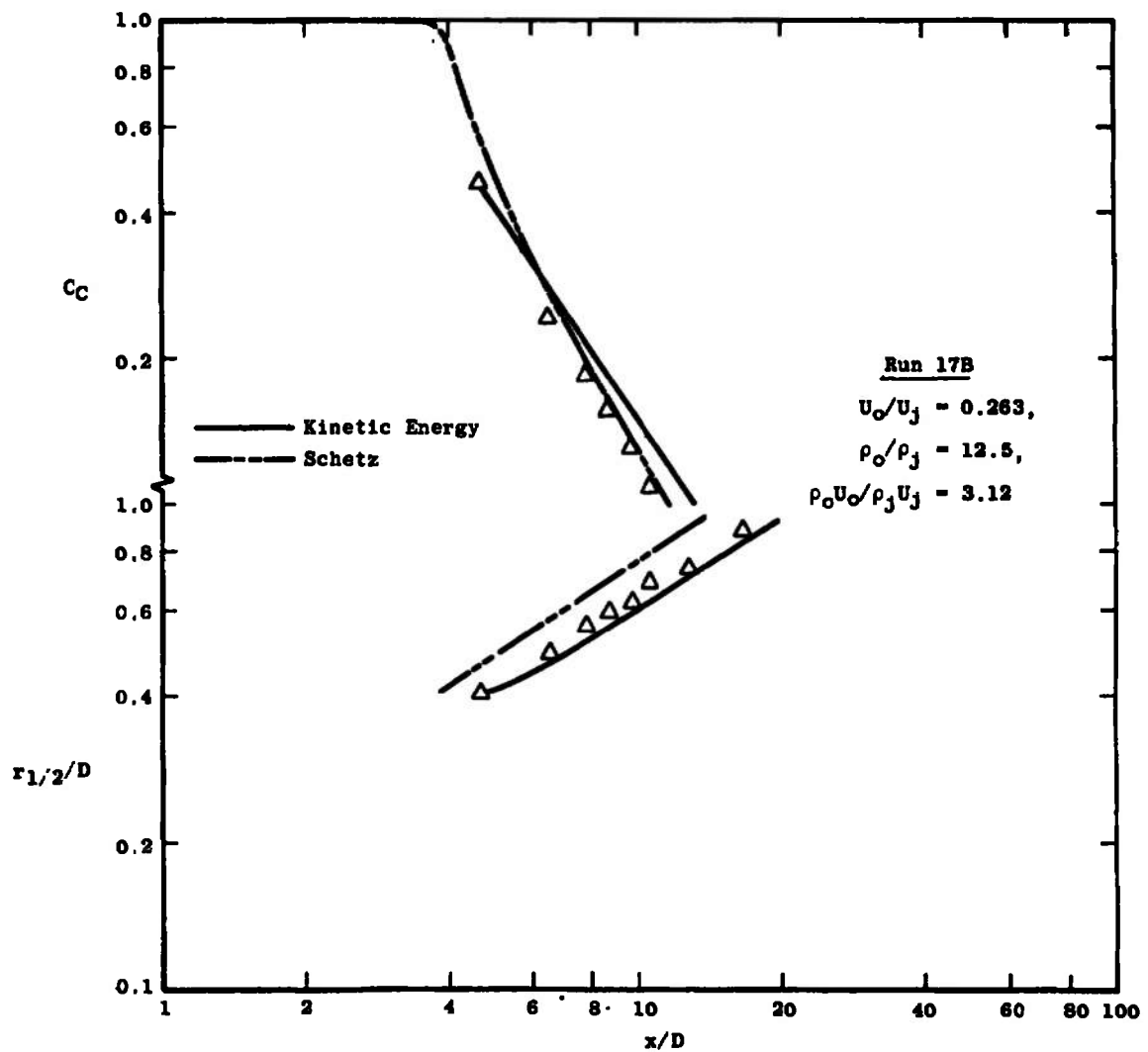


Figure 10.10. (continued)

underpredicted by the Schetz model. Figure 10.10 shows a slight overprediction of the centerline composition, which indicates that the value of the Schmidt number used--0.85--was possibly too large for these data.¹⁰ As would be expected, Figure 10.10 shows a half-radius prediction larger than measured.

Figure 10.11 shows the centerline velocity according to the predictions of the Schetz and kinetic energy models, and Figure 10.12 shows the associated centerline concentration of jet species and half-radius curves for additional coaxial hydrogen-air data. In the case of the kinetic energy calculation these curves show the expected behavior. But for the Schetz calculation, these two figures show an overprediction of both the centerline velocity and the half-radius.

There are two ways that such an apparent discrepancy can occur. One is for the velocity profiles to deviate markedly from the typical shape. The other is for the integral momentum for the calculation to deviate strongly from that for the experiment. Investigation shows that the latter is the case. For Run 17B, the kinetic energy calculation was started at $x/D = 4.7$ using measured velocity, concentration, total enthalpy, and shear stress profiles. At this point the value of the momentum parameter

¹⁰Turbulent Prandtl number was 0.85 and turbulent Lewis number was 1.0.

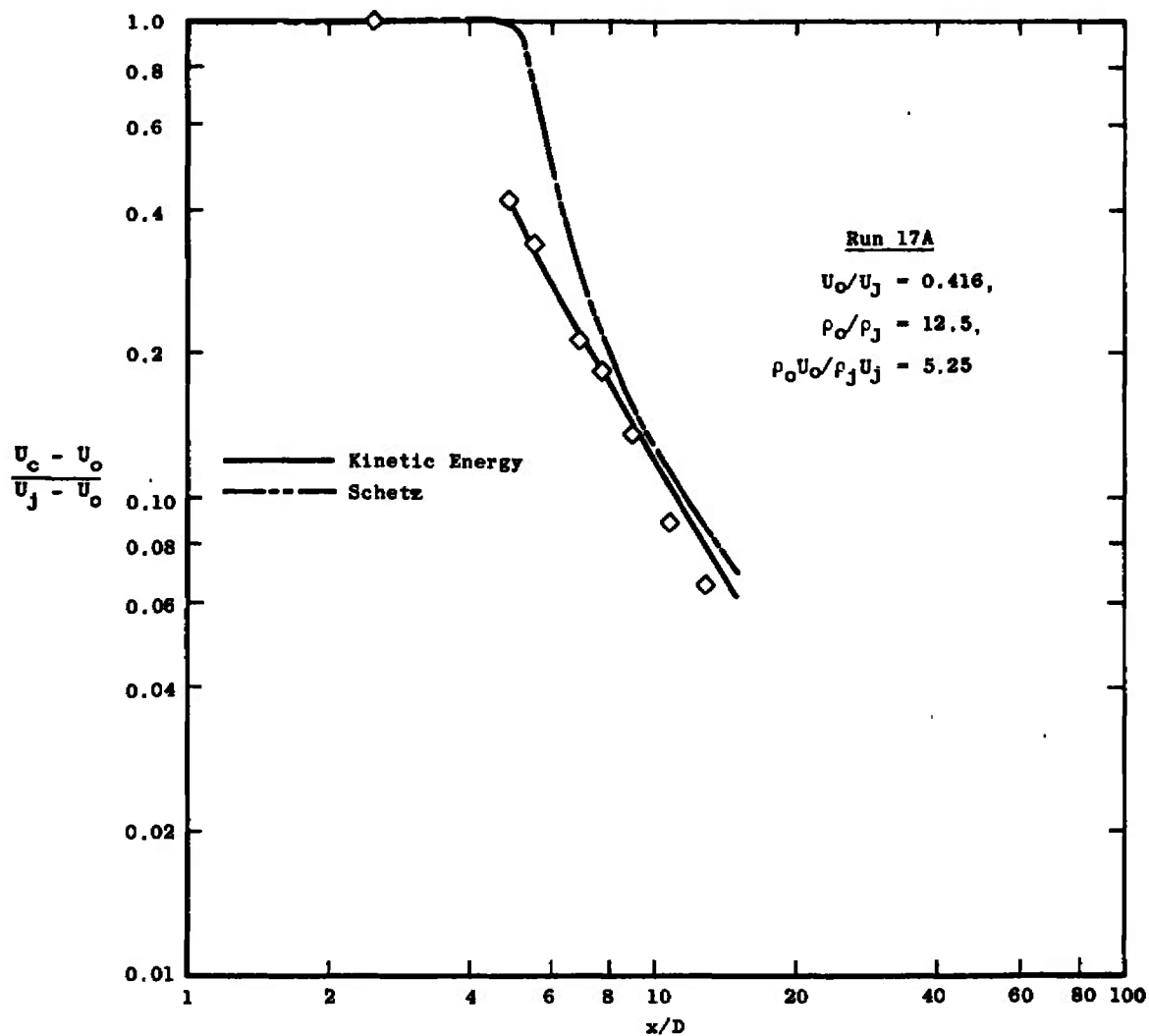


Figure 10.11. Comparison of predicted centerline velocity decay according to Schetz model and kinetic energy theory with hydrogen-air mixing data. Data from Chriss [90].

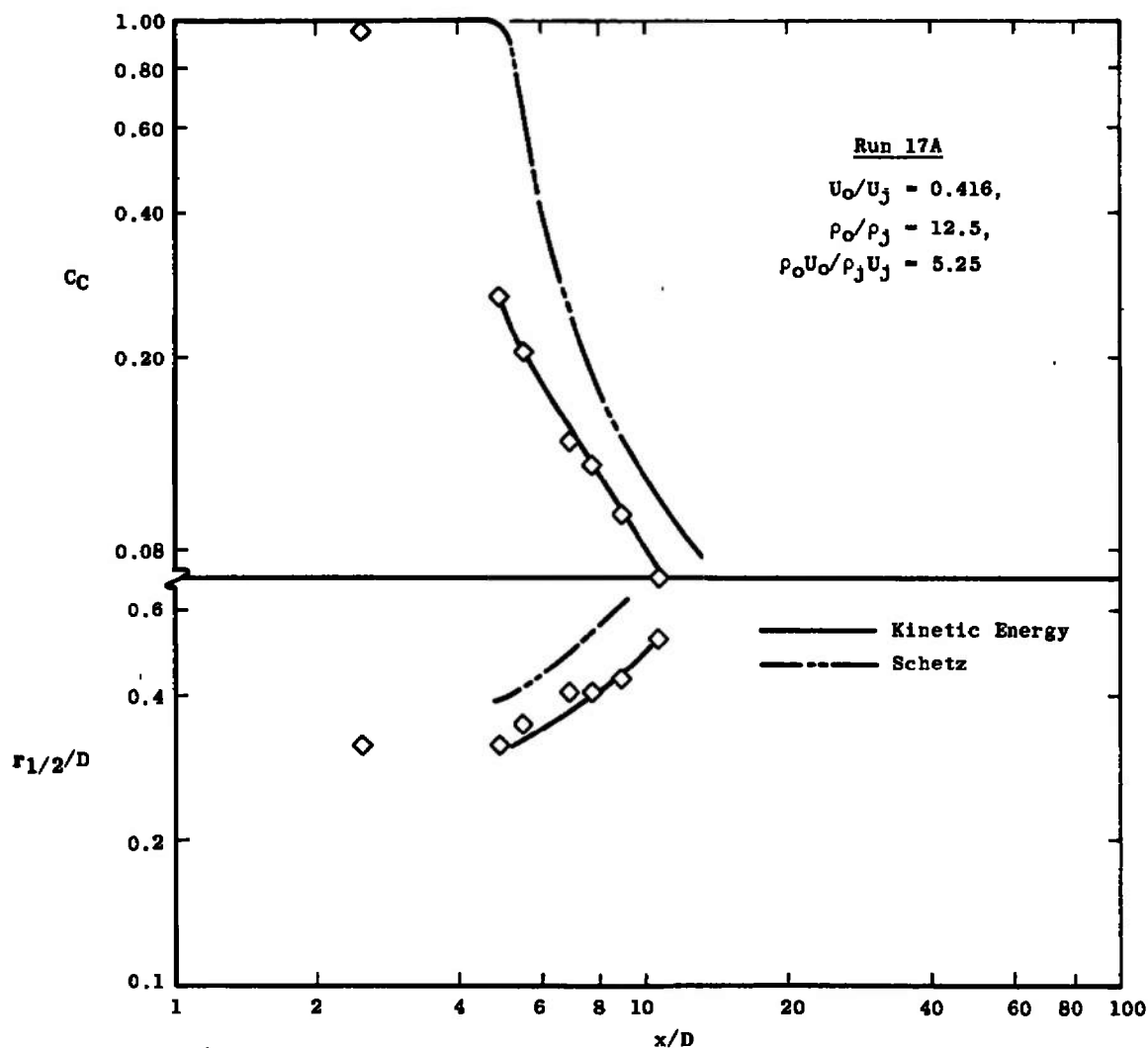


Figure 10.12. Comparison of centerline composition decay and half-radius growth predictions of Schetz model and kinetic energy theory with hydrogen-air data. Data from Chriss [90], $U_o/U_j \approx 0.416$.

$$\int_0^{\infty} \rho U r (U - U_0) dr \quad (10.1)$$

was 9.15 in arbitrary units. On the other hand, the calculations using the Schetz model were started at $x/D = 0$ using a $1/7$ power law velocity profile, a $2/7$ power law enthalpy profile, and a linear concentration profile. The initial boundary layer thickness was taken from Chriss [90]; it was not reported specifically for this case but it was assumed to be approximately the same for all cases. This assumption was naive, for the value of the momentum parameter obtained in this manner was 8.50 in the same arbitrary units, which is greater than that for the data. Given the typical profiles, if a flow calculation overpredicts the centerline velocity and uses a too great value of the momentum parameters, it can also overpredict the half-radius. It is clear that this is the case for the data in question. Clearly a more sophisticated approach would have been to take the boundary layer thickness such as to provide at $x/D = 0$ a value of Equation (10.1) equivalent to that obtained from the downstream data. As the comparisons made and the conclusions reached in this study are based primarily on the trend of the prediction and not the actual values predicted, this problem is not extremely serious. It does point out a major need in future experimental work, which is an accurate measurement and careful reporting of

the flow initial conditions. Such data could prevent serious deviation of the type described from occurring.

Recommendations for Future Experimental Work

For the single gas jet into still surroundings, the asymptotic far-field behavior appears to be very well known, and no additional work would appear to be necessary. However, for the very near-field (the "first transition regime" in Chapter 2), there are no measurements. This is the region at the edge of the nozzle in which the flow undergoes transition from a boundary-layer character to a free-shear layer. Investigation of this region would require the development of quite small instrumentation (or large test apparatus which might be beyond the capabilities of most research organizations), but should be rewarding in developing descriptions for the transition of a flow from a boundary layer flow to a free-shear layer. Of secondary importance is an investigation in which careful measurements in the first regime are extended downstream far enough into the second regime to establish the appropriate axial decay curve. This would obviate the need for using composite data as was done in this study.

The situation with regard to coaxial air-air jets is similar. However, in this case the first mixing regime itself needs to be more extensively investigated in greater detail than has been common in the past. The necessity for ducting the outer stream is understood if far downstream

measurements are to be made, but such a duct must be large enough so as not to interfere with the free-turbulent character of the flow. To this end the axial pressure gradient ought to be monitored and reported. The influence of the duct becomes more important as the outer stream to inner stream velocity ratio U_o/U_j approaches unity because the wall shear becomes larger in relation to the free-turbulent shear; indeed this is the primary reason that few reliable measurements exist for $U_o/U_j \geq 0.5$. This situation should be rectified with appropriate care to insure a zero axial pressure gradient and with careful reporting of the initial conditions of the flow. The importance of the latter cannot be overemphasized.

The lack of reliable and complete reports of the initial conditions of the flow is especially noticeable in the case of mixing of dissimilar gases. For the case of hydrogen-air mixing the lack of adequately reported data is especially noteworthy. Detailed structural measurements in such flows must await the development of radically improved instrumentation, but in the meantime much valuable information can be obtained through mean-flow measurements. In particular, flows with outer-to-jet mass flux ratios $\rho_o U_o / \rho_j U_j$ less than unity should be investigated. Again if a duct must be used to insure an adequate second regime, it must be so designed that it does not influence the development of the flow.

Turbulent wakes, both axisymmetric and two-dimensional, have been investigated in some detail. However, as for the jet into still surroundings, there are no experiments in which near-field and far-field measurements are made in the same flow. Also as for the jet-into-still-air, the transition from a boundary layer to a free-shear layer needs to be extensively investigated.

The author was somewhat surprised to find that there was no data available on a flow configuration in which the outer stream is subsonic and the inner supersonic. This would seem to be a problem of both academic and practical interest. Again the same comments as made above with regard to the initial conditions and the use of an outer duct should apply. On the other hand, the author does not feel that at the present time any basic information on turbulent mixing processes can be obtained from very high speed flows. Such flows may be useful for testing the predictions of a mixing model in extreme situations, but such a model will have to be developed from more basic flows.

The tremendous importance of the measurement of the initial conditions of the flow cannot be overemphasized. This is obviously true when history-dependent models such as the turbulent kinetic energy approach are being used, but accurate knowledge of the initial condition of the flow is important for the testing of any turbulent shear stress model, even if it is locally-dependent. The only fair way

to test a model is to remove all other uncertainties from the calculation.

Recommendations for Turbulent Shear Stress Models--

Present Use

If initial profiles of the turbulent shear stress are known or they can be reliably calculated, none of the locally-dependent methods considered in this study is nearly as powerful as the turbulent kinetic energy method. The capabilities of this method warrant its use wherever possible. However, there are many flow phenomena for which turbulent shear stress profiles or even levels are unknown. For these flows locally dependent models must be used, although the user must recognize that in some cases significant errors can result. Table 10.1 lists the locally-dependent eddy viscosity models (recall that the turbulent shear stress, τ , is given by $\tau = \rho \epsilon \partial U / \partial y$) that are recommended from the results of this study. The numbers in the column labeled "Observed Error" should not be taken as the maximum error to be expected. Rather, they represent typical maximum errors in centerline velocity predictions encountered in the course of this study; they should represent the approximate order of magnitude of the errors to be expected. The most widely applicable model is the Prandtl eddy viscosity model [114] using the constant reported by Ferri [83]; the Ferri model, however, does not work for the dissimilar gas case for which it was designed.

TABLE 10.1

RECOMMENDATIONS FOR THE USE OF LOCALLY-DEPENDENT
TURBULENT SHEAR STRESS MODELS

Type of Flow	Recommended Model	Form of Expression	Constant	Recommended Range	Typical Observed Error this Study ^a
Jet-into-still surroundings	Ferri	$\epsilon = K_F r_{1/2} (U_{\max} - U_{\min})$	0.025	all	15% low transition region)
Coaxial air-air	Prandtl	$\epsilon = K_P b (U_{\max} - U_{\min})$ $b = 2r_{1/2}$	0.007 ^b 0.011 ^c	$0 \leq x/D \leq 20$	26% high (x/D=18)
	Ferri	$\epsilon = K_F r_{1/2} (U_{\max} - U_{\min})$	0.025	$x/D > 20$	40% high (x/D=56)
Coaxial H ₂ -air	Schetz	$\rho \epsilon = K_S (\rho_O U_O \delta_r^2) / r_O$	0.018	all	40% low (x/D=10.4)
Axisymmetric wake	Ferri	$\epsilon = K_F r_{1/2} (U_{\max} - U_{\min})$	0.025	all	small
2D wake	Zakkay	$\epsilon = K_Z r_{1/2} U_{CL}$	0.011	all	small
Compressible jet	Prandtl	$\epsilon = K_P b (U_{\max} - U_{\min})$ $b = 2r_{1/2}$	0.007 ^b 0.011 ^c	$20 \leq x/D \leq 60$	35% low (x/D=15) 30% high (x/D=60)

^aError in prediction of centerline velocity.^bFirst regime.^cSecond regime.

Note also that the Prandtl model is listed in Table 10.1 for the compressible jet-into-still-air, although the error involved in its use is very nearly prohibitive.

Recommendations for Turbulent Shear Stress Models--

Further Development

In the author's opinion, arrived at as a result of this study, further attempts to modify the basic Prandtl eddy viscosity model or the mixing length theory to make them apply to more complex flows is a fruitless avenue of attack. The results of this study have shown that none of the modifications of the Prandtl eddy viscosity model, including the Donaldson and Gray compressibility correction [67] are capable of greatly altering the basic shape of the axial centerline velocity decay curve, and the shape predicted by the Prandtl model and all of its derivatives is incorrect for complex (two-gas) flows. The Libby transform [125], which includes a form of the Prandtl eddy viscosity model, has also been found not to represent any improvement over the basic Prandtl model in its prediction of the centerline velocity decay. The restriction of this approach to unity turbulent Prandtl Lewis numbers makes it less attractive still.

On the other hand, the displacement-thickness model proposed by Schetz [121] is the only locally dependent model to show the proper behavioral trends for hydrogen-air mixing. Because of this, its use should be investigated in

other dissimilar-gas flows. Further work should be done in applying this model or a modification of it to coaxial single-gas flows as well to establish an approach for use in the first regime of mixing. Further investigation of this model and its implications is recommended.

Given some knowledge of the turbulent shear stress, the turbulent kinetic energy method is capable of providing better and more uniform predictions of a wider range of flows than any other model. Because of this, it clearly holds the greatest promise for future development. The most important area for future work is in establishing methods for the generation of the proper initial conditions. The comparison with the data of Forstall, Figure 10.4, page 505, shows how good the predictions of this method can be, given appropriate initial conditions. One suggested approach to this problem is to develop a technique whereby a boundary layer calculation is allowed to proceed from the edge of a nozzle to a fully-developed free shear layer. Another area for further work involves the establishment of better models for the terms of the turbulent kinetic energy equation, or in obtaining better values for the constants in the models now in use. The models and constants used in this study have been developed rather crudely--they seem to work well, but that does not mean that there is no room for improvement.

It is somewhat disturbing that after all of the effort expended on research on free turbulent mixing, there is still no reliable way to make engineering calculations of any but the most basic free turbulent flows. In part this situation is a result of the diffuse nature of free turbulence research, with many workers in many laboratories investigating different facets of the problem. Their work is often not widely reported, with the result that new workers in the field all too often have to repeat all of the previous mistakes in order to become aware of the deficiencies of the various models for the free turbulent shear stress. The lack of a reliable way to make engineering calculations is also in part caused by attempts to analyze complicated flow systems while simple ones are not understood, although this is often due more to necessity than desire. Such analyses bury the turbulent shear stress models so deeply under assumptions for the other variables in the problem that when they fail, as they all too often do, their failure sheds no light on the turbulent shear stress model involved.

The purpose of this study was to establish the state of the art in free turbulent mixing. This involved a critical analysis of the available free turbulent mixing experiments and of the available models for the free turbulent shear stress. One result of this study is the establishment of limits within which various shear stress

models may be used, although often with considerable error. But a potentially far more important result is the demonstration of the accuracy of the history-dependent methods. As the work described in this report has shown, the methods of analysis which take into account the structure of the turbulent flow seem to offer the hope of breaking away from the previous situation. Such methods offer the possibility of being able to predict reliably a broad range of free mixing flows. It is doubtful whether methods which fail to take into account the fact that the flow is turbulent, and not laminar with some badly behaving viscosity, can ever be made to agree with more than a small range of experiments. It is clearly time that the methods of analysis of turbulent flow recognize that it is indeed turbulent.

BIBLIOGRAPHY

BIBLIOGRAPHY

1. Hannum, W. H., and Griffith, W. "On the Intermittency of a Two-Dimensional Jet," Journal of the Aeronautical Sciences, Vol. 22, March 1955, pp. 202-203.
2. Van der Hegge Zijnen, B. G. "Measurements of the Velocity Distribution in a Plane Turbulent Jet of Air," Applied Scientific Research, Section A, Vol. 7, No. 4, 1958, pp. 250-276.
3. Newman, B. G. "Turbulent Jets and Wakes," Fluid Mechanics of Internal Flow, Elsevier, Amsterdam-London-New York, 1967, pp. 170-209.
4. Foss, J. F., and Jones, J. B. "Secondary Flow Effects in a Bounded Rectangular Jet," Journal of Basic Engineering, Transactions ASME, Series D, Vol. 90, No. 2, June 1968, pp. 241-248.
5. Townsend, A. A. The Structure of Turbulent Shear Flow, Cambridge University Press, Cambridge, 1956.
6. Miller, D. R., and Comings, E. W. "Static Pressure Distribution in the Free Turbulent Jet," Journal of Fluid Mechanics, Vol. 3, 1957, pp. 1-16.
7. Heskestad, G. "Hot-Wire Measurements in a Plane Turbulent Jet," Journal of Applied Mechanics, Vol. 32, December 1965, pp. 721-724, Erratum, Journal of Applied Mechanics, Vol. 33, September 1966, p. 710.
8. Albertson, M. L., Dai, Y. B., Jensen, R. A., and Rouse, H. "Diffusion of Submerged Jets," Transactions ASCE, Vol. 115, 1950, pp. 643-664.
9. Flora, J. J., Jr., and Goldschmidt, V. W. "Virtual Origins of a Free Plane Turbulent Jet," AIAA Journal, Vol. 7, No. 12, December 1969, pp. 2344-2346.
10. Prosser, D. W., and Fisher, M. J. "Turbulence as a Producer of Noise in Proportional Fluid Amplifiers," Journal of Applied Mechanics, Vol. 33, December 1966, pp. 728-734.

11. Van der Hegge Zijnen, B. G. "Measurements of Turbulence in a Plane Jet of Air by the Diffusion Method and by the Hot-Wire Method," Applied Scientific Research, Section A, Vol. 7, No. 4, 1968, pp. 293-313.
12. Harsha, P. T., and Lee, S. C. "Correlation between Turbulent Shear Stress and Turbulent Kinetic Energy," AIAA Journal, Vol. 8, No. 8, August 1970, pp. 1508-1510.
13. Csanady, G. T. "On the Energy Balance of a Turbulent Mixing Layer," Journal of Fluid Mechanics, Vol. 15, 1963, pp. 545-559.
14. Mueller, T. J. "On Separation, Reattachment, and Redevelopment of Turbulent Boundary Layers," Ph.D. Thesis, University of Illinois, Urbana, Illinois, May 1961.
15. Haugen, R. L., and Dhanak, A. M. "Momentum Transfer in Turbulent Separated Flow Past a Rectangular Cavity," Journal of Applied Mechanics, Vol. 33, September 1966, pp. 641-646.
16. Chapman, A. J. "Mixing Characteristics of a Free Jet Boundary with Consideration of Initial Boundary Layer Configuration," Ph.D. Thesis, University of Illinois, Urbana, Illinois, July 1953.
17. Liepmann, H. W., and Laufer, J. "Investigation of Free Turbulent Mixing," Technical Note 1257, August 1949, NACA.
18. Bradshaw, P., Ferriss, D. H., and Johnson, R. F. "Turbulence in the Noise-Producing Region of a Circular Jet," Journal of Fluid Mechanics, Vol. 19, 1964, pp. 591-624.
19. Chow, W. L. "Discussion of Liepmann and Laufer's Work on Shear Stress Distribution in Turbulent Free-Jet Mixing Region," unpublished report.
20. Wygnanski, I., and Fiedler, H. "Some Measurements in the Self-Preserving Jet," Journal of Fluid Mechanics, Vol. 38, Part 3, 1969, pp. 577-612.
21. Baines, W. D. "Diffusion of Submerged Jets - Discussion," Proceedings ASCE, Vol. 75, No. 7, September 1949, pp. 1019-29.

22. Binnie, A. M. "The Turbulent Spreading of a Water Jet," Engineering, Vol. 153, June 1942, pp. 503-504.
23. Corrsin, S. "Investigation of Flow in an Axially Symmetrical Heated Jet of Air," Wartime Report W-94, originally issued as ACR 3L 23, December 1943, NACA.
24. Hinze, J. O., and Van der Hegge Zijnen, B. G. "Transfer of Heat and Matter in the Turbulent Mixing Zone of an Axially Symmetrical Jet," Applied Scientific Research, Vol. A1, 1949, pp. 435-461.
25. Corrsin, S., and Uberoi, M. S. "Further Experiments on the Flow and Heat Transfer in a Heated Turbulent Air Jet," Report 998, 1950, NACA.
26. Taylor, J. F., Grimmer, H. L., and Comings, E. W. "Isothermal Free Jets of Air Mixing with Air," Chemical Engineering Progress, Vol. 47, No. 4, 1951, pp. 175-180.
27. Alexander, L. G., Baron, T., and Comings, E. W. "Transport of Momentum, Mass, and Heat in Turbulent Jets," Bulletin 413, May 1953, University of Illinois Engineering Experiment Station.
28. Davies, P. O. A. L., Fisher, M. J., and Barratt, M. J. "The Characteristics of the Turbulence in the Mixing Region of a Round Jet," Journal of Fluid Mechanics, Vol. 15, 1963, pp. 337-369.
29. Sami, S. "Velocity and Pressure Fields of a Diffusing Jet," Ph.D. Thesis, 1966, University of Iowa, Iowa City, Iowa. Also Sami, S., Carmody, T., and Rouse, H. "Jet Diffusion in the Region of Flow Establishment," Journal of Fluid Mechanics, Vol. 27, Part 2, 1967, pp. 231-252, and Sami, S. "Balance of Turbulence Energy in the Region of Jet Flow Establishment," Journal of Fluid Mechanics, Vol. 29, Part 1, 1967, pp. 81-92.
30. Hinze, J. O. Turbulence, McGraw-Hill, New York, 1959.
31. Davies, P. O. A. L. "Turbulence Structure in Free Shear Layers," AIAA Journal, Vol. 4, No. 11, November 1966, pp. 1971-1978.

32. Jezdinsky, V. "Measurement of Turbulence by Pressure Probes," AIAA Journal, Vol. 4, No. 11, November 1966, pp. 2072-2073.
33. Carmody, T. "Establishment of the Wake Behind a Disk," Ph.D. Dissertation, University of Iowa, Iowa City, 1963.
34. Bradbury, L. J. S. "The Structure of a Self-Preserving Plane Turbulent Jet," Journal of Fluid Mechanics, Vol. 23, Part 1, 1965, pp. 31-64.
35. Zawacki, T. S., and Weinstein, H. "Experimental Investigation of Turbulence in the Mixing Region between Coaxial Streams," CR-959, February 1968, NASA.
36. Wagnanski, I., and Fiedler, H. E. "The Two-Dimensional Mixing Region," Journal of Fluid Mechanics, Vol. 41, Part 2, 1970, pp. 327-361.
37. Weinstein, A. S., Osterle, J. F., and Forstall, W. "Momentum Diffusion from a Slot Issuing into a Moving Secondary," Journal of Applied Mechanics, Vol. 23, pp. 437-443.
38. Bradbury, L. J. S., and Riley, J. "The Spread of a Turbulent Plane Jet Issuing into a Parallel Moving Airstream," Journal of Fluid Mechanics, Vol. 27, Part 2, 1967, pp. 381-394.
39. Bradbury, L. J. S. "Simple Expressions for the Spread of Turbulent Jets," The Aeronautical Quarterly, May 1967, pp. 133-142.
40. Forstall, W., Jr. "Material and Momentum Transfer in Coaxial Gas Streams," Ph.D. Thesis, Massachusetts Institute of Technology, Cambridge, Massachusetts, 1949.
41. Forstall, W., Jr., and Shapiro, A. H. "Momentum and Mass Transfer in Coaxial Gas Jets," Journal of Applied Mechanics, Vol. 17, December 1950, pp. 399-408. Discussion: Journal of Applied Mechanics, Vol. 18, June 1951, pp. 219-220.
42. Paulk, R. A. "Experimental Investigation of Free Turbulent Mixing of Nearly Constant Density Coaxial Streams," M.S. Thesis, The University of Tennessee, Knoxville, March 1969.

43. Landis, F., and Shapiro, A. H. "The Turbulent Mixing of Coaxial Jets," Proceedings of the Heat Transfer and Fluid Mechanics Institute, 1951, pp. 133-146.
44. Curtet, R., and Ricou, F. P. "On the Tendency of Self-Preservation in Axisymmetric Ducted Jets," Journal of Basic Engineering, Transaction ASME, Series D, Vol. 86, 1964, pp. 765-776.
45. Fejer, A. A., Torda, T. P., Boehmann, L. I., Ghia, K. N., and Hermann, W. G. "Research on Mixing of Coaxial Streams," Report ARL 67-0058, Aerospace Research Laboratories, March 1967.
46. Maczynski, J. F. J. "A Round Jet in an Ambient Coaxial Stream," Journal of Fluid Mechanics, Vol. 13, 1962, pp. 597-608.
47. Rozenmann, T. "Experimental Investigation of Recirculation Patterns in the Initial Region of Coaxial Jets," Ph.D. Thesis, Illinois Institute of Technology, Chicago, Illinois, January 1969.
48. Squire, H. B., and Trouncer, J. "Round Jets in a General Stream," R & M 1975, January 1944, Aeronautical Research Council (G.B.).
49. Kobashi, Y. "Experimental Studies in Compound Jets," Proceedings Second Japan National Congress for Applied Mechanics, 1952, pp. 223-226.
50. Townsend, A. A. "The Fully Developed Turbulent Wake of a Circular Cylinder," Australian Journal of Scientific Research, Series A, Vol. 2, December 1949, pp. 451-468.
51. Lee, S. C. "A Study of the Two-Dimensional Free Turbulent Mixing between Converging Streams with Initial Boundary Layers," Ph.D. Thesis, University of Washington, Seattle, 1966.
52. Chevray, R., and Kovasznay, L. S. G. "Turbulence Measurements in the Wake of a Thin Flat Plate," AIAA Journal, Vol. 7, No. 8, August 1969, pp. 1641-1643.
53. Grant, H. L. "The Large Eddies of Turbulent Motion," Journal of Fluid Mechanics, Vol. 4, 1958, pp. 149-190.

54. Batchelor, G. K. "Note on Free Turbulent Flows with Special Reference to the Two-Dimensional Wake," Journal of the Aeronautical Sciences, Vol. 17, No. 7, July 1950, pp. 441-445.
55. Bradshaw, P., Ferriss, D. H., and Atwell, N. P. "Calculation of Boundary Layer Development Using the Turbulent Energy Equation," Journal of Fluid Mechanics, Vol. 28, Part 3, 1967, pp. 593-616.
56. Cooper, R. D., and Lutzky, M. "Exploratory Investigation of the Turbulent Wakes Behind Bluff Bodies," Report 963, October 1955, David Taylor Model Basin.
57. Carmody, T. "Establishment of the Wake Behind a Disk," Journal of Basic Engineering, Transactions ASME, Vol. 86, Series D, December 1964, pp. 869-882.
58. Chevray, R. "The Turbulent Wake of a Body of Revolution," Journal of Basic Engineering, Transactions ASME, Vol. 90, Series D, No. 2, June 1968, pp. 275-284.
59. Gibson, C. H., Chen, C. C., and Lin, S. C. "Measurements of Turbulent Velocity and Temperature Fluctuations in the Wake of a Sphere," AIAA Journal, Vol. 6, No. 4, April 1968, pp. 642-649.
60. Hwang, N. H. C., and Baldwin, L. V. "Decay of Turbulence in Axisymmetric Wakes," Journal of Basic Engineering, Transactions ASME, Vol. 88, Series D, pp. 261-268.
61. Naudascher, E. "Flow in the Wake of Self-Propelled Bodies and Related Sources of Turbulence," Journal of Fluid Mechanics, Vol. 22, Part 4, 1965, pp. 625-656.
62. Watt, W. E. "The Velocity-Temperature Mixing Layer," Ph.D. Dissertation, Department of Mechanical Engineering, University of Toronto, Toronto, Canada, 1967.
63. Gooderum, P. B., Wood, G. P., and Brevoort, M. J. "Investigation with an Interferometer of the Turbulent Mixing of a Free Supersonic Jet," Report 963, January 1949, NACA.

64. Bershader, D., and Pai, S. I. "On Turbulent Jet Mixing in Two-Dimensional Supersonic Flow," Journal of Applied Physics, Vol. 21, 1950, p. 616.
65. Broer, L. J. F., and Rietdijk, J. A. "Measurements in Supersonic Free Jets," Applied Scientific Research, Section A, Vol. 9, 1960, pp. 465-477.
66. Anderson, A. R., and Johns, F. R. "Characteristics of Free Supersonic Jets Exhausting into Quiescent Air," Jet Propulsion, Vol. 25, No. 1, January 1955, pp. 13-15.
67. Donaldson, C. duP., and Gray, K. E. "Investigation of Free Mixing of Dissimilar Gases," AIAA Journal, Vol. 4, No. 11, November 1966, pp. 2017-2025.
68. Johannesen, N. H. "The Mixing of Free Axially-Symmetrical Jets of Mach Number 1.40," R & M No. 3291, 1962, Aeronautical Research Council.
69. Johannesen, N. H. "Further Results on the Mixing of Free Axially-Symmetrical Jets of Mach Number 1.40," R & M No. 3292, 1962, Aeronautical Research Council.
70. Warren, W. R. "An Analytical and Experimental Study of Compressible Free Jets," Report 381, 1957, Aeronautical Engineering Laboratory, Princeton University.
71. Pitkin, E. T., and Glassman, I. "Experimental Mixing Profiles of a Mach 2.6 Free Jet," Journal of the Aeronautical Sciences, Vol. 25, 1958, pp. 791-793.
72. Eggers, J. M. "Velocity Profiles and Eddy Viscosity Distributions Downstream of a Mach 2.22 Nozzle Exhausting to Quiescent Air," TN D-3601, September 1966, NASA.
73. Warren, W. R. "The Static Pressure Variation in Compressible Free Jets," Journal of the Aeronautical Sciences, Vol. 22, March 1955, pp. 205-207.
74. Laurence, J. C. "Scale and Spectra of Turbulence in the Mixing Region of a Free Subsonic Jet," Report 1292, 1956, NACA.

75. Cleeves, V., and Boelter, L. M. K. "Isothermal and Non-Isothermal Air Jet Investigations," Chemical Engineering Progress, Vol. 43, No. 3, 1947, pp. 123-134.
76. Keagy, W. R., and Weller, A. E. "A Study of Freely Expanding Inhomogeneous Jets," Proceedings 1949 Heat Transfer and Fluid Mechanics Institute, May 1949, pp. 89-96.
77. O'Connor, T. J., Comfort, E. H., and Cass, L. A. "Turbulent Mixing of an Axisymmetric Jet of Partially Dissociated Nitrogen with Ambient Air," AIAA Journal, Vol. 4, No. 11, November 1966, pp. 2026-2032.
78. Frauenberger, J. H., and Forbister, J. G. "The Axial Decay and Radial Spread of a Supersonic Jet Exhausting into Air at Rest," The Aeronautical Quarterly, May 1961, pp. 131-149.
79. Maydew, R. C., and Reed, J. F. "Turbulent Mixing of Compressible Free Jets," AIAA Journal, Vol. 1, No. 6, June 1963, pp. 1443-1444.
80. Hill, J. A. F., and Nicholson, J. E. "Compressible Effects on Fluid Entrainment by Turbulent Mixing Layers," CR-131, November 1964, NASA.
81. Hill, W. G., Jr. "Initial Development of Compressible Turbulent Free Shear Layers," Ph.D. Thesis, May 1966, Rutgers, The State University, New Brunswick, New Jersey.
82. Rom, J. "Study of Similarity of High Temperature Turbulent Jets," AIAA Journal, Vol. 6, No. 7, July 1968, pp. 1368-1370.
83. Ferri, A., Libby, P. A., and Zakkay, V. "Theoretical and Experimental Investigation of Supersonic Combustion," Report ARL 62-467, September 1962, Aeronautical Research Laboratories; also PIBAL-713, Polytechnic Institute of Brooklyn.
84. Alpinieri, L. J. "An Experimental Investigation of the Turbulent Mixing of Non-Homogeneous Coaxial Jets," Report 789, August 1963, Polytechnic Institute of Brooklyn; also "Turbulent Mixing of Coaxial Jets," AIAA Journal, Vol. 2, No. 9, September 1964, pp. 1560-1567.

85. Zakkay, V., and Krause, E. "Mixing Problems with Chemical Reactions," in Olfe, D. B. and Zakkay, V., eds., Supersonic Flow, Chemical Processes and Radiative Transfer, 1964, Pergamon Press, Oxford, pp. 3-30.
86. Zakkay, V., Krause, E., and Woo, S. D. L. "Turbulent Transport Properties for Axisymmetric Heterogeneous Mixing," AIAA Journal, Vol. 2, No. 11, November 1964, pp. 1939-1947.
87. Bluston, H. S. "An Experimental Study of the Turbulent Mixing of a Subsonic and a Supersonic Jet in a Closed Duct," Report 868, May 1965, Polytechnic Institute of Brooklyn.
88. Forde, J. M. "The Mixing of Turbulent Supersonic Fuel-Air Streams," The Aeronautical Quarterly, Vol. 13, Part 4, November 1965, pp. 377-387.
89. Ragsdale, R. G., and Edwards, O. J. "Turbulent Coaxial Mixing of Dissimilar Gases at Nearly Equal Stream Velocities," TM X-52082, 1965, NASA.
90. Chriss, D. E. "Experimental Study of the Turbulent Mixing of Subsonic Axisymmetric Gas Streams," TR-68-133, August 1968, AEDC.
91. Eggers, J. M., and Torrence, M. G. "An Experimental Investigation of the Mixing of Compressible-Air Jets in a Coaxial Configuration," TN-D-5315, July 1969, NASA.
92. Fejer, A. A., Hermann, W. G., and Torda, T. P. "Factors that Enhance Jet Mixing," Report ARL 69-0175, October 1969, Aerospace Research Laboratories.
93. Zakkay, V., Krause, E., and Woo, S. D. L. "Turbulent Transport Properties for Axisymmetric Heterogeneous Mixing," Report ARL 64-103, June 1963, Aerospace Research Laboratories.
94. Peters, C. E., Chriss, D. E., and Paulk, R. A. "Turbulent Transport Properties in Subsonic Coaxial Free Mixing Systems," AIAA Paper No. 69-681, June 1969.

95. Zakkay, V., and Krause, E. "The Radial Variation of the Eddy Viscosity in Compressible Turbulent Jet Flows," International Journal of Heat and Mass Transfer, Vol. 8, 1965, pp. 1047-1050.
96. Zakkay, V., and Fox, H. "Experimental and Analytical Consideration of Turbulent Heterogeneous Mixing in the Wake," Report NYU-AA-66-54, April 1966, New York University; paper prepared for presentation at 7th AGARD Colloquium on Recent Advances in Aerothermochemistry, Oslo, Norway, 16-20 May 1966; also, "An Experimental and Theoretical Investigation of the Turbulent Far Wake," AIAA Journal, Vol. 5, No. 3, March 1967, pp. 568-574.
97. Demetriades, A. "Turbulent Fluctuation Measurement in Compressible Axisymmetric Wakes," AIAA Journal, Vol. 5, No. 5, May 1967, pp. 1028-1029.
98. Fox, H., Zakkay, V., and Sinha, R. "A Review of Some Problems in Turbulent Mixing," Report NYU-AA-66-63, September 1966, New York University; also, "A Review of Problems in the Nonreacting Turbulent Far Wake," Astronautica Acta, Vol. 14, 1969, pp. 215-228.
99. Demetriades, A. "Mean-Flow Measurements in an Axisymmetric Compressible Turbulent Wake," AIAA Journal, Vol. 6, No. 3, March 1968, pp. 432-439.
100. Sinha, R., and Zakkay, V. "Experimental and Theoretical Investigation of the Near Wake in an Axisymmetric Supersonic Flow with and without Base Injection," Report NYU-AA-68-26, May 1968, New York University; also Zakkay, V. and Sinha, R., same title, Israel Journal of Technology, Vol. 7, No. 1-2, 1969, pp. 43-53.
101. Schlichting, H. "Boundary Layer Theory," 4th edition, McGraw-Hill Book Company, Inc., New York, 1960.
102. Taylor, G. I. "The Transport of Vorticity and Heat Through Fluids in Turbulent Motion," Proceedings of the Royal Society of London, Series A, Vol. 135, 1932, pp. 685-702.
103. Reichardt, H. "On a New Theory of Free Turbulence," Journal of the Royal Aeronautical Society, Vol. 47, 1942, pp. 167-176; translated from Zeitschrift fur angewandte Mathematik und Mechanik, Vol. 21, No. 5, October 1941.

104. Swain, L. M. "On the Turbulent Wake Behind a Body of Revolution," Proceedings of the Royal Society of London, Series A, Vol. 125, 1929, pp. 647-659.
105. Acharya, Y. V. G. "Momentum Transfer Theory Applied to a Turbulent Jet Spreading in Still Air," Applied Scientific Research, Section A, Vol, 5, 1955, pp. 265-267.
106. Kuethe, A. M. "Investigation of the Turbulent Mixing Regions Formed by Jets," Journal of Applied Mechanics, Vol. 2, No. 3, 1935, pp. 87-95.
107. Taylor, G. I. "Distribution of Velocity and Temperature between Concentric Rotating Cylinders," Proceedings of the Royal Society of London, Series A, Vol. 151, 1935, pp. 494-512.
108. Tomotika, S. "Application of the Modified Vorticity Transport Theory to the Turbulent Spreading of a Jet of Air," Proceedings of the Royal Society of London, Series A, Vol. 165, March 1938, pp. 65-72.
109. Howarth, L. "Concerning the Velocity and Temperature Distributions in Plane and Axially Symmetrical Jets," Proceedings of the Cambridge Philosophical Society, Vol. 34, 1938, pp. 185-203.
110. Grodzovskiy, G. L. "Escape of a Free Turbulent Stream into a Moving Medium," Promyshlennaya Aerodinamika, No. 23, 1962, pp. 107-165; translated as FTD TT-65-1971.
111. Squire, H. B. "Reconsideration of the Theory of Free Turbulence," Philosophical Magazine, Series 7, Vol. 39, No. 288, January 1948, pp. 1-20.
112. Vulis, L. A., Leont'eva, T. P., Sakipov, Z. B., Palatnik, I. B., and Ustimenko, B. P. "Transfer Processes in a Free (Jet) Turbulent Boundary Layer," International Journal of Heat and Mass Transfer, Vol. 4, 1961, pp. 111-118.
113. Sforza, P. M., Trentacoste, N., and Mons, R. "Turbulent Mixing: A Review, Evaluation, and Extension," Paper 69-31, January 1969, AIAA.
114. Prandtl, L. "Bermerkungen zur Theorie der freien Turbulenz," Zeitschrift fur angewandte Mathematik und Mechanik, Vol. 22, October 1942, pp. 241-243.

115. Szablewski, W. "The Diffusion of a Hot Air Jet in Air in Motion," TM 1288, December 1950, NACA.
116. Weinstein, H., and Todd, C. A. "Analysis of Mixing of Coaxial Streams of Dissimilar Fluids Including Energy Generation Terms," TN D 2123, March 1964, NASA.
117. Szablewski, W. "Turbulenter Vermischung runder Kalt luftstrahlen mit umgebender ruhender Heissluft," International Journal of Heat and Mass Transfer, Vol. 6, 1963, pp. 739-754.
118. Chapman, A. J., and Korst, H. H. "Free Jet Boundary with Consideration of Initial Boundary Layer," Proceedings 2nd U.S. National Congress of Applied Mechanics, Vol. 1, 1954, pp. 723-731.
119. Peters, C. E. "Turbulent Mixing and Burning of Coaxial Streams Inside a Duct of Arbitrary Shape," TR-68-270, January 1969, AEDC.
120. Schetz, J. A. "Turbulent Mixing of a Jet in a Coflowing Stream," AIAA Journal, Vol. 6, No. 10, October 1968, pp. 2008-2010.
121. Schetz, J. A. "Unified Analysis of Turbulent Jet Mixing," CR-1382, July 1969, NASA.
122. Mager, A. "Transformation of the Compressible Turbulent Boundary Layer," Journal of the Aero/Space Sciences, Vol. 25, May 1958, pp. 305-311.
123. Snyder, W. T. "The Use of the Howarth Transformation in Turbulent Compressible Flow," Journal of the Aero/Space Sciences, Vol. 29, 1962, pp. 235-236.
124. Channapragada, R. S., and Woolley, J. P. "Turbulent Mixing of Parallel Compressible Free Jets," Paper 65-606, 1965, AIAA.
125. Libby, P. A. "Theoretical Analysis of Turbulent Mixing of Reactive Gases with Application to Supersonic Combustion of Hydrogen," ARS Journal, Vol. 32, No. 3, March 1962, pp. 388-396.
126. Ting, L., and Libby, P. A. "Remarks on the Eddy Viscosity in Compressible Mixing Flows," Journal of the Aero/Space Sciences, Vol. 27, October 1960, pp. 797-798.

127. Deverall, L. I., and Channapragada, R. S. "Invariancy of the Total Shear Stress for Compressible Turbulent Flows," AIAA Journal, Vol. 3, No. 8, August 1965, p. 1513.
128. Kleinstein, G. "Mixing in Turbulent Axially Symmetric Free Jets," Journal of Spacecraft, Vol. 1, No. 4, July-August 1964, pp. 403-408.
129. Bradshaw, P. "Boundary-Layer Problems of 1966," Aero Report 1203, 1966, National Physical Laboratory (G.B.); ARC 28 191, Aeronautical Research Council.
130. Nee, V. W., and Kovasznay, L. S. G. "Simple Phenomenological Theory of Turbulent Shear Flows," The Physics of Fluids, Vol. 12, No. 3, March 1969, pp. 473-484.
131. Laster, M. L. "Inhomogeneous Two-Stream Turbulent Mixing Using the Turbulent Kinetic Energy Equation," TR-70-134, May 1970, AEDC.
132. Lee, S. C., and Harsha, P. T. "The Use of Turbulent Kinetic Energy in Free Mixing Studies," AIAA Journal, Vol. 8, No. 6, June 1970, pp. 1026-1032.
133. Kline, S. J., Morkovin, M. V., Sovran, G., and Cockrell, D. J., eds., "Proceedings - Computation of Turbulent Boundary Layers - 1968 AFOSR-IFP-Stanford Conference," Thermosciences Division, Department of Mechanical Engineering, Stanford University, California, 1969.
134. Glushko, G. S. "Turbulent Boundary Layers on a Flat Plate in an Incompressible Fluid," Investia Akademia Nauk SSSR - Mekhanika, Vol. 4, July/August 1965, pp. 13-23. Available in English translation from DDC as AD 638 204, May 1966.
135. Patankar, S. V., and Spalding, D. B. "A Finite-Difference Procedure for Solving the Equations of the Two-Dimensional Boundary Layer," International Journal of Heat and Mass Transfer, Vol. 10, 1967, pp. 1389-1411.
136. Dryden, H. L. Advances in Applied Mechanics, Vol. 1, Academic Press, New York, 1948, pp. 1-40.

137. Donaldson, C. duP., and Rosenbaum, H. "Calculation of Turbulent Shear Flows through Closure of the Reynolds Equation by Invariant Modeling," ARAP Rept. 127, December 1968, Aeronautical Research Associates of Princeton, Inc., Princeton, N. J.
138. Korst, H. H., and Tripp, W. "The Pressure on a Blunt Trailing Edge Separating Two Supersonic Two-Dimensional Air Streams of Different Mach Number and Stagnation Pressure but Identical Stagnation Temperature," Proceedings of the Fifth Midwestern Conference on Fluid Mechanics, University of Michigan, Ann Arbor, Michigan, pp. 187-199, April 1957.
139. Patankar, S. V. "Heat and Mass Transfer in Turbulent Boundary Layers," Ph.D. dissertation, 1967, Imperial College of Science and Technology, Dept. of Mechanical Engineering, London, England. Also available as Spalding, D. B. and Patankar, S. V., same title, Chemical Rubber Company Press, Cleveland, 1968.

APPENDIXES

APPENDIX A

EVALUATION OF THE MOMENTUM INTEGRAL

Axisymmetric Flow

Consider a generalized axisymmetric flow, Figure A.1. Along the centerline, $r = 0$, $V = 0$, and $\tau = 0$ by symmetry. For constant pressure the mean-flow momentum equation is

$$\rho U r \frac{\partial U}{\partial x} + \rho V r \frac{\partial U}{\partial r} = \frac{\partial (r\tau)}{\partial r} \quad (A.1)$$

where $\tau = -\rho \overline{uv}$. Here the instantaneous velocity $U = \bar{U} + u$, Equation (A.1) is appropriate for incompressible flow, under the assumption of constant pressure (as well as the usual boundary layer assumptions). For compressible flow, use of Equation (A.1) implies the approximation $\rho' \ll \rho$, as well as assumptions involving turbulence terms such as $\overline{\rho' uv}$ which enter the definition of τ . Laster [131] has shown that these "compressibility" terms are negligible for the types of flow to be considered here.

The equation of continuity

$$\frac{\partial (\rho U r)}{\partial x} + \frac{\partial (\rho V r)}{\partial r} = 0$$

may be integrated to obtain

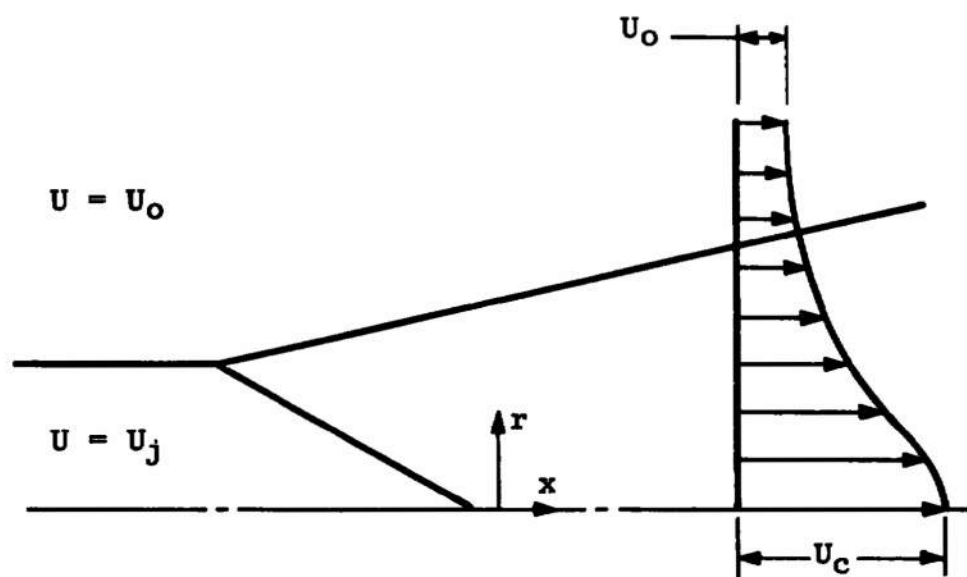


Figure A.1. General axisymmetric flow.

$$\rho V r = - \int_0^r \frac{\partial (\rho U r')}{\partial x} dr' \quad (A.3)$$

Substituting this expression into Equation (A.1) and integrating $r = 0$ to $r = R$ yields

$$\int_0^R \rho U r \frac{\partial U}{\partial x} dr - \int_0^R \int_0^r \frac{\partial (\rho U r')}{\partial x} dr' \frac{\partial U}{\partial r} dr = R \tau_R \quad (A.4)$$

where $\tau_R = \tau$ at $r = R$. If R is taken sufficiently far into the secondary flow so that $U = U_0 = \text{constant}$ (where U_0 may be zero) then

$$\int_0^R \rho U r \frac{\partial U}{\partial x} dr - \int_0^R \int_0^r \frac{\partial (\rho U r')}{\partial x} dr' \frac{\partial U}{\partial r} dr = 0 \quad (A.5)$$

Integrating the second term by parts

$$\begin{aligned} \int_0^R \int_0^r \frac{\partial (\rho U r')}{\partial x} dr' \frac{\partial U}{\partial r} dr &= \left[U \frac{\partial (\rho U r')}{\partial x} dr' \right]_0^R - \\ &- \int_0^R U \frac{\partial (\rho U r)}{\partial x} dr = U_0 \int_0^R \frac{\partial (\rho U r)}{\partial x} dr - \int_0^R U \frac{\partial (\rho U r)}{\partial x} dr \end{aligned} \quad (A.6)$$

so that Equation (A.5) becomes

$$\int_0^R \frac{\partial}{\partial x} (\rho U r^2) dr - U_0 \int_0^R \frac{\partial (\rho U r)}{\partial x} dr = 0 \quad (\text{A.7})$$

Using Liebnitz' rule, Equation (A.7) becomes

$$\frac{d}{dx} \int_0^R \rho U r^2 dr - U_0 \frac{d}{dx} \int_0^R \rho U r dr = 0 \quad (\text{A.8})$$

or

$$\frac{d}{dx} \left[\int_0^R \rho U (U - U_0) r dr \right] = 0 \quad (\text{A.9})$$

where it has been assumed that $dU_0/dx = 0$. This is equivalent to the already stated assumption that the pressure is constant, as the external flow has also been assumed to be inviscid ($\tau = 0$). Thus the momentum integral requirement is that

$$\int_0^R \rho U (U - U_0) r dr = \text{constant} \quad (\text{A.10})$$

for an axisymmetric flow.

Symmetric Two-Dimensional Flow

Here the momentum equation is

$$\rho U \frac{\partial U}{\partial x} + \rho V \frac{\partial U}{\partial y} = \frac{\partial \tau}{\partial y} \quad (\text{A.11})$$

and the continuity equation is

$$\frac{\partial (\rho U)}{\partial x} + \frac{\partial (\rho V)}{\partial y} = 0 \quad (\text{A.12})$$

again assuming constant pressure, and subject to the same remarks about the influence of compressibility effects as were made above for the axisymmetric flow. Because the flow is symmetric, a centerline exists (at $y = 0$) for which $V = 0$ and $\tau = 0$. Thus, integrating the continuity equation (A.12) gives

$$\rho V = - \int_0^y \frac{\partial (\rho U)}{\partial x} dy' \quad (\text{A.13})$$

Performing the same operations as for axisymmetric flow leads to the equation

$$\frac{d}{dx} \left[\int_0^y \rho U (U - U_0) dy \right] = 0 \quad (\text{A.14})$$

again assuming that the integral is carried to a Y sufficiently large so that $U = U_0 = \text{constant}$ (which may be zero)

so that at $y = Y$, $\tau = 0$. Thus the momentum integral requirement for two-dimensional symmetric flow is

$$\int_0^Y \rho U(U - U_0) dy = \text{constant} \quad (\text{A.15})$$

Non-Symmetric Two-Dimensional Flow

Figure A.2 illustrates a non-symmetric two-dimensional flow; a two-dimensional mixing layer is an example. As before, the momentum and continuity equations are

$$\rho U \frac{\partial U}{\partial x} + \rho V \frac{\partial U}{\partial y} = \frac{\partial \tau}{\partial y} \quad (\text{A.16})$$

and

$$\frac{\partial (\rho U)}{\partial x} + \frac{\partial (\rho V)}{\partial y} = 0 \quad (\text{A.17})$$

Here, however, the integration on y must be taken from $y = -Y$, where $U = U_1$ and $V = V_{Y-}$ to $y = Y$, $U = U_0$ and $V = V_Y$. Thus, the integral from (A.17) from $-Y$ to Y is

$$\rho V - \rho_{Y-} V_{Y-} = - \int_{-Y}^Y \frac{\partial (\rho U)}{\partial x} dy' \quad (\text{A.18})$$

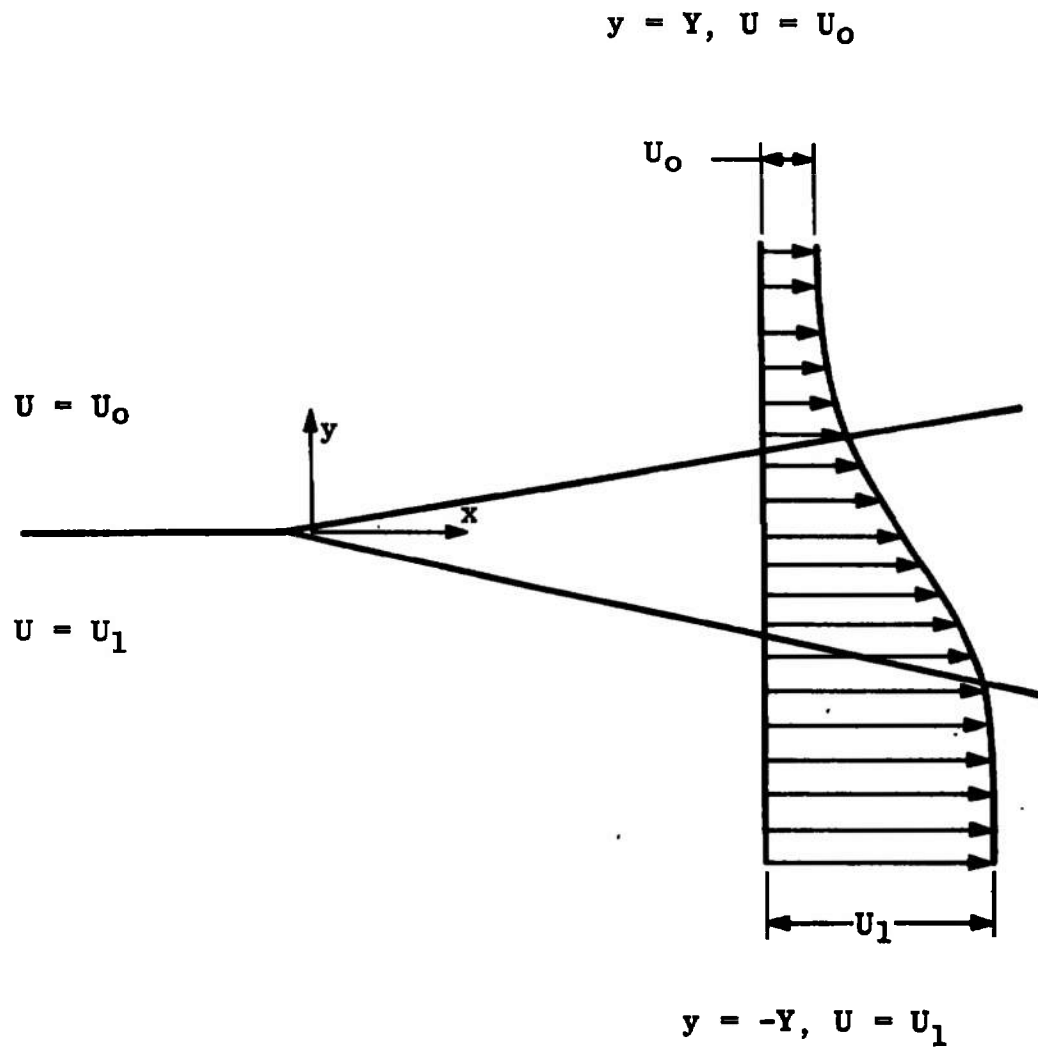


Figure A.2. Non-symmetric two-dimensional flow.

and Equation (A.16) becomes, after integration from $-Y$ to Y

$$\begin{aligned} \int_{-Y}^Y \rho U \frac{\partial U}{\partial x} dy - \int_{-Y}^Y \left[\frac{\partial (\rho U)}{\partial x} dy \right] \frac{\partial U}{\partial y} dy + \rho_{Y-} V_{Y-} \int_{-Y}^Y \frac{\partial U}{\partial y} dy = \\ = \tau_Y - \tau_{Y-} \end{aligned} \quad (\text{A.19})$$

where $\tau_Y = \tau_{Y-} = 0$. Integrating the second term of (A.19) by parts

$$\begin{aligned} \int_{-Y}^Y \int_{-Y}^Y \frac{\partial (\rho U)}{\partial x} dy \frac{\partial U}{\partial y} dy + \rho_{Y-} V_{Y-} \int_{-Y}^Y \frac{\partial U}{\partial y} dy = \\ = U_0 \int_{-Y}^Y \frac{\partial (\rho U)}{\partial x} dy - \int_{-Y}^Y U \frac{\partial (\rho U)}{\partial x} dy + \\ + \rho_{Y-} V_{Y-} (U_0 - U_1) \end{aligned} \quad (\text{A.20})$$

so that Equation (A.19) becomes

$$\begin{aligned} \int_{-Y}^Y \frac{\partial}{\partial x} (\rho U^2) dy - U_0 \int_{-Y}^Y \frac{\partial (\rho U)}{\partial x} dy - \\ - \rho_{Y-} V_{Y-} (U_0 - U_1) = 0 \end{aligned} \quad (\text{A.21})$$

Using Liebnitz' rule:

$$\frac{d}{dx} \int_{-Y}^Y \rho U (U - U_0) dy - \rho_{Y-} V_{Y-} (U_0 - U_1) = 0 \quad (A.22)$$

or

$$\begin{aligned} & \int_{-Y}^Y \rho U (U - U_0) dy + \\ & + (U_1 - U_0) \int_0^x \rho_{Y-} V_{Y-} dx' = \text{constant} \end{aligned} \quad (A.23)$$

so that some knowledge of the behavior of ρ_{Y-} and V_{Y-} is necessary to evaluate the momentum integral for a non-symmetric two-dimensional flow.

APPENDIX B

EVALUATION OF AXIAL DECAY OF CENTERLINE VELOCITY
FOR INCOMPRESSIBLE FLOW

Consider an axisymmetric flow as in Figure B.1. Assume constant pressure and constant density. Then from Appendix A,

$$\int_0^R U(U - U_0) r dr = \text{constant} \quad (\text{B.1})$$

For an ideal flow, at $x = 0$, $U = U_j = \text{constant}$, $0 \leq r \leq r_j$, and $U = U_0 = \text{constant}$, $r_j < r \leq R$. Then

$$\int_0^R U(U - U_0) r dr = r_j^2 U_j (U_j - U_0) \quad (\text{B.2})$$

and at any position x , $x < x_c$

$$\begin{aligned} \int_0^R U(U - U_0) r dr &= r_j^2 U_j (U_j - U_0) + \\ &+ r_I^2 U_j (U_j - U_0) \end{aligned} \quad (\text{B.3})$$

At $x = x_c$, $r_I = 0$, and

$$\int_0^R U(U - U_0) r dr = r_j^2 U_j (U_j - U_0) \quad (\text{B.4})$$

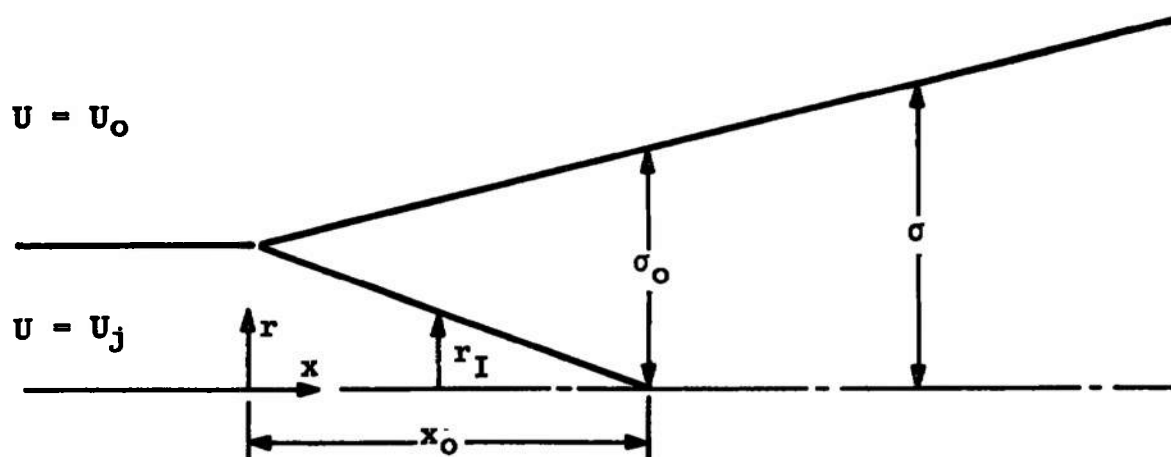


Figure B.1. Nomenclature.

For $x > x_c$, assume

$$\frac{U - U_o}{U_c - U_o} = f\left(\frac{x}{\sigma}\right) = f(\eta) \quad (\text{B.5})$$

so

$$U = U_o + (U_c - U_o)f(\eta) \quad (\text{B.6})$$

so that

$$\sigma = C_1 x^{(1-\lambda)} \quad (\text{B.7})$$

This expression was quoted by Forstall [40, 41] for coaxial jets; it reduces to $\sigma \propto x$ for the jet-into-still air, for which $\lambda = U_o/U_j = 0$. Note that at $x = x_o$, $\sigma = \sigma_o$ and $U_o = U_j$.

The constant C_1 is evaluated by evaluating Equation (B.4) at $x = x_c$. Thus, using

$$\left. \begin{aligned} U - U_o &= (U_j - U_o)f(\eta) \\ x &= \sigma\eta \end{aligned} \right\} \quad (\text{B.8})$$

noting that $U_0 = U_j$ at $x = x_c$

$$\begin{aligned} \int_0^{\infty} [U_0 + (U_j - U_0)f(\eta)] (U_j - U_0)f(\eta) \sigma^2 \eta d\eta &= \\ &= \frac{r_j^2 U_j}{2} (U_j - U_0) \end{aligned} \quad (B.9)$$

so

$$\sigma^2 \left[\int_0^{\infty} U_0 f \eta d\eta + \int_0^{\infty} (U_j - U_0) f^2 \eta d\eta \right] = \frac{r_j^2}{2} U_j \quad (B.10)$$

or

$$\sigma^2 = \frac{r_j^2 U_j}{2} \frac{1}{U_0 \int_0^{\infty} f \eta d\eta + (U_j - U_0) \int_0^{\infty} f^2 \eta d\eta} \quad (B.11)$$

Now $\int_0^{\infty} F(\eta) \eta d\eta = k_1$, $\int_0^{\infty} f^2(\eta) \eta d\eta = k_2$, and $\sigma^2|_{x=x_c} = C_1^2 x_c^{2(1-\lambda)}$

so

$$C_1^2 = \frac{r_j^2 U_j^2}{2 x_c^{2(1-\lambda)}} \frac{1}{U_0 k_1 + (U_j - U_0) k_2} \quad (B.12)$$

for $x > x_c$

$$U - U_0 = (U_c - U_0) f(\eta) \quad (B.13)$$

and Equation (B.4) yields, after some algebra, using (B.13)

$$\begin{aligned} & \left(\frac{U_c - U_o}{U_j - U_o} \right)^2 k_2 + \left(\frac{U_o}{U_j - U_o} \right) \left(\frac{U_c - U_o}{U_j - U_o} \right) k_1 - \\ & - \frac{r_j^2 U_j}{2\sigma^2 (U_j - U_o)} = 0 \end{aligned} \quad (B.14)$$

letting

$$\phi \equiv \frac{U_c - U_o}{U_j - U_o} \quad (B.15)$$

$$\lambda \equiv U_o/U_j \quad (B.16)$$

and solving Equation (B.14)

$$\begin{aligned} \phi = \frac{1}{2} \left[\left(\frac{k_1}{k_2} \right) \left(\frac{\lambda}{1-\lambda} \right)^2 + \frac{4r_j^2}{2k_2} \left(\frac{1}{1-\lambda} \right) \frac{1}{\sigma^2} \right]^{1/2} - \\ - \frac{1}{2} \left(\frac{k_1}{k_2} \right) \left(\frac{\lambda}{1-\lambda} \right) \end{aligned} \quad (B.17)$$

where the plus sign has been taken for the square root to ensure proper behavior for $\lambda \rightarrow 0$. Now $\sigma^2 = C_1^2 x^2 (1-\lambda)$ from (B.7) so, using (B.12) and (B.16),

$$\frac{1}{\sigma^2} = \frac{\frac{k_1}{k_2} \left(\frac{\lambda}{1-\lambda} \right) + 1}{\frac{1}{k_2} \left(\frac{1}{1-\lambda} \right)} \frac{2}{r_j^2} \left(\frac{x}{x_c} \right)^{-2(1-\lambda)} \quad (B.18)$$

which when substituted into (B.17) gives

$$\frac{U_c - U_o}{U_j - U_o} = \frac{1}{2} \left\{ \left(\frac{k_1}{k_2} \right)^2 \left(\frac{\lambda}{1-\lambda} \right)^2 + 4 \left(\frac{x}{x_c} \right)^{-2(1-\lambda)} \right. \\ \left. \left[\frac{k_1}{k_2} \left(\frac{\lambda}{1-\lambda} \right) + 1 \right] \right\}^{1/2} - \frac{1}{2} \left(\frac{k_1}{k_2} \right) \left(\frac{\lambda}{1-\lambda} \right) \quad (B.19)$$

so that under the assumptions of this section,

$(U_c - U_o)/(U_j - U_o)$ can be written as a function only of the velocity ratio U_o/U_j and the potential core length x_c .

Note that for the special case of a jet-into-still air, $\lambda = 0$, and

$$\frac{U_c}{U_j} = \left(\frac{x}{x_c} \right)^{-1} \quad (x \geq x_c) \quad (B.20)$$

APPENDIX C

CONDITIONS FOR SELF-PRESERVATION

The conditions under which a two-dimensional or axisymmetric flow may be self-preserving have been identified by Newman [3]. This development is followed here, with some changes of notation. For a symmetrical, two-dimensional or axisymmetrical jet or wake (Figure C.1) the time-averaged boundary layer equation in the x- (downstream) direction is

$$\begin{aligned}
 U \frac{\partial U}{\partial x} + v \frac{\partial U}{\partial y} + \frac{\partial}{\partial x} (\overline{u^2} - \overline{v^2}) + \frac{1}{y^r} \frac{\partial}{\partial y} (\overline{uv} y^r) \\
 = U_0 \frac{dU_0}{dx} + \frac{v}{y^r} \frac{\partial}{\partial y} (y^r \frac{\partial U}{\partial y})
 \end{aligned}
 \tag{C.1}$$

Here constant-density has been assumed, but constant pressure has not; Equation (C.1) makes use of the approximate equation in the y-direction. The term v is the physical kinematic viscosity of the fluid; u and v are the turbulent fluctuations associated with the average velocities U and V . The time-averaged continuity equation is

$$\frac{\partial U}{\partial x} + \frac{1}{y^r} \frac{\partial}{\partial y} (v y^r) = 0
 \tag{C.2}$$

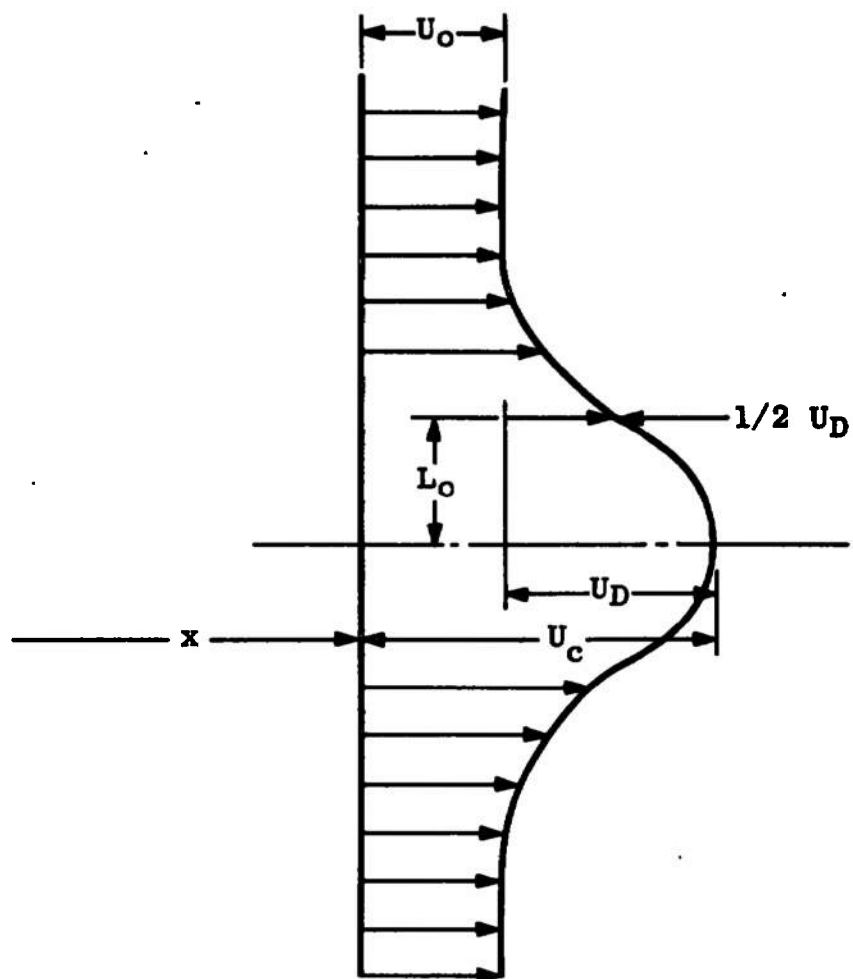


Figure C.1. Symmetrical jet with arbitrary secondary-stream velocity.

where

$r = 0$ for two-dimensional flow

$r = 1$ for axisymmetric three-dimensional flow

For self-preserving flows, for all x :

$$U = U_o + U_D f(y/L_o) \quad (C.3)$$

$$\left. \begin{aligned} \overline{u^2} &= U_D^2 g_{11}(y/L_o) \\ \overline{v^2} &= U_D^2 g_{22}(y/L_o) \\ \overline{uv} &= U_D^2 g_{12}(y/L_o) \end{aligned} \right\} \quad (C.4)$$

where L_o is the value of y for which $U = U_o + U_D/2$, a function of x . Substituting (C.3) in (C.2), noting that if $\eta = y/L_o(x)$

$$\left. \begin{aligned} \frac{\partial}{\partial x} &= \frac{\partial}{\partial x} + \frac{\partial}{\partial \eta} \frac{\partial \eta}{\partial x} = \frac{\partial}{\partial x} - \frac{\eta}{L_o} \frac{dL_o}{dx} \frac{\partial}{\partial \eta} \\ \frac{\partial}{\partial y} &= \frac{\partial}{\partial \eta} \frac{\partial \eta}{\partial y} = \frac{1}{L_o} \frac{\partial}{\partial \eta} \end{aligned} \right\} \quad (C.5)$$

$$\frac{dU_o}{dx} + \frac{\partial}{\partial x}[U_D f] - \frac{\eta}{L_o} \frac{dL_o}{dx} U_D f' + \frac{1}{L_o^r \eta^r} \frac{1}{L_o} \frac{\partial}{\partial \eta} (v \eta^r L_o^r) = 0$$

or

$$\frac{dU_o}{dx} + \frac{dU_D}{dx} f - U_D f' \frac{\eta}{L_o} \frac{dL_o}{dx} + \frac{1}{L_o^r \eta^r} \frac{d}{d\eta} (v \eta^r L_o^r) = 0$$

so

$$\begin{aligned}
 -\frac{d}{d\eta} \eta^r L_O^r V &= L_O^{r+1} \eta^r \frac{dU_D}{dx} + L_O^{r+1} \eta^r f \frac{dU_D}{dx} - \\
 &\quad - U_D f' \eta^{r+1} L_O^r \frac{dL_O}{dx}
 \end{aligned}$$

where the prime indicates $d/d\eta$.

Integrating

$$\begin{aligned}
 -\eta^r L_O^r V &= L_O^{r+1} \frac{dU_O}{dx} \int_0^\eta \eta^r d\eta + L_O^{r+1} \frac{dU_D}{dx} \int_0^\eta \eta^r f(\eta) d\eta - \\
 &\quad - U_D L_O^r \frac{dL_O}{dx} \int_0^\eta \eta^{r+1} f'(\eta) d\eta \\
 &= \frac{L_O^{r+1}}{r+1} \eta^{r+1} \frac{dU_O}{dx} + L_O^{r+1} \frac{dU_D}{dx} \int_0^\eta \eta^r f(\eta) d\eta - \\
 &\quad - U_D L_O^r \frac{dL_O}{dx} f \eta^{r+1} + (r+1) \int_0^\eta \eta^r f d\eta U_D L_O^r \frac{dL_O}{dx} \\
 &= \frac{L_O^{r+1}}{r+1} \eta^{r+1} \frac{dU_O}{dx} + \frac{d}{dx} (U_D L_O^r) \int_0^\eta \eta^r f d\eta - \\
 &\quad - U_D L_O^r \frac{dL_O}{dx} f \eta^{r+1}
 \end{aligned}$$

so that

$$\begin{aligned}
 -v &= \frac{L_o \eta}{r+1} \frac{dU_o}{dx} + \frac{1}{(L_o \eta)^r} \frac{d}{dx} (U_D L_o^r) \int_0^\eta r f d\eta - \\
 &\quad - U_D \eta f \frac{dL_o}{dx}
 \end{aligned} \tag{C.6}$$

Now

$$\begin{aligned}
 U \frac{\partial U}{\partial x} &= (U_o + U_D f) \left(\frac{\partial U_o}{\partial x} + f \frac{\partial U_o}{\partial x} - \frac{\eta}{L_o} \frac{dL_o}{dx} U_D f' \right) \\
 &= U_o \frac{dU_o}{dx} + U_o f \frac{dU_o}{dx} - \frac{\eta}{L_o} \frac{dL_o}{dx} U_D U_o f' + \\
 &\quad + U_D f \frac{dU_o}{dx} + U_D f^2 \frac{dU_D}{dx} - \frac{\eta}{L_o} \frac{dL_o}{dx} U_D^2 f f'
 \end{aligned} \tag{C.7}$$

and

$$\frac{\partial U}{\partial y} = \frac{1}{L_o} U_D f'$$

so

$$\begin{aligned}
 v \frac{\partial U}{\partial y} &= - \frac{\eta}{r+1} U_D \frac{dU_o}{dx} f' - \frac{U_D}{L_o^{r+1} \eta^r} \frac{d}{dx} (U_D L_o^r) \int_0^\eta r f d\eta f' + \\
 &\quad + \frac{U_D^2}{L_o} \eta f f' \frac{dL_o}{dx}
 \end{aligned} \tag{C.8}$$

$$\frac{\partial \overline{u^2}}{\partial x} = \frac{dU_D^2}{dx} g_{11} - \frac{\eta}{L_O} \frac{dL_O}{dx} U_D^2 g'_{11} \quad (C.9)$$

$$\frac{\partial \overline{v^2}}{\partial x} = \frac{dU_D^2}{dx} g_{22} - \frac{\eta}{L_O} \frac{dL_O}{dx} U_D^2 g'_{22} \quad (C.10)$$

$$\begin{aligned} \frac{1}{y^r} \frac{\partial}{\partial y} (\overline{uv} y^r) &= \frac{1}{(L_O \eta)^r} \frac{1}{L_O} \frac{\partial}{\partial \eta} [\overline{uv} (L_O \eta)^r] \\ &= \frac{1}{\eta^r} \frac{U_D^2}{L_O} \frac{d}{d\eta} (\eta^r g_{12}) \end{aligned} \quad (C.11)$$

$$\begin{aligned} \frac{v}{y^r} \frac{\partial}{\partial y} (y^r \frac{\partial U}{\partial y}) &= \frac{v}{(L_O \eta)^r} \frac{1}{L_O} \frac{\partial}{\partial \eta} [(L_O \eta)^r \frac{1}{L_O} U_D f'] \\ &= \frac{v U_D}{L_O^2 \eta^r} \frac{d}{d\eta} [\eta^r f'] \end{aligned} \quad (C.12)$$

Substituting Equations (C.6) through (C.12) into (C.1) yields the equation

$$\begin{aligned} U_O f \frac{dU_D}{dx} - \frac{\eta}{L_O} \frac{dL_O}{dx} U_D U_O f' + U_D f \frac{dU_O}{dx} + U_D f^2 \frac{dU_D}{dx} - \\ - \frac{\eta}{L_O} \frac{dL_O}{dx} U_D^2 f f' - \frac{\eta}{r+1} U_D \frac{dU_O}{dx} f' - \\ - \frac{f'}{L_O^{r+1} \eta^r} \frac{d}{dx} (U_D L_O^r) \int_0^\eta \eta^r f d\eta + \frac{U_D^2}{L_O} \eta f f' \frac{dL_O}{dx} + \end{aligned}$$

$$\begin{aligned}
& + \frac{1}{\eta^r} \frac{U_D^2}{L_O} \frac{d}{d\eta} (\eta^r g_{12}) + g_{11} \frac{dU_D^2}{dx} - \frac{\eta}{L_O} \frac{dL_O}{dx} U_D^2 g'_{11} - \\
& - g_{22} \frac{dU_D^2}{dx} + \frac{\eta}{L_O} \frac{dL_O}{dx} U_D^2 g'_{22} - \\
& - \frac{v}{L_O^2 \eta^r} U_D \frac{d}{d\eta} (\eta^r f') = 0 \quad (C.13)
\end{aligned}$$

Multiplying through L_O/U_D^2 and rearranging yields:

$$\begin{aligned}
& \left\{ \frac{L_O}{U_O} \frac{dU_O}{dx} \right\} [f^2 + 2(g_{11} - g_{22})] + \left\{ \frac{L_O}{U_D^2} \frac{d}{dx} (U_O U_D) \right\} [f] - \\
& - \left\{ \frac{1}{r+1} \frac{1}{U_D L_O^r} \frac{d}{dx} (U_O L_O^{r+1}) \right\} - \\
& - \left\{ \frac{1}{U_D L_O^r} \frac{d}{dx} (U_D L_O^r) \right\} \left[\frac{f'}{\eta^r} \int_0^\eta \eta^r f d\eta \right] - \\
& - \left\{ \frac{dL_O}{dx} \right\} [\eta (g'_{11} - g'_{22})] + \\
& + \left[\frac{1}{\eta^r} \frac{d}{d\eta} (\eta^r g_{12}) \right] - \\
& - \left\{ \frac{v}{L_O U_D} \right\} \left[\frac{1}{\eta^r} \frac{d}{d\eta} (\eta^r f') \right] = 0 \quad (C.14)
\end{aligned}$$

The arrangement of the curly ({}) and square ([]) brackets is purposeful: all quantities in the curly brackets are functions of x only and all quantities in the square brackets are functions of y only. Since the next to the last term has no curly bracket, self-preservation is possible only if the terms in the six curly brackets are constant. For sufficiently large $U_0 L_0 / \nu$, the last term may be neglected. The remaining terms are constant if

$$\begin{aligned}\frac{dL_0}{dx} &= \text{constant} \\ \frac{U_D}{U_0} &= \text{constant} \\ \frac{L_0}{U_D} \frac{dU_D}{dx} &= \text{constant}\end{aligned}\tag{C.15}$$

Thus for true self-preservation, L_0 varies linearly with x , and both U_D and U_0 are proportional to $(x + x_0)^m$ where x_0 is the virtual origin which is constant for a particular flow. The exponent m is not arbitrary but varies with U_D/U_0 . As in Appendix A, integrating Equation (C.1) from $y = 0$ to y very large (so $\overline{uv} = 0$) yields

$$\frac{d}{dx}(\theta^{r+1} U_0^2) + (\delta^*)^{r+1} U_0 \frac{dU_0}{dx} = 0\tag{C.16}$$

i.e.,

$$\theta^{r+1} u_o^{H+2} = \text{constant for constant } H \quad (\text{C.17})$$

where

$$\theta^{r+1} u_o^2 = \frac{2}{r+1} \int_0^\infty u(u - u_o) y^r dy \quad (\text{C.18})$$

$$(\delta^*)^{r+1} u_1 = \frac{2}{r+1} \int_0^\infty (u - u_o) y^r dy$$

and

$$H = (\delta^*/\theta)^{r+1}$$

From Equation (C.17) using the assumption of similar profiles (C.3)

$$\begin{aligned} \theta^{r+1} u_o^{H+2} &= u_o^H \left(\frac{2}{r+1} \right) \int_0^\infty [u_o + u_D f] [u_D f] L_o^{r+1} \eta^r d\eta \\ &= L_o^{r+1} u_o^H u_o^2 \left(\frac{2}{r+1} \right) \\ &\quad \int_0^\infty \left[1 + \frac{u_D}{u_o} f \right] [f] \eta^r d\eta \end{aligned} \quad (\text{C.19})$$

For self-preservation, $U_D/U_O = \text{constant}$, and

$$\left. \begin{array}{l} L_O^{r+1} U_O^{H+2} = \text{constant} \\ \text{or} \\ L_O^{r+1} U_D^{H+2} = \text{constant} \end{array} \right\} \quad (C.20)$$

Now from the condition for self-preservation

$$\frac{L_O}{U_D} \frac{dU_D}{dx} = \text{constant} = C_1$$

But

$$L_O = C_2 x$$

so

$$\frac{1}{U_D} \frac{dU_D}{dx} = \frac{C_1/C_2}{x}$$

so

$$\frac{dU_D}{U_D} = (C_1/C_2) \frac{dx}{x}$$

therefore

$$U_D \propto x^m \quad m = C_1/C_2$$

But

$$U_D^{H+2} \propto L_O^{-(r+1)}$$

So, given

$$\begin{aligned} L_O &\propto x \\ U_D &\propto x^{-\frac{r+1}{H+2}} \end{aligned}$$

and

$$m = - (r+1)/(H+2) \quad (C.21)$$

For the jet into still surroundings $U_D/U_O \rightarrow \infty$, and since for self-similar profiles

$$\frac{1}{H} = \frac{\int_0^{\infty} (1 + \frac{U_D}{U_O} f) f \eta^r d\eta}{\int_0^{\infty} f \eta^r d\eta} \quad (C.22)$$

for $U_D/U_O \rightarrow \infty$

$$H \rightarrow 0$$

and

$$m = -\frac{1+r}{2}$$

Therefore, for the jet into virtually still surroundings, true self-preservation requires

$$\left. \begin{aligned} L_O &\propto (x + x_O) \\ U_D &\propto (x + x_O)^{-1/2} \end{aligned} \right\} \begin{array}{l} \text{for two-dimensional} \\ \text{flow} \end{array} \quad (C.23)$$

$$\left. \begin{aligned} L_O &\propto (x + x_O) \\ U_D &\propto (x + x_O)^{-1} \end{aligned} \right\} \begin{array}{l} \text{for axisymmetric} \\ \text{flow} \end{array} \quad (C.24)$$

The small increment jet, for which $U_D/U_O \rightarrow 0$, $H \rightarrow 1$ is the opposite extreme. For this case

$$\left. \begin{aligned} L_O &\propto (x + x_O) \\ U_D &\propto (x + x_O)^{-1/3} \end{aligned} \right\} \begin{array}{l} \text{two-dimensional} \\ \\ \text{axisymmetric} \end{array} \quad (C.25)$$

For a jet or wake in a zero pressure gradient, the requirement $U_D/U_O = \text{constant}$ precludes exact self-preservation. However in this case, if U_D/U_O is $\ll 1$, Equation (C.14) becomes

$$\begin{aligned} \left\{ \frac{L_O}{U_D^2} \frac{d}{dx} (U_O U_D) \right\} [f] - \left\{ \frac{1}{r+1} \frac{1}{U_D L_O^r} \frac{d}{dx} (U_O L_O^{r+1}) \right\} [\eta f'] + \\ + \left[\frac{1}{\eta^r} \frac{d}{d\eta} (\eta^r g_{12}) \right] = 0 \end{aligned} \quad (C.26)$$

when both the normal turbulent stress term and the viscous term are neglected. The requirement becomes

$$\frac{U_o L_o}{U_D^2} \frac{dU_o}{dx} \text{ and } \frac{U_o}{U_o} \frac{dL_o}{dx} = \text{constant} \quad (C.27)$$

while Equation (C.16) gives

$$\theta^{r+1} = \text{constant}$$

so

$$U_D L_o^{r+1} = \text{constant} \quad (C.28)$$

Substituting (C.28) into (C.27)

$$U_o L_o^{r+1} \frac{dL_o}{dx} = \text{constant}$$

or

$$L_o \propto (x + x_o)^{1/(r+2)}$$

therefore

$$U_D \propto L_o^{-(r+1)}$$

so

$$U_D \propto (x + x_o)^{-[(r+1)/(r+2)]}$$

So that, for $U_D/U_O = U - U_O/U_O \ll 1$,

$$L_O \propto (x + x_O)^{1/r+2}$$

$$U_O \propto (x + x_O)^{-[(r+1)/(r+2)]}$$

$$r = 0 \qquad r = 1$$

$$1/2 \quad \text{and} \quad 1/3$$

$$-1/2 \quad \text{and} \quad -2/3$$

APPENDIX D

DETAILS OF THE TING-LIBBY TRANSFORMATION IN
TWO-DIMENSIONAL AND AXISYMMETRIC FLOW

Two-Dimensional Flow

Following Mager [122], the Howarth transformation for two-dimensional turbulent flow, with the molecular viscosity neglected, is, with X, Y transformed (incompressible) coordinates, and x, y physical (compressible) coordinates:

$$X = x \quad (D.1)$$

$$Y = F \int_0^y \frac{\rho}{\rho_0} dy' \quad (D.2)$$

so that

$$\frac{\partial}{\partial y} = F \left(\frac{\rho}{\rho_0} \right) \frac{\partial}{\partial Y}$$

Still following Mager [122], we postulate that

1. The stream function is invariant under the transformation, i.e.,

$$\Psi = \Psi^* \quad (D.3)$$

where the $*$ indicates the transformed (incompressible) value.

2. The total amount of shear associated with an elemental fluid mass is invariant under the transformation:

$$(\rho \overline{uv}) \rho dx dy dz = (\rho_0 \overline{uv}) * \rho_0 dX dY dZ \quad (D.4)$$

Now in the physical plane the stream function Ψ is defined by

$$\left. \begin{aligned} \rho U &= \rho_0 \partial \Psi / \partial Y \\ (\rho V + \overline{\rho'v}) &= \rho_0 \partial \Psi / \partial X \end{aligned} \right\} \quad (D.5)$$

while in the transformed plane

$$U^* = \frac{\partial \Psi^*}{\partial Y} , \quad V^* = - \frac{\partial \Psi^*}{\partial X} \quad (D.6)$$

Now

$$U^* = \frac{\partial \Psi^*}{\partial Y} = \frac{\partial \Psi}{\partial Y} = \frac{\partial \Psi}{\partial Y} \frac{\partial Y}{\partial Y} = \frac{\rho_0}{\rho} \frac{1}{F} \frac{\partial \Psi}{\partial Y} = \frac{U}{F} \quad (D.7)$$

The infinitesimal element is transformed:

$$\begin{aligned} dXdY &= J \begin{pmatrix} X, Y \\ x, y \end{pmatrix} dx dy \\ &= \frac{\partial (X, Y)}{\partial (x, y)} dx dy \end{aligned} \quad (D.8)$$

$$\begin{aligned}
&= \left(\frac{\partial X}{\partial x} \frac{\partial Y}{\partial y} - \frac{\partial Y}{\partial x} \frac{\partial X}{\partial y} \right) dx dy \\
&= F^2 (\rho / \rho_0) dx dy
\end{aligned} \tag{D.9}$$

so

$$(\rho \overline{uv}) \rho dx dy = (\rho_0 \overline{uv^*}) F^2 \rho dx dy$$

or

$$\rho \overline{uv} = F^2 \rho_0 \overline{uv^*} \tag{D.10}$$

Now

$$\rho \overline{uv} = \rho \epsilon \partial U / \partial y$$

$$\rho \overline{uv^*} = \rho_0 \epsilon^* \partial U^* / \partial Y \tag{D.11}$$

so that

$$\begin{aligned}
\rho \epsilon \frac{\partial U}{\partial y} &= F^2 \rho_0 \epsilon^* \partial U^* / \partial Y \\
&= F^2 \rho_0 \epsilon^* \frac{\partial}{\partial Y} \left(\frac{U}{F} \right) \\
&= F^2 \rho_0 \epsilon^* \frac{\rho_0}{\rho} \frac{1}{F} \frac{\partial}{\partial Y} \left(\frac{U}{F} \right)
\end{aligned}$$

which leads to

$$\rho^2 \epsilon = \rho_0^2 \epsilon^* \tag{D.12}$$

Axisymmetric Flow

Here the transformation becomes

$$X = x \quad (D.13)$$

$$R^2 = F \int_0^r \left(\frac{\rho}{\rho_0} \right) r' dr' \quad (D.14)$$

Again the capital letters refer to the transformed (incompressible) coordinates and lower case letters refer to the physical coordinates.

From Equation (D.14)

$$\frac{\partial}{\partial r} = F \left(\frac{\rho}{\rho_0} \right) \frac{r}{2R} \frac{\partial}{\partial R} \quad (D.15)$$

For axisymmetric flow, we again assume

$$\Psi = \Psi^* \quad (D.16)$$

where the * refers to the transformed (incompressible) coordinate, but we now make the assumption [126] that the "moment of the turbulent shear about an axis of the fluid element is conserved":

$$(r \rho \overline{uv}) \rho (r dr dx) = (R \rho_0 \overline{u^* v^*}) \rho_0 (R dR dx) \quad (D.17)$$

The Jacobian of the transformation of the element is

$$J = F(\rho/\rho_0) r/2R \quad (D.18)$$

so (D.17) becomes

$$\begin{aligned} (r\rho \overline{uv})\rho(rdrdx) &= \\ &= (R\rho_0 \overline{uv^*})\rho_0 F(\rho/\rho_0) \frac{r^2}{2R} drdx \end{aligned}$$

or

$$\rho \overline{uv} = \rho_0 \overline{uv^*} F/2 \quad (D.19)$$

Now

$$\rho Ur = \rho_0 \partial \Psi / \partial r$$

$$U^* R = \partial \Psi^* / \partial R$$

so that

$$\begin{aligned} \rho Ur &= \rho_0 \frac{\partial \Psi}{\partial r} = \rho_0 \frac{\partial \Psi^*}{\partial r} = \rho_0 F \frac{\rho}{\rho_0} \frac{r}{2R} \frac{\partial \Psi^*}{\partial R} = \\ &= \rho_0 F \frac{\rho}{\rho_0} \frac{r}{2R} U^* R \end{aligned}$$

and

$$U = \frac{FU^*}{2} \quad (D.20)$$

further

$$\left. \begin{aligned} \rho \overline{uv} &= \rho \epsilon r \partial U / \partial r \\ \rho_0 \overline{uv^*} &= \rho_0 \epsilon^* R \partial U^* / \partial R \end{aligned} \right\} \quad (D.21)$$

Substituting (D.19) into (D.21)

$$\rho \epsilon r \frac{\partial U}{\partial r} = \rho_0 \epsilon^* R \frac{\partial U^*}{\partial R} \frac{F}{2} \quad (D.22)$$

Using (D.20) and (D.15)

$$\rho \epsilon r \frac{F^2}{2} \frac{\rho}{\rho_0} \frac{r}{2R} \frac{\partial U^*}{\partial R} = \rho_0 \epsilon^* R \frac{F}{2} \frac{\partial U^*}{\partial R}$$

so

$$\rho^2 \epsilon = 2 \rho_0^2 \epsilon^* \frac{R^2}{r^2} \frac{1}{F} \quad (D.23)$$

So, substituting (D.14) for F into (D.23)

$$r^2 \rho^2 \epsilon = 2 \rho_0^2 \epsilon^* \int_0^r \left(\frac{\rho}{\rho_0} \right) r' dr' \quad (D.24)$$

APPENDIX E

THE NUMERICAL SOLUTION TECHNIQUE

The numerical method used to make all of the calculations reported in this study (with the exception of the calculations made to invert the Libby solution [125] back to the real plane) is based on the technique developed by Patankar [139]. This procedure is valid for the numerical solution of an arbitrary number of simultaneous parabolic partial differential equations. It is an implicit technique, which embodies a variable grid size, each lateral increment essentially being a given fraction of the total mass flow in the flow field. This use of a variable grid, combined with the use of a standard form for the parabolic partial differential equations in non-dimensional stream function coordinates results in a considerable economy in computer time for a large scale calculation. For example, a calculation involving the simultaneous solution of three equations (momentum, energy, and species) for a two-gas nonreacting mixture with non-unity turbulent Prandtl and Schmidt numbers, using a forty-point lateral grid and involving of the order of 150 downstream steps, requires approximately four minutes on an IBM 360/50.

This economy of execution time and the accuracy permitted by the variable grid size are the primary factors which allowed the calculations made in this study to be performed in a reasonable time. However, to adapt the Patankar program for the purposes of this study, several major modifications were necessary. The first involves the definition of the turbulent eddy viscosity, ϵ . Patankar [139] wrote the program using the Prandtl mixing length model for the turbulent eddy viscosity. As will be seen, this simplifies the definition of one of the important parameters in the formulation of the problem. Since this study requires the use of a number of models for the turbulent eddy viscosity, the restriction to the Prandtl mixing length model inherent in the definition of the parameter in question had to be removed. Secondly, although the structure of the program written by Patankar allows an arbitrary number of simultaneous parabolic equations to be solved, the actual number allowed in the programming by Patankar was three. Since the most complex problem solved in this study using the turbulent kinetic energy equation involves four governing equations (with the continuity equation absorbed into the momentum equation)--momentum, energy, species, and kinetic energy, this restriction on the number of equations had to be lifted. Additionally, the turbulent kinetic energy equation was written in a form suitable for inclusion in the program, transformed into

non-dimensional stream function coordinates, and the appropriate terms were added to the program. This also involved a modification to the mean flow energy equation.

A third modification involves the accuracy of the computations. Some of the calculations involved in this study proceed to large values of axial distance, which involves a large number of calculations. As will be seen in this section, one of the functions chosen by Patankar to control the variation of the grid size (which also enters the definitions of the coefficients of the equations) proved inaccurate when used for a large number of calculation steps. Thus, this function had to be changed and an alternate one which proved considerably more accurate (but which is limited to free mixing problems) was substituted.

Because a complete description of the basic program is given by Patankar [139], the details will be only briefly discussed in this section. The modifications that have been made will of course be discussed in detail.

Formulation of the System of Equations

In his formulation of the problem, Patankar first converts the system of governing equations from the physical coordinates to the von Mises stream-function coordinate system, where the stream function Ψ is defined so as to satisfy the continuity equation:

$$\frac{\partial \Psi}{\partial y} = \rho U y^\alpha, \quad \frac{\partial \Psi}{\partial x} = -\rho V y^\alpha \quad (\text{E.1})$$

The parameter α is unity for axisymmetric flow and zero for plane flow. Consider now the X-direction momentum equation, written, incorporating the Boussinesq assumption for the turbulent shear stress:

$$\rho U \frac{\partial U}{\partial x} + \rho V \frac{\partial U}{\partial y} = \frac{1}{y^\alpha} \frac{\partial}{\partial y} (y^\alpha \epsilon \frac{\partial U}{\partial y}) - \frac{dP}{dx} \quad (E.2)$$

and the kinetic energy equation in parabolic form (see Chapter 8)

$$\begin{aligned} \rho U \frac{\partial k}{\partial x} + \rho V \frac{\partial k}{\partial y} = \frac{1}{y^\alpha} \frac{\partial}{\partial y} \left(\frac{y^\alpha \epsilon}{Pr_{k2}} \frac{\partial k}{\partial y} \right) + \\ + \epsilon \left(\frac{\partial U}{\partial y} \right)^2 - D_k \end{aligned} \quad (E.3)$$

The energy and species equations are developed in the same manner as Equations (E.2) and (E.3); their development is not given here.

Equations (E.2) and (E.3) are now transformed into the von Mises coordinate system, i.e.,

$$(x, y) \rightarrow (\bar{x}, \psi)$$

where $\bar{x} = x$. Noting that

$$\frac{\partial}{\partial x} = \frac{\partial}{\partial \bar{x}} + \frac{\partial}{\partial \psi} \frac{\partial \psi}{\partial x} = \frac{\partial}{\partial \bar{x}} - \rho V y^\alpha \frac{\partial}{\partial \psi} \quad (E.4)$$

$$\frac{\partial}{\partial y} = \frac{\partial}{\partial \Psi} \frac{\partial \Psi}{\partial y} = \rho U y^\alpha \frac{\partial}{\partial \Psi} \quad (\text{E.5})$$

and setting $\bar{x} = x$, the transformed momentum and kinetic energy equations become

$$\frac{\partial}{\partial \bar{x}} = \frac{\partial}{\partial \Psi} (y^{2\alpha} \rho U \epsilon \frac{\partial U}{\partial \Psi}) - \frac{1}{\rho U} \frac{dP}{d\bar{x}} \quad (\text{E.6})$$

$$\frac{\partial k}{\partial \bar{x}} = \frac{\partial}{\partial \Psi} (y^{2\alpha} \frac{\rho U \epsilon}{Pr_k} \frac{\partial k}{\partial \bar{x}}) + \rho U y^{2\alpha} \epsilon \left(\frac{\partial U}{\partial \Psi} \right)^2 - \frac{D_k}{\rho U} \quad (\text{E.7})$$

Now define

$$\omega = \frac{\Psi - \Psi_I}{\Psi_E - \Psi_I} \quad (\text{E.8})$$

where Ψ_E is the value of the stream function Ψ on the outer or "external" edge of the mixing layer, and Ψ_I is the value of the inner or "internal" edge. Thus, the value of ω will be from zero to one. The coordinate system transformation

$$(x, \Psi) \rightarrow (\bar{x}, \omega)$$

where $\bar{x} = x$ is now performed. The transformation equations are

$$\frac{\partial}{\partial \bar{x}} = \frac{\partial}{\partial \bar{x}} + \frac{1}{\Psi_E - \Psi_I} \left[- \frac{d\Psi_I}{d\bar{x}} - \frac{\Psi - \Psi_I}{\Psi_E - \Psi_I} \left(\frac{d\Psi_E}{d\bar{x}} - \frac{d\Psi_I}{d\bar{x}} \right) \right] \frac{\partial}{\partial \omega}$$

$$\frac{\partial}{\partial \Psi} = \frac{\partial}{\partial \omega} \frac{\partial \omega}{\partial \Psi} = \frac{1}{\Psi_E - \Psi_I} \frac{\partial}{\partial \omega}$$

The terms Ψ_I and Ψ_E are functions only of x ; using the continuity equation (E.1)

$$-\frac{d\Psi_E}{dx} = \rho_E V_E r_E \frac{\Delta}{r_E \dot{m}_E} \quad (E.9)$$

$$-\frac{d\Psi_I}{dx} = \rho_I V_I r_I \frac{\Delta}{r_I \dot{m}_I} \quad (E.10)$$

where \dot{m}_E represents the mass flow rate per unit area entrained at the outer edge of the layer and \dot{m}_I the same quantity at the inner edge, the transformation equations become

$$\frac{\partial}{\partial x} = \frac{\partial}{\partial \bar{x}} + \frac{1}{\Psi_E - \Psi_I} [r_I \dot{m}_I + \omega(r_E \dot{m}_E - r_I \dot{m}_I)] \frac{\partial}{\partial \omega} \quad (E.11)$$

$$\frac{\partial}{\partial \Psi} = \frac{1}{\Psi_E - \Psi_I} \frac{\partial}{\partial \omega} \quad (E.12)$$

Using Equations (E.11) and (E.12), Equations (E.6) and (E.7), as well as the energy and species equations all transform to a standard form which can be written, taking $\bar{x} = x$ again,

$$\frac{\partial \phi}{\partial x} + (a+b\omega) \frac{\partial \phi}{\partial \omega} = \frac{\partial}{\partial \omega} (c \frac{\partial \phi}{\partial \omega}) + d \quad (E.13)$$

where

$$a = r_I \dot{m}_I / (\Psi_E - \Psi_I) \quad (E.14)$$

$$b = (r_E \dot{m}_E - r_I \dot{m}_I) / (\Psi_E - \Psi_I) \quad (E.15)$$

$$c = y^{2\alpha} \rho U \epsilon / \sigma (\Psi_E - \Psi_I)^2 \quad (E.16)$$

and where, for various ϕ , the values of σ and d are as given in Table E.1.

In forming the expressions that appear in Table E.1, it has been assumed that no chemical reactions occur, and that a two-gas mixture which can be characterized by the concentration of a single species C is involved. It should be noted that the term $(1/Pr_k - 1/Pr) \partial k / \partial \omega$ included in the expression for d for the total enthalpy equation (H) in Table E.1 was not included by Patankar [139] as he did not consider the kinetic energy equation. Pr represents the turbulent (mean-flow energy) Prandtl number, Sc the turbulent Schmidt number, and Pr_k the turbulent kinetic energy Prandtl number, described in Chapter 8.

Development of the Auxiliary Relations

It is in the evaluation of the terms $(\Psi_E - \Psi_I)$, $r_E \dot{m}_E$, and $r_I \dot{m}_I$ that substantial differences have evolved between the formulation used by Patankar [139] and that were

TABLE E.1

SOURCE TERMS IN THE TRANSFORMED EQUATIONS

ϕ	σ	d
U	1	$-\frac{1}{\rho U} \frac{dP}{dx}$
k	Pr_k	$\frac{(y^{2\alpha} \rho U \epsilon)}{(\psi_E - \psi_I)^2} \left(\frac{\partial U}{\partial \omega} \right)^2 - \frac{D_k}{\rho U}$
C	Sc	-
H	Pr	$\frac{\partial}{\partial \omega} \left\{ \frac{y^{2\alpha} \rho U \epsilon}{(\psi_E - \psi_I)^2} \left[\left(1 - \frac{1}{Pr} \right) \frac{\partial}{\partial \omega} \left(\frac{U^2}{2} \right) + \left(\frac{1}{Pr_k} - \frac{1}{Pr} \right) \frac{\partial k}{\partial \omega} \right] \right\}$

used in this study. The terms used by Patankar and the modifications made to them in this study are described in this section.

The terms $r_I \dot{m}_I$ and $r_E \dot{m}_E$ can be evaluated from the axial momentum equation. Consider the axial momentum equation applied along a free boundary, denoted by the subscript G. Just outside of the G boundary

$$\left(\frac{\partial U}{\partial x}\right)_G = - \left(\frac{1}{\rho U} \frac{dP}{dx}\right)_G \quad (E.17)$$

from the inviscid Bernoulli equation. If it is assumed that this relation also holds just inside of the G boundary, the axial momentum equation becomes

$$\begin{aligned} \frac{1}{\Psi_E - \Psi_I} [r_I \dot{m}_I + (r_E \dot{m}_E - r_I \dot{m}_I) \omega_G] \frac{\partial U}{\partial \omega} \Big|_G &= \\ &= \left[\frac{\partial}{\partial \omega} \frac{y_G^{2\alpha} \rho_U U_G^\epsilon}{(\Psi_E - \Psi_I)^2} \frac{\partial u}{\partial \omega} \right]_{\omega=\omega_G} \end{aligned} \quad (E.18)$$

For $\omega_G \rightarrow 1$, this becomes

$$r_E \dot{m}_E = \lim_{\omega \rightarrow \omega_G} \left[\frac{\frac{\partial U}{\partial \omega} \left(\frac{y_G^{2\alpha} \rho_U U_G^\epsilon}{\Psi_E - \Psi_I} \frac{\partial u}{\partial \omega} \right)}{\partial U / \partial \omega} \right] \quad (E.19)$$

while for $\omega_G \rightarrow 0$

$$r_I \dot{m}_I = \lim_{\omega \rightarrow \omega_G} \left[\frac{\frac{\partial U}{\partial \omega} \left(\frac{y_I^{2\alpha} \rho_I U_I^\epsilon}{\Psi_E - \Psi_I} \frac{\partial U}{\partial \omega} \right)}{\partial U / \partial \omega} \right]$$

For the Prandtl mixing length model

$$\epsilon = \rho l^2 \left| \frac{\partial U}{\partial y} \right| = \frac{\rho^2 U y^{\alpha} l^2}{\psi_E - \psi_I} \left| \frac{\partial U}{\partial \omega} \right| \quad (\text{E.20})$$

and the limit in Equation (E.19) is finite. This remains true as long as $\epsilon \propto \partial U / \partial y$. However, most eddy viscosity models considered in this study do not have this feature, so that it is necessary to evaluate $r_G \dot{m}_G$ in some other manner.

If the axial momentum equation is evaluated somewhere away from the edge of the mixing layer, say at $\omega = \omega_G$, then

$$\begin{aligned} r_I \dot{m}_I + \omega_B (r_E \dot{m}_E - r_I \dot{m}_I) = & \left\{ \frac{\frac{\partial}{\partial \omega} \left[\frac{y^{2\alpha} \rho U \epsilon}{(\psi_E - \psi_I)^2} \frac{\partial U}{\partial \omega} \right]}{\partial U / \partial \omega} \right\}_B - \\ & - \frac{\psi_E - \psi_I}{(\partial U / \partial \omega)_B} \left(\frac{dU_B}{dx} + \frac{1}{\rho_B U_B} \frac{dP}{dx} \right) \end{aligned} \quad (\text{E.21})$$

In practice, dP/dx is taken to be zero for the free mixing flows considered in this study. A value of ω_B , say $\omega_B = 0.95$ is then selected and it is demanded that at $\omega = \omega_B$, $U_B = \tilde{U}_B = 0.99 U_E$. The term dU_B/dx is then evaluated by comparing the value of U_B obtained with that desired at the downstream station U_B , so that

$$\frac{dU_B}{dx} \approx \frac{\tilde{U}_B - U_B}{x_D - x_U} \quad (\text{E.22})$$

In practice the value $x_D - x_U$ is not yet known, so the value of $x_D - x_U$ from the preceding step must be used. If one boundary is free, the known value of the entrainment from the other boundary is used with (E.22) in (E.21) to obtain the free-boundary entrainment; if both boundaries are free the entrainment rate must be obtained at both boundaries simultaneously, perhaps taking $\omega_B = 0.005$ and $U_B = 0.99 U_I$ at the inner edge.

In the numerical procedure devised by Patankar [139], the coefficients a , b , and c are all defined at the upstream station, denoted by subscript U . For an arbitrary dependent variable ϕ , the term at the downstream station, subscript D , is evaluated using the expression

$$d_D = d_U + \left(\frac{\partial d}{\partial \phi} \right)_U (\phi_D - \phi_U) \quad (E.23)$$

Using the coefficients a_U , b_U , c_U , and d_U , the value of ϕ_D is then obtained by a simultaneous solution of the governing equations, written in the form of Equation (E.13) at the downstream station. This technique puts considerable emphasis on the proper definition of the terms a_U , b_U , c_U , and d_U , which in turn emphasizes the terms $r_I \dot{m}_I$, $r_E \dot{m}_E$, and $\psi_E - \psi_I$. The method of obtaining $r_I \dot{m}_I$ and $r_E \dot{m}_E$ has already been shown. Patankar obtains $\psi_E - \psi_I$ from Equations (E.9) and (E.10):

$$(\psi_E - \psi_I)_D \approx (r_I \dot{m}_I - r_E \dot{m}_E)_U (x_D - x_U) \quad (E.24)$$

where $r_I \dot{m}_I$ and $r_E \dot{m}_E$ are evaluated at the upstream station and $x_D - x_U$ is the x-step used to get to the upstream station from the one preceding it. The next step length is obtained by requiring that the step length be such that a given fraction of the total mass flow at the upstream step is entrained. Using the data at the former downstream station, which now becomes the upstream station for the next calculation, the entrainment terms $r_I \dot{m}_I$ and $r_E \dot{m}_E$ are defined, and the step length is taken as

$$x_D - x_U = \Delta x \approx C \cdot (\psi_E - \psi_I)_U / (r_I \dot{m}_I - r_E \dot{m}_E)_U \quad (E.25)$$

The effect of a very high predicted entrainment will be to decrease the step length, but there is no way in this formulation to correct the effect that an erroneous prediction of the entrainment has on the specification of $(\psi_E - \psi_I)_U$ for the next step. The effect that manifested itself in the course of this study was a steady deviation from the requirement, true for a free mixing flow, that the value of the momentum integral be a constant. Since deviations of from 30-40 percent were found, the situation was clearly unacceptable. However, for a free mixing flow, one can write for the momentum integral

$$\int_0^{\infty} \rho U (U - U_E) y^a dy = \text{constant}$$

or

$$\int_0^{\infty} (U - U_E) d\psi = \text{constant}$$

which becomes

$$(\psi_E - \psi_I) \int_0^1 (U - U_E) d\omega = \text{constant}$$

Thus, instead of Equation (E.24), the equation

$$(\psi_E - \psi_I)_D = \frac{\int_0^1 (U - U_E) d\omega_U}{\int_0^1 (U - U_E) d\omega_D} (\psi_E - \psi_I)_U \quad (\text{E.26})$$

was used in this study. This results in a definition of $(\psi_E - \psi_I)$ which is not directly dependent on the entrainment flow rates evaluated upstream, and which serves to keep the value of the momentum integral constant. Few calculations made with Equation (E.26) have been found to deviate more than 6 percent from the criterion that the momentum integral be a constant, and most have been considerably better. As important, the deviations oscillate slowly about zero rather than monotonically increasing, as they do when (E.24) is used.

The plan of the calculations is thus as follows: given a set of profiles of dependent values, ϕ , at the downstream station, a value of $(\Psi_E - \Psi_I)$ is calculated from Equation (E.26). The entrainment rates are calculated from Equation (E.21), and these define the constants a , b , and c in Equations (E.14) to (E.16), and the x -step length Δx from Equation (E.25), where C is commonly taken to be 0.05. The constants a , b , and c , and the value of d_D computed from the upstream profile are used to calculate the values of ϕ at the downstream station, and the process is repeated.

The Numerical Procedures

The details of the numerical procedures are given by Patankar [139]. However, his formulation of the difference equations is sufficiently different from other formulations to warrant a brief description. Consider the numerical grid shown on Figure E.1. The points $U-$, U , and $U+$ correspond to three values of ω , ω_{U-} , ω_U , and ω_{U+} ; the corresponding downstream points, which have the same values of ω are denoted by $D-$, D , and $D+$. It is assumed that between grid points the dependent variables ϕ vary linearly with ω , and that along the x -coordinate between x_U and x_D the value of ϕ is ϕ_U except at $x = x_D$, where it becomes, with a step change, ϕ_D . The values of ϕ at $x = x_U$ are all known, and the values of ϕ at $x = x_D$ are to be solved for simultaneously, using these values; the method is thus implicit. If a linear variation in ϕ from x_U to x_D is

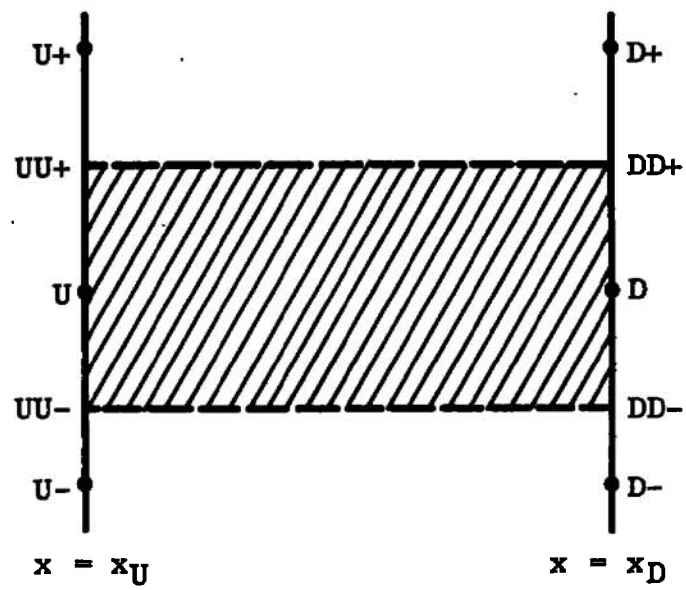


Figure E.1. Finite-difference grid.

assumed, the method would correspond to the Crank-Nicholson technique. To formulate the difference equation, the values of the derivatives are obtained as the mean values integrated over the control volume shown cross-hatched in Figure E.1. The points UU-, UU+, DD-, and DD+ are all located halfway between their respective data points on an x- ω grid. In keeping with this formulation of the difference equation as a "miniature integral equation," the fundamental derivatives are expressed as

$$\frac{\partial \phi}{\partial x} \approx \left(\frac{1}{x_D - x_U} \right) \left(\frac{1}{\omega_{DD+} - \omega_{DD-}} \right) \int_{x_U}^{x_D} \int_{\omega_{DD-}}^{\omega_{DD+}} \frac{\partial \phi}{\partial x} d\omega dx \quad (E.27)$$

$$\frac{\partial \phi}{\partial \omega} \approx \left(\frac{1}{\omega_{DD+} - \omega_{DD-}} \right) \int_{\omega_{DD-}}^{\omega_{DD+}} \frac{\partial \phi}{\partial \omega} d\omega \quad (E.28)$$

The integrals are evaluated using the assumed linear profiles between grid points; thus

$$\begin{aligned}
\int_{x_D}^{x_U} \int_{\omega_{DD-}}^{\omega_{DD+}} \frac{\partial \phi}{\partial x} d\omega dx &= \int_{\omega_{DD-}}^{\omega_{DD+}} \int_{x_U}^{x_D} \frac{\partial \phi}{\partial x} dx d\omega \\
&= \int_{\omega_{DD-}}^{\omega_{DD+}} (\phi_D - \phi_U) d\omega \\
&= \int_{\omega_{DD-}}^{\omega_D} (\phi_D - \phi_U) d\omega + \int_{\omega_D}^{\omega_{DD+}} (\phi_D - \phi_U) d\omega \\
&= \int_{\omega_{DD-}}^{\omega_D} f_1(\omega) d\omega + \int_{\omega_D}^{\omega_{DD+}} f_2(\omega) d\omega \quad (E.29)
\end{aligned}$$

where, in general

$$\omega_{DD-} \leq \omega \leq \omega_D \quad \phi = f_1(\omega) = \phi_{DD-} + k_1(\omega - \omega_{DD-}) \quad (E.30)$$

$$\omega_D \leq \omega \leq \omega_{DD+} \quad \phi = f_2(\omega) = \phi_D + k_2(\omega - \omega_D) \quad (E.31)$$

Substitution of Equations (E.30) and (E.31) into (E.29) leads to the expression

$$\begin{aligned}
\frac{\partial \phi}{\partial x} &\approx \frac{(\phi_D - \phi_U)(\omega_D - \omega_{DD-})}{4(x_D - x_U)(\omega_{D+} - \omega_{D-})} + \frac{3}{4} \frac{(\phi_D - \phi_U)}{(x_D - x_U)} + \\
&+ \frac{(\phi_{D+} - \phi_{U+})(\omega_{D+} - \omega_D)}{4(x_D - x_U)(\omega - \omega_{D-})} \quad (E.32)
\end{aligned}$$

For $\partial\phi/\partial\omega$, evaluation of (E.28) yields

$$\begin{aligned}\frac{\partial\phi}{\partial\omega} &\approx \left(\frac{1}{\omega_{DD+} - \omega_{DD-}} \int_{\omega_{DD-}}^{\omega_{DD+}} d\phi \right) \\ &= \frac{\phi_{DD+} - \phi_{DD-}}{\omega_{DD+} - \omega_{DD-}} \\ &= \frac{\frac{1}{2}(\phi_D + \phi_{D+}) - \frac{1}{2}(\phi_D + \phi_{D-})}{\frac{1}{2}(\omega_D + \omega_{D+}) - \frac{1}{2}(\omega_D + \omega_{D-})}\end{aligned}$$

so that

$$\frac{\partial\phi}{\partial\omega} \approx \frac{\phi_{D+} - \phi_{D-}}{\omega_{D+} - \omega_{D-}} \quad (\text{E.33})$$

Concluding Remarks

As described in the introduction to this section, the program written by Patankar [139] provides an economical means for the solution of an arbitrary number of parabolic partial differential equations. However, the version prepared by Patankar for the calculation of turbulent mixing problems is valid only for the Prandtl mixing length theory. The modifications described in this section have considerably broadened the range of applicability of this technique, and have improved its accuracy. The definitions of the entrainment and the parameter $\psi_E - \psi_I$ have been

generalized and it becomes a simple matter to include any arbitrary eddy viscosity model. The only model used in this study which requires an important further modification is the Schetz "unified theory" model [120, 121] which requires the calculation of the displacement thickness:

$$\begin{aligned} \int_0^{\infty} \left| 1 - \frac{\rho U}{\rho_E U_E} \right| y^{\alpha} dy &= \int_0^{\infty} \rho U y^{\alpha} \left| \frac{1}{\rho U} - \frac{1}{\rho_E U_E} \right| dy = \\ &= (\Psi_E - \Psi_I) \int_0^1 \left| \frac{1}{\rho U} - \frac{1}{\rho_E U_E} \right| d\omega \quad (E.34) \end{aligned}$$

All the other eddy viscosity models considered require no significant changes to the program.

APPENDIX F

INITIAL CONDITIONS FOR THE CALCULATIONS

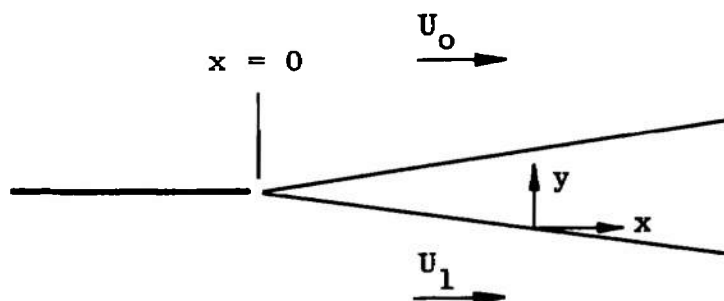
The initial conditions used to begin the finite-difference calculations made in this study are listed in the following sixteen tables. The data in the tables are largely self-explanatory; where they are not, nomenclature sketches are included.

TABLE F-1

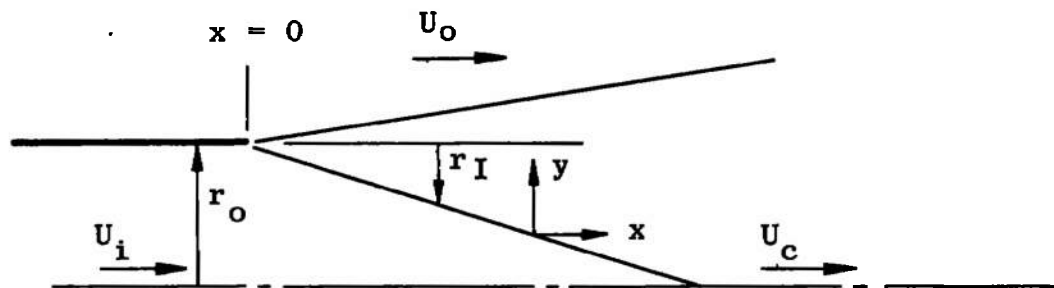
INITIAL PROFILES FOR INCOMPRESSIBLE JET-INTO-STILL AIR
DATA FROM BRADSHAW, et al (18)

$x/D = 2.0$ $r_o = 0.0833$ ft $r_I = 0.0333$ ft $U_j = 100$ ft/sec (nominal)			
y/r_o	U/U_j	k/U_j^2	
0	1.0	2.8	
0.01	0.998	3.1	
0.02	0.996	3.5	
0.03	0.994	3.8	
0.04	0.992	4.1	
0.05	0.990	4.5	
0.06	0.987	4.9	
0.07	0.984	5.3	
0.08	0.980	5.7	
0.09	0.976	6.1	
0.10	0.972	6.6	
0.11	0.968	7.1	
0.12	0.964	7.5	
0.13	0.960	8.1	
0.14	0.955	8.6	
0.15	0.950	9.3	
0.16	0.940	10.0	
0.17	0.930	10.6	
0.18	0.920	11.3	
0.20	0.910	12.8	
0.22	0.900	14.5	
0.24	0.880	16.7	
0.26	0.850	18.8	
0.30	0.780	22.4	
0.35	0.710	25.2	
0.40	0.630	27.2	
0.50	0.500	26.7	
0.60	0.360	22.4	
0.80	0.160	9.8	
1.0	0.060	2.3	
1.2	0.010	0	

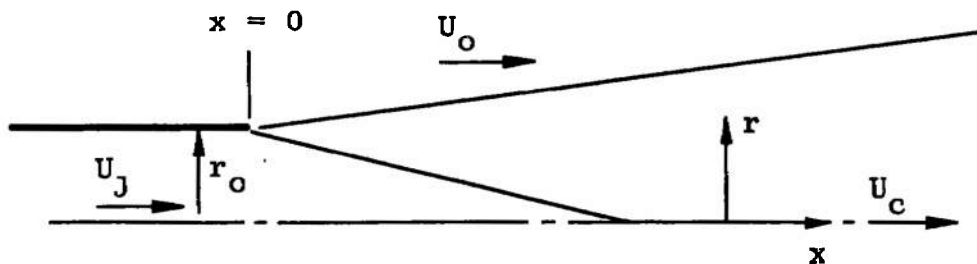
See Figure F-1 for Nomenclature



a. Two-Dimensional Flow



b. Axisymmetric Flow, First Regime



c. Axisymmetric Flow, Second Regime

Figure F-1 Nomenclature for Initial Profile Tabulation

TABLE F-2
INITIAL PROFILES FOR COMPRESSIBLE JET-INTO-STILL AIR
DATA FROM EGGERS (72)

**A. Profiles for Eddy
Viscosity Calculations**

**B. Profiles for Kinetic
Energy Calculations**

$x/D = 0$ $r_I = 0.0034$ ft		$r_o = 0.0419$ ft $U_j = 1765$ ft/sec		$x/D = 14.45$ $r_o = 0.0419$ ft $U_j = 1765$ ft/sec	
r/r_o	U/U_j	r/r_o	U/U_j	$\epsilon/U_j r_o$	
0	1.0	0	0.9077	1.00	
0.002	0.995	0.1225	0.9049	2.10	
0.004	0.991	0.2218	0.8956	1.75	
0.006	0.988	0.3078	0.8846	1.55	
0.008	0.983	0.3774	0.8787	1.35	
0.010	0.980	0.4800	0.8476	1.35	
0.012	0.977	0.5660	0.8200	1.39	
0.014	0.972	0.6489	0.7886	1.40	
0.016	0.968	0.6951	0.7715	1.45	
0.018	0.961	0.7414	0.7534	1.50	
0.020	0.956	0.8044	0.7336	1.57	
0.022	0.948	0.8606	0.7128	1.63	
0.024	0.938	0.9269	0.6898	1.70	
0.026	0.926	0.9964	0.6650	1.81	
0.028	0.917	1.0592	0.6432	1.90	
0.030	0.908	1.1255	0.6195	1.97	
0.032	0.895	1.2050	0.5928	2.05	
0.034	0.885	1.2975	0.5628	2.15	
0.036	0.875	1.3968	0.5278	2.21	
0.038	0.865	1.4632	0.5077	2.25	
0.042	0.844	1.5293	0.4860	2.25	
0.046	0.820	1.6022	0.4613	2.20	
0.050	0.790	1.7047	0.4337	2.12	
0.054	0.760	1.8139	0.4026	2.03	
0.058	0.732	1.8802	0.3851	1.93	
0.062	0.700	1.9597	0.3663	1.85	
0.066	0.675	2.0234	0.3456	1.80	
0.070	0.615	2.1186	0.3235	1.70	
0.074	0.565	2.2111	0.2975	1.60	
0.076	0.535	2.3303	0.2688	1.48	
0.078	0.370	2.4628	0.2355	1.35	
0.079	0.250	2.6316	0.1938	1.20	
0.080	0.070	2.8367	0.1385	1.05	
		3.0453	0.0988	0.90	
		3.2109	0.0698	0.80	
		3.2900	0.0570	0.70	
		3.3800	0.0450	0.65	
		3.4650	0.0325	0.60	
		3.5600	0.0200	0.50	
		3.6450	0.0100	0.48	
		3.7000	0.0040	0.40	

See Figure F-1 for Nomenclature

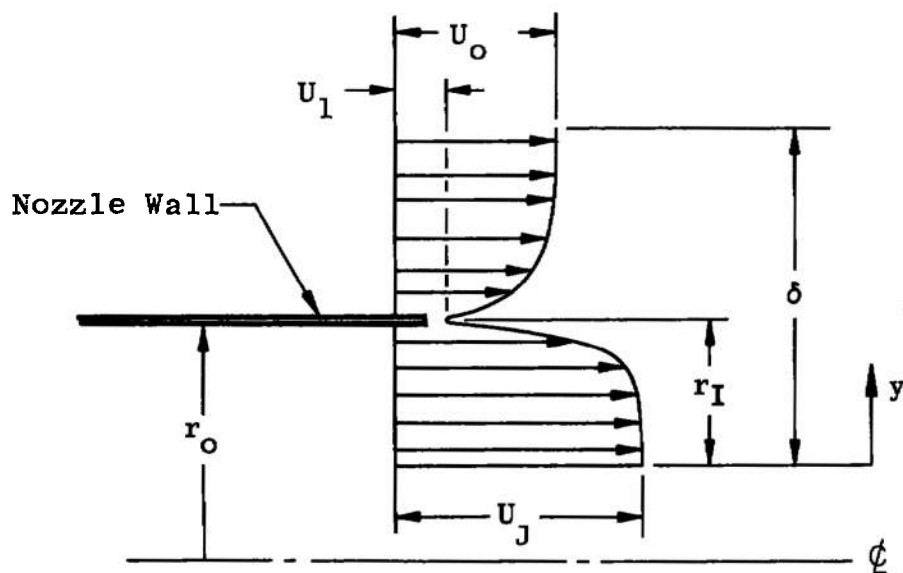


Figure F-2 Nomenclature for Coaxial Mixing,
Using Power-Law Profiles

TABLE F-3

INITIAL PROFILES FOR COAXIAL AIR-AIR MIXING
 DATA FROM FORSTALL (40)
 $U_o/U_j = 0.25$

a. Locally Dependent Models

Assumed profile: 1/7 power law. Thus Figure F-2

$$U = U_1 + (U_j - U_1) \left(\frac{r_I - y}{r_I} \right)^{1/7} \quad 0 \leq y \leq r_I \quad (F-1)$$

$$U = U_1 + (U_o - U_1) \left(\frac{y - r_I}{\delta - r_I} \right)^{1/7} \quad r_I \leq y \leq \delta \quad (F-2)$$

$$U_o = 30 \text{ ft/sec}$$

$$U_j = 120 \text{ ft/sec}$$

$$U_1 = 16.05 \text{ ft/sec}$$

$$r_o = 0.0417 \text{ ft}$$

$$r_I = 0.0113 \text{ ft}$$

$$\delta = 0.0258 \text{ ft}$$

$$T_t = \text{constant} = 540^\circ \text{R}$$

b. Kinetic Energy Calculation

As Table F-3a, with turbulent shear stress profile obtained from

$$\tau = 0.007 \rho \delta \left| U_j - U_o \right| \frac{\partial U}{\partial y} \quad (F-3)$$

TABLE F-4

INITIAL PROFILES FOR COAXIAL AIR-AIR MIXING
DATA FROM FORSTALL (40)

$$U_o/U_j = 0.20$$

a. Locally Dependent Models

Assumed Profile: Equations (F-1) and (F-2)

$$U_o = 45 \text{ ft/sec}$$

$$U_j = 225 \text{ ft/sec}$$

$$U_1 = 7.2 \text{ ft/sec}$$

$$r_o = 0.0104 \text{ ft}$$

$$r_I = 0.0010 \text{ ft}$$

$$\delta = 0.0072 \text{ ft}$$

$$T_t = \text{constant} = 540^\circ \text{R}$$

b. Kinetic Energy Calculation

Turbulent shear stress obtained from data
of Table F-4a using Equation (F-3)

TABLE F-5

INITIAL PROFILES FOR COAXIAL AIR-AIR MIXING
 DATA FROM PAULK (42)
 $U_o/U_j = 0.125$

a. Locally Dependent Models

Assumed Velocity Profile: Equations (F-1) and (F-2)

Assumed Total Temperature Profile:
 linear (see Figure F-2, page 607)

$$T_t = T_{t_j} + \left(T_{t_o} - T_{t_j} \right) (y/\delta) \quad (F-4)$$

$$U_o = 50.5 \text{ ft/sec}$$

$$U_j = 405 \text{ ft/sec}$$

$$U_l = 1.0 \text{ ft/sec}$$

$$r_o = 0.0208 \text{ ft}$$

$$r_l = 0.0013 \text{ ft}$$

$$\delta = 0.0030 \text{ ft}$$

$$T_{t_o} = 530.5 \text{ }^\circ\text{R}$$

$$T_{t_j} = 569.6 \text{ }^\circ\text{R}$$

TABLE F-5 Concluded

B. Kinetic Energy Calculation (Fig. F-1)

$x/D = 6.94$ $r_o = 0.0208 \text{ ft}$ $U_j = 405 \text{ ft/sec}$			
$r, \text{ ft}$ $\times 10^3$	$U, \text{ ft/sec}$	$\tau, \text{ lbf/ft}^2$	$H_t, \text{ Btu/lbm}$
0	367	0	137.1
1	366.5	0.3	137.06
2	366	0.55	137.0
3	364	0.76	136.91
4	362	1.0	136.83
5	359	1.23	136.70
6	355	1.45	136.55
7	351	1.67	136.40
8	346	1.90	136.20
9	340	2.13	136.02
10	334	2.34	135.85
11	329	2.55	135.60
12	322	2.73	135.40
13	315	2.85	135.20
14	308	2.98	135.0
15	300	3.08	134.75
16	293	3.17	134.5
17	285	3.24	134.3
18	277.5	3.30	134.0
19	270	3.33	133.8
20	263	3.37	133.55
21	254	3.39	133.25
22	249	3.40	133.0
23	239	3.37	132.8
24	230	3.34	132.5
26	215	3.23	132.05
28	200	3.08	131.6
30	186	2.96	131.1
32	173	2.80	130.65
36	147	2.50	129.8
40	123	2.22	129.0
44	103	1.92	128.25
48	85	1.65	127.55
52	72	1.33	126.95
56	63	1.04	126.6
60	59	0.77	126.4
64	56	0.54	126.3
68	55	0.31	126.2
72	54	0.13	126.13
76	53	0.05	126.1
78	52.5	0.01	126.1

TABLE F-6

INITIAL PROFILES FOR COAXIAL AIR-AIR MIXING
 DATA FROM PAULK (42)
 $U_o/U_j = 0.477$

a. Locally Dependent Models

Assumed Velocity Profile: Equations (F-1) and (F-2)

Assumed Total Temperature Profile: Equation (F-4)

$$U_o = 191 \text{ ft/sec}$$

$$U_j = 401 \text{ ft/sec}$$

$$U_l = 1.0 \text{ ft/sec}$$

$$r_o = 0.0208 \text{ ft}$$

$$r_I = 0.0013 \text{ ft}$$

$$\delta = 0.0030 \text{ ft}$$

$$T_{t_o} = 510.3 \text{ }^\circ\text{R}$$

$$T_{t_j} = 563.2 \text{ }^\circ\text{R}$$

Nomenclature Defined by Figure F-2, page 607

TABLE F-6 Concluded

B. Kinetic Energy Calculation (Fig. F-1c)

$X/D = 8.4$ $r_o = 0.0208 \text{ ft}$ $U_j = 401 \text{ ft/sec}$			
$r, \text{ ft}$ $\times 10^3$	$U, \text{ ft/sec}$	$\tau, \text{ lbf/ft}^2$	$H_t, \text{ Btu/lbm}$
0	381	0	136.3
1	380	0.03	136.2
2	380	0.08	136.2
3	379	0.13	136.1
4	378	0.19	136.0
5	376	0.25	135.8
6	374	0.33	135.6
7	372	0.41	135.4
8	369	0.51	135.2
9	366	0.63	134.9
10	363	0.76	134.5
11	358	0.87	134.2
12	353	0.99	133.9
13	345	1.08	133.5
14	337	1.16	132.8
15	329	1.23	132.3
16	321	1.29	131.9
17	313	1.33	131.5
18	306	1.37	130.6
19	297	1.44	130.0
20	290	1.40	129.3
21	283	1.40	128.6
22	276	1.38	127.9
23	269	1.33	127.4
24	263	1.28	126.8
25	257	1.22	126.1
26	251	1.16	125.4
27	245	1.09	124.8
28	240	1.02	124.2
29	234	0.93	123.6
30	227	0.83	123.1
31	223	0.74	122.5
32	218	0.64	122.3
33	213	0.58	122.0
34	209	0.49	121.8
35	204	0.42	121.6
36	200	0.35	121.5
37	197	0.29	121.4
38	195	0.15	121.3
39	191	0.05	121.2
40	188	0.01	121.0

TABLE F-7

INITIAL PROFILES FOR COAXIAL H_2 - AIR MIXING

DATA FROM CHRISS (90)

$$\rho_o U_o / \rho_j U_j = 1.61$$

a. Locally Dependent Models

Assumed Velocity Profile: Equations (F-1) and (F-2)

Assumed Total Temperature Profile: Equation (F-4)

Assumed Concentration Profile:

$$C = 1 - y/\delta \quad (F-5)$$

$$U_o = 673 \text{ ft/sec}$$

$$U_j = 3100 \text{ ft/sec}$$

$$U_l = 1.0 \text{ ft/sec}$$

$$r_o = 0.0208 \text{ ft}$$

$$r_I = 0.0013 \text{ ft}$$

$$\delta = 0.0030 \text{ ft}$$

$$T_{t_o} = 1050 \text{ }^\circ\text{R}$$

$$T_{t_j} = 550 \text{ }^\circ\text{R}$$

$$C_j = 1.0 \text{ (hydrogen jet)}$$

$$C_{p_j} = 3.42 \text{ Btu/lbm }^\circ\text{R}$$

$$C_{p_o} = 0.24 \text{ Btu/lbm }^\circ\text{R}$$

Nomenclature Defined by Figure F-2, page 607

TABLE F-7 Concluded

B: Kinetic Energy Calculations

$X/D = 4.59$		$r_o = 0.0208 \text{ ft}$	$U_j = 3100 \text{ ft/sec}$	
$r, \text{ ft}$ $\times 10^3$	$U, \text{ ft/sec}$	$\tau, \text{ lbf/ft}^2$	$H_t, \text{ Btu/lbm}$	C
0	3070	0	1900	0.948
1	3065	2.4	1890	0.942
2	3060	4.8	1885	0.940
3	3050	7.4	1870	0.932
4	3030	9.6	1850	0.924
5	3020	11.7	1830	0.905
6	2990	13.7	1800	0.890
7	2970	15.5	1775	0.865
8	2930	17.4	1755	0.842
9	2880	18.8	1700	0.820
10	2820	20.3	1650	0.800
11	2770	21.7	1590	0.765
12	2730	23.2	1510	0.730
13	2680	24.4	1470	0.700
14	2580	25.7	1400	0.665
15	2520	26.8	1330	0.630
16	2460	28.0	1270	0.600
17	2350	29.2	1230	0.565
18	2250	29.9	1170	0.530
19	2140	30.4	1110	0.490
20	2040	30.5	1050	0.452
21	1930	30.2	990	0.420
22	1840	29.7	930	0.390
23	1740	28.4	860	0.355
24	1640	27.3	800	0.325
25	1530	25.6	750	0.300
26	1470	24.8	700	0.272
27	1390	23.3	650	0.255
28	1290	21.6	602	0.230
29	1230	20.0	580	0.208
30	1150	18.2	550	0.192
31	1080	16.5	510	0.170
32	1040	14.7	490	0.155
33	970	12.8	460	0.140
34	930	11.6	439	0.128
35	870	10.3	410	0.110
37	800	7.8	380	0.084
39	730	5.7	350	0.065
41	690	3.8	310	0.045
43	650	2.3	290	0.038
45	640	1.0	270	0.018

TABLE F-8

INITIAL PROFILES FOR COAXIAL H_2 - AIR MIXING

DATA FROM CHRISS (90)

$$\rho_o U_o / \rho_j U_j = 1.785$$

a. Locally Dependent Models

Assumed Velocity Profile: Equations (F-1) and (F-2)

Assumed Total Temperature Profile: Equation (F-4)

Assumed Concentration Profile: Equation (F-5)

$$U_o = 526 \text{ ft/sec}$$

$$U_j = 3300 \text{ ft/sec}$$

$$U_l = 1.0 \text{ ft/sec}$$

$$r_o = 0.0208 \text{ ft}$$

$$r_I = 0.0013 \text{ ft}$$

$$\delta = 0.0030 \text{ ft}$$

$$T_{t_o} = 650 \text{ }^\circ\text{R}$$

$$T_{t_j} = 550 \text{ }^\circ\text{R}$$

$$C_j = 1 \text{ (hydrogen jet)}$$

$$C_{p_j} = 3.42 \text{ Btu/lbm }^\circ\text{R}$$

$$C_{p_o} = 0.24 \text{ Btu/lbm }^\circ\text{R}$$

Nomenclature Defined by Figure F-2, page 607

TABLE F-8 Concluded

B. Kinetic Energy Calculations

$X/D = 5.34$ $r_o = 0.0208 \text{ ft}$ $U_j = 3300 \text{ ft/sec}$				
$r, \text{ ft}$ $\times 10^3$	$U, \text{ ft/sec}$	$\tau, \text{ lbf/ft}^2$	$H_t, \text{ Btu/lbm}$	C
0	3050	0	1570	0.822
1	3050	2.8	1560	0.820
2	3040	5.5	1550	0.817
3	3010	7.5	1530	0.808
4	2980	9.8	1510	0.799
5	2940	12.2	1480	0.780
6	2870	14.3	1450	0.756
7	2840	16.3	1400	0.730
8	2780	18.0	1350	0.700
9	2720	19.8	1290	0.669
10	2630	21.7	1250	0.645
11	2540	23.4	1190	0.615
12	2440	25.5	1130	0.585
13	2370	26.5	1080	0.545
14	2260	27.8	1030	0.508
15	2170	28.9	970	0.470
16	2070	29.7	910	0.435
17	1940	30.2	850	0.395
18	1840	30.6	770	0.365
19	1740	30.8	710	0.330
20	1630	31.6	670	0.300
21	1540	30.0	610	0.275
22	1451	29.5	580	0.255
23	1380	28.7	530	0.231
24	1279	27.5	500	0.212
25	1220	26.3	465	0.190
26	1130	24.8	430	0.170
27	1070	23.3	400	0.153
28	1010	21.7	380	0.140
29	947	20.2	350	0.125
30	920	17.9	330	0.112
31	850	16.3	310	0.100
32	810	14.2	290	0.082
33	750	12.3	270	0.078
34	720	10.3	260	0.068
35	670	9.3	250	0.057
36	640	6.4	240	0.049
37	610	5.5	230	0.030
38	590	3.8	210	0.020
40	570	2.9	180	0.008
43	540	1.8	160	0.001

TABLE F-9

INITIAL PROFILES FOR COAXIAL H_2 - AIR MIXING

DATA FROM CHRISS (90).

$$\rho_o U_o / \rho_j U_j = 2.44$$

a. Locally Dependent Models

Assumed Velocity Profile: Equations (F-1) and (F-2)

Assumed Total Temperature Profile: Equation (F-4)

Assumed Concentration Profile: Equation (F-5)

$$U_o = 765 \text{ ft/sec}$$

$$U_j = 2450 \text{ ft/sec}$$

$$U_1 = 1.0 \text{ ft/sec}$$

$$r_o = 0.0208 \text{ ft}$$

$$r_i = 0.0013 \text{ ft}$$

$$\delta = 0.003 \text{ ft}$$

$$T_{to} = 1050 \text{ }^\circ\text{R}$$

$$T_{tj} = 550 \text{ }^\circ\text{R}$$

$$C_j = 1.0 \text{ (hydrogen jet)}$$

$$C_{pj} = 3.42 \text{ Btu/lbm }^\circ\text{R}$$

$$C_{po} = 0.24 \text{ Btu/lbm }^\circ\text{R}$$

Nomenclature Defined by Figure F-2, page 607

TABLE F-9 Concluded

B. Kinetic Energy Calculations

$x/D = 5.2$		$r_o = 0.0208 \text{ ft}$	$U_j = 2450 \text{ ft/sec}$	
$r, \text{ ft}$ $\times 10^3$	$U, \text{ ft/sec}$	$\tau, \text{ lbf/ft}^2$	$H_t, \text{ Btu/lbm}$	C
0	2010	0	1290	0.565
1	2008	1.5	1280	0.562
2	2000	3.2	1270	0.553
3	1980	4.5	1240	0.545
4	1960	5.8	1200	0.532
5	1940	7.3	1178	0.523
6	1910	8.2	1145	0.508
7	1880	9.4	1113	0.494
8	1860	10.3	1085	0.478
9	1820	11.4	1055	0.463
10	1790	12.3	1025	0.450
11	1760	13.0	990	0.425
12	1720	13.8	965	0.407
13	1680	14.6	932	0.390
14	1640	15.2	910	0.373
15	1595	15.6	875	0.355
16	1550	16.3	840	0.342
17	1510	16.5	810	0.325
18	1470	16.8	770	0.308
19	1410	16.8	740	0.295
20	1350	16.8	710	0.275
21	1330	16.5	685	0.263
22	1280	16.2	650	0.250
23	1230	15.7	625	0.232
24	1190	15.2	600	0.218
25	1130	14.8	570	0.203
26	1090	13.9	540	0.192
27	1050	13.3	520	0.173
28	1010	12.4	495	0.153
29	970	11.5	465	0.142
30	940	10.5	435	0.225
31	910	9.4	405	0.217
32	880	8.3	385	0.200
33	860	6.9	365	0.092
34	850	5.7	350	0.081
35	835	4.9	328	0.069
36	825	4.1	306	0.058
37	815	3.3	284	0.048
38	810	2.4	262	0.036
39	805	1.8	258	0.025
40	800	1.2	252	0.014

TABLE F-10

INITIAL PROFILES FOR COAXIAL H_2 - AIR MIXING

DATA FROM CHRISS (90)

$$\frac{\rho_o U_o}{\rho_j U_j} = 2.57$$

a. Locally Dependent Models

Assumed Velocity Profile: Equations (F-1) and (F-2)

Assumed Total Temperature Profile: Equation (F-4)

Assumed Concentration Profile: Equation (F-5)

$$U_o = 727.5 \text{ ft/sec}$$

$$U_j = 3300 \text{ ft/sec}$$

$$U_l = 1.0 \text{ ft/sec}$$

$$r_o = 0.0208 \text{ ft}$$

$$r_i = 0.0013 \text{ ft}$$

$$\delta = 0.0030 \text{ ft}$$

$$T_{t_o} = 650^\circ \text{R}$$

$$T_{t_j} = 550^\circ \text{R}$$

$$C_j = 1.0 \text{ (hydrogen jet)}$$

$$C_{p_j} = 3.42 \text{ Btu/lbm }^\circ \text{R}$$

$$C_{p_o} = 0.24 \text{ Btu/lbm }^\circ \text{R}$$

Nomenclature Defined by Figure F-2, page 607

TABLE F-10 Concluded

B. Kinetic Energy Calculations

$X/D = 4.55$		$r_o = 0.0208 \text{ ft}$	$U_j = 3300 \text{ ft/sec}$	
$r, \text{ ft}$ $\times 10^3$	$U, \text{ ft/sec}$	$\tau, \text{ lbf/ft}^2$	$H_t, \text{ Btu/lbm}$	C
0	2720	0	1185	0.615
1	2700	3.3	1175	0.615
2	2675	6.5	1155	0.605
3	2650	9.3	1135	0.590
4	2610	12.3	1105	0.575
5	2575	15.0	1080	0.555
6	2520	17.7	1050	0.535
7	2475	20.5	1020	0.520
8	2430	23.0	990	0.500
9	2380	25.0	950	0.475
10	2320	27.5	915	0.455
11	2270	30.0	875	0.425
12	2200	32.5	835	0.400
13	2130	33.3	800	0.375
14	2040	35.2	755	0.350
15	1950	36.3	710	0.325
16	1840	37.3	665	0.300
17	1740	38.0	620	0.280
18	1650	38.3	580	0.260
19	1560	38.0	535	0.243
20	1480	37.6	510	0.220
22	1350	36.0	450	0.190
24	1230	33.5	400	0.155
26	1140	30.5	340	0.125
28	1050	26.0	300	0.098
30	970	20.3	265	0.072
32	900	14.5	235	0.050
34	850	10.0	215	0.033
36	810	7.0	195	0.065
38	775	4.0	185	0.018
40	755	2.2	175	0.011
42	745	1.0	170	0.008
45	740	0	160	0.001

TABLE F-11

INITIAL PROFILES FOR COAXIAL H_2 - AIR MIXING

DATA FROM CHRISS (90)

$$\rho_o U_o / \rho_j U_j = 3.12$$

a. Locally Dependent Models

Assumed Velocity Profile: Equations (F-1) and (F-2)

Assumed Total Temperature Profile: Equation (F-4)

Assumed Concentration Profile: Equation (F-5)

$$U_o = 803 \text{ ft/sec}$$

$$U_j = 3050 \text{ ft/sec}$$

$$U_1 = 1.0 \text{ ft/sec}$$

$$r_o = 0.0208 \text{ ft}$$

$$r_I = 0.0013 \text{ ft}$$

$$\delta = 0.0030 \text{ ft}$$

$$T_{to} = 650^\circ R$$

$$T_{tj} = 550^\circ R$$

$$C_j = 1.0 \text{ (hydrogen jet)}$$

$$C_{pj} = 3.42 \text{ Btu/lbm } ^\circ R$$

$$C_{po} = 0.24 \text{ Btu/lbm } ^\circ R$$

Nomenclature Defined by Figure F-2, page 607

TABLE F-11 Concluded

B. Kinetic Energy Calculations

$X/D = 4.65$		$r_o = 0.0208 \text{ ft}$	$U_j = 3050 \text{ ft/sec}$	
$r, \text{ ft}$ $\times 10^3$	$U, \text{ ft/sec}$	$\tau, \text{ lbf/ft}^2$	$H_t, \text{ Btu/lbm}$	C
0	2300	0	940	0.460
1	2290	3.8	939	0.460
2	2280	7.0	925	0.460
3	2250	9.8	914	0.452
4	2200	12.4	890	0.443
5	2175	14.9	857	0.431
6	2130	17.3	830	0.415
7	2080	20.0	802	0.400
8	2040	21.8	770	0.384
9	1970	24.0	740	0.365
10	1930	25.7	710	0.347
11	1890	27.4	685	0.327
12	1830	28.8	655	0.303
13	1770	30.4	625	0.298
14	1720	31.7	600	0.209
15	1670	32.7	570	0.250
16	1605	33.4	545	0.235
17	1550	33.8	525	0.215
18	1490	34.0	495	0.205
19	1430	33.8	463	0.188
20	1380	33.5	443	0.172
21	1320	32.7	415	0.161
22	1270	31.7	395	0.142
23	1230	30.4	370	0.130
24	1170	29.7	345	0.120
25	1120	26.8	320	0.105
26	1110	24.7	300	0.098
27	1080	22.5	280	0.083
28	1030	20.0	265	0.075
29	985	17.3	250	0.065
30	930	13.8	235	0.058
31	910	11.6	220	0.047
32	890	9.5	210	0.041
33	870	8.2	200	0.037
34	850	6.7	190	0.030
35	830	5.4	180	0.025
36	820	4.4	179	0.015
37	818	3.6	171	0.011
38	810	2.7	167	0.007
39	805	2.3	160	0.005
40	802	1.6	152	0.003

TABLE F-12

INITIAL PROFILES FOR COAXIAL H_2 - AIR MIXING

DATA FROM CHRISS (90)

$$\rho_o U_o / \rho_j U_j = 3.33$$

a. Locally Dependent Models

Assumed Velocity Profile: Equations (F-1) and (F-2)

Assumed Total Temperature Profile: Equation (F-4)

Assumed Concentration Profile: Equation (F-5)

$$U_o = 780 \text{ ft/sec}$$

$$U_j = 1950 \text{ ft/sec}$$

$$U_l = 1.0 \text{ ft/sec}$$

$$r_o = 0.0208 \text{ ft}$$

$$r_I = 0.0013 \text{ ft}$$

$$\delta = 0.0030 \text{ ft}$$

$$T_{t_o} = 1050 \text{ }^\circ\text{R}$$

$$T_{t_j} = 550 \text{ }^\circ\text{R}$$

$$C_j = 1.0 \text{ (hydrogen jet)}$$

$$C_{p_j} = 3.42 \text{ Btu/lbm }^\circ\text{R}$$

$$C_{p_o} = 0.24 \text{ Btu/lbm }^\circ\text{R}$$

Nomenclature Defined by Figure F-2, page 607

TABLE F-12 Concluded

B. Kinetic Energy Calculations

$X/D = 4.82$		$r_o = 0.0208 \text{ ft}$	$U_j = 1950 \text{ ft/sec}$	
$r, \text{ ft}$ $\times 10^3$	$U, \text{ ft/sec}$	$\tau, \text{ lbf/ft}^2$	$H_t, \text{ Btu/lbm}$	C
0	1725	0	1380	0.635
1	1723	0.9	1370	0.633
2	1719	1.9	1365	0.627
3	1702	2.6	1350	0.615
4	1690	3.4	1330	0.602
5	1670	4.2	1300	0.588
6	1650	5.0	1270	0.570
7	1630	5.7	1250	0.555
8	1609	6.4	1200	0.530
9	1575	7.0	1150	0.515
10	1545	7.6	1100	0.495
11	1510	8.2	1060	0.470
12	1480	8.6	1000	0.450
13	1440	9.0	970	0.430
14	1400	9.4	930	0.405
15	1365	9.7	890	0.385
16	1320	10.0	850	0.360
17	1285	10.0	800	0.335
18	1245	10.0	780	0.315
19	1200	10.0	730	0.290
20	1170	10.0	690	0.262
21	1120	10.0	650	0.295
22	1085	9.5	630	0.225
23	1035	9.2	590	0.200
24	975	8.8	550	0.175
25	950	8.4	520	0.159
26	940	7.7	490	0.140
27	900	7.3	460	0.120
28	880	6.7	430	0.105
29	862	6.2	500	0.090
30	845	5.5	380	0.080
31	835	5.0	350	0.070
32	825	4.4	330	0.054
33	812	3.8	300	0.045
34	802	3.4	290	0.037
35	795	2.8	280	0.030
36	789	2.4	270	0.029
37	788	2.1	260	0.020
38	782	1.7	255	0.012
39	780	1.2	250	0.007
41	775	1.0	250	0.001

TABLE F-13

INITIAL PROFILES FOR COAXIAL H_2 - AIR MIXING

DATA FROM CHRISS (90)

$$\rho_o U_o / \rho_j U_j = 4.16$$

a. Locally Dependent Models

Assumed Velocity Profile: Equations (F-1) and (F-2)

Assumed Total Temperature Profile: Equation (F-4)

Assumed Concentration Profile: Equation (F-5)

$$U_o = 800 \text{ ft/sec}$$

$$U_j = 2400 \text{ ft/sec}$$

$$U_l = 1.0 \text{ ft/sec}$$

$$r_o = 0.0208 \text{ ft}$$

$$r_I = 0.0013 \text{ ft}$$

$$\delta = 0.0030 \text{ ft}$$

$$T_o = 650 \text{ }^\circ\text{R}$$

$$T_{tj} = 550 \text{ }^\circ\text{R}$$

$$C_j = 1.0 \text{ (hydrogen jet)}$$

$$C_{pj} = 3.42 \text{ Btu/lbm }^\circ\text{R}$$

$$C_{po} = 0.24 \text{ Btu/lbm }^\circ\text{R}$$

Nomenclature Defined by Figure F-2, page 607

TABLE F-13 Concluded

B. Kinetic Energy Calculations

$X/D = 3.98$		$r_o = 0.0208 \text{ ft}$		$U_j = 2400 \text{ ft/sec}$	
$r, \text{ ft}$ $\times 10^3$	$U, \text{ ft/sec}$	$\tau, \text{ lbf/ft}^2$	$H_t, \text{ Btu/lbm}$	C	
0	1945	0	1125	0.565	
1	1942	2.2	1124	0.565	
2	1938	4.3	1118	0.560	
3	1915	5.6	1090	0.548	
4	1870	7.2	1055	0.520	
5	1830	9.0	1020	0.500	
6	1775	10.6	975	0.475	
7	1735	12.0	935	0.448	
8	1675	13.3	880	0.418	
9	1625	14.5	830	0.375	
10	1565	15.6	775	0.336	
11	1500	16.5	710	0.305	
12	1450	17.5	660	0.280	
12.5	1420	17.9	635	0.270	
13	1385	18.2	610	0.255	
13.5	1365	18.4	585	0.240	
14	1330	18.6	570	0.230	
14.5	1300	18.7	550	0.220	
15	1265	18.8	520	0.205	
16	1210	19.0	480	0.190	
17	1175	18.7	450	0.175	
18	1130	18.2	420	0.155	
19	1082	17.6	395	0.145	
20	1050	16.8	365	0.130	
21	1000	15.6	330	0.115	
22	955	14.4	305	0.100	
23	920	13.0	265	0.090	
24	880	11.5	245	0.075	
25	852	9.9	230	0.065	
26	835	8.0	218	0.055	
27	820	6.5	202	0.045	
28	813	4.9	190	0.030	
29	808	3.0	184	0.020	
30	803	1.5	175	0.010	
31	800	0.3	170	0	

TABLE F-14

INITIAL PROFILES FOR COAXIAL H_2 - AIR MIXING

DATA FROM CHRISS (90)

$$\rho_o U_o / \rho_j U_j = 5.25$$

a. Locally Dependent Models

Assumed Velocity Profile: Equations (F-1) and (F-2)

Assumed Total Temperature Profile: Equation (F-4)

Assumed Concentration Profile: Equation (F-5)

$$U_o = 792 \text{ ft/sec}$$

$$U_j = 1900 \text{ ft/sec}$$

$$U_l = 1.0 \text{ ft/sec}$$

$$r_o = 0.0208 \text{ ft}$$

$$r_I = 0.0013 \text{ ft}$$

$$\delta = 0.0030 \text{ ft}$$

$$T_{t_o} = 650 \text{ }^\circ\text{R}$$

$$T_{t_j} = 550 \text{ }^\circ\text{R}$$

$$C_j = 1.0 \text{ (hydrogen jet)}$$

$$C_{p_j} = 3.42 \text{ Btu/lbm }^\circ\text{R}$$

$$C_{p_o} = 0.24 \text{ Btu/lbm }^\circ\text{R}$$

Nomenclature Defined by Figure F-2, page 607

TABLE F-14 Concluded

B. Kinetic Energy Calculations

$X/D = 4.87$		$r_o = 0.0208 \text{ ft}$		$U_j = 1900 \text{ ft/sec}$	
$r, \text{ ft}$ $\times 10^3$	$U, \text{ ft/sec}$	$\tau, \text{ lbf/ft}^2$	$H_t, \text{ Btu/lbm}$	C	
0	1260	0	605	0.265	
0.6	1257	1.0	600	0.264	
1.2	1253	2.0	594	0.263	
1.8	1250	2.7	589	0.260	
2.4	1244	3.5	584	0.258	
3.0	1237	4.0	575	0.254	
3.6	1228	4.5	568	0.251	
4.2	1223	4.9	563	0.246	
4.8	1212	5.4	552	0.240	
5.4	1204	6.0	543	0.235	
6.0	1194	6.5	536	0.230	
6.6	1183	6.9	523	0.225	
7.2	1172	7.3	512	0.220	
7.8	1162	7.5	500	0.210	
8.6	1143	7.7	483	0.200	
9.2	1129	8.1	473	0.194	
9.8	1113	8.3	462	0.186	
10.4	1099	8.4	450	0.178	
11.0	1082	8.6	437	0.173	
12.0	1057	8.8	417	0.159	
13.0	1033	9.0	397	0.148	
14.0	1004	9.1	379	0.134	
15.0	977	9.2	362	0.133	
16.0	952	9.2	345	0.112	
17.0	932	9.2	327	0.110	
18.0	910	9.1	310	0.090	
18.6	897	8.9	303	0.088	
19.2	886	8.8	288	0.082	
19.8	874	8.7	280	0.076	
20.4	862	8.5	268	0.074	
21.0	850	8.4	258	0.064	
21.6	838	8.3	248	0.058	
22.2	828	8.0	237	0.054	
22.8	813	7.8	232	0.049	
23.4	802	7.6	223	0.044	
24.0	794	7.3	214	0.040	
24.6	788	7.2	208	0.038	
25.2	782	6.9	202	0.035	
25.8	776	6.5	198	0.025	
26.4	774	6.1	193	0.021	
27.0	772	5.8	188	0.017	

TABLE F-15

INITIAL PROFILES FOR THE AXISYMMETRIC WAKE
DATA FROM CHEVRAY (58)

$r_o = 0.0832 \text{ ft}$	$U_o = 90 \text{ ft/sec}$	$\rho = 0.073 \text{ lbm/ft}^3$
$r, \text{ in.}$	$U, \text{ ft/sec}$	$\tau/\rho U_o^2 \times 10^4$
0	0	0
0.025	0.5	0.555
0.05	1.25	0.770
0.075	2.50	0.905
0.10	4.00	1.000
0.125	6.50	1.075
0.150	10.0	1.130
0.175	14.0	1.180
0.20	18.0	1.220
0.225	23.5	1.240
0.25	29.0	1.220
0.275	34.5	1.165
0.30	40.5	1.105
0.325	46.5	1.035
0.35	52.0	0.950
0.375	56.5	0.850
0.40	60.5	0.730
0.425	64.0	0.560
0.45	70.5	0.440
0.475	74.0	0.355
0.50	76.5	0.290
0.525	79.0	0.230
0.55	81.0	0.185
0.575	82.8	0.145
0.60	84.4	0.115
0.625	85.3	0.085
0.65	86.4	0.060
0.675	87.0	0.050
0.70	87.6	0.040
0.725	88.0	0.035
0.75	88.5	0.025
0.775	89.0	0.019
0.80	89.1	0.012
0.825	89.3	0.010
0.85	89.4	0.005
0.875	89.5	0.004
0.90	89.6	0.003
0.925	89.7	0.002
0.95	89.8	0.001
0.975	89.9	0
1.0	90.0	0

TABLE F-16

INITIAL PROFILES FOR THE TWO-DIMENSIONAL WAKE
DATA FROM CHEVRAY AND KOVASZNAY (52)

$U_o = 13.07 \text{ ft/sec}$ $\rho = 0.073 \text{ lbm/ft}^3$		
$y, \text{ ft}$ $\times 10^{-1}$	$U, \text{ ft/sec}$	$\tau/\rho U_o^2 \times 10^4$
0	0	0
0.095	7.123	24.00
0.190	8.234	22.40
0.285	8.979	20.95
0.381	9.567	19.30
0.476	10.170	17.50
0.571	10.530	15.55
0.667	10.940	13.50
0.761	11.305	11.80
0.856	11.620	10.15
0.952	11.890	8.05
0.105	12.130	7.25
0.114	12.350	6.00
0.124	12.530	4.85
0.133	12.680	3.85
0.143	12.810	2.95
0.152	12.930	2.15
0.162	13.000	1.50
0.171	13.040	0.95
0.181	13.060	0.45
0.190	13.070	0.15

DOCUMENT CONTROL DATA - R & D

(Security classification of title, body of abstract and indexing annotation must be entered when the overall report is classified)

1. ORIGINATING ACTIVITY (Corporate author) Arnold Engineering Development Center, ARO, Inc., Operating Contractor, Arnold Air Force Station, Tennessee 37389		2a. REPORT SECURITY CLASSIFICATION UNCLASSIFIED	
		2b. GROUP N/A	
3. REPORT TITLE FREE TURBULENT MIXING: A CRITICAL EVALUATION OF THEORY AND EXPERIMENT			
4. DESCRIPTIVE NOTES (Type of report and inclusive dates) June 1969 to June 1970--Final Report			
5. AUTHOR(S) (First name, middle initial, last name) Philip Thomas Harsha, ARO, Inc.			
6. REPORT DATE February 1971		7a. TOTAL NO. OF PAGES 668	7b. NO. OF REFS 139
8a. CONTRACT OR GRANT NO. F40600-71-C-0002		9a. ORIGINATOR'S REPORT NUMBER(S) AEDC-TR-71-36	
b. PROJECT NO. 9711			
c. Program Element 61102F		9b. OTHER REPORT NO(S) (Any other numbers that may be assigned this report) ARO-ETF-TR-70-273	
d.			
10. DISTRIBUTION STATEMENT This document has been approved for public release and sale; its distribution is unlimited.			
11. SUPPLEMENTARY NOTES Available in DDC		12. SPONSORING MILITARY ACTIVITY Arnold Engineering Development Center (XON), Air Force Systems Command, Arnold AF Station, Tennessee 37389	
13. ABSTRACT The problem of the analysis of free turbulent mixing is complex, and some empiricism is always necessary to obtain a solution. This has led to a proliferation of experiments and of semi-empirical models for the turbulent shear stress. All of these models will correlate experimental data well in some region of a particular flow, but not in others. None has been tested over as broad a range as is possible. The ultimate goal of this study is to confront each important model for the turbulent shear stress with as broad a range of experimental data as possible. From this confrontation come two sets of conclusions--one detailing those models presently suitable for engineering use, and the second establishing the models which show promise of becoming more generally applicable with further development.			

14	KEY WORDS	LINK A		LINK B		LINK C	
		ROLE	WT	ROLE	WT	ROLE	WT
	turbulent flow mixing evaluation experimental data viscosity shear stress turbulent diffusion						